

University of Warwick institutional repository: <http://go.warwick.ac.uk/wrap>

A Thesis Submitted for the Degree of PhD at the University of Warwick

<http://go.warwick.ac.uk/wrap/2783>

This thesis is made available online and is protected by original copyright.

Please scroll down to view the document itself.

Please refer to the repository record for this item for information to help you to cite it. Our policy information is available from the repository home page.

Modern Mass Spectrometry
Investigations into the Gas-
Phase Behaviour of Derivatised
Fullerenes and Amino Acid
supported Silver Clusters

Leanne Claire Nye

Thesis submission for the qualification of Doctor of Philosophy

University of Warwick

Chemistry Department

August 2009

Table of Contents

Table of Contents.....	i
Lists of Table and Figure Legends.....	v
List of Figure Legends.....	v
Chapter 1.....	v
Chapter 2.....	v
Chapter 3.....	vi
Chapter 4.....	vi
Chapter 5.....	vii
Chapter 6.....	viii
Chapter 7.....	x
Chapter 8.....	xii
List of Table Legends.....	xvi
Chapter 2.....	xvi
Chapter 3.....	xvi
Chapter 5.....	xvi
Chapter 7.....	xvi
Chapter 8.....	xvii
Acknowledgements.....	xix
Declaration.....	xxi
Publications.....	xxi
Abstract.....	xxii
Abbreviations Key.....	xxiii
Chapter 1: Introduction.....	1
Fullerenes.....	1
History.....	1
Derivatised Fullerenes.....	2
Techniques.....	7
MALDI (Matrix-Assisted Laser Desorption Ionisation).....	7
ESI (ElectroSpray Ionisation).....	22
References.....	35

Chapter 2: Experimental.....	41
Sample Preparation.....	41
Common Samples/Solvents	41
MALDI.....	42
Bruker Ultraflex II	42
ESI	44
esquire2000.....	44
Chapter 3: Study of Novel Fullerene Derivatives.....	47
Introduction.....	47
Open Cage Fullerenes.....	47
Experimental	53
Open-Cage Fullerenes:	53
Other Fullerene Derivatives	56
Results	64
MALDI Analysis	64
Cage re-healing by “harsh” MALDI and direct LDI	74
Appendix of related experimental efforts.....	79
Conclusion	85
References.....	86
Chapter 4: An Investigation into C₆₀H₂ using MALDI and LDI mass spectrometry.....	88
Introduction.....	88
Experimental	92
Results and Discussion	93
Conclusion	96
References.....	97
Chapter 5: Investigation into MALDI Matrices.....	99
Introduction.....	99
DCTB.....	99
Pencil Lead.....	102
Experimental	106
Results	109
Pencil as a matrix.....	109
Pencil lead performance check against LDI and (conventional) DCTB-MALDI.....	113

Sodium and Potassium adduct formation with different analytes using pencil lead ..	119
Conclusion	144
References.....	145
Chapter 6: Synthesis of C₆₀ Polycyclic Aromatic Hydrocarbon (PAH) Complexes and Analysis with MALDI and ESI.....	146
Introduction.....	146
Synthesis.....	147
Reaction Pathway.....	148
Previous Attempts at Mass Spectrometry	149
Cis-bis[60]fullerene adduct of 6,13-diphenylpentacene.....	154
Experimental	156
Synthesis of C ₆₀ Anthracene, C ₆₀ Tetracene and C ₆₀ Pentacene	156
MALDI Analysis.....	156
ESI Analysis	156
Results	158
Analysis of C ₆₀ PAH complexes by MALDI and ESI.....	158
Testing the Validity of MALDI as soft ionisation approach	167
Other Observations	170
Conclusion	183
References.....	184
Chapter 7: Formation of Amino Acid – Silver Complexes in ESI.....	186
Introduction.....	186
Amino Acids.....	186
Silver	187
ESI of Silver and Amino Acids	188
Experimental	192
Results	193
Tryptophan-Silver Cluster Production.....	193
MS/MS Experiments.....	207
Conclusion	217
References.....	219
Chapter 8: Use of Silver as a cationising agent, and ESI as an analytical tool for the analysis of pure fullerenes and unpolar fullerene derivatives.....	221

Introduction.....	221
The Kinetic Method	221
Silver bound dimers of Fullerenes and Fullerene Derivatives.....	222
ESI as an analytical tool for fullerenes	225
Experimental	226
Positive Ion Silver ESI-MS	226
Positive-ion and Negative-ion mode ESI-MS without Silver	228
Results	229
Positive-ion Mode Silver ESI with Fullerenes and Related Compounds.....	229
C ₆₀ , C ₆₀ PAH and Gold	274
Standard ESI of Fullerenes.....	277
Conclusion	284
References.....	286
Chapter 9: Conclusion.....	287
Appendix.....	291
Chapter 3 Additional Spectra	291
MALDI spectra	291
High Laser power MALDI spectra of OCF's.....	320
Chapter 5 Additional Spectra	328
Additional OCF on pencil spectra	328
Additional (Z)- and (E)-acenaphthalene (“Cis” and “Trans”) Spectra.....	332
Chapter 6 Additional Spectra	333
C ₆₀ P Spectra at elevated Laser Fluences	333
Chapter 7 Additional Spectra	337
Actual and Simulated Isotopic pattern of the different Clusters	337
MS/MS of Trp-Ag clusters, positive-ion mode ESI spectra.....	359
MS/MS of Silver clusters, positive-ion mode ESI spectra.....	377
MS(3) of the Trp-Ag clusters, positive-ion mode ESI spectra.....	379
MS(3) of Silver clusters, positive-ion mode ESI spectra	386
Chapter 8 Additional Spectra	389
Homo-dimer formation with silver, positive-ion mode ESI spectra.....	389

Lists of Table and Figure Legends

List of Figure Legends

Chapter 1		
1.1	Structure of C ₆₀	1
1.2	Structure of C ₇₀	2
1.3	Arrangements of pentagon and hexagons within a fullerene.....	4
1.4	Location of bridges on a fullerene surface.....	4
1.5	[4+2] reaction.....	5
1.6	[2+2] addition reaction.....	5
1.7	Structure of DCTB.....	10
1.8	Schematic of linear time-of-flight detector.....	13
1.9	Schematic of reflectron time-of-flight detection.....	14
1.10	Schematic of a discrete dynode.....	14
1.11	Schematic of a continuous dynode.....	15
1.12	Photo of the Kratos Kompact MALDI IV.....	17
1.13	Schematic of the Kratos Kompact MALDI IV.....	18
1.14	Photo of the inside of the Kratos Kompact MALDI IV.....	18
1.15	Photo of the Bruker Ultraflex II.....	19
1.16	Schematic of the Bruker Ultraflex II.....	19
1.17	Nascent drop at tip of electrospray needle.....	23
1.18	Schematic of an electrospray instrument.....	24
1.19	Schematic of a quadrupole mass analyser.....	27
1.20	Schematic of an ion trap.....	29
1.21	Photo of the Bruker esquire2000.....	31
1.22	Schematic of the Bruker esquire2000.....	32
Chapter 2		
2.1	Photo of the MALDI slide.....	44

Chapter 3

3.1	First OCF created.....	48
3.2	Nitrogen atom linkage replacing a C-C bond.....	52
3.3	Structure of $C_{60}N_2MEM_2$	52
3.4	Structure and negative-ion mode MALDI spectrum of 1.2.....	67
3.5	Structure and negative-ion mode MALDI spectrum of 1.5.....	68
3.6	Enhanced molecular ion region of 1.5, left, and simulated mass spectrum of 1.5, right.....	68
3.7	Structure and negative-ion mode spectrum of 2.3.....	69
3.8	Enhanced molecular ion region of 2.3, left, and simulated mass spectrum of 2.3, right.....	69
3.9	Structure and negative-ion mode MALDI spectrum of 2.12.....	70
3.10	Structure and negative-ion mode MALDI spectrum of 3.10.....	71
3.11	Enhanced molecular ion region of 3.10, left, and simulated mass spectrum of 3.10, right.....	71
3.12	Structure and negative-ion mode MALDI of 5.2.....	72
3.13	Enhanced molecular ion region of 5.2.....	72
3.14	Structure and negative-ion mode MALDI of 8.13.....	73
3.15	Enhanced molecular ion region of 8.13.....	73
3.16	Structure of 2.12.....	78
3.17	Low laser fluence, target: $C_{60}N_2MEM_2$	80
3.18	High laser fluence, target: $C_{60}N_2MEM_2$	81
3.19	Plot of $C_{60}/C_{59}N$ peak intensity ratio vs. laser power for experiments in both ion modes, with or without a matrix (DCTB) present.....	81
3.20	Plot of the ratio of N containing peaks: All C containing peaks vs. The number of atoms present in the fullerene fragment.....	82
3.21	CID spectra of C_{60} using either Helium or Argon gas as the collision gas.....	84

Chapter 4

4.1	Negative-ion mode FAB spectrum of $C_{60}H_2$ from the first reported
-----	---

	synthesis - science, 1993, 259, 1885.....	90
4.2	C ₆₀ H ₂ direct laser desorption/ionization mass spectra: a) negative-ion and b) positive-ion mode. Pure C ₆₀ for comparison: c) positive-ion LDI. C ₆₀ H ₂ MALDI mass spectra (DCTB as matrix, analyte-to-matrix ratio 1:50): d) negative-ion mode and e) positive-ion mode.....	93
4.3	C ₆₀ H ₂ ageing monitored by negative-ion DCTB MALDI: a) one day, b) three and c) fourteen days after synthesis. d) same a c) but positive-ion DCTB MALDI.....	95
Chapter 5		
5.1	Structure of "Isopropyl Mono".....	106
5.2	Structure of "Mono".....	106
5.3	Structure of "Bis".....	106
5.4	Structure of "Tris".....	106
5.5	Structures of 2.1 (above left) and 2.2 (above right).....	107
5.6	Structures of 2.3 (above left) and 2.4 (above right).....	107
5.7	Structures of 2.5 (above left) and 2.6 (above right).....	108
5.8	Positive-ion and negative-ion mode LDI and DCTB-MALDI of Isopropyl mono.....	109
5.9	Spectra of isopropyl mono on 6B and 8B pencil.....	110
5.10	Light and heavy application of pencil as a matrix for isopropyl mono...	111
5.11	Light and heavy application of pencil as a matrix for isopropyl mono...	112
5.12	LDI, 6B-, 8B-, DCTB-MALDI spectra of isopropyl mono at 8%.....	115
5.13	LDI, 6B-, 8B-, DCTB-MALDI spectra of isopropyl mono at 16%.....	116
5.14	LDI, 6B-, 8B-, DCTB-MALDI spectra of isopropyl mono at 20%.....	117
5.15	Positive and negative-ion mode LDI spectra of 6B and 8B pencil.....	118
5.16	Structure of 8.13.....	119
5.17	Positive and negative-ion mode LDI of 8.13 on 6B and 8B pencil.....	120
5.18	Positive and negative-ion mode LDI of 8.13 on 6B and 8B pencil.....	120
5.19	Positive-ion mode LIFT of the Na and K adducts of 8.13 on 6B and 8B pencil.....	122

5.20	Positive-ion mode LIFT of the Na and K adducts of 8.13 on 6B and 8B pencil.....	123
5.21	Fragmentation - [Crown+Na] ⁺ (m/z 287) and [Crown+K] ⁺ (m/z 303) during LIFT.....	124
5.22	Positive-ion mode LIFT of the Na and K adducts of 8.13 on 6B and 8B pencil.....	125
5.23	Mono, bis and tris on 6B and 8B pencil.....	127
5.24	Enhancement of the molecular regions of mono, bis, tris on 6B and 8B pencil.....	127
5.25	LIFT of molecular ions of 2.3 and 2.4 with DCTB-MALDI.....	131
5.26	Enhancement of fragment peaks from LIFT of molecular ions of 2.3 and 2.4.....	132
5.27	2.3 and 2.4 on 6B and 8B pencil.....	133
5.28	Enhancement of molecular ion region of 2.3 and 2.4 on 6B and 8B pencil.....	133
5.29	Positive-ion mode LIFT of Na and K adduct of 2.3 and 2.4.....	134
5.30	Positive-ion mode LIFT of Na and K adduct of 2.3 and 2.4 on 8B pencil.....	135
5.31	Positive-ion mode LIFT of the Na and K adducts of 2.1 and 2.2.....	137
5.32	2.1 and 2.2 on HB pencil.....	138
5.33	2.1 and 2.2 on HB pencil.....	138
5.34	2.5 and 2.6 with DCTB on Pencil.....	139
5.35	2.5 and 2.6 with DCTB on Pencil.....	139
5.36	Structure of "cis", left, and "trans", right.....	140
5.37	"Cis" and "trans" on 6B and 8B pencil.....	141
5.38	"Cis" and "trans" on 6B and 8B pencil.....	142
5.39	Positive-ion mode of the Na and K adducts of "cis".....	142
Chapter 6		
6.1	The structure of anthracene, C ₁₄ H ₁₀	146
6.2	The structure of tetracene (2,3-Benzanthracene), C ₁₈ H ₁₂	146

6.3	The structure of pentacene, $C_{22}H_{14}$	146
6.4	Mechanism of a Diels-Alder reaction.....	148
6.5	Left to right, the structures of C_{60} anthracene, C_{60} tetracene, C_{60} pentacene.....	149
6.6	C_{60} tagged with a crown ether.....	151
6.7	Spectrum from Detection of Methoxylated anions of Fullerenes by Electrospray-Ionization Mass-Spectrometry, Journal of the American Chemical Society, 1993, 115 (22), 10334-10337.....	152
6.8	Structure of cis-bis[60]fullerene adduct of 6,13-diphenylpentacene.....	154
6.9	Negative-ion mode MALDI spectra of $C_{60}A$, left, $C_{60}T$, centre, $C_{60}P$, right.....	158
6.10	Negative-ion mode MALDI spectra of $C_{60}A$, left, $C_{60}T$, centre and $C_{60}P$, right.....	158
6.11	Positive-ion mode MALDI spectra of $C_{60}A$, left, $C_{60}T$, centre and $C_{60}P$, right.....	159
6.12	Positive-ion mode MALDI spectra of $C_{60}A$, left, $C_{60}T$, centre and $C_{60}P$, right.....	160
6.13	Negative-ion mode ESI spectrum of $C_{60}A$	160
6.14	Negative-ion mode ESI spectrum of $C_{60}A$, demonstrating the $C_{60}+1 /$ $+31$ and $C_{60}A+1 / +31$ peaks.....	161
6.15	Isotopic patterns in the C_{60} region, left, and in the $C_{60}A$ region, right	162
6.16	Negative-ion mode ESI spectrum of $C_{60}T$	163
6.17	Negative-ion mode ESI spectrum of $C_{60}T$, showing the $C_{60}+1$ and $C_{60}T+1$ peaks.....	164
6.18	Isotopic patterns of C_{60} , left and $C_{60}T$, right.....	164
6.19	Negative-ion mode ESI spectrum of $C_{60}P$	165
6.20	Negative-ion mode ESI spectrum demonstrating the C_{60} and $C_{60}P$ peaks.....	166
6.21	Isotopic pattern of $C_{60}+1$, left and $C_{60}P+1$, right.....	166
6.22	Negative-ion mode MALDI of $C_{60}P$ at laser powers: 6%, left, and	

	11%, right.....	168
6.23	Negative-ion mode MALDI of purified C ₆₀ P at 6% laser.....	169
6.24	Negative-ion mode MALDI of C ₆₀ T.....	170
6.25	Negative-ion mode LIFT of C ₆₀ T and C ₆₀ T ₂	172
6.26	Positive and negative-ion mode LDI spectra with linear and reflectron detection of C ₆₀ A at elevated laser fluences.....	173
6.27	Positive and negative-ion mode LDI spectra with linear and reflectron detection of C ₆₀ A at elevated laser fluences.....	174
6.28	Positive and negative-ion mode LDI spectra with linear and reflectron detection of C ₆₀ T at elevated laser fluences.....	175
6.29	Positive and negative-ion mode LDI spectra with linear and reflectron detection of C ₆₀ T at elevated laser fluences.....	176
6.30	Positive and negative-ion mode LDI spectra with linear and reflectron detection of C ₆₀ and Anthracene at elevated laser fluences.....	177
6.31	Positive and negative-ion mode LDI spectra with linear and reflectron detection of C ₆₀ and Anthracene at elevated laser fluences.....	178
6.32	Positive and negative-ion mode LDI spectra with linear and reflectron detection of C ₆₀ and Tetracene at elevated laser fluences.....	180
6.33	Positive and negative-ion mode LDI spectra with linear and reflectron detection of C ₆₀ and Tetracene at elevated laser fluences.....	181
Chapter 7		
7.1	Basic structure of an Amino Acid.....	186
7.2	Structure of Tryptophan.....	187
7.3	Full positive-ion mode ESI spectrum of Tryptophan and AgTFA.....	193
7.4	Positive-ion mode ESI spectrum of Trp and AgTFA.....	196
7.5	Simulated isotopic pattern of [Trp ₂ Ag ₃ minus 2H] ⁺ , left, and Ag ₇ ⁺ , right.....	197
7.6	Positive-ion mode ESI spectrum of Trp and Ag.....	197
7.7	Simulated isotopic pattern of [Ag ₅ Trp ₃ minus 4H] ⁺ , left, and [Ag ₇ Trp ₂ minus 4H] ⁺ , right.....	198

7.8	Simulated isotopic pattern of $[\text{Ag}_9\text{Trp minus 2H}]^+$, left, and Ag_{11}^+ , right.....	198
7.9	Positive-ion mode ESI spectrum of Trp and AgTFA.....	199
7.10	Simulated isotopic pattern of $[\text{Ag}_{11}\text{Trp}_4 \text{ minus 8H}]^+$, left, and $[\text{Ag}_{13}\text{Trp}_3 \text{ minus 6H}]^+$, right.....	199
7.11	Positive-ion mode ESI spectrum of AgTFA and Trp at 100% compound stability.....	201
7.12	Positive-ion mode ESI spectrum of AgTFA.....	202
7.13	Actual (top) and simulated (bottom) isotopic pattern of Ag_3^+ , left, and Ag_9^+ , right.....	204
7.14	Actual (top) and simulated (bottom) isotopic pattern of Ag_{11}^+ , left, and Ag_{13}^+ , right.....	205
7.15	Actual (top) and simulated (bottom) isotopic pattern of Ag_{17}^+ , left and Ag_{20}^+ , right.....	205
7.16	Positive and negative-ion mode MALDI with linear and reflectron detection of AgTFA.....	206
7.17	Positive-ion mode MALDI of AgTFA with linear and reflectron detection.....	206
7.18	MS/MS of 1792.0, left, and 1794.0, right.....	207
7.19	MS/MS of Ag_3Trp_2 , MS^3 of Ag_3Trp , left. MS/MS Ag_6Trp , MS^3 Ag_4Trp , right.....	211
7.20	MS/MS of Ag_6Trp_3 , MS^3 of Ag_6Trp_2 , left. MS/MS Ag_9Trp_3 , MS^3 Ag_9Trp_2 , right.....	212
7.21	MS/MS $\text{Ag}_{11}\text{Trp}_2$, MS^3 of Ag_{11}Trp , left; MS/MS $\text{Ag}_{11}\text{Trp}_4$, MS^3 $\text{Ag}_{11}\text{Trp}_3$, right.....	212
7.22	Structure of tryptophan demonstrating the position of exchangeable hydrogen.....	213
7.23	Positive-ion mode MS/MS of Ag_7^+ , left, Ag_9^+ , right.....	214
7.24	Positive-ion mode MS/MS of Ag_{13}^+ , left, and Ag_{15}^+ , right.....	214
7.25	Positive-ion mode MS/MS of Ag_9^+ , followed by MS^3 of Ag_8^+	215

7.26	Positive-ion mode ESI of AgTFA and Tryptophan, m/z region 2150 – 2200.....	217
Chapter 8		
8.1	Structure of C ₆₀ derivatised with a phenathroline.....	223
8.2	Structures of “cis”, left and “trans”, right.....	226
8.3	Structure of C ₅₀ H ₂₀	226
8.4	Structures of C ₆₀ C ₈ H ₈ , left and cis-bis[60]fullerene adduct of 6,13-diphenylpentacene, right.....	227
8.5	Structure of Isopropyl Mono.....	228
8.6	Positive-ion mode ESI spectrum of C ₆₀ with AgTFA.....	229
8.7	Positive-ion mode MS/MS spectrum of m/z 1548.8.....	230
8.8	Positive-ion mode ESI spectrum of (C ₅₉ N) ₂ with AgTFA.....	231
8.9	Measured, top, and simulated, bottom, isotopic pattern of [(C ₅₉ N) ₂ Ag] ⁺	232
8.10	Positive-ion mode ESI mass spectrum of C ₂₄ H ₁₂ with AgTFA.....	232
8.11	Measured, top, and simulated, bottom, isotopic pattern of [(C ₂₄ H ₁₂) ₂ Ag] ⁺	233
8.12	Positive-ion mode ESI spectrum of [(C ₈₄) ₂ Ag] ⁺	234
8.13	The molecular ion peak of C ₈₄ in the positive-ion mode ESI spectrum..	234
8.14	Measured, top, and simulated, bottom, isotopic pattern of [(C ₈₄) ₂ Ag] ⁺ ..	235
8.15	Positive-ion mode MS/MS spectrum of m/z 2125.1.....	235
8.16	Positive-ion mode ESI spectrum of C ₆₀ , C ₇₀ and AgTFA.....	237
8.17	Positive-ion mode DCTB-MALDI spectra of fullerene combinations with AgTFA.....	238
8.18	Enhancement of the [Fullerene _A -Ag-Fullerene _B] ⁺ m/z region of the DCTB-MALDI spectra of fullerenes and AgTFA.....	239
8.19	Full positive-ion mode ESI spectrum of C ₂₀ H ₁₀ with AgTFA.....	240
8.20	Measured, top, and simulated isotopic pattern, bottom, of [(C ₂₀ H ₁₀) ₂ Ag] ⁺	241
8.21	MS/MS positive-ion mode ESI spectrum of [(C ₂₀ H ₁₀) ₂ Ag] ⁺	241
8.22	Positive-ion mode ESI spectrum of C ₂₄ H ₁₂ (coronene), C ₂₆ H ₁₂ and	

	AgTFA.....	242
8.23	Measured, top, and simulated, bottom, isotopic pattern of [C ₂₄ H ₁₂ AgC ₂₆ H ₁₂] ⁺	242
8.24	MS/MS of [C ₇₀ AgC ₅₉ N] ⁺ , left, MS/MS of [C ₇₀ AgC ₈₄] ⁺ , right.....	246
8.25	MS/MS of [C ₂₆ H ₁₂ AgC ₆₀] ⁺ , left and [C ₂₆ H ₁₂ AgC ₂₄ H ₁₂] ⁺ , right.....	247
8.26	Positive-ion mode ESI spectrum of C ₆₀ A with AgTFA.....	248
8.27	Measured, top, and simulated, bottom, isotopic pattern of [(C ₆₀ A)Ag(C ₆₀ A ₂)] ⁺	249
8.28	DCTB-MALDI of C ₆₀ PAH's with AgTFA.....	250
8.29	The m/z regions of [C ₆₀ PAH-Ag] ⁺ complexes.....	250
8.30	Positive-ion mode ESI spectrum of C ₆₀ C ₈ H ₈ and AgTFA.....	251
8.31	The measured, top, and simulated, bottom, isotope pattern of [(C ₆₀ C ₈ H ₈) ₂ Ag] ⁺	252
8.32	Positive-ion mode MALDI of C ₆₀ C ₈ H ₈ and AgTFA.....	252
8.33	Molecular ion region of [C ₆₀ C ₈ H ₈ Ag] ⁺	253
8.34	Positive-ion mode ESI spectrum of (C ₆₀) ₂ C ₂₂ H ₁₂ (C ₆ H ₅) ₂ and AgTFA....	253
8.35	Positive-ion mode DCTB-MALDI of (C ₆₀) ₂ C ₂₂ H ₁₂ (C ₆ H ₅) ₂ with AgTFA....	254
8.36	The isotopic pattern of C ₆₀ C ₂₂ H ₁₂ (C ₆ H ₅) ₂ Ag ⁺	255
8.37	Positive-ion mode MS/MS spectrum of m/z 1057.0.....	255
8.38	DCTB-MALDI spectra of the C ₆₀ PAH complexes with AgTFA.....	257
8.39	Positive-ion mode MS/MS spectrum of m/z 931.1.....	258
8.40	The m/z region 822 to 850 of the ESI spectrum of C ₆₀ C ₈ H ₈ and AgTFA.....	259
8.41	Positive-ion mode LIFT spectrum of m/z 933.....	260
8.42	m/z region 823 to 833 of the positive-ion mode LIFT spectrum of m/z 933.....	260
8.43	Positive-ion mode MS/MS spectrum of m/z 1979.1.....	261
8.44	Positive-ion mode LIFT spectrum of m/z 1259.....	262
8.45	Positive-ion mode MS/MS spectrum of m/z 1259.1.....	262
8.46	Positive-ion mode ESI spectrum of C ₆₀ , Anthracene and AgTFA.....	263

8.47	Positive-ion mode MALDI spectrum of C ₆₀ , Anthracene and AgTFA.....	264
8.48	Positive-ion mode MALDI of C ₆₀ , Anthracene and AgTFA.....	264
8.49	Positive-ion mode LIFT spectrum of m/z 1005.....	265
8.50	Positive-ion mode ESI spectrum of “cis”, enhanced molecular ion region on right.....	266
8.51	Positive-ion mode ESI spectrum of “trans”, enhanced molecular ion region on right.....	266
8.52	Positive-ion mode ESI spectrum of “cis” and AgTFA.....	267
8.53	Positive-ion mode of “cis” and AgTFA, MS/MS of m/z 413.0.....	268
8.54	Positive-ion mode ESI spectrum of “trans” and AgTFA.....	269
8.55	The isotopic pattern of the peak at m/z 717.1 from the ESI spectrum of “trans” and AgTFA.....	270
8.56	Positive-ion mode spectrum of “trans” and AgTFA, MS/MS of m/z 717.1.....	270
8.57	Structure of “cis”, left, and “trans”, right.....	271
8.58	LDI and MALDI spectra of “cis” and “trans” with AgTFA.....	272
8.59	Positive-ion mode LDI and MALDI of “cis” and “trans” with AgTFA.....	273
8.60	Positive-ion mode LDI of “trans” with AgTFA, m/z region 712 to 721....	273
8.61	Positive-ion mode LIFT of 411 for “cis” and “trans” with AgTFA, LDI and MALDI.....	274
8.62	Positive-ion mode ESI spectrum of C ₆₀ A with AuCl ₃	275
8.63	Positive-ion mode MS/MS spectrum of m/z 2121.9.....	276
8.64	Positive and negative-ion mode MALDI of C ₆₀ A with Au.....	276
8.65	Positive and negative-ion mode MALDI of C ₆₀ A and Au, m/z region 1088 to 1104.....	277
8.66	Positive-ion mode ESI spectrum of isopropyl mono with sodium acetate.....	278
8.67	Positive-ion mode ESI spectrum of isopropyl mono with sodium acetate.....	279
8.68	Isotopic pattern from the measured mass spectrum of m/z 929, left,	

	and m/z 1836, right.....	280
8.69	Positive-ion mode ESI spectrum of isopropyl mono and sodium, MS/MS of m/z 1836.2.....	280
8.70	Negative-ion mode ESI spectrum of C ₆₀ with sodium methoxide.....	281
8.71	Negative-ion mode ESI spectrum of C ₈₄ at 500% Compound Stability.	282
8.72	Negative-ion mode ESI spectrum of C ₈₄ at 100% Compound Stability.	283

List of Table Legends

Chapter 2

2.1	Information on the mostly used samples/solvents.....	41-42
2.2	Instrument parameters of the Bruker Ultraflex II (“normal” mass spectra).....	43
2.3	Instrument parameters for the LIFT methods (positive and negative ions) on the Bruker Ultraflex II.....	43
2.4	Laser parameters for the Bruker Ultraflex II.....	43
2.5	Parameters for the Bruker esquire2000.....	45
2.6	Variables on the Bruker esquire2000.....	45

Chapter 3

3.1	Structures of the OCFs.....	53-55
3.2	Structures of monoligated azafullerenes.....	56
3.3	Structures of the remaining fullerene derivatives.....	57-62
3.4	Results of DCTB-MALDI analysis of all samples in both ion modes.....	64-66
3.5	Results of increased laser fluence on the OCFs.....	74-75
3.6	Structures of OCFs with ring orifices containing less than 13 atoms.....	76
3.7	Structures of OCFs with ring orifices containing 16 members.....	77-78

Chapter 5

5.1	Results of using DCTB as a matrix for various compounds.....	102
5.2	LDI, 6B-, 8B- and DCTB-MALDI of Isopropyl Mono at different laser powers.....	114-115

Chapter 7

7.1	Full listing of the Trp-Ag clusters formed, with their associated hydrogen loss.....	194-196
7.2	Silver clusters produced in positive-ion mode ESI.....	203-204
7.3	Daughter ion analysis through MS/MS experiments of Ag-Trp clusters.....	208-209

7.4	Fragment peaks resulting from MS ³ experiments of Trp-Ag clusters.....	210
7.5	MS/MS experiments with Ag clusters: parent and daughter ions.....	213
7.6	MS ³ experiments with the pure Ag clusters.....	215
Chapter 8		
8.1	Final concentrations of samples initially dissolved in dichloromethane....	227
8.2	Final concentrations of samples initially dissolved in 1:1 toluene:dichloromethane.....	227
8.3	Identification of the peaks in the C ₆₀ and AgTFA positive-ion mode ESI spectrum.....	229-230
8.4	Identification of peaks in the MS/MS spectrum of 1548.8.....	230
8.5	Peaks from the MS/MS spectrum of m/z 2125.1.....	236
8.6	Formation and MS/MS spectra of the hetero-dimers of series 1.....	236
8.7	Peaks from the positive-ion mode ESI spectrum of C ₆₀ , C ₇₀ and AgTFA.....	237
8.8	Formation and MS/MS spectra of the hetero-dimers of series 2.....	239-240
8.9	m/z values of the hetero-dimers of series 1.....	243
8.10	m/z values of the hetero-dimers of series 2.....	243
8.11	Fragment intensities of series 1.....	244
8.12	Fragment intensities of series 2.....	244
8.13	Total fragment intensities of series 1.....	245
8.14	Total fragment intensities of series 2.....	245
8.15	Table of peaks for the ESI spectrum of C ₆₀ A with AgTFA.....	248-249
8.16	Peaks from the ESI spectrum of C ₆₀ C ₈ H ₈ and AgTFA.....	251
8.17	Peaks of the ESI spectrum of (C ₆₀) ₂ C ₂₂ H ₁₂ (C ₆ H ₅) ₂ and AgTFA.....	254

8.18	Intensities of the fragments resulting from MS/MS of $[C_{60}PAHAg]^+$ complexes.....	256
8.19	Intensities of C_{60} fragments and PAH fragments.....	256
8.20	Fragment intensities of LIFT experiments of $[C_{60}-Ag-PAH]^+$	257
8.21	Total intensities of C_{60} fragments and PAH fragments.....	258
8.22	Peaks in the positive-ion mode spectrum of “trans” and AGTFA, MS/MS of m/z 717.1.....	271
8.23	Peaks from the negative-ion mode ESI spectrum of C_{60} and Sodium Methoxide.....	281

Acknowledgements

There are many people I would like to thank for their help and support during the course of my research and the production of this thesis.

Initial thanks go to my supervisors for their support and providing the opportunity for this PhD: Professor Dr Thomas Drewello (now based at the Friedrich-Alexander-Universität Erlangen-Nürnberg, Germany, previously University of Warwick) for providing me with the opportunity to undertake such fascinating research both at home and abroad; also Dr Rob Deeth, who very kindly accepted the challenge of being my supervisor after Tom's departure, and supporting me through the final stages.

I would like to thank the EPSRC and the University of Warwick Chemistry Department for providing the funding.

I would like to thank the various students I have had the pleasure of working with: Deena Modeshia, James Hendicott, Raïssa Marques, Kym Wells, Christ Hart, Jing (Joan) Li, Toks Fowowe, and ManTo (Henry) Chan. I would also like to thank fellow group members and office companions for their discussions and friendship: Marie Anderson, Marc von Gernler, Dr Mark Barrow, Lewis Mark, Matthew Gill and Azhar Iqbal.

I would also like to thank other colleagues in the Chemistry department for their services and assistance during the course of the PhD: Dr Lijiang Song and John Bickerton (RIP) for technical support and training on various mass spectrometers; Professor Alison Rodger for provision of amino acids.

Without the assistance of our external collaborators, some of the research would not have been possible, so I am of course very grateful to the following people:

Professor Mike Orfanopoulos and Manolis Tzirakis from the University of Crete, Greece, for providing many interesting fullerene derivatives, including the open-cage fullerenes.

Professor Glen P. Miller from the University of New Hampshire, USA, for providing the purified C₆₀pentacene sample in addition to the C₆₀-PAH derivative.

Professor Lawrence T. Scott from Boston College, USA, for providing the fullerene precursors.

Professor Helena Grennberg at Uppsala University, Sweden, for providing the two stereoisomers "cis" and "trans".

I would also like to thank the friends I have made in the department for their friendship and support, in particular Angeliki Damianoglou and Rachel Athersmith.

Special thanks go to my family, my parents Sally and Stephen Nye and my brothers Andrew and Rob who have had to cope with me being an eternal student!

And finally, a special mention for my rabbits, the cats and friends from outside of the department, both at home and at Warwick.

Declaration

I hereby declare that this thesis represents original material and that to the best of my knowledge, it contains material not previously created nor published by a person other than myself, unless otherwise acknowledged in the text. The material presented in this thesis has also not been submitted for an award at an establishment other than the University of Warwick; the following thesis has been submitted solely to the University of Warwick, UK, for the degree of Doctor of Philosophy.

Leanne Claire Nye

Publications

“One-step Synthesis of Fullerene Hydride C₆₀H₂ via Hydrolysis of Acylated Fullerenes”

Manolis D. Tzirakis, Mariza N. Alberti, Leanne C. Nye, Thomas Drewello and Michael Orfanopoulos, *J. Org. Chem.*, **2009**, *74* (15), 5746–5749

Abstract

A variety of mass spectrometry experiments have been performed with the aim of further understanding of the ionisation processes involved and the gas-phase behaviour of various organic molecules within two ionisation techniques: Matrix-Assisted Laser Desorption Ionisation (MALDI) and Electrospray Ionisation (ESI).

The majority of the studied compounds were C_{60} derivatised in various ways, either with addition of a ligand, or by the creation of an orifice within the cage structure with heteroatoms – Open-Cage Fullerenes (OCFs).

The DCTB-MALDI investigations into the OCFs revealed a possible correlation between orifice size and the heteroatoms present in the orifice, to how the OCF behaved under elevated laser fluence.

An extended investigation into the smallest hydrofullerene, $C_{60}H_2$, established for the first time decomposition-free conditions for its analysis, so that its oxidation over time, which has been controversial in the literature, could be studied.

The use of pencil lead as a matrix was compared to the traditional matrix for fullerenes, DCTB. Pencil lead was found to be inferior as a matrix, however, proved an exceptionally easy way of creating sodium and potassium adducts, which was found to be useful in the differentiation of isomers of some of the OCFs.

The formation of polyaromatic hydrocarbons adducts to C_{60} were synthesized and analysed with both MALDI and ESI-MS. These complexes are notoriously labile, yet a larger $C_{60}PAH:C_{60}$ peak intensity ratio was achieved than had been previously reported.

The use of silver in ESI experiments was explored in depth. Initially, heterodimers of amino acids bound by silver (I) ions were created and fragmented in order to ascertain relative silver binding affinities, by use of the kinetic method. The same technique was applied to compounds that have been traditionally difficult to ionise with ESI-MS. These included pure fullerenes, fullerene derivatives, and various fullerene precursors. These compounds have been successfully arranged into order of their silver-ion affinities.

Abbreviations Key

^{13}C -NMR	Carbon-13 Nuclear Magnetic Resonance
^1H -NMR	Hydrogen-1 Nuclear Magnetic Resonance
APCI	Atmospheric Photo Chemical Ionisation
CID	Collision Induced Dissociation
DCTB	Trans-2-[3-(4-tert-Butylphenyl)-2-methyl-2-propenylidene]malononitrile
DFT	Density Functional Theory
EA	Electron Affinity
EI	Electron Impact
ESI	ElectroSpray Ionisation
FAB	Fast Atom Bombardment
IE	Ionisation Energy
IR	Infra Red spectroscopy
LDI	Laser Desorption Ionisation
MALDI	Matrix Assisted Laser Desorption Ionisation
MS	Mass Spectrometry
OCF	Open-cage fullerene/cage-open fullerene
P1/P2	Ground plate/Plate 2
PAH	Polycyclic Aromatic Hydrocarbon
PCIS	PreCursor Ion Selector
PIE	Pulsed Ion Extraction
PLMS	Post LIFT Metastable Suppressor
PSD	Post Source Decay
RF	Radio Frequency
TGA	Thermal Gravimetric Analysis
ToF	Time-of-Flight
UV-Vis	Ultraviolet-Visible Spectroscopy

Chapter 1: Introduction

Fullerenes

History

The search for cyanopolyynes, long carbon chains terminated at either end by a hydrogen and a nitrogen atom and which are believed to be responsible for interstellar bands, started in the late 1970's and resulted in the discovery of the fullerenes in September 1985¹⁻⁴. The fullerenes – the third allotrope of carbon – were first discovered in laser ablation experiments of graphite which were conducted at Rice University (Texas, USA) by H. W. Kroto, R. E. Smalley, J. R. Heath, S. C. O'Brien, and R. F. Curl¹. Prior to its physical discovery, different groups had speculated on the existence of C_{60} as far back as 1970^{2, 3}. Theoretical calculations on the stability of C_{60} had also been performed^{2, 5, 6}. Creation of the fullerenes had in fact occurred prior to the elucidation of the structures; in 1984 by a group at Exxon Research and Engineering Co⁷. However, the slight prominence of the signals for C_{60} and C_{70} could not be explained and no significance was attached to them.

In 1990, W. Kratschmer, D. Huffman, K. Fostiropoulos, and L. Lamb developed a method to produce macroscopic quantities of fullerenes (mainly C_{60}) which provided a broader community access to the new material⁸. Other synthetic methods have also been developed⁹.

The most stable and well known of the fullerenes is Buckminsterfullerene, C_{60} . Its stability is derived from its configuration¹⁰⁻¹². There are 1760 ways of arranging 60 atoms in a sphere, yet there is only one configuration with total symmetry, in which none of the pentagon structures are adjacent. This configuration has essentially the form of a football.

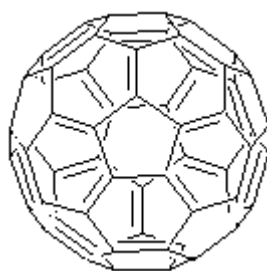


Figure 1.1: Structure of C_{60}

Proof of the structure came when a ^{13}C -NMR spectrum was obtained of C_{60} which consisted of a single line^{13, 14}. Further confirmation of the structures came from the ^{13}C -NMR spectrum of C_{70} , which consisted of five lines. Field Ion Microscopy has also confirmed the structures¹⁵.

Fullerene molecules are composed of adjoining pentagon and hexagon structures. As pentagons do not contain any double bonds, two adjacent pentagons will interrupt the alternation of double bonds in the sphere, which reduces stability (isolated pentagon rule).

C_{60} is the smallest fullerene which obeys the rule of no adjacent pentagons. Progressing through the fullerenes, by formally adding C_2 to C_{60} , C_{70} is the next fullerene with no adjacent pentagons, and is the second most stable fullerene after C_{60} . It has the following structure:



Figure 1.2: Structure of C_{70}

C_{70} also has a fairly symmetrical structure, as it is an elongated C_{60} with a band of hexagons around its centre. Technically the smallest fullerene is C_{20} , which would have a structure composed entirely of twelve adjoining pentagons. This is confirmed by Euler's Law which states that compounds of these configurations consist of twelve pentagon structures and any number of hexagon structures. The derived equation also explains why fullerenes always consist of an even number of carbon atoms – number of carbon atoms (vertices) = $20 + 2xH$ (number of hexagon structures present).

Derivatised Fullerenes

Fullerenes have been derivatised in a number of ways in order to create new uses for these compounds, for example for biological and medicinal purposes¹⁶⁻²⁴.

There exist four different ways to modify a fullerene:

- Endohedral doping – by placing an atom or molecule inside of the cage

- Substitutional doping – by substituting a carbon within the framework at the sphere by another atom
- Exohedral doping – by attaching a ligand to the outside of the cage
- Cage opening – by creating an orifice into the cage through implementation of heteroatoms

After the initial discovery, attempts were made to place atoms and small molecules inside the cage structure, for example lanthanum^{3, 25, 26}. This was part of the process which proved C₆₀ has a closed shell structure - a lanthanum atom was placed inside the cage by impregnating graphite with lanthanum and vaporising with a laser^{2, 25-27}. Additionally, a potassium atom was placed inside the cage to create K@C₆₀. The cage was “shrink-wrapped” by activation of K@C₆₀ with laser light, which removed C₂ units, essentially shrinking the cage²⁸. It was possible to shrink the cage down to C₄₄, creating K@C₄₄. The fact that further C₂ units could not be removed demonstrated that the structure was a closed shell and the potassium atom inside was restricting further shrinkage. When caesium was inserted into the cage, the laser activation only reduced the cage to Cs@C₄₈, due to the caesium atoms larger size.

Exohedral doping is achieved by a chemical reaction with the carbon atoms of the cage. For a better understanding of these reactions it is essential to look at the bonding situation of the carbon atoms of the cage and the reactions that can be conducted. The hybridisation of carbon in C₆₀ is mainly sp²; however, because of the curvature of the cage, there is some slight sp³ character present too. With increasing fullerene size, the curvature decreases and the fullerenes tend towards graphitic behaviour.

Initially it was believed that C₆₀ would behave as an aromatic compound, however, it actually behaves more like an alkene. This is because the pentagons present in the cage structure prevent delocalisation of the π electrons, and the double bonds remain localised on their specific sites. The double bonds prefer not to be part of a pentagon, because of the increase in strain. As a result, this leaves few sites which will react. There are three main possibilities for the location of two pentagons around a hexagon²⁹, as shown below:

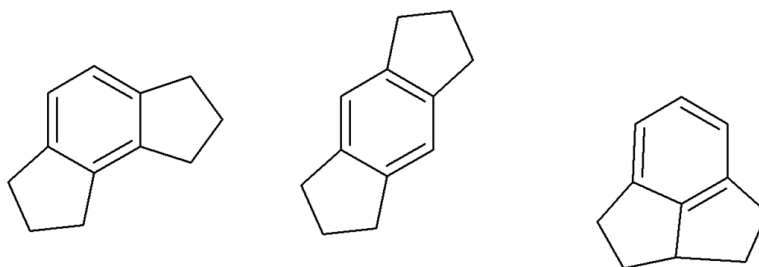


Figure 1.3: Arrangements of pentagon and hexagons, L-R: meta, para, ortho

The most likely configuration where reaction will occur is the meta arrangement on the left, as there are no double bonds located on either pentagon.

C_{60} is electrophilic and easily reduced, and as such can be employed as a mild oxidising agent. It undergoes a variety of reactions²⁹⁻³²:

- Halogenation
- Cycloaddition
- Polymerisation
- Hydrogenation
- Alkylation
- Amination

Bridging reactions occur either between two hexagons, or between a hexagon and a pentagon, as shown below:

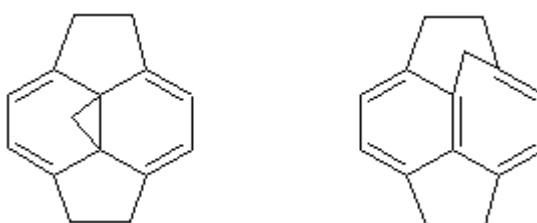


Figure 1.4: Location of bridges on a fullerene surface

One C_{60} derivative with a bridge has shown activity against HIV-1 protease^{21, 23}.

There are two types of cycloaddition reactions, [4+2] - a Diels-Alder reaction, and [2+2] reactions.

In [4+2] cycloaddition reactions, four electrons are provided by a conjugated diene and two from the C_{60} , reacting as the dienophile which underlies the slight electron deficient character of the double bond in C_{60} .

[4+2] reactions occur as follows:

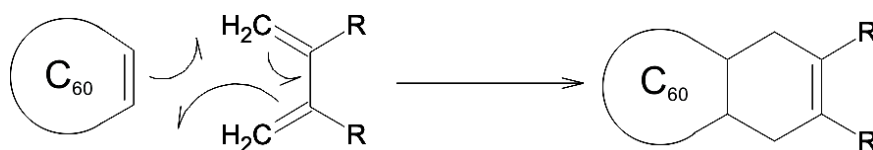


Figure 1.5: [4+2] reaction

[2+2] additions can occur, for example, between two fullerene cages, resulting in:



Figure 1.6: [2+2] addition reaction

Many of the compounds studied in the course of this thesis are fullerenes that have been derivatised by exohedral doping.

The majority of the derivatives have been studied in conjunction with Professor Michael Orfanopoulos at the University of Crete. His group is engaged with the synthesis of a variety of novel derivatised fullerenes, including some open cage fullerenes, for which a hole is created in the cage structure using strategically placed heteroatoms. These unique compounds could be of interest for transporting molecules.

Besides the method development for the structure elucidation of such compounds by mass spectrometry, experiments were performed with the aim to fragment and coalesce particular precursors in order to study the formation of larger entities, similar to research by Beck et al³³. Both these approaches involved predominantly laser desorption/ionisation methods, which differed in the extent of the excitation of the target materials.

Further experiments were concerned with the attachment of silver cations to adducts of polyaromatic hydrocarbons to C₆₀. In these experiments the character of the silver cation binding to such species was studied. The aim was here to use this interaction analytically and to provide thermochemical insight into preferred interactions of the silver cation and the respective π -electron system.

In addition to laser desorption methods, these experiments also used electrospray ionisation (ESI).

Finally, the use of silver ions in ESI led to a comprehensive investigation into the formation of silver clusters by electrospray ionisation. The role of an amino acid as aid for the formation of mixed and pure silver clusters was studied and insight into the structure of cluster ions was obtained in MS/MS experiments.

Techniques

Mass spectrometry has been used for the analysis of fullerenes since their discovery³⁴⁻⁴⁵, and is the analytical technique of choice for this research. Two different ionisation techniques have been used, and are presented below.

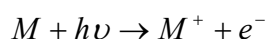
MALDI (Matrix-Assisted Laser Desorption Ionisation)

This mass spectrometry-based ionisation method, developed in the late 1980's⁴⁶⁻⁴⁸, is very useful for the analysis of large, thermally labile compounds, in particular for biomolecules such as peptides⁴⁹⁻⁵¹. Coupled with time-of-flight detection, this gentle ionisation method provides a valuable tool to detect very large masses⁵².

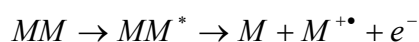
Ionisation Mechanism

The analyte is mixed with a matrix compound in solution or in the solid state. The matrix is a low mass compound chosen for having a λ_{max} close to the wavelength of the laser light and is in excess. The mixture is applied to a sample holder slide, allowed to dry if a solution, and inserted into the ion source of the instrument. Laser light is fired in pulses at the mixture. The excess matrix absorbs the laser light and is energised. This causes localised sublimation and ionisation of the matrix, which expands into the gas phase, carrying the analyte with it.

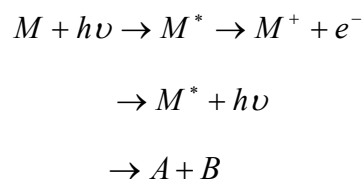
Photoionisation of the matrix can occur as follows^{53, 54}:



Often matrix ions are observed even though the ionisation energy of its molecular constituent exceeds the energy of one laser light photon. Up to two photons can hit one molecule to result in ionisation but the probability of a three photon accumulation to result in ionisation is so low that this process can be discounted as a responsible mechanism of ionisation. However, it is not uncommon to observe matrix ions even though three photons are needed for the removal of the electron. For such cases which exclude direct photoionisation alternative mechanisms are proposed. This includes for instance the reaction of two matrix molecules

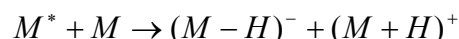


Ionisation can occur via an excited intermediate:



Where A and B can be neutral, or an ion pair.

The excited intermediates can also react with other matrix molecules:

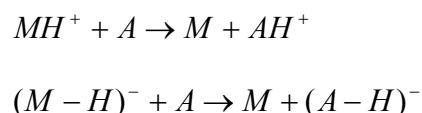


The actual ionisation or ion formation processes of the analyte can be very different in nature and are often the subject of intense research; especially as it is thought that ionisation of the analyte will occur at any time within the plume. The analyte may be ionised directly by the laser, however this will usually result in fragmentation, as is the case with direct LDI – Laser Desorption/Ionisation, where no matrix is present to protect the sample.

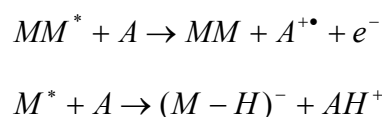
The various processes of analyte ion formation may include⁵⁵⁻⁵⁷:

- Gas-phase proton transfer
- Gas-phase cationisation
- Gas-phase photoionisation
- Excited state proton transfer
- Ion-molecule reactions
- Desorption of pre-formed ions.

The main process is widely believed to be gas-phase proton transfer. In this process the matrix will exchange a proton with the sample in the gas phase:



Other reactions involve an excited matrix molecule:



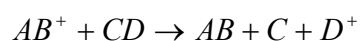
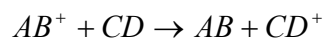
Ion-molecule reactions may involve⁵⁵⁻⁵⁷:

- Charge transfer/transfer of an electron
- Charge transfer followed by dissociation

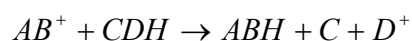
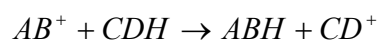
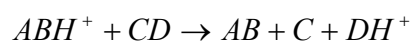
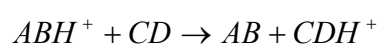
- Transfer of heavy ions
- Transfer of heavy ions followed by dissociation
- Transfer of neutral groups

In the following, examples of key reactions are given.

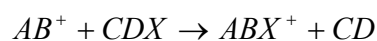
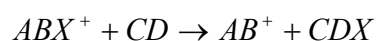
Charge transfer:



Transfer of heavy ions:



Transfer of neutral groups:



Where X is usually hydrogen, but can also be nitrogen, oxygen, iodine, chlorine, bromine and various alkyl groups.

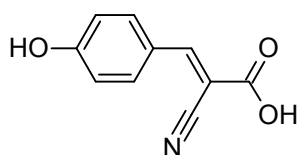
The mechanisms described above apply mainly to large biological molecules.

Ionisation Mechanism for Fullerenes

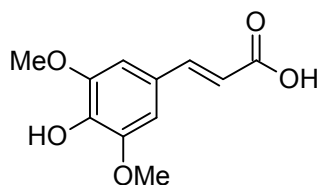
The MALDI ion formation mechanism for fullerene differs from the one for biological molecules and occurs through electron transfer reactions with matrix-derived ions.

Examples of fairly standard matrices for the MALDI analysis of common biological analytes include:

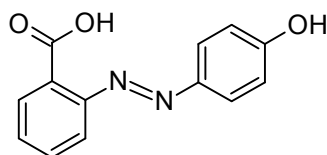
- α -HCCA: α -cyano-4-hydroxycinnamic acid:



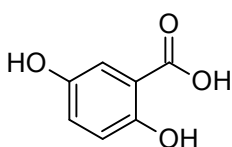
- Sinapinic acid: 3,5-dimethoxy-4-hydroxycinnamic acid:



- HABA 2-(4-Hydroxyphenylazo)benzoic acid



- DHB 2,5-Dihydroxybenzoic acid



All of these matrix materials contain loosely bound hydrogen atoms which can be easily converted into protons for the protonation of the analyte upon laser activation.

The best matrix for MALDI analysis of fullerenes has been found to be DCTB, 2-[(2 E)-3-(4-tert-butylphenyl)-2-methylprop-2-enylidene] malononitrile, which has a λ_{max} of 355nm.

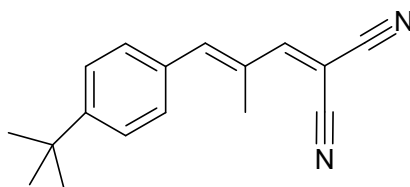


Figure 1.7: Structure of DCTB

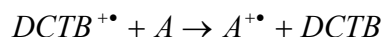
This compound was found to outperform the previous standard fullerene matrix – 9-nitroanthracene, in both positive and negative mode, producing more abundant analyte ions at lower laser powers, and leading to less fragmentation^{42, 58}.

Comparison with the protonating matrices shown above reveals the entire absence of acidic hydrogen atoms in DCTB. Protonation can be consequently discounted when DCTB is used as a matrix and in fact instead of producing the protonated (or diprotonated) analyte normally the molecular cation (or anion) of the analyte is observed.

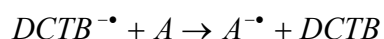
Fullerenes are ionised in both positive and negative-ion mode as the result of electron transfer reactions. It has been demonstrated that electron transfer with DCTB ions is

favourable with analytes within the thermochemical frame provided by the respective ionisation energies and electron affinities involved⁵⁹.

To form positive ions, DCTB and the analyte might react as below, assuming that the ionisation energy of DCTB is greater than the ionisation energy of the analyte:



To form negative ions, DCTB and the analyte may react as below, assuming that the electron affinity of the analyte exceeds the electron affinity of DCTB:



The adiabatic ionisation energy of DCTB has been calculated as 8.05 ± 0.05 eV, and the vertical ionisation energy has been measured by PE spectroscopy as 8.54 ± 0.05 eV. The electron affinity has been calculated to lie between 2.0 and 2.3 eV⁵⁹. This means that positive ion MALDI is achievable with any sample with an ionisation energy below 8.54 eV, and negative ion MALDI with samples with an electron affinity greater than 2.3 eV.

For standard fullerenes, such as C₆₀ and C₇₀, the ionisation energies are 7.58 eV and 7.61 eV, respectively, and their electron affinities are 2.65 ± 0.05 eV and 2.72 eV, respectively. These are within the required parameters to be ionised using DCTB as the matrix. For polycyclic aromatic hydrocarbons (PAHs) with ionisation energies below 8.54 eV and electron affinities below 2.3 eV it was shown that as expected only positively charged analyte ions could be formed from DCTB-MALDI while negative ions remained (also as expected) absent.

For fluorofullerenes, such as C₆₀F_{46/48}, the ionisation energy is 12 eV, and the electron affinity is 4.06 ± 0.25 eV³⁹. As expected from the thermochemistry these fluorofullerenes are not observed in positive-ion mode, only in negative-ion mode.

Matrix Suppression

One of the drawbacks in MALDI mass spectrometry is that matrix peaks will often obscure the lower mass range. Moreover, being the primary absorbant of the laser light the matrix may also entirely fragment. DCTB, for example, has a RMM (relative molecular mass) of 250.34 g mol⁻¹. This means that any peak below m/z 250 cannot be confidently assigned to the sample, as it is more likely to be caused by the matrix. DCTB dimers can also be

formed, resulting in peaks at m/z 500. DCTB can occasionally add to the sample, creating, for example, $[C_{60}DCTB]$ ions. However, under certain circumstances matrix peaks can be suppressed in the MALDI experiment.

Matrix suppression occurs only occasionally, leading to spectra that have little or no matrix peaks visible. This is advantageous for the analysis of small molecules as the matrix peaks could otherwise obscure the sample peaks⁶⁰⁻⁶². It is thought that matrix suppression occurs when all of the matrix ions donate their charge to the sample, leaving itself neutral and therefore undetected. The reaction of analyte and matrix ions is so efficient that matrix ions will not survive under these conditions. The optimum conditions for matrix suppression include the laser power being low, and close to the threshold for ion formation. It appears that the ratio of analyte:matrix also plays an important role, as does the preparation of the slide (mixed solution of matrix and analyte applied versus solutions applied separately in layers). DCTB is the first matrix that shows suppression in both ion modes. Normally, matrix suppression is observed either in positive or negative ion mode for a particular matrix. This is because earlier investigations covered only proton-transfer matrices⁶¹⁻⁶³, where it is difficult to both protonate and de-protonate the analytes, or vice versa. DCTB is an electron-transfer matrix, which can produce analyte ions in both ion modes. The thermochemical boundaries in which this is possible were outlined above. Matrix suppression in both ion modes simultaneously is observed for the first time in the course of our investigation with the DCTB matrix and in turn underlines the effectiveness of the charge transfer reactions with this matrix.

Time-of-Flight Mass Analyser and Detection

As the laser light is pulsed, analysis is usually with time-of-flight (ToF) mass spectrometry, which is ideally suited for the recording of pulsed ion beams. The ToF measurement needs a start and end point for the flight time of the ion of interest. The start is provided by the laser pulse, which generates the ion and the time measurement is stopped when the ion is registered by the detector. ToF spectra are recorded either in linear (using a linear flight tube) or in reflectron mode (using an ion mirror to improve the resolution).

In linear detection, ions are formed in the ion source, accelerated to a certain kinetic energy, and then allowed to drift in a field free region within a linear flight tube, until they hit a detector^{53, 54}.

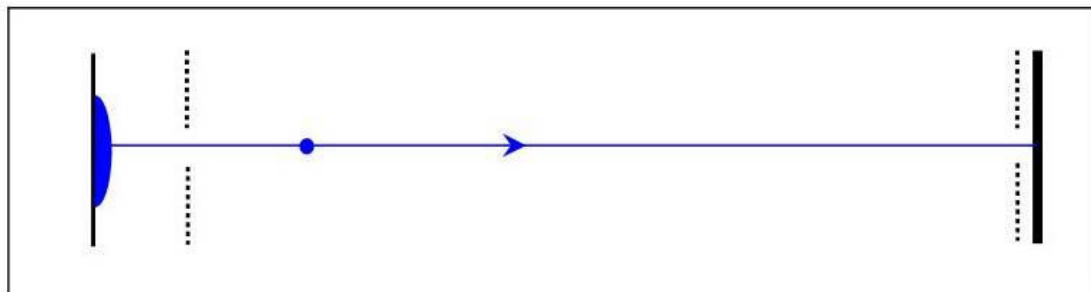


Figure 1.8: Schematic of linear time-of-flight detector

The masses of the ions are calculated as follows.

The ions are accelerated by a potential, V . They fly a distance, d , in a certain time, t , before reaching the detector, and are in possession of a kinetic energy given by:

$$E_{kin} = \frac{1}{2}mv^2$$

The total charge of the ion, q :

$$q = ze$$

$$E_{kin} = \frac{1}{2}mv^2 = qV = zeV$$

$$t = \frac{d}{v} \rightarrow v = \frac{d}{t}$$

V is the accelerating voltage, and z is the charge on the ion.

Rearranging results in the following equations:

$$\frac{1}{2}m\left(\frac{d}{t}\right)^2 = zeV$$

$$t^2 = \frac{m}{z}\left(\frac{d^2}{2Ve}\right)$$

So knowing the time taken for the ion to reach the detector, the length of the flight tube, and the accelerating voltage, the m/z value can be calculated.

Detection after reflectron analysis improves the resolution, as the reflectron compensates for the intrinsic velocity and therefore energy spread that accompanies the ionisation process

and which with a linear flight tube only would result in ions of the same mass being detected at different times, and therefore leading to a low resolution signal. The reflectron introduces an electric potential gradient, which deflects ions according to their kinetic energy^{53, 54}.

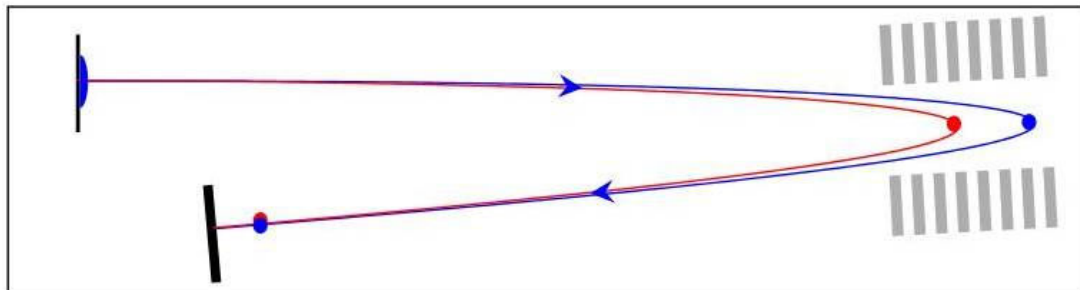


Figure 1.9: Schematic of reflectron time-of-flight detection

Ions of the same kinetic energy and m/z will penetrate the reflectron to the same extent and spend the same time in it. Ions of higher or lower kinetic energy but with the same m/z will spend longer or shorter times in the reflectron, so that kinetic energy differences are compensated for, and ions of the same m/z reach the detector after leaving the reflectron at the same time.

Linear time-of-flight analysers theoretically have no upper mass limit and frequently detect very large proteins and polymers of up to tens of thousands of Daltons. The reflectron, however, limits the upper mass to several ten thousands of Daltons, beyond which the ion becomes too large/heavy to be successfully transferred through the reflectron.

The detector commonly employed for time-of-flight mass analysers is the Ion-Electron Multiplier. There are two types of dynode, the discrete and the continuous dynode.

The discrete dynode is a series of 12 to 20 beryllium-copper dynodes, which are situated as shown below to allow detection by multiplication of the signal.

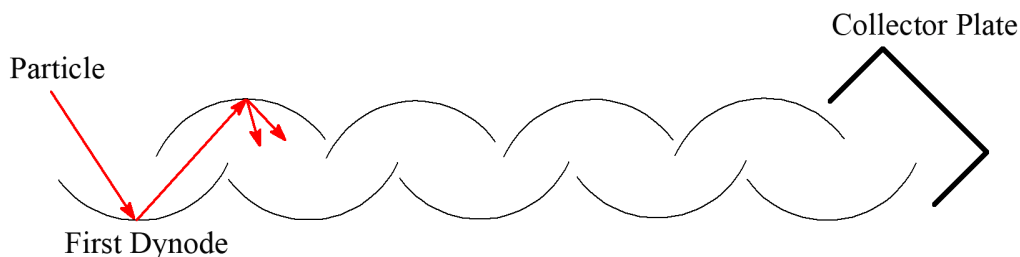


Figure 1.10: Schematic of a discrete dynode

The dynodes are connected electrically through a resistive network. A positive ion will hit the first dynode, which is held at a negative potential, with an energy of between 5,000 and 10,000 eV. This will release between 2 and 3 secondary electrons, which are accelerated by the applied voltage, and will hit the second dynode, releasing more secondary electrons, which hit the next detector, and so forth.

By the final electrode, as many as 10^6 electrons have been formed for each ion that hits the first dynode. These electrons then reach the collector plate, which converts the output current into a voltage that is suitable for recording.

For detection of negative ions, a conversion dynode is placed prior to the initial dynode. It is held at a positive potential, and when negative ions hit it, positive ions are released, and hit the first dynode, which releases electrons, and so forth.

Continuous dynodes, or Continuous Channel Multipliers, are curved tubes made from lead doped glass, which have a voltage applied to them.

They have good secondary emission properties and are electrically resistive. The voltage creates a uniform field along the length of the tube. An ion will hit the wall of the tube, which releases secondary electrons, which are accelerated by the field, and will then hit the wall further down, releasing further electrons, and so forth.

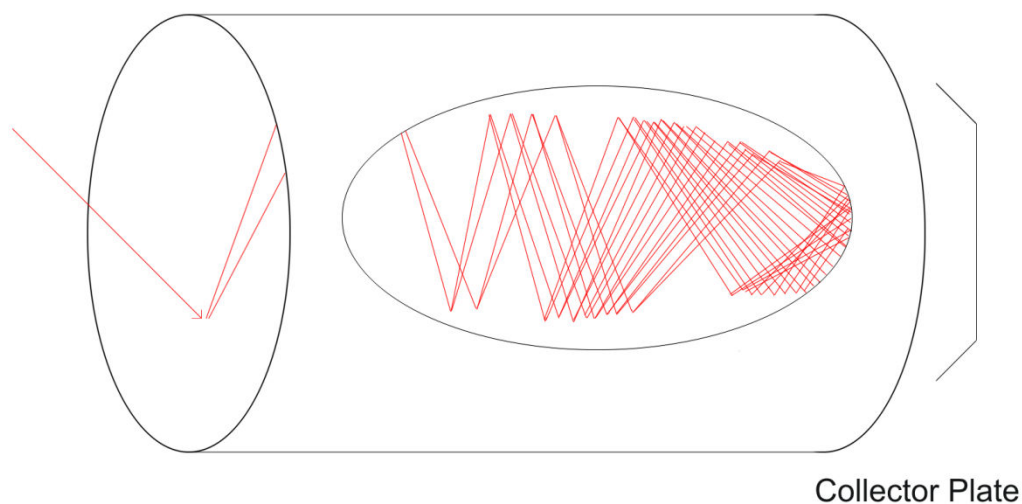


Figure 1.11: Schematic of a continuous dynode

At the end of the tube, the electrons will hit a collector plate, as is the case for the discrete dynodes.

Very often the tube will have an elongated bell-shaped end piece preceding it, through which the ions traverse initially. This design prevents slow moving and neutral ions from creating false signals.

Instrumentation

Two MALDI instruments were used in the course of this research; the Kratos (now Shimadzu) Kompact MALDI IV, purchased in the early 1990's; and the Bruker Ultraflex II, purchased in September 2006. Both instruments have several distinct differences. The most notable being the length of the flight tube, the types of reflectron and the types of laser used. As a consequence, the more recent MALDI instrument shows higher sensitivity at markedly enhanced resolving power (resolution).

The resolving power (resolution) is the ability to produce distinct signals for ions with a particular mass difference. It is, for example, desirable to be able to detect a molecular ion of interest isotopically resolved, so that in addition to the mass the resolved isotopic pattern may be used to elucidate the elemental composition. Another important issue which is concerned with the resolution is the ability to separate ions that have different elemental compositions but show the same nominal mass (so-called isotopic ions).

For two peaks to be considered resolved, the valley between the two peaks must be only 10% of the height of the less intense peak. (10% valley definition)

A numerical value for resolution can be calculated either by using two peaks, with masses of m and $m + \delta m$, where δm is the mass difference between the two as below:

$$R = \frac{m}{\delta m}$$

Or, the same equation can also be applied to individual peaks, where δm is the peak width at half the height. This is the FWHM – full width at half maximum method.

Kratos Kompact MALDI IV (now Shimadzu)

This instrument is a desktop mass spectrometer, built in the early 1990's. It is equipped with a Nitrogen laser with a wavelength of 337 nm and a pulse length of 3 ns.

The machine allows detection of ions in linear and reflectron mode. Unfortunately, the resolving power is very low, even in reflectron mode – i.e., well below 1000. With its continuous acceleration voltage it does not employ delayed extraction to further improve the resolution.

The machine allows the recording of daughter-ion spectra of selected precursor ions (tandem MS, MS/MS, post source decay) through the use of an ion gate for the selection of the parent ion and the use of a reflectron for the daughter ion analysis.

The reflectron is a curved-field ion mirror which allows the simultaneous detection of all daughter ions without the need of variation of the reflectron potentials. However, although the acquisition speed in MS/MS experiments is advantageous, the low resolution is problematic for the reliable assignment of even relatively low masses.



Figure 1.12: Photo of the Kratos Kompact MALDI IV

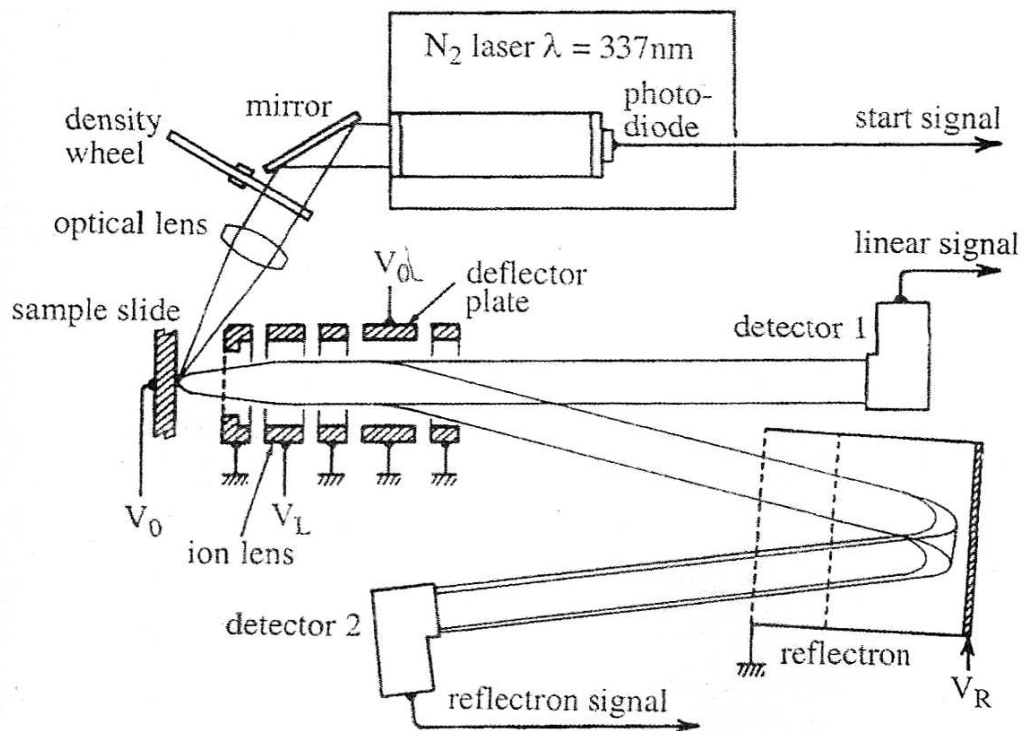


Figure 1.13: Schematic of the Kratos Kompact MALDI IV

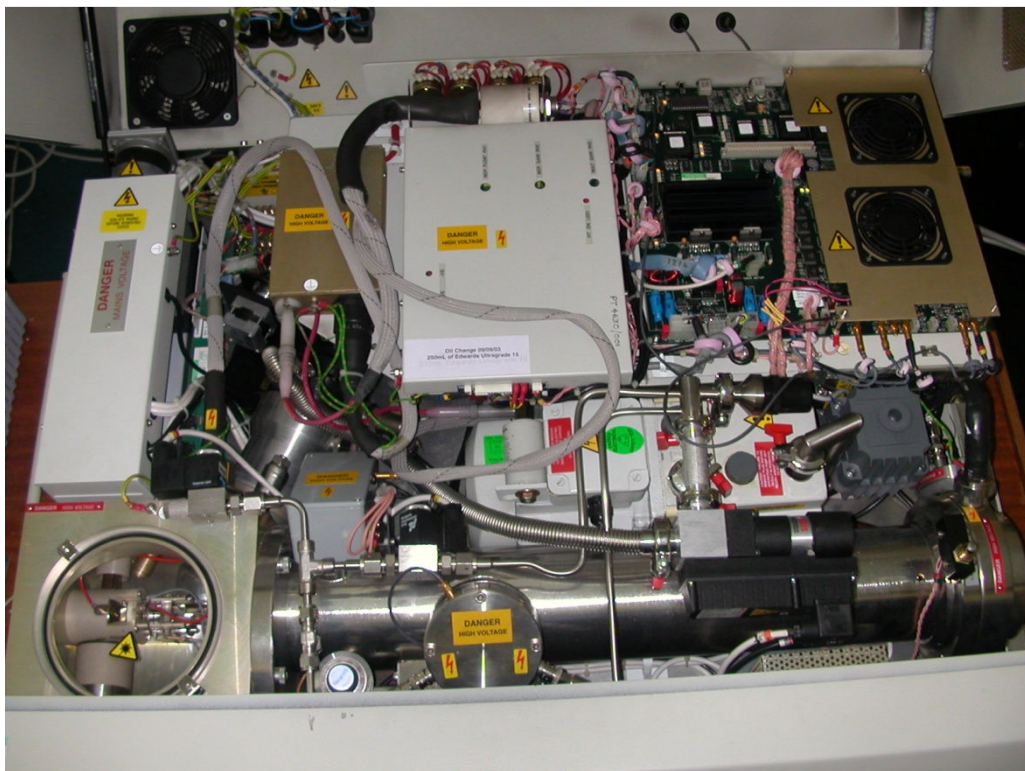


Figure 1.14: Photo of the inside of the Kratos Kompact MALDI IV

Bruker Ultraflex II

Purchased in September 2006, this MALDI mass spectrometer has an Nd:YAG laser with a wavelength of 355 nm and a variable repetition rate of between 1 and 200 Hz.

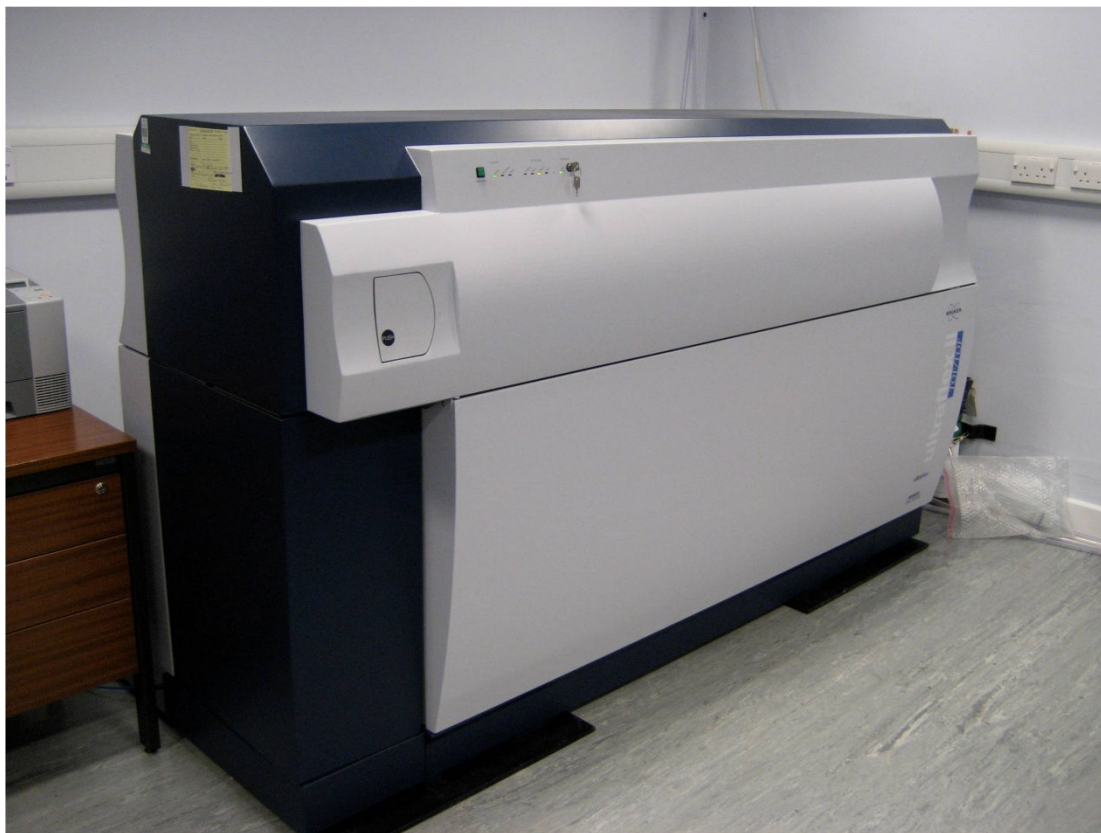


Figure 1.15: Photo of the Bruker Ultraflex II

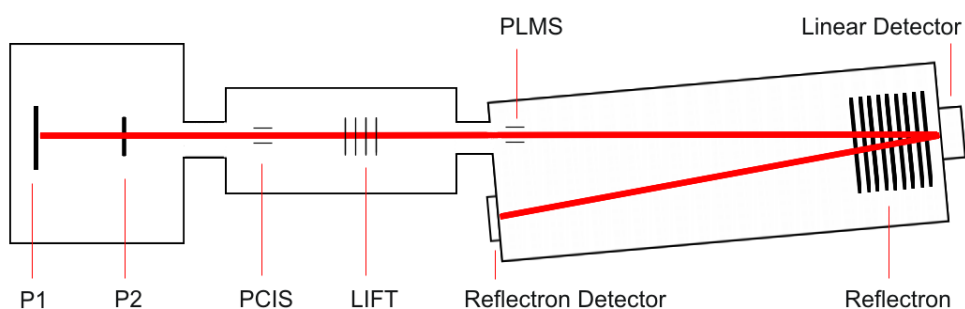


Figure 1.16: Schematic of the Bruker Ultraflex II

P1 – this is the target plate, on which the sample is located inside the source.

P2 – this is a plate which is used for delayed extraction to improve the resolution. When the laser is fired at the sample, the ions are produced with a range of kinetic energies. As a consequence ions of the same m/z will arrive at the detector at different times, resulting in

poorly resolved peaks. Therefore, continuous extraction, which introduces a static electrical field to accelerate the ions directly after formation, leads to mass spectra of only poor resolution. However, delayed extraction employs a voltage on P2, which initially prevents acceleration of the ions. These travel for a few nanoseconds without or with a very low potential difference towards P2. After passing through a hole in P2, the ions will experience the full acceleration voltage. The delay in extraction, that is, the field-free drift between P1 and P2 has the effect that the initial velocity spread is compensated so that the ions will reach the detector in a more simultaneous manner.

There are two methods of applying the voltage to P2 – Pulsed Ion Extraction, PIE, and Panoramic Extraction, PAN.

For PIE a sharp pulse is applied to P2. This allows very high resolution, however only over a small m/z range. For PAN the pulse is “softened” (applied over a longer time span, gradually increasing and decreasing) and a moderately high resolution is achieved over a larger m/z range.

P2 is followed by a ground plate for the acceleration, and a lens plate for the focus of the ions. Located after these plates is the collision cell. Here the ions are collided with an inert collision gas. In the present Collision-Induced Dissociation (CID) experiments argon was commonly used as the collision gas.

The following items will be discussed later in the context of tandem mass spectrometry experiments. These include:

PCIS –the Pre-Cursor Ion Selector,

LIFT optics – essential part of the daughter ion analysis.

PLMS – Post LIFT Metastable Suppressor, a final stage to LIFT.

The Reflectron is an ion mirror consisting of several plates and is held at a potential in order to “mirror” ions in reflectron mode.

Detectors – there are two, one for the linear mode, and one for the reflectron mode.

The linear detector consists of two single multi channel plate detectors. The reflectron detector consists of a single, tiltable multi channel plate cartridge.

A unique feature of the Bruker Ultraflex is LIFT⁶⁴, a method to achieve the fragmentation of one selected precursor ion and the detection of all resulting fragment ions without the time-consuming variation of the reflectron potentials.

The problem of any fragmentation ion detection in reflectron mode is that the kinetic energy of the parent ion is distributed between the neutral and the charged fragment. The fragment ion kinetic energy is therefore always lower than that of the parent ion and given by:

$$E_{kin, Daughter Ion} = \left(\frac{\ln MASS_{Daughter ion}}{\ln MASS_{Parent ion}} \right) E_{kin, Parent Ion}$$

The reflectron for the Bruker Ultraflex II, however, is only able to focus fragment ions if their kinetic energy is not lower than 70% of the 100% value of the parent ion. Daughter ions of lower E_{kin} will not reach the detector.

LIFT solves this problem by “lifting” the energies of the fragments, so that all the ions formed will have a kinetic energy within 70% of the parent ion.

The parent ions are initially accelerated with only 8kV, compared to between 22 and 25kV in the normal operating mode. This means the fragments can have energies of between 0 and 8kV. When they pass through the LIFT mechanism, the fragments and parent ions receive another 19kV, altering the range of energies from 0 – 8kV, to 19 – 27kV. 19kV is 70.37% of 27kV, so all the fragments can be focussed by the reflector and detected.

The actual LIFT process can be summarised in detail as follows:

The sample is ionised and accelerated by a voltage of 8kV. The ions traverse through to the PCIS. The PCIS is an ion gate, which is held at a positive potential which deflects the ions until the selected ion family passes through, at which point the voltage is switched off, and shortly afterwards, typically between 50 and 100 ns, the potential will switch back to the opposite polarity. The total change in polarity allows very short switching times, which results in a very precise mass selection. The PCIS consists of a series of deflection plates which are parallel to the flight path of the ions.

The ions then enter the LIFT ion optics. This part consists of four electrodes, whose voltages are altered in order to add the 19kV as the selected ion family passes through. As the ions pass the first electrode they experience a high voltage which is applied to the first and the second electrodes. As the family pass the second electrode they experience the potential on the third electrode which is reduced to start the second acceleration.

The lifted ions then pass through the PLMS. This is another ion gate which is timed to deflect the parent ion. It is held at ground whilst the fragments pass, yet raised to a high potential when the parent reaches it. It is important to deflect the parent ion, as the second acceleration may encourage further fragmentation – post LIFT decay. The resulting fragments from this second acceleration would have differing kinetic energies to the fragments of the same m/z , and this would decrease the resolution. LIFT experiments could be performed with or without the collision cell active. It has been shown that the collisions the ions undergo do not always affect the dissociation spectra (i.e. no extra fragmentations peaks observed)⁶⁵, and this was also seen in some of the experiments presented here.

ESI (ElectroSpray Ionisation)

Electrospray Ionisation is another soft ionisation method particularly suited to analyse large biomolecules and biomolecular complexes⁶⁶⁻⁶⁹. The link with biologically important molecules and complexes is particularly prominent as the analysis can be performed on aqueous solutions and as the softness of the process reduces fragmentation, without the need for a matrix. Therefore, ESI can be utilised to study non covalent interactions of complexes⁷⁰. Developed in the early 1980's⁷¹⁻⁷⁷, prompted by research in the late 1960's^{78, 79}, it involves the direct injection of a solution at atmospheric pressure through a charged needle.

Ionisation Mechanism

The sample is dissolved in a volatile solvent, and this solution is slowly pumped through a stainless steel capillary. A typical flow is in the range of several μl per minute. This capillary is held at a potential of around 3-4 kV, resulting in a spray of highly charged droplets.

There is a counter electrode, held at ground potential and positioned 1 to 3 cm away from the exit of the capillary. It is also possible to leave the capillary at ground potential and put a potential onto the counter electrode. The net effect is the same. Both types of sources are commercially available and a particular preference is mainly determined by patent regulations. The counter electrode has a hole in its centre so that ions can traverse further into the mass spectrometer.

As the voltage increases, the shape of the nascent drop at the very tip of the capillary will change. This is due to the repulsion between the ions overcoming the surface tension. The sphere will elongate and eventually expand into the Taylor cone, (as shown in the figure below on the far right) breaking into a mist of highly charged droplets which are at most 10 μ m in diameter.

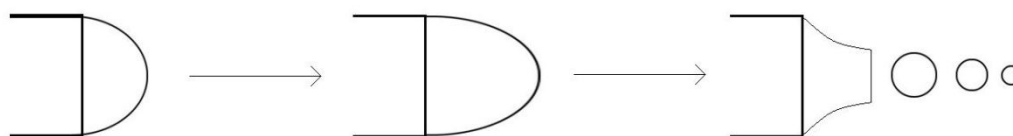


Figure 1.17: Nascent drop at tip of electro spray needle

These droplets carry multiple charges. The droplets shrink and decay, first through solvent evaporation, which is aided by a stream of nitrogen gas at 300°C, and also by charge repulsion as the coulombic forces come close to the cohesion forces (Rayleigh equation⁸⁰). This decay process produces smaller and smaller drops, until finally the electric field on the surface of the drop becomes large enough that ions desorb from the surface - the Ion Evaporation (Desorption) Model⁸¹⁻⁸³. Alternatively, the Charged Residue Model involves coulomb explosions of the droplets when their charge density becomes too high to be retained by the droplet^{53, 54, 84, 85}. Both models predict basically the same ions as the result of the spray process, and some research suggests both models apply^{86, 87}.

Most large molecules, generally with masses above 1000Da, will become multiply charged, i.e. through the attachment of many protons as the charge carriers. One benefit of the multiple protonation process is the reduction of the m/z value into a mass range that can be accessed by even less sophisticated mass spectrometers.

Finally ions travel through a small hole in the counter electrode into a pre vacuum section. As the ionisation occurs at atmospheric pressure, and the mass analyser is held at a high vacuum, the ions must traverse regions of decreasing pressure. A stainless steel skimmer removes any last solvent molecules prior to mass analysis.

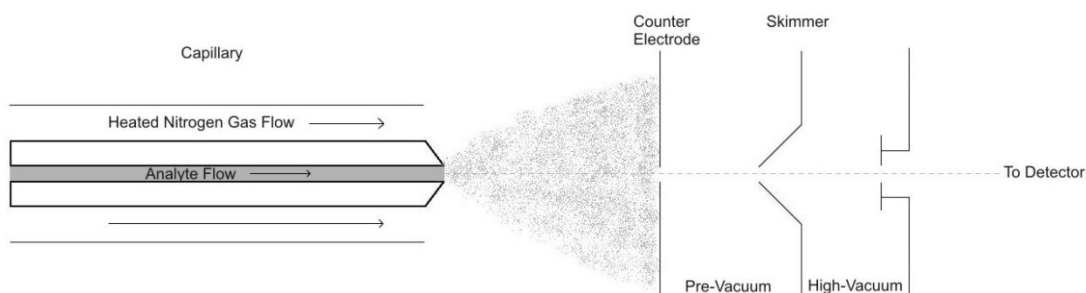


Figure 1.18: Schematic of an electrospray instrument

The ion formation process in ESI has similarities with processes occurring in an electrochemical cell. If positive ions are being detected, then these will be pushed to the front of the capillary, into the nascent tip and the negative charges will be “pumped” away.

This idea of electrophoretic charging, where there is a partial separation of positive ions from negative ions due to the imposed electric field and leading to the excess of a positive charge on the surface of the liquid, which then destabilises the surface leading to the emission of droplets, assumes that ions are already present in the solution.

While the electric current is achieved by movement of electrons through the wire that provides the potential for the electrodes, the current in solution is achieved by the movement of ions. Therefore, there must be an electrochemical conversion of electrons to ions at the liquid-metal interface of the capillary tip.

If an oxidation reaction occurs at the tip, this will create the required excess of ions by removing electrons from negatively charged ions, and creating positively charged ions.

This was confirmed by constructing a capillary with a tip made of a metal with a favourable oxidation potential, which would therefore produce ions which could be detected in the spray. The chosen metal was Zinc, and when the zinc tip was at the very end of the capillary, Zn^{2+} ions were seen in the resulting spectra. To confirm that it was not just a corrosion of the zinc tip that was creating these ions, the zinc tip was placed in the tubing prior to the start of the capillary, and was electrically insulated from the rest of the system. It was found as expected that in this situation, no zinc ions were formed⁸⁸.

These reactions that occur at the tip – oxidation for the detection of positive ions and reduction for the detection of negative – create a current that limits the number of ions that will go through to the detector. It is called the limiting current, I_M , and generally will not exceed $1\mu\text{A}$, and is only dependent on concentration of the sample, not the flow rate.

For ions of both polarities, ions of an analyte, A, are desorbed from the droplets producing a theoretical current⁵⁴:

$$I_A = k_A[A]$$

Where k_A is a rate constant, dependent on A.

If another analyte, B, will form ions:

$$I_B = k_B[B]$$

The total current produced, I_T :

$$I_T = (I_A + I_B)$$

As this current is limited by the process at the capillary tip:

$$I_M = I_T$$

The current for each ion is proportional to their relative desorption rate, as below:

$$I_A = I_M \left(\frac{k_A[A]}{k_A[A] + k_B[B]} \right)$$

and:

$$I_B = I_M \left(\frac{k_B[B]}{k_A[A] + k_B[B]} \right)$$

Consider the following scenario. If the concentration of B remains constant, and the concentration of A varies.

If $k_B[B] \gg k_A[A]$

Then:

$$I_A \approx I_M \left(\frac{k_A[A]}{k_B[B]} \right) \text{ and } I_B \approx I_M \left(\frac{k_B[B]}{k_B[B]} \right) = I_M$$

Therefore, the intensity of the signal for A will be proportional to its concentration and the sensitivity will be inversely proportional to the concentration of B. It appears that the limiting current in this situation is dependent upon B.

If the scenario is reversed, with $k_B[B] \ll k_A[A]$, then:

$$I_A \approx I_M \left(\frac{k_A[A]}{k_A[A]} \right) \approx I_M \text{ and } I_B \approx I_M \left(\frac{k_B[B]}{k_A[A]} \right)$$

In this situation, the total current is almost entirely dependent on A, quantitation of the concentration of A is impossible, and the intensity of the signal for B will decrease with increasing concentration of A.

This partially demonstrates how many variables are involved in achieving repeatable, accurate ESI spectra.

Ionisation Mechanism for Fullerenes

The ionisation mechanism of fullerenes by ESI is still under investigation. Typically, non polar compounds are very difficult to ionise with ESI as these contain neither a pre-formed charge, nor heteroatoms that could easily protonate. Previous experiments have been performed by either altering the fullerenes with a polar ligand, or by adding salts to the solution⁸⁹⁻⁹².

The properties of the ESI source acting as an electrochemical cell can be exploited for ionising fullerenes and other non polar compounds⁴¹, however, the redox potentials have to lie between the values of -0.8 to +1.0 V⁹². For C₆₀ and C₇₀, molecular ions could only be found in negative mode. Otherwise, off line electrolysis had to be used to produce the ions prior to injection into the ESI. Of course, this only works if the oxidised or reduced species are stable for the period of time it takes to produce them and analyse them.

In the course of this research conditions have been found in which ionisation of the raw compounds has been achieved.

Ion-Trap Mass Analyser and Detection

The Ion Trap mass analyser is based upon the quadrupole mass analyser which was developed in 1953⁹³. It consists of four perfectly formed and perfectly aligned parallel rods:

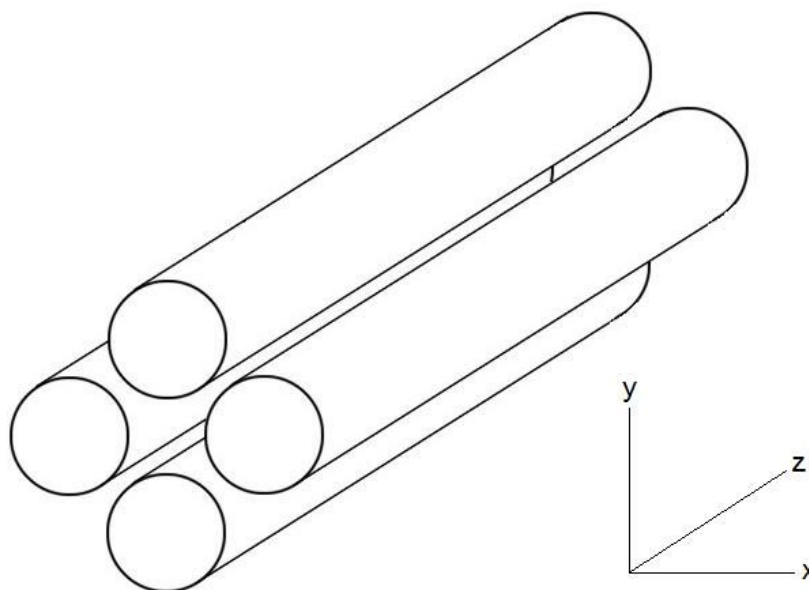


Figure 1.19: Schematic of a quadrupole mass analyser

The rods have a potential applied across them, with opposite rods bearing the same charge. The idea is that an ion travelling through the quadrupole, along the z-axis, will be attracted to the oppositely charged rod. If the potential changes rapidly, the ion will be deflected away, and will then be attracted to one of the rods either side. Then the polarity will change again, and the ion will change direction. As long as the ion does not reach one of the rods and discharge, it will make its way through to the detector.

The voltage applied to the rods consists of a direct potential and a radio frequency voltage.

Ions travelling along the z-axis are subject to this electric field:

$$\Phi_o = -(U - V \cos \omega t) \text{ and } \Phi_o = +(U - V \cos \omega t)$$

Φ_o = potential applied to rod

ω = angular frequency, rad s^{-1} , = $2\pi u$, where u = frequency of the radio frequency, RF, field

V = zero to peak amplitude of RF voltage – this alternates from 0 – 3000 V (-3000 to +3000)

U = direct potential – typically 500 to 2000 V

The ions are accelerated in the z – direction and maintain this velocity between the poles.

The accelerations in the x and y directions induced by the electric fields are calculated as follows:

$$F_x = m \frac{d^2 x}{dt^2} = -ze \frac{\partial \Phi}{\partial x}$$

$$F_y = m \frac{d^2 y}{dt^2} = -ze \frac{\partial \Phi}{\partial y}$$

Where z is the charge on the ion and F is the field.

Φ is a function of Φ_o , and is given by:

$$\Phi_{(x,y)} = \Phi_o \frac{(x^2 - y^2)}{r_o^2} = \frac{(x^2 - y^2)(U - V \cos \omega t)}{r_o^2}$$

Where r_o is the radius of the gap between the rods. Derivatising leads to:

$$\frac{d^2 x}{dt^2} + \frac{2ze}{mr_o^2} (U - V \cos \omega t) x = 0$$

$$\frac{d^2 y}{dt^2} - \frac{2ze}{mr_o^2} (U - V \cos \omega t) y = 0$$

The trajectory is stable as long as x and y remain less than r_o .

The above equations correspond nicely with the Mathieu equation, used to study the propagation of waves in membranes:

$$\frac{d^2 u}{d\xi^2} + (a_u - 2q_u \cos 2\xi) u = 0$$

From this,

$$\xi = \frac{\omega t}{2}$$

Taking into account that the potential along y is the opposite of that along x :

$$a_u = a_x = -a_y = \frac{8zeU}{m\omega^2 r_o^2}$$

$$q_u = q_x = -q_y = \frac{4zeV}{m\omega^2 r_o^2}$$

For a quadrupole, r_o is constant. $\omega = 2\pi\nu$ is also constant, which leaves U and V as the variables.

Plotting "a" vs. "q" gives two stability plots, one for x and one for y . Overlapping the two plots gives areas where the values of a and q will allow safe trajectory through the quadrupole.

Rearrangement of the equations allows for more clearly seeing the effect of U and V on a and q :

$$U = a_u \frac{m \omega^2 r_o^2}{z 8e} \text{ and } V = q_u \frac{m \omega^2 r_o^2}{z 4e}$$

As $\frac{\omega^2 r_o^2}{8e}$ and $\frac{\omega^2 r_o^2}{4e}$ are constant for any given quadrupole analyser, any change in U and

V will change a and q for any given m/z. Also, different m/z values will have different a and q values at any given voltage.

Therefore, changing voltages allows only certain ions to have a stable trajectory through the quadrupole, with other ions discharging on the rods. This allows for separation of the ions.

Quadrupole Ion Traps are based upon the design for the Quadrupole, however, they consist of a circular, or ring electrode, with two end caps⁹⁴. Typically, the potential is only applied to the ring electrode.

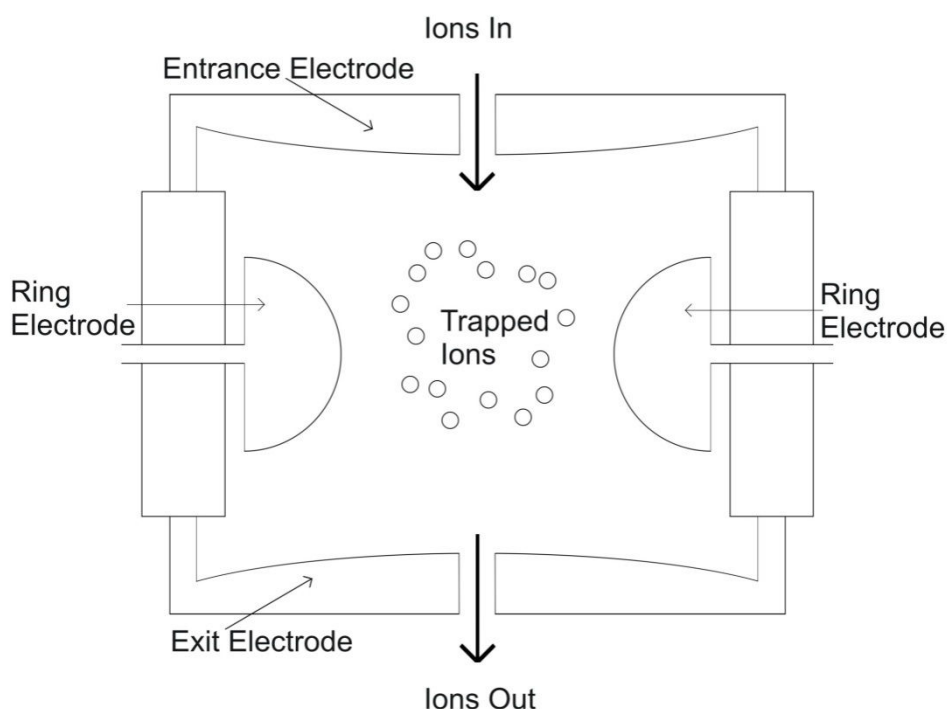


Figure 1.20: Schematic of an ion trap

Initially, however, with both instruments, only ions of a single m/z value could be held within the trap; all others were ejected and wasted. As such, their potential for mass spectrometry and chemical purposes were not realised until 1984, where two improvements to the design were made⁹⁵. The first was that ions could be ejected from the trap sequentially in the order of their m/z values with subsequent detection through a mode of operation called “Mass-Selective Instability”. The second development was that the introduction of gaseous helium

into the trap improved the resolution, by reducing the kinetic energies of the ions through terminating collisions and constricting their orbits.

Ions enter the trap and the voltage applied to the ring electrode causes the ions to oscillate in an orbit inside the trap. Increasing the RF voltage increases ion motion along the z-axis which causes the orbits to destabilise. Ions with a low m/z will start to exit, 50% through the entrance electrode and 50% through the exit electrode through to the detector. With increasing RF amplitude, the larger m/z ions are ejected.

Low pressure helium gas is present to decrease the kinetic energy of the ions through collisions, which increases the probability of the ions staying trapped. As many ions are present, they will constantly repel one another, causing the oscillations to increase in size. Helium-induced collisions help in preventing this.

The same principle of rapid field reversal in Quadrupole analysers is applied to Ion Traps. The ions are alternately accelerated and decelerated in the z direction, and vice versa in the radial – x and y combined – direction. Mathieu plots are again used to determine the a and q values in which the orbits are stable.

Because of the cylindrical symmetry inside a trap, it follows that:

$$x^2 + y^2 = r^2$$

Therefore movement can be expressed in terms of z_0 and r_0 and the Quadrupole equations can be adapted as follows:

$$\frac{d^2 z}{dt^2} - \frac{4Ze}{m(r_0^2 + 2z_0^2)}(U - V \cos \omega t)z = 0 \text{ and}$$

$$\frac{d^2 r}{dt^2} + \frac{2Ze}{m(r_0^2 + 2z_0^2)}(U - V \cos \omega t)r = 0$$

Z is the number of charges, z is the distance in the z direction.

Adapting the general Mathieu equation results in:

$$\xi = \frac{\omega t}{2}$$

$$a_u = a_z = -2a_r = \frac{-16ZeU}{m(r_0^2 + 2z_0^2)\omega^2}$$

$$q_u = q_z = -2q_r = \frac{8ZeU}{m(r_o^2 + 2z_o^2)\omega^2}$$

Instrumentation

The main body of the ESI research was carried out on a quadrupole ion trap mass spectrometer (Bruker esquire2000), with a few experiments performed on an ESI orthogonal time-of-flight mass spectrometer (Bruker MicrOTOF).

Bruker esquire2000

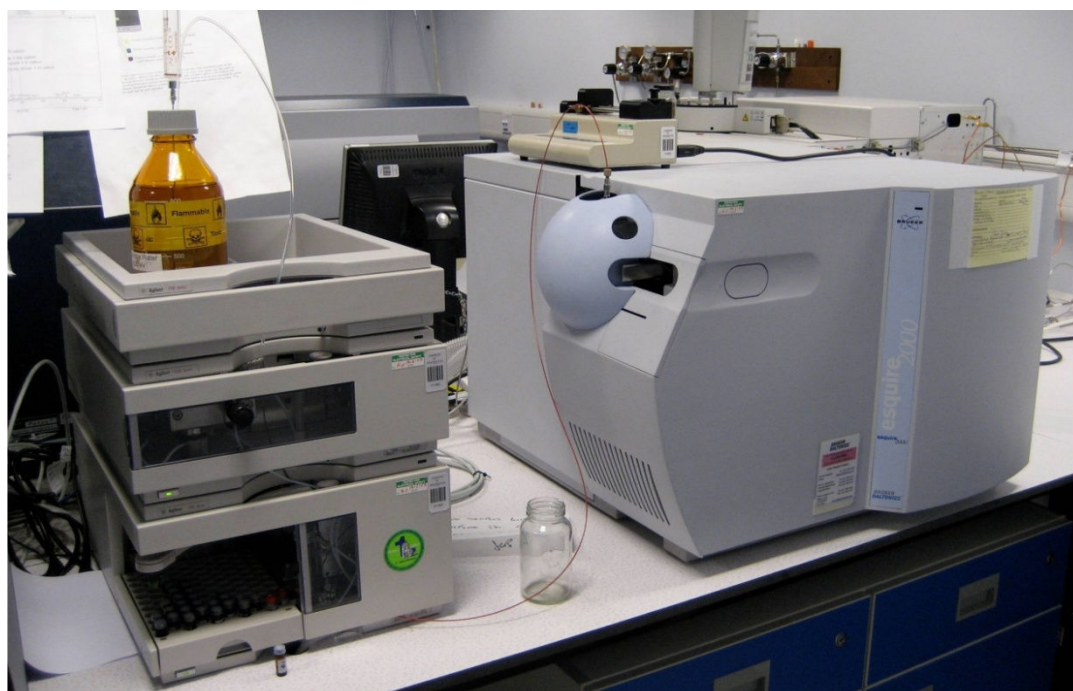


Figure 1.21: Photo of the Bruker esquire2000

The Bruker Esquire2000 is equipped with an ion trap mass analyser with an upper mass limit of 2200 m/z.

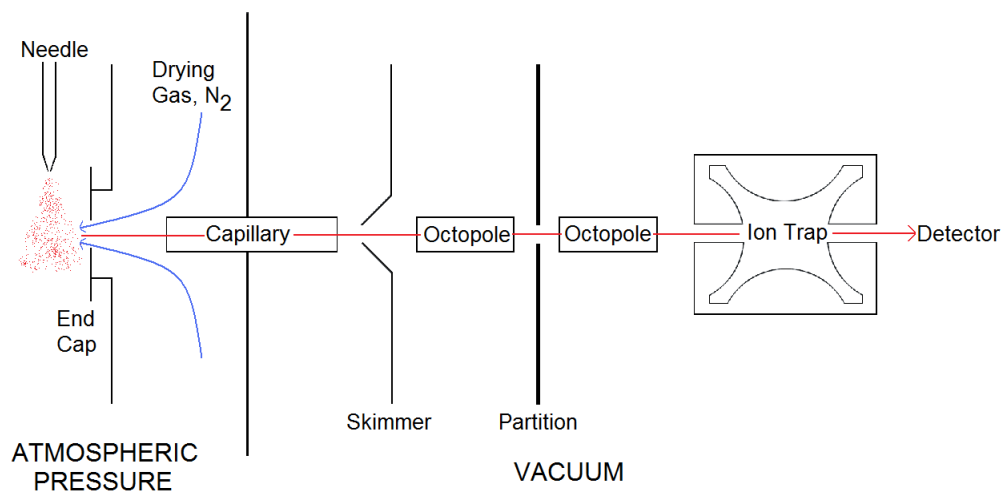


Figure 1.22: Schematic of the Bruker esquire2000

For this particular mass spectrometer, the spray direction is at right angles to the capillary. The spray is formed at the charged needle. Between the end cap and the metal end caps of the capillary, a potential is held which creates an electrostatic gradient to help the ions into and through the capillary. For the ions to pass through the end cap, it is held at a lower potential than the needle. In addition, the entrance and exit caps of the capillary are held at a lower potential than the end cap and the needle.

Heated nitrogen gas helps to evaporate the solvents, and also heats up part of the capillary as it flows past it into the source.

The capillary acts as a barrier between the source, which is held at atmospheric pressure and the rest of the system which is held at vacuum. The pressure gradient across it also helps guide ions through the capillary, and means the ions leave the capillary as a subsonic jet flow.

The exit cap of the capillary is held at a higher voltage than the skimmer, so the ions are attracted to the skimmer. As the ions pass through, the skimmer removes the bulk of the drying gas. The ions then pass through the octopoles, which focus and guide the ions into the ion trap for analysis. From this they may exit into the detector, which for this instrument is based on a conversion dynode.

The scan rate of this machine is 1 mass unit every 76 μs . This is equivalent to 13,158 mass units per second.

Fragmentation experiments can be performed on this machine. Initially, the ion of interest the precursor ion - has to be selected and isolated. This is achieved in the ion trap. Each

mass will have its own resonance, and by synthesizing a range of frequencies, except the one for the precursor ion, all other ions will be ejected from the trap. This broadband frequency spectrum is generated by the electronics system.

Once isolated, the energy of the ion is increased through resonance excitation with the dipole field. With increased energy, the ion will collide with the helium background gas and fragment. This whole process takes between 20 and 60 ms.

There is a drawback – if the RF level is too high, then all the low mass fragments will be ejected. If it is too low, then the ions will not be excited enough for fragmentation. In order to compromise, there is a lower mass limit of ion detection, at one third of the mass of the precursor ion.

One advantage over quadrupole MS/MS experiments is that in the ion trap, only the parent ions are sufficiently excited to fragment. Therefore only the parent ions will dissociate and successive dissociations from the fragment ions can be mostly discounted as these will not have enough energy to participate in follow up dissociations. In contrast, CID in the quadrupole often leads to grand-daughter ions because of successive reactions occurring under the multiple collision conditions.

After a certain time, the RF level is ramped back up, in order to either obtain the spectrum, or to excite fragment ions to perform further MSⁿ experiments.

With the present instrument, up to MS⁴ can be performed; however, there is a loss of signal with each stage of the dissociation. If a signal is strong enough, the method can be useful for the elucidation of fragmentation pathways.

The possibility to perform MSⁿ experiments ($n > 2$) with one analyser is the other advantage that the ion trap (including FT-ICR) possesses over other mass spectrometers as these would require one additional analyser for each additional selection step.

Bruker MicrOTOF

The Bruker MicrOTOF employs the same ESI source as the esquire2000. It has, however, theoretically no upper mass limit and provides over a mass range a sufficiently medium high resolution and mass accuracy to allow the establishment of the elemental composition. The analyser consists of an orthogonal time-of-flight mass spectrometer without MS/MS

capability. In the present study, the instrument was used when it was necessary to extend the limited mass range covered by the esquire2000 ion trap.

References

1. Kroto, H. W.; Heath, J. R.; O'Brien, S. C.; Curl, R. F.; Smalley, R. E., *Nature* **1985**, *318*, 162.
2. Baggott, J. E., *Perfect symmetry: the accidental discovery of Buckminsterfullerene*. Oxford University Press: Oxford, 1994; p ix,315p.
3. Aldersey-Williams, H., *The most beautiful molecule: the discovery of the buckyball*. J. Wiley: New York; Chichester, 1995; p ix, 340 p.
4. Kroto, H.; Allaf, A.; Balm, S., *Chemical Reviews* **1991**, *91* (6), 1213-1235.
5. Haymet, A., *Journal of the American Chemical Society* **1986**, *108* (2), 319-321.
6. Davidson, R., *Theoretica Chimica Acta* **1981**, *58* (3), 193-231.
7. Rohlfling, E.; Cox, D.; Kaldor, A., *Journal of Chemical Physics* **1984**, *81* (7), 3322-3330.
8. Kratschmer, W.; Lamb, L.; Fostiropoulos, K.; Huffman, D., *Nature* **1990**, *347* (6291), 354-358.
9. Chen, Y.; Zhang, H.; Zhu, Y.; Yu, D.; Tang, Z.; He, Y.; Wu, C.; Wang, J., *Materials Science and Engineering B-Solid State Materials for Advanced Technology* **2002**, *95* (1), 29-32.
10. Klein, D.; Schmalz, T.; Hite, G.; Seitz, W., *Journal of the American Chemical Society* **1986**, *108* (6), 1301-1302.
11. Schmalz, T. G.; Seitz, W. A.; Klein, D. J.; Hite, G. E., *Chemical Physical Letters* **1986**, *130* (3), 203.
12. Newton, M.; Stanton, R., *Journal of the American Chemical Society* **1986**, *108* (9), 2469-2470.
13. Taylor, R.; Hare, J.; Abdulsada, A.; Kroto, H., *Journal of the Chemical Society-Chemical Communications* **1990**, (20), 1423-1424.
14. Kroto, H., *Angewandte Chemie-International Edition in English* **1992**, *31* (2), 111-129.
15. Ohmae, N.; Tagawa, M.; Umeno, M., *Journal of Physical Chemistry* **1993**, *97* (44), 11366-11367.

16. Ungurenasu, C.; Airinei, A., *Journal of Medicinal Chemistry* **2000**, *43* (16), 3186-3188.
17. Katz, A.; Redlich, M.; Rapoport, L.; Wagner, H.; Tenne, R., *Tribology Letters* **2006**, *21* (2), 135-139.
18. Simon, F.; Peterlik, H.; Pfeiffer, R.; Bernardi, J.; Kuzmany, H., *Chemical Physics Letters* **2007**, *445* (4-6), 288-292.
19. Innocenzi, P.; Brusatin, G., *Chemistry of Materials* **2001**, *13* (10), 3126-3139.
20. Bosi, S.; Da Ros, T.; Spalluto, G.; Prato, M., *European Journal of Medicinal Chemistry* **2003**, *38* (11-12), 913-923.
21. Friedman, S.; Decamp, D.; Sijbesma, R.; Srdanov, G.; Wudl, F.; Kenyon, G., *Journal of the American Chemical Society* **1993**, *115* (15), 6506-6509.
22. Schinazi, R.; Sijbesma, R.; Srdanov, G.; Hill, C.; Wudl, F., *Antimicrobial Agents and Chemotherapy* **1993**, *37* (8), 1707-1710.
23. Sijbesma, R.; Srdanov, G.; Wudl, F.; Castoro, J.; Wilkins, C.; Friedman, S.; Decamp, D.; Kenyon, G., *Journal of the American Chemical Society* **1993**, *115* (15), 6510-6512.
24. Prassides, K., *Current Opinion in Solid State & Materials Science* **1997**, *2* (4), 433-439.
25. Billups, W. E.; Ciufolini, M. A., *Buckminsterfullerenes*. VCH: New York; London, 1993; p xv, 339p.
26. Heath, J.; O'Brien, S.; Zhang, Q.; Liu, Y.; Curl, R.; Kroto, H.; Tittel, F.; Smalley, R., *Journal of the American Chemical Society* **1985**, *107* (25), 7779-7780.
27. Weltner, W.; Vanzee, R., *Chemical Reviews* **1989**, *89* (8), 1713-1747.
28. Curl, R.; Smalley, R., *Science* **1988**, *242* (4881), 1017-1022.
29. Hirsch, A.; Brettreich, M., *Fullerenes: chemistry and reactions*. Wiley-VCH: Weinheim, 2005; p xvii, 423 p.
30. Taylor, R.; Walton, D., *Nature* **1993**, *363* (6431), 685-693.
31. Wang, S.; Jansen, S., *Journal of Physical Chemistry* **1995**, *99* (21), 8556-8561.
32. Miller, G., *Comptes Rendus Chimie* **2006**, *9* (7-8), 952-959.

33. Beck, R.; Weis, P.; Hirsch, A.; Lamparth, I., *Journal of Physical Chemistry* **1994**, *98* (39), 9683-9687.
34. McElvany, S.; Ross, M., *Journal of the American Society for Mass Spectrometry* **1992**, *3* (4), 268-280.
35. Saldi, F.; Marie, Y.; Gao, Y.; Simon, C.; Migeon, H.; Begin, D.; Mareche, J., *European Mass Spectrometry* **1995**, *1* (5), 487-492.
36. Campbell, E. E. B.; Ulmer, G.; Busmann, H. G.; Hertel, I. V., *Chemical Physics Letters* **1990**, *175* (5), 505-510.
37. Ulmer, G.; Campbell, E. E. B.; Kühnle, R.; Busmann, H. G.; Hertel, I. V., *Chemical Physics Letters* **1991**, *182* (2), 114-119.
38. Cordero, M.; Cornish, T.; Cotter, R., *Journal of the American Society for Mass Spectrometry* **1996**, *7* (6), 590-597.
39. Cozzolino, R.; Belgacem, O.; Drewello, T.; Kaseberg, L.; Herzsuh, R.; Suslov, S.; Boltalina, O., *European Mass Spectrometry* **1997**, *3* (6), 407-414.
40. Gross, J.; Giesa, S.; Kratschmer, W., *Rapid Communications in Mass Spectrometry* **1999**, *13* (9), 815-820.
41. Barrow, M.; Feng, X.; Wallace, J.; Boltalina, O.; Taylor, R.; Derrick, P.; Drewello, T., *Chemical Physics Letters* **2000**, *330* (3-4), 267-274.
42. Brown, T.; Clipston, N.; Simjee, N.; Luftmann, H.; Hungerbuhler, H.; Drewello, T., *International Journal of Mass Spectrometry* **2001**, *210* (1-3), 249-263.
43. Streletskii, A.; Ioffe, I.; Kotsiris, S.; Barrow, M.; Drewello, T.; Strauss, S.; Boltalina, O., *Journal of Physical Chemistry A* **2005**, *109* (4), 714-719.
44. Kotsiris, S.; Vasil'ev, Y.; Streletskii, A.; Han, M.; Mark, L.; Boltalina, O.; Chronakis, N.; Orfanopoulos, M.; Hungerbuhler, H.; Drewello, T., *European Journal of Mass Spectrometry* **2006**, *12* (6), 397-408.
45. Markov, V.; Aleshina, V.; Borschevskiy, A.; Khatymov, R.; Tuktarov, R.; Pogulay, A.; Maximov, A.; Kardashev, S.; Ioffe, I.; Avdoshenko, S.; Dorozhkin, E.; Goryunkov, A.; Ignat'eva, D.; Gruzinskaya, N.; Sidorov, L., *International Journal of Mass Spectrometry* **2006**, *251* (1), 16-22.
46. Karas, M.; Hillenkamp, F., *Analytical Chemistry* **1988**, *60* (20), 2299-2301.

47. Tanaka, K.; Waki, H.; Ido, Y.; Akita, S.; Yoshida, Y.; Yoshida, T., *Rapid Communications in Mass Spectrometry* **1988**, 2 (8), 3.
48. Tanaka, K.; Ido, Y.; Akita, S.; Yoshida, Y.; Yoshida, T., *Second Japan-China Joint Symposium on Mass Spectrometry Abstract* **1987**, 4.
49. Tang, K.; Allman, S.; Jones, R.; Chen, C., *Analytical Chemistry* **1993**, 65 (15), 2164-2166.
50. Chen, H.; He, M.; Pei, J.; He, H., *Analytical Chemistry* **2003**, 75 (23).
51. Trimpin, S.; Keune, S.; Rader, H.; Mullen, K., *Journal of the American Society for Mass Spectrometry* **2006**, 17 (5), 661-671.
52. Williams, J.; Chapman, T.; Hercules, D., *Analytical Chemistry* **2003**, 75 (13), 3092-3100.
53. Chapman, J. R., *Practical organic mass spectrometry: a guide for chemical and biochemical analysis*. 2nd ed. ed.; Wiley: 1993.
54. Hoffmann, E. d.; Stroobant, V., *Mass spectrometry: principles and applications*. 2nd ed.; John Wiley: Chichester, 2001; p xii, 407 p.
55. *Ion-Molecule Reactions: Volume 1*. Butterworth & Co.: New York, 1972; Vol. 1.
56. Knewstubb, P. F., *Mass spectrometry and ion-molecule reactions*. Cambridge U.P.: London, 1969; p vii, 136 p.
57. Knochenmuss, R.; Stortelder, A.; Breuker, K.; Zenobi, R., *Journal of Mass Spectrometry* **2000**, 35 (11), 1237-1245.
58. Ulmer, L.; Mattay, J.; Torres-Garcia, H.; Luftmann, H., *European Journal of Mass Spectrometry* **2000**, 6 (1), 49-52.
59. Vasil'ev, Y. V.; Khvostenko, O. G.; Streletskii, A. V.; Boltalina, O. V.; Kotsiris, S. G.; Drewello, T., *The Journal of Physical Chemistry A* **2006**, 110 (18), 5967-5972.
60. Cohen, L.; Gusev, A., *Analytical and Bio analytical Chemistry* **2002**, 373 (7), 571-586.
61. Donegan, M.; Tomlinson, A.; Nair, H.; Juhasz, P., *Rapid Communications in Mass Spectrometry* **2004**, 18 (17), 1885-1888.
62. McCombie, G.; Knochenmuss, R., *Analytical Chemistry* **2004**, 76 (17), 4990-4997.

63. Smirnov, I.; Zhu, X.; Taylor, T.; Huang, Y.; Ross, P.; Papayanopoulos, I.; Martin, S.; Pappin, D., *Analytical Chemistry* **2004**, 76 (10), 2958-2965.
64. Suckau, D.; Resemann, A.; Schuerenberg, M.; Hufnagel, P.; Franzen, J.; Holle, A., *Analytical and bioanalytical chemistry* **2003**, 376 (7), 952-965.
65. Moneti, G.; Francese, S.; Mastrobuoni, G.; Pieraccini, G.; Seraglia, R.; Valitutti, G.; Traldi, P., *Journal of mass spectrometry : JMS* **2007**, 42 (1), 117-126.
66. Smith, R.; Loo, J.; Edmonds, C.; Barinaga, C.; Udseth, H., *Analytical Chemistry* **1990**, 62 (9), 882-899.
67. Snyder, A., *Biochemical and Biotechnological Applications of Electrospray Ionization Mass Spectrometry* **1996**, 619, 1-20.
68. Fenn, J.; Mann, M.; Meng, C.; Wong, S.; Whitehouse, C., *Science* **1989**, 246 (4926), 64-71.
69. Manisali, I.; Chen, D.; Schneider, B., *Trac-Trends in Analytical Chemistry* **2006**, 25 (3), 243-256.
70. Pramanik, B.; Bartner, P.; Mirza, U.; Liu, Y.; Ganguly, A., *Journal of Mass Spectrometry* **1998**, 33 (10), 911-920.
71. Yamashita, M.; Fenn, J., *Journal of Physical Chemistry* **1984**, 88 (20), 4451-4459.
72. Yamashita, M.; Fenn, J., *Journal of Physical Chemistry* **1984**, 88 (20), 4671-4675.
73. Whitehouse, C.; Dreyer, R.; Yamashita, M.; Fenn, J., *Analytical Chemistry* **1985**, 57 (3), 675-679.
74. Smith, R.; Barinaga, C.; Udseth, H., *Analytical Chemistry* **1988**, 60 (18), 1948-1952.
75. Smith, R.; Olivares, J.; Nguyen, N.; Udseth, H., *Analytical Chemistry* **1988**, 60 (5), 436-441.
76. Vanberkel, G.; Glish, G.; Mcluckey, S., *Analytical Chemistry* **1990**, 62 (13), 1284-1295.
77. Fenn, J. B., *Journal of Biomolecular Techniques* **2002**, 13 (3), 18.
78. Dole, M.; Mack, L. L.; Hines, R. L.; Mobley, R. C.; Ferguson, L. D.; Alice, M. B., *The Journal of Chemical Physics* **1968**, 49 (5), 10.
79. Mack, L. L.; Kralik, P.; Rheude, A.; Dole, M., *The Journal of Chemical Physics* **1970**, 52 (10), 10.

80. Peters, J. M. H., *European Journal of Physics* **1980**, 1 (3), 4.
81. Iribarne, J.; Thomson, B., *Journal of Chemical Physics* **1976**, 64 (6), 2287-2294.
82. Thomson, B.; Iribarne, J., *Journal of Chemical Physics* **1979**, 71 (11), 4451-4463.
83. Fenn, J., *Journal of the American Society for Mass Spectrometry* **1993**, 4 (7), 524-535.
84. Kebarle, P., *Journal of Mass Spectrometry* **2000**, 35 (7), 804-817.
85. de la Mora, J., *Analytica Chimica Acta* **2000**, 406 (1), 93-104.
86. Wang, G.; Cole, R., *Analytica Chimica Acta* **2000**, 406 (1), 53-65.
87. Gamero-Castano, M.; de la Mora, J., *Analytica Chimica Acta* **2000**, 406 (1), 67-91.
88. Blades, A.; Ikonomou, M.; Kebarle, P., *Analytical Chemistry* **1991**, 63 (19), 2109-2114.
89. Wilson, S.; Wu, Y., *Journal of the American Society for Mass Spectrometry* **1993**, 4 (7), 596-603.
90. Wilson, S.; Wu, Y., *Journal of the Chemical Society-Chemical Communications* **1993**, (9), 784-786.
91. Wilson, S.; Wu, Y., *Journal of the American Chemical Society* **1993**, 115 (22), 10334-10337.
92. Dupont, A.; Gisselbrecht, J.; Leize, E.; Wagner, L.; Vandorselaer, A., *Tetrahedron Letters* **1994**, 35 (33), 6083-6086.
93. Paul, W., *Angewandte Chemie-International Edition in English* **1990**, 29 (7), 739-748.
94. March, R., *Journal of Mass Spectrometry* **1997**, 32 (4), 351-369.
95. Stafford, G.; Kelley, P.; Syka, J.; Reynolds, W.; Todd, J., *International Journal of Mass Spectrometry and Ion Processes* **1984**, 60 (SEP), 85-98.

Chapter 2: Experimental

Sample Preparation

For the majority of the MALDI-MS and all of the ESI-MS experiments, solutions of the samples were prepared. To decrease the risk of contamination a clean glass pipette was used to measure out each individual compound, which was disposed of after use. The samples were weighed using a Precisa Gravimetrics AG Precisa 125 weighing balance. 1ml, 200 μ l and 20 μ l Gilson pipettes and the corresponding tips were used to measure solvents/solutions. A 10 μ l Barky μ tipette was used for pipetting solutions onto the MALDI target slide. Each tip was used only once.

Solutions were thoroughly dissolved via vibrations created by a Fisherbrand Whirlimixer.

For solid state LDI/MALDI-MS, samples were ground into finer particles using a marble pestle and mortar. Double sided tape was used to attach the powders to the target slide. For solid state MALDI-MS, DCTB and the sample were weighed prior to being ground, and were ground together to ensure that the DCTB and sample were evenly dispersed. It was vital to ensure no loose powder remained on the target plate, as this would disturb the vacuum inside the source or result in contamination of the ion source with sample material. Therefore, the target plate was placed in an air stream prior to analysis in order to remove material that was only loosely attached.

Common Samples/Solvents

The samples and solvents used most frequently are listed below with supplier and purity information. Information on other samples is mentioned in the relevant chapters.

Sample	Supplier	Purity/Grade
C ₆₀	Term-USA	99.5%
C ₇₀	Southern Chemical Group, LLC	98%
C ₈₄	Laboratory stock	Not known
Fullerene Mixture	Laboratory stock	Not known
DCTB	Fluka (Sigma-Aldrich)	99%, HPLC grade

Toluene	Fisher Chemicals	99%, Laboratory reagent grade
Dichloromethane	Fisher Chemicals	99.8%, HPLC grade
Methanol	Acros Organics	99.9%
Methanol	Fisher Chemicals	99.99%, HPLC grade
Water	Fisher Chemicals	HPLC grade

Table 2.1: Information on mostly used samples/solvents

MALDI

Bruker Ultraflex II

The MALDI-ToF could be operated in 6 modes –

Positive-ion or negative-ion mode with Reflectron analysis

Positive-ion or negative-ion mode with Linear analysis

Positive-ion or negative-ion mode LIFT

The Ultraflex II was supplied with several generic methods that had been optimised for standard use, mainly for large molecular weight polymers and proteins. Due to the lack of specific fullerene/low mass methods, the standard methods optimised for fairly low m/z ranges were further optimised to produce fullerene signals with a good resolution and accurate isotopic pattern.

For the recording of “normal” mass spectra and of LIFT mass spectra (MS/MS experiments which have been discussed in detail in the introduction) the optimised instrumental parameters are listed below separately.

Parameters altered included:

“IS1”, Ion Source 1, is the potential applied to the target plate, P1.

“IS2”, Ion Source 2, is the potential applied to P2.

“Lens” is the voltage applied to the lens plate located directly after P2.

“Ref1” and “Ref2” refer to the reflectron when reflectron analysis is used.

“LIFT1” and “LIFT2” refer to the LIFT optics.

PIE, Pulsed Ion Extraction, is the time a sharp pulse is applied to P2.

P and N refer to positive-ion and negative-ion mode; L and R refer to linear and reflectron detection respectively.

Method	IS1 / kV	IS2 / kV	Lens / kV	Ref1 / kV	Ref2 / kV	PIE / ns
PR	25	21.3	9	26.3	13.8	40
PL	25	23.8	6.5	-	-	40
NR	20	17	7	21	11	20
NL	20	19	5.4	-	-	20

Table 2.2: Instrument parameters of the Bruker Ultraflex II (“normal” mass spectra)

The LIFT methods are optimised by the manufacturer and internally calibrated. The parameters cannot be changed without invalidating the calibration.

IS1 / kV	IS2 / kV	Lens / kV	Ref1 / kV	Ref2 / kV	LIFT1 / kV	LIFT2 / kV	PIE / ns
8	7.2	3.6	29.5	13.85	19	3.80	0

Table 2.3: Instrument parameters for the LIFT methods (positive and negative ions) on the Bruker Ultraflex II

The laser parameters are identical between the “normal” methods and the LIFT methods and are as follows:

	Variables	Normal Methods	LIFT methods
Laser attenuator	Offset	66%	66%
	Range	15%	20%
	Set	3_medium	4_large
Laser Focus:	Offset	1%	1%
	Range	98%	98%
	Value	35%	16%

Table 2.4: Laser parameters for the Bruker Ultraflex II

This means that for every group of spectra obtained, the only variable in the laser is the % power.

The offset and range in the laser attenuator section refer to objects, for example mirrors, in the path of the laser, which can increase or decrease the amount of laser light getting through to the sample.

The target plate to which samples are applied has 384 individual target spots arranged in 16 rows and 24 columns. The rows are lettered A to P and the columns are arranged 1 - 24; a photo is shown below:



Figure 2.1: Photo of the MALDI slide

The standard plate is the MTP 384 target plate ground steel T F.

Made of stainless steel, it has to be mounted in a holder prior to insertion into the machine.

ESI

esquire2000

The sample solution can be introduced to the esquire2000 in two different ways. The first way involves an automated sampling system, which allows for fast throughput yet has limited access to the many variables that can be changed. The second option is manual injection, which is more time consuming but allows for a greater control and real time optimisation of the method.

Certain parameters of the mass spectrometer remained constant whether the automated sampler or manual injection was used and these are listed below. The parameters are separated according to the tab (left column) under which they are found in the software which controls the esquire2000:

Mode	Save Spectra	Yes
	Scan Mode	Normal
	Threshold	1000
	Divert Valve	To Source
Tune	Nebulae	10.0 phi
	Dry Gas	5.0 l/min
	Trap Drive Level	100%
	Optimise	Normal
Optimise	Smart Ramp	Capillary
	Ramp Range	-4500.0 to -1500.0 V
	Adapt Scan Range	Yes
	Averages	1
Polarity/Spectra	Link Edit	Yes
	ICC	Yes
	Target	20000
	Max. Ace Time	200.00 ms
	Averages	7

Table 2.5: Parameters for the Bruker esquire2000

When using the autosampler, pre-set methods have to be used which vary: polarity, compound stability (at set values between 20 and 100%) and the mass optimization range (in ranges of 500 m/z, for example: m/z 0 - 500, m/z 500 – 1000). The drying gas temperature was usually set at 300°C. Another pre-requisite of these methods was that the sample had to be dissolved in 80:20 v/v acetonitrile:water.

When using the manual injection, the main variables altered were as follows:

Polarity	Positive or Negative
Dry Temperature (temperature of the drying gas)	Between 100 and 300°C
Target Mass (enhanced sensitivity for a certain m/z)	Chosen m/z between 1 and 2200
Scan (selected m/z range to scan)	Between m/z 1 and 2200
Compound Stability (source voltage)	Between 0 and 1000%

Table 2.6: Variables on the Bruker esquire2000

The option of using solvents other than acetonitrile and water was another reason that manual injection was preferable, as the fullerenes and related compounds analysed here dissolve preferably in non-polar solvents. With ESI some solvents cannot be used, for example dichloromethane cannot be used alone as it is too volatile and no signal is produced, however, if mixed with methanol the signal improves. Toluene, the primary solvent for the fullerenes, is another solvent which cannot be used, due to its non-polar nature. Another factor for consideration of solvent choice is that the solvent should not erode parts of the equipment, such as the PTFE tubing that transfers the sample from the injection needle to the ESI needle.

Chapter 3: Study of Novel Fullerene Derivatives

Introduction

Open Cage Fullerenes

Fullerenes can be derivatised in many ways as explained in the introduction. One derivatisation of interest involves creating an orifice within the fullerene shell by introducing new atoms to the structure, such as nitrogen, oxygen and sulphur. These fullerene derivatives are called Open-Cage Fullerenes (OCFs).

Open-cage fullerenes are potentially interesting because they can be used to encapsulate small atoms and compounds within the cage structure. They are of interest as they resemble hemicarplexes, a host-guest complex where the host molecule has a small portal within its structure, which enables entry of the guest molecule. Hemicarplexes have several possible uses ranging from medicinal purposes to catalysts¹. Medicinal functions could include the time release of drugs, or the entrapment of salts of radioactive materials to help with radiation diagnosis or therapy.

The environment within these hemicarplexes is totally unique. They can be used to provide very selective reaction sites, and as such can act as catalysts, where only compounds that are present within the complex would react. Another use would be as transport mechanisms across membranes – if the host can insert itself into a membrane it can easily trap and then release the guest across the membrane. The guests within the hosts are protected from the outside world, as they usually cannot escape without the escape being initiated by, for instance, higher temperatures or electrically.

The theoretical applications of OCFs are similar to those mentioned for hemicarplexes, and they have also been considered as a possible means of hydrogen storage. Computer modelling of H₂ within the C₆₀ cage has shown that encapsulation should be possible, and that the H₂ would be unhindered enough to be able to rotate freely inside the cage, with negligible distortion of the fullerene cage².

The first OCF was created in 1995 by Wudl et al.³. The reaction of C₆₀ with azides affords [5,6]azafulleroids, in which a C-C bond is cleaved and the C=C bonds adjacent to the nitrogen atom are susceptible to the formation of bisazafulleroids.

The orifice on this first OCF consisted of 11 members and has ketolactam functionality:



Figure 3.1: First OCF created

The creation of this OCF is fairly straightforward, with N-methoxyethoxymethyl(MEM)-substituted [5,6]azafulleroid being dissolved in 1,2-dichlorobenzene and subjected to a light source for 3 hours at between 25 and 30°C.

As there is an obvious potential for these molecules to entrap molecules easily through the orifice, attempts were made to increase the size of the orifice. It was assumed that a larger orifice would increase the ease of entrapment.

The energy barriers to the helium entry and exit into a 13-membered ring orifice OCF were calculated and compared to an OCF with a smaller orifice. It was easier for the OCF with the larger orifice to encapsulate the helium⁴.

A 12-membered ring orifice OCF was formed by reacting C₆₀ with 4,6-dimethyl-1,2,3-triazine, in *o*-dichlorobenzene for 24 hours at 180°C. This formed two products – an azacyclohexadiene-fused derivative and an OCF with an 8-membered ring orifice. This orifice was enlarged to 12 members by simply leaving the compound dissolved in CS₂, exposed to air and room light for one hour. The reaction involved oxidative cleavage of the double bond leading to the larger orifice⁵.

A 12-membered ring orifice OCF without organic addends on the rim was first created in 2004 by G. C. Vougioukalakis et al by creating a 12-membered ring orifice OCF with an N-MEM protective group attached, which was removed by heating in a degassed ODCB solution at 150°C in the presence of *p*-toluenesulfonic acid monohydrate⁶.

13-membered ring orifice OCFs were developed by enlarging existing OCFs through different reaction stages. To start, an 8-membered ring orifice OCF was created by reacting

C₆₀ with a 1,2,4-triazine derivative in *o*-dichlorobenzene for 17 hours at 180°C. Photochemical oxidation of this 8-membered ring orifice OCF gave two products – a 10-membered and a 12-membered ring orifice OCF. Interestingly, the same group observed that reacting C₆₀ with phthalazine by two different methods - one solid state with a high-speed vibration milling technique, the other solution state; resulted in production of a C₆₀ dimer with the high-speed vibration milling technique and an OCF using a one-pot synthetic reaction⁷.

The 12-membered ring orifice OCF was then enlarged to a 13-membered ring orifice OCF via sulphur insertion into an activated C-C bond⁸.

Using the original 11-membered ring orifice OCF created by Wudl "et al". 15-membered ring orifice OCFs have been developed using various phenyl hydrazine derivatives, in a fairly straightforward one pot synthesis. The different functional groups present from the various phenyl hydrazine derivatives allow for further regioselective reaction to create new OCFs⁹.

The synthesis of ten 16-membered ring orifice OCFs has been reported by our collaborators on this project¹⁰. Two isomeric 12-membered ring orifice OCFs were reacted with phenyl hydrazine, *p*-Br-phenylhydrazine, *p*-MeO-phenylhydrazine, diphenylhydrazine and benzophenone hydrazone, to create the ten different 16-membered ring orifice OCFs. The reaction times for the reactions with the phenylhydrazine derivatives varied between 2 and 9 hours, and were performed either at room temperature or at 60°C. For the reaction with benzophenone hydrazone, the reaction was performed at 100°C for 18 hours.

With synthesis of OCFs with large orifices possible, encapsulation of various small molecules has been attempted.

The initial attempt to trap H₂ and He gases within an OCF resulted in yields of the trapped gases of 1.5% for He and 5% for H₂¹¹.

Entrapment of the gases involves fairly forceful conditions. For He encapsulation it involved heating the OCF as a powder at around 300°C, with a He pressure of 475 atm for 7.5 hours. For H₂, the conditions involved heating at 400°C for 48 hours, under a H₂ pressure of 100 atm.

The OCF in question was synthesized by reacting C₆₀ with diazidobutadiene at 55°C under argon for 4 days in *o*-dichlorobenzene. It had an 14-membered elliptical ring orifice¹².

Unfortunately it was also discovered that these gases readily escaped at elevated temperatures of around 150°C.

It was because of this that steps have been devised to perform “molecular surgery” - a procedure involving several steps which would allow the capture and retention of various small molecules. The initial step is to create the orifice within the cage structure. The second step is to trap the small molecule or atom, and the third step is to re-heal the cage structure, back to a pure fullerene, with the small molecule trapped inside.

So with the success of producing OCFs with large enough orifices to incorporate a variety of small molecules, the next step was to increase the encapsulation.

A 13-membered ring orifice OCF was treated with a H₂ pressure of 800 atm at 200°C for 8 hours, which produced H₂@OCF in a much greater yield than previously seen¹³. ¹H-NMR verified the structure to be H₂@OCF. HPLC of the H₂@OCF and the empty OCF showed no difference, which also suggests the H₂ has not attached in an exohedral manner to the outside of the OCF.

MALDI was performed on the H₂@OCF complex, and as well as molecular ion peaks for H₂@OCF, and the empty OCF, there was also a peak at m/z 722 assigned to H₂@C₆₀. It appeared that the laser rehealed the OCF of the H₂@OCF complex to its original fullerene form, trapping the H₂ inside. To check that it was not exohedral C₆₀H₂ that had been formed, MALDI was performed on a sample of exohedral C₆₀H₂ under the same conditions, which produced m/z 720 and 721 but the molecular ion of C₆₀H₂ at m/z 722 was not observed.

Using various 19-membered ring orifice OCFs, H₂O was encapsulated¹⁴. The original 19-membered ring orifice OCF was created by enlarging a previous OCF through the reaction with o-phenyldiamine, pyridine and PhCl at 80°C. The various side groups on the 19-membered ring orifice OCF could be altered through various reactions, and so the water molecule encapsulation was tested on 3 of these variants. And although all three could encapsulate the water molecule, the various side groups appeared to affect the ability of the OCF to encapsulate the water.

A yield of 83% H₂ encapsulation was achieved using an OCF with a 16-membered ring orifice, with an H₂ pressure of 13.5 MPa at 100°C. To test the effect of temperature and pressure on the encapsulation the pressure of the H₂ ranged from 0.6 – 13.5 MPa (~6 - 133

atm), and the temperature varied between 50 and 150°C. These two variables had a great effect on the efficiency of the encapsulation¹⁵.

Carbon monoxide is another compound that has been inserted into an OCF. The encapsulation of CO was produced by dissolving a mixture of H₂O@OCF and the empty OCF in 1,1,2,2-tetrachloroethane and heating under a CO pressure of 9 MPa (≈89 atm).

The resulting CO@OCF complex was confirmed by ¹³C-NMR, ESI mass spectrometry and IR spectroscopy. The gradual leakage of CO from the OCF resulted in the spontaneous formation of H₂O@OCF, which suggests that H₂O somehow interacts more strongly within the cage of the OCF¹⁶.

The position of the compound within the cage is another matter of interest. X-ray diffraction patterns taken of an OCF with and without an encapsulated H₂ molecule demonstrated that the H₂ sits almost exactly in the centre of the internal dimensions of the OCF¹⁷.

With increasing yields of encapsulation of the molecules of interest, the next step was to perform “molecular surgery” to close the orifice, whilst avoiding loss of the encapsulated molecule. Obviously the encapsulated molecules tend to exit the OCF when the temperature exceeds 150°C, so the “surgery” must be performed at lower temperatures.

One example is of H₂ encapsulated in a 13-membered ring orifice OCF¹⁸. With the H₂ encapsulated a series of reactions were performed to close the cage. The first was the oxidation of a sulphide unit on the orifice, which was performed at room temperature. The second reaction was the removal of the SO unit by a photochemical reaction, also at room temperature. The third reaction was to reductively couple two carbonyl groups on the rim using Ti(0) at 80°C. At this stage, the orifice had been reduced to 8 members. The final step was to heat at 340°C under vacuum for 2 hours, which led to the creation of H₂@C₆₀.

As the orifice had been reduced in size, the application of such a high temperature meant that very little H₂ escaped.

H₂@C₆₀ was found to be almost as stable as C₆₀ and even when it was heated for 10 minutes at 500°C, the H₂ did not escape.

Using methods for the verification of the entrapment, other than mass spectrometry is vital, when the fact that laser ablation of various fullerene derivatives can also form C₅₉N, which has essentially the same m/z as H₂@C₆₀ is taken into consideration.

To differentiate between $H_2@C_{60}$, or even $C_{60}H_2$ and $C_{59}N$ would require an extremely high resolution. $C_{59}N$ was found to form when fullerene derivatives, which had an organic ligand bound to the carbon cage through a nitrogen atom, were analysed with positive-ion mode LDI, with an elevated laser power¹⁹. The nitrogen atom linkage replaced a single C-C bond (represented as a dashed line in figure 3.2, below) shared by a 6-membered and 5-membered ring on the fullerene cage:

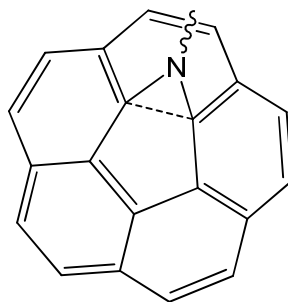


Figure 3.2: Nitrogen atom linkage replacing a C-C bond

Of the fullerene derivatives with these organic ligands ablated with a high laser power, all formed both C_{60} and $C_{59}N$ as fragments, and two of these formed C_{60} in preference to $C_{59}N$. Using a high resolution mass spectrometer, it was proved that m/z 722 was composed primarily of $^{12}C_{59}^{14}N$, with a very minor contribution from $^{12}C_{58}^{13}C_2$. $^{12}C_{60}H_2$ was not present. $(C_{59}N)_2$ was also studied, and CID of the $C_{59}N$ monomer unit demonstrated that the nitrogen is incorporated into the cage, as the resultant fragments did not contain nitrogen. The C-N unit was lost first, followed by the typical fragmentation pattern of C_2 units lost by C_{60} . $C_{60}N_2MEM_2$ was also studied and showed similar behaviour:

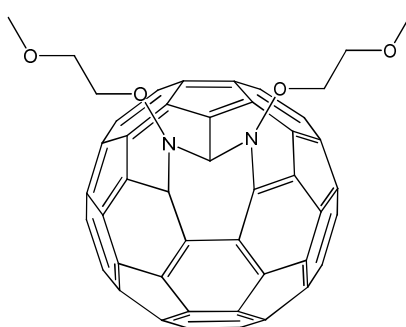
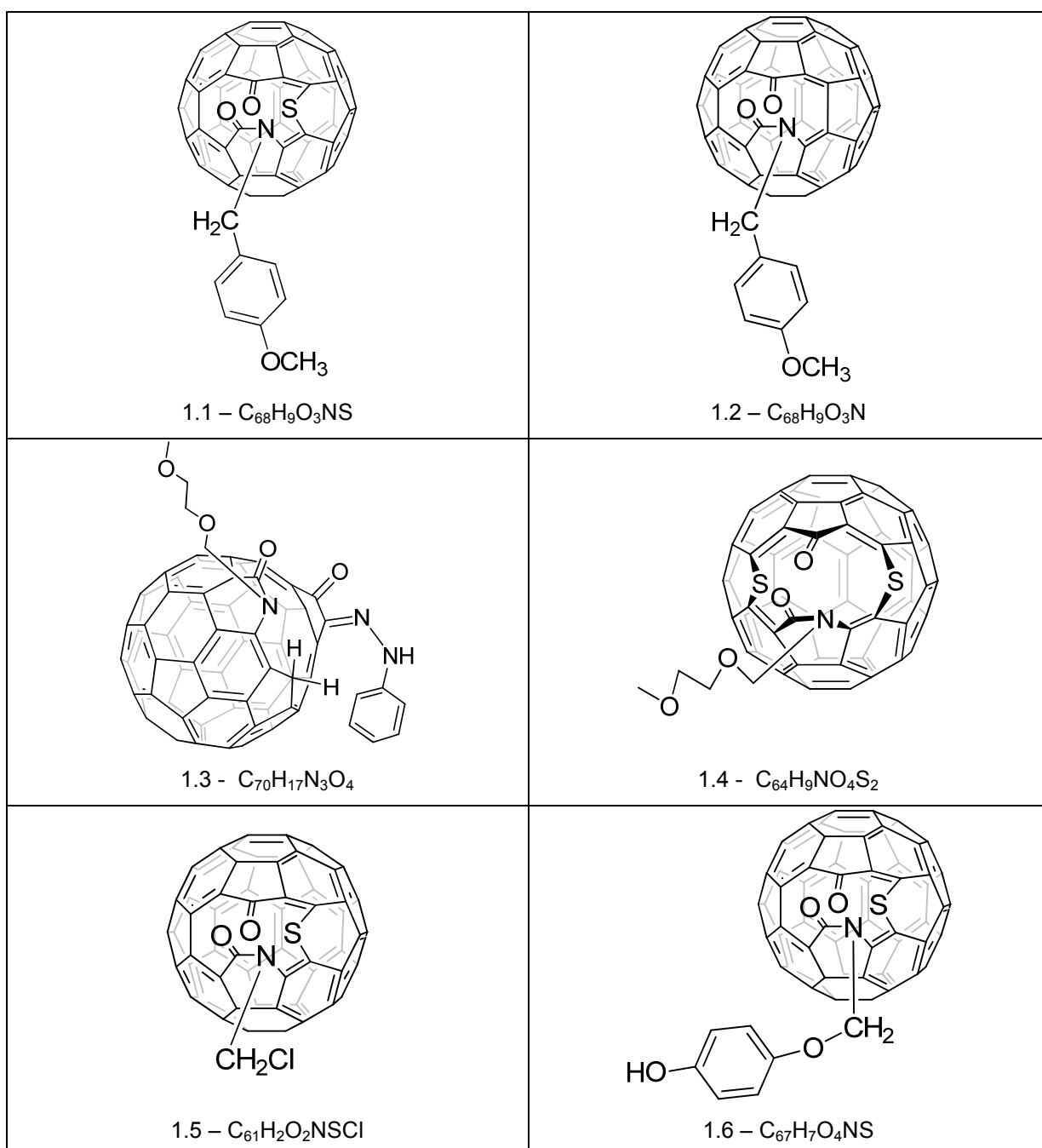


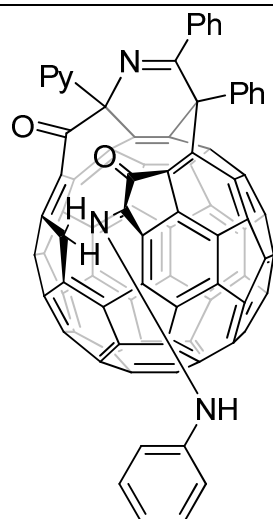
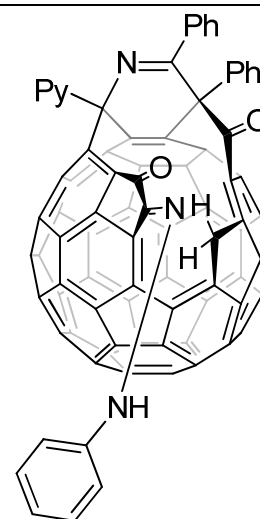
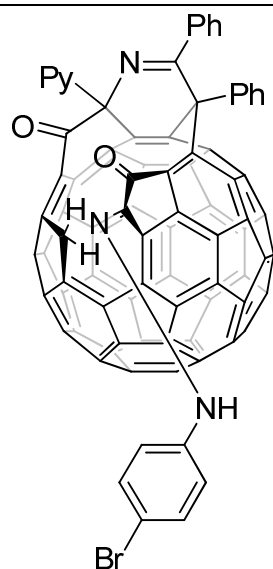
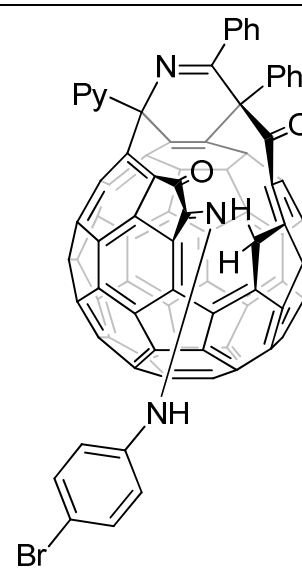
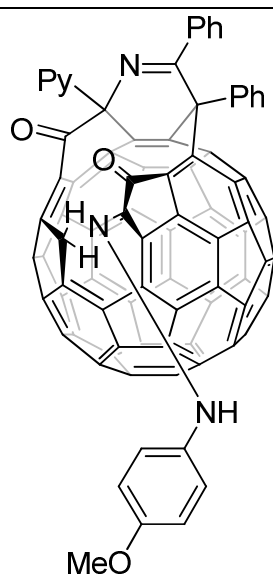
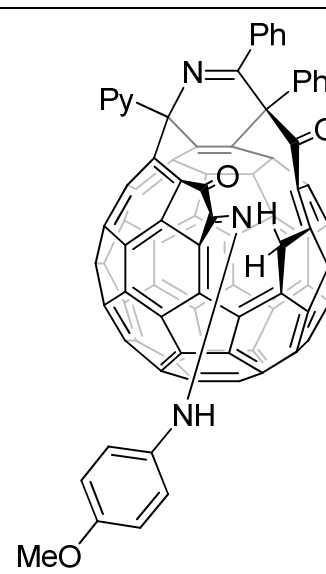
Figure 3.3: Structure of $C_{60}N_2MEM_2$

Experimental

All samples were synthesized by Manolis Tzirakis and Professor Mike Orfanopoulos at the University of Crete, and were used as received.

Open-Cage Fullerenes:



2.1 - $C_{86}H_{22}N_4O_2$ 2.2 - $C_{86}H_{22}N_4O_2$ 2.3 - $C_{86}H_{21}N_4O_2Br$ 2.4 - $C_{86}H_{21}N_4O_2Br$ 2.5 - $C_{87}H_{24}N_4O_3$ 2.6 - $C_{87}H_{24}N_4O_3$

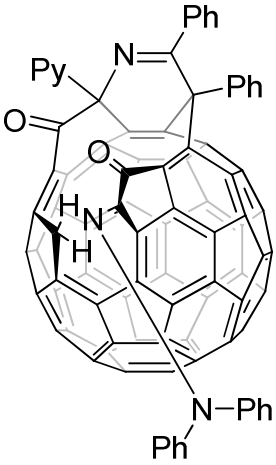
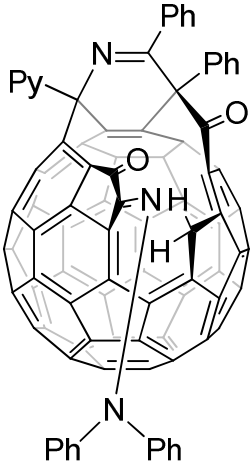
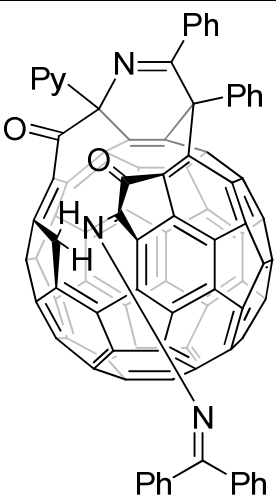
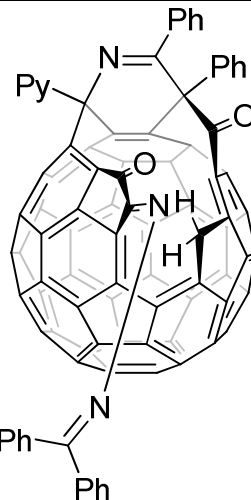

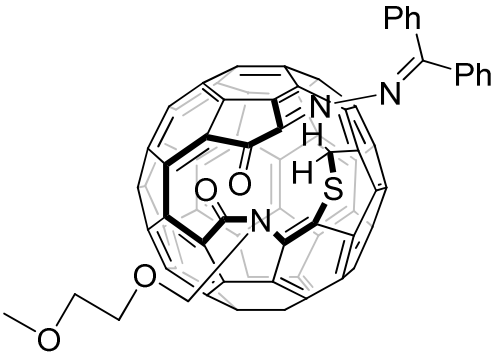
 <p>2.7 - $C_{92}H_{26}N_4O_2$</p>	 <p>2.8 - $C_{92}H_{26}N_4O_2$</p>
 <p>2.9 - $C_{93}H_{26}N_4O_2$</p>	 <p>2.10 - $C_{93}H_{26}N_4O_2$</p>
 <p>2.11 - $C_{60}HNO_2S_2$</p>	 <p>2.12 - $C_{77}H_{21}N_3O_4S$</p>

Table 3.1: Structures of the OCFs

Other Fullerene Derivatives

Other novel fullerene derivatives synthesized included the formal exchange of a carbon for a nitrogen atom in the sphere and then addition of a ligand:

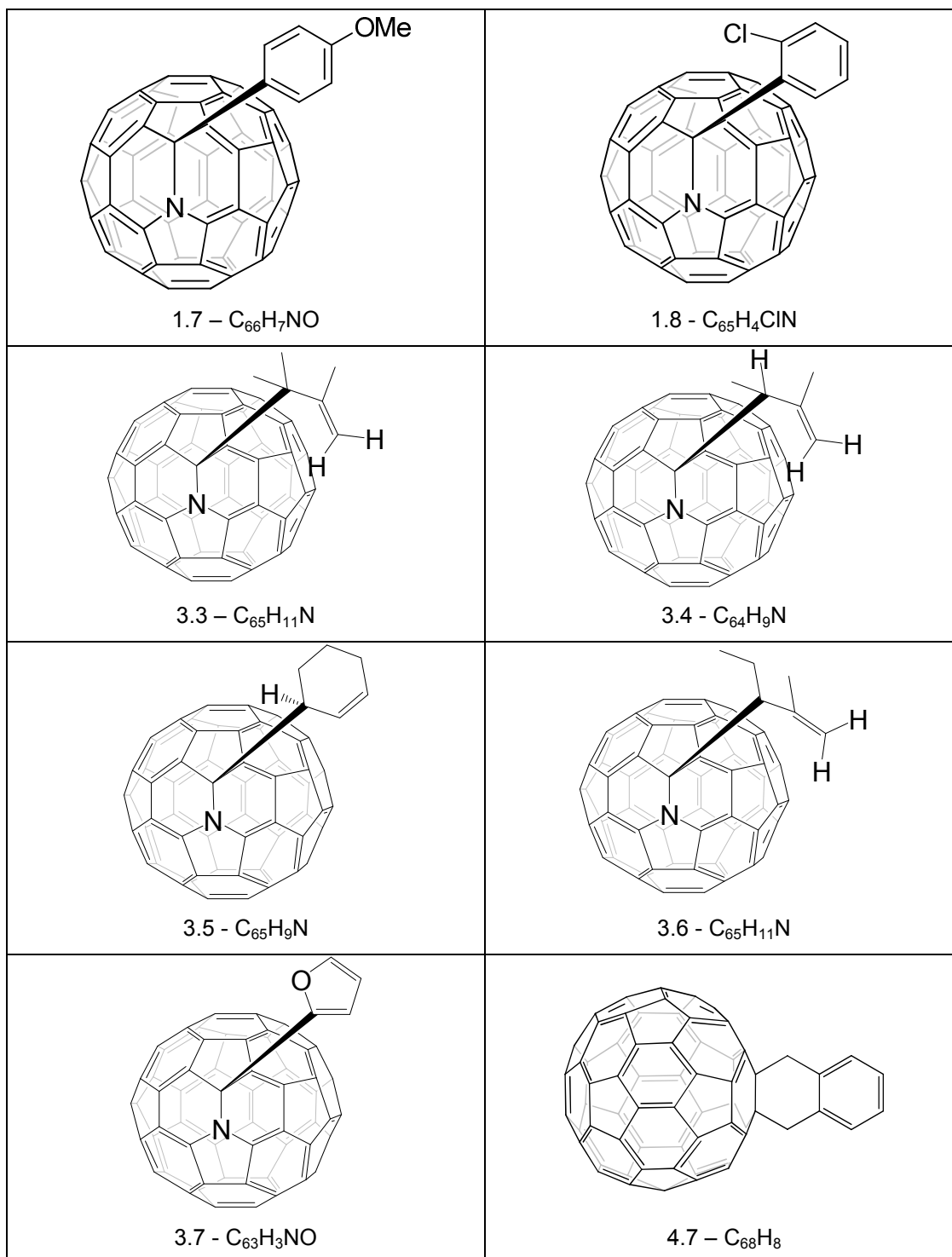
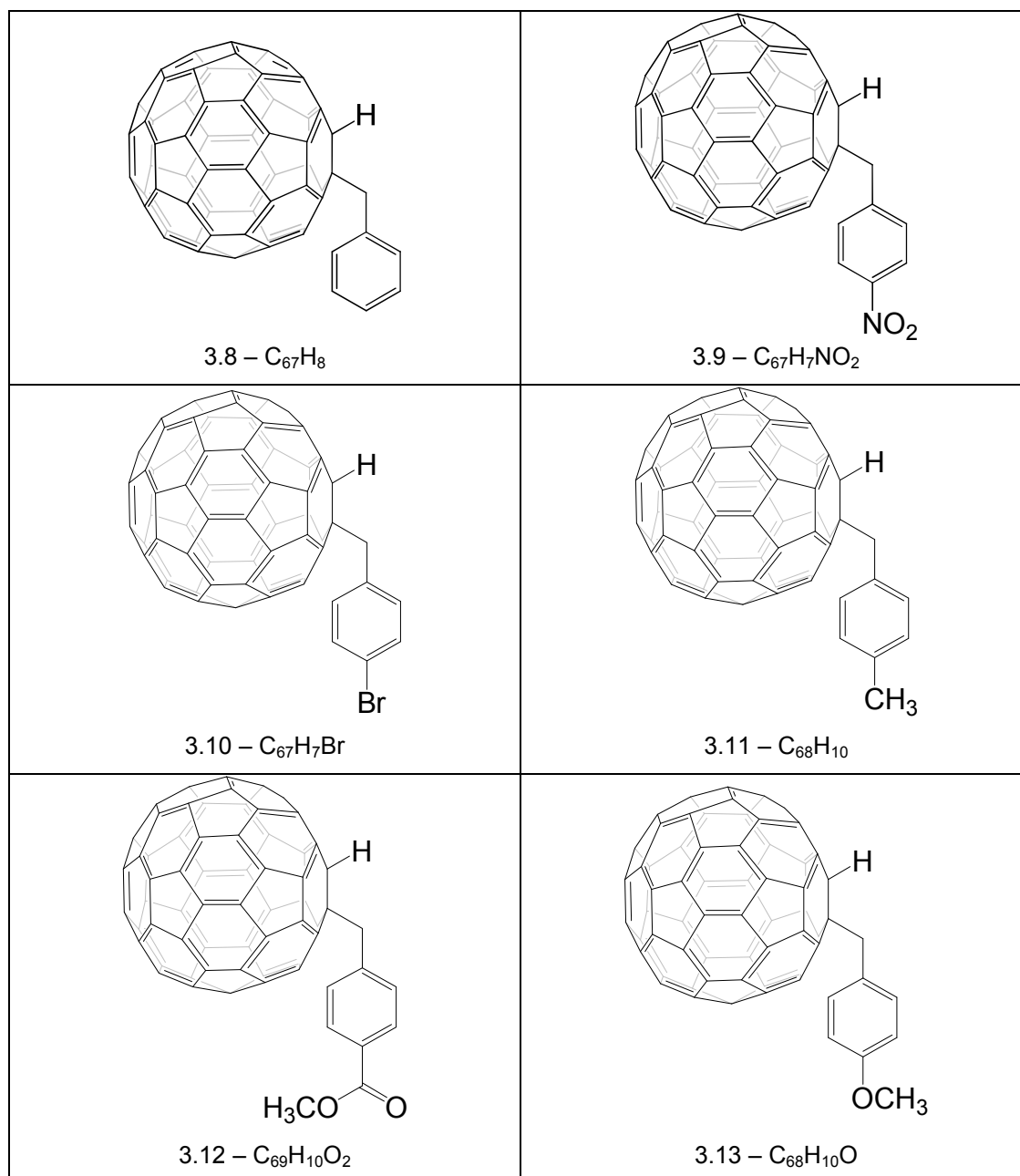


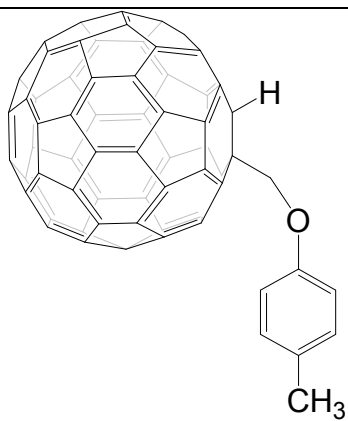
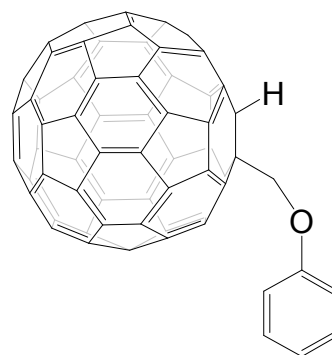
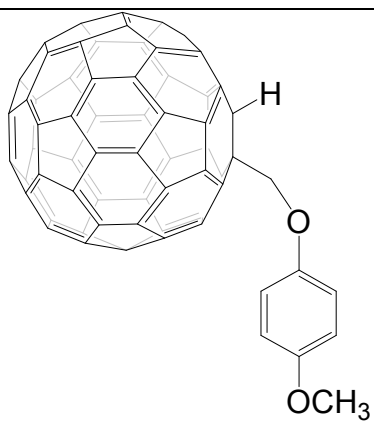
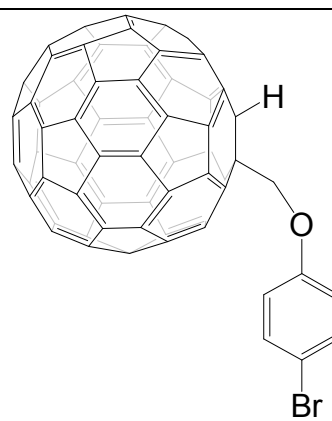
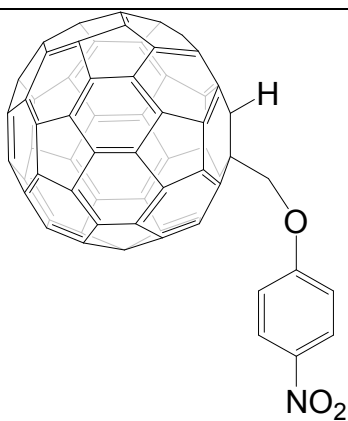
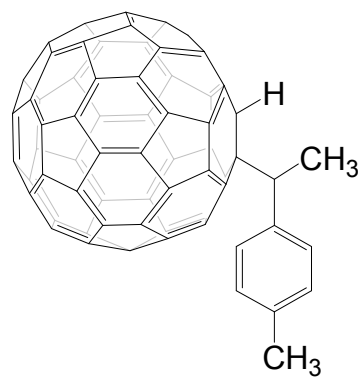
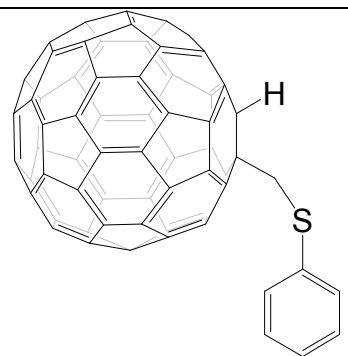
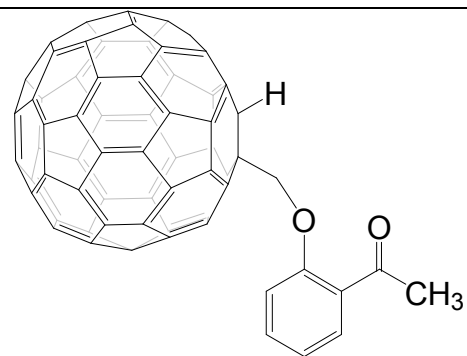
Table 3.2: Structures of monoligated azafullerenes

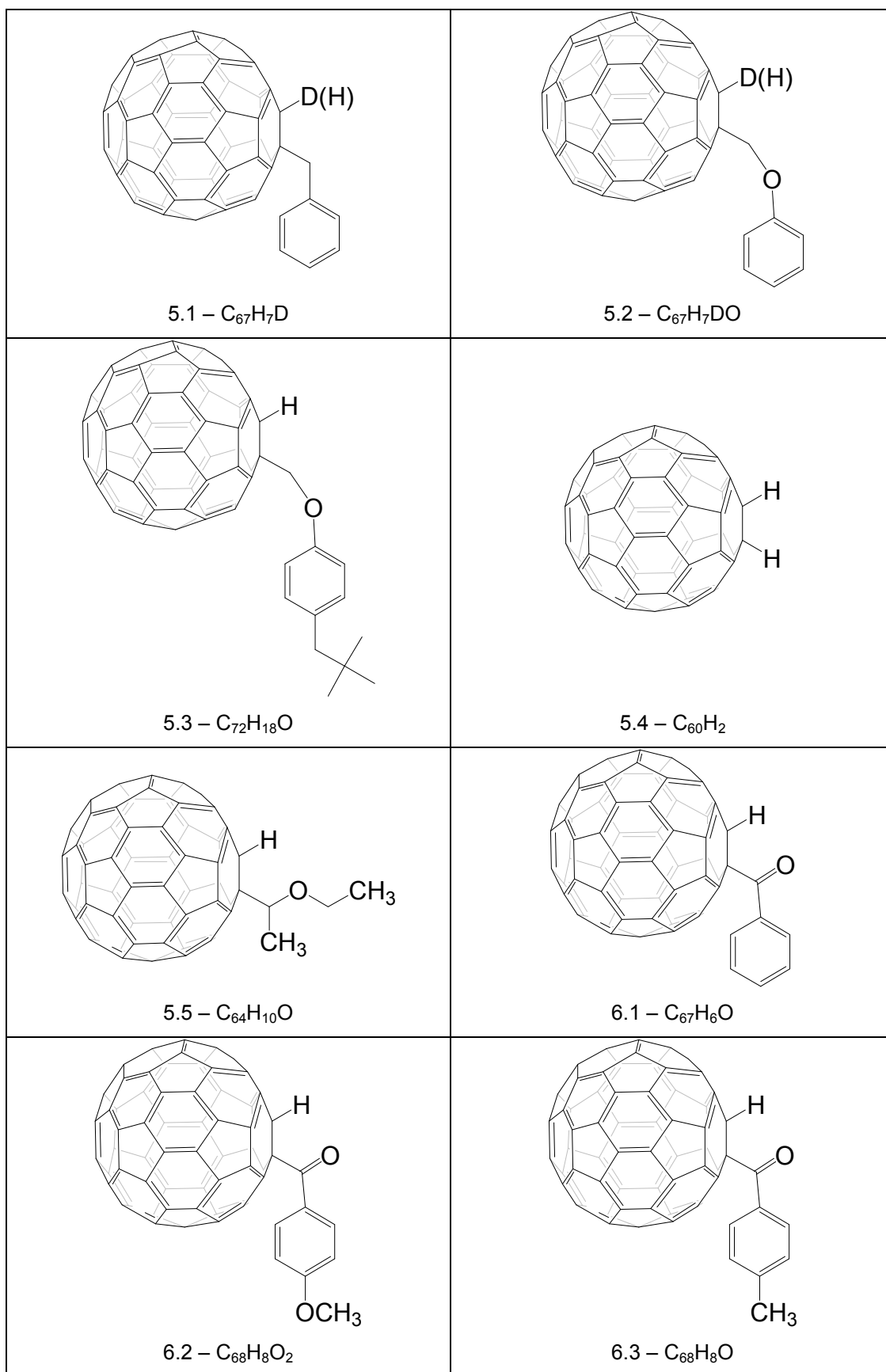
Note that compound 4.7 is displayed here although it does not belong to the class of monoligated azafullerenes. However, compound 4.7 is a cycloaddition [60] fullerene

derivative which was also synthesised in collaboration by the Orfanopoulos group as an important target molecule for our silver cation experiments (chapter 8).

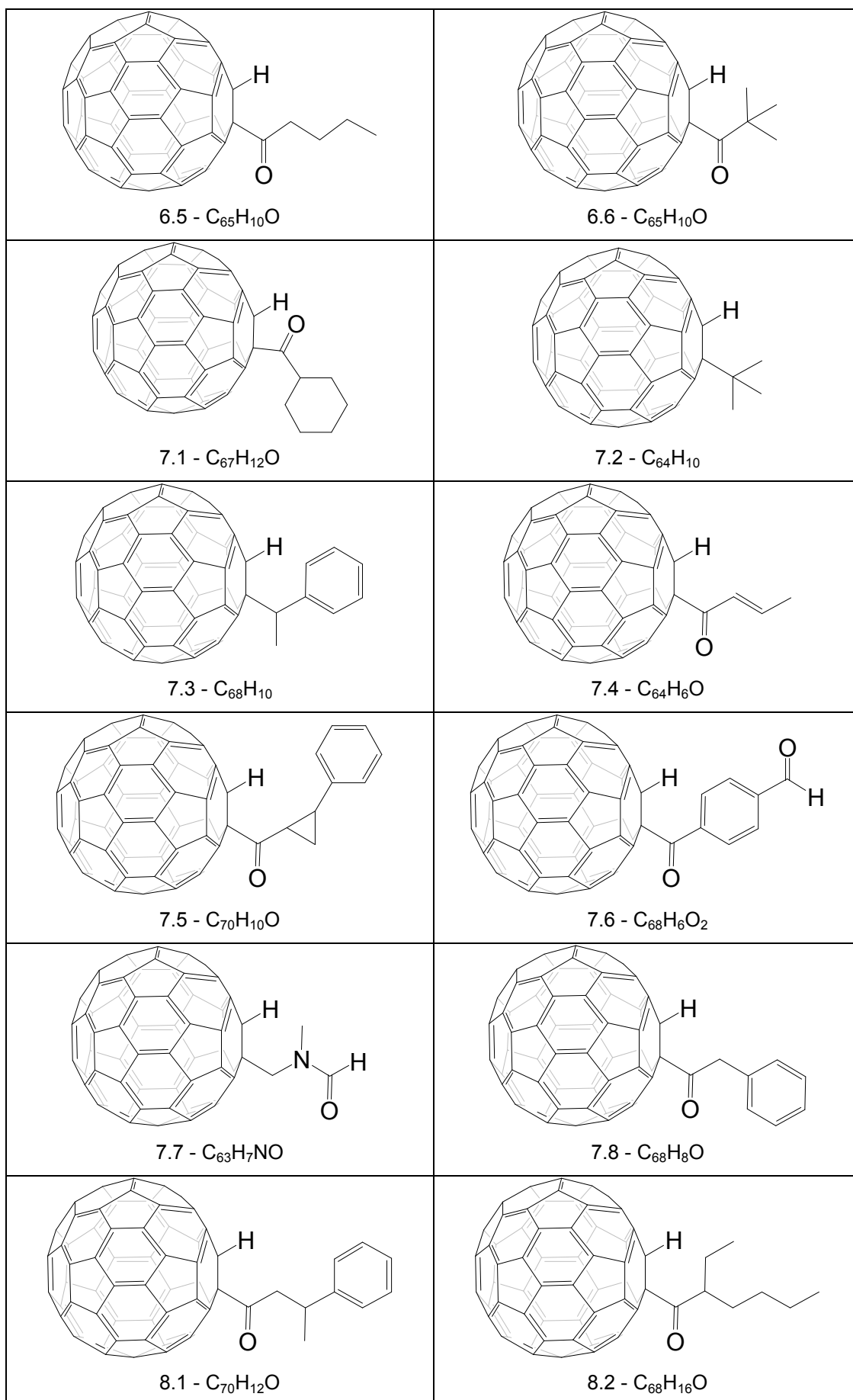
Formally replacing the nitrogen atom in compounds 1.7, 1.8, 3.3 – 3.7 leads to [60] fullerene derivatives with one hydrogen and one organic ligand attached to the sphere:

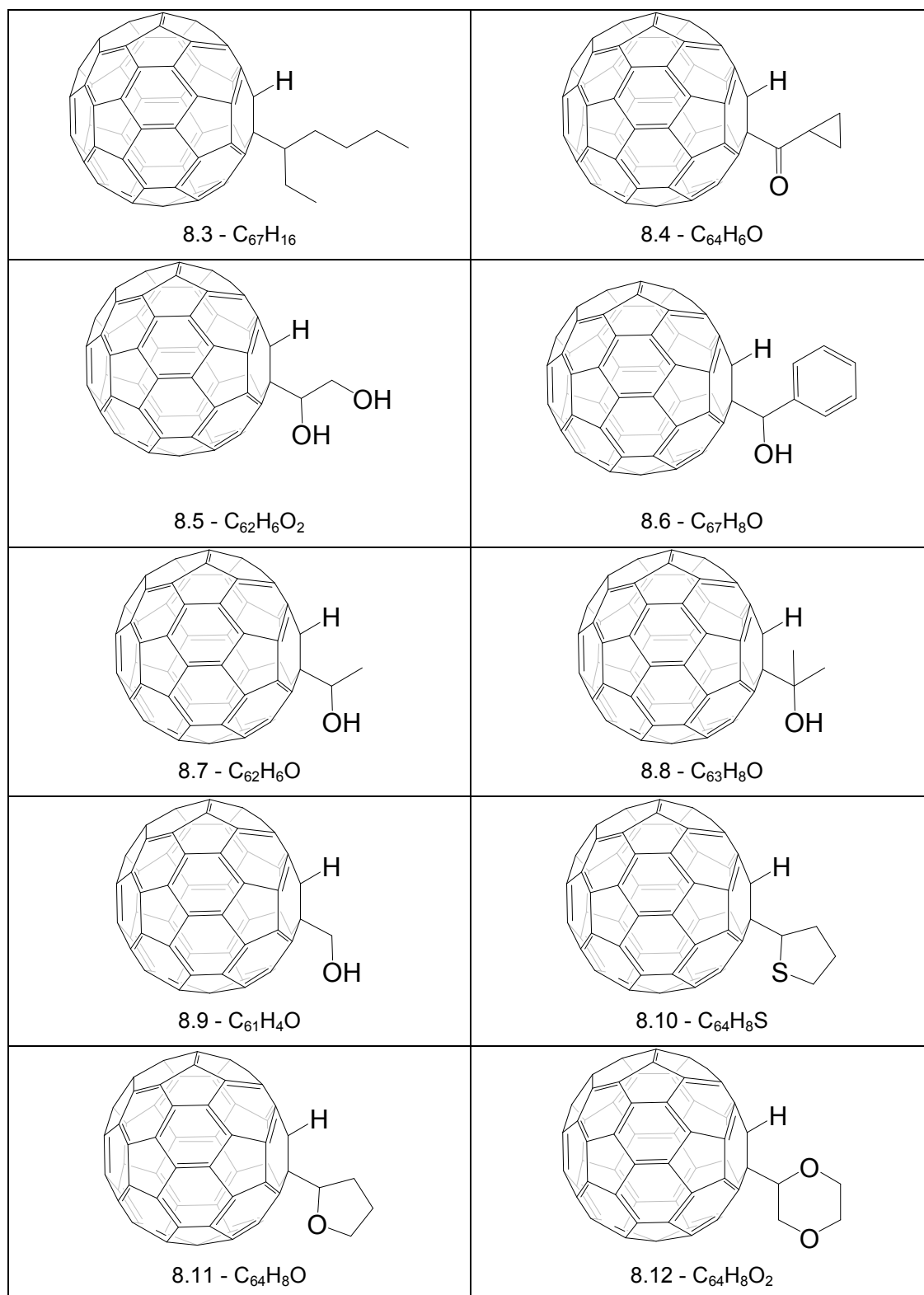


3.14 - C₆₈H₁₀O3.15 - C₆₇H₈O4.1 - C₆₈H₁₀O₂4.2 - C₆₇H₇OBr4.3 - C₆₇H₇NO₃4.4 - C₆₉H₁₂4.5 - C₆₇H₈S4.6 - C₆₉H₁₀O₂



In compound 5.4, the organic ligand was replaced by another hydrogen, leading to $C_{60}H_2$





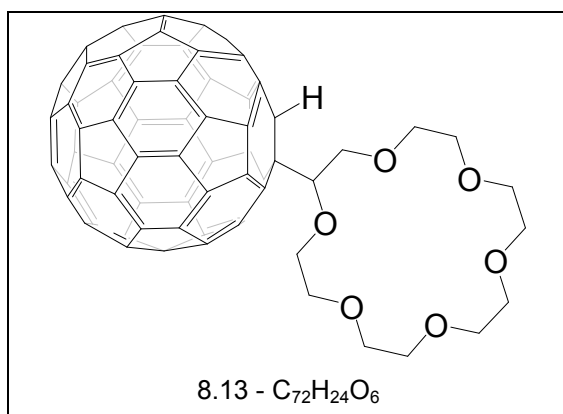


Table 3.3: Structures of the remaining fullerene derivatives

The numbering system is of no real importance and is related to the order in which sets of compounds were received. As a result there may appear to be “missing samples”: samples 3.1 and 3.2 are purified versions of samples 2.5 and 2.8 respectively. Sample 6.4 was the same as sample 3.8. Hence, these samples are not listed above.

For all MALDI experiments, DCTB was used as the matrix.

A fullerene mixture was used to calibrate the Bruker Ultraflex. It consisted mainly of C₆₀ and C₇₀, with small amounts of C₈₄, C₉₀, C₉₆.

Sample and matrix were both dissolved in toluene, individually. DCTB was prepared in a 10 mg/ml solution.

The sample and matrix were mixed in an approximately 1:50 molar ratio. As the amount of DCTB solution to add was based on what the molecular weight of the sample was thought to be, if a sample had not been synthesized as expected, then the molecular ratio of DCTB:sample would not be 50:1. A typical sample preparation is listed below:

Sample 5.3, R.M.M 898 Da, was dissolved in an approximately* 1 mg/ml concentration solution, and thoroughly dissolved using a Whirlimixer. (*Due to the very small amounts of sample received, less than a milligram, weighing the sample would not have been as accurate as for larger amounts.)

10µl of the 1 mg/ml solution of sample 5.3, was mixed with 14 µl of a 10 mg/ml DCTB solution, thoroughly mixed with the Whirlimixer, and then applied to the MALDI slide using a 1-10µl Baryk µtipipette. Typically between 3 and 5µl was applied per target spot. The solution was applied a drop at a time, which was allowed to dry between each application. The drying was assisted by a MALDI IV slide drying machine, which blew a stream of room

temperature air over the surface of the target slide. The calibration mixture was applied in close proximity to the sample spots. Machine calibration occurred at the start of the experiment and after every two samples that had been analysed. A final calibration was performed on the spectra after acquisition, as part of the processing.

The spectra were saved and processed collectively after data acquisition had finished. Processing included the final calibration, and the production of a mass list which labelled all the peaks with their m/z value to at least 3 decimal places.

For collision induced dissociation experiments, LIFT mode was employed on the Bruker Ultraflex II. Samples were prepared as normal.

Results

MALDI Analysis

As a first step the identity of the synthetic samples was checked by applying DCTB-MALDI in both ion modes. The majority of the compounds had been synthesized as expected and a summary is presented in the table below. The experiments provided also evidence of the applicability of DCTB-MALDI with open cage fullerenes, as a means to generate molecular ions with only little fragmentation. In general, molecular ion peaks were seen using both ion modes. Negative-ion mode generally produced cleaner spectra, with the intensity of the molecular ion peak being more abundant than that of any fragmentation. Most negative-ion spectra showed reduced fragmentation. The possible oxidation of the samples was also better seen for negative ions. If both polarities are listed in the table below, then the molecular ion was clearly present and mostly abundant for both, however, the polarity listed first produced spectra of a slightly higher quality. Few samples were only successfully analysed in one ion-mode and if so, this tended to be in negative-ion mode.

Sample	Expected R.M.M	Present in Spectra	Best Polarity
1.1	919	Yes	Negative and Positive
1.2	887	Yes	Negative
1.3	963	No	-
1.4	919	No	-
1.5	847.5 (Cl)	Yes	Positive and Negative
1.6	921	Yes	Negative
1.7	829	Yes	Negative
1.8	833.5 (Cl)	Yes	Positive and Negative
2.1	1142	Yes	Negative
2.2	1142	Yes	Negative
2.3	1221 (Br)	Yes	Negative
2.4	1221 (Br)	Yes	Negative
2.5	1172	Yes	Negative and Positive

2.6	1172	Yes	Negative
2.7	1218	Yes	Positive and Negative
2.8	1218	Yes	Negative and Positive
2.9	1230	Yes	Negative
2.10	1230	Yes	Negative
2.11	831	Yes	Negative
2.12	1083	Yes	Negative
3.3	805	No	-
3.4	791	No	-
3.5	803	No	-
3.6	805	No	-
3.7	789	Yes	Positive and Negative
3.8	812	Yes	Negative and Positive
3.9	857	Yes	Negative and Positive
3.10	891	Yes	Negative and Positive
3.11	826	Yes	Negative and Positive
3.12	870	Yes	Negative and Positive
3.13	842	Yes	Negative and Positive
3.14	842	Yes	Negative and Positive
3.15	828	Yes	Negative and Positive
4.1	858	Yes	Negative and Positive
4.2	907	Yes	Negative and Positive
4.3	873	Yes	Negative and Positive
4.4	840	No	-
4.5	844	Yes	Negative and Positive
4.6	870	Yes	Negative
4.7	824	Yes	Positive and Negative
5.1	813 (D)	Yes	Negative and Positive
5.2	829 (D)	Yes	Negative and Positive

5.3	898	Yes	Negative and Positive
5.4	722	Yes	Positive and Negative
5.5	794	Yes	Negative and Positive
6.1	826	Yes	Negative and Positive
6.2	856	Yes	Negative
6.3	840	Yes	Negative
6.5	806	Yes	Negative and Positive
6.6	806	Yes	Negative and Positive
7.1	832	Yes	Negative and Positive
7.2	778	Yes	Negative and Positive
7.3	826	Yes	Negative and Positive
7.4	790	Yes	Negative and Positive
7.5	866	Yes	Negative and Positive
7.6	854	Yes	Negative and Positive
7.7	793	Yes	Negative and Positive
7.8	840	Yes	Negative and Positive
8.1	868	Yes	Negative and Positive
8.2	848	Yes	Negative and Positive
8.3	820	Yes	Negative and Positive
8.4	790	Yes	Negative and Positive
8.5	782	Yes	Negative and Positive
8.6	828	Yes	Negative
8.7	766	Yes	Negative and Positive
8.8	780	Yes	Negative
8.9	752	Yes	Negative and Positive
8.10	808	No	-
8.11	792	Yes	Negative and Positive
8.12	808	Yes	Negative and Positive
8.13	984	Yes	Negative and Positive

Table 3.4: Results of DCTB-MALDI analysis of all samples in both ion modes

With the exception of samples 1.3, 1.4, 3.3, 3.4, 3.5, 3.6, 4.4 and 8.10, all samples produced molecular ion peaks at the expected m/z values.

The samples were not purified prior to analysis, as was evidenced by the appearance of a peak at m/z 1034 in the spectra of the open cage fullerenes in set 2 (samples labelled 2.x) – this was the mass of the precursor molecule in the synthesis.

For compounds that contained an element with distinctive isotopes, the isotopic pattern was very useful in showing that synthesis had been successful through comparison with the calculated pattern.

A few representative MALDI mass spectra are displayed and discussed below. The remaining spectra can be found in the appendix.

1.2 – $C_{68}H_9O_3N$

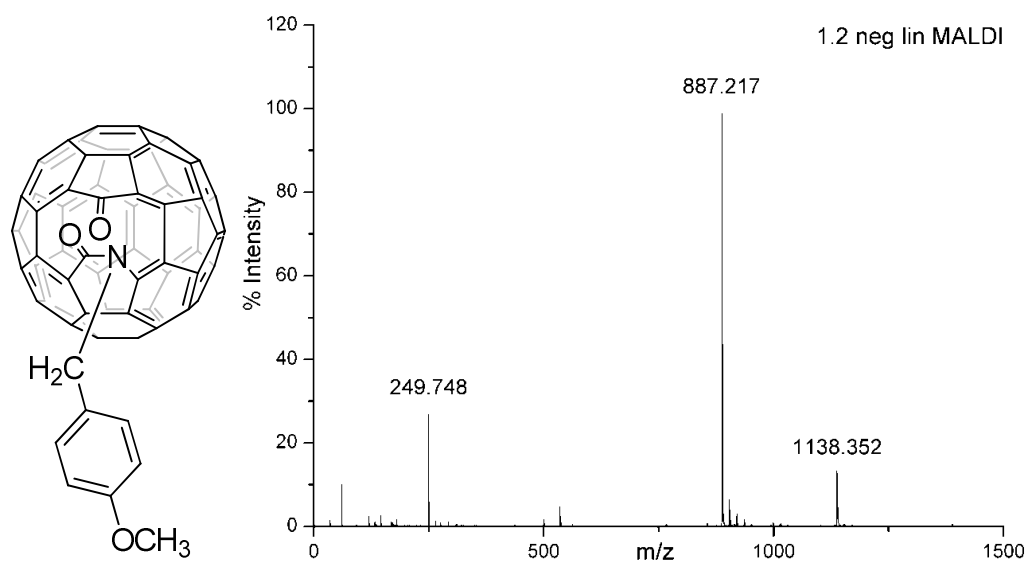


Figure 3.4: Structure and negative-ion mode MALDI spectrum of 1.2

The molecular ion peak is the most intense in the spectrum, at m/z 887.2. The peak at m/z 249.7 is $DCTB^-$, and the peak at m/z 1138.3 is $[C_{68}H_9O_3N-DCTB-H]^-$. Some oxidation of the molecular ion is evident. The spectrum was obtained in negative-ion mode with linear detection.

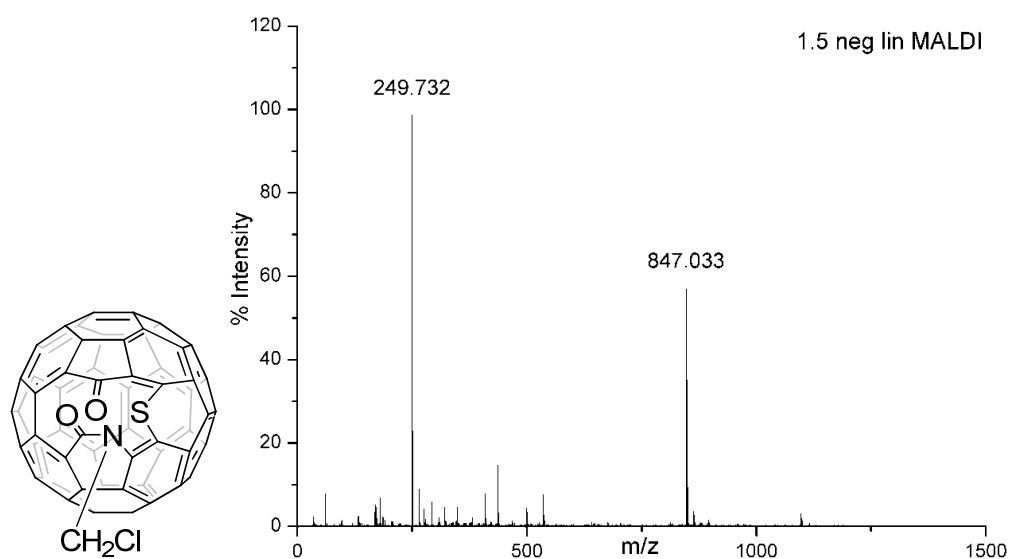
1.5 – C₆₁H₂O₂NSCl

Figure 3.5: Structure and negative-ion mode MALDI spectrum of 1.5

In this spectrum the DCTB⁻ peak at m/z 249.7 is the most intense, followed by the molecular ion at m/z 847.0. The spectrum was obtained in negative-ion mode, with linear detection. By enlarging the molecular ion region, the isotopic pattern is clearly displayed. A simulated pattern of the isotopic pattern, created by Bruker software – Bruker Daltonics IsotopePattern, shows the excellent match with the measured isotopic pattern, further confirmation that the empirical formula is correct and that the true molecular ion had been obtained, as opposed to the deprotonated (negative-ion mode) or the protonated species (positive-ion mode).

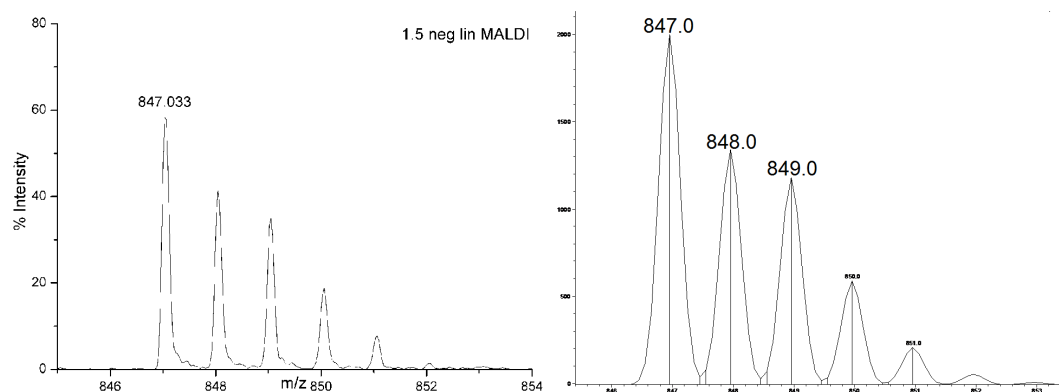


Figure 3.6: Enhanced molecular ion region of 1.5, left, and simulated mass spectrum of 1.5, right

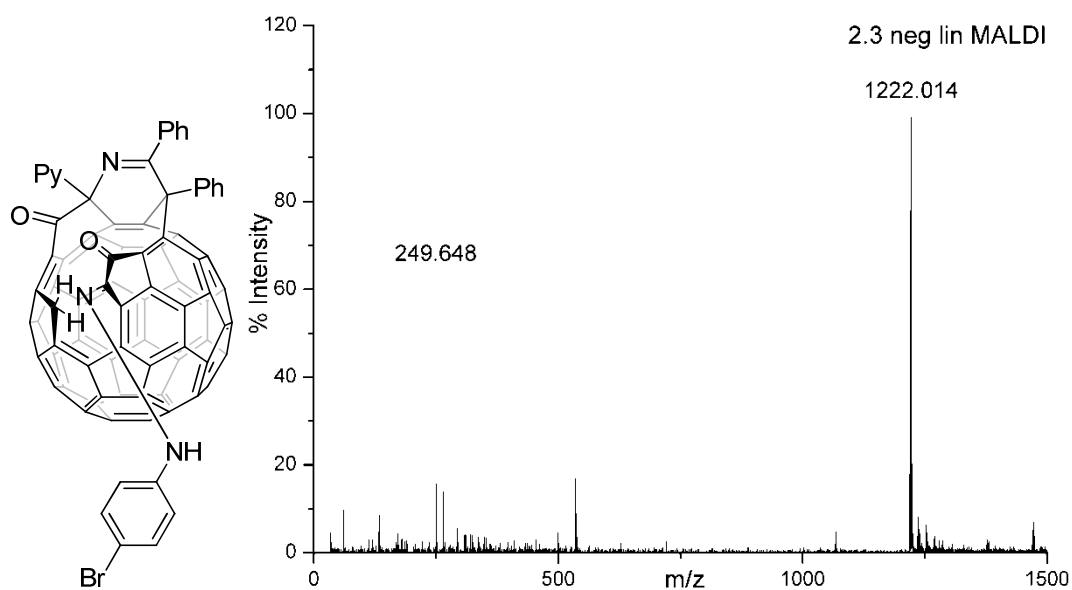
2.3 - C₈₆H₂₁N₄O₂Br

Figure 3.7: Structure and negative-ion mode spectrum of 2.3

In this negative-ion mode spectrum obtained with linear detection, the molecular ion peak at m/z 1222.0, is the most intense. DCTB⁻ is also present. Examination of the isotopic pattern demonstrates the presence of bromine, and matches the simulated (Bruker software) isotopic pattern.

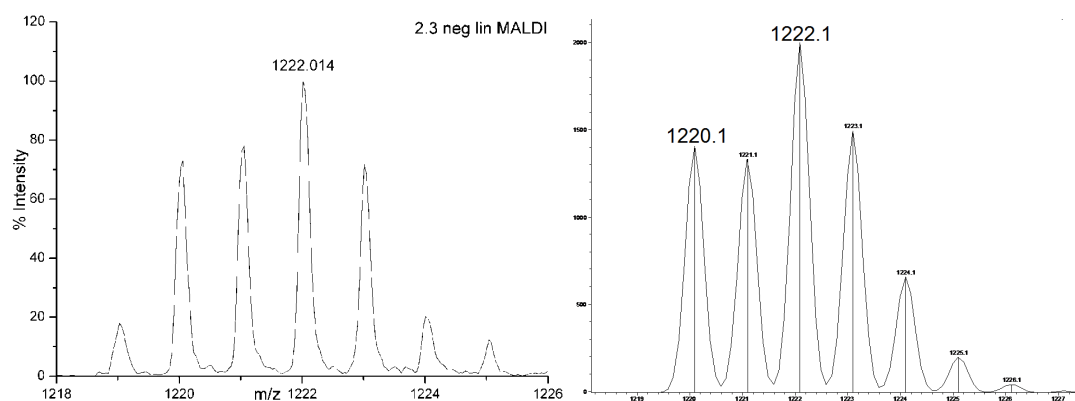


Figure 3.8: Enhanced molecular ion region of 2.3, left, and simulated mass spectrum of 2.3, right

There is a slight hydrogen loss evident, as can be observed by the appearance of a peak at m/z 1219. This could also explain the slight enhancement of the peak at m/z 1221, in relation to the peak at m/z 1220.

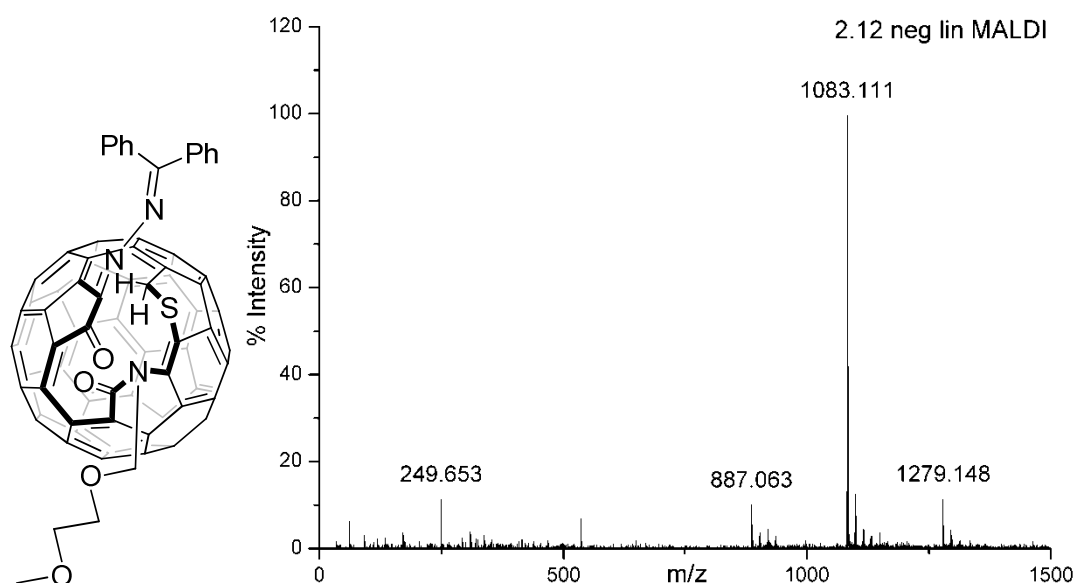
2.12 - $C_{77}H_{21}N_3O_4S$ 

Figure 3.9: Structure and negative-ion mode MALDI spectrum of 2.12

The molecular ion of sample 2.12, at m/z 1083.1, is the most prominent peak in the spectrum. DCTB⁻ is also present in this negative-ion mode spectrum. Two peaks, spaced 196 mass units either side of the molecular ion peak, suggest that this sample had an additional $-N=N=CPh_2$ group attached in very small quantities and that the $-N=N=CPh_2$ is easily lost from the open-cage fullerene. Oxidation is evident for all of these compounds, through the appearance of additional signals at the high mass end spaced by 16 mass units (additional oxygen atoms) These were also observed for the smaller peaks either side of the molecular ion. This suggests that these compounds were present in the sample, and not produced during the experiment.

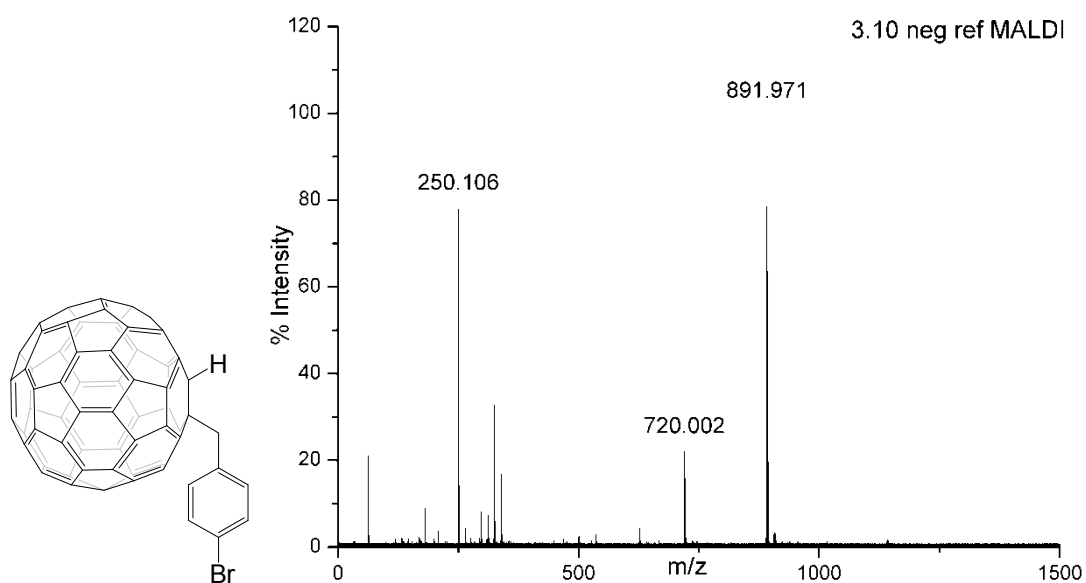
3.10 - C₆₇H₇Br

Figure 3.10: Structure and negative-ion mode MALDI spectrum of 3.10

In this negative-ion mode spectrum, detected with the reflectron detector, the most intense peak is the molecular ion peak, at m/z 891.9. The C₆₀⁻ fragment is present at m/z 720. DCTB⁻ is present at m/z 250.1.

Comparison of the molecular ion peak to the simulated isotopic pattern is shown below. The isotopic pattern clearly demonstrates the presence of bromine and is a perfect match to the simulated pattern. There is a very small peak at m/z 889, which represents the loss of a hydrogen atom.

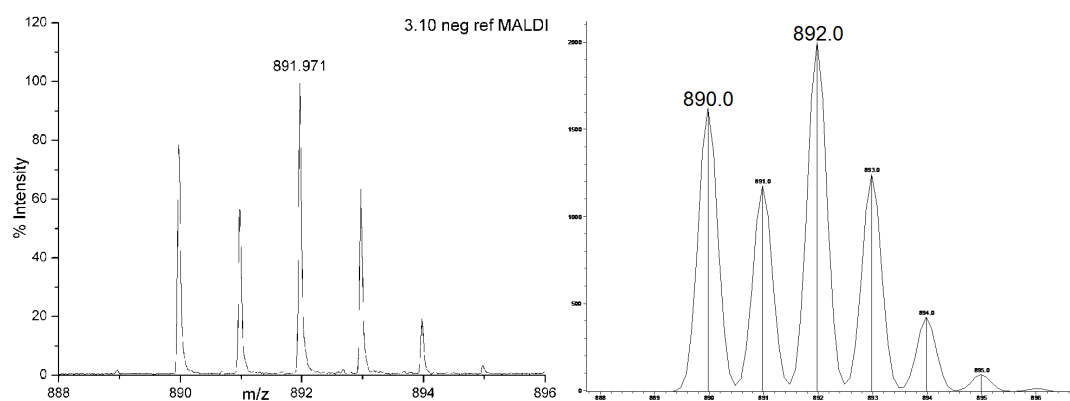


Figure 3.11: Enhanced molecular ion region of 3.10, left, and simulated mass spectrum of 3.10, right

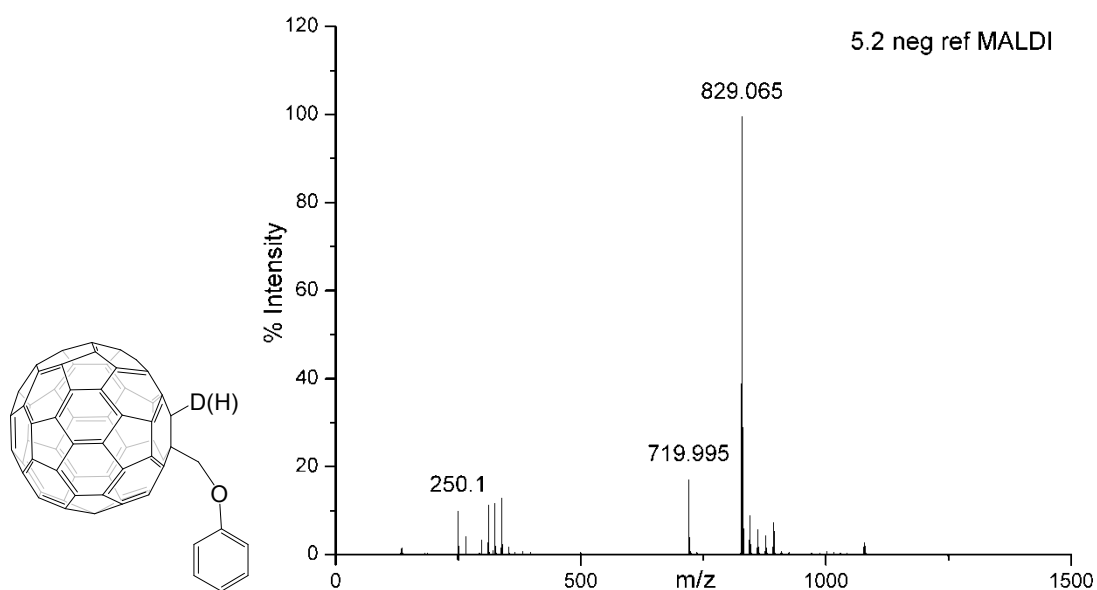
5.2 - C₆₇H₇DO

Figure 3.12: Structure and negative-ion mode MALDI of 5.2

The molecular ion is present at m/z 829.0, with $DCTB^-$ at m/z 250.1, and C_{60}^- at m/z 719.9. Enhancement of the molecular ion peak, shown below, demonstrates the isotopic pattern of $C_{60}DCH_2OC_6H_5$, with the dominant peak at m/z 829.065. The m/z values from 830 to 832 represent the normal isotopic pattern of this compound. The peak at m/z 828 is from the undeuterated molecule as only about 70% of the product was successfully deuterated in the synthesis. The peak at m/z 827 is loss of either the hydrogen or deuterium.

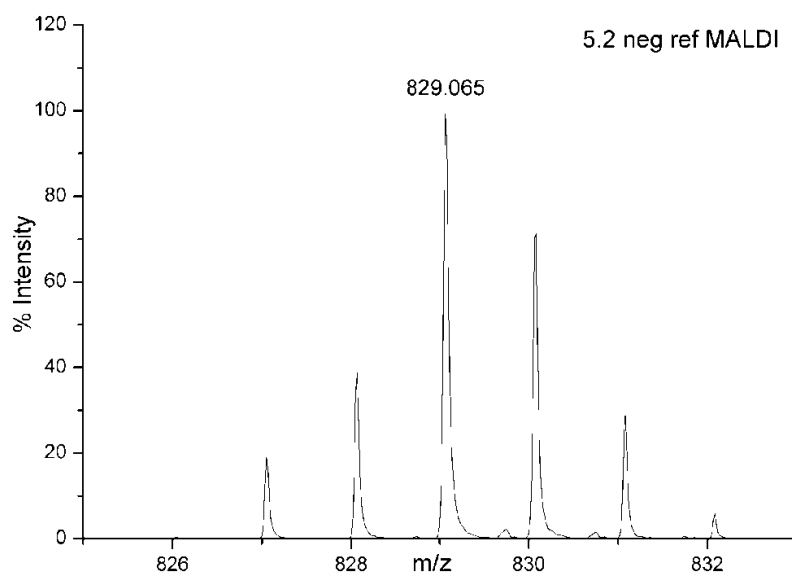


Figure 3.13: Enhanced molecular ion region of 5.2

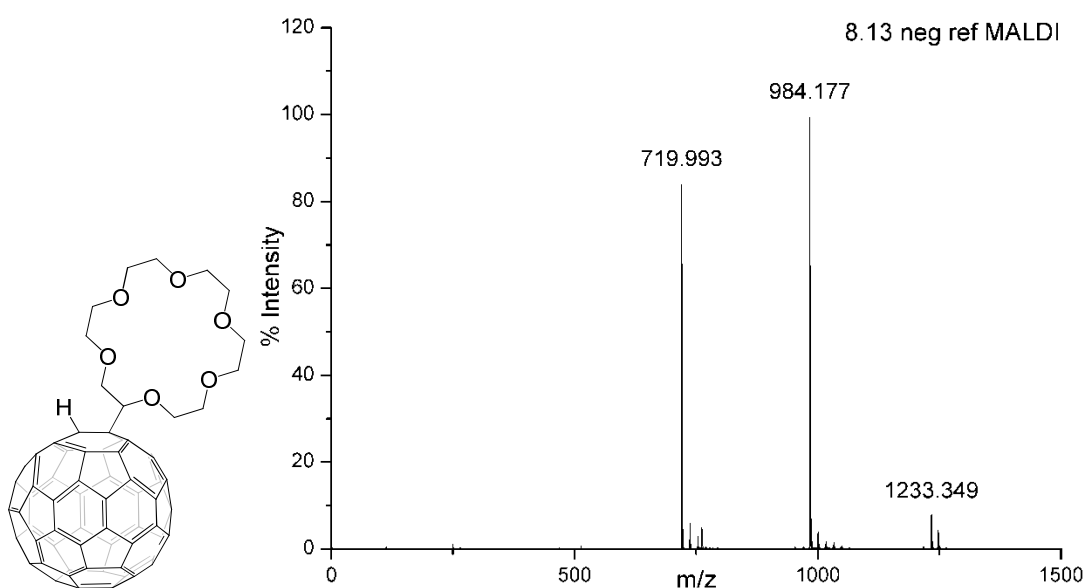
8.13 - $C_{72}H_{24}O_6$ 

Figure 3.14: Structure and negative-ion mode MALDI of 8.13

The molecular ion peak is at m/z 984.1, with prominent fragmentation in the form of C_{60}^- at 719.9, and DCTB addition (with the loss of a hydrogen from 8.13) at m/z 1233.3. Studying the isotopic pattern of the molecular ion from m/z 984 to 987, demonstrates the loss of one hydrogen atom with the peak at m/z 983.

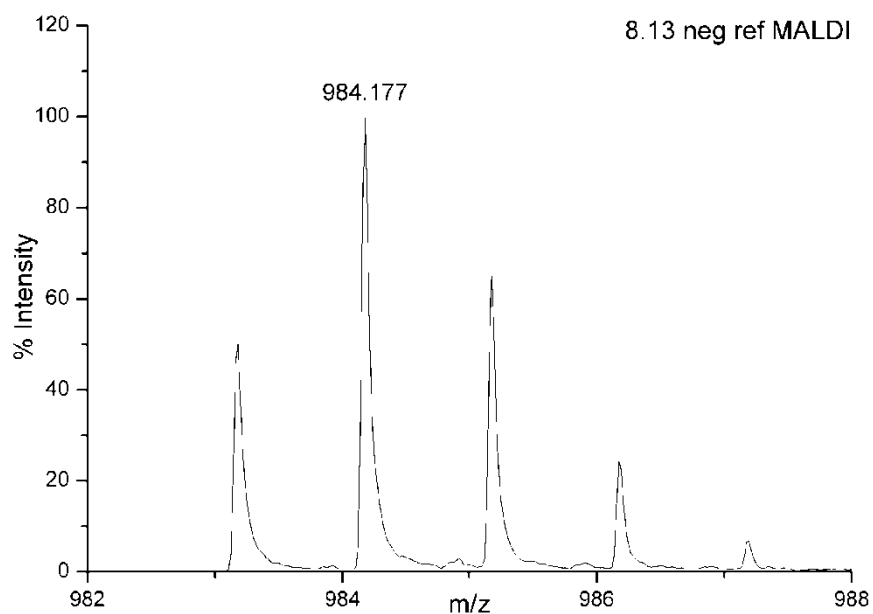


Figure 3.15: Enhanced molecular ion region of 8.13

Cage re-healing by “harsh” MALDI and direct LDI

Activation of the compounds under study by increasing the laser fluence was used in order to deliberately induce fragmentation. In the case of the open cage fullerenes, it was hoped that the laser activation would reheat the cage back to either C_{60} or even $C_{59}N$.

Previous MALDI experiments with increased laser power have shown that fullerene derivatives with an exohedral nitrogen tend to fragment to $C_{59}N$ as well as C_{60} , with $C_{59}N$ occasionally being produced in greater quantities¹⁹. This has interesting implications for experiments where helium has been trapped in an open cage fullerene which has then been reheated to C_{60} via laser irradiation¹³. As $He@C_{60}$ and $C_{59}N$ have almost exactly the same m/z , this would require an extremely high resolution and mass accuracy to distinguish between the two species.

Provided that for future experiments OCF's with an endohedral guest were available, the present experiments would indicate how the cage would close upon activation. Starting with an open cage C_{60} fullerene with endohedral guest, laser treatment could trap the endohedral guest within a $C_{59}N$ cage to which the OCF has collapsed.

The resulting cage closures applying MALDI and LDI experiments with increased laser fluence are described in the table below:

OCF	Positive LDI	Negative LDI	Positive MALDI	Negative MALDI
1.1	$C_{59}N$	$C_{59}N$	C_{60}	C_{60} and $C_{59}N$
1.2	Mainly $C_{59}N$	$C_{59}N$	$C_{59}N$	Mainly $C_{59}N$
1.5	Mainly $C_{59}N$	Mainly $C_{59}N$	$C_{59}N$	Mainly $C_{59}N$
1.6	Mainly $C_{59}N$	Mainly $C_{59}N$	$C_{59}N$	Mainly $C_{59}N$
2.1	Mainly $C_{59}N$	C_{60} and $C_{59}N$	C_{60} and $C_{59}N$	C_{60}
2.2	Mainly $C_{59}N$	C_{60} and $C_{59}N$	Mainly $C_{59}N$	C_{60}
2.3	Mainly $C_{59}N$	C_{60} and $C_{59}N$	Mainly C_{60}	C_{60}
2.4	Mainly $C_{59}N$	C_{60} and $C_{59}N$	C_{60}	C_{60}
2.5	Mainly $C_{59}N$	Mainly C_{60}	C_{60}	C_{60}
2.6	Mainly $C_{59}N$	C_{60} and $C_{59}N$	C_{60}	C_{60}
2.7	Mainly $C_{59}N$	C_{60} and $C_{59}N$	C_{60} and $C_{59}N$	C_{60}

2.8	Mainly C ₅₉ N	Mainly C ₆₀	C ₆₀ and C ₅₉ N	C ₆₀
2.9	Mainly C ₅₉ N	C ₆₀ and C ₅₉ N	Mainly C ₅₉ N	C ₆₀
2.10	Mainly C ₅₉ N	Mainly C ₅₉ N	C ₆₀ and C ₅₉ N	C ₆₀
2.11	C ₅₉ N	C ₅₉ N	Mainly C ₅₉ N	C ₅₉ N
2.12	C ₅₉ N, C ₅₈ N ₂	C ₅₈ N ₂ , low C ₅₉ N	C ₅₉ N, C ₅₈ N ₂	C ₅₉ N, C ₅₈ N ₂

Table 3.5: Results of increased laser fluence on the OCFs

The above table shows results that were obtained by activation of the sample at elevated laser fluences under normal operating conditions; that is neither LIFT nor CID were applied in these experiments (no MS/MS at this stage).

The experiments lead to interesting observations; linking original structure with the resulting heated fragment; also MALDI and LDI lead to different results. For example, LDI of samples 2.1 to 2.10 leads predominantly to the formation of C₅₉N, while MALDI leads to C₆₀ as the dominant or only fragment.

Sample 2.12 produced an entirely unexpected result in the formation of what appeared to be mainly C₅₈N₂, with small amounts of C₅₉N and even less, if any, amounts of C₆₀. This was the case for both MALDI and LDI. This was not a matter of calibration, as the mass spectrometer was carefully calibrated in between the study of each sample, using a fullerene mixture located on a target spot adjacent to the sample.

In the following the observations made when harshly activating the sample to close the open cage fullerene are correlated with structural features of the sample molecules.

Samples 1.1, 1.2, 1.5, 1.6 and 2.11 behave identically, fragmenting predominantly to C₅₉N in all modes, with the exception of sample 1.1 when studied with positive-ion mode MALDI. Studying their structure reveals similarities: all of these samples have a ring orifice with a maximum of 13 atoms forming the opening. Sample 1.2 has a ring orifice of 11 members, samples 1.1, 1.5 and 1.6, possess ring orifices of 12 members, and 2.11 has a ring orifice of 13 members. The arrangement of heteroatoms around the rim is very similar in this group of compounds. Also, these samples contain only one nitrogen atom at most and therefore cannot induce more than one nitrogen atom into the sphere upon activation.

Samples 1.1, 1.2, 1.5, 1.6 and 2.11 are shown below in numerical order:

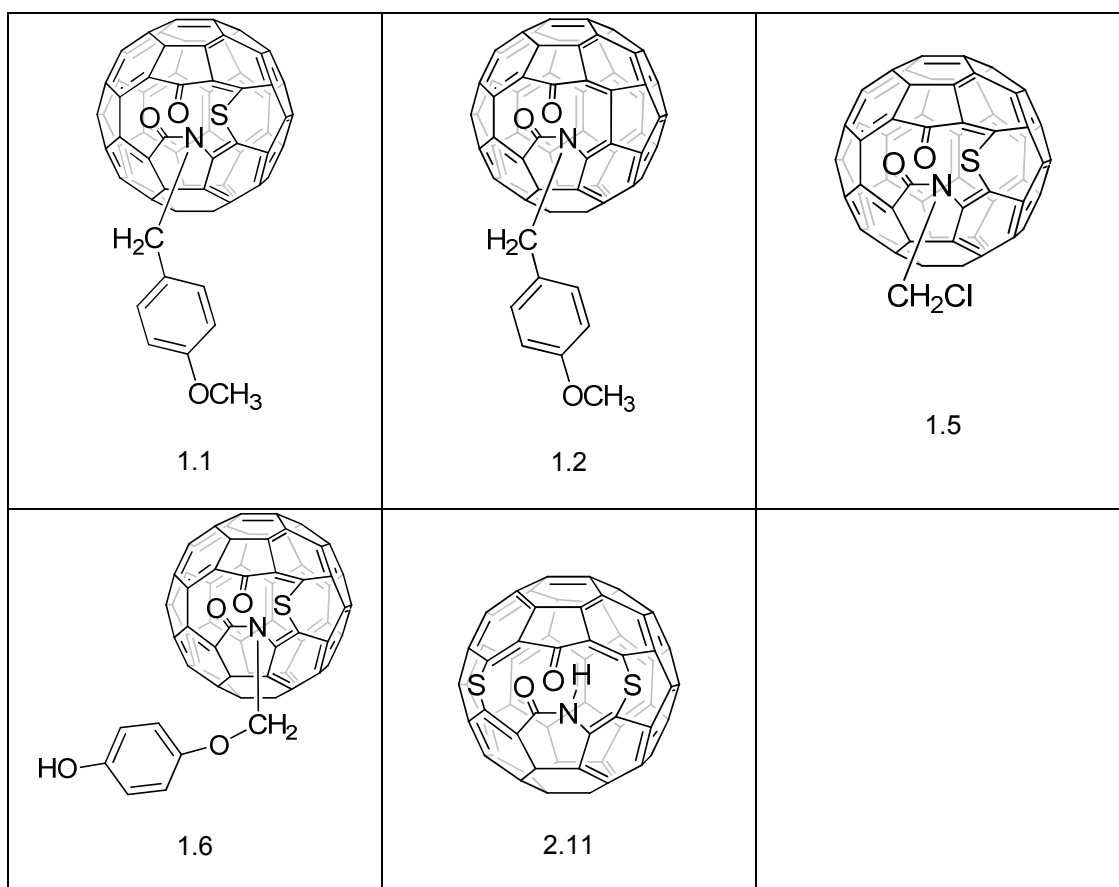
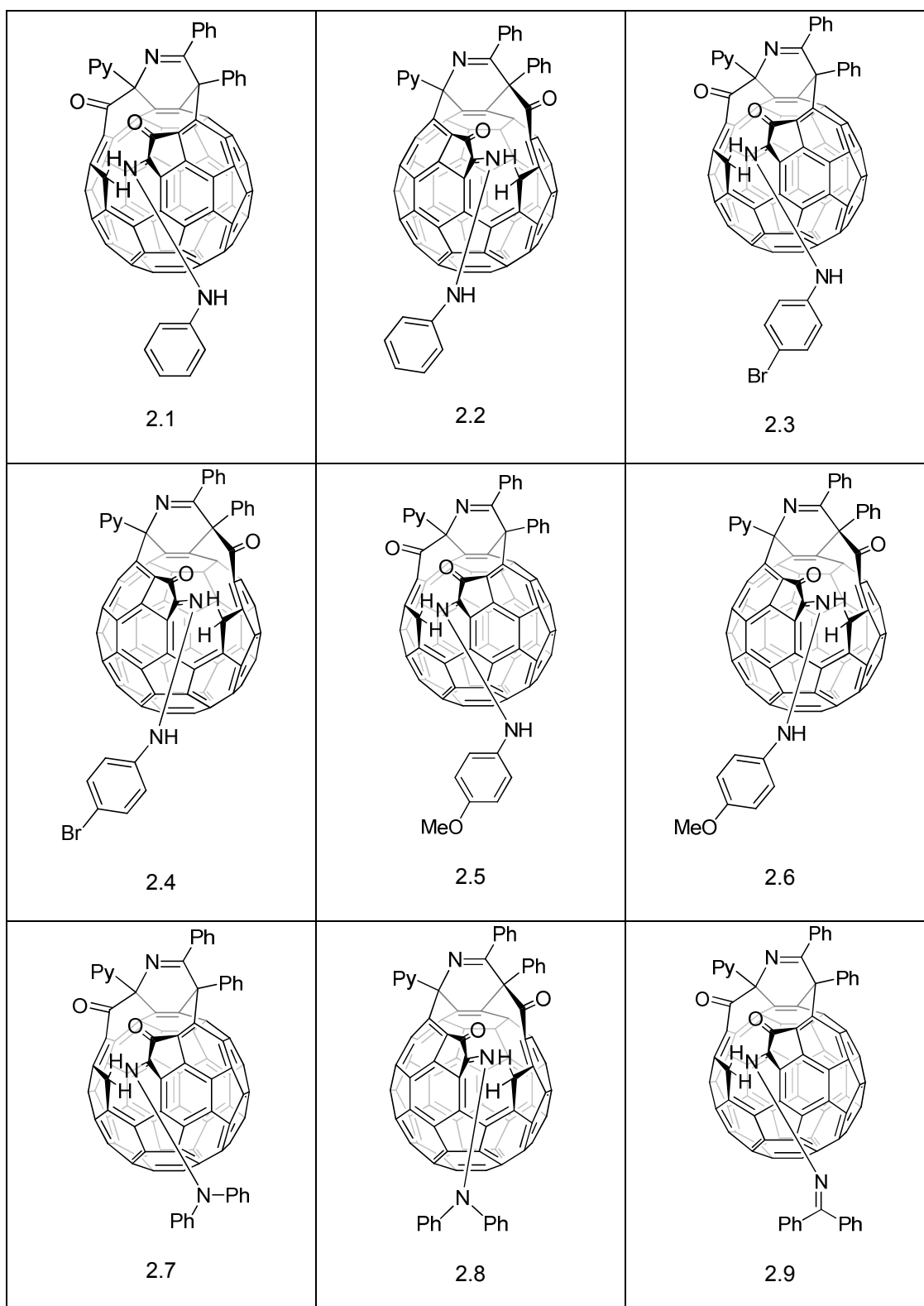


Table 3.6: Structures of OCFs with ring orifices containing less than 13 atoms

In contrast, samples 2.1 through to 2.10 and 2.12 have ring orifices of 16 members and, perhaps even more importantly, the arrangement of the heteroatoms that keep the sphere open are arranged in a completely different manner to the first set of samples, but are very similar within this group. Samples 2.1 through 2.10 also behave similarly with raised laser fluence, fragmenting predominantly to C_{60} under MALDI conditions, and $C_{59}N$ under LDI conditions.

Samples 2.1 to 2.10 are shown below in numerical order:



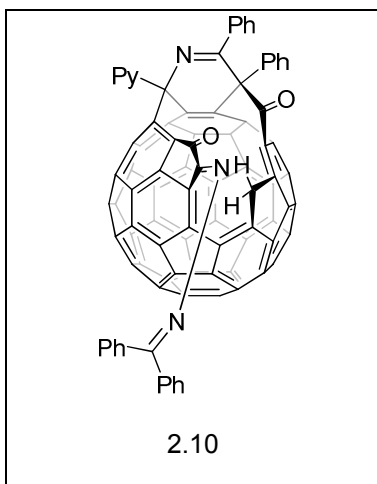


Table 3.7: Structures of OCFs with ring orifices containing 16 members

Although it cannot be predicted which products may result from the starting material, it is nevertheless obvious that structural elements determine the outcome of the decay. The two sets of samples discussed above show within the groups that possess a similar fragmentation behaviour also similarities in their structures. One must assume that the formation of C_{60} is of lower energy requirement than the production of $C_{59}N$, as C_{60} is only formed preferentially when MALDI is applied.

Sample 2.12, shown below, behaves in an entirely different fashion to the other samples. It has a ring orifice with 16 members, much like samples 2.1 through 2.10 and features an arrangement of heteroatoms at the rim which shows motifs of both the sets of samples studied above. Sample 2.12 does not fragment to $C_{59}N$ or C_{60} , its main fragment appears to be $C_{58}N_2$.

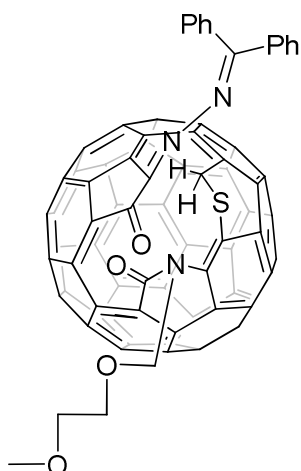


Figure 3.16: Structure of 2.12

The reason why sample 2.12 behaves differently from the other 16 membered ring orifice OCFs must be due to its structure – it is the only 16-membered ring orifice OCF with an additional sulfur atom present in the orifice. Obviously, the different design at the rim facilitates the insertion of a second nitrogen atom into the shell.

Unfortunately, further mechanistic insight into the fragmentation cannot be obtained from the present experiments. Future work in the form of laser ablation experiments on differently structured OCFs may shed more light on the role of the atom arrangement at the rim influencing the formation of C_{60} , $C_{59}N$ and $C_{58}N_2$. Computational investigations into the mechanism could also be helpful to enhance the understanding of the processes involved.

Appendix of related experimental efforts

$C_{60}:C_{59}N$ formation from $C_{60}N_2MEM_2$ and CID experiments with $C_{60}N_2MEM_2$, C_{60} and Open Cage Fullerenes

In an earlier investigation it had been noted that $C_{60}N_2MEM_2$ (figure 3.3) produces $C_{59}N$ and C_{60} when laser activated¹⁹. As the present instrument is more sensitive and much higher resolving, these experiments were conducted here in more detail for comparison

The present experiments showed for positive-ion mode MALDI and LDI, and for negative ion-mode LDI, that at low laser fluence, $C_{60}N_2MEM_2$ predominantly fragments to $C_{59}N$ with very small quantities of C_{60} (the intensity of the C_{60} peak was less than 5% of the $C_{59}N$ peak in positive-ion mode LDI). At higher laser fluences, both $C_{59}N$ and C_{60} are formed; however with increasing laser power the ratio of $C_{59}N:C_{60}$ falls, with both being produced in almost equal amounts at high laser powers (for negative-ion mode LDI, the ratio of $C_{60}:C_{59}N$ is 75:100).

For negative-ion mode MALDI, the situation was reversed. C_{60} is the dominant fragment at low laser powers, with the amount of $C_{59}N$ increasing with increasing laser fluence, until again both were formed in almost equal amounts.

The spectra shown below contrast the ratio of $C_{60}:C_{59}N$ at low laser power (figure 3.20) and higher laser power (figure 3.21) for each ion mode.

For the higher laser power spectra the peaks are broader than and not as resolved as the peaks in the spectra at lower powers. This is due to the much higher internal energy of the parent ion, $C_{60}N_2MEM_2$. At higher laser fluences the fragments have a wider range of energies compared to at lower laser fluences; therefore they will be detected over a wider m/z range. Even though reflectron detection is designed to prevent this, and was employed for the detection of the spectra below, the spread of energies is too enhanced and leads to a decrease in resolution.

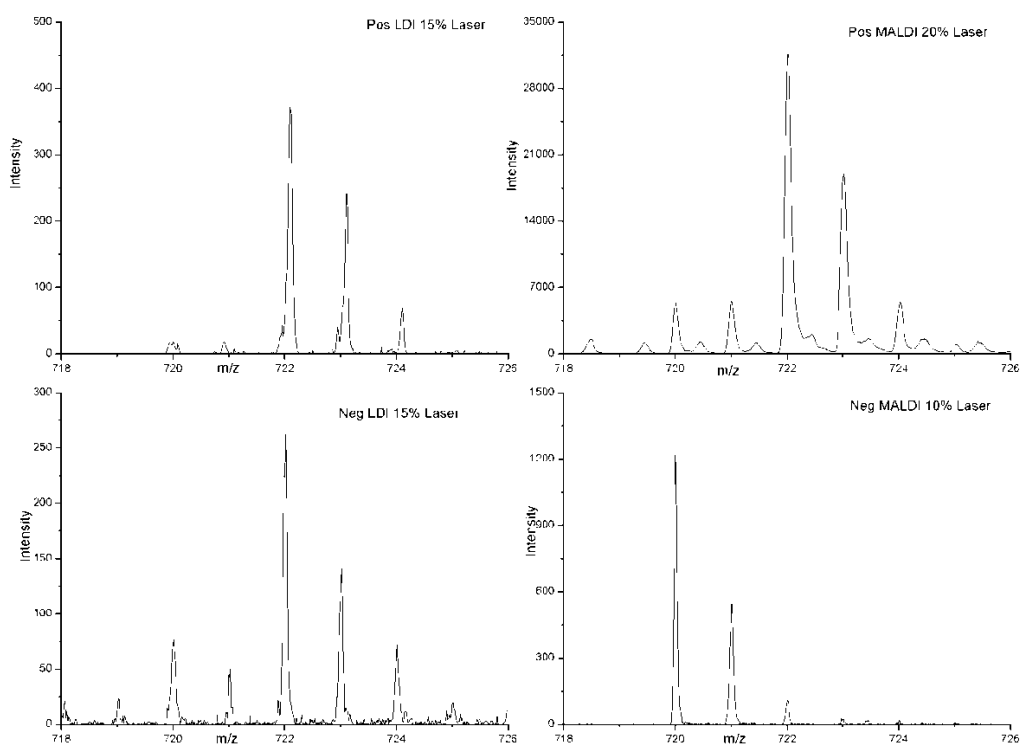


Figure 3.17: Low laser fluence, target: $C_{60}N_2MEM_2$

At low laser fluence, above, it is obvious that in the negative-ion mode MALDI spectrum, shown bottom right, there is very little, if any $C_{59}N$ present. The signal at m/z 722 is most likely from $^{13}C_2^{12}C_{58}$.

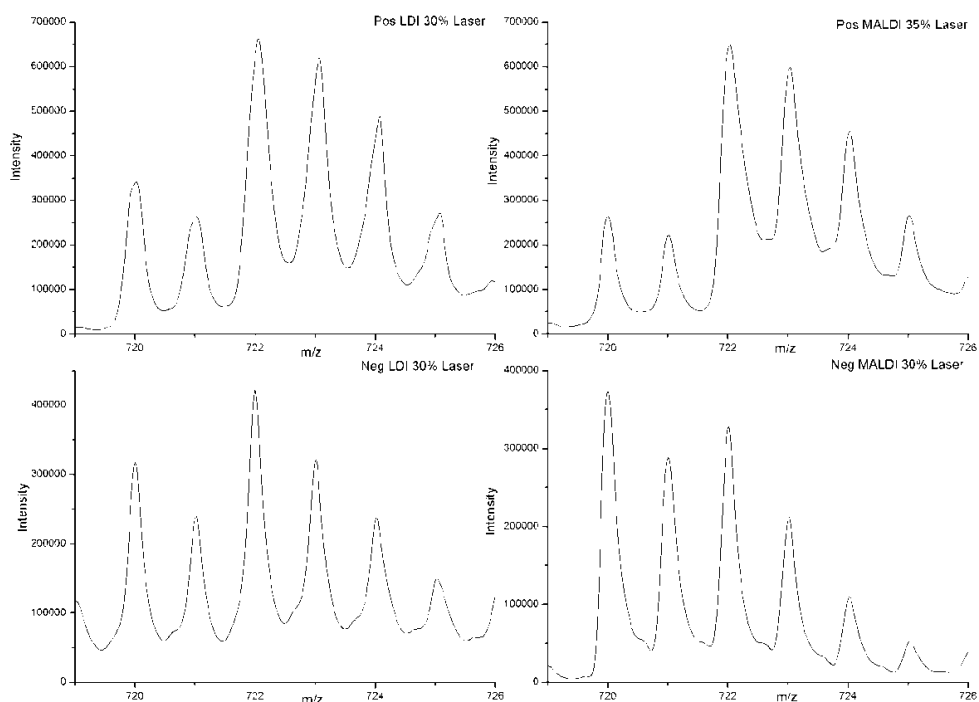


Figure 3.18: High laser fluence, target: $C_{60}N_2MEM_2$

Spectra were obtained at a range of laser powers. What could be observed from these is that the ratio of $C_{60}:C_{59}N$ alters with increasing laser fluence. This can be demonstrated graphically, as below:

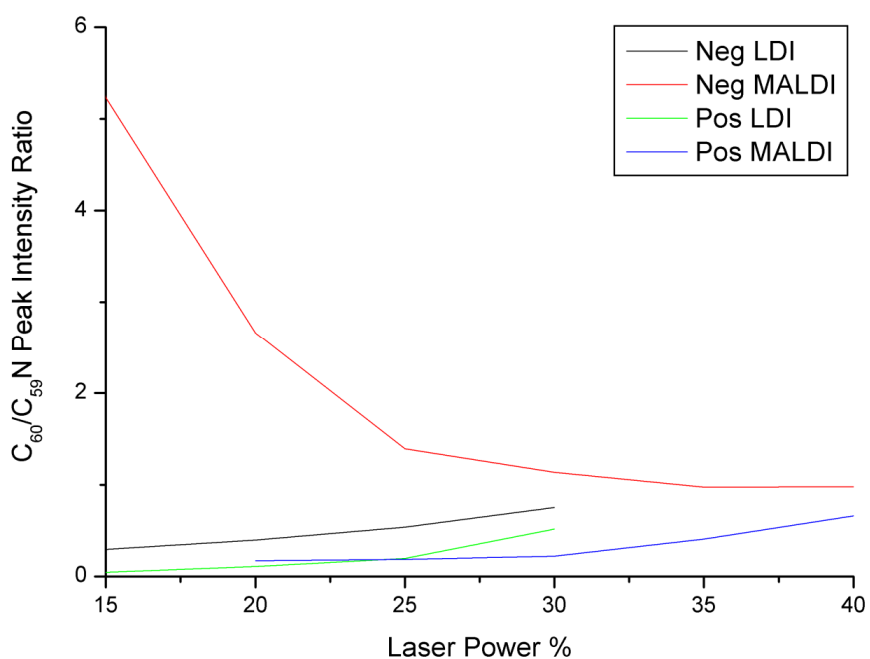


Figure 3.19: Plot of $C_{60}/C_{59}N$ peak intensity ratio vs. laser power for experiments in both ion modes, with or without a matrix (DCTB) present

The above graph clearly demonstrates the increase of the $C_{60}:C_{59}N$ ratio for negative-ion and positive-ion mode LDI and MALDI with increasing laser power. The decreasing $C_{60}:C_{59}N$ ratio is also very apparent for the negative-ion mode MALDI.

Measurements were only taken from 15 to 30% laser power for the LDI spectra, and up to 40% laser power for the MALDI spectra. At even higher laser powers, LDI spectra become saturated and the intensities of the peaks were not accurate anymore.

Overall, the behaviour of $C_{60}N_2MEM_2$ is similar to what has been previously reported, with the exception of the experiments performed in negative-ion mode LDI.

Another interesting observation that can be made due to the enhanced resolution is that the already known loss of CN from the cage followed by further cage shrinkage through C_2 loss, is accompanied by C_2 losses from $C_{59}N$ without CN loss. The resolved pattern of the fragment ions shows the presence of nitrogen in fragments that were as small as $C_{43}N$ (for negative-ion mode LDI). However, CN loss is the favoured fragmentation pathway, as can be seen by the decreasing amounts of nitrogen containing fragments relative to the “all-carbon” fragments. The graph below shows the ratio of the peak intensities versus the number of atoms remaining in the fragment ions.

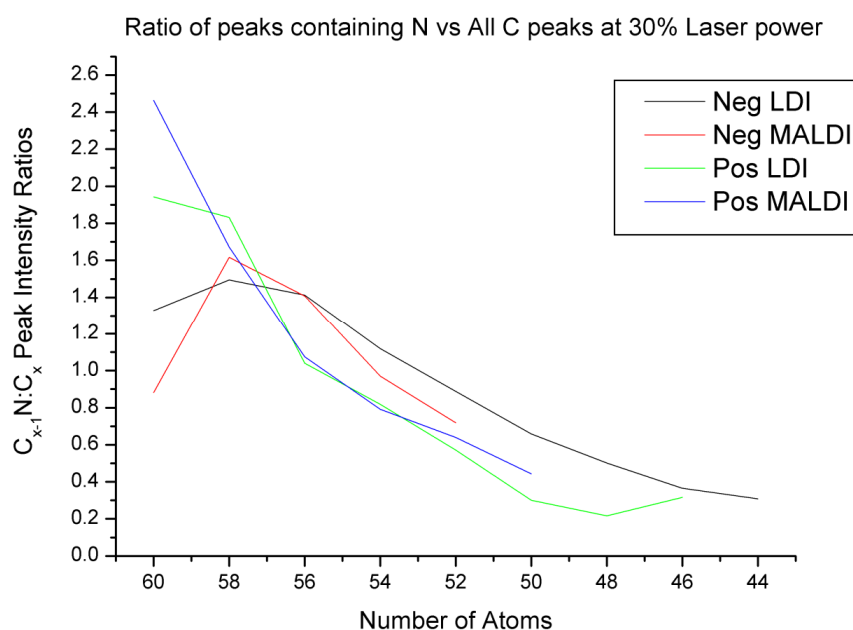


Figure 3.20: Plot of the ratio of N containing peaks: All C containing peaks vs. the number of atoms present in the fullerene fragment

The graph illustrates that the ratio of nitrogen containing fragment peaks to “all-carbon” fragment peaks decreases with decreasing size. Only the initial loss of 2 atoms shows in the

case of negative-ion mode spectra an actual increase, which suggests that for the first fragmentation, C_2 is preferentially lost.

This graph also demonstrates how much greater the impact of direct LDI is on the extent of fragmentation, allowing the detection of much smaller fragments compared to the MALDI spectra obtained at the same laser fluence.

The $C_{x-1}N$ peaks were of too low intensity to allow their distinction from the standard isotopic pattern of the corresponding C_x fragments beyond the following lower mass fragment sizes: 52 atoms for the negative-ion mode MALDI spectra, 50 atoms for the positive-ion mode MALDI spectra, 46 atoms for the positive-ion mode LDI spectra and 44 atoms for the negative-ion mode LDI spectra,.

For this graph, no corrections were made for the contribution to the nitrogen containing peak from the $^{13}C_2\ ^{12}C_{(x-2)}$ peak, as this correction would not have affected the shape of graph.

For a second set of experiments $C_{60}N_2MEM_2$ functioned as a model compound to test the experimental performance. The experimental idea was to change the standard collision gas argon to helium with the intention to insert helium into the open cage fullerenes (OCFs) in CID/Lift experiments. However, as the OCFs were available in only very low amounts, $C_{60}N_2MEM_2$ was used for the initial tests. Unfortunately, when CID was performed on $C_{60}N_2MEM_2$ with helium as the collision gas, a parent ion peak could not be detected to perform CID on and subsequently no spectra were obtained. The LIFT method requires a detectable amount of ions; otherwise the experiment cannot be performed. The conditions for ion formation are different in CID/LIFT mode. Occasionally the peak formation/detection was difficult in LIFT mode and sometimes even impossible. The negative result with $C_{60}N_2MEM_2$ meant that its molecular ion completely dissociated prior to the experiment. Often in CID experiments, a very high laser power is required to obtain sufficient amounts of a particular parent ion. The reason for this has to be seen in the different ion source conditions compared to "normal" mass spectra, for instance, the acceleration voltage is only 8kV and cannot be changed, as this would have effects on the validation of the calibration. As a consequence, severe decomposition may sometimes be the result for labile starting ions. Since the OCFs were available in so low amounts that they could only be studied after prior optimisation of the CID/LIFT experiment by the $C_{60}N_2MEM_2$ model compound, the

helium insertion experiments could not be conducted. “Standard” CID/Lift experiments using argon as collision gas were possible with the OCFs and are discussed in chapter 5 in comparison with metal attachment experiments using the pencil lead matrix.

CID experiments with helium gas were, however, possible and performed with the much more stable C_{60} fullerene, for which the formation of a parent ion was abundant. However, the resulting fragment ions were of only weak abundances and fewer were formed compared to what is obtained in “normal” LDI spectra of C_{60} . The resulting CID/LIFT spectra using both argon and helium as collision gases are shown below.

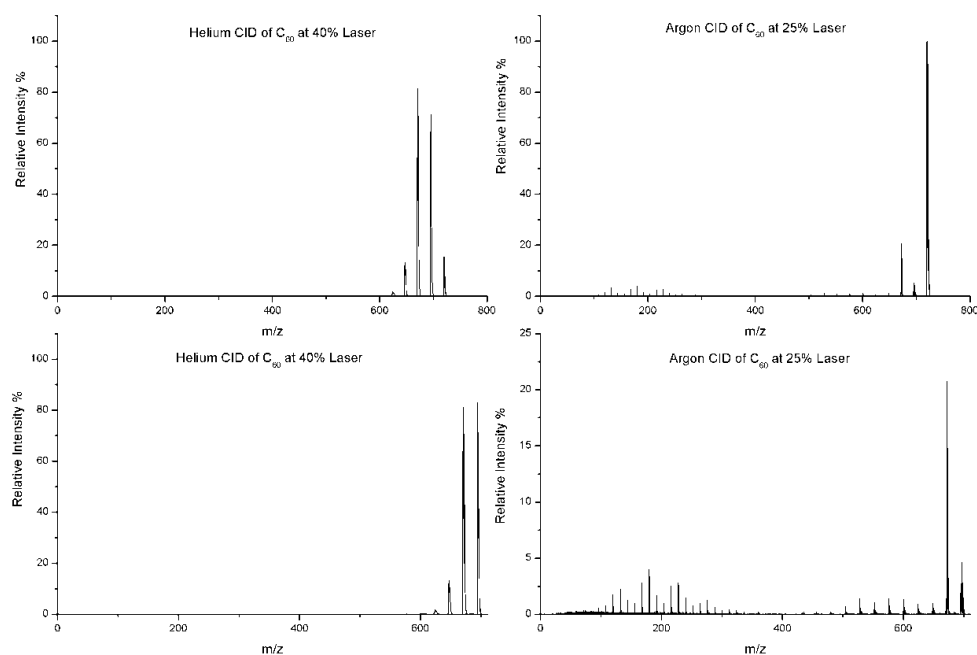


Figure 3.21: CID spectra of C_{60} using either Helium or Argon gas as the collision gas

When argon is used as the collision gas, the close up of the fragments (bottom right spectrum, above) verifies the standard fragmentation pattern of C_{60} . For the use of helium as the collision gas, it is observed that only a small amount of fragmentation has been induced. It is also noteworthy that for the helium CID experiments, the laser power had to be much higher to induce any fragmentation. In the spectra shown above, when helium was used; the laser power was set at 40%, for the CID experiments with argon; the laser power was set at 25%.

Conclusion

Various fullerene derivatives have been successfully analysed using DCTB-MALDI-MS, and in the majority of cases unwanted fragmentation could be reduced. Negative-ion mode was found to produce cleaner spectra.

Experiments with increased laser power were performed with open-cage fullerenes and cage re-healing was studied, leading to C_{60} , $C_{59}N$, or for the case of one of the 16-membered ring orifices, to the formation of $C_{58}N_2$.

Future research would involve the analysis of a wider range of OCF's, to determine the influence of orifice size and connectivity of the atoms at the rim onto the outcome of the laser-induced cage re-healing process.

A second dissociation path of $C_{59}N$ was established by the enhanced resolving power of the instrument. It was found that C_2 loss can compete with the preferred CN loss, leading to several nitrogen containing fragment ions.

Attempts to incorporate helium inside the open cage fullerenes by using the LIFT method on the Bruker Ultraflex II and re-healing them to $He@C_{60}$, $He@C_{59}N$ or $He@C_{58}N_2$ were unsuccessful. The required source conditions for parent ions were too harsh to allow their intact survival and experiments with C_{60} showed only minute fragmentation in collisions with helium.

References

1. Cram, D. J.; Cram, J. M.; Royal Society of Chemistry (Great Britain), *Container molecules and their guests*. Royal Society of Chemistry: Cambridge, 1994; p xiv,223
2. Cross, R. J., *Journal of Physical Chemistry A* **2001**, *105* (28), 6943.
3. Hummelen, J. C.; Prato, M.; Wudl, F., *Journal of the American Chemical Society* **1995**, *117* (26), 7003.
4. Stanisky, C. M.; Cross, R. J.; Saunders, M.; Murata, M.; Murata, Y.; Komatsu, K., *Journal of the American Chemical Society* **2005**, *127* (1), 299-302.
5. Murata, Y.; Murata, M.; Komatsu, K., *The Journal of organic chemistry* **2001**, *66* (24), 8187-8191.
6. Vougioukalakis, G. C.; Prassides, K.; Orfanopoulos, M., *Organic letters* **2004**, *6* (8), 1245-1247.
7. Murata, Y.; Kato, N.; Komatsu, K., *The Journal of organic chemistry* **2001**, *66* (22), 7235-7239.
8. Murata, Y.; Murata, M.; Komatsu, K., *Chemistry (Weinheim an der Bergstrasse, Germany)* **2003**, *9* (7), 1600-1609.
9. Vougioukalakis, G. C.; Prassides, K.; Campanera, J. M.; Heggie, M. I.; Orfanopoulos, M., *The Journal of organic chemistry* **2004**, *69* (13), 4524-4526.
10. Roubelakis, M. M.; Murata, Y.; Komatsu, K.; Orfanopoulos, M., *The Journal of organic chemistry* **2007**, *72* (18), 7042-7045.
11. Rubin, Y.; Jarrosson, T.; Wang, G.; Bartberger, M.; Houk, K.; Schick, G.; Saunders, M.; Cross, R., *Angewandte Chemie-International Edition* **2001**, *40* (8), 1543-+.
12. Schick, G.; Jarrosson, T.; Rubin, Y., *Angewandte Chemie-International Edition* **1999**, *38* (16), 2360-2363.
13. Murata, Y.; Murata, M.; Komatsu, K., *Journal of the American Chemical Society* **2003**, *125* (24), 7152-7153.
14. Iwamatsu, S.; Murata, S., *Tetrahedron Letters* **2004**, *45* (34), 6391-6394.
15. Iwamatsu, S.; Murata, S.; Andoh, Y.; Minoura, M.; Kobayashi, K.; Mizorogi, N.; Nagase, S., *The Journal of organic chemistry* **2005**, *70* (12), 4820-4825.

16. Iwamatsu, S.; Stanisky, C. M.; Cross, R. J.; Saunders, M.; Mizorogi, N.; Nagase, S.; Murata, S., *Angewandte Chemie (International ed.in English)* **2006**, *45* (32), 5337-5340.
17. Sawa, H.; Wakabayashi, Y.; Murata, Y.; Murata, M.; Komatsu, K., *Angewandte Chemie-International Edition* **2005**, *44* (13), 1981-1983.
18. Komatsu, K.; Murata, M.; Murata, Y., *Science (New York, N.Y.)* **2005**, *307* (5707), 238-240.
19. Clipston, N. L.; Brown, T.; Vasil'ev, Y. V.; Barrow, M. P.; Herzsuh, R.; Reuther, U.; Hirsch, A.; Drewello, T., *Journal of Physical Chemistry A* **2000**, *104* (40), 9171.

Chapter 4: An Investigation into C₆₀H₂ using MALDI and LDI mass spectrometry

Introduction

This study was inspired by a recent comprehensive review covering the synthesis and characterization of hydrogenated fullerenes¹. It was noted that C₆₀H₂, the smallest hydrofullerene, has been successfully characterised applying LDI². In contrast, C₆₀H₃₆ suffered such tremendous decomposition when studied by the softer ionisation method of MALDI that a characterisation was initially difficult.

As LDI involves using the laser directly on the sample with no protective matrix, it is a lot more destructive than MALDI. This in turn appears to imply that C₆₀H₂ is of such a greater stability than C₆₀H₃₆ that direct laser ablation leads successfully to desorption and ionisation whereas even matrix assistance could not prevent the decay of C₆₀H₃₆. This assumption seems further corroborated by the fact that the CH bond in C₆₀H₂ (70.5 kcal mol⁻¹) is stronger than in C₆₀H₃₆ (66.7 kcal mol⁻¹)³.

Following earlier investigations into the gas phase behaviour of C₆₀H₃₆ and C₆₀H₁₈ it would be of interest to evaluate these assumptions through dedicated LDI and MALDI experiments with C₆₀H₂.

C₆₀H₂ is of interest as it, along with other hydrogenated fullerenes, may be utilised for hydrogen storage, especially as hydrogen atoms can be attached via both endohedral and exohedral means⁴.

For C₆₀H₂ it has been found that the lowest energy conformation has two hydrogen atoms attached to adjacent carbon atoms which are part of the same 6-membered ring⁵.

Despite the close proximity of the hydrogen atoms, dehydrogenation does not appear to occur via a one step concerted mechanism, rather via a multiple step radical chain reaction⁶.

Hydrogenated fullerenes can be synthesized in various ways. For example, transfer hydrogenation via 9,10-dihydroanthracene, catalysed by [7H]benzanthrene, results in production of C₆₀H_x and C₇₀H_x, where x is between 0 - 36 for both C₆₀ and C₇₀, and 42-44 for

C_{60} ⁷. Without [7H]benzanthrene present, there is still hydrogenation when C_{60} is heated with 9,10-dihydroanthracene to produce $C_{60}H_{36}$ and $C_{60}H_{18}$ ⁸.

Another example - exposing C_{60} in powder form to a temperature of 300°C with various high H_2 pressures, for between 20 and 119 hours created $C_{60}H_x$, where x was between 2 and 18⁴. Heating fullerenes with a polyamine, such as diethylenetriamine or triethylenetetramine, was also found to create hydrogenated fullerenes, for C_{60} , C_{70} and larger fullerenes such as C_{84} and C_{96} ⁹.

Rhodium can be used to catalyse the reaction between C_{60} and H_2 , with $C_{60}H_2$ as the main hydrogenated fullerene present¹⁰.

$C_{60}H_2$ has been studied with a comprehensive array of ionisation methods, including negative-ion fast atom bombardment (FAB)^{5, 11, 12}, atmospheric pressure chemical ionisation (APCI), electron ionisation (EI), field desorption / field ionisation (FD/FI) as well as LDI and MALDI. Common to these different attempts towards gas-phase ionisation is that $C_{60}H_2$ shows tremendous degradation into C_{60} , so that $C_{60}H_2$ was only identified through a combination of methods. For instance a separation of $C_{60}H_2$ prior to its ionisation excludes the possibility of having C_{60} and higher hydrogenated fullerenes in the sample.

A study using negative-ion mode MALDI-MS had a confusing mass assignment¹³. It reported peaks with their respective intensities and assignments as follows:

724 (87%) – $^{13}C^{12}C_{59}H_2$

723 (100%) – $^{12}C_{60}H_2$

722 (93%) – $^{13}C^{12}C_{59}$

721 (68%) – $^{12}C_{60}$

Disregarding the calibration, the intensities of the ^{13}C peaks at m/z 722 and 724 are far higher than they should be for the assignment. The peak at m/z 724 should be approximately 66%, and the peak at m/z 722 should be at approximately 45%. This study also suggested that $C_{60}H_2$ can be stored for several weeks in solution without degradation, and for even longer as a solid. It was reported however, that $C_{60}H_2$ rapidly degrades to C_{60} when in contact with alumina.

FD was found to produce less fragmentation of higher hydrogenated fullerenes, such as $C_{60}H_{18}$ and $C_{60}H_{36}$, when compared to EI¹⁴. Although not tested directly on $C_{60}H_2$, as FD

produced almost fragmentation free spectra for $C_{60}H_{36}$, which is known to fragment extensively under even soft conditions, this method should have produced fragmentation free spectra for $C_{60}H_2$.

However, as negative-ion FAB accompanied the first syntheses of $C_{60}H_2$,⁵ this became the mass spectrometric method of choice for analysis of hydrogenated fullerenes. In this work, the reaction of C_{60} with BH_3 :tetrahydrofuran was employed to produce $C_{60}H_2$ which was obtained in yields of 10 to 30%. HPLC was used to separate the unreacted C_{60} from $C_{60}H_2$. In the negative-ion FAB experiments more than half of the initial $C_{60}H_2$ undergoes hydrogen loss so that the resulting spectrum is dominated by the C_{60}^- anion at m/z 720 and its isotopomers, figure 4.1, shown below:

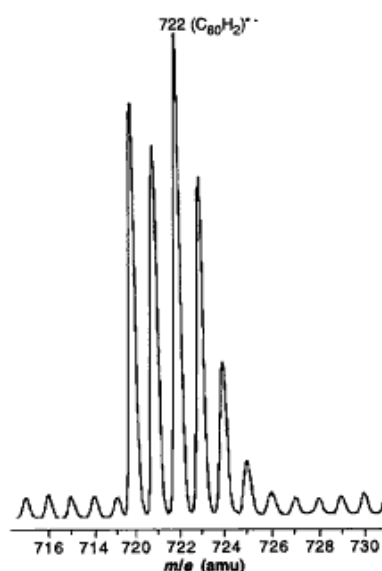


Figure 4.1: Negative-ion mode FAB spectrum of $C_{60}H_2$ from the first reported synthesis⁵

$C_{60}H_2^-$ is identified through the enhancement of the signal at m/z 722 (composed of $^{12}C_{58}^{13}C_2$ and $^{12}C_{60}H_2$). The fairly extensive fragmentation makes it difficult to apply this approach to quantitation of $C_{60}H_2$ or to identify accurately small amounts of C_{60} impurities that might be present in unpurified samples. Also small amounts of $C_{60}H_n$ with $n > 2$ could remain undetected while contributing through fragmentation.

In retrospect it is evident that negative-ion mass spectrometry has to be used with great caution for the identification of hydrofullerenes. The tendency to accept an extra electron decreases with increasing hydrogen content, so that for $C_{60}H_n$ with n in the range of 10 or

12, the electron affinity turns positive and anions become unstable. $C_{60}H_{18}$ represents an exception, possessing an E_A of between 1.4 and 1.6 eV¹⁵ and stable molecular anions.

Previous reports on the application of LDI and MALDI are particularly intriguing. In one study $C_{60}H_2$ was identified in LDI experiments by its accurate mass². Unfortunately, no details about the experiment were given, except that the experiment was performed in positive-ion mode. No spectra were provided that may have shown fragmentation. In the likely case that dissociation into C_{60} had occurred, the separation of $C_{60}H_2$ and $^{13}C_2^{12}C_{58}$ would have afforded a resolving power in excess of 80000. A further study applied direct LDI to characterise $C_{60}H_2$ as produced by sonochemistry¹⁶. The detection by FT-ICR was, however, affected by a space charge phenomenon that led to peak coalescence. The occurrence of this phenomenon, which can be prevented through the use of stronger fields, led to mass spectra in which the $C_{60}H_2$ signal could neither be separated isotopically (too low resolution), nor would it appear at the expected nominal m/z values (too low mass accuracy). $C_{60}H_2$ was also identified by electron transfer negative-ion MALDI, but the data were not more conclusive compared to the early negative-ion FAB experiments.

In the present investigation, $C_{60}H_2$ is studied by LDI and MALDI in both ion modes with a view to evaluate the usefulness of these methods in achieving the formation of molecular ions and reducing fragmentation.

Experimental

$C_{60}H_2$ was synthesized by Manolis Tzirakis of the Orfanopoulos group at the University of Crete¹⁷. Initially, $C_{60}H_2$ was part of the set of samples discussed in the previous chapter. When it became obvious that MALDI would provide an appropriate means to generate molecular ions free of dissociations, a dedicated sample was prepared for the investigation covered in this chapter and in particular great care was taken to purify the $C_{60}H_2$ by chromatographic means to avoid the presence of any impurity.

The sample was synthesised on July 14th 2007. The crude reaction mixture was kept under argon for ten days, and then purified on July 24th, using a semipreparative HPLC technique, on a Marathon III instrument equipped with a Cosmosil 5PBB column (10 x 250 mm, Nacalai Tesque) with detection at 310 nm. The eluent was a 4:1 v/v mixture of toluene and acetonitrile, and the flow rate was 5 ml/min.

The samples were posted on the 25th July, and received on 31st July 2007.

DCTB was used as the matrix material in MALDI, and was mixed with the sample as a 50:1 molar ratio, respectively.

MALDI and LDI experiments were performed on the Bruker Ultraflex II, in both ion modes.

For the experiments where $C_{60}H_2$ was monitored over time to observe degradation, the $C_{60}H_2$ was kept as a solid in the dark at room temperature. It was analysed twice a week, for 4 weeks. Day 0 was the day the sample was received, and the first analysis performed. Subsequent analysis was performed on days 3, 7, 10, 14, 17, 21, 24 and 28.

Due to the time involved in receiving the sample, analysis was initially performed one week after purification, with subsequent analyses performed 10, 14, 17, 21, 24, 28, 31 and 35 days after purification.

Spectra were obtained several times for each ion mode, at a variety of different laser powers (marked in percentages).

Results and Discussion

Figure 4.2 displays the mass spectra resulting from the initial laser desorption experiments with $C_{60}H_2$.

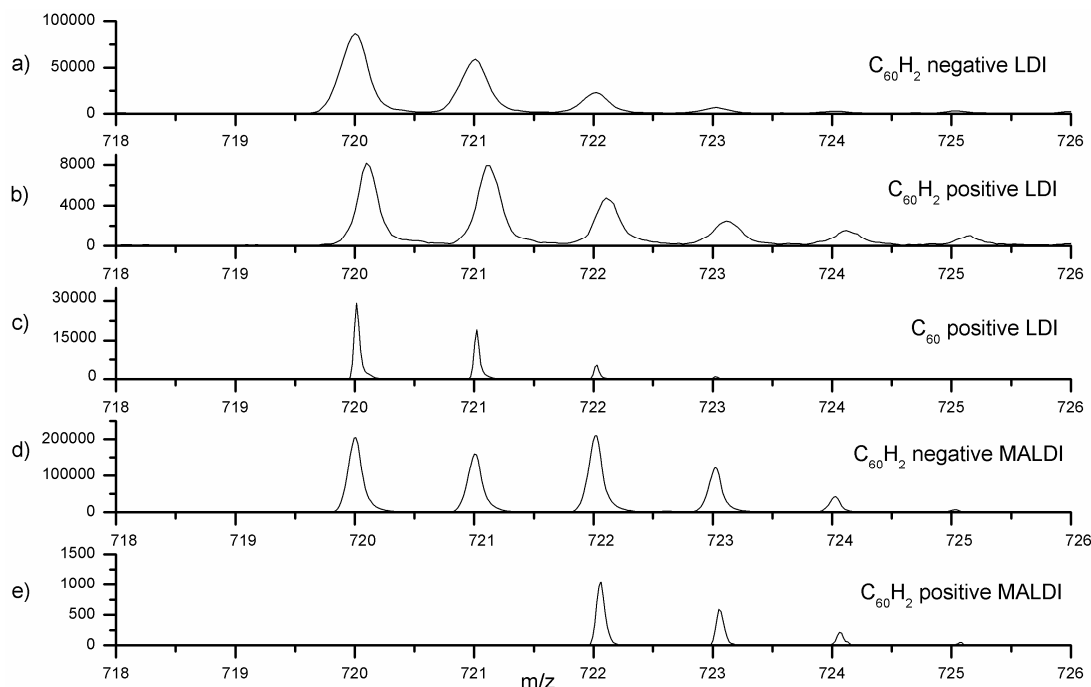


Figure 4.2: $C_{60}H_2$ direct laser desorption/ionization mass spectra: a) negative-ion and b) positive-ion mode. Pure C_{60} for comparison: c) positive-ion LDI. $C_{60}H_2$ MALDI mass spectra (DCTB as matrix, analyte-to-matrix ratio 1:50): d) negative-ion mode and e) positive-ion mode

LDI of $C_{60}H_2$ led in the negative-ion mode to the pattern shown in Fig. 4.2 a) and in the positive-ion mode to a distribution shown in Fig. 4.2 b). The comparison with Fig. 4.2 c), which shows LDI of pure C_{60} in positive ion mode, reveals that LDI of $C_{60}H_2$ leads predominantly to the formation of C_{60} . The pattern obtained for negative-ion LDI of $C_{60}H_2$ is within experimental error identical to the isotopic pattern of pure C_{60} . In the positive ion mode, m/z 721 and 722 appear enhanced indicating the formation of $C_{60}H^+$ and minute amounts of $C_{60}H_2^+$. Although the observation of $C_{60}H_2^+$ is in line with earlier LDI studies, it becomes also evident that the tremendous degree of fragmentation is problematic. As is the case with all other previous approaches, identification and quantitation of $C_{60}H_2$ is complicated and for unpurified samples, the influence of impurities such as C_{60} or

hydrofullerenes with a slightly higher hydrogen content than $C_{60}H_2$ would not be obvious. Consequently, LDI is not suited as a reliable tool to quantify or even identify $C_{60}H_2$.

Very similar considerations are true when MALDI is used in the negative-ion mode.

Figure 4.2 d) shows the molecular ion region for negative-ion MALDI of $C_{60}H_2$ using DCTB as the matrix material. However, the molecular anion at m/z 722 is now clearly evident. The high degree of fragmentation is similar to the extent observed in the pioneering negative-ion FAB experiments. Finally, Fig. 4.2 e) shows the outcome of the positive-ion DCTB-MALDI experiment. The molecular ion $C_{60}H_2^+$ at m/z 722 is formed practically without dissociation.

As explained previously, the ionisation energy of DCTB was recently determined as 8.54 eV and computational estimations locate the electron affinity at about 2 – 2.3 eV. The analyte $C_{60}H_2$ has an estimated ionisation energy of 7.28 eV and electron affinity estimations lie in a range of 2.45 - 2.68 eV. Consequently, $C_{60}H_2$ would transfer an electron in reaction with the DCTB cation radical and accept an electron in reaction with the DCTB anion radical. Although these data clearly support the thermochemical feasibility of ion formation through electron transfer, a more comprehensive description of the thermochemistry surrounding the $C_{60}H_2$ ions is necessary to obtain more detailed insight. For instance, the current data would imply that $C_{60}H_2$ cations are formed with greater excess energy than the $C_{60}H_2$ anions. However, positive-ion DCTB-MALDI generates $C_{60}H_2^+$ free of dissociations while the corresponding anions suffer severe decomposition. Depending on the energetics involved, these two findings are not necessarily contradictory.

The sensitivity of $C_{60}H_2$ towards oxygen has been controversial. Therefore, it was decided to evaluate this question through the use of MALDI. A purified $C_{60}H_2$ sample of several mg in weight was kept at room temperature as a solid in a small glass vial in the dark. Twice a week, as explained in the experimental section, the vial was opened and material removed for analysis. The corresponding positive and negative-ion DCTB-MALDI mass spectra are shown in Fig. 4.3, below.

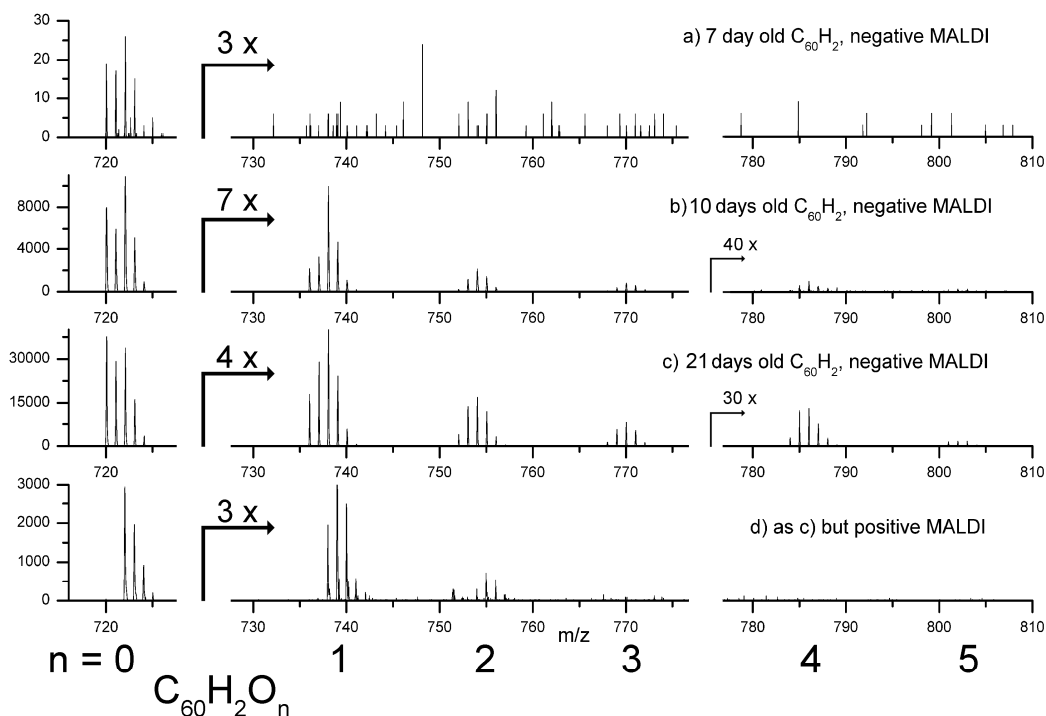


Figure 4.3: $C_{60}H_2$ ageing monitored by negative-ion DCTB MALDI: a) seven days, b) ten and c) twenty-one days after purification. d) same as c) but positive-ion DCTB MALDI

Despite the successful characterisation of $C_{60}H_2$ by positive-ion MALDI, previous work on fullerene oxides would suggest a more sensitive approach in the negative ion mode when oxidation products are of interest. The sample was studied in both ion modes, confirming these assumptions.

The negative-ion MALDI mass spectra of the ageing $C_{60}H_2$ sample are displayed in Fig. 4.3 a) seven days after purification, in Fig. 4.3 b) when the sample had aged ten days and Fig. 4.3 c) after twenty-one days.

It is clearly visible that the oxygen attainment increases with time. This is true for both the number of oxygen atoms attached to the fullerene and the amount of oxidised material. While shortly after the synthesis oxides were barely observed, the attachment of up to five oxygen atoms was evident after ten days and the overall amount of these oxides increased with further ageing. The sample was investigated for up to thirty-five days after purification, but the overall appearance of the spectra was similar to the one obtained after twenty-one days, although the overall oxide abundance seemed lower for samples that were older than

twenty-one days. A typical example of the positive ion MALDI experiment, which was run in parallel, is shown in Fig. 4.3 d) with the sample being twenty-one days old. In line with other investigations, oxidation products are less abundantly observed by this approach and only the attainment of up to two oxygen atoms is just about detected. However, the positive-ion mass spectrum shows hardly any signs of C_{60} , the signal of which is increasingly observed over time in the negative mode. It follows that the C_{60} formation is not caused by hydrogen release from the $C_{60}H_2$ sample over time, but through dissociations of anions in the negative-ion experiment. In general, there seems very little decomposition of the sample in terms of hydrogen loss or cage shrinkage. The latter is corroborated by the very low abundances of C_{58} or C_{59} ions in both ion modes (not shown), which would be indicative of cage shrinkage.

Even though our analysis is not quantitative and lacks comparison with pure C_{60} , the fact that the attachment of up to 5 oxygen atoms can be monitored in a matter of days clearly indicates that solid $C_{60}H_2$ is susceptible to oxidation.

Conclusion

Previous research into the mass spectrometry of $C_{60}H_2$ was particularly affected by unwanted decomposition. Positive-ion mode DCTB-MALDI has been demonstrated here to allow for fragmentation-free formation of molecular ions of $C_{60}H_2$. Negative-ion mode DCTB-MALDI has shown the degradation of $C_{60}H_2$ through addition of up to five oxygen atoms when the solid is kept under ambient conditions. It has also demonstrated how rapidly oxygenation of the sample occurs. Hydrogen loss and cage shrinkage are not evident.

References

1. Nossal, J.; Saini, R.; Alemany, L.; Meier, M.; Billups, W., *European Journal of Organic Chemistry* **2001**, (22), 4167-4180.
2. Ballenweg, S.; Gleiter, R.; Kratschmer, W., *Tetrahedron Letters* **1993**, 34 (23), 3737-3740.
3. Tkachenko, L.; Lobach, A.; Strelets, V., *Russian Chemical Bulletin* **1998**, 47 (6), 1105-1107.
4. Jin, C.; Hettich, R.; Compton, R.; Joyce, D.; Blencoe, J.; Burch, T., *Journal of Physical Chemistry* **1994**, 98 (16), 4215-4217.
5. Henderson, C.; Cahill, P., *Science* **1993**, 259 (5103), 1885-1887.
6. Bettinger, H.; Rabuck, A.; Scuseria, G.; Wang, N.; Litosh, V.; Saini, R.; Billups, W., *Chemical Physics Letters* **2002**, 360 (5-6), 509-514.
7. Gerst, M.; Beckhaus, H.; Ruchardt, C.; Campbell, E.; Tellmann, R., *Tetrahedron Letters* **1993**, 34 (48), 7729-7732.
8. Ruchardt, C.; Gerst, M.; Ebenhoch, J.; Beckhaus, H.; Campbell, E.; Tellmann, R.; Schwarz, H.; Weiske, T.; Pitter, S., *Angewandte Chemie-International Edition in English* **1993**, 32 (4), 584-586.
9. Kintigh, J.; Briggs, J.; Letourneau, K.; Miller, G., *Journal of Materials Chemistry* **2007**, 17 (44), 4647-4651.
10. Becker, L.; Evans, T.; Bada, J., *J Org Chem* **1993**, 58 (27), 7630-1.
11. Meier, M.; Corbin, F.; Vance, V.; Clayton, M.; Mollman, M., *Tetrahedron Letters* **1994**, 35 (32), 5789-5792.
12. Nozu, R.; Matsumoto, O., *Journal of the Electrochemical Society* **1996**, 143 (6), 1919-1923.
13. Siedschlag, C.; Luftmann, H.; Wolff, C.; Mattay, J., *Tetrahedron* **1999**, 55 (25), 7805-7818.
14. Lobach, A.; Perov, A.; Rebrov, A.; Roshchupkina, O.; Tkacheva, V.; Stepanov, A., *Russian Chemical Bulletin* **1997**, 46 (4), 641-648.
15. Vasil'ev, Y.; Absalimov, R.; Nasibullaev, S.; Lobach, A.; Drewello, T., *Journal of Physical Chemistry A* **2001**, 105 (4), 661-665.

16. Mandrus, D.; Kele, M.; Hettich, R.; Guiochon, G.; Sales, B.; Boatner, L., *Journal of Physical Chemistry B* **1997**, *101* (2), 123-128.
17. Tzirakis, M. D.; Alberti, M. N.; Nye, L. C.; Drewello, T.; Orfanopoulos, M., *The Journal of Organic Chemistry* **2009**, *74* (15), 5746–5749

Chapter 5: Investigation into MALDI Matrices

Introduction

As outlined previously, the matrix is a low molecular weight compound used in MALDI analysis for the protection of the sample, but also as a promoter of soft gas-phase transfer and ionisation of the sample. Ideally its absorption maximum is very close to the wavelength of the laser light. It enables soft ionisation of the sample by absorbing the majority of the energy from the laser, ionising and desorbing into the gas phase. The sample of interest will also desorb into the gas phase, and it is within this plume that matrix – sample interactions will ionise the sample. Generally ionisation is by protonation or deprotonation, however, some matrices work by electron transfer.

Unfortunately there is not a single matrix material that is suitable for every compound analysed with MALDI. For different analytes the interaction with a given matrix material may be different and structural features may afford a particular way of ion formation. Consequently, the features of the matrix and the analyte must complement each other.

There are, however, some matrices whose usage is fairly prevalent. These include:

- 2,5-dihydroxybenzoic acid, DHB
- α -cyano-4-hydroxycinnamic acid, α -HCCA
- 3,5-dimethoxy-4-hydroxycinnamic acid, Sinapinic acid
- 9-nitroanthracene, 9-NA

Prior to the use of DCTB, the MALDI analysis of fullerenes and their derivatives was typically performed employing 9-NA as the matrix. DCTB was first used as a matrix for various fullerene derivatives in 1999^{1, 2}. DCTB led to more abundantly observed molecular ions in both positive-ion and negative-ion mode and the degree of fragmentation was markedly reduced.

DCTB

DCTB was first studied seriously in 2000, by comparing it to the traditional fullerene matrix 9-NA, and the universally used matrix, DHB³. Using the substituted fullerene: bis(4-methoxy-

phenyl)methano[60]fullerene, positive-ion and negative-ion mode spectra were obtained. The matrices and samples were mixed in 100/1 to 1000/1 molecular ratios. In negative-ion mode, clean spectra with a dominant molecular ion peak were obtained. In positive-ion mode, the molecular ion peak was also the most intense signal, however, there was also adduct formation of the type $[M+H]^+$, $[M+Na]^+$ and $[M+K]^+$; and loss of a methyl group – $[M-CH_3]^+$.

When the other matrices were used, however, there was fragmentation of the sample and the most intense peaks in the spectra resulted from the matrices.

A more in depth study of suitable matrices for fullerenes and their derivatives appeared in 2001, with 14 different matrices, including DCTB being tested⁴. These matrices were:

- 9-NA
- DHB
- Sudan Orange G
- α -HCCA
- Sinapinic Acid
- 5-Methoxysalicylic Acid, MSA
- 2-(4-hydroxyphenylazo)benzoic Acid, HABA
- DCTB
- 6 related β -carboline alkaloids:
 - Norharmane
 - Harmane
 - Harmine
 - Harmol
 - Harmalol
 - Harmaline

This study was aimed at finding a replacement matrix for the fullerene standard 9-NA, as this compound has the following drawbacks:

- It easily transfers oxygen to the analyte, which is problematic if one is not sure about the oxygen content of the analyte.
- At higher laser fluence the matrix clusters and this can obscure peaks of interest.

The matrices behaved differently depending on the polarity of the instrument. In positive-ion mode, only two of the matrices produced an intact molecular ion peak – these were DCTB and 9-NA.

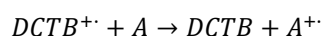
In negative-ion mode, only 3 of the possible candidates did not produce an intact molecular ion – harmalol, MSA, and HABA. Of the remaining 11 matrices only 3 gave an abundant ion signal – DCTB, norharmane, and harmane. Of these 3, only DCTB produced a clean spectrum with very little fragmentation.

It appeared from this study that DCTB gave the best performance as a fullerene matrix for both ion modes.

From this and previous studies DCTB was identified as an electron transfer matrix, as there was no protonation/deprotonation of the sample and only the radical ions of the analyte were observed. This was confirmed by a study into the thermochemistry of DCTB⁵.

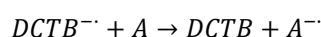
If DCTB does indeed ionise the samples via electron transfer, then the following reactivities can be expected:

In positive-ion mode:



This reaction will occur provided $IE_{DCTB} > IE_A$.

In negative-ion mode:



This reaction will occur provided $EA_{DCTB} < EA_A$.

The vertical ionisation energy of DCTB was obtained by photo-electron spectroscopy as 8.54 ± 0.05 eV, which is in excellent agreement with the calculated value of 8.47 eV (AM1 calculations). The electron affinity has only been obtained so far by quantum chemical calculations to lie between 2.31 eV and 2.0 eV, depending on the method used.

Using these values, DCTB was used as a matrix for the following samples:

- Phenanthrene: IE = 7.9 eV
- Anthracene: EA = 530 ± 5 meV
- C₆₀F_{46/48}: IE = 12 eV, EA = 4.06 ± 0.25 eV

Using the calculated values for the IE and EA of DCTB, it is possible to predict the appearance of the spectra for the aforementioned analytes:

Phenanthrene:

$IE_{\text{phenanthrene}} < IE_{\text{DCTB}} \rightarrow$ Molecular ions should be detected in positive-ion mode MALDI

Anthracene:

$EA_{\text{anthracene}} < EA_{\text{DCTB}} \rightarrow$ Molecular ions should not be detected in negative-ion mode MALDI

$C_{60}F_{46/48}$:

$IE_{C_{60}F_{46/48}} > IE_{\text{DCTB}} \rightarrow$ Molecular ions should not be detected in positive-ion mode MALDI

$EA_{C_{60}F_{46/48}} > EA_{\text{DCTB}} \rightarrow$ Molecular ions should be detected in negative-ion mode MALDI

The actual experiments performed reflected the above predictions, as tabulated below:

Phenanthrene	Positive LDI Positive MALDI	No M^+ Intense M^+
Anthracene	Negative LDI Negative MALDI	M^- No M^-
$C_{60}F_{46/48}$	Positive LDI Positive MALDI Negative LDI Negative MALDI	No M^+ No M^+ M^- , fragmentation M^- , low degree of fragmentation

Table 5.1: Results of using DCTB as a matrix for various compounds

As a result it was shown that MALDI analysis with DCTB proceeds in fact within the boundaries of this thermodynamic frame provided by the respective ionisation energies and electron affinities.

Pencil Lead

Graphite has been used in various forms as a matrix for MALDI; however, it is typically very difficult to apply to the target plate as well as to achieve an even reproducible surface coverage. Graphite particles were combined in solution with more common matrix materials and such suspensions were used for MALDI analysis in an attempt to alleviate the application problems.

Graphite has been shown to be an effective matrix material for various analytes, such as peptides, proteins and polymers, so it is therefore desirable to find an easy way of using graphite as a MALDI matrix.

Pencil lead consists of graphite mixed with clay and varying levels of oils and waxes. It is produced in different levels of hardness and blackness - ranging from 9H, which is the very hardest and creates a very light grey mark upon paper, to 9B, which is very soft and will leave a very dark mark upon paper. Generally the softer the pencil, the more graphite it contains. There are many reasons why pencil lead would be a desirable matrix – its usage is safe, cheap and quick and easy to prepare – one would just have to draw on the target plate. Also, there are no solvent compatibility issues, and the hydrophobic surface tends to help in producing a sweet spot: as the sample solution is applied, it will dry in one place. Also, there are benefits from the additives in pencils – the wax appears to help with ensuring an even reproducible coverage of graphite on the surface.

Pencil lead was first used as a matrix in 2006, in the analysis of various samples including peptides such as substance P, polymers, actinide metals such as uranium, and terfanadine⁶. The results were impressive, in particular, as a matrix for Uranium. The laser power could be reduced from 100% for LDI, to 50% with pencil lead, and a better signal-to-noise ratio was achieved. There was also complete matrix suppression, so that no unwanted matrix signals had to be considered.

In cases where the matrix was not suppressed, it was found that the matrix produced carbon cluster peaks in the low mass range, ranging from C₉ to C₂₄, which could then be used for calibration.

Interestingly enough, when used as a matrix for Substance P, fragment ions were produced which were adducted by sodium and potassium. This demonstrated that the pencil lead had partially protected the sample and aided the ion formation, since if the fragments had been formed as a direct result of laser irradiation, they would be lacking these adducts.

For this study a range of pencil grades were tested, ranging from 4H to 6B. It was found that 6B gave the best performance and this was assumed to be caused by it having the highest graphite content of all the pencils tested. Moreover, the softness of the pencil, which led to easier application and a more even coverage, appeared to offer a better reproducibility.

A follow up study tested a wider range of pencils on a selection of 50 small molecules, which included peptides, polymers, steroids and sugars. This included such molecules as α -cyclodextrin, atropine, caffeine, cocaine, disopyramide, and haloperidol. This study led to

slightly differing results. Here, the 2B pencil was found to give the best results for the range of samples tested⁷.

Of the 50 molecules tested, pencil lead did not work as a matrix for six of them. This study also found that the 6B pencil gave only poor ionisation, possibly as a result of too much graphite being deposited on the surface.

Of course the differences could also have arisen from the different brands of pencil used, as the additives differ both in what is added and the amounts used. However, in both studies a wide range of pencil brands were employed as matrices and were tested on all the different samples.

Pencil lead was considered in further detail as a matrix for polymers in a study looking specifically at silyl hydride functionalised polystyrenes, which are particularly sensitive to the preparation methods commonly used in MALDI for polymers⁸.

The common method for MALDI analysis of polymers is to use dithranol as the matrix, with silver trifluoroacetate (AgTFA) as an additive. If this method is used for the derivatised polystyrenes, then the silane moiety is oxidised.

Mass spectra of non-functionalised polystyrene were obtained using a 6B pencil as a matrix, with and without AgTFA as an additive. The sample was successfully ionised and sufficiently protected. With the AgTFA additive present, the peaks were the most intense of all the spectra obtained, with a good signal-to-noise ratio, with the silver adducted peaks the most intense of all. Without the AgTFA additive, the most intense peaks present were sodiated. It was found that using AgTFA and pencil lead as the matrix, better spectra were obtained than for the typical method of dithranol/AgTFA.

To apply this to the silyl hydride functionalised polystyrene, spectra were obtained and compared using as a matrix either a 6B pencil, or dithranol, with the additives lithium trifluoroacetate (LiTFA) and AgTFA, respectively.

It was important to find conditions under which the integrity of the end groups could be preserved, as they easily underwent side reactions using dithranol/AgTFA.

It was found that using pencil lead and LiTFA, there were no side reactions, and the only adducts formed were lithium adducts.

In summary, pencil lead is looking promising as a new matrix with a broad range of applications. In the present investigation, several fullerene derivatives were tested with the use of pencil lead in order to test the suitability of it as a matrix material for this class of compounds. Comparison was made with DCTB as the benchmark matrix and samples were chosen which would allow easy cationisation by the pencil lead matrix.

Experimental

The fullerene derivatives studied in this chapter are below. (Note the abbreviations underneath the structures, which were used throughout to characterise the sample)

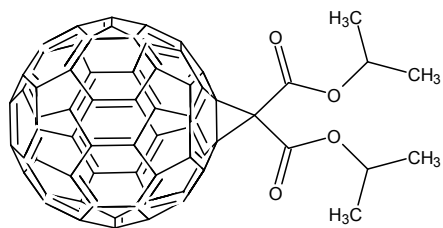


Figure 5.1: Structure of "Isopropyl Mono"

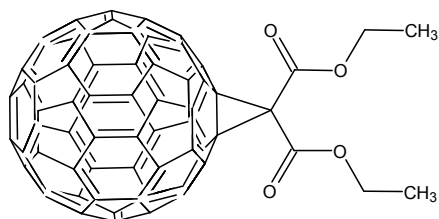


Figure 5.2: Structure of "Mono"

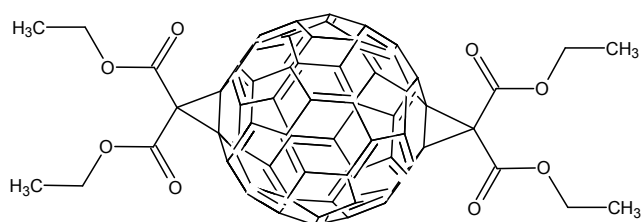


Figure 5.3: Structure of "Bis"

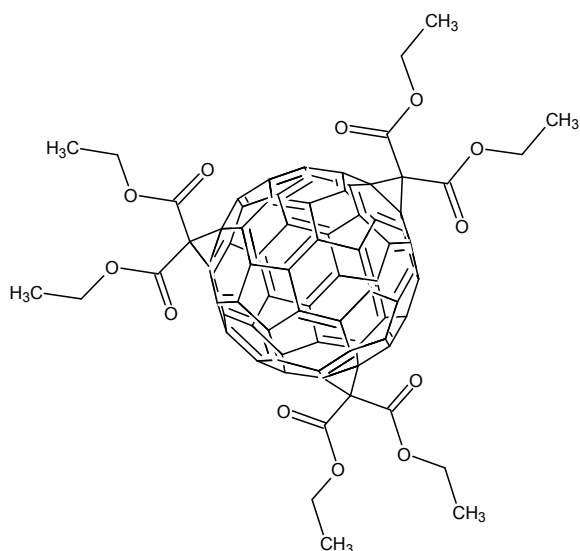


Figure 5.4: Structure of "Tris"

These compounds were isomerically pure. Since these compounds are already several years old they showed slight signs of oxidation. This, however, was of no relevance to the present investigation.

Some of the open cage fullerenes from chapter 3 were also studied. Here the following isomers were of interest:

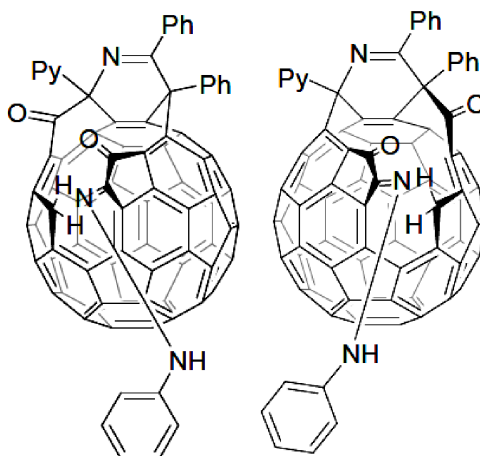


Figure 5.5: Structures of 2.1 (above left) and 2.2 (above right)

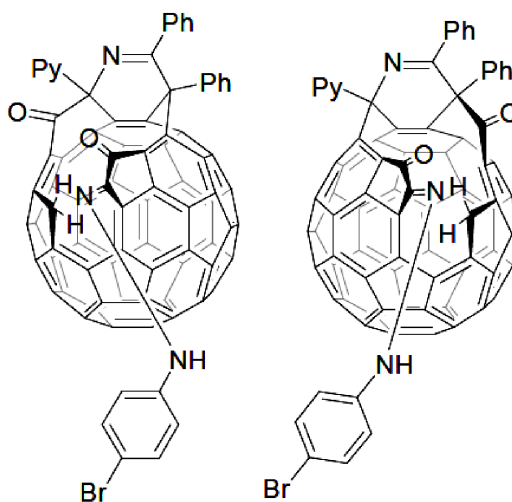


Figure 5.6: Structures of 2.3 (above left) and 2.4 (above right)

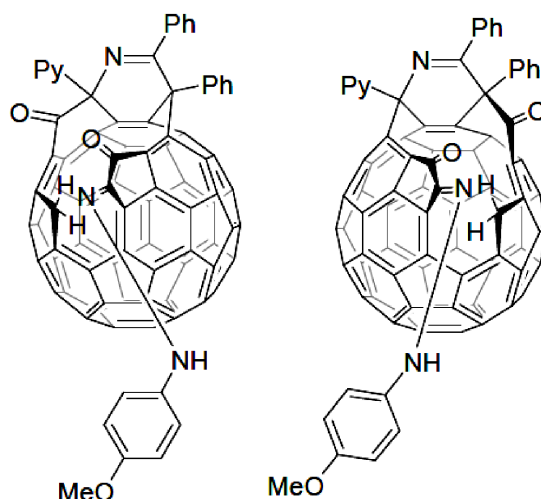


Figure 5.7: Structures of 2.5 (above left) and 2.6 (above right)

A typical sample preparation method involved dissolving the sample in toluene at a 1 mg/ml concentration. A Whirlimixer was used to ensure complete dissolution.

DCTB was prepared in a 10 mg/ml solution, which was added to the sample as required, typically in a 1:50 sample:DCTB molar ratio.

6B and 8B Staedtler branded Mars Lumograph pencils were used throughout and were applied individually on the target spots. A Grafix branded HB pencil was also tested. A pressure equivalent to writing was used to transfer pencil lead to the target plate, except in the experiments where the pressure used to apply was harder or lighter, in an attempt to increase and decrease the amount of pencil lead on the target plate. The entire slide was held in an air stream to remove any loose pencil lead prior to sample application.

The sample solutions were applied one drop at a time using a 1-10 μl Barksy $\mu\text{tipipette}$ and allowed to dry between applications. Typically 5 μl of the solution was applied to each target spot.

For the DCTB experiments, the DCTB solution and sample were mixed and applied together and typically 5 μl of this solution was used per target spot.

Results

Pencil as a matrix

As an initial step, test experiments were performed to evaluate the viability of pencil as a matrix for derivatised fullerenes. Experiments were performed in both ion modes and in comparison with direct LDI and DCTB-MALDI. The methano-bridged [60]fullerenes: isopropyl mono, mono, bis and tris (all displayed in the introduction to this chapter) were chosen as the test compounds, as their behaviour under LDI and MALDI conditions has been described in detail earlier⁴.

Isopropyl Mono

Isopropyl mono was chosen as an ideal representation of a fullerene derivative with which to test the use of pencil as a matrix, as it severely dissociates under direct LDI conditions, but delivers a molecular ion almost free of decomposition when protected under true MALDI conditions. Comparing standard DCTB-MALDI and LDI spectra of isopropyl mono, below, shows how important a matrix is in order to achieve a molecular ion peak:

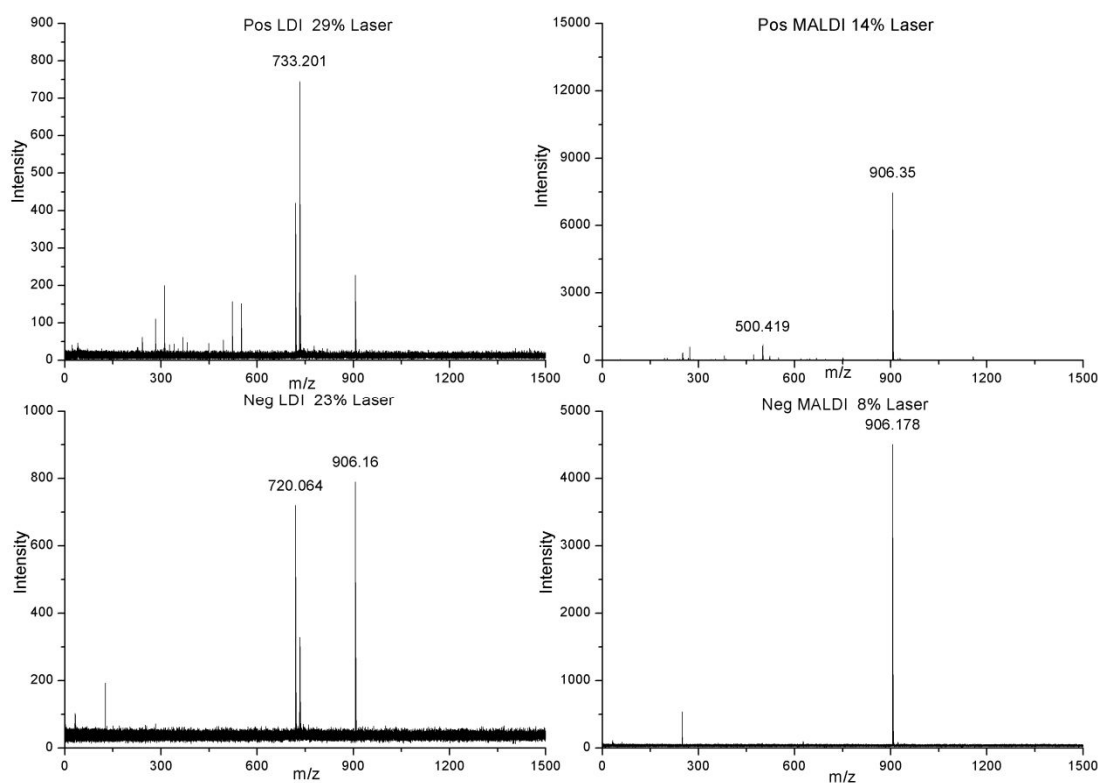


Figure 5.8: Positive-ion and negative-ion mode LDI and DCTB-MALDI of Isopropyl mono

It was noted that the laser power had to be markedly enhanced for LDI compared to MALDI, in order to obtain a molecular ion peak, however, this also results in extensive fragmentation. By comparing actual intensity values it is obvious how few ions are produced with the LDI method, there is also a smaller signal-to-noise ratio when compared to DCTB-MALDI.

Initial positive-ion mode spectra of isopropyl mono on 6B and 8B pencil are below. The fragmentation peaks at m/z 720 (C_{60}) and 733 ($C_{61}H$) are immediately obvious. Also, there is not an obvious peak at m/z 906, but peaks are present at m/z 929 and 945, which indicate addition of sodium and potassium.

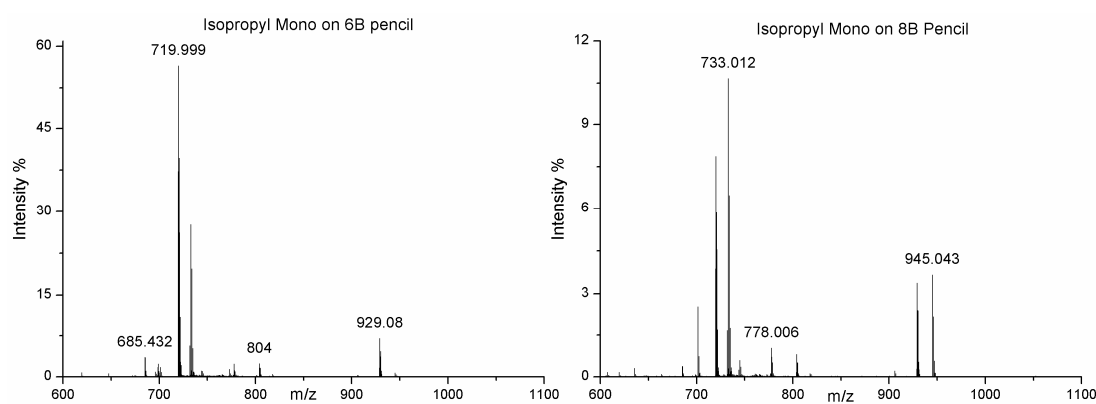


Figure 5.9: Spectra of isopropyl mono on 6B and 8B pencil

Varying the application of the pencil

The matrix-to-analyte ratio is of crucial influence to the outcome of a MALDI experiment. Therefore, it was decided to test how different applications of the pencil might affect its ability to behave as a matrix. For the majority of experiments, the pencil was applied at a normal writing pressure. For the present experiments the pencil was either lightly scraped over or heavily pressed across the surface of the target plate, leaving less or more pencil lead attached to the target plate, respectively, the excess material was blown from the target plate with an air stream. The light or heavy application of pencil lead was obvious to the eye. Spectra of isopropyl mono were obtained in both positive-ion and negative-ion mode, with linear detection, at a range of laser powers.

The positive-ion mode spectra are shown below. It can be observed that there are no great differences between the spectra. This is the case when comparing either between light and

heavy application, or between the hardness of pencil (6B vs. 8B). All spectra below were obtained at 40% laser power.

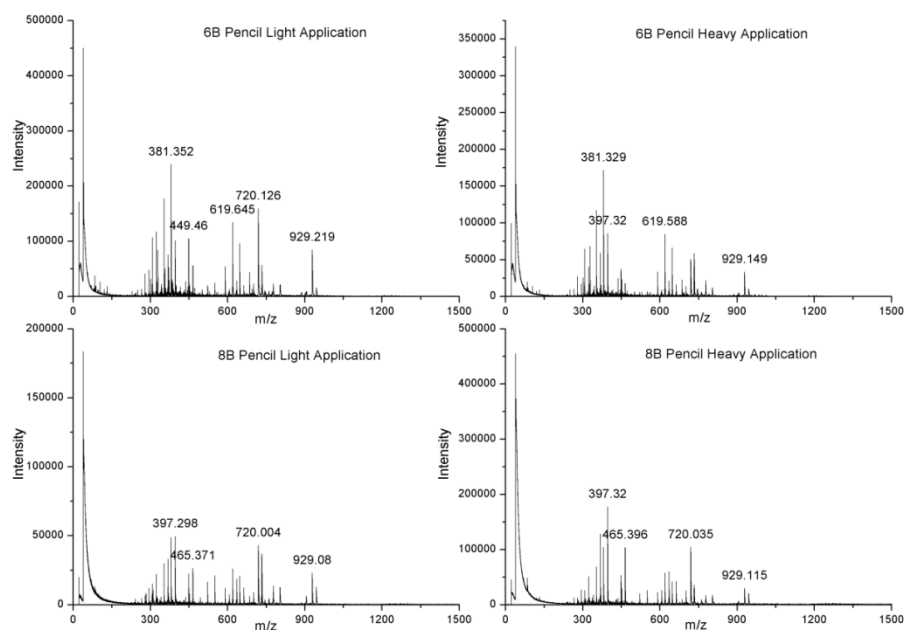


Figure 5.10: Light and heavy application of pencil as a matrix for isopropyl mono

There is extensive fragmentation. The dominant peak in each spectrum is K^+ . The molecular ion peak at m/z 906 is of very low abundance, however, it can be noted that there is abundant sodium and potassium ion attachment to the isopropyl mono at m/z 929 and 945. Clearly, variation of the amount of pencil lead has little influence on the appearance of the positive-ion mode spectra.

The following are the corresponding spectra in negative-ion mode, all at 50% laser power.

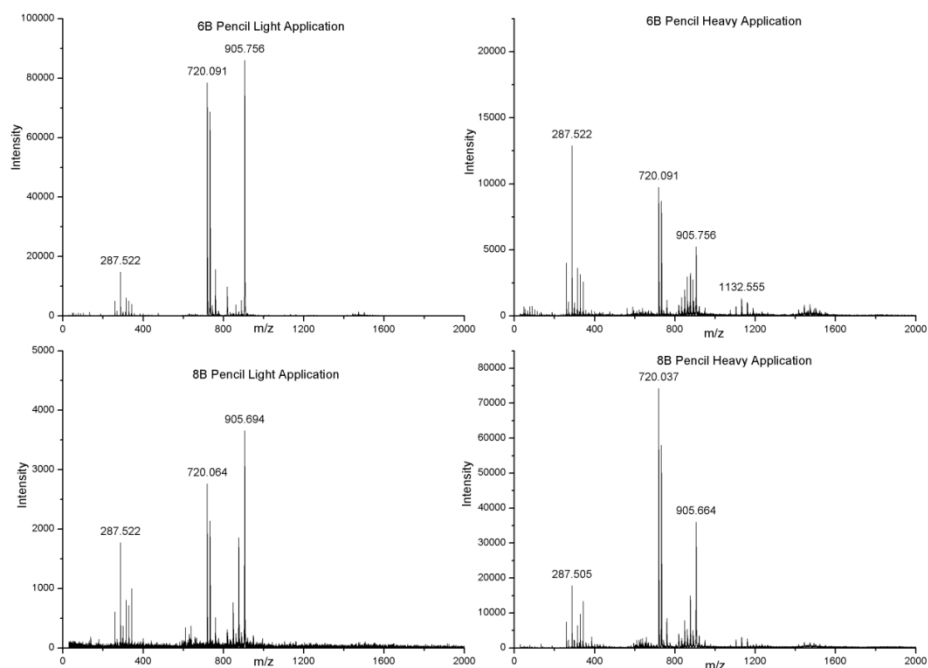


Figure 5.11: Light and heavy application of pencil as a matrix for isopropyl mono

Here a slight difference can be observed between light and heavy application – the ratio of the C_{60} fragment to the molecular ion peak increases when going from light to heavy application. The trend is the same for both the 6B and the 8B pencils, suggesting that this pattern is real and not just a random event. It appears that the light application protects the sample more; the fragmentation signals are less intense than the molecular ion peak. It is clear that metal ion attachment is not a mechanistic option for the ion production in the negative-ion mode. Two mechanisms may be operative in this case. On the one hand, there can be electron attachment to desorbed molecules which may be also followed by fragmentation and on the other hand there can be fragment ion formation by direct laser desorption ionisation. Both of these processes may contribute to a different extent when the pencil lead loading is varied. The observation that a higher pencil lead loading leads to spectra that would result from harsher conditions could, for instance, be explained by assuming that ionisation through electron attachment becomes less favoured. Too much pencil lead may hinder the release of electrons from the surface that would be needed for the ion formation and direct laser ablation may be more prominent, leading to more fragment ions. Alternatively, with more pencil lead on the target, each laser pulse would release more matrix into the plume, which would alter the heating and cooling processes within leading to fragmentation.

A heavier loading of the 6B pencil seems to enhance the overall ion yield, whereas the use of the 8B pencil seems to have the opposite effect. At this point it can only be speculated if this is caused by the different composition of the two types of pencil.

Although the spectra are much cleaner than in the positive-ion mode, there are still low mass ions abundantly observed which have their origin in the pencil lead and thus would interfere with analyte-derived ion signals. Also, the fragment ion production in the negative-ion mode is as severe as in the positive-ion mode. In comparison with negative-ion MALDI using DCTB, one has to conclude that the pencil has some protecting effect, but does not match the high quality spectra obtainable in negative-ion MALDI.

In summary, it appears that the use of pencil lead as matrix for negative ion analysis has some major disadvantages compared to the application of DCTB-MALDI. However, pencil lead may more successfully compete in the positive-ion mode with conventional MALDI, as ion formation through metal cation attachment is clearly the dominating mechanism by which positive ions are formed. In order to accurately compare the matrix performance of pencil lead a careful comparison of 6B and 8B pencil lead to direct LDI and DCTB-MALDI was performed in the following. The four different types of targets were tested while the activating laser power was varied.

Pencil lead performance check against LDI and (conventional) DCTB-MALDI

Isopropyl mono was again chosen as the test compound and comparison was made for the four different targets: direct LDI (no matrix), DCTB-MALDI, 6B and 8B pencil. To ensure a "fair" testing, the same isopropyl mono solution was used and all experiments were performed at the same time ("in one sitting" on the same day) to ensure that machine conditions could not alter the results. The spectra were obtained in positive-ion mode, using reflectron detection and over a wide range of laser powers. The laser powers chosen ranged from 4% to 24% changed in intervals of 4%.

Below 4% it was difficult to obtain a signal for any method and above 24% the spectra did not alter much with higher laser fluences.

The spectral data were analysed and the results are summarised in the following table.

Laser Power %	LDI	DCTB-MALDI	6B Pencil MALDI	8B Pencil MALDI
4	No signal	Intense peak at m/z 906	No signal	No signal
8	No signal	Intense peak at m/z 906	No signal	No signal
12	Small peak at m/z 720	Intense peak at m/z 906. Small peaks at m/z 720, 796, 805, 818, 949, 1026, 1156	Small peak at m/z 733	No signal
16	Small peaks at m/z 720 and 733	Most dominant peak still at m/z 906, other fragmentation increasing	Peaks at m/z 23, 39, 720 and 733	Peak at m/z 39 dominant. Smaller peaks at m/z 23, 720, 733, 804, 945.
20	Peaks at m/z 720, 733, 778, 745, 804	Most dominant peak at m/z 906, extensive fragmentation	Peak at m/z 39 dominant, other peaks at m/z 23, 720, 733, 778, 804, 929, with smaller peaks at m/z 906 and 945. Extensive fragmentation between m/z 250 – 500.	Peak at m/z 39 dominant. Smaller peaks at m/z 23, 720, 733, 745, 778, 804, and 906. Slightly larger peaks at m/z 929 and 945. Fragmentation between m/z 250 – 500
24	Peaks at m/z 720, 733, 778,	Most dominant peak at m/z 906,	Peak at m/z 39 dominant, other	Peak at m/z 39 dominant. Smaller

	745, 804	extensive fragmentation	peaks at m/z 23, 720, 733, 778, 804, 929, with smaller peaks at m/z 906 and 945. Extensive fragmentation between m/z 250 – 500.	peaks at m/z 23, 720, 733, 745, 778, 804, 906 and 945. Slightly larger peak at m/z 929. Fragmentation between m/z 250 – 500
--	----------	-------------------------	---	---

Table 5.2: LDI, 6B-, 8B- and DCTB-MALDI of Isopropyl Mono at different laser powers

Example spectra are shown below, showing the four methods at three of the different laser powers. The first set depicted at 8%, shows a clear molecular ion peak when DCTB is used as the matrix. The spectra for LDI and where 6B and 8B pencils are used as matrices show only noise. The y-axis displays actual intensities, rather than relative intensities as percentages to the dominant peak. This allows for comparison between each method. In the LDI, 6B and 8B pencil spectra, the peaks are not higher than 20 (intensity units). Comparison to the DCTB-MALDI spectrum, where the isopropyl mono peak is at a value of approximately 19000, shows the effectiveness of the DCTB-MALDI performance.

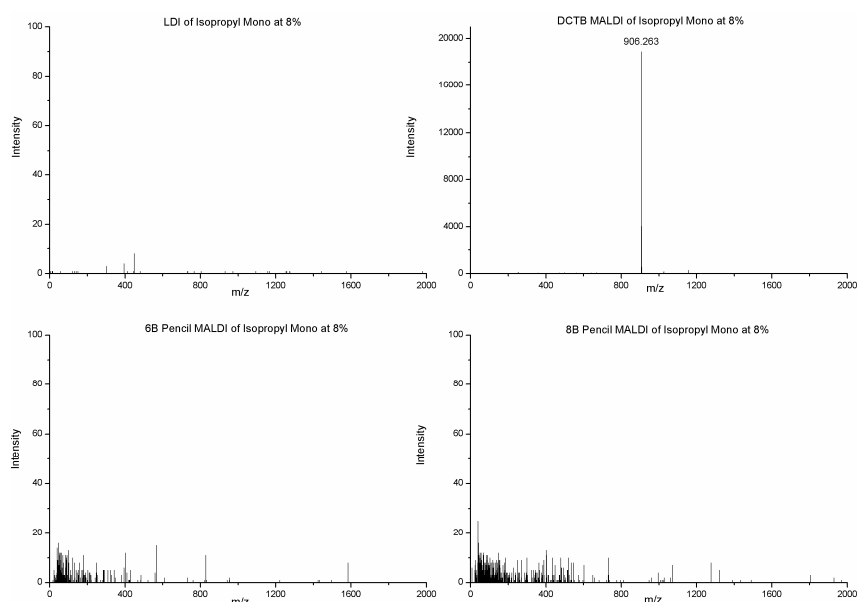


Figure 5.12: LDI, 6B-, 8B-, DCTB-MALDI spectra of isopropyl mono at 8%

At 16% laser power, shown below, peaks are present in all spectra; however, for the LDI, 6B and 8B pencil spectra, these peaks are only due to fragmentation and the molecular ion or

quasi-molecular ion is not observed. The peaks at m/z 720 (C_{60}^+) and m/z 733 ($C_{61}H^+$) are fragment ions, which either arise from complete decomposition of directly ionised isopropyl mono or through ionisation of fragments that result from decomposition of neutral isopropyl mono. In any case, these ions indicate that only fairly drastic conditions prevail.

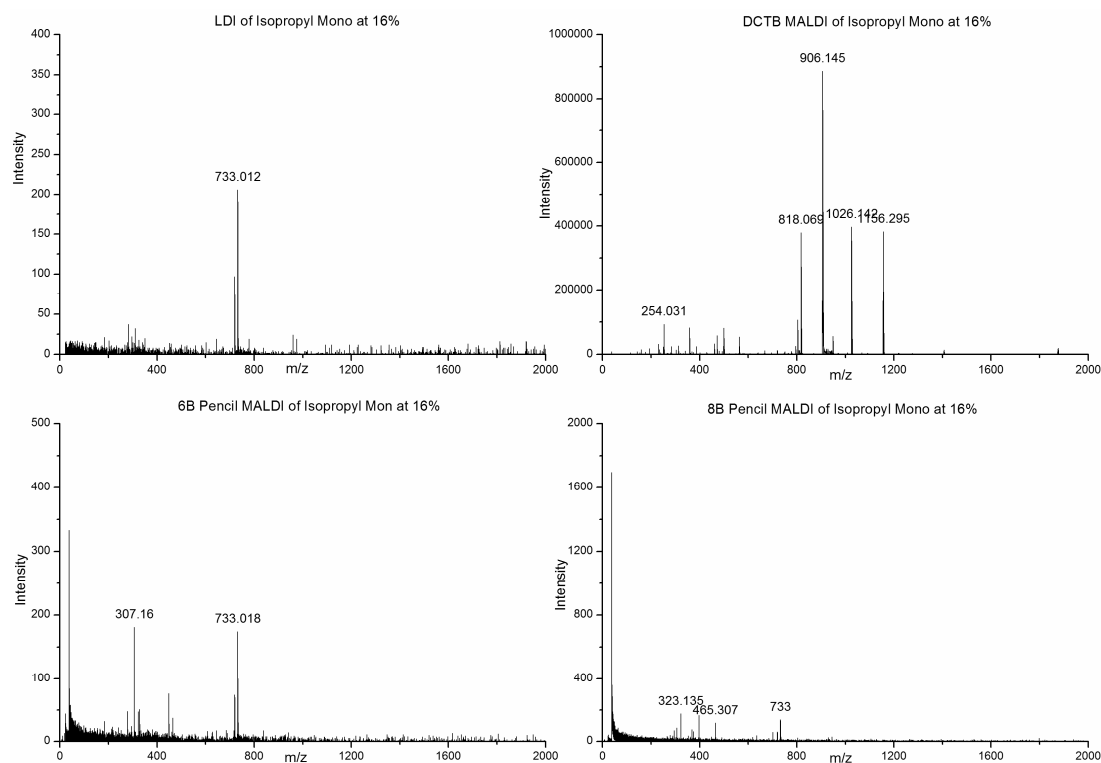


Figure 5.13: LDI, 6B-, 8B-, DCTB-MALDI spectra of isopropyl mono at 16%

In the DCTB-MALDI spectrum the molecular ion is still the base peak, although additional signals appear. The peaks at lower masses than m/z 906 may result from fragmentation (besides those derived from the matrix) and higher mass signals can be attributed to the addition of DCTB to the analyte molecule. However, important is that the fragmentation down to C_{60} is still rather minute with the molecular analyte ion representing the most abundant peak.

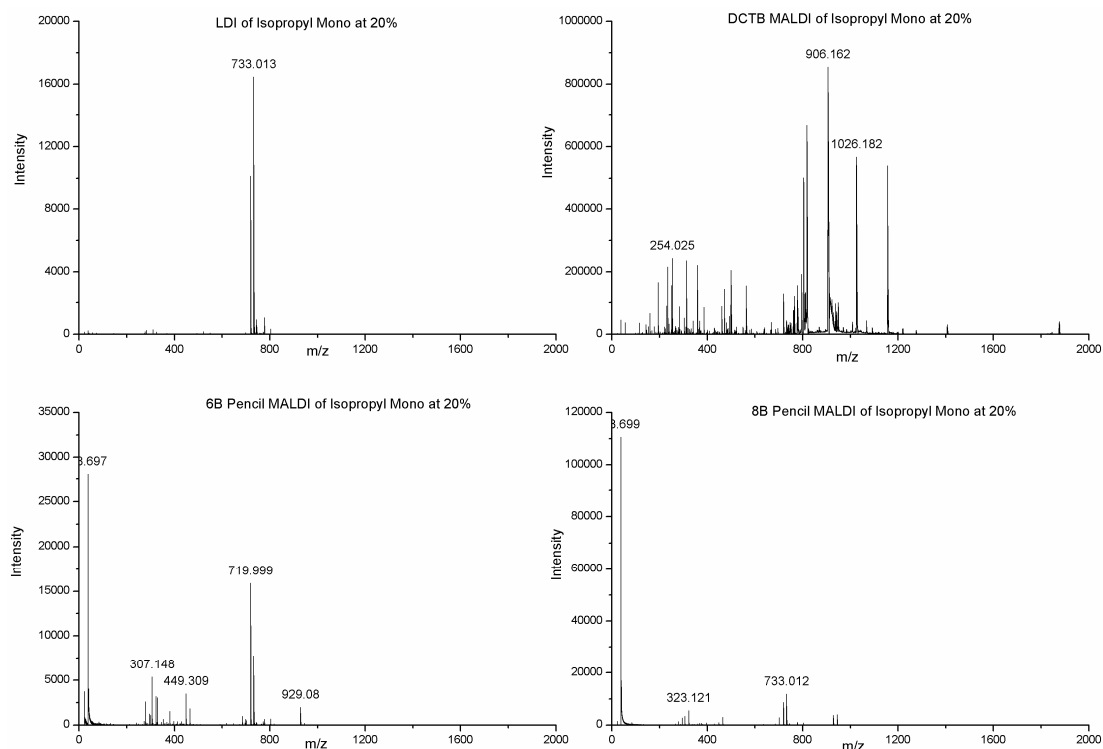


Figure 5.14: LDI, 6B-, 8B-, DCTB-MALDI spectra of isopropyl mono at 20%

The 20% laser power mass spectra are shown above. The main difference is that at this laser power, the sodium and potassium adducts of the analyte are starting to appear in the pencil spectra. The fragmentation peaks are, however, of a greater intensity than the sodium and potassium adducts. K^+ dominates each of the pencil spectra.

The LDI spectrum is still only producing fragmentation peaks. The DCTB-MALDI spectrum shows extensive matrix peaks and fragmentation, yet the dominant signal is still the molecular ion. The overall intensity is far greater with MALDI than with the other methods, which demonstrates how efficient desorption and soft ion formation is using DCTB-MALDI.

In summary, using isopropyl mono as the analyte, pencil lead is inefficient as a MALDI matrix. The formation of quasi-molecular ions is observed in the form of sodium and potassium adducts to the analyte. However, the formation of such quasi-molecular ions occurs at such enhanced laser powers that severe fragmentation is always observed as well. There is also a low abundant molecular ion present, however, the production of which is rather minute. Fragmentation is already abundantly observed at lower laser powers than needed to observe the quasi-molecular ions. Therefore, a large fraction of the fragmentation may be caused by direct laser activation of analyte that remains unprotected through the

pencil matrix. DCTB comes out as a far superior matrix, producing a molecular ion peak at low laser powers, with much reduced or no fragmentation at all.

Finally, positive-ion and negative-ion mass spectra of the 6B and 8B pencil lead are shown without the presence of the analyte. Sodium and potassium ions are abundantly observed in the positive-ion mode, identifying the pencil lead as the source of these ions. There is little difference between 6B and 8B when considering either positive or negative polarity. Positive-ion mode spectra are dominated by the potassium peaks, more so in 8B than 6B. The latter is also corroborated by more pronounced potassium adducts when analytes are present and 8B pencil is used.

It is also obvious that there are many interfering signals produced from the pencil lead which were observed in the experiments above and which are actually counterproductive for a straightforward analysis. These unwanted impurity signals were observed in both modes at enhanced laser powers. Unfortunately, the sodiated and potassiated molecular ions also occurred at such enhanced laser powers that wanted and unwanted signals co-exist in these spectra. The spectra below were obtained of just the pencil lead, and were the result of 35% laser power for positive, and 50% laser power for negative:

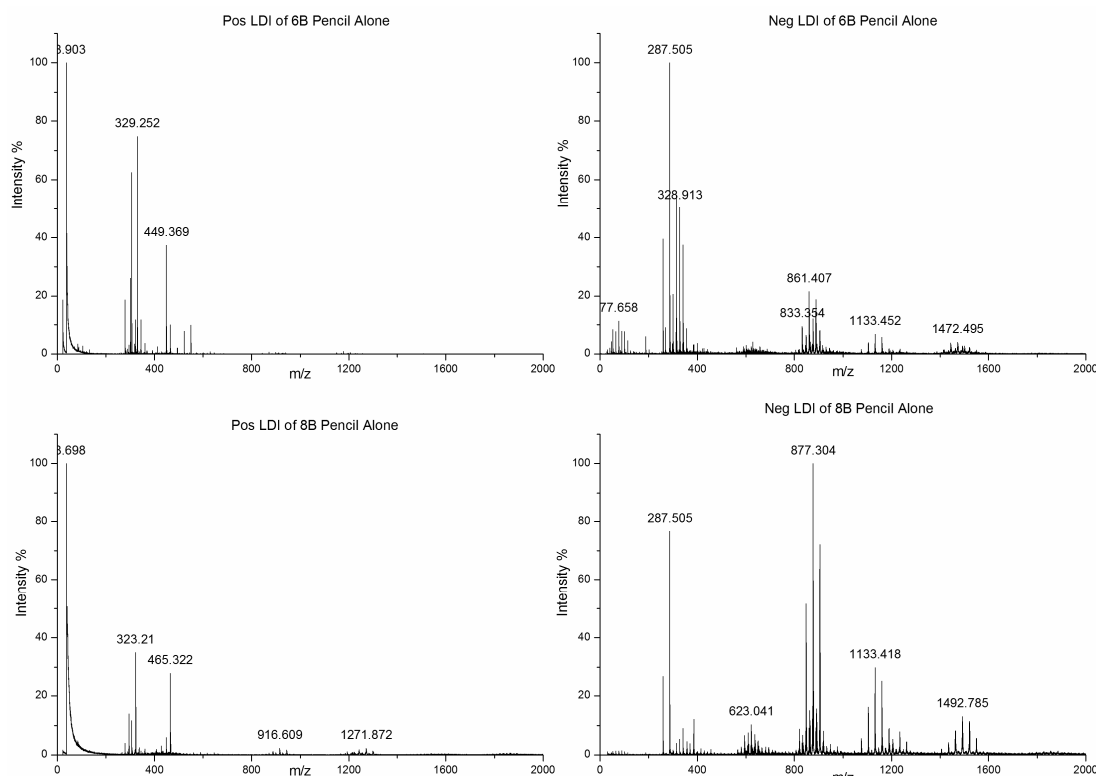


Figure 5.15: Positive and negative-ion mode LDI spectra of 6B and 8B pencil

Sodium and Potassium adduct formation with different analytes using pencil lead

One of the key features of using pencil lead as target substrate or “MALDI matrix” is the abundant formation of sodiated and potassiated analyte molecules. Despite the shortcomings that were identified in the preceding sections connected with the use of pencil lead, sodium and potassium cation addition is comparatively easily achieved. Conventional MALDI approaches would afford the preparation of an additional salt layer to the target if the formation of sodiated or potassiated analyte ions were the aim of the experiment. In summary, the relative ease by which these adducts seem to be formed carries a certain attraction. In the following, this type of adduct formation is investigated for a variety of different analytes with the aim to learn more about the attachment of alkali metal cations from pencil lead as a means of ion formation in laser desorption experiments.

Fullerene derivative with Crown Ether ligand

Initial tests of sodium and potassium addition were conducted with one of the compounds analysed in chapter 2, compound 8.13:

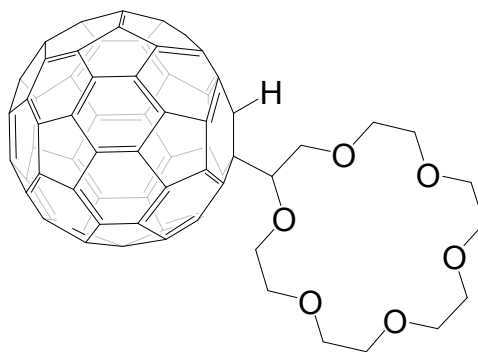


Figure 5.16: Structure of 8.13

This compound was thought to be interesting to study potassium and sodium attachment, due to the presence of the 18-crown-6 ether, which is known for its high affinity for potassium ions⁹.

A similar crown ether adduct to [60]fullerene was used earlier as a model compound in electrospray ionisation of fullerenes. The idea was at the time to link the fullerene synthetically to a crown ether which then would act as the target for cationisation with

sodium or potassium ions¹⁰. Therefore it is interesting to elucidate the behaviour of this model compound for a successful ESI experiment under MALDI conditions.

8.13 was applied to 6B and 8B, and laser activated. The resulting mass spectra are shown below for both ion modes.

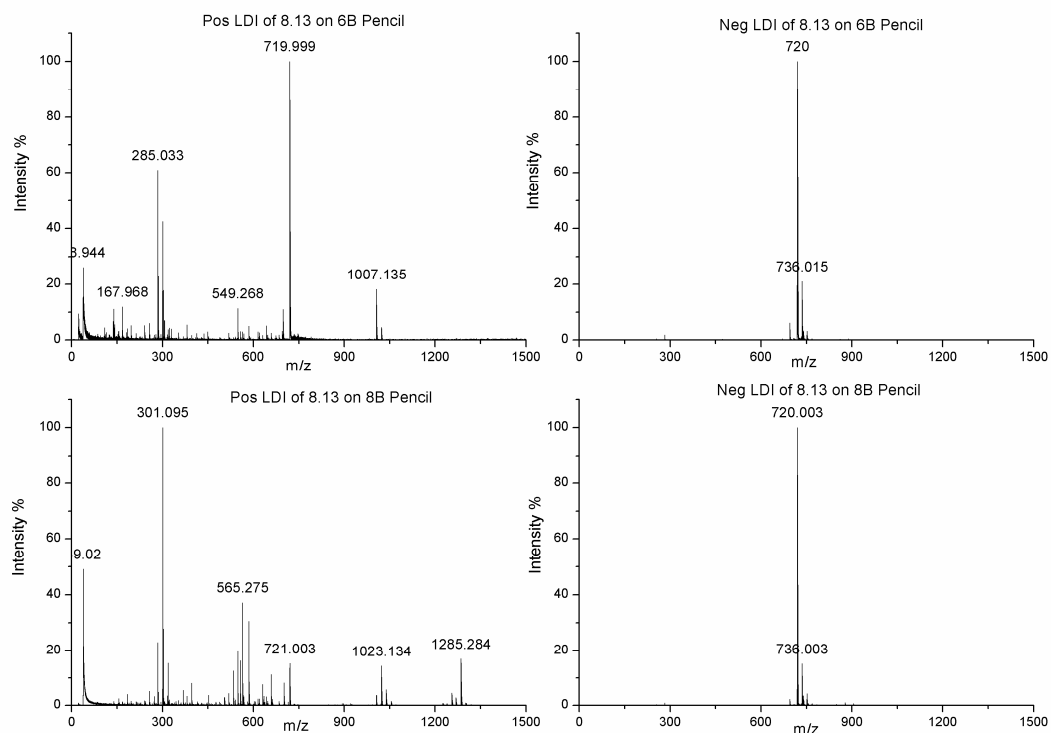


Figure 5.17: Positive and negative-ion mode LDI of 8.13 on 6B and 8B pencil

Enhancement of the molecular ion region is shown below:

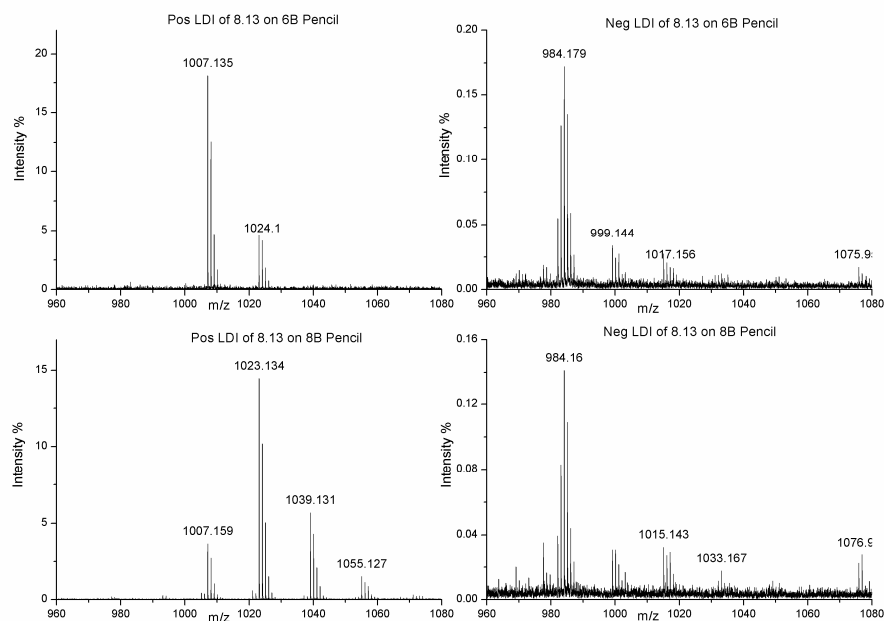


Figure 5.18: Positive and negative-ion mode LDI of 8.13 on 6B and 8B pencil

In the positive-ion mode spectra on the left, there is prominent sodium and potassium addition at m/z values 1007 and 1023, respectively. The bare molecular ion peak, at m/z 984, is at an extremely low intensity for both ion modes. All spectra are dominated by the C_{60} fragment ion, suggesting that pencil is not a very effective matrix for this compound. 6B and 8B pencil are again differentiated by the differences in intensity between the sodium and potassium adducts. The peaks at m/z 1039 and 1055 could be from oxygen addition. m/z 1039 could be either $[8.13-K-O]^+$, or $[8.13-Na-O_2]^+$. m/z 1055 could be either $[8.13-K-O_2]^+$, or $[8.13-Na-O_3]^+$. The negative-ion spectra also confirm addition of up to 2 oxygen atoms. Most likely, the sample has oxidised over time by adding a certain amount of oxygen. Depending on the softness of the experiment, these oxidation products were either observed or not. This is also supported by the DCTB-MALDI spectrum of sample 8.13 (shown in Chapter 3, figure 3.17), which clearly identifies the attachment of several oxygen atoms to the compound.

In summary, efficient sodium and potassium addition can be observed, but the overall appearance of the pencil spectra confirms that this approach is not comparable in softness and cleanliness compared to conventional MALDI. Having produced the cationised ions, MS/MS experiments (LIFT) are of interest to elucidate their fragmentation behaviour. Therefore, LIFT experiments were conducted with these quasi-molecular ions in the positive-ion mode.

Positive-ion mode LIFT-MS were obtained, resulting in the following spectra:

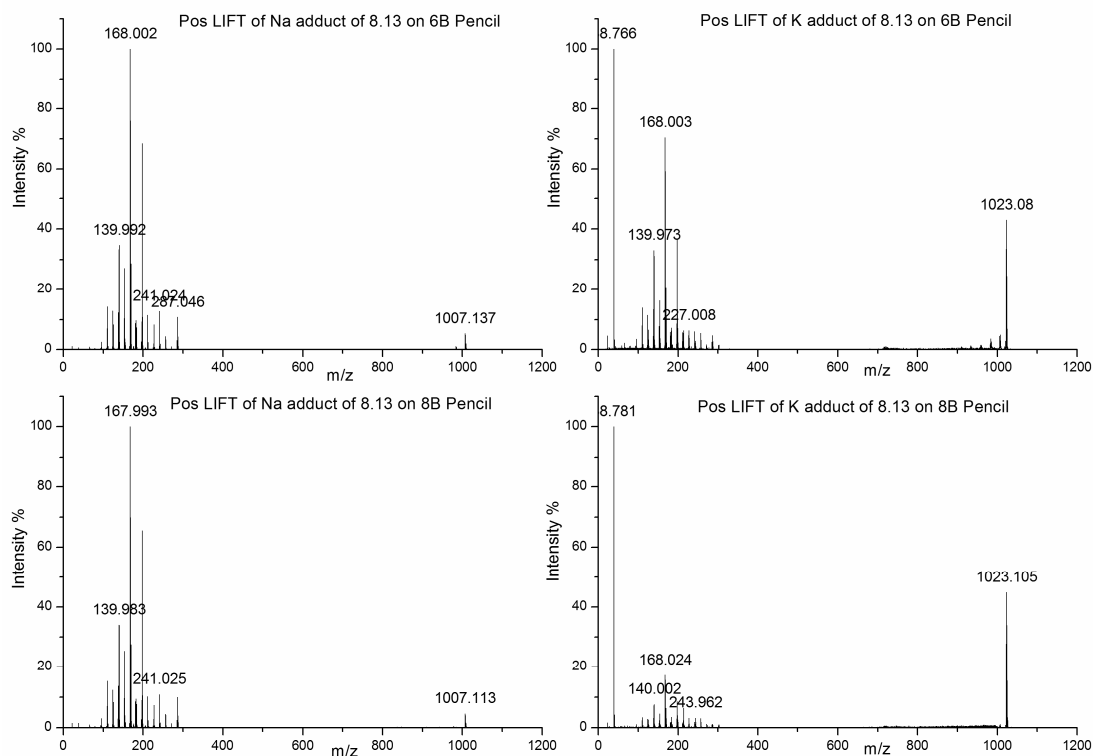


Figure 5.19: Positive-ion mode LIFT of the Na and K adducts of 8.13 on 6B and 8B pencil

At first sight, the daughter ion spectra of the alkali adducts show an unusual appearance. In particular, there is only the merest hint of a peak at m/z 720, corresponding to C_{60}^+ , and this can only be found in the LIFT spectra of the potassium adducts. In other words, the fullerene is not observed as fragment ion, which is indeed unusual, as dissociations of fullerene derivatives are often characterised by the loss of the ligand leading to a C_{60} fragment ion, which may fragment even further. Upon closer inspection, however, the present candidates do not behave differently; the distinct appearance of the spectra is caused by the unusual charge distribution of the compound. The charge is firmly located on the crown ether, so that charge migration to C_{60} is not occurring and C_{60} is in this case the neutral (uncharged) component of the fragmentation.

In order to elucidate this in more detail, the enhancement of the low mass region of the spectra is shown below, as the only region with a sizeable amount of fragment ions.

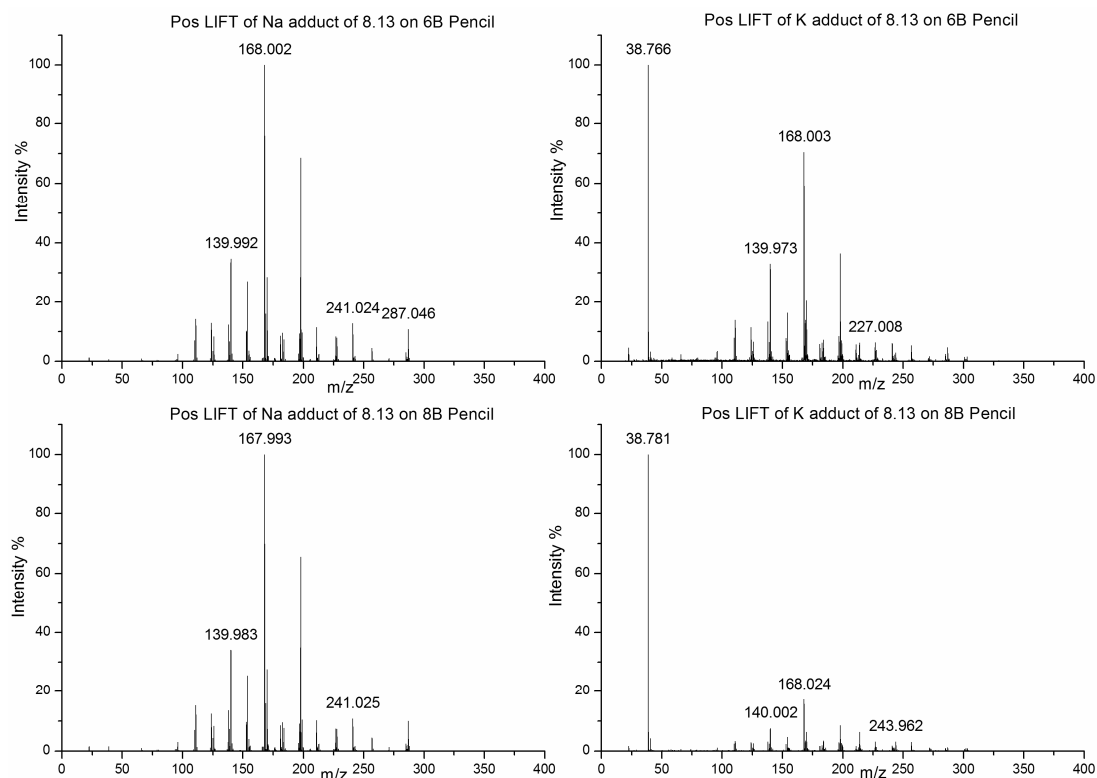


Figure 5.20: Positive-ion mode LIFT of the Na and K adducts of 8.13 on 6B and 8B pencil

The LIFT spectra of both the $[8.13\text{-Na}]^+$ and the $[8.13\text{-K}]^+$ adduct are almost identical with the only obvious difference being the dominating K^+ fragment ion in the spectra of the potassium adduct. However, the similarity of both spectra is an artefact and the less obvious difference of both provides a clue for the assignment of the signals: the highest mass in the low mass ion series of the $[8.13\text{-Na}]^+$ adduct is m/z 287 and the highest mass in the low mass ion series of the $[8.13\text{-K}]^+$ adduct is m/z 303. Both these ions correspond to the respective alkali ion adduct to the crown ether. In the dissociation, the cationised crown ether ligand is separated from the fullerene, whereby the hydrogen atom moves from the fullerene to the crown ether, which continues to carry the charge and C_{60} is lost as the neutral fragment. The low mass region is then dominated by fragment ions that result from further dissociations of the sodiated crown ether. Also the potassium adduct spectrum is dominated by the fragmentation pattern of the sodiated crown ether which explains why both spectra do literally contain the same ions, demonstrated by the spectra below:

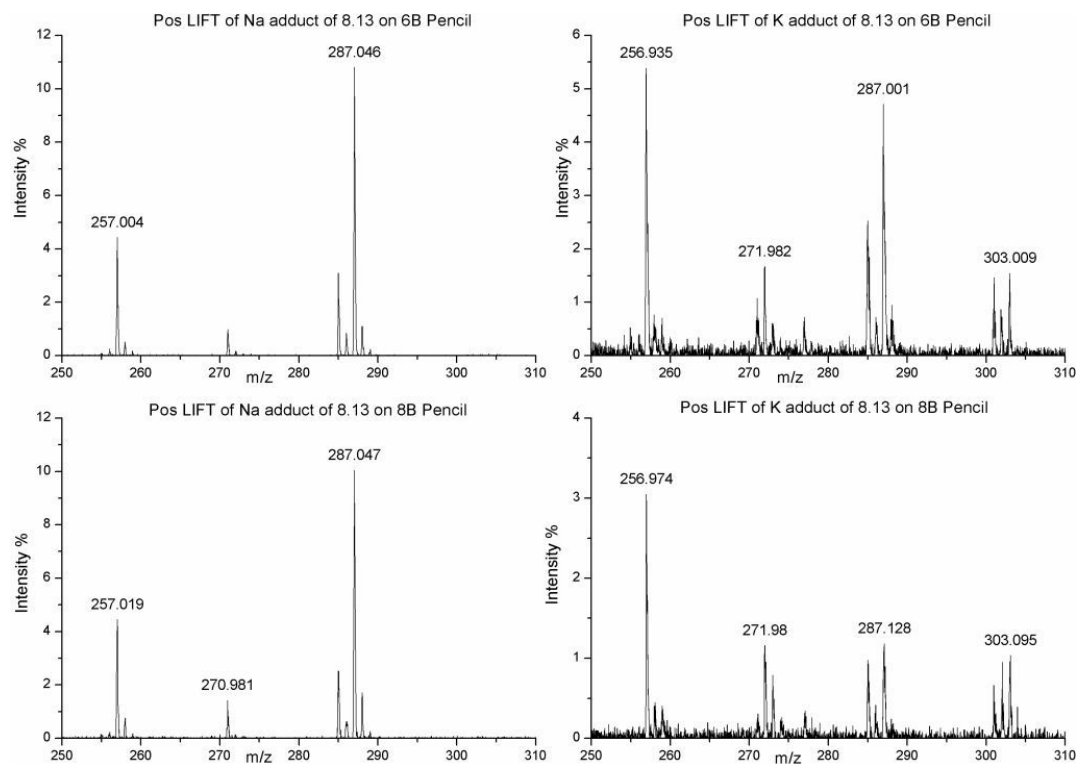


Figure 5.21: Fragmentation - $[\text{Crown}+\text{Na}]^+$ (m/z 287) and $[\text{Crown}+\text{K}]^+$ (m/z 303) during LIFT

The main (and almost only) fragment ion from the potassiated crown ether is in fact K^+ . This interpretation is in perfect agreement with the findings of Maleknia and Brodbeldt, who investigated the fragmentation behaviour of crown ether/alkali metal adducts and found that all metals show the same fragmentation behaviour while metal ion loss was enhanced with increasing size of the metal¹¹. Perfectly in line with these considerations it is found that the sodiated crown ether fragment ion dissociates by the loss of small neutrals with very little Na^+ being formed, while the corresponding potassiated crown almost entirely dissociates into K^+ . The seemingly absurd observation of sodiated crown ether in the dissociation spectrum of the selected potassium adduct can be explained by shortcomings of the ion gate. The resolving power (selectivity) of the ion gate is not high enough to achieve a complete separation of the sodiated and the potassiated species in this mass range. Consequently, both species will contribute to their respective daughter ion spectra, for instance, Na^+ and K^+ ions are present in the LIFT spectra of both adducts. As far as the relative contributions are concerned, the LIFT spectra of $[\text{8.13-Na}]^+$ are clearly less contaminated by contributions of $[\text{8.13-K}]^+$. There are several reasons for this. For the LIFT of either adduct on the 6B surface, there is much lower production of $[\text{8.13-K}]^+$ on this surface. On the 8B surface, $[\text{8.13-K}]^+$ is much more abundant than $[\text{8.13-Na}]^+$, but

contributions to the LIFT of $[8.13\text{-Na}]^+$ are much less severe as the $[8.13\text{-K}]^+$ adduct has a much lower tendency to fragment compared with $[8.13\text{-Na}]^+$. This is obvious when comparing the LIFT spectra of both ions; the $[8.13\text{-K}]^+$ adduct shows less fragmentation and a huge signal of $[8.13\text{-K}]^+$ is evident as comparatively more species survive the LIFT experiment intact. Consequently, $[8.13\text{-K}]^+$ produces less interfering signals when contributing to the LIFT spectrum of $[8.13\text{-Na}]^+$ on 8B. Comparing the LIFT spectra of $[8.13\text{-K}]^+$ obtained on 6B and 8B pencil, it becomes obvious that the interfering contributions of co-selected $[8.13\text{-Na}]^+$ are markedly reduced in the 8B experiment as $[8.13\text{-Na}]^+$ is produced in lower abundance.

The enhancement of the area around the molecular ion peak confirms, with a peak at m/z 1007, the sodium contribution to the potassium adduct. Furthermore, the 6B spectra show a series of ions spaced by C_2 losses, indicating fullerene fragmentation. These signals are due to coalescence of the target into larger fullerenes (at around C_{84} (m/z 1008)). These are produced upon laser activation of less protected target areas and are co-selected in the present experiment. Because of their much lower tendency to fragment, there are no fragment ions of pure fullerenes in the lower part of these LIFT spectra.

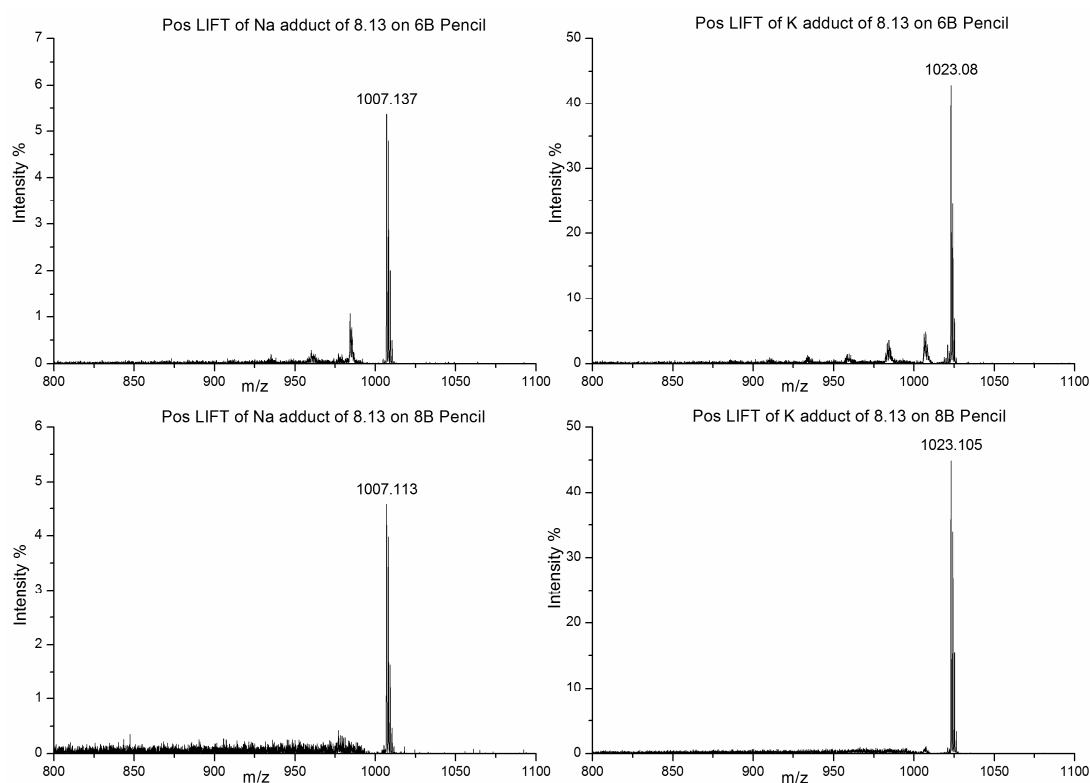


Figure 5.22: Positive-ion mode LIFT of the Na and K adducts of 8.13 on 6B and 8B pencil

Analytically it is important to note that the spectra obtained with the 6B pencil are of slightly better quality than the 8B pencil spectra, leading to larger peak intensities. This was another trend observed throughout the experiments. This trend has also been noted previously, with other groups reporting that lower B number rated pencils produced better spectra. A smaller B number has less graphite and more clays and waxes, to give a harder lead. This may have implications as to which component of the pencil is providing the matrix effect of analyte protection.

In summary, pencil lead provides a less efficient means of MALDI compared with the conventional use of a matrix. However, the ease of formation of sodiated and potassiated adducts with certain analytes makes it an interesting tool for the generation of these species. In the case of crown ether attached fullerenes an unusual fragmentation pattern is obtained without the usual occurrence of fullerene fragment ions, since the cationising metal resides firmly on the crown ether, leading to the loss of a neutral fullerene. This type of charge localisation implies that compound 8.13 is a crown ether with a fullerene ligand attached to it, rather than representing a fullerene with a crown ether ligand.

Mono, Bis and Tris – Fullerene Derivatives by “Pencil-MALDI”

Pencil was tested as a matrix for three fullerene derivatives with different numbers of the same ligand – mono, bis and tris, the structures of which were shown in the experimental section of this chapter. These derivatives are structurally closely related to Isopropyl mono. They incorporate an ethyl ester instead of the isopropyl ester. Their MALDI and LDI behaviour is very similar to that of isopropyl mono. The three derivatives allow testing of the use of pencil lead for quantitation. A 1:1:1 molar ratio of mono:bis:tris was tested with 6B and 8B pencil lead to evaluate the recovery of these analytes when laser activated. The resulting spectra are shown below:

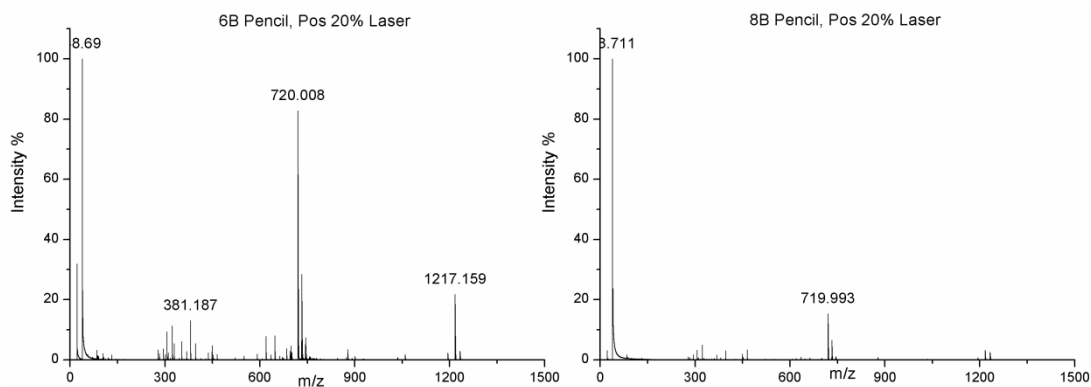


Figure 5.23: Mono, bis and tris on 6B and 8B pencil

The huge signal at m/z 720, representing fragmentation of mono, bis and tris into C_{60} provides yet another indication of how unsuitable pencil lead is as a MALDI matrix for fullerene derivatives, beyond isopropyl mono and the crown ether adduct to C_{60} , compound 8.13. Enhancement of the m/z region of 800 to 1300 shows the molecular ions and the sodium and potassium adducts:

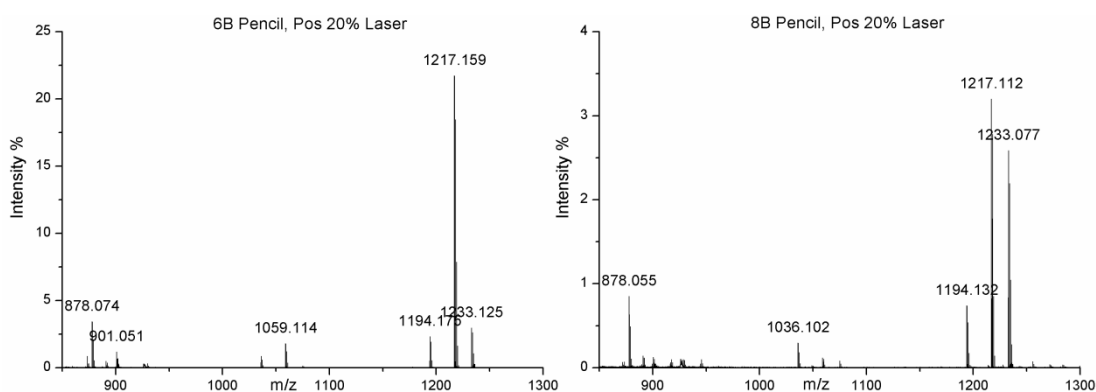


Figure 5.24: Enhancement of the molecular regions of mono, bis, tris on 6B and 8B pencil

Again, mono, bis and tris were mixed in a 1:1:1 molar ratio to form a single solution, which was thoroughly shaken prior to application to the target plate to ensure the ratio on the target plate was as close to the solution ratio as possible. In previous DCTB-MALDI experiments the molecular ions were detected from a 1:1:1 target and the ratio of the peak intensities has been observed to be approximately 1:2:3 in positive-ion mode for mono:bis:tris, and 3:2:1 in negative-ion mode. Quantitation in MALDI is possible, but involves the time consuming recording of calibration curves for every component. In our DCTB-MALDI experiments the ratios obtained for the molecular ions remained constant over a wide range of laser powers and from one experiment to the next. As a consequence, one could have used DCTB-

MALDI in principle for the quantitation of mono, bis and tris, for instance to check their relative yields in a synthesis.

Perhaps even more important than reproducibility for the applicability of quantitation is the fact that DCTB-MALDI produced molecular ions free of fragmentation. Therefore, the rates by which the three compounds would decompose into C_{60} are not important, as no dissociation occurs. This is in contrast to the use of pencil lead, where the C_{60} fragment was dominant. It is not likely that the C_{60} fragment ion originates from the alkali adducts of mono, bis or tris, as the charge would reside with any metal containing fragment. However, the neutral compounds could decompose to C_{60} followed by ionisation and the relative rates for these reactions are not known. Therefore, pencil lead is not suited for the quantitation of fullerene derivatives of the type studied here.

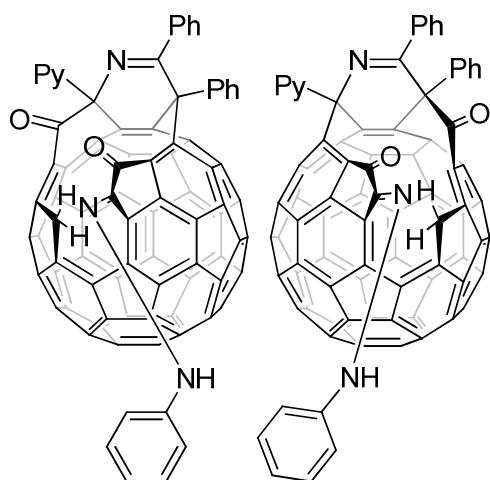
Furthermore, in the experiments above the relative abundances of mono, bis and tris do not follow the previously observed ratio, and indeed the uptake of potassium or sodium ion differs greatly. Mono, with the molecular ion at m/z 878 shows very little sodium and even less potassium adduct formation, yet for tris, with the molecular ion at m/z 1194, there is a huge sodium adduct formed at m/z 1217 and a considerable potassium adduct at m/z 1233, increased when on 8B pencil. Bis at m/z 1036 does not appear to form any potassium adducts with the 6B pencil, only a sodium adduct at m/z 1059, which appears reduced relative to the molecular ion when 8B pencil is used.

The only tendency obvious in these experiments is again a more pronounced potassium uptake when the 8B pencil lead is used. However, other more general tendencies cannot be deduced as the metal adduct formation seems rather random. One might conclude that tris shows more metal attachment than the other two compounds but some kind of indication of the quantitative composition of the target are absent from the data. Consequently, the alkali attachment occurs but shows more irregularities than general trends, so that any effort into the direction of using this approach for quantitation will be much more complicated than the use of DCTB-MALDI. Furthermore, adduct formation gave such low absolute abundances that LIFT experiments could not be conducted.

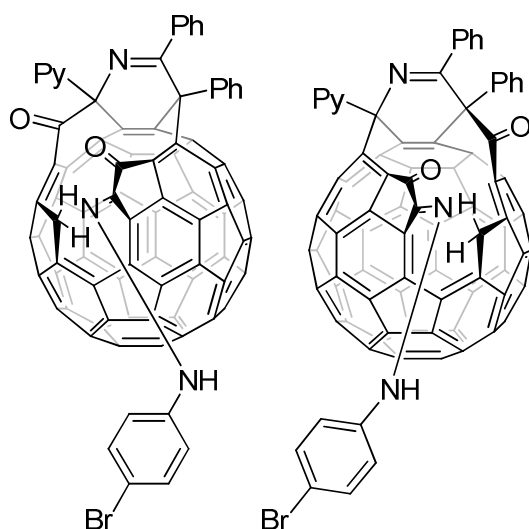
Use of adduct formation to distinguish isomers

Building on the ease of alkali metal addition to the crown ether derivative 8.13, the following investigation was aimed at the distinction of isomeric OCFs through the dissociations of their sodiated and potassiated isomers. Isomer OCFs provide almost identical DCTB-MALDI spectra without any indication as to which isomer was responsible for the data. As will be shown below, the same is true for the LIFT spectra of the molecular ions. The motivation of this investigation comes from the speculative idea that sodium and/or potassium may attach to the heteroatoms at the rim of each isomer in a distinct manner, so that dissociations would lead to the release of different entities. The investigations were conducted with three of the isomeric OCF pairs, including the pairs 2.1, 2.2, as well as 2.3, 2.4 and 2.5, 2.6. The corresponding DCTB-MALDI experiments were discussed in chapter 3 and the structures are again depicted below.

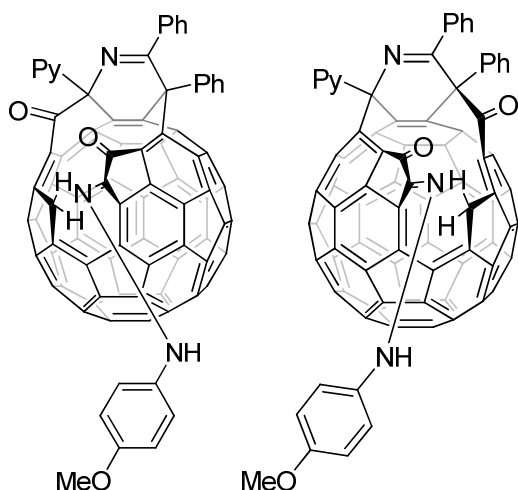
Compounds 2.1, left, and 2.2, right:



Compounds 2.3, left, and 2.4, right:



Compounds 2.5, left, and 2.6, right:



The three pairs of the isomeric OCFs were studied as follows. LIFT spectra of the molecular ions were obtained using DCTB-MALDI as a method of ion production. LIFT experiments of the sodiated and potassiated quasi-molecular ions were recorded by employing 6B, 8B and HB pencil lead as ablation surfaces in different sets of experiments for all six compounds. Tandem and “normal” mass spectra therefore included a minimum set of 36 different experiments. Further experiments were conducted in which the HB pencil lead was spiked with DCTB; together with repeat experiments the actual volume of experiments was much greater. All data from these experiments were carefully considered in the elucidation of the gas-phase dissociation behaviour of the cationised OCFs and it was concluded to lead the

argument in the following way based only on the set of data that were obtained for the OCF pair 2.3 and 2.4. Two reasons are responsible for this procedure. Firstly, the three pairs show a common dissociation scheme which can be explained by discussing just one of the pairs. Secondly, the OCF pair 2.3 and 2.4 gave the “best” set of spectra; “best” in this context means free of contributions of unwanted ions. The LIFT experiments of the crown ether adduct 8.13 already revealed that the ion gate is not able to separate the sodiated and the potassiated complexes when studying their respective dissociation. Both adducts had contributions from the other adduct in their LIFT spectra. The same situation was observed for the three pairs of OCFs. While mass resolution and accuracy were perfectly suited to identify the daughter ions, the separation of parent ions could not be sufficiently achieved. Therefore, interference-free daughter ion spectra (LIFT) could only be obtained in those cases where the unwanted parent ion was initially produced in too low abundances to interfere. Such conditions were coincidentally achieved for the 2.3/2.4 pair. While the DCTB-MALDI experiments did not produce any sodiated and potassiated adducts that would contribute to the LIFT of the molecular ions, in LIFT of the sodiated adduct the potassiated adduct was not generated in a high enough abundance to contribute and vice versa. Following the discussion of the dissociation behaviour, illustrative examples of LIFT spectra with such unwanted contributions will be shown.

The LIFT spectra of the molecular ions of OCFs 2.3 and 2.4 are shown below:

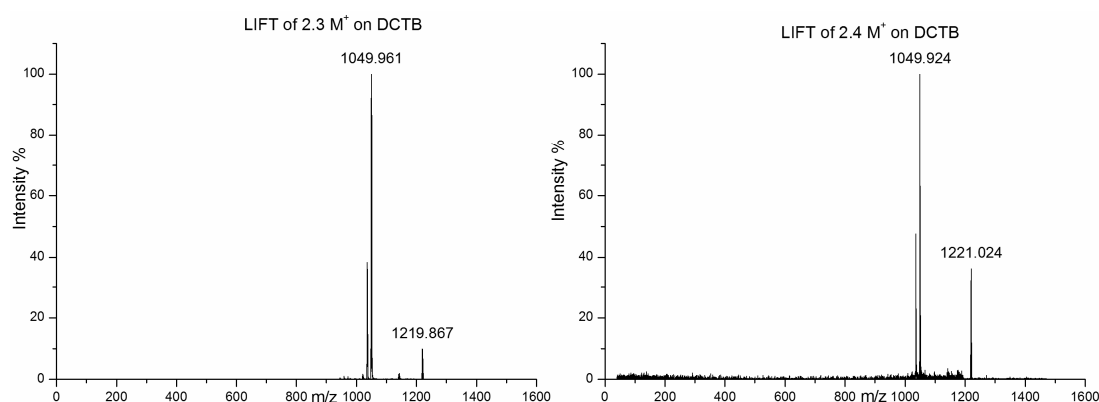


Figure 5.25: LIFT of molecular ions of 2.3 and 2.4 with DCTB-MALDI

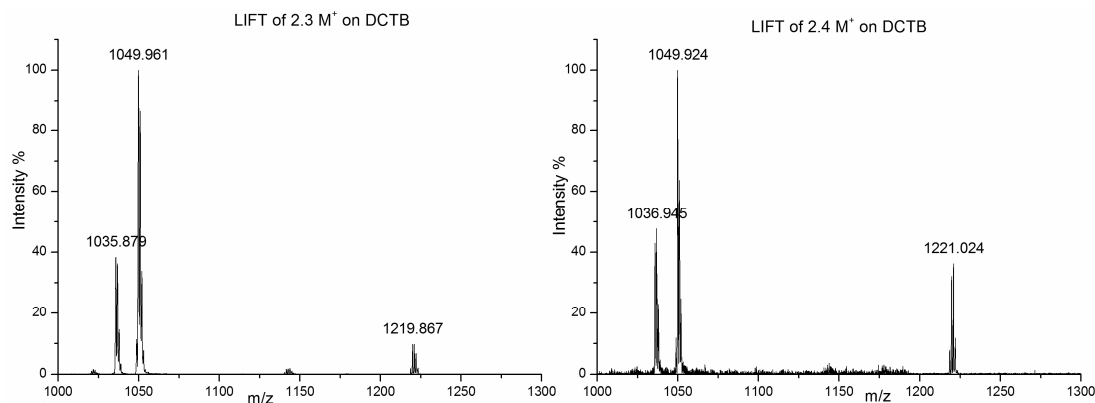


Figure 5.26: Enhancement of fragment peaks from LIFT of molecular ions of 2.3 and 2.4

The LIFT spectra of the OCF pair 2.3 and 2.4 are representative for all three pairs investigated in that two major daughter ions are observed at m/z 1049 and m/z 1036. There is no isomer specific intensity order so that both ions are found abundantly with one or the other dominating. Since the three OCF pairs differ through the par substituent on the benzene unit ligated to the rim, the observation that a set of identical daughter ions is generated from the different OCFs means that the ligand which differentiates the three pairs is lost in the dissociation. The mass difference from the respective molecular ion to m/z 1049 indicates that in each case one additional hydrogen atom was transferred to the released ligand, so that each pair lost a $\text{H}_2\text{N}-\text{C}_6\text{H}_4-\text{X}$ moiety with $\text{X} = \text{H}$ for the 2.1/2.2 pair, $\text{X} = \text{Br}$ for the 2.3/2.4 pair and $\text{X} = \text{OMe}$ for the 2.5/2.6 pair. The other peak at m/z 1036 corresponds to loss of the $\text{NNHC}_6\text{H}_4\text{X}$ ligand of each compound. In summary, the dissociations of the molecular ions of all six compounds involve the hydrazone ligand without providing a distinction between them.

The following spectra were obtained for samples 2.3 and 2.4 on 6B and 8B pencil:

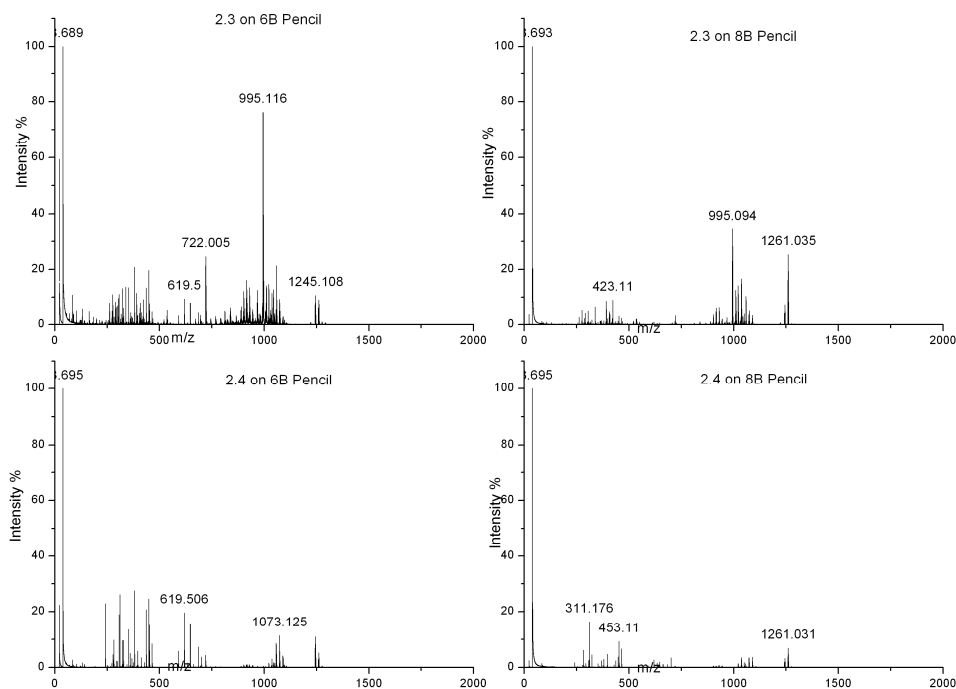


Figure 5.27: 2.3 and 2.4 on 6B and 8B pencil

As a first impression, the spectra are dominated by unwanted signals that originate from the pencil lead. The molecular ion region is enlarged in order to view more clearly the relative ratios of molecular ion versus sodiated and potassiumated quasi molecular ion:

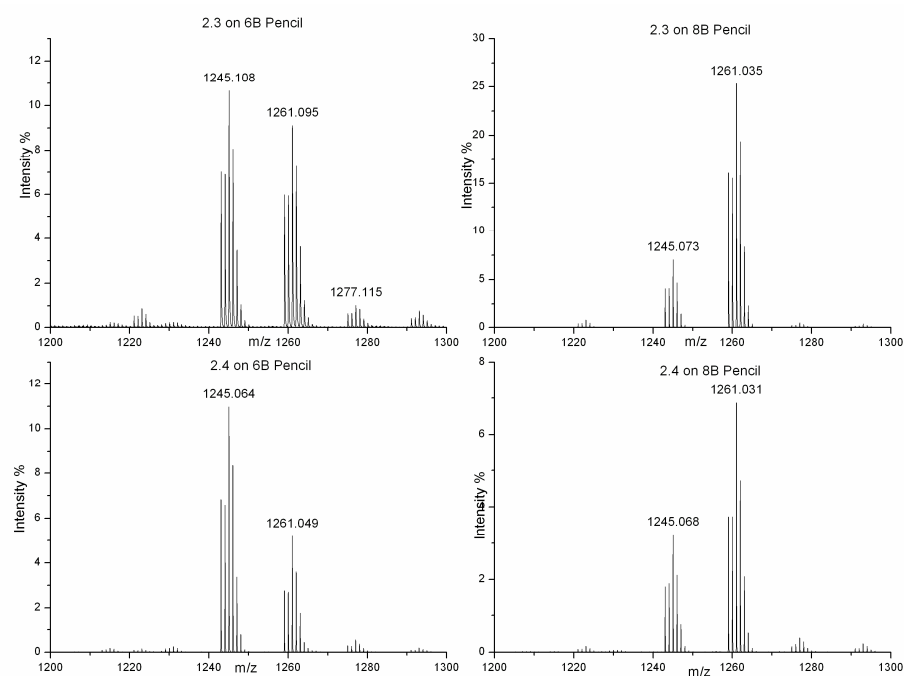


Figure 5.28: Enhancement of molecular ion region of 2.3 and 2.4 on 6B and 8B pencil

As seen in the previous experiments the 8B pencil produces potassium adducts in far greater quantities than the 6B pencil surface.

The empirical formula for 2.3 and 2.4 is $C_{86}H_{21}N_4O_2Br$, with relative molecular mass of 1221 Da (1220 Da includes the ^{79}Br isotope). The molecular ions are only present in minute abundances. The presence of bromine influences the isotopic patterns seen above. The sodium adducts are centred at m/z 1245 (1243 Da includes the ^{79}Br isotope) and the potassium adducts are centred at m/z 1261 (1259 Da includes the ^{79}Br isotope).

Similar results were obtained for all three pairs with marginal differences. Also the normal pencil spectra do not provide a means of distinguishing the isomers of each pair.

After ascertaining that sodium and potassium adducts could be formed with the isomeric open cage fullerenes, in the next stage positive-ion mode LIFT experiments were performed. The dissociation behaviour of the sodiated and potassiated adducts of compounds 2.3 and 2.4 is provided by the positive-ion LIFT mass spectra obtained on 8B pencil. The complete spectra are shown below:

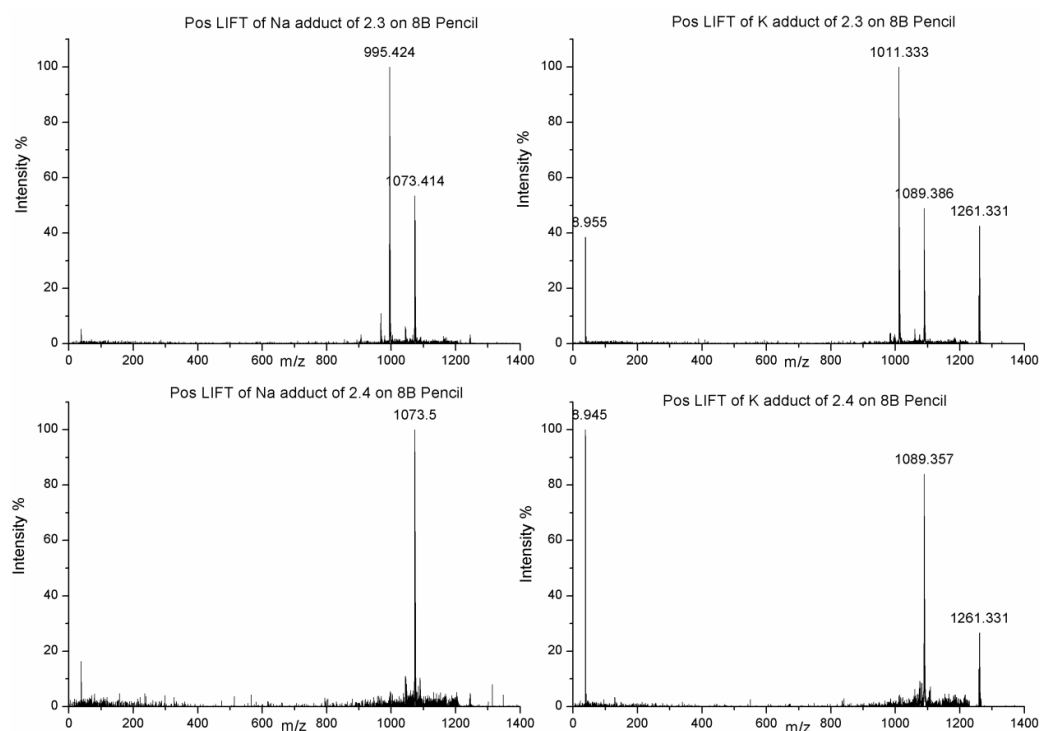


Figure 5.29: Positive-ion mode LIFT of Na and K adduct of 2.3 and 2.4

Enhancement of the m/z region 1000 to 1300 provides closer insight into the main fragment ions:

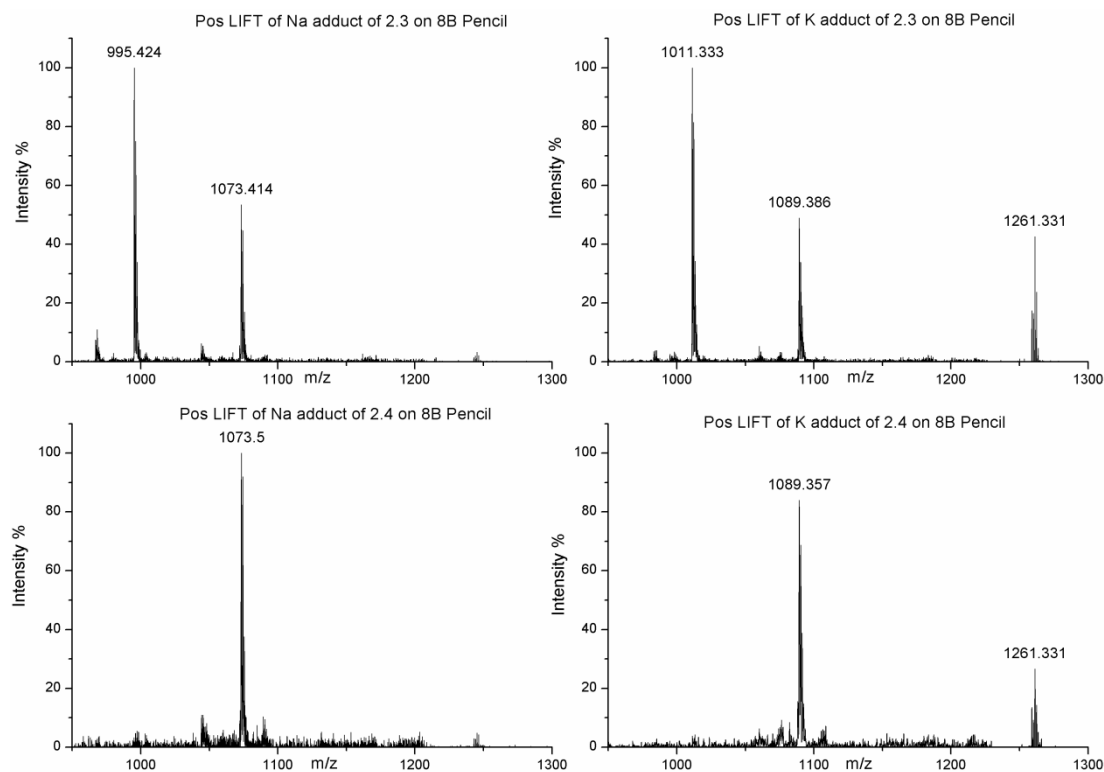


Figure 5.30: Positive-ion mode LIFT of Na and K adduct of 2.3 and 2.4 on 8B pencil

The LIFT spectra of the sodium and potassium adduct of 2.3 and 2.4 were recorded from the quasi molecular ion incorporating the ^{81}Br isotope. The sodium adduct of isotope 2.3 shows two fragment ions. The fragment ion at m/z 1073 is caused by the loss of a neutral of 172 mass units which is given by the $\text{NH-C}_6\text{H}_4\text{-Br}$ entity of the hydrazone ligand. This assignment is also corroborated by the fact that the LIFT spectrum of potassiated 2.3 displays the same fragmentation through the corresponding mass shifted ions. Notably, the fragmentation of the sodium adduct involves the loss of a radical (odd electron species) whereby the molecular ion shows only losses of closed shell neutrals (even electron species). The same fragmentation is the only reaction that occurs for the alkali adducts of isomer 2.4. The LIFT experiment brings with it the first “clear-cut” distinction between the two isomers, through a very pronounced additional fragmentation which is not observed for the 2.4 isomer. The distinguishing fragmentation shows the loss of a neutral of mass 78. There are two options for this fragmentation: loss of C_6H_6 or loss of $\text{C}_5\text{H}_4\text{N}^\cdot$. Without specific labelling experiments a distinction of these two options cannot be achieved, so that the current assignment must remain speculative. Since the other fragmentation of the metal cationised isomers features the loss of an odd electron species and while in contrast the

molecular ions lose only closed shell neutrals, it seems likely to assume that the $C_5H_4N^{\cdot}$ radical is lost.

The dissociation behaviour for sodium and potassium adducts is the same. The change of the metal cation does not induce a distinct behaviour, however, the metal ion induces a distinction between the two isomeric OCF forms, which is not observed in dissociations of the true molecular ions. This behaviour may be explained through the coordination of the cation to the heteroatoms of the rim. In those isomers that show the additional loss of the pyridyl radical, the heteroatoms are more situated around this ligand. In the other type of isomers, the pyridin moiety is further away from the heteroatoms. It is tempting to speculate that the cation interaction may occur with several of the heteroatoms simultaneously and may cause in isomers 2.1, 2.3 and 2.5 a repulsion that pushes the ligand away from the rim. In the isomers 2.2, 2.4 and 2.6 the complexed cation is located further away from the pyridyl ligand and the repulsive interaction is therefore reduced.

Obviously, cationisation leads to a clear distinction of OCF isomers through their fragmentation behaviour, yet the structural interactions that cause these effects must remain speculative. Future work may involve computational approaches to provide more insight into the interaction of the cation and the atoms at the rim.

As an example of the kind of interferences that occurred in many of the spectra of this study, the LIFT spectra of compounds 2.1 and 2.2 are shown below as obtained on 6B pencil. All spectra are dominated by the presence of the potassiated isomers. The LIFT spectrum of 2.1- Na^+ shows the same signals as seen in the 2.1- K^+ and 2.2- Na^+ shows the same major fragment ion seen in the decomposition of 2.2- K^+ . The potassium adduct spectra possess a slight mass inaccuracy due to a slightly inaccurate calibration and the signals in the sodiated adduct spectra are clearly shifted to lower masses. This latter mass shift is probably a result of the origin of these signals as interferences that were co-selected as potassiated adducts at the masses of the sodiated adducts.

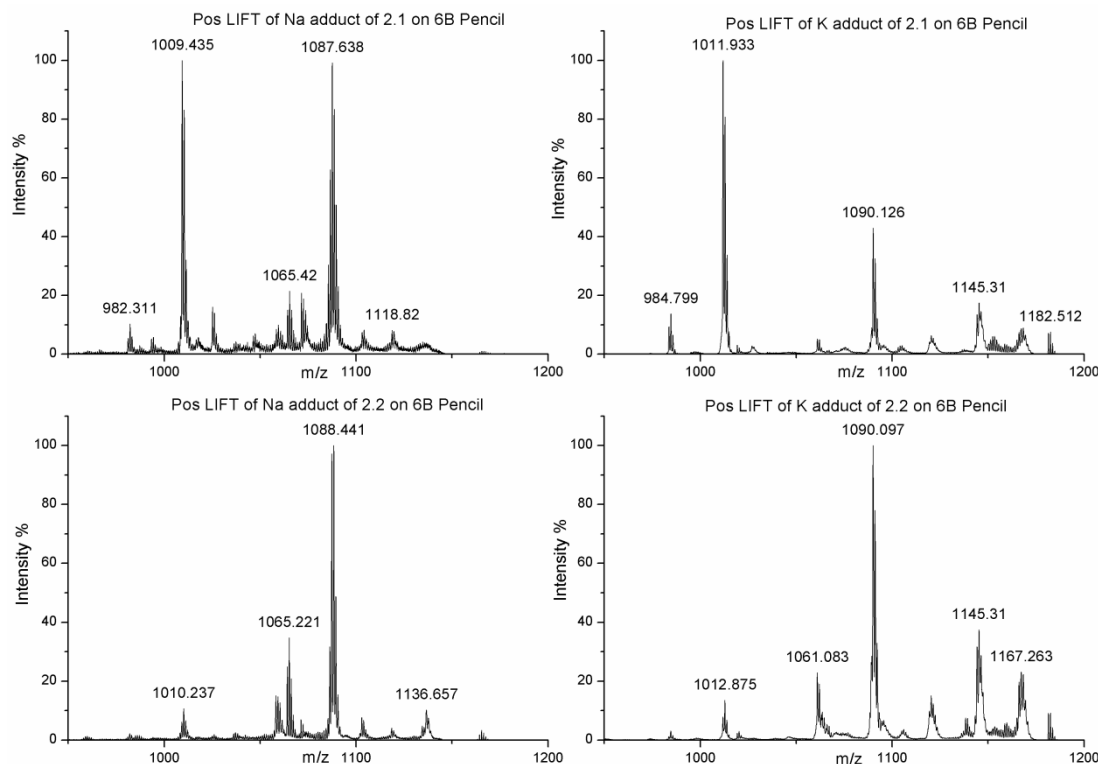


Figure 5.31: Positive-ion mode LIFT of the Na and K adducts of 2.1 and 2.2

Comparison of 6B, 8B and HB pencil lead spiked with DCTB

The motivation to examine the HB pencil in addition to 6B and 8B results from the fact that it was reported previously that lower B rated pencils provide better spectra. The motivation to add DCTB to the HB pencil resulted from the observation that the alkali adducts were always accompanied by a substantial degree of fragmentation signals. It was hoped the DCTB would aid the gentle desorption of the species into the gas-phase and thus increase the softness of the process (minimise neutral decomposition), so that cationisation could still take place, induced by the pencil lead, but with much reduced decomposition.

The results are summarised as follows:

None of the pencil applications could compete with DCTB-MALDI regarding the cleanliness of spectra, the abundant production of molecular ions and the reduction of fragmentation. 6B and 8B generated minute amounts of the molecular ions, however, sodium and potassium addition was predominantly observed. 8B produced commonly more pronounced potassium adducts. HB did not enhance the performance. There was still pronounced fragmentation. The molecular ions were enhanced with HB and the alkali adducts less abundant than with 6B or 8B. The addition of DCTB to HB pencil did not enhance the performance in terms of a

softer, more pronounced production of the alkali adducts. DCTB addition to the pencil resulted in a change of ion formation mechanism: self protonation of the analytes in contrast to metal attachment or charge exchange.

To illustrate the above summarised findings, HB pencil spectra (without DCTB) of some of the isomeric OCF pairs are shown below. The full spectra illustrate the dominant presence of impurities from the pencil lead and of fragments of the alkali adducts.

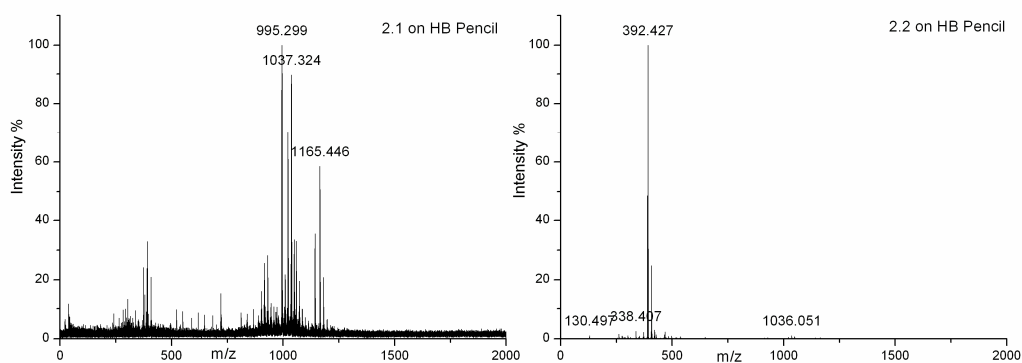


Figure 5.32: 2.1 and 2.2 on HB pencil

The enlarged molecular ion region shows that the molecular ion peak is stronger in relation to the adduct peaks. The overall formation of molecular ions is not comparable to the use of DCTB.

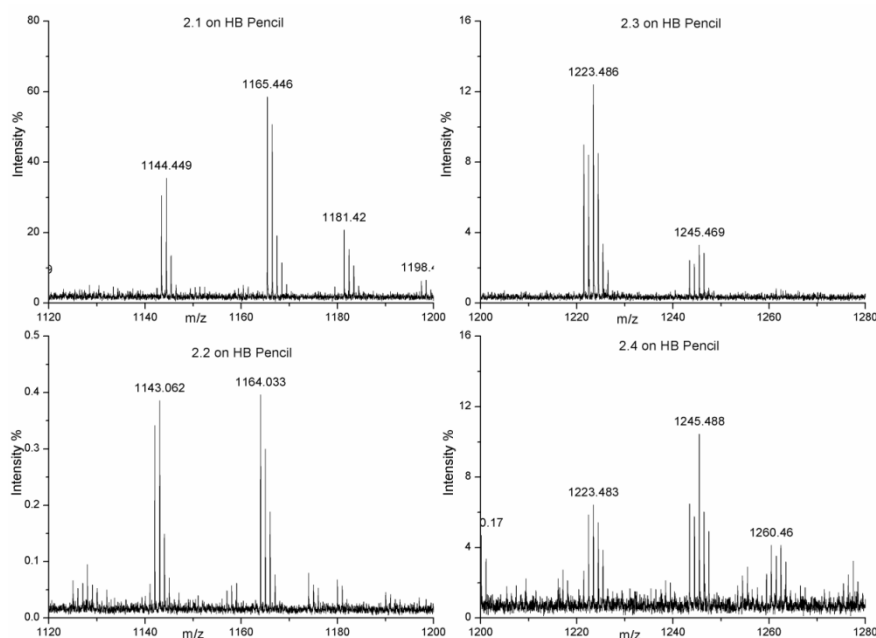


Figure 5.33: 2.1 and 2.2 on HB pencil

Experiments were also performed by mixing DCTB with the compounds prior to application to the pencil, in an attempt to increase the production of the adducts. The presence of DCTB

could have hindered adduct formation, so the amount of DCTB was reduced relative to “normal” experiments, to ensure some protection, without hopefully reducing adduct formation. The experimental results are illustrated initially by the spectra of the isomeric open cage fullerenes 2.5 and 2.6:

These isomeric open cage fullerenes have the empirical formula $C_{87}H_{24}N_4O_3$, and a relative molecular mass of 1172 Da.

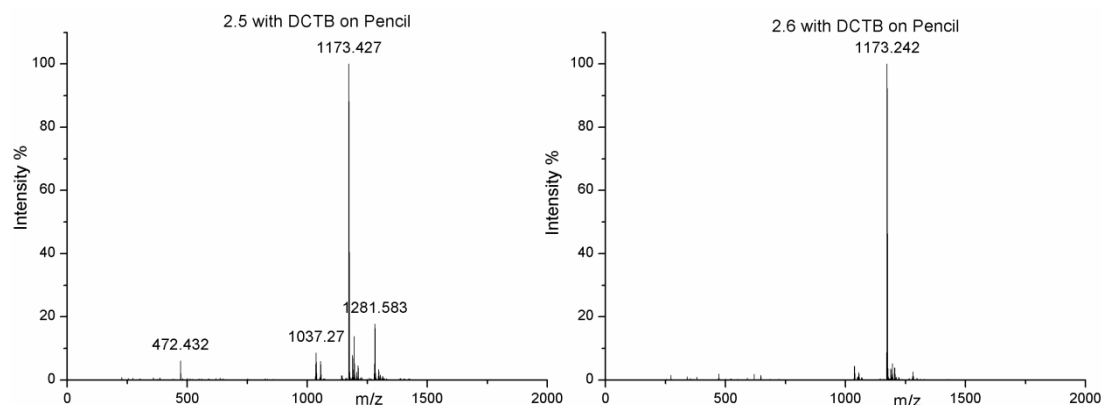


Figure 5.34: 2.5 and 2.6 with DCTB on Pencil

Adduct formation is demonstrated when the m/z region 1180 to 1220 is enhanced, below:

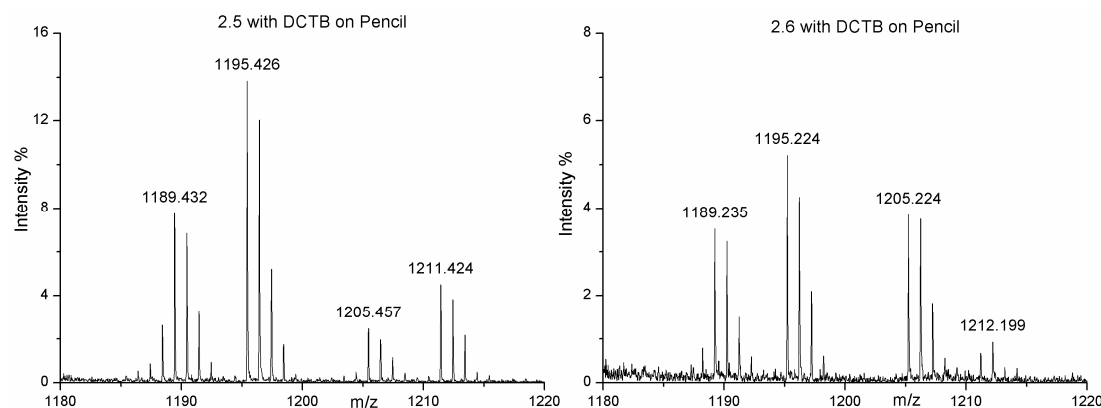


Figure 5.35: 2.5 and 2.6 with DCTB on Pencil

All six OCFs show a similar behaviour in their DCTB-spiked HB pencil analysis. Neither the metal adduct formation, nor charge transfer as in DCTB-MALDI is the dominant process. Instead, all six molecules are protonated. Since the amount of DCTB was reduced in these experiments, and since normal DCTB-MALDI does not show the protonation, it can be assumed that the ion formation is the result of self protonation of the analytes. The present data suggest that DCTB provides a soft gas phase transfer followed by self protonation as DCTB is not present in abundant amounts to allow for charge exchange to occur. A detailed

investigation into this interesting change in ion formation mechanism is beyond the scope of this work and will be followed up in future studies.

Laser Activation of (Z)- and (E)-acenaphthylene dimer ("Cis" and "Trans") on Pencil

Inspired by the distinction of OCFs through the fragmentation behaviour of their alkali metal adducts, this part of the investigation of the use of pencil lead surface is aimed to elucidate the laser ablation of a pair of isomeric hydrocarbons. While silver cations are well known to strongly interact with the π -system of unsaturated hydrocarbons, alkali metal cations are not particularly renowned for this type of interaction, as these tend to more readily attach to heteroatoms. A detailed investigation into the interaction with silver cations follows in chapter 8, where the species were investigated by electrospray ionisation. However, the ease of pencil lead MALDI led us to check if alkali interactions could be seen as well. The two isomers were the (Z)- and (E)-acenaphthylene dimer, which were termed in the following as "cis" and "trans" and which were provided by Professor Helena Grennberg, Uppsala University, Sweden. The structures of both are as follows:

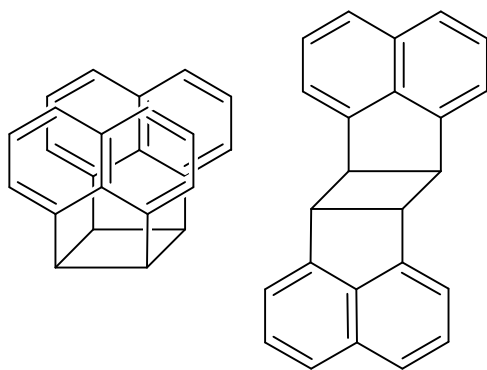


Figure 5.36: Structure of "cis", left, and "trans", right

The positive-ion mode spectra below demonstrate "cis" and "trans" individually analysed with either 6B or 8B pencil.

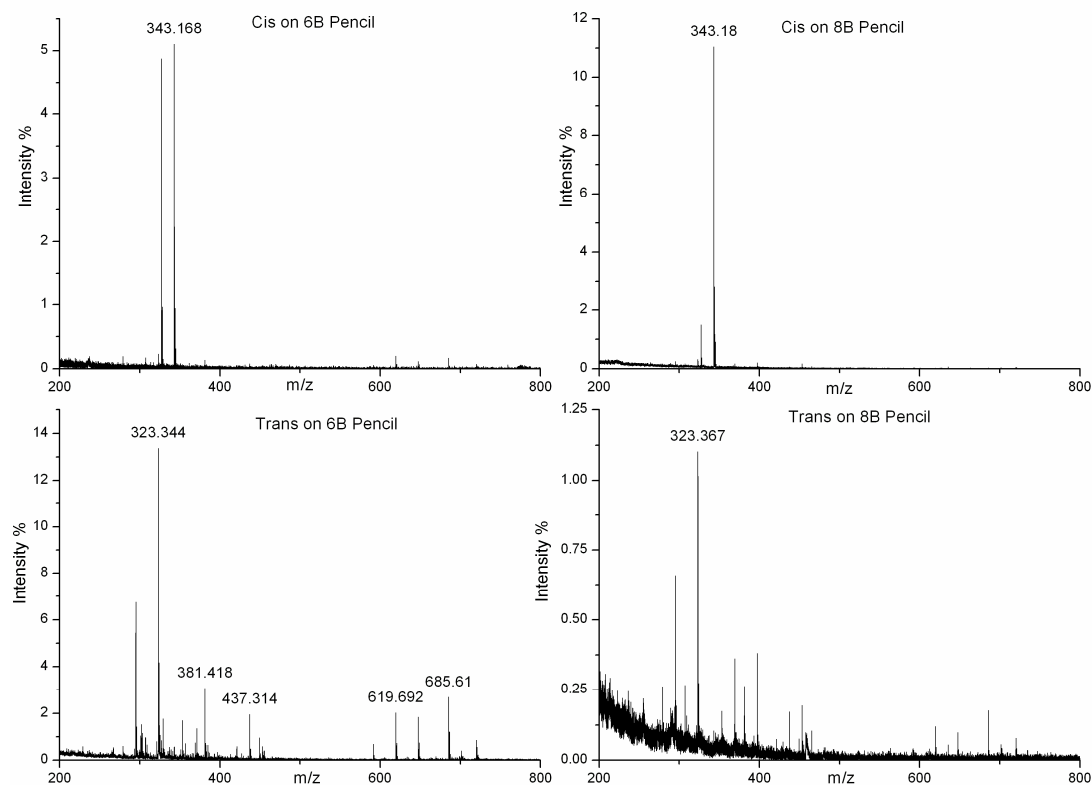


Figure 5.37: “Cis” and “trans” on 6B and 8B pencil

The molecular ion of “cis” and “trans” would appear at m/z 304, the sodium and potassium adducts as m/z 327 and m/z 343 respectively. The spectra only show the mass range from m/z 200 upwards as there were enormously abundant signals of unattached sodium and potassium ions, which dominated the spectra. The tail of the potassium peak is still very obvious in the spectrum of “trans” on 8B pencil. The intensities of the peaks shown are relative to the potassium peak at 100%, the values of the peak intensities in the above spectra demonstrate just how large the contribution from potassium was.

Focussing on the m/z region between 300 and 400 portrays the molecular ion peaks and the adduct formation:

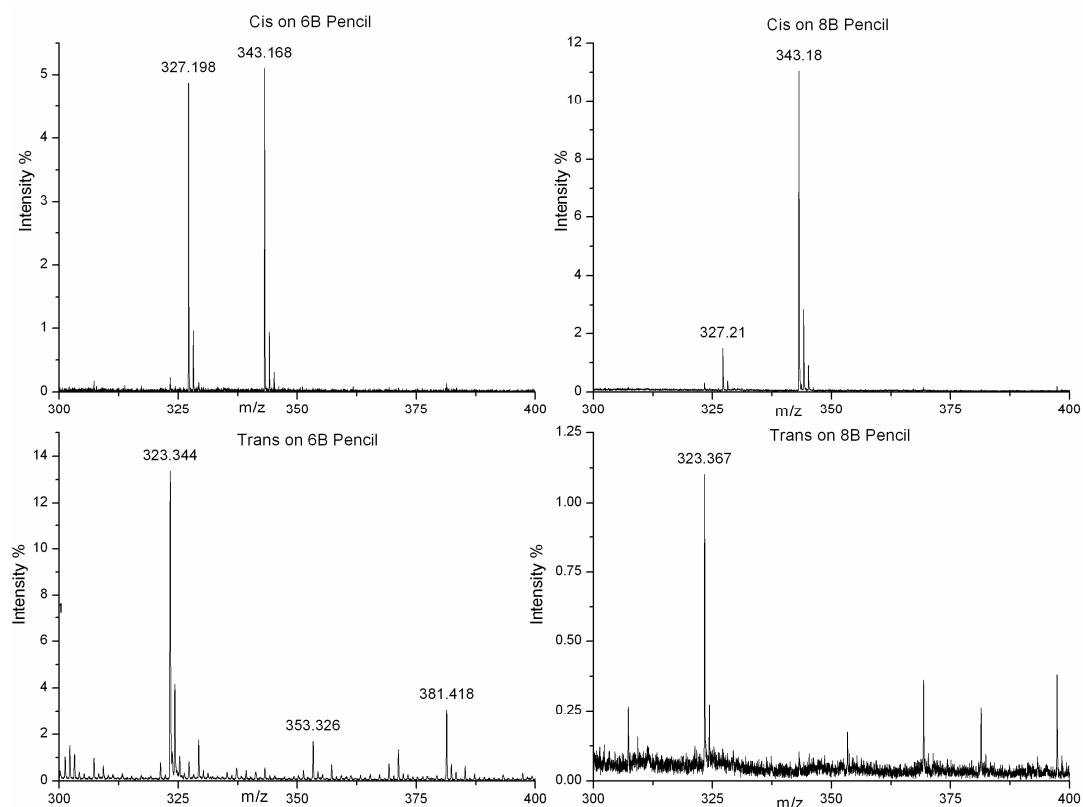


Figure 5.38: “Cis” and “Trans” on 6B and 8B pencil

For “cis”, on 6B and 8B pencil, the same peaks are present; however, the ratio of the intensity alters. The peak at m/z 327 is the sodium adduct of “cis”. The peak at m/z 343 is the potassium adduct of “cis”. The increased potassium addition on 8B pencil is a trend that was observed in all experiments comparing 6B to 8B pencil. Obviously “cis” is readily sodiated and potassiated. This is also corroborated by the collision-induced dissociation (CID) spectra of these ions, which reveal sodium and potassium cations as the only daughter ions of these adducts. The charge resides 100% with the metal cation.

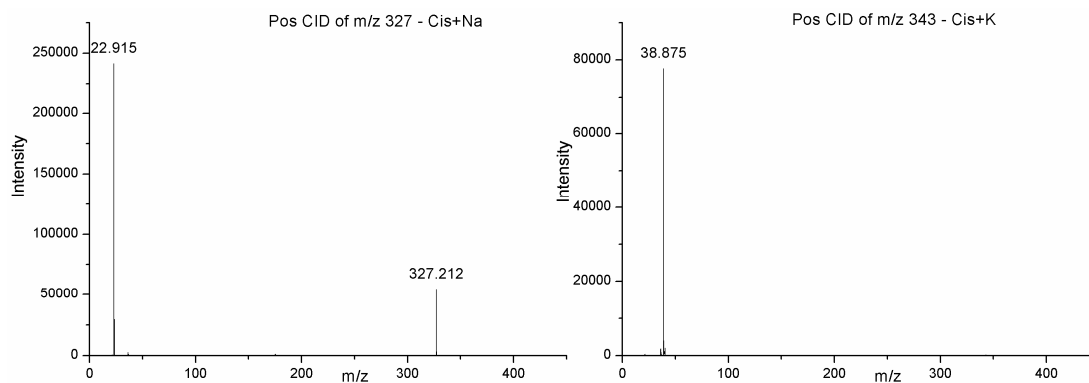


Figure 5.39: Positive-ion mode of the Na and K adducts of “cis”

With “trans”, the alkali adducts are not readily formed. Only a tiny potassium adduct was obtained on 8B pencil and identified through its CID spectrum which gave the same result as for the “cis” adduct. The signals observed for “trans” in the region just above m/z 300 and the m/z 600 are “impurities” that result from the pencil lead and are produced when pencil is alone on the target.

Both isomers gave unexpectedly poor results with DCTB-MALDI. CID experiments of m/z 304 ions did not show the expected dissociation into two halves, so that one cannot be certain that molecular ions were formed at all. Since thermochemical data such as IP, EA or dissociation energies of “cis” and “trans” are currently not available, the reasons for this failure remain unclear.

As indicated above, the behaviour of “trans” showing practically no alkali metal addition is the expected case and the relative readiness by which adduct formation occurs with “cis” is unexpected. One may assume that the commonly weak interaction between the system and the alkali cation is strengthened in “cis” by the fact that the two sides of the molecule may interact simultaneously with the cation. In summary, the two isomers show a distinct behaviour in reactions with sodium and potassium cations whereby “cis” shows some addition and “trans” almost no addition at all. CID of the adducts would not provide a distinction of the isomers as shown by the potassiated adducts produced for both isomers which gave the potassium cation as the only daughter ion. This fairly unspectacular behaviour has to be seen in relation to the rich and illustrative behaviour when silver is used as the cationising metal, as will be discussed in chapter 8.

Conclusion

Pencil has been shown to be an unsatisfactory matrix for fullerenes and their derivatives, especially when compared to the benchmark of DCTB-MALDI. There is extensive fragmentation and the production of the molecular ion peak is commonly of low intensity. In general, higher laser fluences are needed than in DCTB-MALDI. Analytically valuable is the addition of sodium and potassium to analytes with heteroatoms. This could be used for identification, but also can be useful as a means to produce such adducts for further experiments.

As an example isomeric OCFs could be distinguished through a clearly different fragment ion ratio in dissociations of their sodiated and potassiated adduct ions, indicating that the cation interaction is distinct and brings about a differentiation, which could not be achieved in DCTB-MALDI and in dissociations of isomeric molecular ions. Direct alkali cation addition was also able to distinguish a model pair of isomeric hydrocarbons.

The difference between 6B and 8B pencil was not pronounced in terms of matrix performance, however 8B spectra produced higher quantities of potassium addition. Use of the 8B pencil did also occasionally seem to hinder ion production, resulting in lower quality spectra overall.

HB pencil appeared to produce bare molecular ion peaks in somewhat greater intensity relative to the adduct peaks. DCTB-spiked HB pencil experiments lead to self protonation of the analytes, a process that will be followed up in future work. Analysis in the negative-ion mode is not successful.

In summary, pencil lead-MALDI does not match the quality of DCTB-MALDI regarding softness, cleanliness of spectra and sensitivity, but could have its merits as a facile approach to generate sodium and potassium adducts of structurally suited fullerene derivatives.

References

1. Gigante, B.; Santos, C.; Fonseca, T.; Curto, M.; Luftmann, H.; Bergander, K.; Berberan-Santos, M., *Tetrahedron* **1999**, *55* (19), 6175-6182.
2. Siedschlag, C.; Luftmann, H.; Wolff, C.; Mattay, J., *Tetrahedron* **1999**, *55* (25), 7805-7818.
3. Ulmer, L.; Mattay, J.; Torres-Garcia, H.; Luftmann, H., *European Journal of Mass Spectrometry* **2000**, *6* (1), 49-52.
4. Brown, T.; Clipston, N.; Simjee, N.; Luftmann, H.; Hungerbuhler, H.; Drewello, T., *International Journal of Mass Spectrometry* **2001**, *210* (1-3), 249-263.
5. Vasil'ev, Y. V.; Khvostenko, O. G.; Streletskii, A. V.; Boltalina, O. V.; Kotsiris, S. G.; Drewello, T., *The Journal of Physical Chemistry A* **2006**, *110* (18), 5967-5972.
6. Black, C.; Poile, C.; Langley, J.; Herniman, J., *Rapid communications in mass spectrometry: RCM* **2006**, *20* (7), 1053-1060.
7. Langley, G. J.; Herniman, J. M.; Townell, M. S., *Rapid communications in mass spectrometry: RCM* **2007**, *21* (2), 180-190.
8. Berger-Nicoletti, E.; Wurm, F.; Kilbinger, A. F. M.; Frey, H., *Macromolecules* **2006**, *40* (3), 6.
9. Pedersen, C. J., *Journal of the American Chemical Society* **1967**, *89* (10), 2495-2496.
10. Wilson, S.; Wu, Y., *Journal of the Chemical Society-Chemical Communications* **1993**, (9), 784-786.
11. Maleknia, S.; Brodbelt, J., *Rapid Communications in Mass Spectrometry* **1992**, *6* (6), 376-381.

Chapter 6: Synthesis of C₆₀ Polycyclic Aromatic Hydrocarbon (PAH) Complexes and Analysis with MALDI and ESI

Introduction

C₆₀ and other fullerenes react with polycyclic aromatic hydrocarbons (PAHs) to produce a range of complexes, which, due to their very labile nature are interesting fullerene derivatives to study with mass spectrometry. The lability of these adducts represents the benchmark to test the softness of the ionisation method applied. Adduct formation of anthracene to C₆₀ was initially reported in 1992¹, however, these adducts were not analysed in any depth until 1993, when the structures of it and related complexes were confirmed using ¹H-NMR, ¹³C-NMR,^{2,3} thermal gravimetric analysis (TGA), UV-Vis and IR spectroscopy². The compounds are difficult to observe with mass spectrometry, due to the tendency of the complex to undergo a retro Diels-Alder reaction to leave C₆₀ and anthracene as separate entities.

The research performed in this context is primarily concerned with the complexes of C₆₀ with anthracene, tetracene and pentacene. The PAHs are shown below:

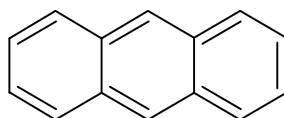


Figure 6.1: The structure of anthracene, C₁₄H₁₀

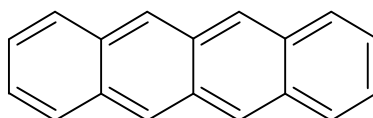


Figure 6.2: The structure of tetracene (2,3-Benzanthracene), C₁₈H₁₂

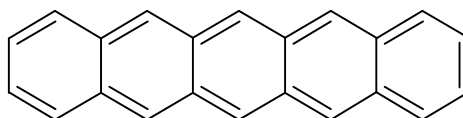


Figure 6.3: The structure of pentacene, C₂₂H₁₄

Part of this research was performed in conjunction with a third year undergraduate student, ManTo (Henry) Chan, as part of his third year laboratory project. These projects have only

15 days of laboratory time devoted to them, and in this instance was used for the synthesis of the different complexes and the initial MALDI mass spectrometric analysis. The ESI analysis and subsequent in-depth MALDI mass spectrometric analysis, discussed in chapter 8, were performed after the project's completion, without the assistance of ManTo Chan.

Synthesis

Various synthetic methods of the C_{60} -anthracene ($C_{60}(C_{14}H_{10})$) complex have been employed previously, the most prevalent being the refluxing of the reagents for several hours.

Initial attempts at synthesis involved dissolving C_{60} and anthracene in toluene in a 1:10 molar ratio (respectively) and refluxing for 3 days². C_{60} -anthracene was produced, and found to be stable in a freezer at -10°C for several weeks.

A second method developed in 1993 dissolved C_{60} and anthracene in a 5:6 molar ratio (respectively) in benzene, then refluxed for 12 hours under N_2 . The reaction was performed at different temperatures and production of the mono-adduct was found to be inversely affected by increasing temperature³. At room temperature the yield of the mono-adduct C_{60} anthracene was 25%, with the yield of the di-adduct, C_{60} anthracene₂, 24%. It was found that heating the mono-adduct at greater than 60°C produced the reactants, confirming that the reaction is easily reversible.

C_{60} anthracene has also been formed by dissolving a 1:1 molar ratio of C_{60} and anthracene in naphthalene and stirring at 200°C whilst sealed in a pyrex glass tube under vacuum for 2 days. The complex was produced in a 67% yield⁴.

A rapid method of production involves the modification of a domestic microwave oven⁵. It produced C_{60} anthracene in a yield of 35%, in only 15 minutes. Similar to reflux experiments, the C_{60} and anthracene were mixed in a 1:10 molar ratio (respectively) and dissolved in toluene. The power of the microwave oven was set to 800 W.

High Speed Vibration Milling (HSVM) is another fairly rapid method of producing C_{60} anthracene⁶. This is a solvent free method that is assumed to work with localised high pressure spots activating local reaction sites. Due to the lack of solvent molecules the reacting species can come into a very close proximity, which can be assumed to help

promote the reaction. C_{60} and anthracene were vibrated in a 5:6 molar ratio (respectively) in a stainless steel capsule, for 1 hour at 3500 cycles per minute. A stainless steel milling ball was also present inside the capsule. It produced C_{60} anthracene in a 55% yield, and C_{60} anthracene₂ in a 19% yield.

This method of production was also applied to the reaction between C_{60} and pentacene, and produced the following complexes: C_{60} pentacene in 19% yield, $(C_{60})_2$ pentacene in 11% yield, and C_{60} pentacene₂ in 15% yield. The synthesis was also applied to C_{60} and tetracene, producing the mono adduct in a 61% yield.

The synthetic method employed for this experiment is listed in the experimental section of this chapter. It is based on the method developed by Schlueter et al².

Reaction Pathway

The reaction between C_{60} and anthracene, tetracene and pentacene proceeds via a Diels-Alder, or [4+2] cycloaddition reaction. For the reaction between C_{60} and anthracene, the reaction has been confirmed as a concerted Diels-Alder reactions⁷. C_{60} undergoes a wide range of cycloaddition reactions, of which the [4+2] has been most studied. The C_{60} -PAH complexes easily undergo the retro Diels-Alder reaction, hence the difficulty in analysing these complexes using mass spectrometry. Even very soft mass spectrometric techniques result in the separation of the PAH from the C_{60} . Prior to the present investigation, ratios of intact molecular ions of C_{60} anthracene complexes relative to the C_{60} fragment ion were typically only a few per cent (typically around 3%), even when soft ionisation methods such as Fast Atom Bombardment (FAB) were used⁸.

The Diels-Alder reaction proceeds as follows:

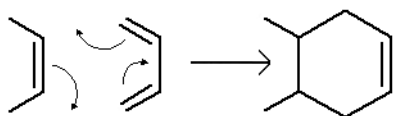


Figure 6.4: Mechanism of a Diels-Alder reaction

Naturally, the resultant effect of the reaction to the C_{60} PAH complexes is disruption to the delocalisation of the PAH aromatic π system. The structures of the complexes formed are shown below:

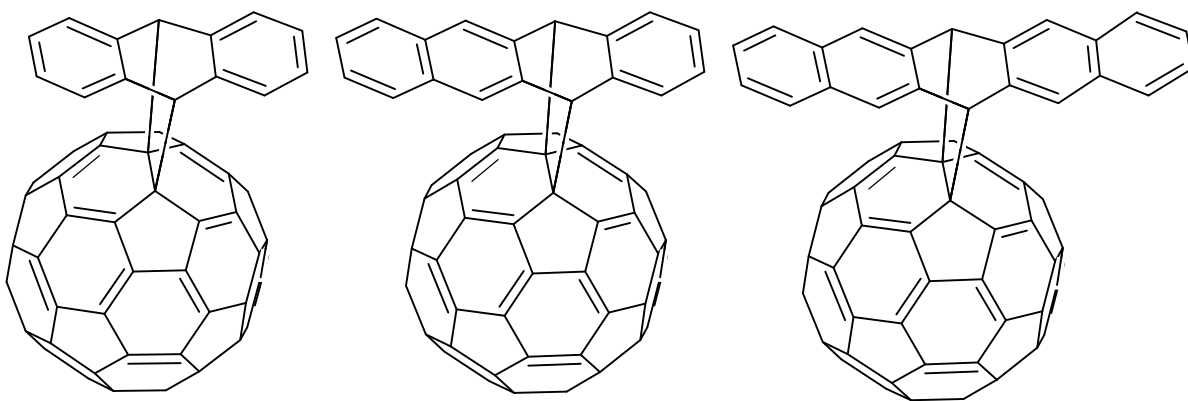


Figure 6.5: Left to right, the structures of C_{60} anthracene, C_{60} tetracene, C_{60} pentacene

For the PAH, addition will always be located across a central ring. Proof for the structure of C_{60} anthracene was confirmed by $^1\text{H-NMR}$, TGA, UV-Vis and IR spectroscopy².

The $^1\text{H-NMR}$ spectrum also confirmed that anthracene adds across a reactive 6-6 ring junction on C_{60} , as is expected of most addition reactions to C_{60} .

TGA confirmed that C_{60} and anthracene were bound. Comparison of the UV-Vis spectra of C_{60} , anthracene, and the C_{60} anthracene complex showed that the aromatic system of the anthracene had been destroyed by binding with C_{60} , whereas C_{60} was largely unchanged; a similar outcome was obtained by analysis of the IR spectra.

The C_{60} tetracene adduct is slightly different from the C_{60} anthracene and the C_{60} pentacene adducts in that the PAH ligand is composed of an even number of benzene rings, however the addition still occurs as close to the centre as possible. Proof of its structure came from $^1\text{H-NMR}$, UV-Vis spectroscopy and Atmospheric Photo Chemical Ionisation (APCI) MS⁶. The crystal structure of C_{60} pentacene was obtained in 2003⁹, and confirms quite clearly that addition occurs across the central benzene ring.

Previous Attempts at Mass Spectrometry

The first attempt to study C_{60} anthracene with mass spectrometry was in 1993, when LD-ToF was performed¹⁰. It was apparent that the synthesis had been successful, as after the reaction an insoluble brown substance precipitated out of the solution. However, the mass spectrum resulted in only a single peak at m/z 720 for C_{60} .

The next attempt at mass spectrometry utilised negative-ion mode FAB, which produced a very small molecular ion peak for C₆₀anthracene at m/z 898. m-Nitrobenzyl alcohol was used as the matrix, and the Xe beam had an energy of 8 kV³. There was also a weak signal for C₆₀Anthracene₂, the dianthracene adduct. The strongest signal by far, however, was for C₆₀. A related compound, the anthracene adduct to C₇₀Ph₈ was studied using EI and FAB mass spectrometry resulting in spectra that resembled those of C₇₀Ph₈ alone. The synthesis had been successful in this case as well, as the anthracene addition had been confirmed with ¹H- and ¹³C-NMR¹¹. FAB-MS has also been used in conjunction with ¹H-NMR and UV/Vis to study the bis adducts of the reaction between C₆₀ and anthracene¹². The use of EI-MS to study the adduct of anthracene to C₆₀F₁₈ resulted only in fragmentation peaks for C₆₀F₁₈ and anthracene¹³.

Electrospray mass spectrometry has been used for the analysis of similar [4+2] adducts. During a 30 hour reflux in benzene of C₆₀ with a crown ether substituted diene, aliquots were removed, diluted with toluene and methanol, and potassium acetate added. These aliquots were sprayed in positive-ion mode, and the progression of the reaction monitored. The only peak in the spectrum was the potassium adduct of the desired molecular ion¹⁴. Electrospray is a much softer ionisation method than FAB, which could explain the lack of fragmentation. It could also be that the C₆₀-crown ether substituted diene adduct is less labile than the C₆₀PAH adducts being studied here.

Electrospray of “bare” fullerene derivatives has always been difficult to achieve as non-polar molecules tend to be “ESI inactive”. Generally, either polar molecules or solutions with already pre-formed ions are best suited for ESI-MS analysis.

Nevertheless, it has been observed that conditions can be achieved inside the ESI source that would mimic an electrochemical cell¹⁵, and that it is possible to obtain C₆₀ and C₇₀ ions in negative-ion mode through reduction with careful optimisation of the conditions. However, the formation of positive ions could still not be achieved¹⁶.

To overcome this issue, C₆₀ has been tagged with a crown ether to produce the C₆₁-fulleroid shown below, on the right:

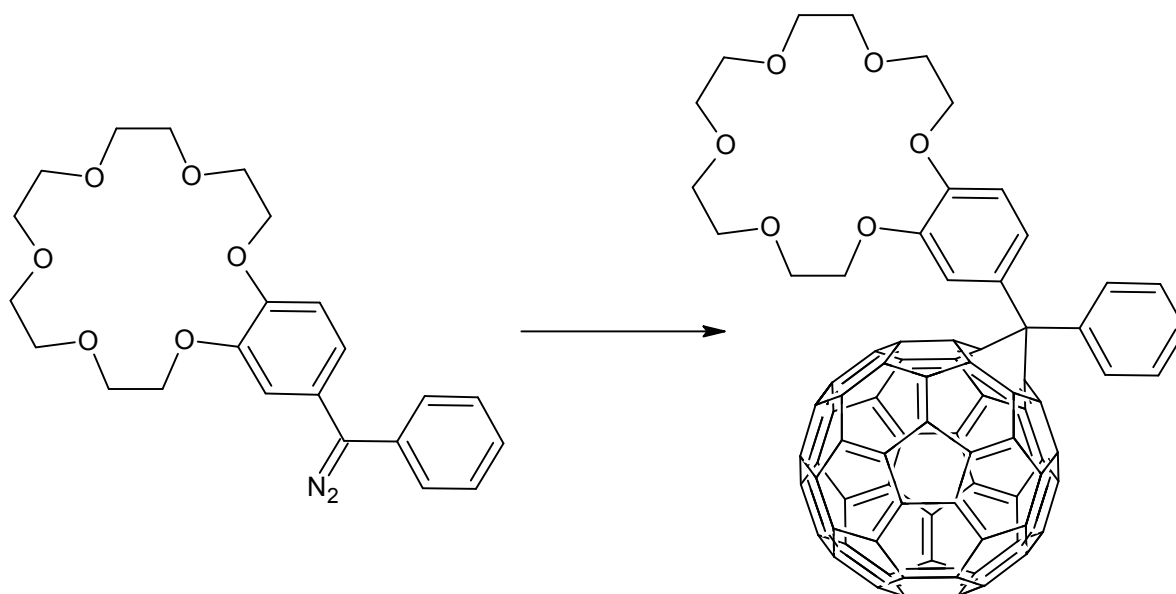


Figure 6.6: C_{60} tagged with a crown ether

In positive-ion mode ESI, crown ethers become charged through either sodium or potassium cation attachment, depending on the salt solutions added. A typical preparation for the C_{61} -fulleroid includes dissolving in benzene and mixing with a $10^{-3} \text{ mol dm}^{-3}$ potassium acetate in methanol solution to create a solvent ratio of 4:1 benzene: methanol.

The resulting spectra produced a single peak of the potassiated molecular ion: $[M+K]^+$. There was no fragmentation. When this method of tagging with the crown ether was performed on a C_{60}/C_{70} mixture, peaks were produced for the C_{61} -fulleroid with potassium and the C_{71} -fulleroid with potassium¹⁷. The method of tagging with a crown ether and addition of a cation to it for ion formation in ESI was also found to work for other neutral organic molecules such as vitamin D, carboxylic acids, cholesterol and amino acids¹⁸.

The crown ether C_{61} -fulleroid was used to monitor C_{60} reactivity by ESI. The idea here has been that the C_{61} -fulleroid would be used in reactions in place of pure C_{60} , mimicking its reactivity and the attached crown ether would allow ESI analysis through metal attachment. One illustrative example was the Diels-Alder reaction with vitamin D. This was followed with ESI, and it was found that two vitamin D molecules attach consequentially to the C_{60} ¹⁸.

The research group involved with the tagging of fullerenes with crown ethers for positive-ion detection in ESI also developed an interesting approach for negative-ion detection. The authors found that methoxy ions in solutions with bare fullerenes would create molecular ions of the fullerenes in negative-ion mode without optimisation of the conditions inside the ESI source¹⁹.

Using a solution of C_{60} in toluene, and adding to this sodium methoxide in methanol to create a solution with a 1:1 toluene:methanol by volume, negative-ion mode ESI was performed. A range of compounds were formed, including C_{60}^- , $C_{60}O^-$, $C_{60}(OCH_3)_n^-$ and $C_{60}O(OCH_3)_n^-$, where n was an odd number up to 5, $C_{60}O_3(OCH_3)_3^-$, and $C_{60}O_2(CH_2C_6H_5)^-$. Other solvent combinations were also tested, such as toluene/ethanol, benzene/methanol, and ethylbenzene/methanol. It appeared that toluene/methanol produced the best spectra. The method was also tested with C_{70} , and similar adducts were produced as for C_{60} . One issue with these experiments, however, is that they were performed with an instrument of only low resolution, and as such the isotopic pattern is not easily distinguishable. However, simply enlarging the published spectra seems to reveal that the $[M+1]^-$ peak is actually more abundant than the M^- peak for the majority of the peaks in the spectrum below:

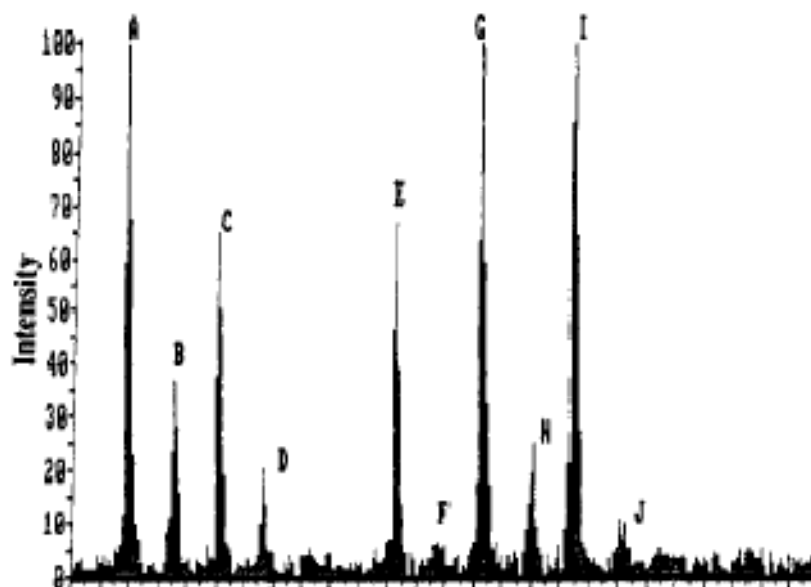
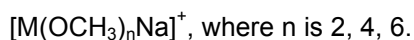
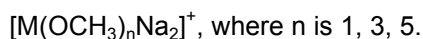


Figure 6.7: Spectrum from Detection of Methoxylated anions of Fullerenes by Electrospray-Ionization Mass-Spectrometry, *Journal of the American Chemical Society*, 1993, 115 (22), 10334-10337

The findings obtained in this thesis clearly show that the formal addition of hydrogen (or hydride) to create MH^- is significant in addition to production of the “bare” anions.

This “methoxide” method was applied to the C_{61} -fulleroid compound shown in figure 6.6, in positive-ion and negative-ion mode. In negative-ion mode, peaks for M^- , $M(OCH_3)^-$, $M(OCH_3)_3^-$ and $M(OCH_3)_5^-$ were produced. In positive-ion mode, both odd and even numbers of methoxy groups added to the C_{61} -fulleroid. However, for odd numbers of methoxy groups

added, 2 sodium cations also attached. For even numbers of methoxy groups, only 1 sodium cation attached, to produce:



The sodium adduct of the molecular ion peak was also found, $[\text{MNa}]^+$.

A demonstration of how conditions within the ESI source affect ionisation through redox reactions comes from the study of dianions of higher fullerenes, in particular C_{84} and C_{90} ²⁰. These experiments also emphasised how important the properties of the analytes themselves are. For instance the electron affinity, as well as solution concentration and choice of solvent also affect the formation of ions. The fullerene mixture was analysed in negative-ion mode and was dissolved in a variety of different solvents and solvent combinations. The sample contained 41% C_{84} , 5% C_{90} , and other fullerenes of between 60 and 96 carbon atoms, all at around 5% intensity each. In the resulting spectra C_{90} dominated, due to it possessing a higher electron affinity. Dianions were also formed, however, only from C_{90} and C_{84} . The negative-ion ESI-MS was performed without additives and used such solvents as benzene, o-dichlorobenzene; either alone or mixed with methanol or dimethyl sulphoxide.

A similar technique to ESI, nanospray, involves modification of the electrospray source. This technique analyses much smaller amounts than used for ESI-MS to produce similar quality spectra. It has been utilised for the detection of non derivatised fullerenes in both positive and negative mode, without the addition of salts, and found to be successful²¹. Modifications included altering the stainless steel capillary to a gold/palladium coated glass needle which is kept at ground potential. There is also the introduction of a pyrex tube with nickel end caps, held at different potentials, directly after the spray formation. The spray goes through this tube prior to analysis and subsequent detection. It appears that such modifications promote the ability of the source to function as an electrochemical cell.

Another benefit is that the fullerenes could be dissolved and analysed in toluene, which cannot be used in traditional ESI-MS. There was no protonation or deprotonation of the sample, and molecular ion peaks of C_{60} and various other fullerene derivatives were observed in both ion modes, with no or very little fragmentation.

However, this technique does involve the modification of an ESI source, which is not always an option. Ideally, it is desirable that conditions are found where the C₆₀-PAH complexes can be analysed with reduced or no fragmentation, and that the intensity of the molecular ion can be increased. In this chapter the both most promising soft ionisation methods MALDI and ESI were applied to the analysis of the C₆₀PAH adducts. The experiments conducted are beyond a simple testing of the suitability of the ionisation methods, they rather represent the method development to make the ionisation methods work for the analytes under investigation.

Cis-bis[60]fullerene adduct of 6,13-diphenylpentacene

This complex was synthesized by Prof. Glen Miller of the University of New Hampshire (USA) and is composed of two C₆₀ molecules which attach in a cis fashion across the 6,13-diphenylpentacene backbone^{9, 22}:

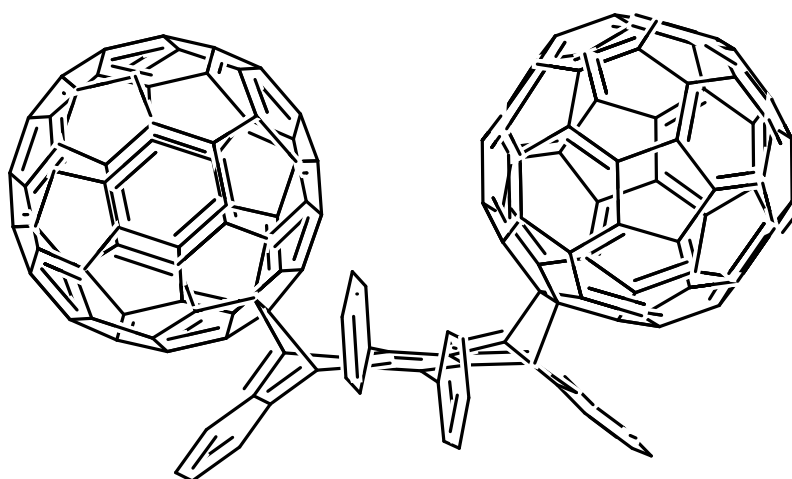


Figure 6.8: Structure of cis-bis[60]fullerene adduct of 6,13-diphenylpentacene

This structure is stabilised by van der Waals interactions between the two fullerenes – each fullerene has a five-membered ring directly opposite a five-membered ring of the other fullerene. These five-membered rings, however, are not exactly aligned with one another⁹.

Although the structure has been confirmed with a single crystal x-ray, the molecular ion peak has never been seen in mass spectrometry, due to the ease with which the compound loses the C₆₀ molecules. The molecule can be expected to be even more labile than the C₆₀PAH complexes also being studied for this chapter. As such, it is an excellent test molecule of

which to attempt MALDI and ESI-MS analysis of, in order to test the softness of the methods developed.

Experimental

Synthesis of C₆₀Anthracene, C₆₀Tetracene and C₆₀Pentacene

50mg C₆₀ and the PAH of interest: anthracene, tetracene or pentacene, (Acros Organics 98%) were dissolved in a 1:10 molar ratio in 15ml of toluene in a 100 ml round bottomed flask. The flask was covered with foil to exclude light, and the mixture stirred using a magnetic stirrer and hot plate without heating for an hour to ensure complete dissolution of the reactants. The solution was then refluxed for 72 hours at 50°C. A guard tube containing CaCl₂ was attached to the end of the condenser.

At the end of the 72 hours the solvent was removed by a rotary evaporator, with care taken to ensure the water bath was kept below 30°C to prevent the retro Diels-Alder reaction. Due to time constraints the sample was analysed as formed without further purification. The products were stored in a refrigerator.

MALDI Analysis

The solid samples were dissolved in toluene to make a 1 mg/ml solution.

DCTB was dissolved in toluene to make a 10 mg/ml solution.

DCTB and the sample were mixed in an approximately 1:50 molar ratio, the calculation was based on the assumption of 100% yield, and applied to the target spot. Typically, 5µl was applied per spot. The fullerene calibration mixture was applied to spots adjacent to the sample spots. The samples were analysed in positive-ion and negative-ion mode with the Bruker Ultraflex II, with both linear and reflectron time-of-flight analysis used.

ESI Analysis

0.5mg product was dissolved in 2ml DCM. 400µl of this solution was diluted by addition of 1600µl DCM, to form solutions with concentrations of approximately 50µM. 1ml of this solution was mixed with 1ml methanol for ESI analysis. The final concentrations for ESI analysis, the calculation based on 100% yield, were C₆₀anthracene: 27.8µM, C₆₀tetracene: 26.3µM and C₆₀pentacene: 25.0µM. In practise the actual concentration would have been

lower. It should be emphasized that no methoxy salt was added, so that the C₆₀PAHs were sprayed directly from a DCM/methanol solution.

Results

Analysis of C₆₀PAH complexes by MALDI and ESI

As confirmation of a successful synthesis of the C₆₀PAH complexes, both MALDI and ESI were utilised. For MALDI the most promising matrix: DCTB was employed and for ESI spraying a solvent combination in the negative-ion mode was tested, as outlined in the introduction to this chapter. The C₆₀PAH complexes are abbreviated in the following as C₆₀A, C₆₀T and C₆₀P, representing the raw product of the respective addition reaction of anthracene, tetracene and pentacene with C₆₀.

MALDI

MALDI was employed in both ion modes, however; only in the negative-ion mode could molecular ions be obtained:

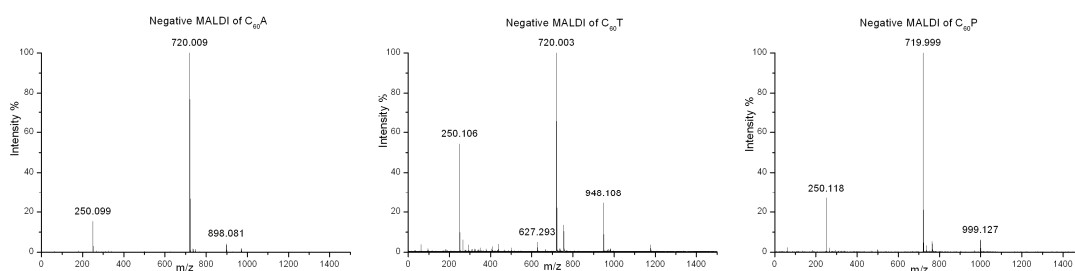


Figure 6.9: Negative-ion mode MALDI spectra of C₆₀A, left, C₆₀T, centre, C₆₀P, right

The molecular ions can be seen at m/z 898, 948 and 998, respectively.

Enhancing the molecular ion region of the spectra shows in more detail the isotopic pattern of each compound:

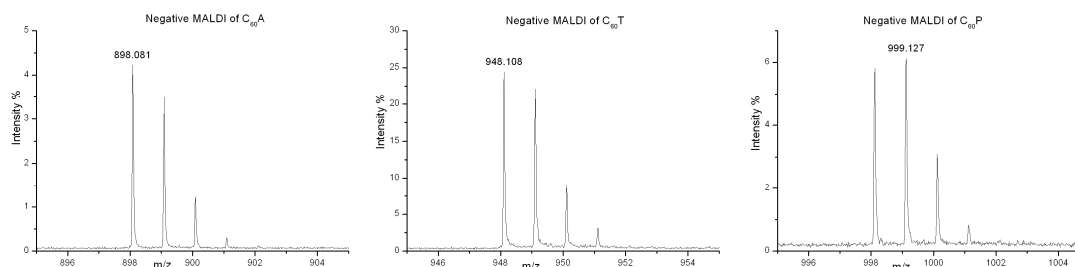


Figure 6.10: Negative-ion mode MALDI spectra of C₆₀A, left, C₆₀T, centre and C₆₀P, right

For all three ions, the isotopic abundances differ slightly from the expected appearance for molecular ions. The M+1 peak is too high in intensity compared to the M peak. The

theoretical intensity ratios of M:M+1 peaks are calculated below (based on the $^{12}\text{C}_{n-1}^{13}\text{C}$ peak intensity equalling 1.1n% of the intensity of the $^{12}\text{C}_n$ peak, set at 100%).

C_{60} Anthracene: 100%:81.4%

C_{60} Tetracene: 100%:85.8%

C_{60} Pentacene: 100%:90.2%

The reason for the deviation of the observed isotopic pattern from what is expected for the pure molecular ions is most probably due to the very low intensity at which these signals are obtained. At very low intensities, we have observed in several other experiments on the Bruker Ultraflex II that the isotopic pattern is not always obtained accurately. We discount the possibility of protonation as the experiments are run in the negative-ion mode.

Positive-ion mode MALDI does not produce a molecular ion peak of the complexes. Only peaks for the corresponding PAH and C_{60} are seen, indicating that decomposition is complete under these conditions.

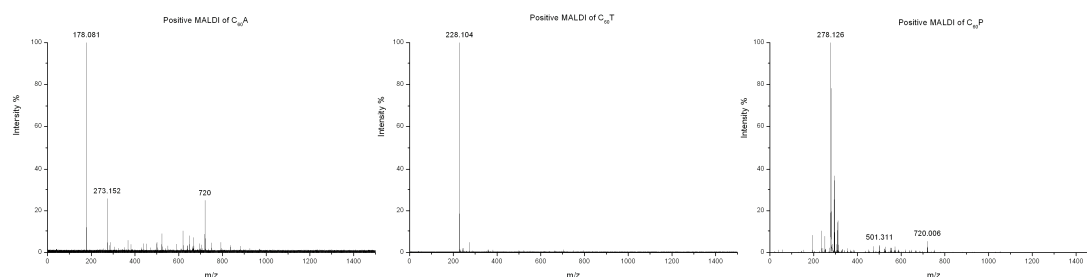


Figure 6.11: Positive-ion mode MALDI spectra of C_{60}A , left, C_{60}T , centre and C_{60}P , right

The dominant peak in each spectrum is the signal of the PAH. This would be due in part to dissociation of the synthesized product; however, an even higher contribution would result from the fact that the PAHs were in excess during the synthesis. This also explains why the polyaromatic hydrocarbon peaks are at a far greater intensity than the C_{60} peak, although it cannot be excluded that the charge may reside preferably on the PAH.

The absence of a molecular ion peak for the C_{60} -PAH in positive-ion mode is demonstrated by enhancing the m/z region 700 - 1100:

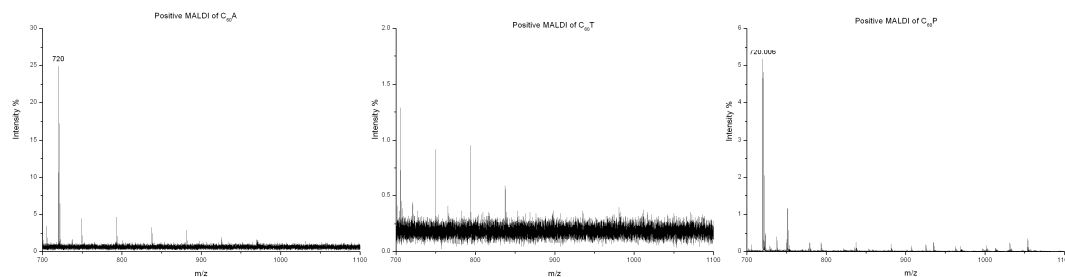


Figure 6.12: Positive-ion mode MALDI spectra of $C_{60}A$, left, $C_{60}T$, centre and $C_{60}P$, right

ESI

The $C_{60}PAH$ complexes were also examined by ESI spraying from DCM/methanol solution in the negative-ion mode on the Bruker esquire2000 as outlined in the experimental section. As ESI is in general a softer ionisation technique than MALDI, it was hoped that this would decrease the appearance of fragmentation and increase the intensity of the molecular ion peak.

C_{60} Anthracene:

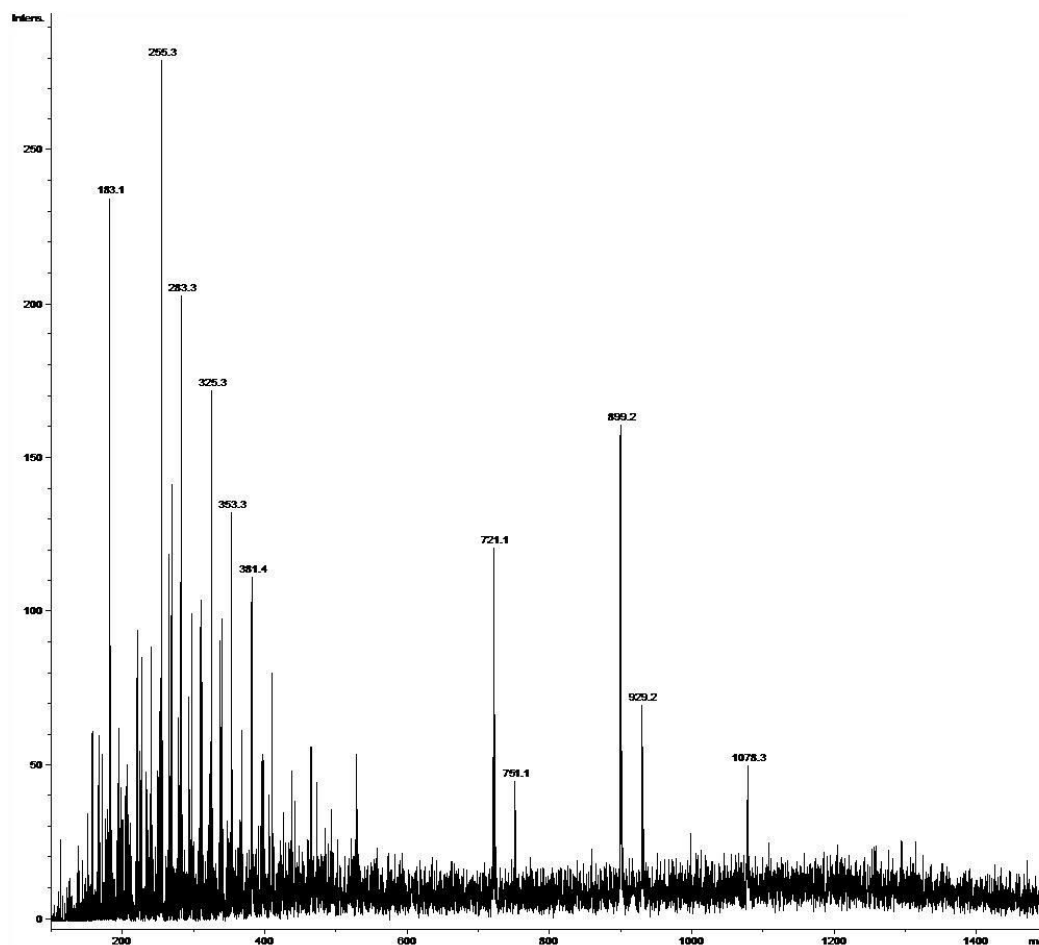


Figure 6.13: Negative-ion mode ESI spectrum of $C_{60}A$

Despite a considerable amount of noise in the low mass region, the quasi-molecular ion peak for $C_{60}A$ and the related fragmentation peaks are present.

The enhancements of the respective mass regions below, clearly indicate that the observed masses are accurate and that the peaks observed at m/z 721.1 and m/z 899.2 are in fact due to $C_{60}+1$ and $C_{60}A+1$, i.e. each plus one additional mass.

Enhancement of the m/z region 700 to 900 shows the most important peaks:

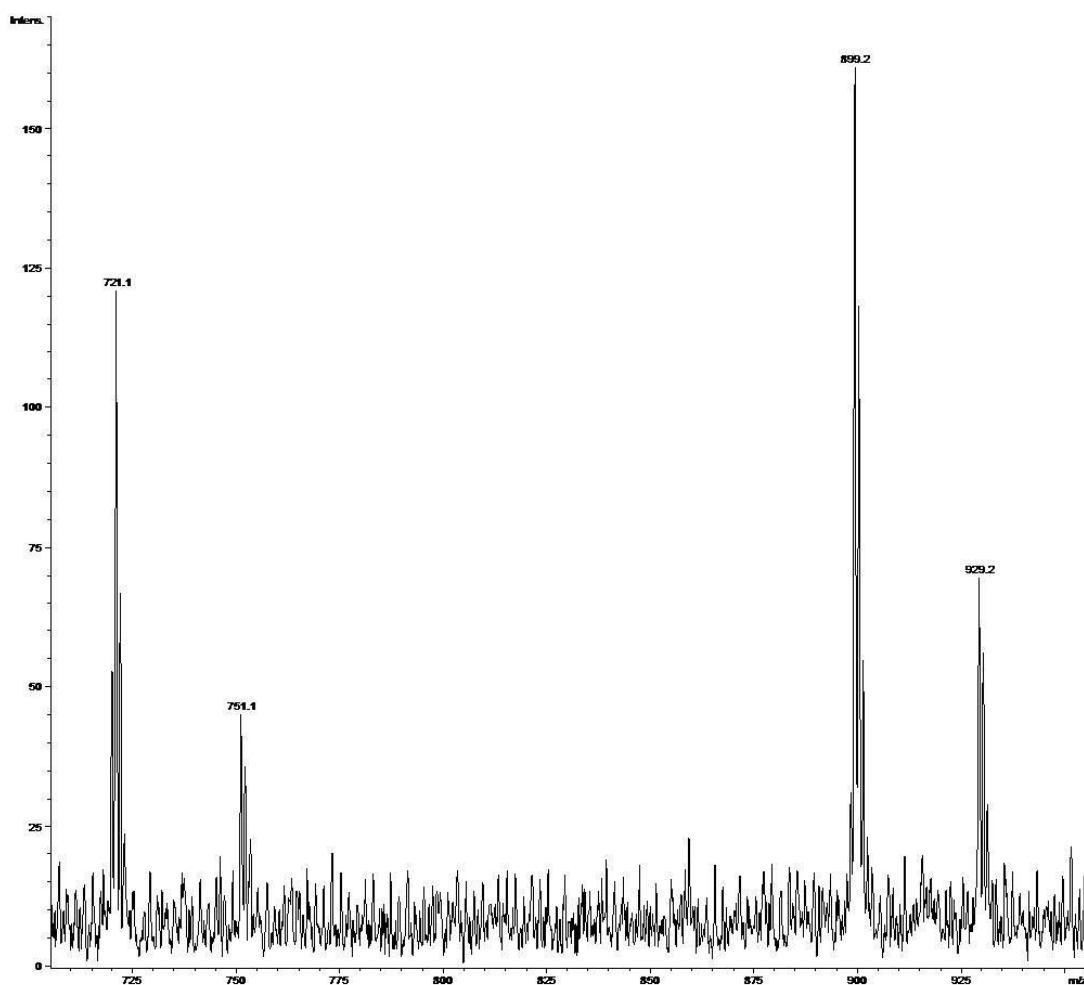


Figure 6.14: Negative-ion mode ESI spectrum of $C_{60}A$, demonstrating the $C_{60}+1 / +31$ and $C_{60}A+1 / +31$ peaks

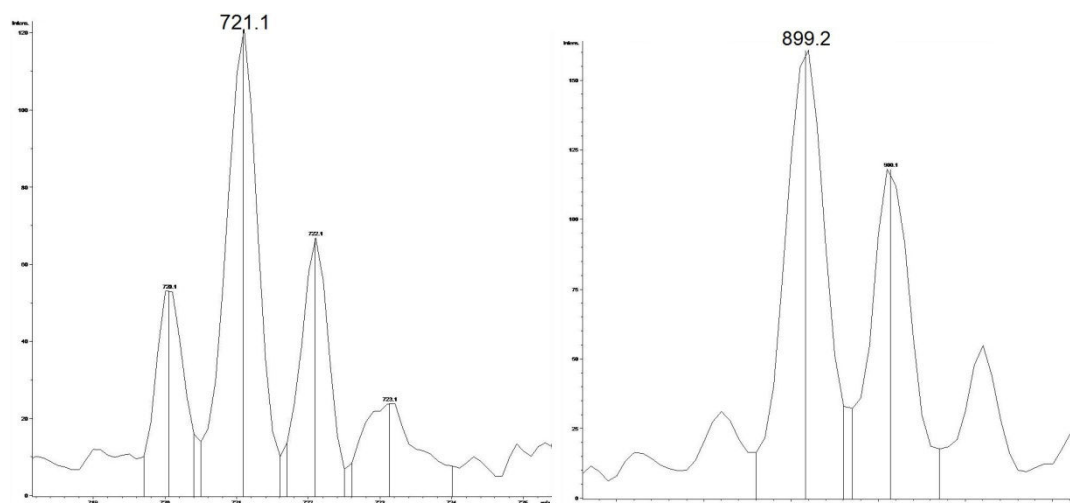


Figure 6.15: Isotopic patterns in the C_{60} region, left, and in the $C_{60}A$ region, right

This indicates addition of a hydrogen atom. Mechanistically it seems likely that the ion formation occurs through the addition of hydride (H^-) to C_{60} and $C_{60}A$. However, there are also peaks at 30 mass units higher for both $C_{60}+1$ and $C_{60}A+1$. These would represent the formal addition of OCH_3 , to the $M+1$ species, in other words: methanol addition to the molecular anions. At present, it can only be speculated about the actual mechanism by which these ions are formed. Since ESI was conducted without methoxy salt addition, the most likely source for both anionic attachments to the fullerene seems to be the solvent. The fact remains, however, that the $C_{60}A$ -containing ions are more abundant than the fragments, indicating that the overall process is much softer than DCTB-MALDI. For the observed ions there is no obvious formation mechanism at hand and its elucidation was not the prime focus of this investigation. Therefore, future experiments are planned to elucidate in more detail the actual ion formation mechanism.

For C_{60} Tetracene the following results were obtained when electrosprayed under the same conditions:

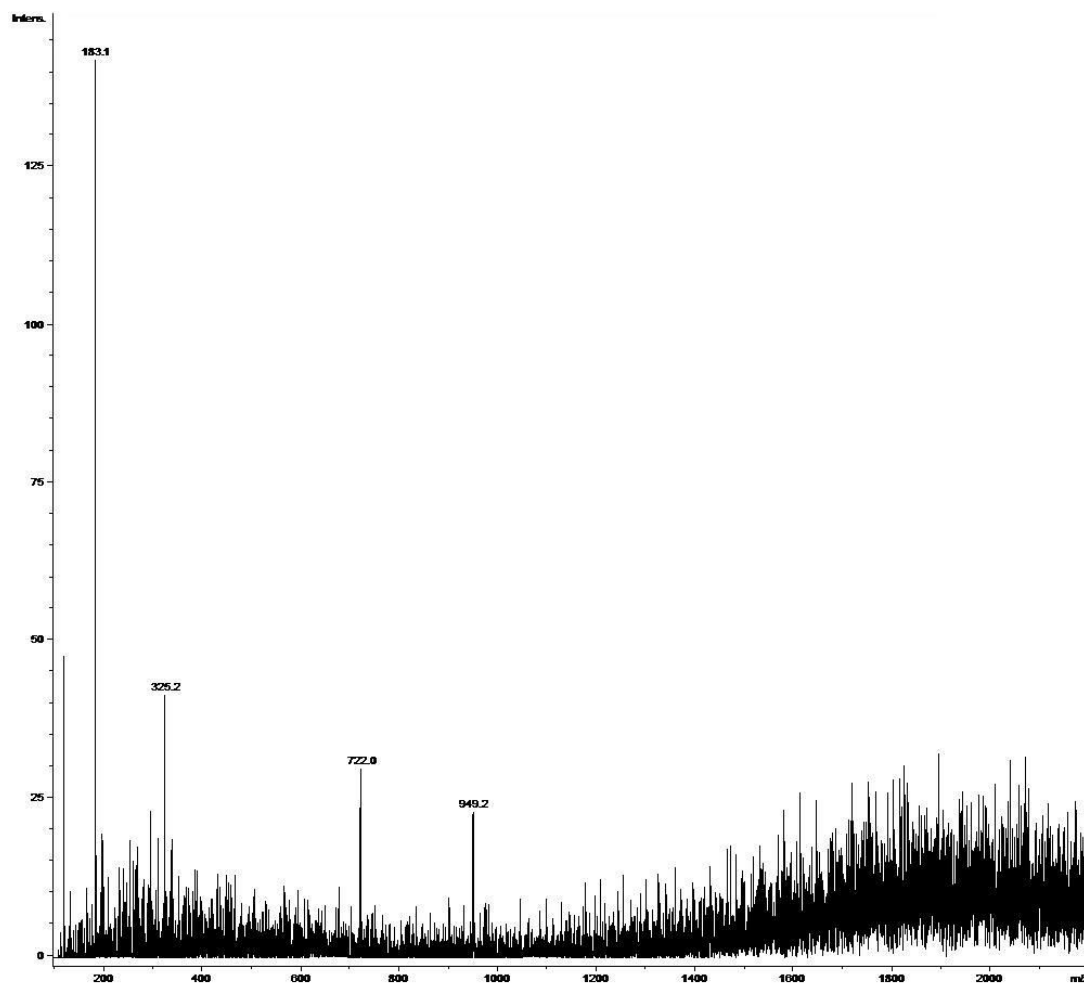


Figure 6.16: Negative-ion mode ESI spectrum of $C_{60}T$

As for $C_{60}A$, the spectrum produced is noisy; however, peaks for $C_{60}+1$ and $C_{60}Tetracene+1$ are present. The most intense peak in the isotopic pattern in the C_{60} region is at m/z 722 ($C_{60}+2$) and for the $C_{60}T$ region, the most intense peak is at m/z 949.2 ($C_{60}T+1$).

The m/z region of 700 to 975 is enlarged in the following:

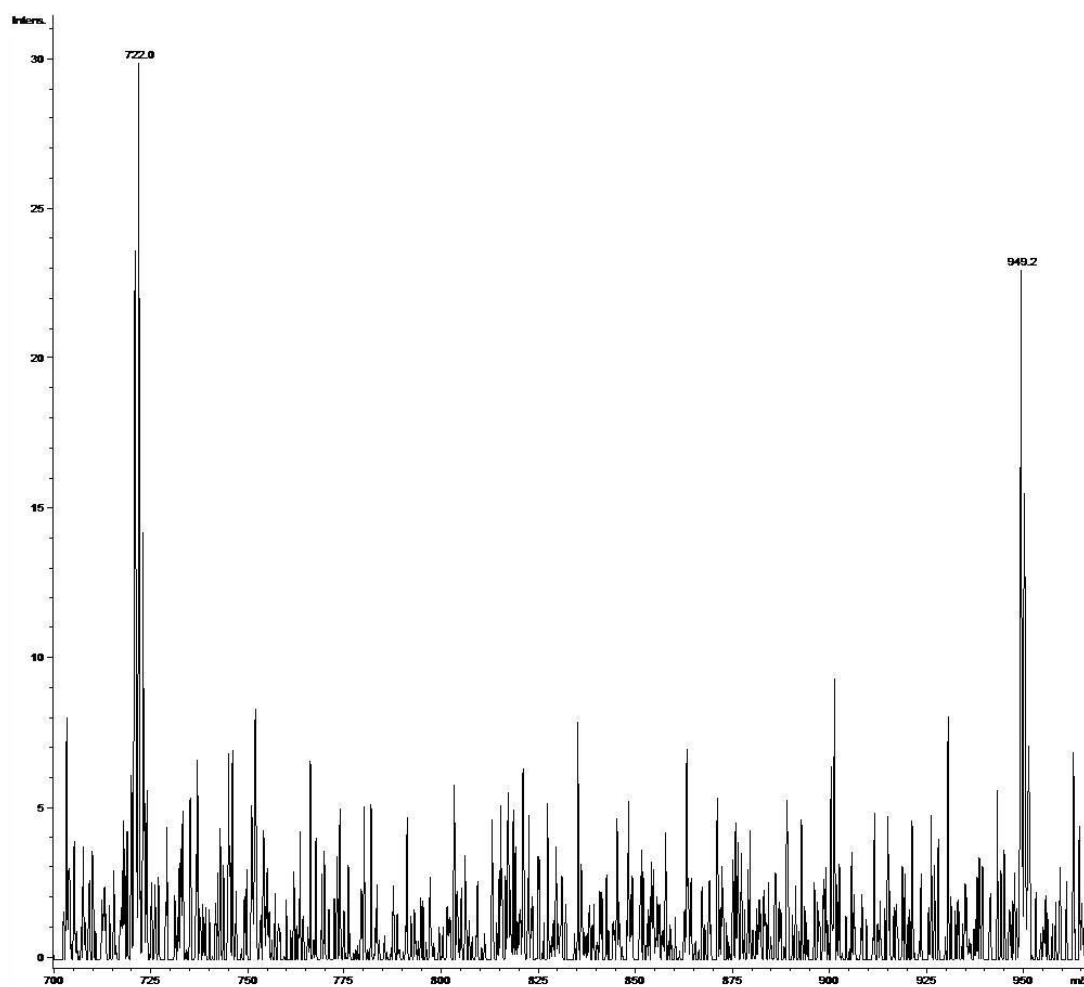


Figure 6.17: Negative-ion mode ESI spectrum of $C_{60}T$, showing the $C_{60}+1$ and $C_{60}T+1$ peaks

The two peaks are again enlarged in the following:

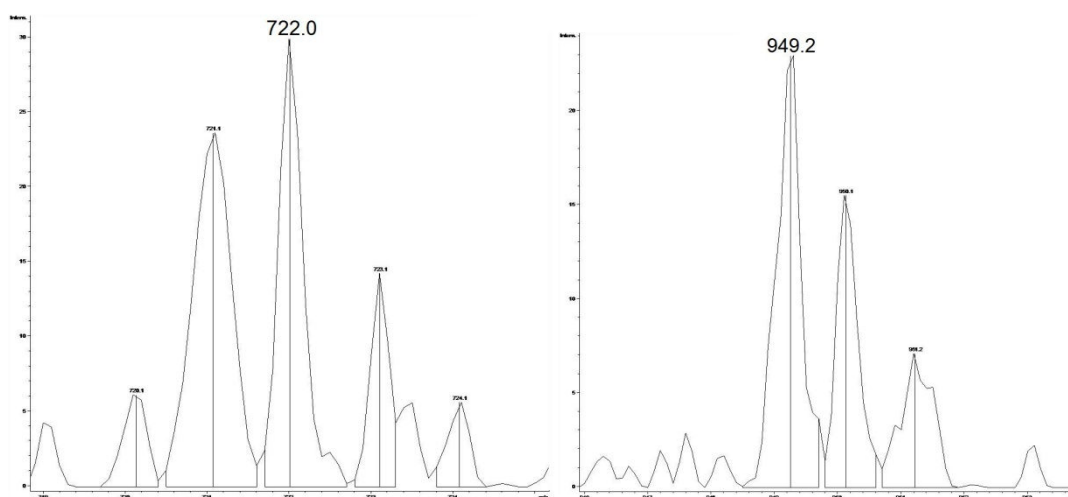


Figure 6.18: Isotopic patterns of C_{60} , left and $C_{60}T$, right

It seems likely that the low abundance of the ions leads to the observed inaccuracy of the isotope pattern in the $C_{60}+1$ region. For all three compounds, $C_{60}T$ gave the weakest ions

and this was the only slight deviation from the $C_{60}+1$ and $C_{60}PAH+1$ pattern. For $C_{60}T$ no peaks appear at 30 m/z unit higher for either of the important peaks. This is most likely due to the decreased signal to noise ratio compared to the $C_{60}A$ spectrum.

$C_{60}P$ gave the following ESI data when sprayed under identical conditions:

The negative-ion mode ESI spectrum of $C_{60}P$ appears cleaner and shows greater intensity signals than the spectra for $C_{60}A$ and $C_{60}T$. At first glance, no signals seem to be present in the C_{60} region, but a small peak in the m/z 1000 region could be indicative of $C_{60}P$:

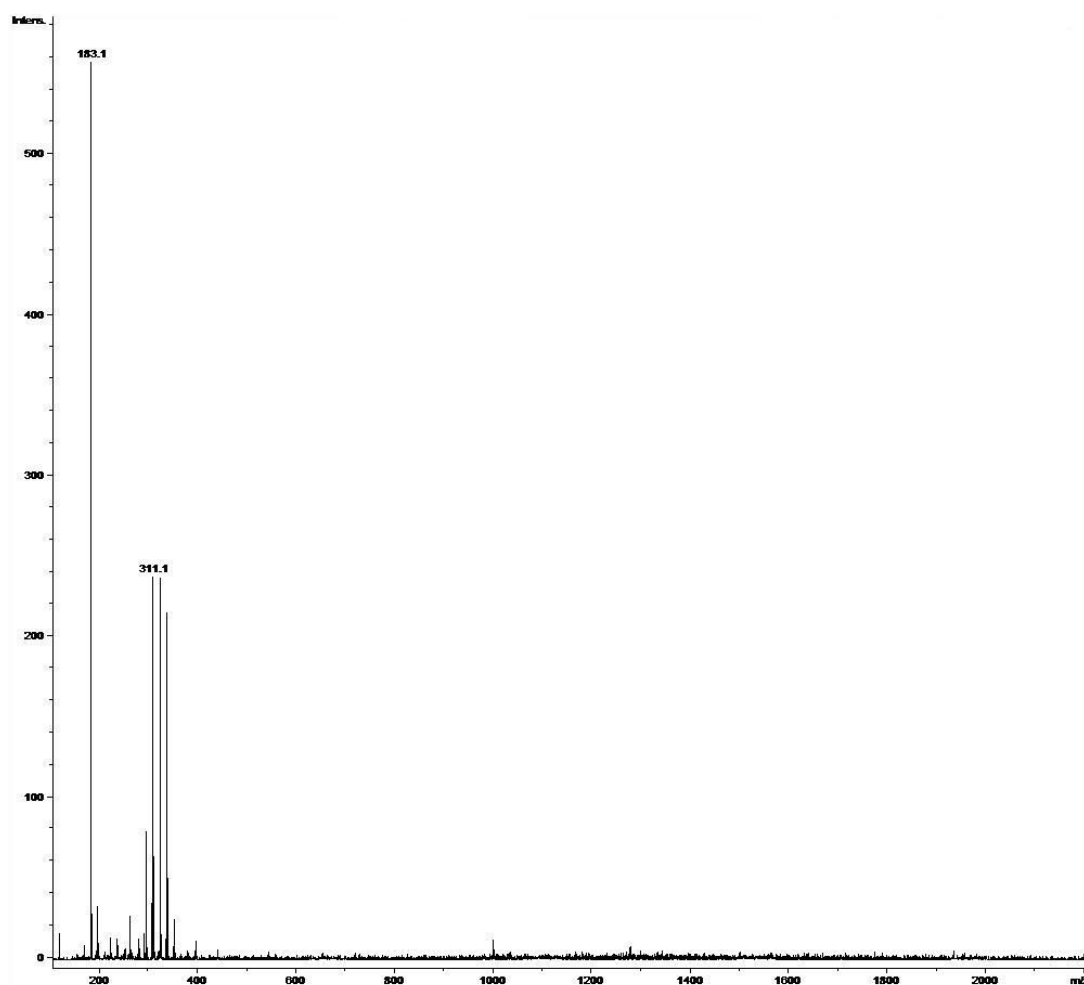


Figure 6.19: Negative-ion mode ESI spectrum of $C_{60}P$

Enlarging the m/z region 700 to 1015 allows for a better inspection of the peaks in question. $C_{60}+1$ is observed at m/z 720.9 in this spectrum and is of very low abundance. As for $C_{60}A$ and $C_{60}T$ the $C_{60}P+1$ signal is clearly observed:

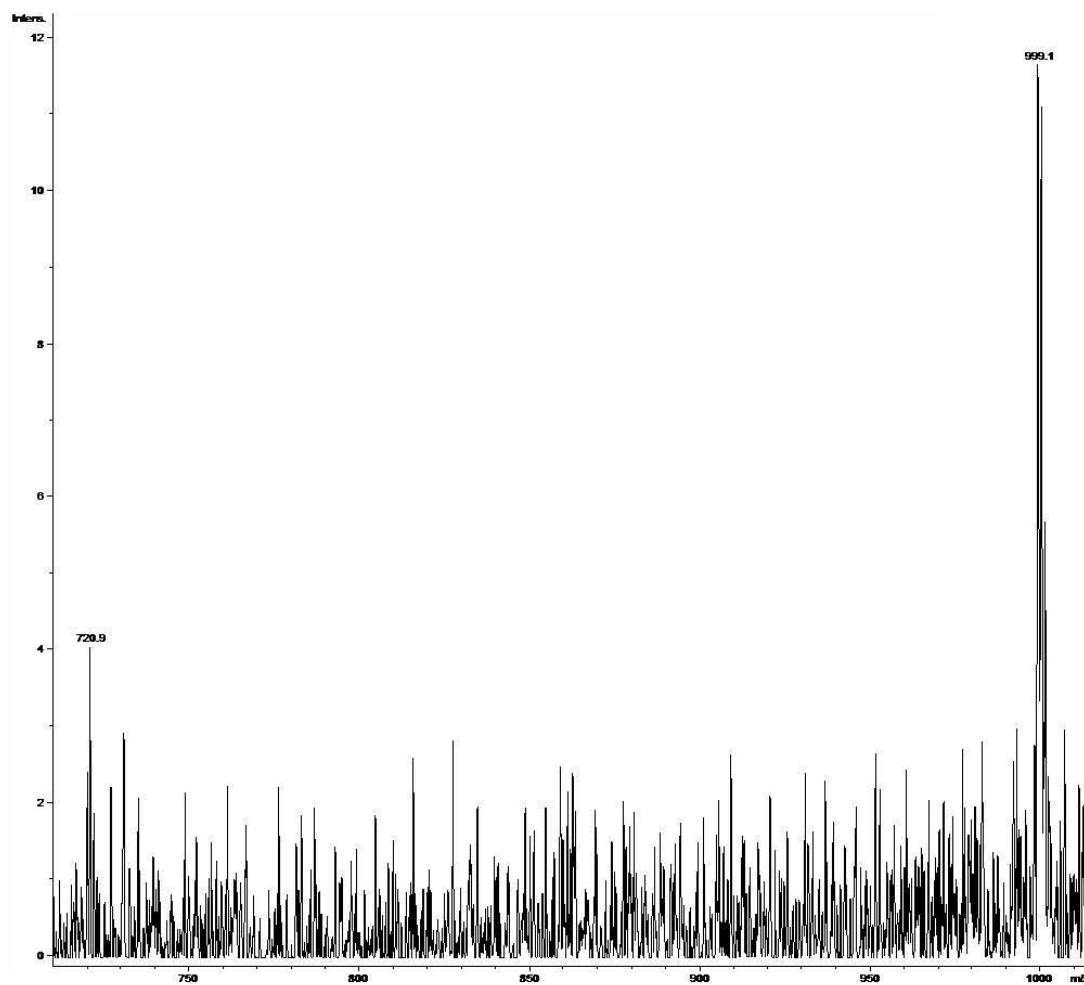


Figure 6.20: Negative-ion mode ESI spectrum demonstrating the C_{60} and $C_{60}P$ peaks

It is obvious that the C_{60} Pentacene peak is much more intense than the C_{60} peak. The ratio is an indication of how much softer this ESI method is compared to MALDI-MS. The isotopic patterns of the C_{60} and C_{60} Pentacene region, displayed in more detail below, again demonstrate the addition of one mass unit, respectively.

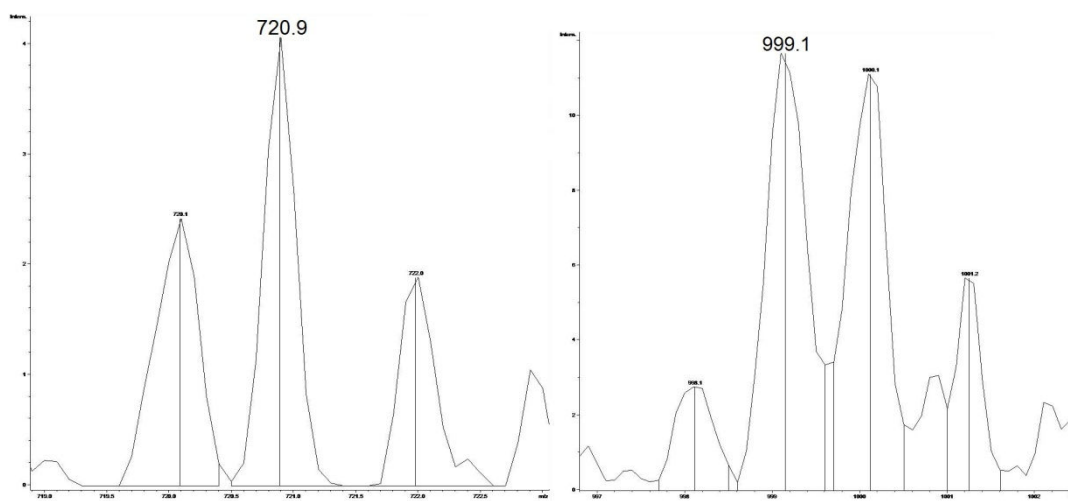


Figure 6.21: Isotopic pattern of $C_{60}+1$, left and $C_{60}P+1$, right

The ESI spectra reveal that this ionisation method is even softer than MALDI. However, the C₆₀PAHs produce fewer ions in ESI. The fragmentation into C₆₀ appears much reduced in ESI. One must also keep in mind that C₆₀ ions would be present regardless, because of the lack of purification. As the present spectra were obtained from the raw products, the C₆₀ peak present in these spectra could be entirely due to the unreacted reactant. Methanol addition was only seen for C₆₀Anthracene. This is perhaps due to the more intense signal produced for C₆₀Anthracene compared with the other C₆₀PAH complexes.

The most interesting observation of these ESI experiments is the addition of one additional mass unit in the ion formation. The calibration of the esquire2000 is very accurate, and does not change over the course of an experiment. It is therefore certain that the peaks appear at 1 m/z value higher than they would do if the anions were formed only by reduction through electron attachment. Often a small peak for the pure anions is seen in the enlarged isotope pattern confirming the existence of the more abundant “plus-one-peaks”. Unfortunately, MS/MS experiments could not be performed at a high enough resolution that would shed more light on the ion formation mechanism. To obtain detailed insight into the ion formation mechanism was beyond the scope of this investigation. The present data suggest that hydride (H⁻) addition and in the case of C₆₀A also methoxy (⁻OCH₃) addition may be the way by which the ions were formed. This may involve predominantly the solvent. However, only future experiments will bring clarity.

Testing the Validity of MALDI as soft ionisation approach

The MALDI spectra of the PAH raw products indicated extensive fragmentation into C₆₀. This is also expected as the compounds are well-known for their lability. However, as the samples had not been purified prior to analysis the extent of fragmentation in relation to the presence of unreacted C₆₀ was not clear. To test the validity of MALDI as a soft ionisation method for analysis of these compounds, a purified sample of C₆₀P, provided by Glen Miller from the University of New Hampshire (USA), was subjected to the same analytical conditions as the samples synthesized for this project.

The purified C₆₀P sample was analysed with MALDI in negative-ion mode over a range of laser powers. Two example spectra are shown below:

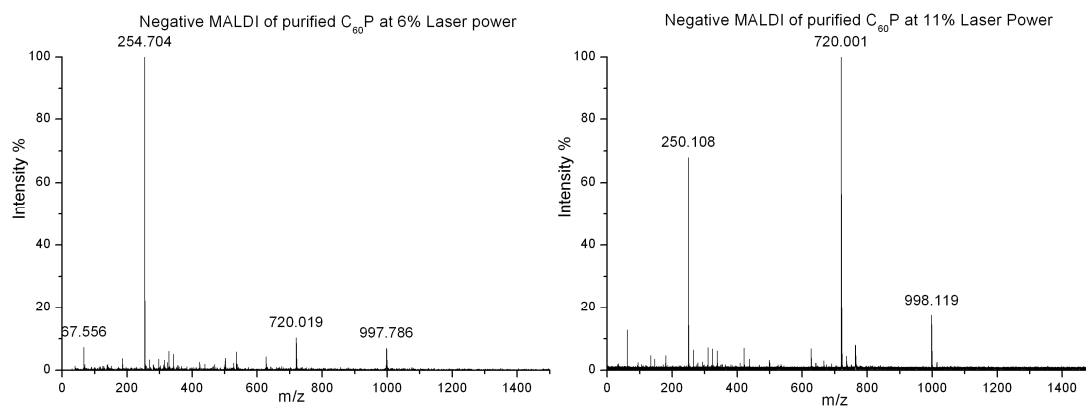


Figure 6.22: Negative-ion mode MALDI of C₆₀P at laser powers: 6%, left, and 11%, right

The above spectra were obtained at different laser powers. The laser power is given in arbitrary units. These percent values are not converted to laser power or laser fluence values with units that would have a physical meaning, as the laser power is used here only qualitatively. In other words, if the laser power percentage increases, more energy is deposited into the sample; the sample is energetically more activated. For the purified C₆₀P, the negative-ion DCTB-MALDI is shown with 6% laser power (LP), displayed on the left and with 11% LP, displayed on the right. In the 6% LP spectrum, the intensity of the C₆₀ peak at m/z 720 is almost equal to the C₆₀P peak at m/z 998. The peak at m/z 254 is due to the DCTB matrix and can be ignored. A ratio this large has not been observed or published previously, and suggests that the MALDI method employed here is more efficient at protecting the sample than previous methods. There is still fragmentation into C₆₀, and increasing the laser power merely increases the fragmentation as would be expected. A close up of the C₆₀ and C₆₀P peaks in the 6% LP spectrum is below:

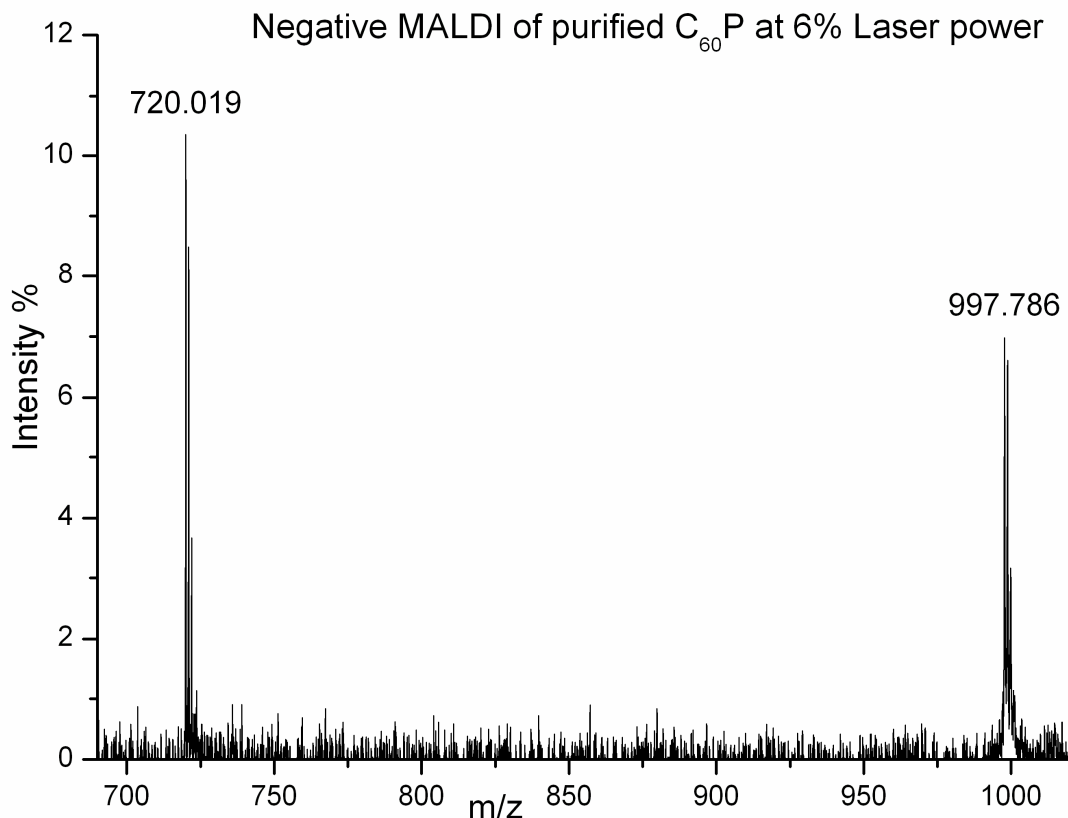


Figure 6.23: Negative-ion mode MALDI of purified C₆₀P at 6% laser

For a low laser power, adjusted at the threshold of ion formation, the signal-to-noise ratio is also low. This is evident by the “grass” present in the spectrum. Unfortunately the low laser power is necessary in order to reduce fragmentation that will produce a strong C₆₀P signal relative to C₆₀. The actual measured intensities of the peaks are 913 for ¹²C₆₀, and 616 for ¹²C₆₀P. This corresponds to a ratio of 100:67.5. This is greater than has been observed previously by other MS approaches in the literature. This confirms negative-ion DCTB-MALDI as an appropriate soft ionisation approach for the analysis of these compounds.

Finally, in comparison with our ESI experiments employing the negative-ion mode, even less fragmentation of the raw product C₆₀P into C₆₀ was obtained. However, the spectrum showed much more noise and less ion abundances when compared to MALDI, so that MALDI would be the method of choice to apply to the C₆₀PAH analysis. One must, however, keep in mind that both ESI and MALDI experiments were performed on different instruments and the influence of the analyser on the sensitivity of the experiment is important but not known in this context.

Other Observations

Several other observations were made throughout these investigations which are discussed in the following.

$C_{60}T_2$

It was observed during the MALDI analysis of the raw products that a small peak, corresponding to the addition of two tetracene molecules to C_{60} had occurred. This was not observed for the $C_{60}A$ or $C_{60}P$ complexes and was also not observed in ESI experiments.

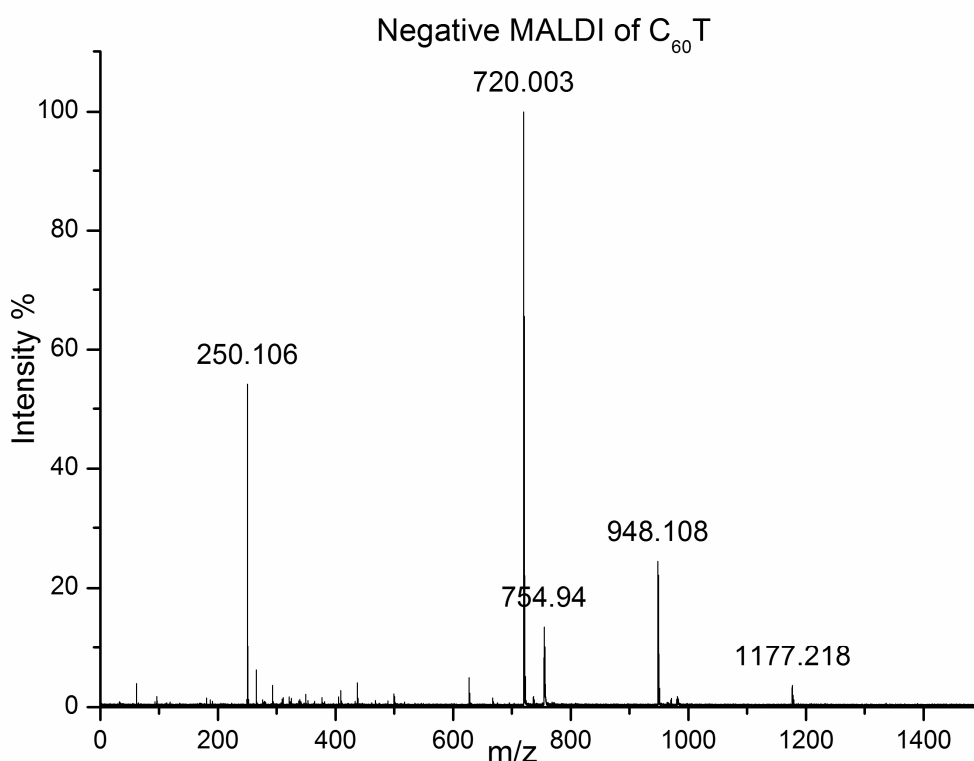


Figure 6.24: Negative-ion mode MALDI of $C_{60}T$

The small peak at m/z 1177.218 is close to the expected m/z of $[C_{60}Tetracene_2]^-$.

To confirm that this peak was $[C_{60}Tetracene_2]^-$, negative-ion mode LIFT was performed on both m/z 948 (left spectrum, below) and m/z 1177 (right spectrum, below). The resulting spectra show that for LIFT of m/z 948, one fragment peak is obtained at m/z 720 - the loss of tetracene. For LIFT of m/z 1177, there are two peaks, at m/z 720 and m/z 948, corresponding to C_{60} and $C_{60}T$, respectively, demonstrating consecutive tetracene loss:

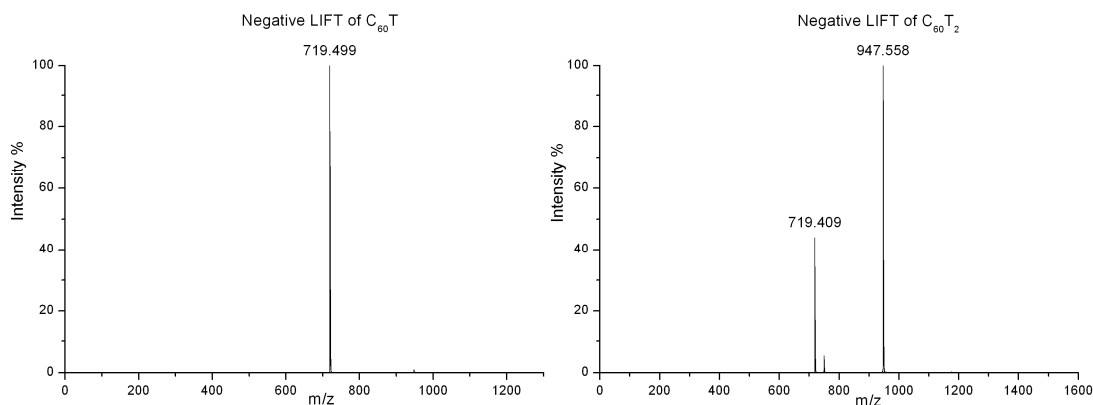


Figure 6.25: Negative-ion mode LIFT of $C_{60}T$ and $C_{60}T_2$

The peaks are shifted by approximately 0.5 m/z from the correct values due to the internal calibration of the LIFT method. Nevertheless, these experiments confirm that a bis adduct was produced when tetracene reacted with C_{60} . It must be assumed that the bis adduct formation is coincidental, as the structural difference of tetracene compared to anthracene and pentacene do not allow to explain a preference for the bis addition. However, it is evident that negative-ion DCTB-MALDI is more sensitive than the negative-ion ESI experiment, which did not show the bis adduct.

Appearance of $C_{60}PAH$ at High Laser Fluences

The initial synthetic paper² on the initial production of $C_{60}A$ claimed identification of the compound through the detection of a small molecular ion in positive-ion direct laser desorption ionisation. In light of the lability of $C_{60}A$ it seems amazing that even a small molecular ion should be observable without the use of an appropriate matrix molecule. In order to elucidate the validity of such claims, LDI experiments were performed on each $C_{60}PAH$ compound at a range of laser powers, in both positive and negative-ion mode, with linear and reflectron detection. At the lower laser powers decomposition appeared to be in fact complete, as molecular ion peaks for the complexes were absent in the LDI spectra. At high laser powers, however, it was observed that there appeared to be small signals, corresponding to the relevant $C_{60}PAH$ under investigation. These peaks were small but distinct from the fragmentation peaks. This was observed for both negative-ion and positive-ion mode.

It is somewhat unexpected that tiny molecular ions are seen when the laser power is increased, as one would tentatively assume that if fragmentation prevails already at low laser fluences, this should be especially the case at higher laser powers.

One possible explanation of this observation could involve fragmentation of the C_{60} PAH in combination with recombination of the fragments.

To test this theory, C_{60} and each of the PAHs were mixed individually and analysed under the same conditions as operative for the detection of molecular ions from the C_{60} PAH compounds. If molecular ion peaks relating to C_{60} PAH were observed in the experiments where C_{60} and the PAH were simply mixed, then this would be the result of the C_{60} and the PAH reacting inside the source. The LDI spectra of the C_{60} PAH complexes which gave rise to the initial observation are shown below first, starting with $C_{60}A$:

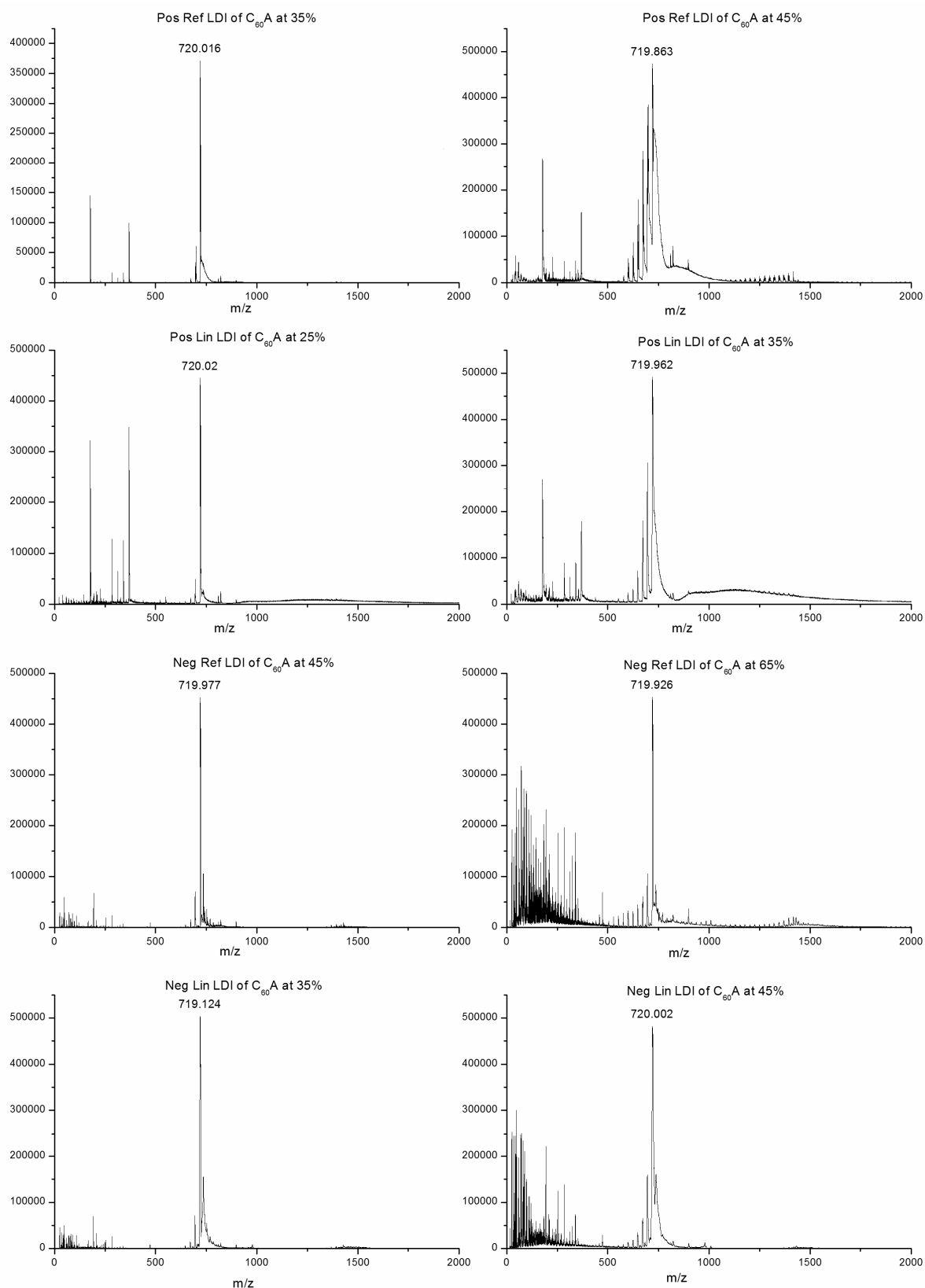


Figure 6.26: Positive and negative-ion mode LDI spectra with linear and reflectron detection of $C_{60}A$ at elevated laser fluences

The possible molecular ion peak at m/z 898 is of very small intensity relative to the other peaks. Enhancing the molecular ion region demonstrates this:

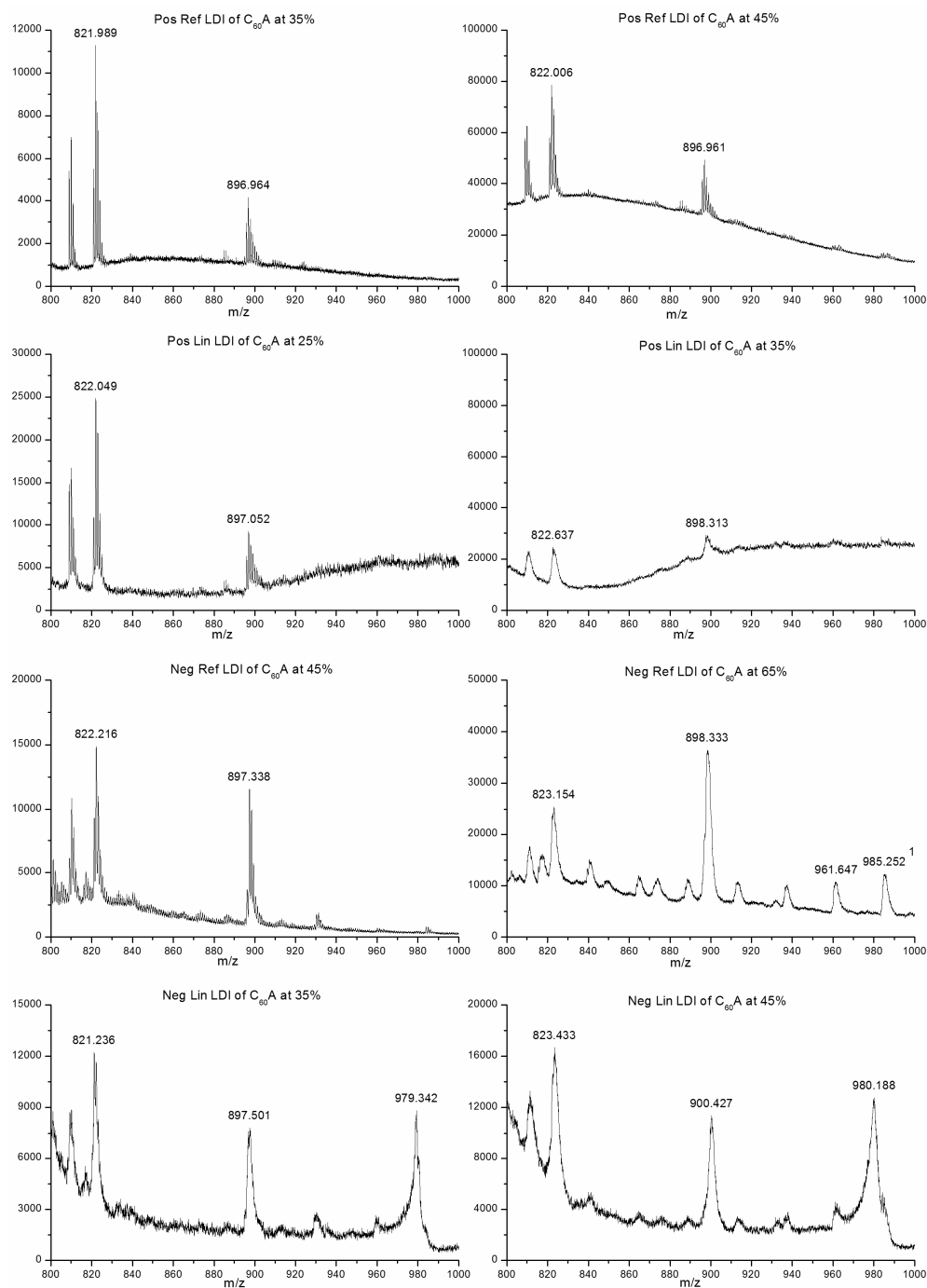


Figure 6.27: Positive and negative-ion mode LDI spectra with linear and reflectron detection of $C_{60}A$ at elevated laser fluences

Peaks at approximately the correct m/z for $C_{60}A$ (m/z 898) are present in all of the above spectra. Most molecular ion signals are only very low abundant relative to the surrounding

noise. The combination of low ion abundances and high laser fluences can result in the inaccuracies in the observed m/z values.

$C_{60}T$ and $C_{60}P$ behaved very similar to $C_{60}A$. All three provide low abundant signals in the molecular ion region. Only the data for $C_{60}T$ are shown here, the $C_{60}P$ spectra are shown in the appendix.

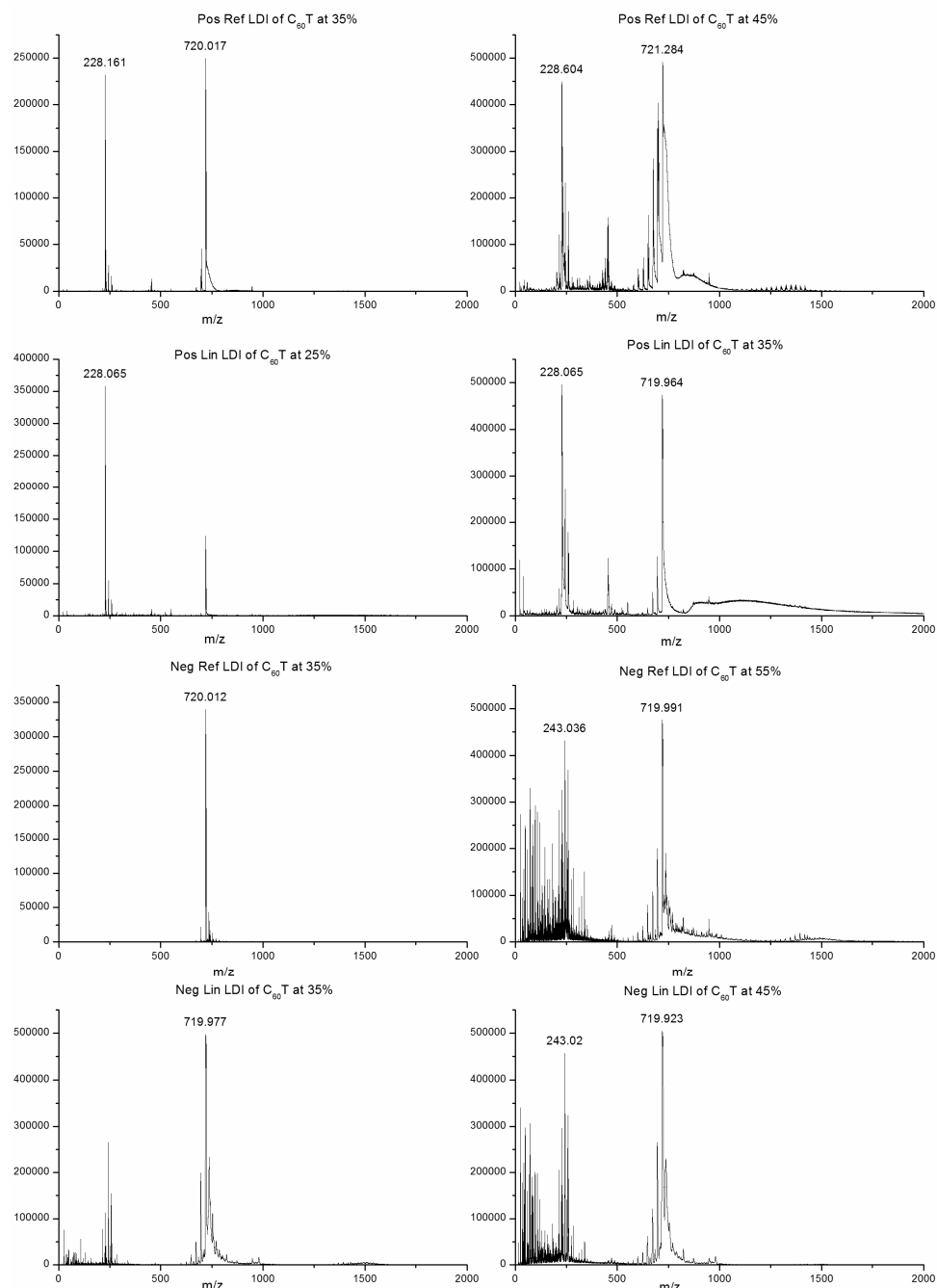


Figure 6.28: Positive and negative-ion mode LDI spectra with linear and reflectron detection of $C_{60}T$ at elevated laser fluences

The molecular ion region for $C_{60}T$ enhanced; the molecular ion is expected at m/z 948:

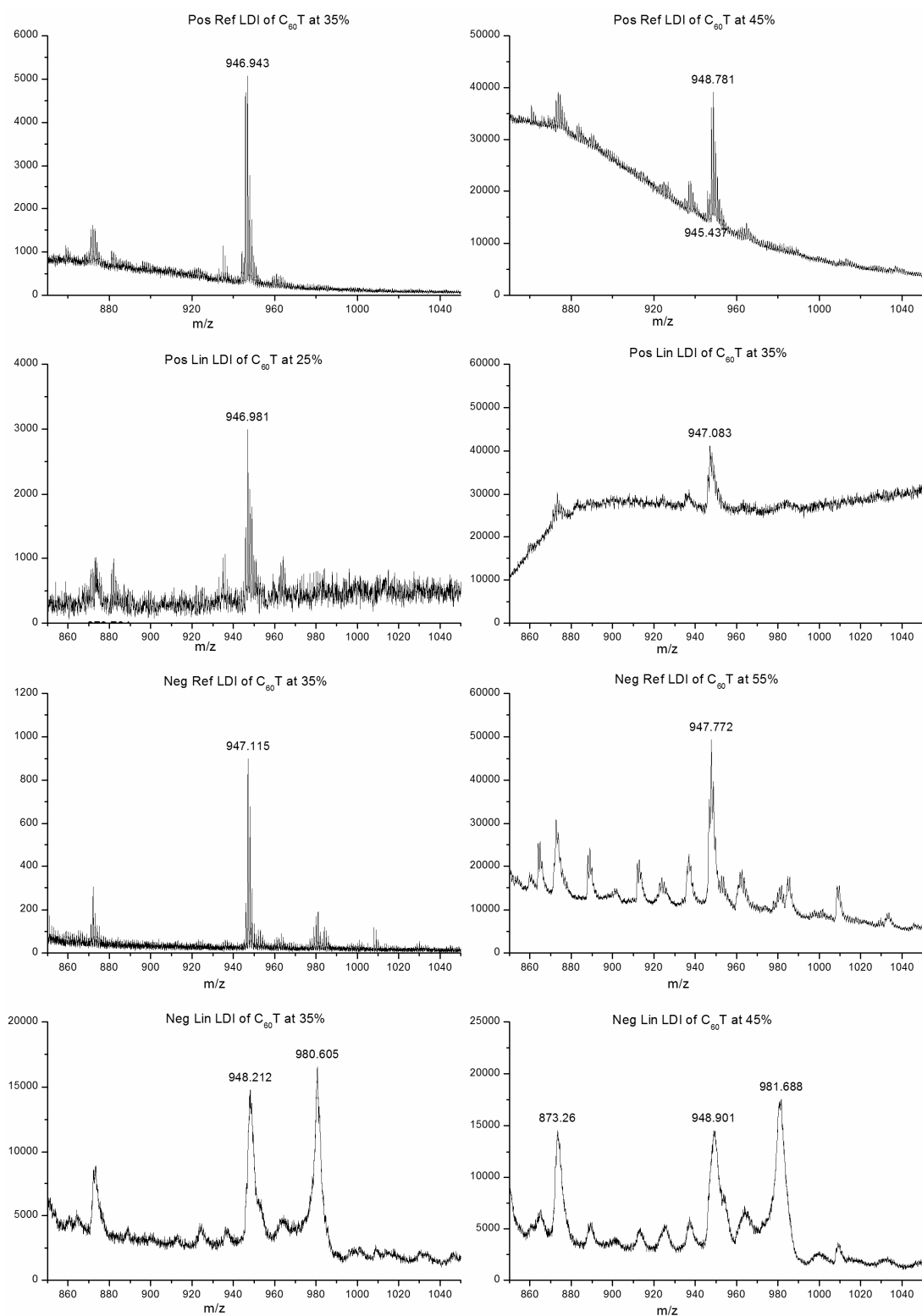


Figure 6.29: Positive and negative-ion mode LDI spectra with linear and reflectron detection of $C_{60}T$ at elevated laser fluences

All three complexes provide low abundant peaks at approximately the correct m/z values under the harsh conditions of LDI mass spectrometry, and even in positive-ion mode. Since

all three C_{60} PAH compounds have molecular ions at different m/z values it can be excluded that the observed peaks are coincidental.

The next step of this project was to study the mixed samples of C_{60} and the respective PAH under the same conditions. The C_{60} and PAHs were mixed in a 1:1 molar ratio. Initially, C_{60} and anthracene were studied:

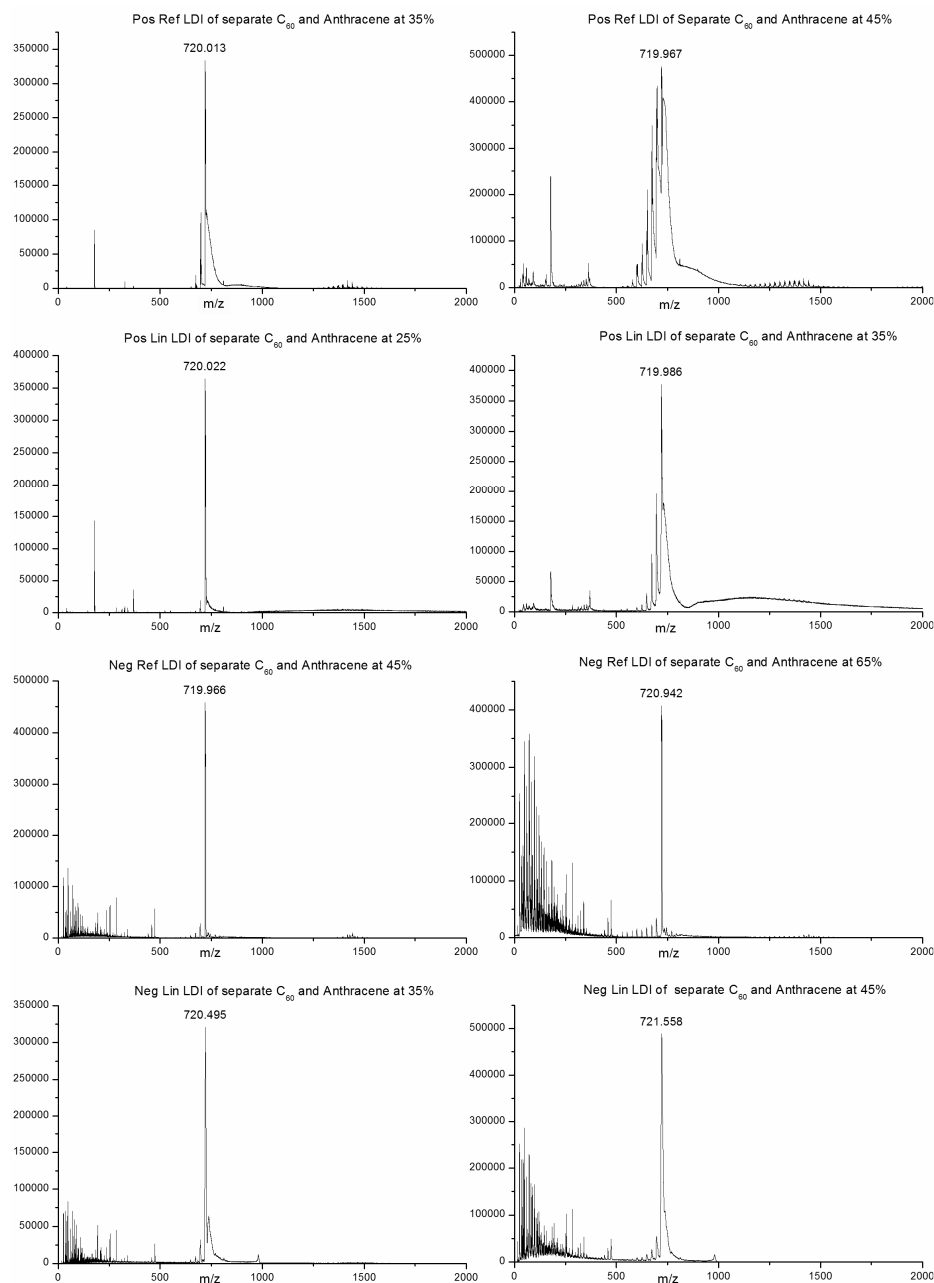


Figure 6.30: Positive and negative-ion mode LDI spectra with linear and reflectron detection of C_{60} and Anthracene at elevated laser fluences

Enhancement of the molecular ion region:

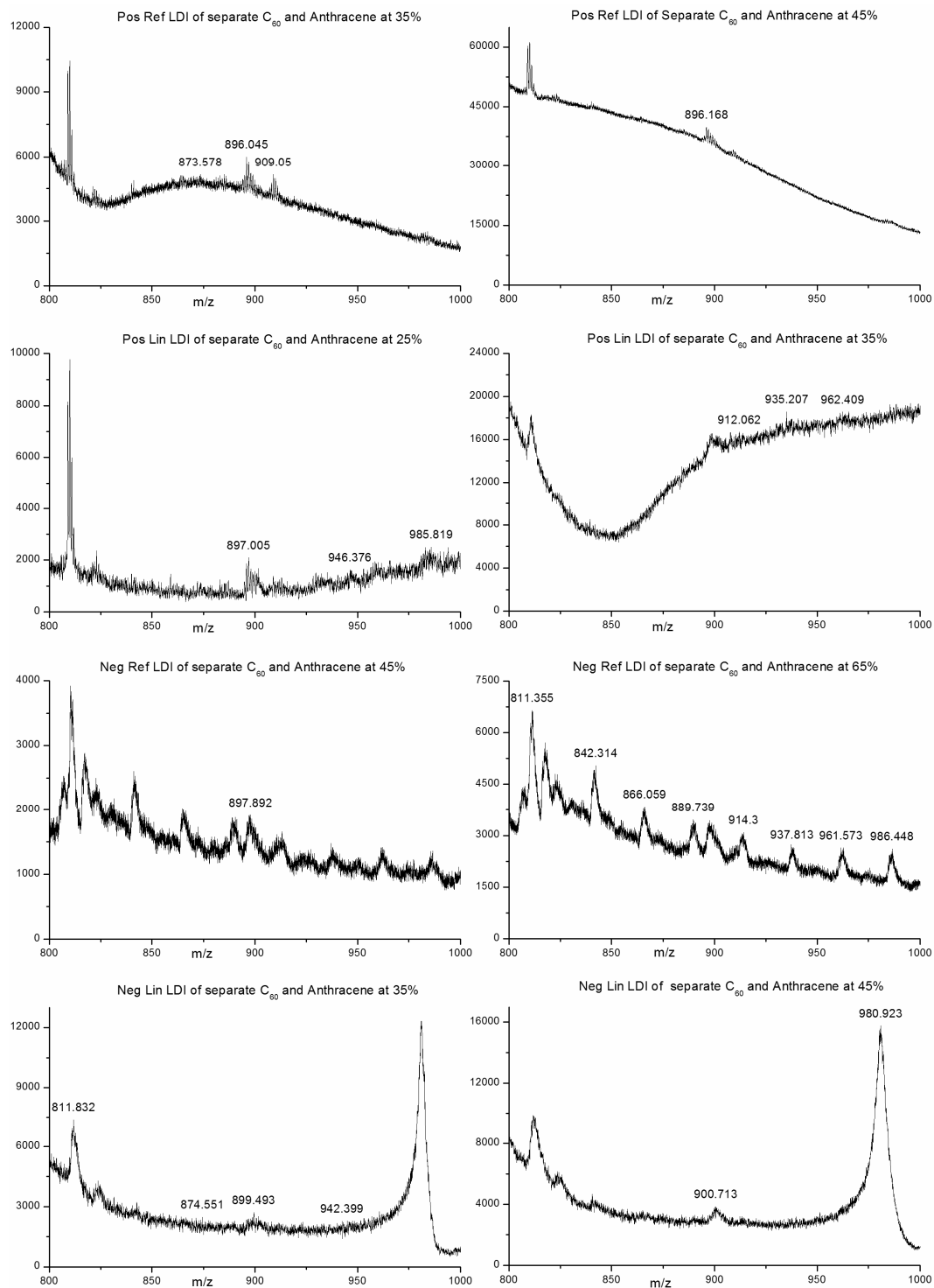


Figure 6.31: Positive and negative-ion mode LDI spectra with linear and reflectron detection of C_{60} and Anthracene at elevated laser fluences

The background noise is high in these spectra, as would be expected from the harsh condition. There are, however, some tiny signals at approximately the right m/z values which could be attributed to the possible formation of $C_{60}A$. These signals are greatly reduced compared to the $C_{60}A$ peaks in the LDI spectra of the reacted $C_{60}A$ complex.

The peak at m/z 980, found when the spectra are obtained in negative-ion mode with reflectron detection, is present regardless of the compound being analysed, which suggests it is either linked to the C_{60} or is an artefact of the analytical method. It is an addition of 260 Daltons to C_{60} , assuming the peak is singly charged.

The experiments with C_{60} and tetracene and pentacene did not reveal the formation of the respective C_{60} PAH complexes. The data for tetracene are shown below; the pentacene data are displayed in the appendix.

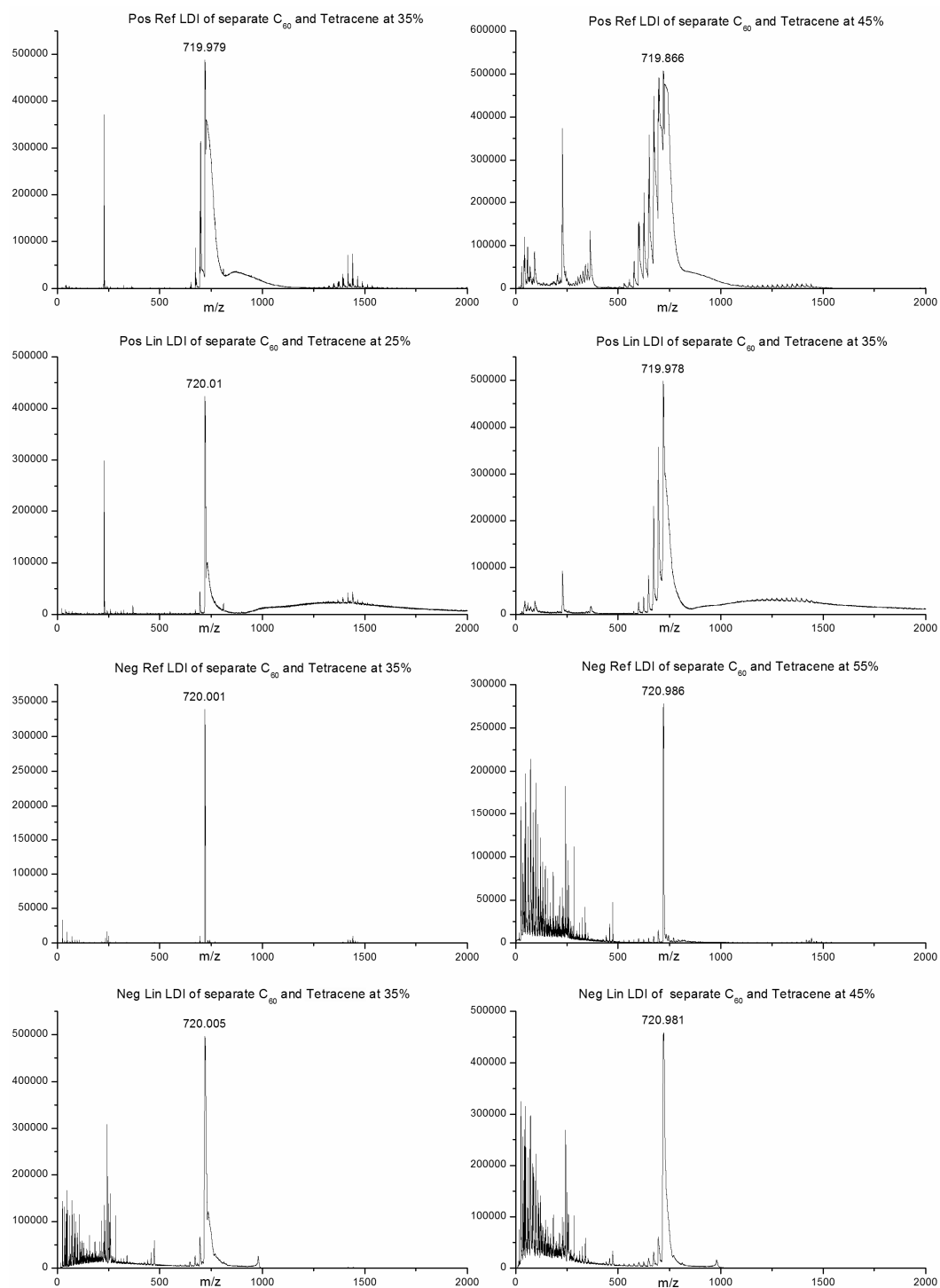


Figure 6.32: Positive and negative-ion mode LDI spectra with linear and reflectron detection of C_{60} and Tetracene at elevated laser fluences

Enhancement of the m/z region for the $C_{60}T$ complex (m/z 948):

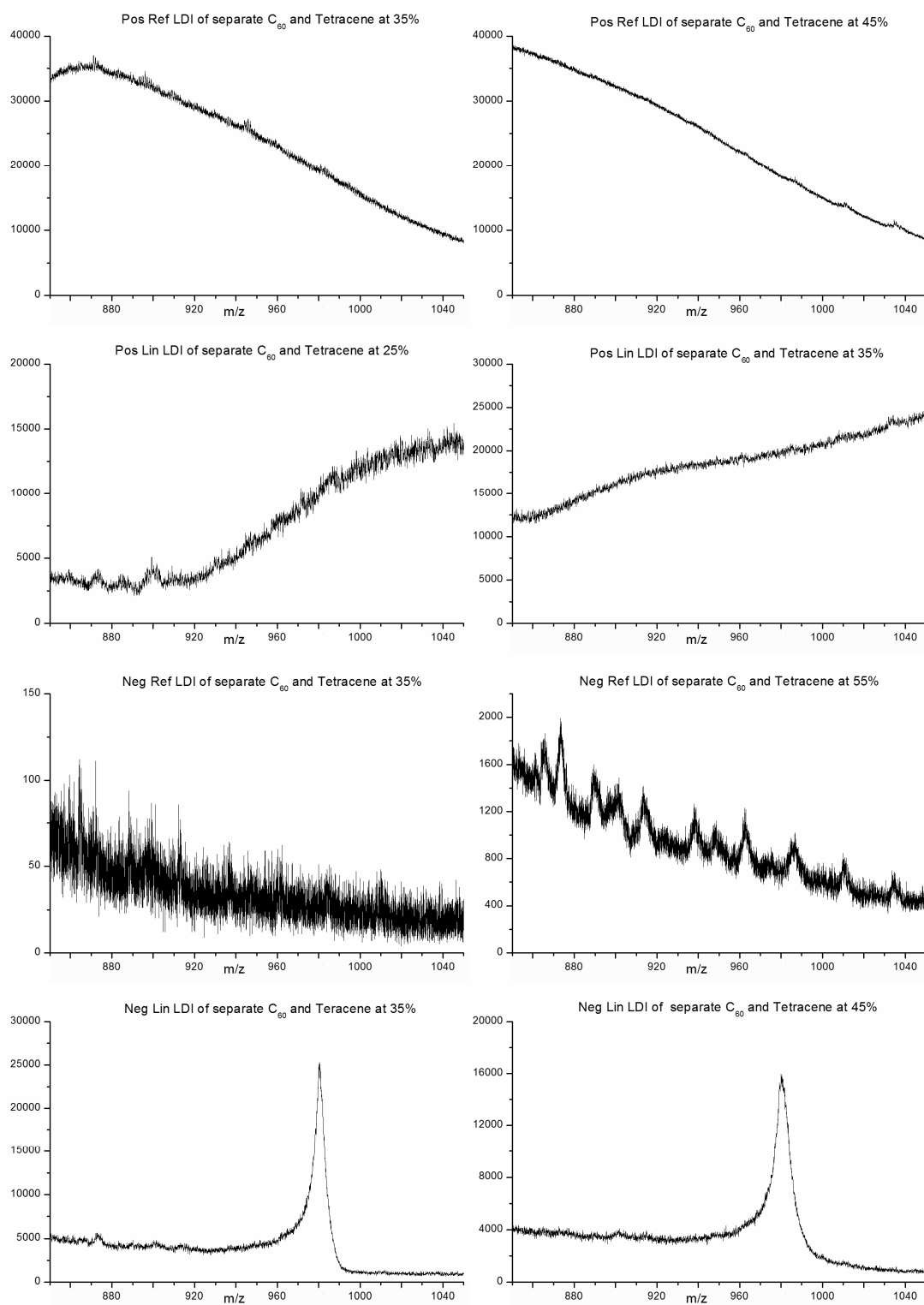


Figure 6.33: Positive and negative-ion mode LDI spectra with linear and reflectron detection of C_{60} and Tetracene at elevated laser fluences

For C_{60} mixed with either tetracene or pentacene there are no signals that are obvious above the noise. This suggests that there has been no formation of the C_{60} -PAH compound through laser-induced fusion of fullerene and PAH within the source.

The experiments with the C_{60} and the unattached PAHs were performed at the same laser power as the original experiments with the synthesised complexes. Given that the conditions were very similar, the formation of the C_{60} PAH complex could be expected if the complex was being reformed in the source. The conditions were not entirely identical, however, as C_{60} and the PAH were mixed in a 1:1 molar ratio for the experiments with “separate” moieties. In the original synthesis the concentration of the PAH was ten times that of C_{60} , and there was no purification prior to analysis.

Future work could involve the same experiments with differing ratios of C_{60} to the PAH.

In summary, C_{60} A, C_{60} T and C_{60} P produce minute but intact molecular ions under harsh laser desorption conditions. Only C_{60} and anthracene combine under these conditions to a low amount of the complex. This seems to indicate that recombination of the separated moieties is not the prevailing mechanism of complex formation. At present it can be only speculated about the way in which the intact complex survives the harsh activation. A further option may involve cooling and/or protection within the ablated material plume. If one assumes that enhanced laser activation increases the amount of material that is ablated from the target. This could lead to protection of a small amount of species that may survive the ablation/ionisation process intact, provided the laser power is high enough.

Conclusion

C_{60} Anthracene, C_{60} Tetracene and C_{60} Pentacene have been successfully synthesized and characterized using MALDI-MS and ESI-MS. In particular the negative-ion analysis has suffered less from fragmentation.

The approximate 1:0.7 ratio of the C_{60} : C_{60} Pentacene peaks observed in negative-ion mode DCTB-MALDI-MS of the purified C_{60} Pentacene sample is higher than any ratio reported previously. Only negative-ion ESI produces less fragmentation, but with an overall lower abundance of the quasi-molecular ion. Additionally, the appearance of the ions in negative-ion mode ESI-MS is highly dependent on the conditions within the source. This makes MALDI the more appropriate approach, although ESI is softer. The enhanced sensitivity of DCTB-MALDI is also confirmed through the detection of a tetracene bis adduct, which escapes the detection by ESI. While DCTB-MALDI produces ions through electron transfer, leading to the true molecular ions of the analyte, the ion formation in negative ESI will be the topic of future investigations. At present, there is indication of ion formation through hydride attachment (H^-) as the main process, leading to $M+1$ quasi-molecular ions. Future investigations are aimed at the elucidation of the role of the solvent in the ion formation mechanism, as in addition to hydride addition, there is occasional methoxy attachment. Both anionic attachments seem to result from the solvent.

Investigation into the possible appearances of C_{60} PAH complexes at high laser powers, in both ion modes under LDI conditions has demonstrated that all complexes under investigation provide low abundant but intact molecular ions. The complexes are not fragmenting and recombining inside the source. The reason for the appearance of the complexes at high laser fluence is still to be determined. We currently assume that from a certain laser power onwards the amount of material ablated is functioning as cooling and/or protecting environment in which the complexes may survive the harsh conditions.

References

1. Wudl, F., *Accounts of Chemical Research* **1992**, 25 (3), 157-161.
2. Schlueter, J.; Seaman, J.; Taha, S.; Cohen, H.; Lykke, K.; Wang, H.; Williams, J., *Journal of the Chemical Society-Chemical Communications* **1993**, (11), 972-974.
3. Tsuda, M.; Ishida, T.; Nogami, T.; Kurono, S.; Ohashi, M., *Journal of the Chemical Society-Chemical Communications* **1993**, (16), 1296-1298.
4. Komatsu, K.; Murata, Y.; Sugita, N.; Takeuchi, K.; Wan, T., *Tetrahedron Letters* **1993**, 34 (52), 8473-8476.
5. de la Cruz, P.; de la Hoz, A.; Langa, F.; Illescas, B.; Martin, N., *Tetrahedron* **1997**, 53 (7), 10.
6. Murata, Y.; Kato, N.; Fujiwara, K.; Komatsu, K., *Journal of Organic Chemistry* **1999**, 64 (10), 3483-3488.
7. Chronakis, N.; Orfanopoulos, M., *Tetrahedron Letters* **2001**, 42 (6), 1201-1204.
8. Duarte-Ruiz, A.; Muller, T.; Wurst, K.; Krautler, B., *Tetrahedron* **2001**, 57 (17), 3709-3714.
9. Miller, G.; Briggs, J.; Mack, J.; Lord, P.; Olmstead, M.; Balch, A., *Organic Letters* **2003**, 5 (22), 4199-4202.
10. Rubin, Y.; Khan, S.; Freedberg, D.; Yeretjian, C., *Journal of the American Chemical Society* **1993**, 115 (1), 344-345.
11. Avent, A.; Benito, A.; Birkett, P.; Darwish, A.; Hitchcock, P.; Kroto, H.; Locke, I.; Meidine, M.; O'Donovan, B.; Prassides, K.; Taylor, R.; Walton, D.; van Wijnkoop, M., *Journal of Molecular Structure* **1997**, 437, 1-9.
12. Alvaro Duarte-Ruiz; Klaus Wurst; Bernhard Kräutler, *Helvetica Chimica Acta* **2001**, 84 (8), 2167-2177.
13. Avent, A.; Boltalina, O.; Street, J.; Taylor, R.; Wei, X., *Journal of the Chemical Society-Perkin Transactions 2* **2001**, (6), 994-997.
14. Wilson, S. R.; Lu, Q., *Tetrahedron Letters* **1993**, 34 (50), 4.
15. Blades, A.; Ikonomou, M.; Kebarle, P., *Analytical Chemistry* **1991**, 63 (19), 2109-2114.

16. Dupont, A.; Gisselbrecht, J.; Leize, E.; Wagner, L.; Vandorsselaer, A., *Tetrahedron Letters* **1994**, 35 (33), 6083-6086.
17. Wilson, S.; Wu, Y., *Journal of the Chemical Society-Chemical Communications* **1993**, (9), 784-786.
18. Wilson, S.; Wu, Y., *Journal of the American Society for Mass Spectrometry* **1993**, 4 (7), 596-603.
19. Wilson, S.; Wu, Y., *Journal of the American Chemical Society* **1993**, 115 (22), 10334-10337.
20. Khairallah, G.; Peel, J., *Chemical Physics Letters* **1998**, 296 (5-6), 545-548.
21. Barrow, M.; Feng, X.; Wallace, J.; Boltalina, O.; Taylor, R.; Derrick, P.; Drewello, T., *Chemical Physics Letters* **2000**, 330 (3-4), 267-274.
22. Miller, G.; Briggs, J., *Organic Letters* **2003**, 5 (22), 4203-4206.

Chapter 7: Formation of Amino Acid – Silver Complexes in ESI

Introduction

In recent ESI experiments it has been observed that the amino acid tryptophan can form clusters with silver. MS/MS experiments showed that these complexes can be dissociated into either smaller clusters, or “bare” silver clusters – silver nanoparticles¹.

The motivation of the work presented in this chapter is twofold. Firstly, a dedicated analysis of the cluster composition and the investigation of their dissociation behaviour is conducted to obtain a better understanding of the principles that determine the formation of these aggregates regarding both their electronic and geometric structure. Secondly, the experimental conditions are evaluated for the production of mixed molecule/silver and of pure silver clusters, aiming at the development of new ways to generate silver nanoparticles or clusters in a controlled fashion.

Amino Acids

Amino acids are compounds containing an amino group and a carboxylic acid group, which are attached to adjacent carbon atoms:

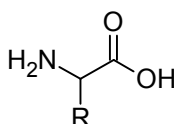


Figure 7.1: Basic structure of an Amino Acid

There are 20 α -amino acids; all are chiral with the exception of glycine and they all naturally occur in the L configuration. They generally exist as zwitterions through the transfer of the hydrogen atom from the carboxylic acid to the amino group. Essential for human survival, they are used principally by the body for protein synthesis. Individually, some amino acids also have other specific roles. As has been discussed in the introduction, ESI-MS is exceptionally suited for the analysis of biological compounds; and amino acids have been found to form ions through the ion evaporation (desorption) model as discussed in the introduction².

Tryptophan, (s)-2-amino-3-(1H-indol-3-yl)propanoic acid, $C_{11}H_{12}N_2O_2$, R.M.M. = 204.23 g mol^{-1} , is the amino acid studied for this chapter. It is a precursor for the neurotransmitter serotonin, the hormone melatonin and vitamin B3, niacin.

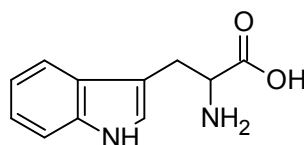


Figure 7.2: Structure of Tryptophan

Silver

Silver is a metallic element with two naturally occurring isotopes – ^{107}Ag (106.9 g mol^{-1}) and ^{109}Ag (108.9 g mol^{-1}). These are found in an approximately 1:1 ratio, with ^{107}Ag being slightly more abundant.

Silver has been used for a variety of different applications throughout history. A recent observation concerns its toxicity to bacteria³. In the bacteria, silver forms complexes with sulphur, nitrogen and oxygen atoms present in the functional groups of organic compounds.

This interaction results in:

- Defects in the cell wall resulting in loss of plasma
- Disturbance of the metabolism of the bacteria

Both of these effects are fatal for the cell. Silver can also interact with DNA, preventing reproduction.

Recently, research has also focused on medical applications of silver nano-clusters.

For example, silver nano-clusters have been found to be effective in controlling proliferation of peripheral blood mononuclear cells. Allergies and infectious inflammation cause an increase in cytokine production and the production of the peripheral blood mononuclear cells. Silver nanoclusters were found to inhibit the proliferation in doses that were not large enough to be cytotoxic and therefore could possibly be used as anti-inflammatories⁴. The production of such silver nano-clusters follows a complex mechanism, essential; however, is the chemical reduction of the silver ion. The nano-clusters produced were typically 1.5 nm in size.

Silver nanoparticles are even more effective than silver alone in their antimicrobial impact. Polyamide 6, a material which is used in the production of wound sutures, artificial tendons and medical packaging, was spiked with either silver nanoparticles or silver⁵.

Polyamide 6 containing 0.06 wt % of silver nanoparticles killed 100% of the E.Coli bacteria within 24 hours.

Polyamide 6 containing 1.9 wt % silver ions killed only 80% of the E. Coli bacteria within 24 hours.

It appeared that silver ions are released faster from the silver nanoparticles and are able to attack the bacteria more effectively, despite the relatively reduced amount of silver present.

Several approaches made use of silver nanoclusters that were mounted on a carrier, from which silver ions escape over time to fight bacteria. In one instance the silver nanoclusters were created in sizes of 3 to 5 nm inside a semi-IPN hydrogel⁶. Another example mounts it onto a nano SiO₂ carrier, which was also found to be effective against bacteria⁷.

ESI of Silver and Amino Acids

Previously, silver and amino acids have been electrosprayed with the aim of studying the gas-phase interactions of these molecules with the silver cation. After desorption of the solvent molecules, an environment is created which allows the study of the interaction of the silver ions and the amino acids free of any other interactions (no solvent effects). Silver (I) bound heterodimers of various amino acids were produced in 1998 by electrospraying a solution of silver ions and the two amino acids under study⁸. This enabled the evaluation of the relative silver (I) binding energies of 19 of the α -amino acids, by the kinetic method, which shall be discussed in more detail in chapter 8.

More recent studies showed that water, and to a lesser extent methanol, can form adducts with the amino acid-silver complex^{9, 10}.

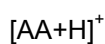
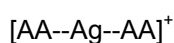
The different amino acids studied initially⁹ were:

- Phenylalanine
- Tyrosine
- Tryptophan
- 4-fluorophenylalanine

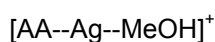
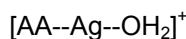
- Alanine
- Valine
- tert-Leucine
- α -aminocyclohexanepropionic acid

These were electrosprayed individually with silver nitrate, both dissolved in 1:1 methanol:water. When the amino acid-silver complex was formed, the individual complexes were selected and stored in the ion trap for between 3 and 3000 ms, without any activation.

The most intense peak in the normal spectra was from the amino acid-silver complex, however other complexes that formed included (where AA stands for amino acid):

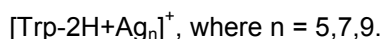
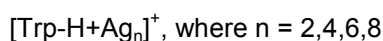
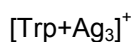
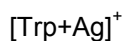


Amino acids with aliphatic side chains produced the following complexes in addition to those listed above:



Collision induced dissociation (CID) experiments on these adducts restored the amino acid-silver complex. Evidently, all earlier investigations revealed the preference of the silver cation to bind two intact molecules.

In a recent investigation, solutions of tryptophan and silver nitrate were electrosprayed together and led to mostly unexpected complexes of the following forms¹:



In particular aggregates were composed of several silver atom and one tryptophan molecule that had lost one or two hydrogen atoms. These complexes have an even number of electrons, and it was deduced that the silver had not replaced the hydrogen atoms lost by

the tryptophan, as tryptophan has a total of four exchangeable hydrogen atoms and only up to two were absent from these complexes.

Dissociating these complexes followed similar patterns, and it was found that loss of the tryptophan was in competition with the loss of a neutral Ag_2 , if the silver cluster was smaller than Ag_7 . For $[\text{Trp-Ag}_7]^+$ and larger, the tryptophan was released, leading to a pure silver cluster.

If the resultant silver cluster contained an even number of silver atoms, then one neutral silver atom would be lost, to generate a cluster with an odd number of silver atoms, as these have an even number of electrons and are more stable than the even numbered clusters.

For example, multi stage dissociation of $[\text{Trp-2H+Ag}_9]^+$ was observed as follows:



The formation of the clusters was dependent on the difference between the capillary and the tube lens. Formation was not affected by other source conditions, which suggests that clustering occurs within the capillary, and that they are not present in the solution initially.

To confirm this, a UV-Vis spectrum was obtained of the solution, and this showed no sign of nanoparticles formation. Interestingly, the silver clusters did not form if tryptophan was not present, which suggested it plays an integral part in the formation of these clusters.

These initial findings were followed by a series of investigations by the same researchers whereby it was tried to shed more light on the structural features of these clusters. These studies employed collision-induced (CID) and photo-fragmentation in combination with quantum chemical calculations¹¹⁻¹⁴. However, these studies were performed on a very limited amount of clusters and the reported findings are also in part somewhat confusing. For instance, while initially the $[\text{Ag}_9\text{Trp-2H}]^+$ cluster was reported as the CID precursor for Ag_9^+ , later work refers to a Ag_9Trp cluster without hydrogen deficiency (i.e. the tryptophan was intact) and with very different fragmentation behaviour in CID.

The motivation for the work of this chapter was therefore to conduct clarifying experiments into this new form of mixed metal and bio-molecular clusters. In summary, the present investigation provides a much more comprehensive insight into a greatly enlarged population of silver/tryptophan aggregates.

Experimental

D,L-Tryptophan (Sigma (Sigma-Aldrich), 99%) was dissolved in water to produce a solution with a concentration of 200 μ M.

Silver nitrate (AgNO₃, VWR BDH Prolab, 99.5%) and silver trifluoroacetate (AgTFA, Aldrich (Sigma-Aldrich), 98%) were dissolved in methanol to make a concentration of 1mM.

The tryptophan solution and one of the silver solutions were mixed in a 1:1 ratio, giving final concentrations of 100 μ M for tryptophan, and 500 μ M for the silver.

Silver was electrosprayed alone, in this instance the 1ml of the silver solution was mixed with 1ml of water, to ensure the same concentration and solvent ratio as for the tryptophan and silver experiments.

Various conditions on the ESI were altered including the target mass, compound stability, the drying temperature and the length of time the spectrum was collected. The average spectrum was collected for three minutes; however, some experiments such as MS/MS were collected for longer due to the reduced signal intensity.

For some experiments a drop of formic acid (3% solution, laboratory stock) was added.

Results

Tryptophan-Silver Cluster Production

Tryptophan and silver clusters were produced using the conditions described in the experimental section. In contrast to the earlier work by Dugourd and co-workers the present study reveals a much richer distribution of the silver/tryptophan hybrids. In particular larger clusters could be produced more abundantly than in previous investigations. Other interesting observations concern the number of hydrogen atoms that were lost from the tryptophan molecules according to the size of the silver cluster attached and to the number of tryptophan molecules present.

The spectrum displayed below demonstrates the full range of cluster formation and includes some pure silver clusters:

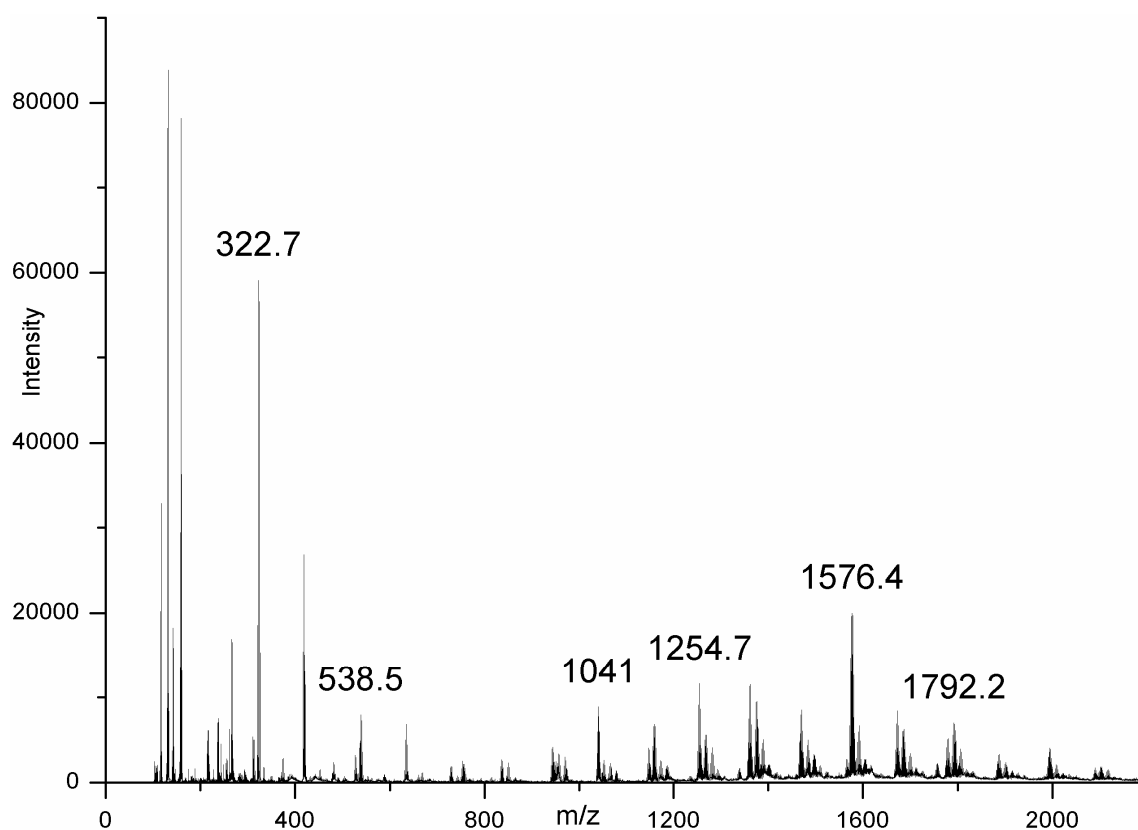


Figure 7.3: Full positive-ion mode ESI spectrum of Tryptophan and AgTFA

The list of tryptophan-silver clusters discovered using the esquire2000 is given below. It is arranged in series of increasing tryptophan molecules. The column entitled “m/z” refers to the m/z value of the central or most intense peak in the isotopic pattern. Due to the presence

of the two silver isotopes, the isotopic pattern of these clusters is complex, particularly when larger cluster sizes are involved.

The isotopic pattern was important in confirming the number of tryptophan molecules and silver atoms involved in each cluster, and also demonstrated that there has been apparent hydrogen loss. The number of neutral hydrogen atoms lost is displayed in the third column, and was deduced by comparing the actual to the simulated isotopic pattern for each cluster.

Series	m/z	Hydrogen atoms lost
AgTrp	311.0	0
Ag ₂ Trp	418.9	1
Ag ₃ Trp	526.8	0
Ag ₄ Trp	634.7	1
Ag ₅ Trp	742.5	0
Ag ₆ Trp	850.5	1
Ag ₇ Trp	956.4	2
Ag ₈ Trp	1064.3	1
Ag ₉ Trp	1172.3	2
Ag ₁₀ Trp	1282.0	1
Ag ₁₁ Trp	1388.0	2
Ag ₁₂ Trp	1496.6	2
Ag ₁₃ Trp	1604.4	2
Ag ₁₄ Trp	1712.3	2
Ag ₁₅ Trp	1818.2	2
Ag ₁₆ Trp	1928.3	2
Ag ₁₇ Trp	2036.2	Unclear

Ag ₃ Trp ₂	728.9	2
Ag ₄ Trp ₂	836.8	3
Ag ₅ Trp ₂	942.7	4
Ag ₆ Trp ₂	1052.6	3

Ag ₇ Trp ₂	1158.5	4
Ag ₈ Trp ₂	1268.3	3
Ag ₉ Trp ₂	1374.3	4
Ag ₁₀ Trp ₂	1482.1	3
Ag ₁₁ Trp ₂	1591.9	4
Ag ₁₂ Trp ₂	1699.8	3
Ag ₁₃ Trp ₂	1805.9	4
Ag ₁₄ Trp ₂	1915.7	3
Ag ₁₅ Trp ₂	2022.5	Unclear
Ag ₁₆ Trp ₂	2130.4	Unclear

Ag ₄ Trp ₃	1040.9	3
Ag ₅ Trp ₃	1146.7	4
Ag ₆ Trp ₃	1254.7	5
Ag ₇ Trp ₃	1360.6	6
Ag ₈ Trp ₃	1470.4	5
Ag ₉ Trp ₃	1576.3	6
Ag ₁₀ Trp ₃	1686.1	5
Ag ₁₁ Trp ₃	1792.2	6
Ag ₁₂ Trp ₃	1902.1	5
Ag ₁₃ Trp ₃	2008.0	6
Ag ₁₄ Trp ₃	2117.9	5

Ag ₈ Trp ₄	1672.5	7
Ag ₉ Trp ₄	1780.3	8
Ag ₁₀ Trp ₄	1886.2	7
Ag ₁₁ Trp ₄	1994.1	8
Ag ₁₂ Trp ₄	2103.9	7

$\text{Ag}_{10}\text{Trp}_5$	2090.2	9
$\text{Ag}_{11}\text{Trp}_5$	2196.3	10

Table 7.1: Full listing of the Trp-Ag clusters formed, with their associated hydrogen loss

For the larger clusters, the signal abundance was sometimes so low that the isotopic pattern was nearly indistinguishable from the surrounding background peaks. This resulted in the occasional “unclear” labels which appear in the “hydrogen atoms lost” column in the above table. However, for these cases it can be assumed that the hydrogen loss pattern follows the alternations found for the preceding and more abundantly observed clusters.

Some example spectra are shown below. For comparison the corresponding simulated isotopic pattern is provided. Clusters $[\text{Ag}_3\text{Trp}_2 \text{ minus } 2\text{H}]^+$ and Ag_7^+ are displayed in the spectrum below at m/z 728.9 and 754.3, respectively:

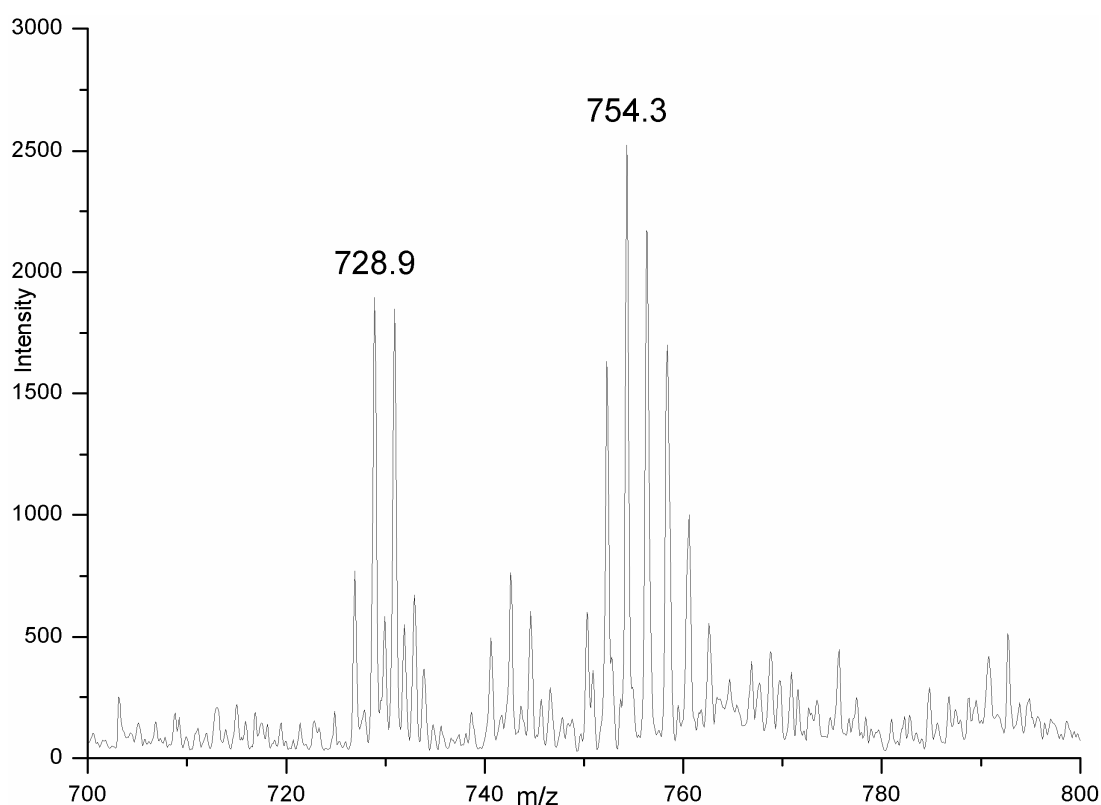


Figure 7.4: Positive-ion mode ESI spectrum of Trp and AgTFA

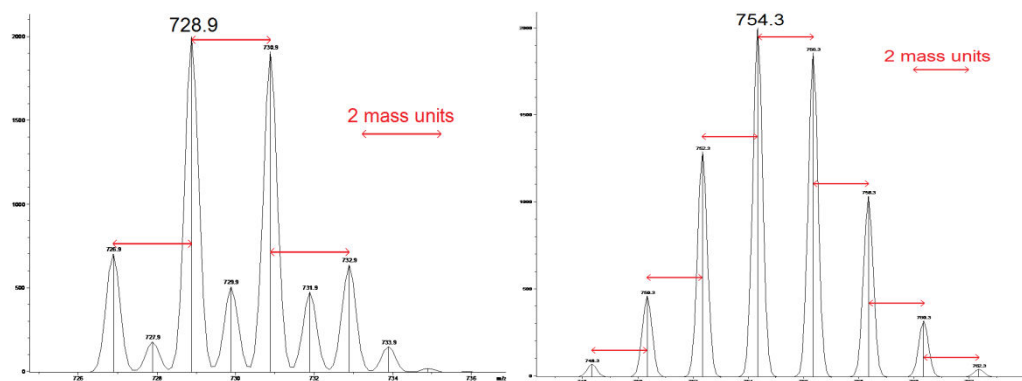


Figure 7.5: Simulated isotopic pattern of $[\text{Trp}_2\text{Ag}_3 \text{ minus } 2\text{H}]^+$, left, and Ag_7^+ , right

Clusters $[\text{Ag}_5\text{Trp}_3 \text{ minus } 4\text{H}]^+$, $[\text{Ag}_7\text{Trp}_2 \text{ minus } 4\text{H}]^+$, $[\text{Ag}_9\text{Trp} \text{ minus } 2\text{H}]^+$ and Ag_{11}^+ are displayed at m/z 1146.9, 1158.6, 1172.3 and 1186, respectively:

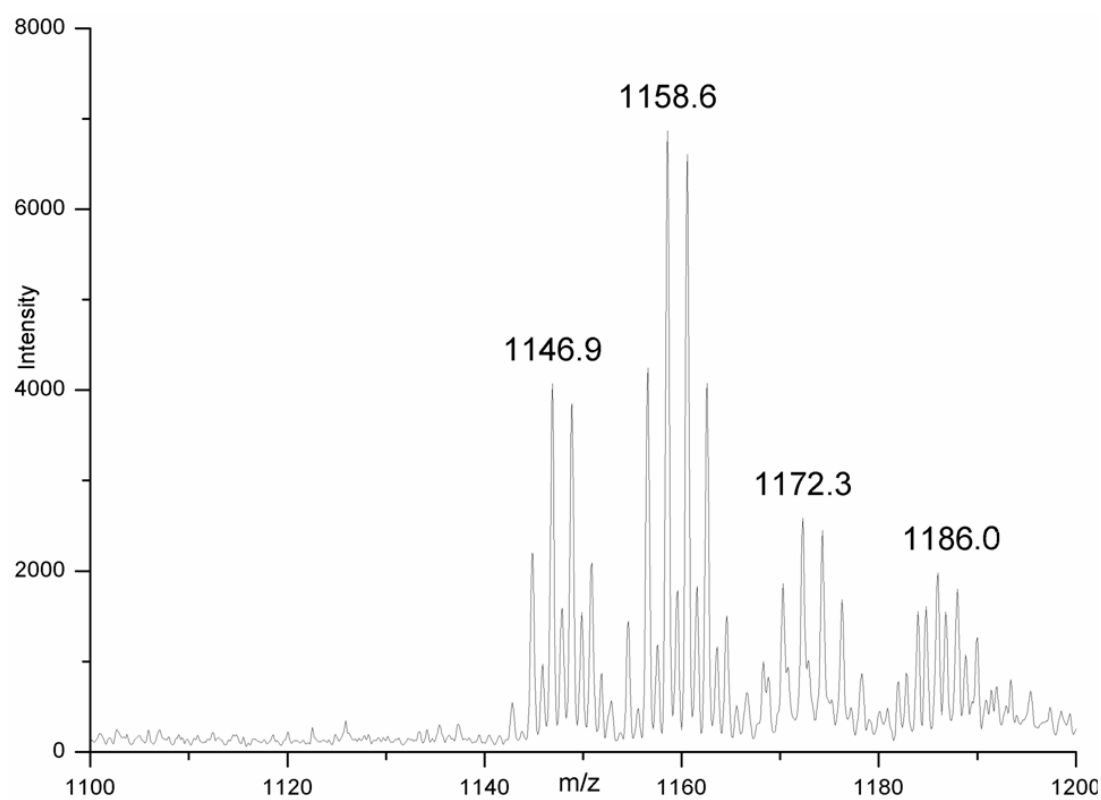


Figure 7.6: Positive-ion mode ESI spectrum of Trp and Ag

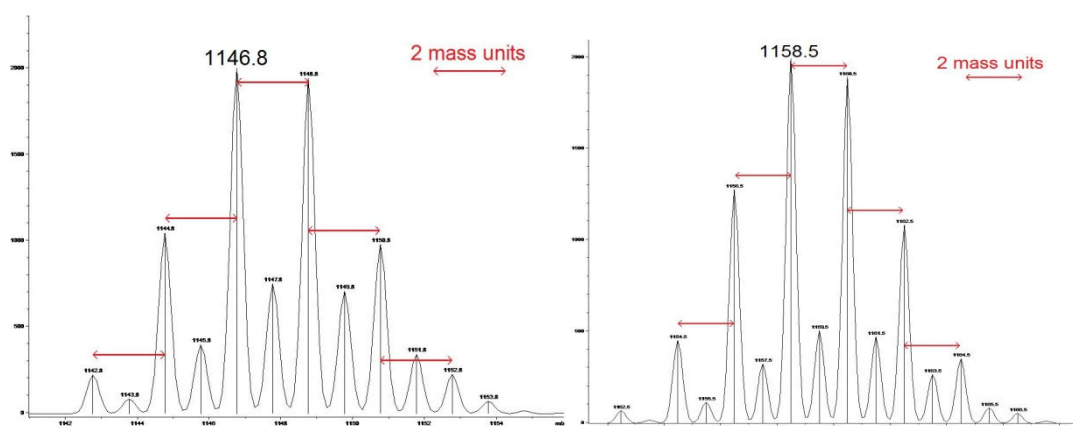


Figure 7.7: Simulated isotopic pattern of $[Ag_5Trp_3 \text{ minus } 4H]^+$, left, and $[Ag_7Trp_2 \text{ minus } 4H]^+$, right

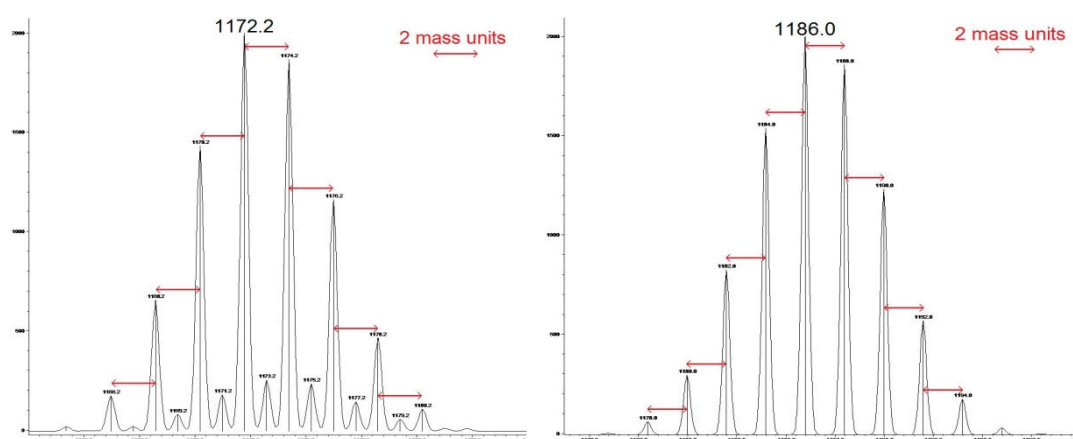


Figure 7.8: Simulated isotopic pattern of $[Ag_9Trp \text{ minus } 2H]^+$, left, and Ag_{11}^+ , right

Clusters $[\text{Ag}_{11}\text{Trp}_4 \text{ minus } 8\text{H}]^+$ and $[\text{Ag}_{13}\text{Trp}_3 \text{ minus } 6\text{H}]^+$ are displayed at m/z 1994.3 and 2008 respectively:

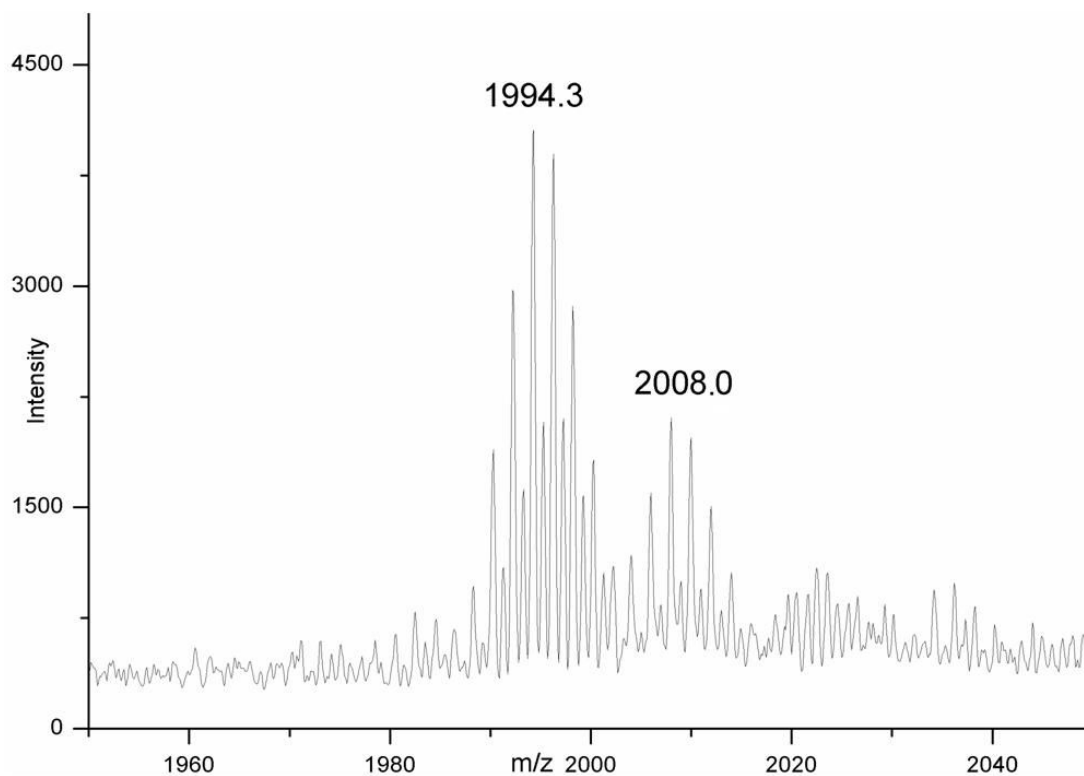


Figure 7.9: Positive-ion mode ESI spectrum of Trp and AgTFA

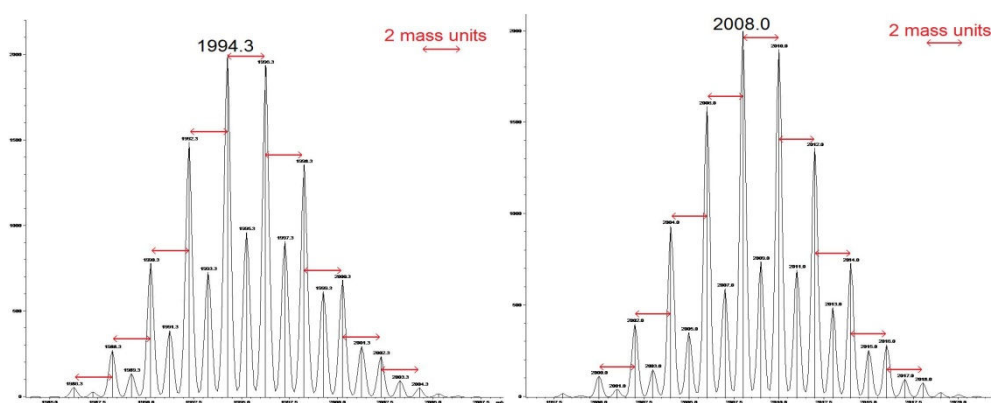


Figure 7.10: Simulated isotopic pattern of $[\text{Ag}_{11}\text{Trp}_4 \text{ minus } 8\text{H}]^+$, left, and $[\text{Ag}_{13}\text{Trp}_3 \text{ minus } 6\text{H}]^+$, right

Hydrogen Loss

The table reveals that a maximum of 2 hydrogen atoms can be lost per tryptophan molecule when a part of the cluster. The silver content seems to determine the extent of the hydrogen loss. In general, the hydrogen loss increases with increasing silver content up to the

maximum hydrogen loss possible (that is two hydrogen atoms per tryptophan molecule). An even numbered silver content results in a loss of an odd number of hydrogen atoms and vice versa. Only in the case of one tryptophan molecule attached to increasing amounts of silver, does the odd/even-alternation seem to fade for the large silver contents and consequentially two hydrogen atoms are “missing” continuously. It seems that the clusters with more than one tryptophan molecule do not reach a high enough silver content for the odd/even-alternation to become unimportant.

To answer the question as to whether these clusters are formed in solution or in the ESI process, control experiments with MALDI were conducted. Positive-ion mode MALDI spectra were obtained with the DCTB matrix. DCTB functions as a soft electron transfer matrix and would not destroy a potential cluster through protonation. No sign of any tryptophan-silver clusters were produced; merely Ag^+ , Ag_2^+ and Ag_3^+ could be observed.

This provides further support for the assumption that silver and tryptophan do not cluster prior to injection, but that the conditions within the ESI source are responsible for cluster formation.

Further proof that the formation of the clusters is dependent upon conditions inside the source, results from variation of the parameters that control the conditions. Optimisation of the ESI method to produce the clusters was time-consuming, as a variety of different parameters needed adjustment. However, the most important factor was found to be the value of the “compound stability”. This refers to the voltage difference between the capillary end cap and the skimmer inside the source. The voltage difference is referred to as cone-skimmer voltage in the literature and is used to induce collisions in that transfer region in order to dissociate the ions. A high “compound stability” parameter implies a higher voltage difference and more collisions. The “compound stability” (CS) for the majority of experiments performed on the ESI is between 20 and 100%. For production of the clusters the compound stability had to be set at 500%. This equates to a fairly high voltage. At 100% CS, only small clusters would form, for example Ag_3^+ , which is a very stable silver cluster, an example spectrum is shown below:

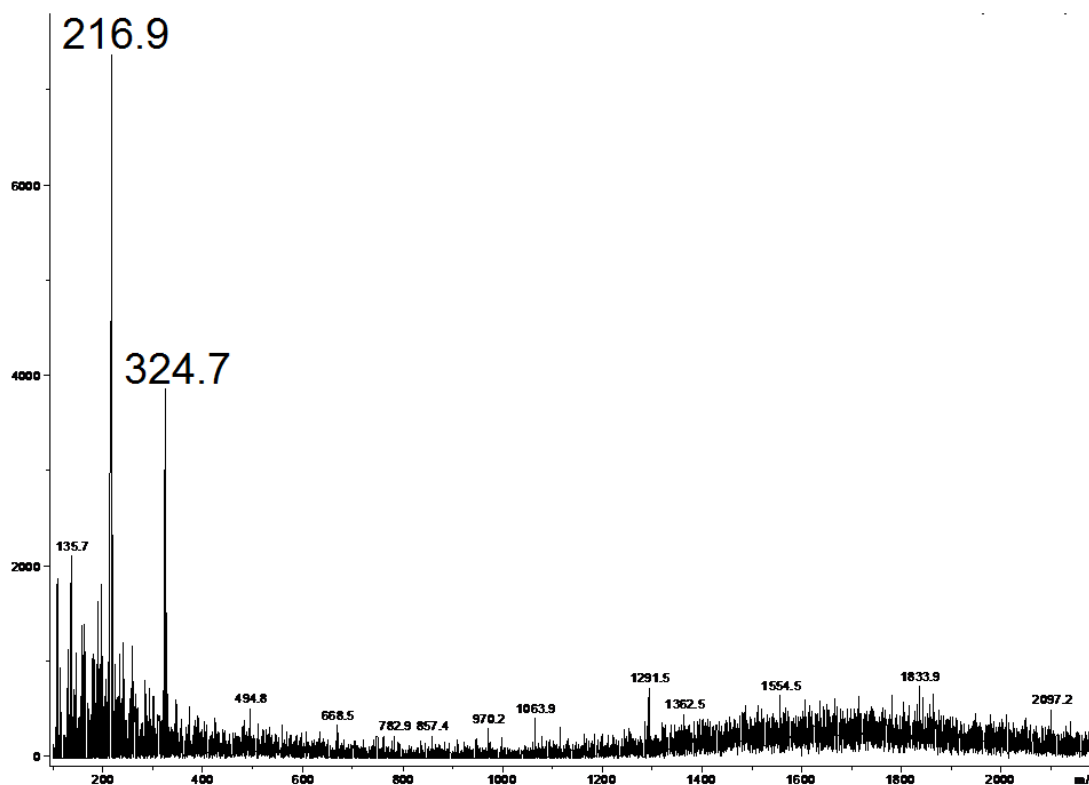


Figure 7.11: Positive-ion mode ESI spectrum of AgTFA and Trp at 100% compound stability. Ag_3^+ has been reported previously in ESI-MS spectra of aqueous solutions of AgNO_3 ¹⁵, which suggests that the optimised source conditions are perhaps only necessary for the larger clusters.

The addition of formic acid was also found to be unnecessary.

Production of Pure Silver Clusters

In the pioneering publication¹ in which tryptophan and silver clusters were first observed, pure silver clusters could only be produced through dissociation of a tryptophan-silver cluster. These dissociations were accomplished through collision inside an ion trap mass analyser. The experiments discussed above indicate that pure silver cluster ions can be generated through the increase of the “compound stability” parameter. In other words, pure silver clusters can be produced from the tryptophan/silver hybrid clusters through collision induced dissociation inside the ESI ion source. This is a gradual improvement of the initial approach as no ion trap is necessary to produce pure silver clusters, so that these silver clusters are already produced in the ESI ion source as opposed to their production further on in the initial analyser.

However, the pure silver clusters are still accompanied by undissociated tryptophan/silver cluster ions. Advantageous would be a situation that allowed the production of pure silver clusters without any unwanted or interfering by-products.

Exactly this was achieved in the following experiments when pure AgNO_3 or AgO_2CCF_3 (Silver trifluoroacetic acid) solutions were sprayed without the addition of tryptophan, but under exactly those ion source conditions which were optimised for the production of silver clusters from the tryptophan/silver experiments. The result obtained when a pure AgTFA solution is sprayed under such condition is shown below:

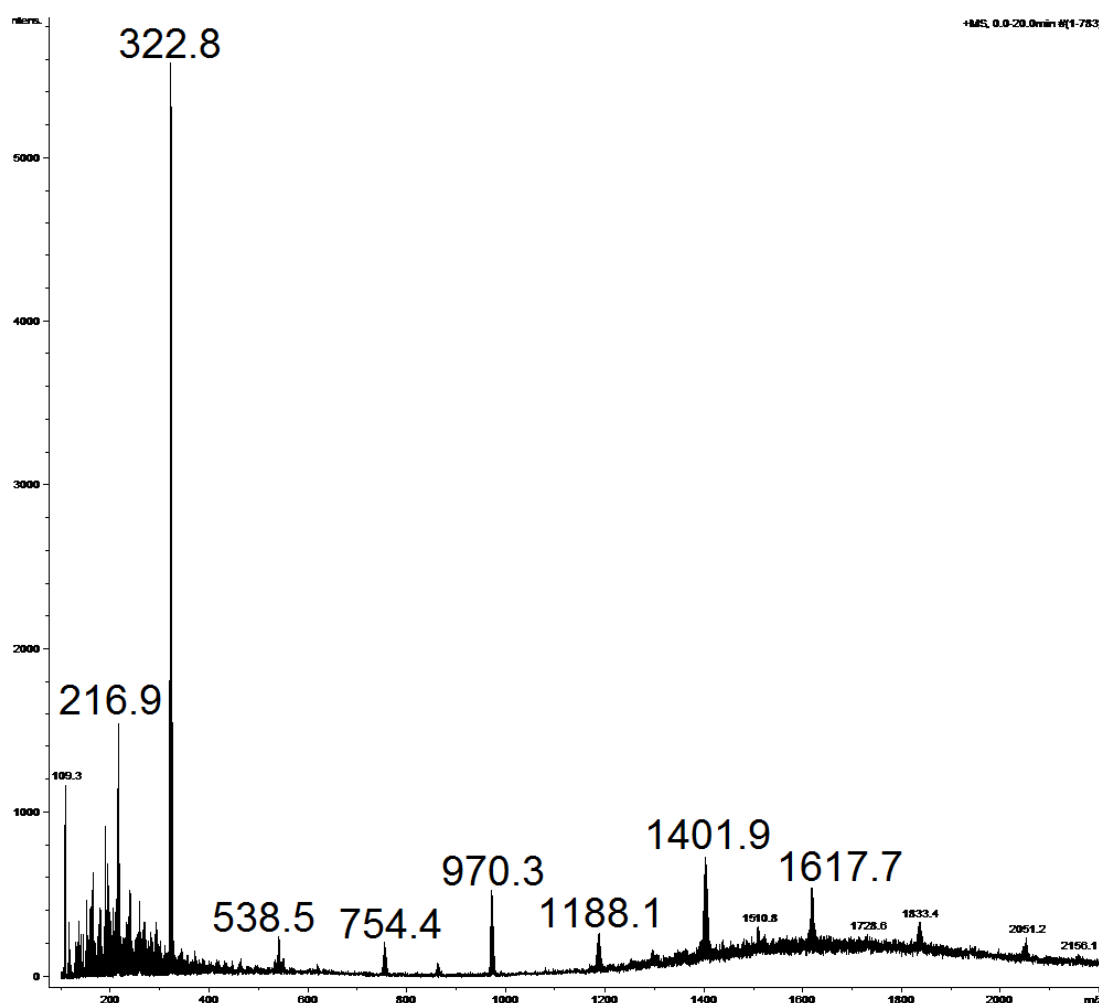


Figure 7.12: Positive-ion mode ESI spectrum of AgTFA

A spectrum is obtained which only contains pure silver cluster ions without any contributing signals beyond Ag_3^+ . Obviously, conditions are achieved whereby silver clusters are formed through stabilising conditions. The production of these silver clusters from pure silver salt solutions was somewhat “temperamental” in that under seemingly identical conditions silver clusters would sometimes not form. It cannot be excluded that these pure silver clusters are

generated by a similar mechanisms being operative in the tryptophan/silver case, however, triggered by compounds that are only present in trace amounts. These could aid the cluster formation through their presence but would not appear in the spectrum because of the minute abundance.

The ESI spectrum obtained when AgTFA is sprayed under harsh conditions shows the following features: Ag_3^+ dominates at m/z 322.8. All other clusters appear at less than half the intensity of the Ag_3^+ peak. Ag_{13}^+ at m/z 1401.9 and Ag_9^+ at m/z 970.3 are particularly dominant. The odd numbered clusters produced signals of greater abundance than the even clusters, which is most likely a sign of enhanced stability. A few even numbered clusters are apparent including Ag_2^+ , Ag_8^+ , and Ag_{14}^+ . Only vaguely present are Ag_{12}^+ , Ag_{16}^+ , Ag_{18}^+ and Ag_{20}^+ , their assignment is, however, tentative. When the spectrum is displayed over a wide m/z range as above, it is apparent that there are small peaks present at the correct m/z values for these even-numbered clusters. However, when enhancing the m/z regions it becomes obvious that the isotopic patterns do not appear very distinct above the background noise, which hinders a confident assignment.

The silver clusters produced by this method are listed below, including the even-numbered clusters of low intensity. The m/z column refers to the dominant peak in the isotopic pattern:

Cluster	m/z
Ag	109.3
Ag_2	216.9
Ag_3	322.8
Ag_5	538.5
Ag_7	754.4
Ag_8	861.3
Ag_9	970.3
Ag_{11}	1188.1
Ag_{12}	1298.0
Ag_{13}	1401.9
Ag_{14}	1510.8
Ag_{15}	1617.7

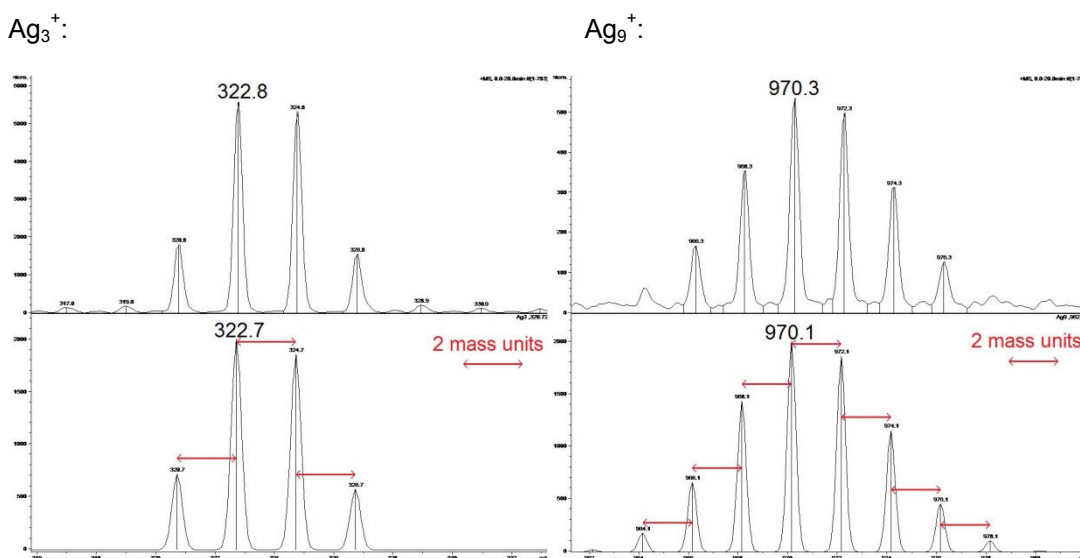
Ag ₁₆	1728.6
Ag ₁₇	1833.4
Ag ₁₈	1940.0
Ag ₁₉	2051.2
Ag ₂₀	2156.1

Table 7.2: Silver clusters produced in positive-ion mode ESI

Examples with the related simulated isotopic patterns are shown below. The simulated isotopic pattern is generated within the Bruker Compass software, and is displayed below the actual mass spectrum.

For Ag₃⁺ and Ag₉⁺, the actual isotopic pattern and the simulated isotopic pattern are identical, demonstrating that the identification of these clusters is correct.

By enhancing the m/z regions of the respective clusters, in particular Ag₁₇⁺ and Ag₂₀⁺, it becomes apparent just how little of the larger clusters is produced. Obviously the conditions within the source favour the production of smaller clusters preferably with an odd number of silver atoms. The resulting mass spectrum seems to reflect the harsh conditions within the source.

Figure 7.13: Actual (top) and simulated (bottom) isotopic pattern of Ag₃⁺, left, and Ag₉⁺, right

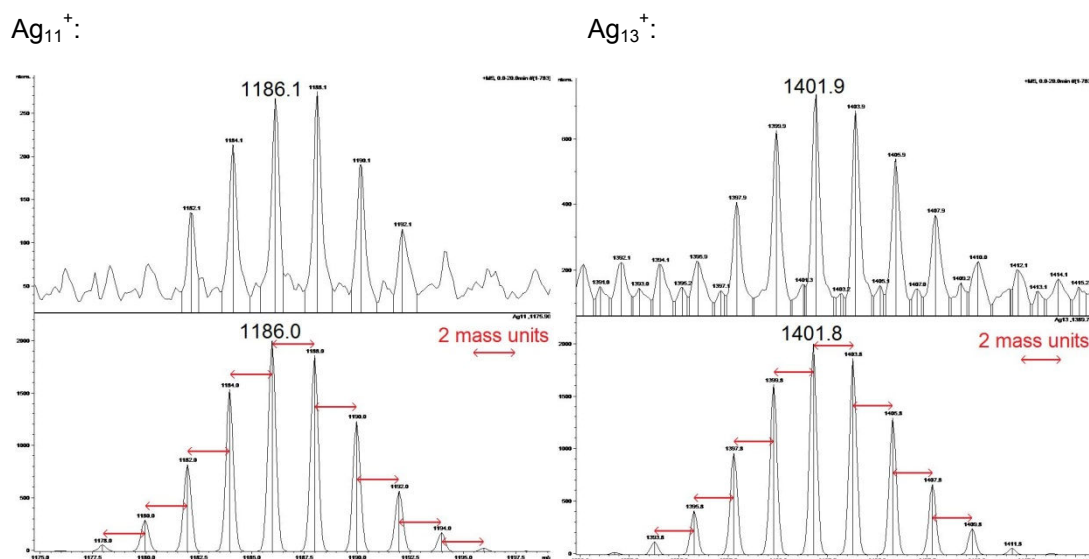


Figure 7.14: Actual (top) and simulated (bottom) isotopic pattern of Ag_{11}^+ , left, and Ag_{13}^+ , right

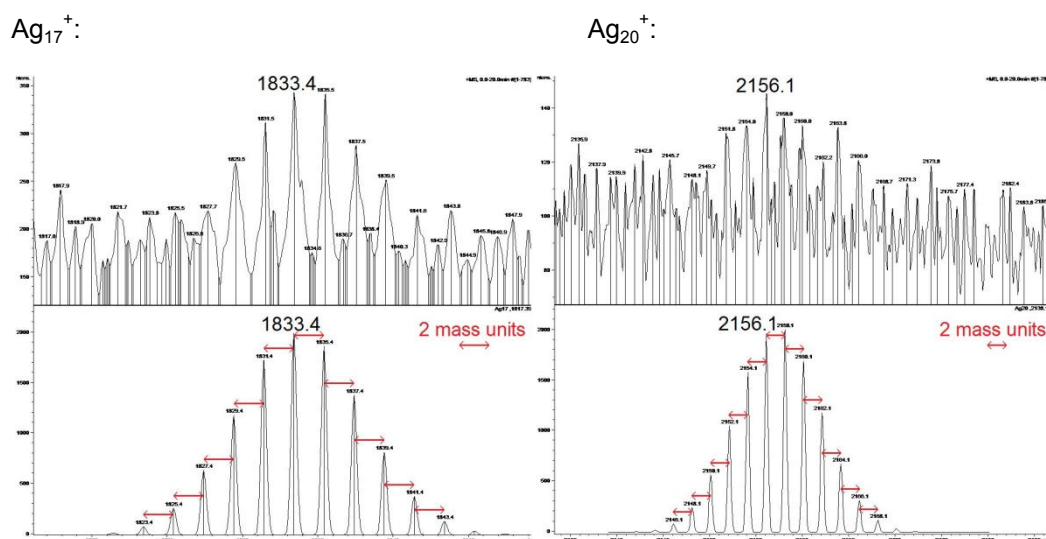


Figure 7.15: Actual (top) and simulated (bottom) isotopic pattern of Ag_{17}^+ , left and Ag_{20}^+ , right

In order to ascertain whether the silver clusters were a result of conditions inside the source, or whether formation had occurred in the initial solution, MALDI-MS was performed. The silver solution was applied to a target plate which had previously a DCTB solution applied to it. Positive and negative-ion mode MALDI-MS was employed, using both linear and reflectron detection. The resulting spectra demonstrate each set of conditions:

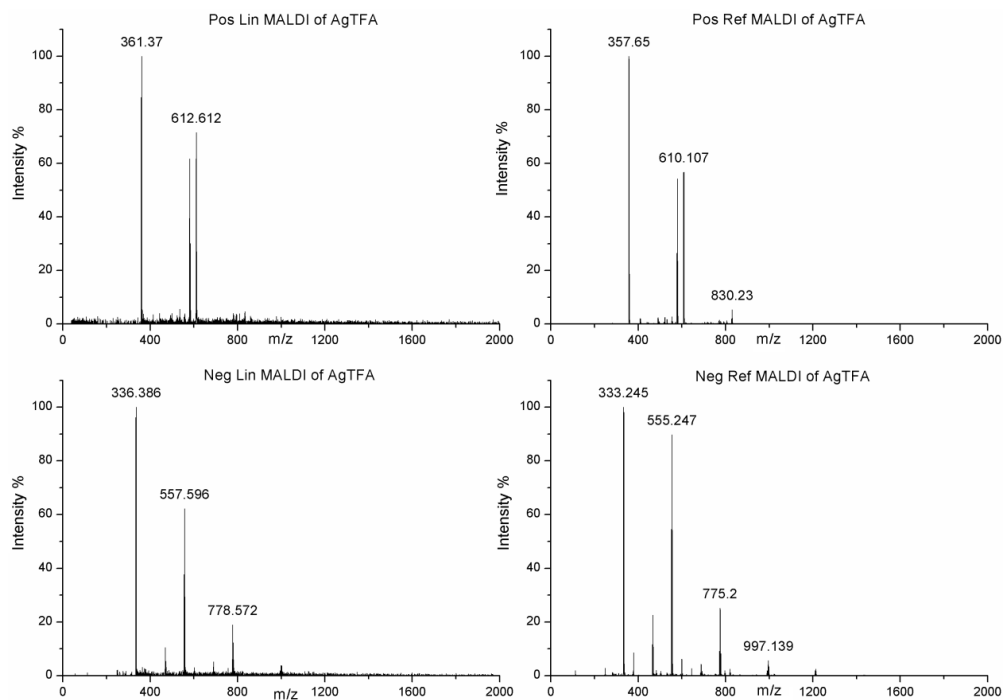


Figure 7.16: Positive and negative-ion mode MALDI with linear and reflectron detection of AgTFA

Enhancing the m/z region 300 to 700 in the positive-ion spectra allows study of the dominant peaks:

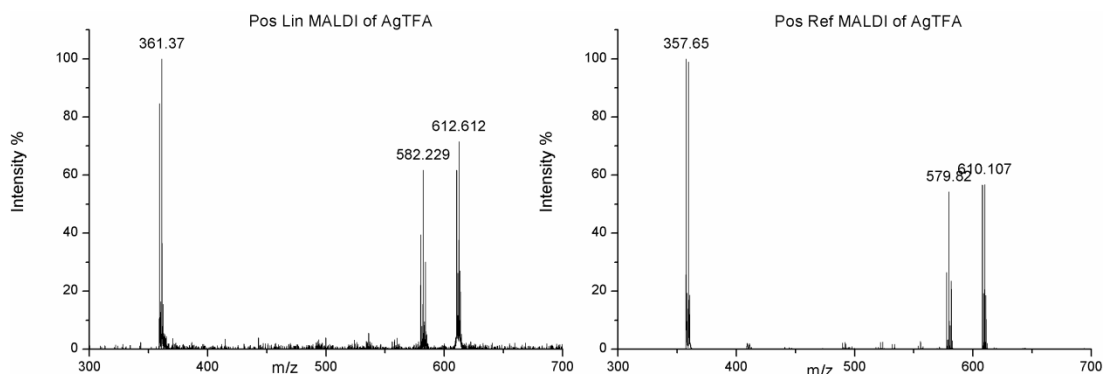


Figure 7.17: Positive-ion mode MALDI of AgTFA with linear and reflectron detection

There is no sign of any silver clusters in that region, which would appear centred at m/z values 324 (Ag_3^+), 432 (Ag_4^+), 540 (Ag_5^+) and 648 (Ag_6^+).

These spectra support the idea that the cluster formation is entirely a result of the conditions within the ESI source. For clusters formed in solution there is a high probability that the MALDI experiment would have shown some signs of silver clusters as well.

The conditions within the source have to be precisely set as mentioned previously; altering the “compound stability” parameter greatly reduced the size of the clusters produced.

However, external factors also appeared to affect the formation of the clusters – once the conditions had been optimised, still some experimental runs would lead to no cluster formation at all. Compared to AgNO_3 , the production of pure silver clusters was always more pronounced when AgTFA was used.

MS/MS Experiments

MS/MS experiments were conducted in which a parent ion of choice was selected and allowed to fragment following collisional activation. The motivation here was to obtain structural information about the clusters through their fragmentation behaviour.

Tryptophan-Silver Clusters

MS/MS experiments were performed with the majority of the clusters ions produced. If the signal was intense enough, MS^3 experiments were performed on the fragments, in order to establish fragmentation pathways even further. The fragmentation of a selected cluster ion is characterised by the composition of the daughter ion and its abundance. The dissociation is caused by low energy collisions with He inside the ion trap. As a result, the MS/MS spectrum will feature fragment ions that are energetically accessible in such collisions. The MS/MS experiments aims at the elucidation of the parent ion structure through the analysis of its dissociations.

An example is the actual appearance of such spectra; the MS/MS experiment of $[\text{Ag}_{11}\text{Trp}_3-6\text{H}]$ is shown below for the selection and dissociation of m/z 1792.0 and 1794.0, respectively.

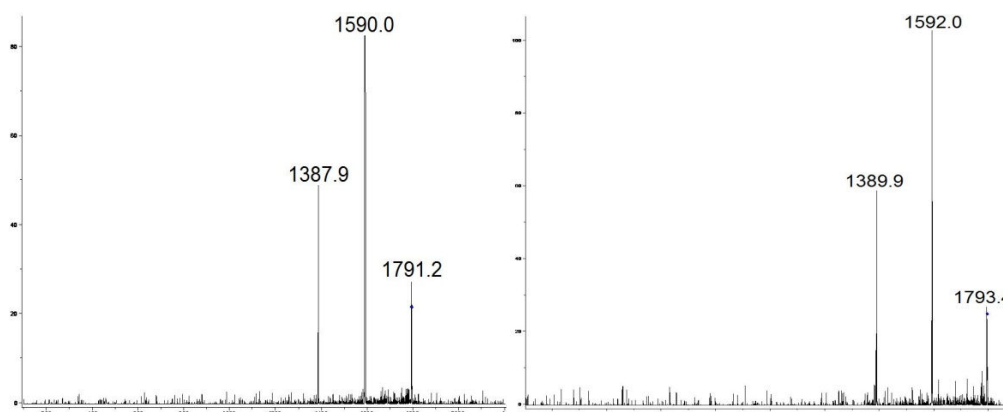


Figure 7.18: MS/MS of 1792.0, left, and 1794.0, right

The two parent ions are the most abundant ions of the corresponding isotope pattern. The difference between m/z 1794.0 and m/z 1792.0 is that one ^{107}Ag is replaced by one ^{109}Ag , which increases the mass by two mass units. Both MS/MS spectra feature the successive loss of 202 mass units and corresponding daughter ions are also shifted by two mass units, which indicates that the isotope composition of the silver in the cluster has not been changed in the dissociation. As a result, the experiment features the loss of two of the three tryptophan-2H units in that cluster.

The table below lists the parent cluster ion of choice and the major fragment ions that resulted from its dissociation. The actual MS/MS spectra are shown in the appendix.

MS/MS of m/z	Cluster	Main Fragment	Second fragment	Other fragments
418.9	Ag_2Trp	No fragments	-	-
528.7	Ag_3Trp	AgTrp	Ag_3	m/z 266/268, 483.7
634.7	Ag_4Trp	Ag_2Trp	m/z 480/482, 374	524, 588, 265/267
728.8	Ag_3Trp_2	Ag_3Trp	Ag_3 , AgTrp	Ag_2Trp
740.6	Ag_5Trp	Ag_3Trp	-	-
836.7	Ag_4Trp_2	Ag_4Trp	Ag_2Trp	-
850.0	Ag_6Trp	Ag_4Trp	Ag_2Trp	-
942.7	Ag_5Trp_2	Ag_3Trp	Ag_5Trp , $\text{Ag}_7?$	AgTrp , Ag_3
958.4	Ag_7Trp	Ag_7	m/z 885	-
1040.8	Ag_4Trp_3	Ag_4Trp_2	-	-
1056.6	Ag_6Trp_2	Ag_6Trp	-	-
1064.3	Ag_8Trp	Ag_6Trp	Ag_4Trp	-
1146.7	Ag_5Trp_3	Ag_5Trp_2	-	-
1158.5	Ag_7Trp_2	Ag_7Trp	Ag_7	Ag_5Trp_2
1170.6	Ag_9Trp	Ag_9	Ag_7Trp	-
1254.7	Ag_6Trp_3	Ag_6Trp_2	Ag_6Trp	Ag_5Trp_2 , 382
1268.4	Ag_8Trp_2	Ag_8Trp	Ag_6Trp_2	Ag_9 , Ag_6Trp
1282.0	Ag_{10}Trp	m/z 1236	Ag_{10}	Ag_8Trp , Ag_9

1361.6	Ag ₇ Trp ₃	Ag ₇ Trp ₂	Ag ₇ Trp	Ag ₇
1376.2	Ag ₉ Trp ₂	Ag ₉ Trp	Ag ₉	-
1388.7	Ag ₁₁ Trp	Ag ₁₁	-	-
1470.5	Ag ₈ Trp ₃	Ag ₈ Trp ₂	Ag ₈ Trp	Ag ₆ Trp
1482.1	Ag ₁₀ Trp ₂	Ag ₁₀ Trp	-	-
1496.6	Ag ₁₂ Trp	Ag ₁₂	Ag ₁₀ Trp, m/z 1092	Ag ₁₀ , m/z 876
1578.1	Ag ₉ Trp ₃	Ag ₉ Trp ₂	Ag ₉ Trp	Ag ₉
1591.9	Ag ₁₁ Trp ₂	Ag ₁₁ Trp	m/z 1518	Ag ₁₁
1604.4	Ag ₁₃ Trp	Ag ₁₃	Ag ₁₁ Trp	m/z 1198
1672.5	Ag ₈ Trp ₄	Ag ₈ Trp ₃	Ag ₈ Trp ₂	-
1699.8	Ag ₁₂ Trp ₂	Ag ₁₂ Trp	Ag ₁₀ Trp	-
1712.3	Ag ₁₄ Trp	Ag ₁₄	m/z 1308	-
1780.3	Ag ₉ Trp ₄	Ag ₉ Trp ₃	Ag ₉ Trp ₂	-
1792.0	Ag ₁₁ Trp ₃	Ag ₁₁ Trp ₂	Ag ₁₁ Trp	-
1818.2	Ag ₁₅ Trp	Ag ₁₅	m/z 1414	-
1886.2	Ag ₁₀ Trp ₄	Ag ₁₀ Trp ₃	Ag ₁₀ Trp ₂	-
1928.1	Ag ₁₆ Trp	No fragments	-	-
1994.1	Ag ₁₁ Trp ₄	Ag ₁₁ Trp ₃	Ag ₁₁ Trp ₂	Ag ₁₁ Trp
2036.1	Ag ₁₇ Trp	No fragments	-	-
2090.2	Ag ₁₀ Trp ₅	No fragments	-	-
2103.9	Ag ₁₂ Trp ₄	No fragments	-	-

Table 7.3: Daughter ion analysis through MS/MS experiments of Ag-Trp clusters. Note that the hydrogen deficiency has been ignored for simplicity in the table. As indicated earlier, one Trp has lost up to 2 hydrogen atom.

For the majority of the clusters in the table above, the dominant fragmentation channel is the loss of one tryptophan molecule. The smaller clusters in the series of clusters with one tryptophan appear to lose two silver atoms preferentially. This is the case for Ag₃Trp, Ag₄Trp, Ag₅Trp, Ag₆Trp and Ag₈Trp. For some reason, Ag₇Trp dissociates into Ag₇. This would suggest that the smaller silver clusters, up to Ag₈, are stabilised by the presence of

tryptophan, the exception being Ag₇ which is stable without tryptophan. The fact that Ag₇ has a greater stability is also seen in the dissociation of silver clusters, explored in more detail later in this chapter.

MS³ experiments, for which a fragment ion resulting from an MS² (MS/MS) experiment is selected and fragmented further, were performed. MS³ experiments can only be performed when the initial fragment ion is abundantly enough generated in MS/MS step and usually results in spectra of very low quality.

MS/MS	Cluster	MS ³	Cluster	Main fragment	Other fragments
728.9	Ag ₃ Trp ₂	526.7	Ag ₃ Trp	AgTrp	Ag ₃
836.7	Ag ₄ Trp ₂	634.6	Ag ₄ Trp	Ag ₂ Trp	Ag ₃ Trp
850.0	Ag ₆ Trp	634.5	Ag ₄ Trp	Ag ₂ Trp	-
1064.3	Ag ₈ Trp	848.4	Ag ₆ Trp	Ag ₄ Trp	Ag ₂ Trp
1254.6	Ag ₆ Trp ₃	850.5	Ag ₆ Trp	Ag ₄ Trp	Ag ₂ Trp
1254.6	Ag ₆ Trp ₃	1052.6	Ag ₆ Trp ₂	Ag ₆ Trp	Ag ₄ Trp
1482.1	Ag ₁₀ Trp ₂	1280.1	Ag ₁₀ Trp	m/z 1234	m/z 1103, Ag ₉
1496.6	Ag ₁₂ Trp	1292.5	Ag ₁₂	m/z 1092	Ag ₁₀ , 876
1576.3	Ag ₉ Trp ₃	1374.2	Ag ₉ Trp ₂	Ag ₉ Trp	Ag ₉
1591.9	Ag ₁₁ Trp ₂	1390.0	Ag ₁₁ Trp	Ag ₁₁	-
1604.4	Ag ₁₃ Trp	1401.6	Ag ₁₃	Ag ₁₂	Ag ₁₁
1672.5	Ag ₈ Trp ₄	1467.4	Ag ₈ Trp ₃	m/z 1394	Ag ₈ Trp ₂
1699.8	Ag ₁₂ Trp ₂	1497.9	Ag ₁₂ Trp	Ag ₁₀ Trp	-
1712.3	Ag ₁₄ Trp	1511.4	Ag ₁₄	¹⁰⁹ Ag ₁₂ *	-
1780.3	Ag ₉ Trp ₄	1374.3	Ag ₉ Trp ₂	Ag ₉ Trp	Ag ₉
1780.3	Ag ₉ Trp ₄	1577.3	Ag ₉ Trp ₃	Ag ₉ Trp ₂	m/z 1502
1792.0	Ag ₁₁ Trp ₃	1590.0	Ag ₁₁ Trp ₂	Ag ₁₁ Trp	-
1818.2	Ag ₁₅ Trp	1615.4	Ag ₁₅	No fragments	-
1886.2	Ag ₁₀ Trp ₄	1482.0	Ag ₁₀ Trp ₂	Ag ₁₀ Trp	-
1994.1	Ag ₁₁ Trp ₄	1791.0	Ag ₁₁ Trp ₃	Ag ₁₁ Trp ₂	Ag ₁₁ Trp

Table 7.4: Fragment peaks resulting from MS³ experiments of Trp-Ag clusters. As before, the hydrogen deficiency has been ignored for simplicity in the table.

* There appears to be a small contribution from an all ^{109}Ag cluster at m/z 1308. The mass of $^{109}\text{Ag}_{12}\text{Trp}_2$ is 1712 is the same as for $^{107}\text{Ag}_8^{109}\text{Ag}_6\text{Trp}$, which was the ion of interest for the MS/MS experiment. Obviously both ions were selected together and contributed to the MS/MS spectrum. This may also be the explanation for the appearance of peaks of unknown origin in other spectra. Some of these contributions are evident through a silver composition that differs from the selected one.

With these considerations in mind, the fragmentation behaviour of the different clusters can be analysed. Two major dissociation pathways are evident: the simultaneous loss of two silver atoms and the loss of one tryptophan molecule. As discussed above, the latter species may show a hydrogen deficiency of up to two hydrogen atoms.

The majority of these clusters prefer to lose a tryptophan molecule initially. For the larger clusters, the tryptophan is preferentially lost until the bare silver cluster is obtained. For the smaller clusters, tryptophan is preferentially lost until one tryptophan remains with the silver cluster, and then two silver atoms are lost.

This confirms the observation that for smaller silver clusters, it is preferable that one tryptophan molecule remains with the cluster. Again, it seems that clusters which contain up to 8 silver atoms will prefer to retain the tryptophan molecule, and that larger silver clusters lose tryptophan preferentially. Some example spectra are shown below.

MS/MS: 728.8, MS³: 526.7:

MS/MS: 850.0, MS³: 634.5:

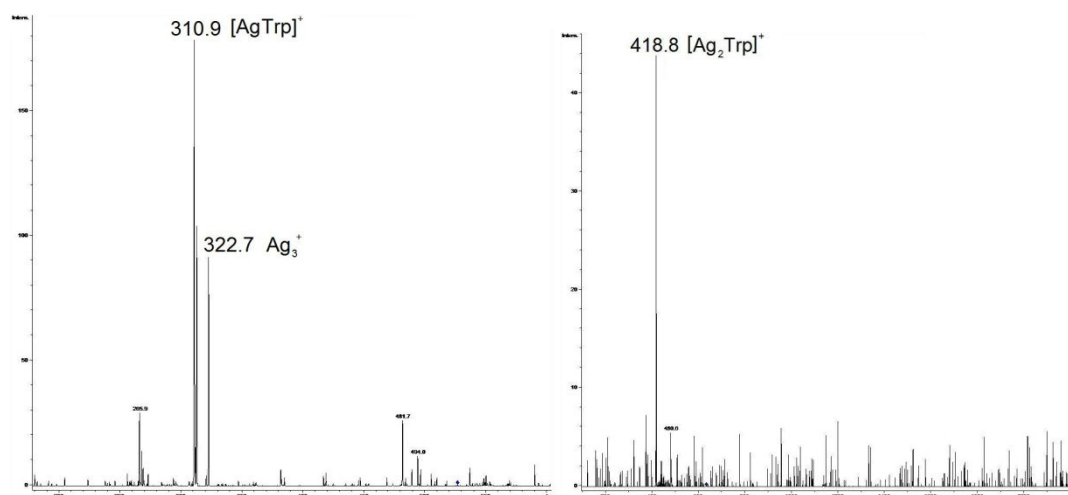
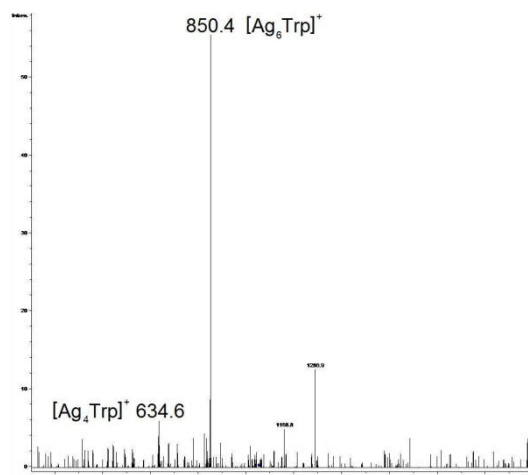
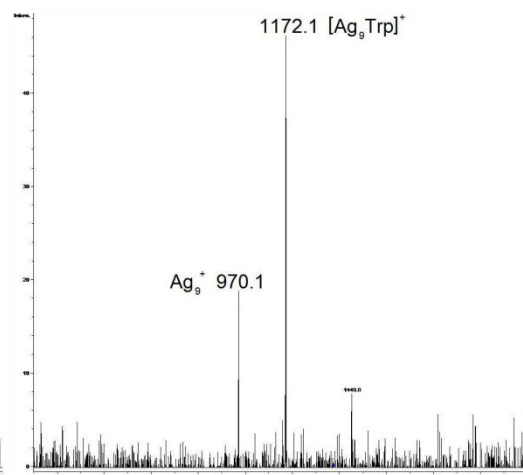
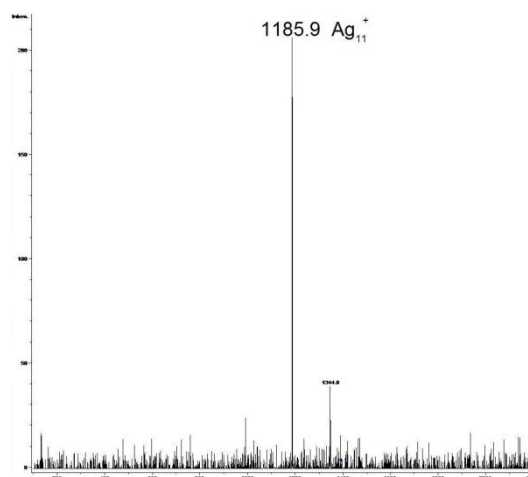
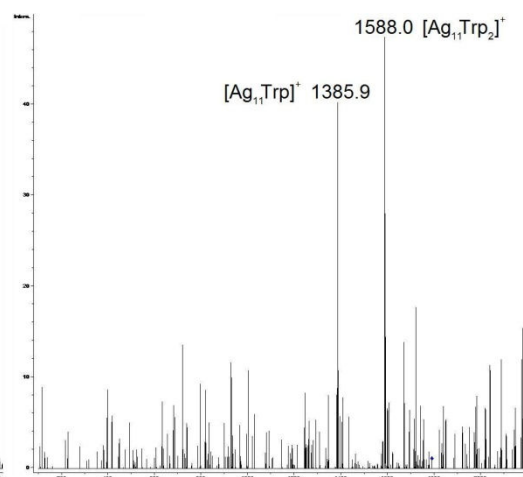


Figure 7.19: MS/MS of Ag_3Trp_2 , MS³ of Ag_3Trp , left. MS/MS Ag_6Trp , MS³ Ag_4Trp , right

MS/MS: 1254.6, MS³: 1052.6:MS/MS: 1576.3, MS³: 1374.2:Figure 7.20: MS/MS of Ag₆Trp₃, MS³ of Ag₆Trp₂, left. MS/MS Ag₉Trp₃, MS³ Ag₉Trp₂, rightMS/MS: 1591.0, MS³: 1390.0:MS/MS: 1994.1, MS³: 1791.0:Figure 7.21: MS/MS Ag₁₁Trp₂, MS³ of Ag₁₁Trp, left; MS/MS Ag₁₁Trp₄, MS³ Ag₁₁Trp₃, right

In summary, the observed fragmentation behaviour would indicate that the silver/tryptophan hybrid clusters are composed of a silver cluster which contains at its periphery a certain amount of tryptophan moieties, as these are preferably evaporated leading to pure silver clusters.

Experiments have been performed in conjunction with the project student Chris Hart. These were aimed at the elucidation of the origin of the hydrogen atoms that are lost in these hybrid clusters. In D₂O solution, all four exchangeable hydrogen atoms in tryptophan were

exchanged by deuterium. When this Trp(4D) was used to produce the hybrid clusters with silver, it was found that only D and no H was lost in the production of these clusters.

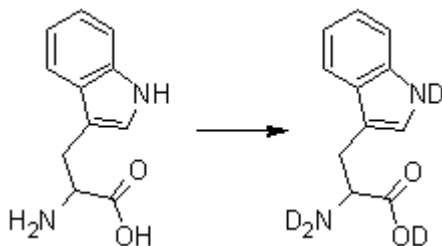


Figure 7.22: Structure of tryptophan demonstrating the position of exchangeable hydrogen

These experiments confirm that the hydrogen atoms lost in the initial clusters were from the above locations on the tryptophan, and not from the aromatic rings.

Silver Clusters

The fragmentation pathways of pure silver clusters were also analysed by MS/MS and MS³ experiments.

m/z	Cluster	Main fragment	Other fragments
538.4	Ag ₅ ⁺	Ag ₃ ⁺	-
756.3	Ag ₇ ⁺	Ag ₅ ⁺	Ag ₃ ⁺
863.1	Ag ₈ ⁺	Ag ₇ ⁺	-
972.1	Ag ₉ ⁺	Ag ₈ ⁺	Ag ₇ ⁺
1188.0	Ag ₁₁ ⁺	Ag ₉ ⁺	-
1401.6	Ag ₁₃ ⁺	Ag ₁₂ ⁺	Ag ₁₁ ⁺
1617.5	Ag ₁₅ ⁺	Ag ₁₄ ⁺	Ag ₁₃ ⁺
1831.5	Ag ₁₇ ⁺	Ag ₁₆ ⁺	Ag ₁₅ ⁺

Table 7.5: MS/MS experiments with Ag clusters: parent and daughter ions

Larger silver clusters show the loss of one silver atom, followed by a second loss, to ultimately produce an odd-numbered silver cluster. MS/MS/MS (MS³) experiments below show that the even silver cluster daughter ion is an intermediate on the way to the more stable odd-numbered fragment ion. Smaller clusters do not even show this even-numbered intermediate fragment. Ag₇⁺ dissociates directly into Ag₅⁺, and Ag₅⁺ fragments further into Ag₃⁺. Ag₃⁺ is a particularly stable cluster, which was abundantly in most ESI experiments.

Ag_8^+ was the only even numbered silver cluster which had a large enough intensity to perform MS/MS. Ag_8^+ undergoes the loss of only one silver atom, to create Ag_7^+ . Ag_9^+ fragments into Ag_8^+ and then into Ag_7^+ – the fragment ion intensities seem to indicate that Ag_7^+ has an enhanced stability compared to other smaller clusters.

In summary, these MS/MS experiments provide further proof that the odd numbered silver clusters are much more stable than their even numbered counterparts. Some example spectra are depicted below.

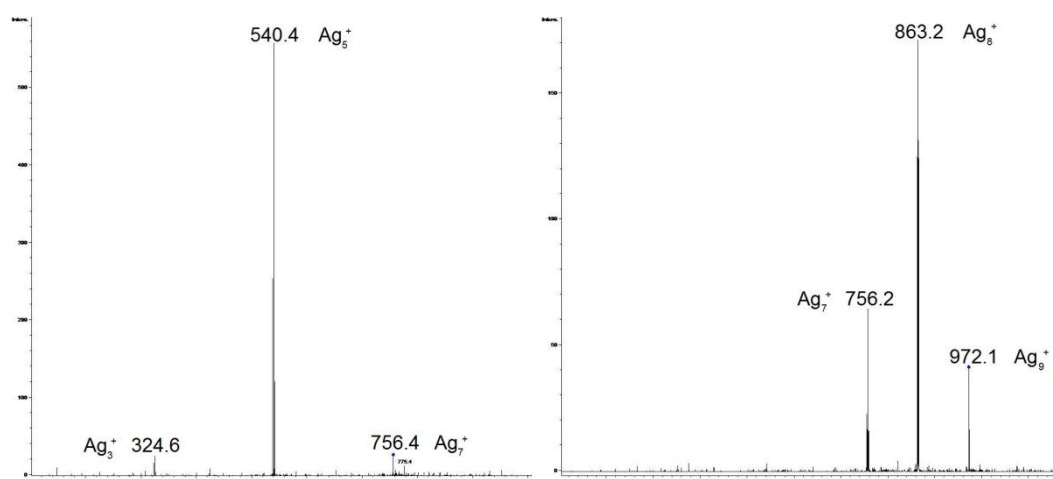


Figure 7.23: Positive-ion mode MS/MS of Ag_7^+ , left, Ag_9^+ , right

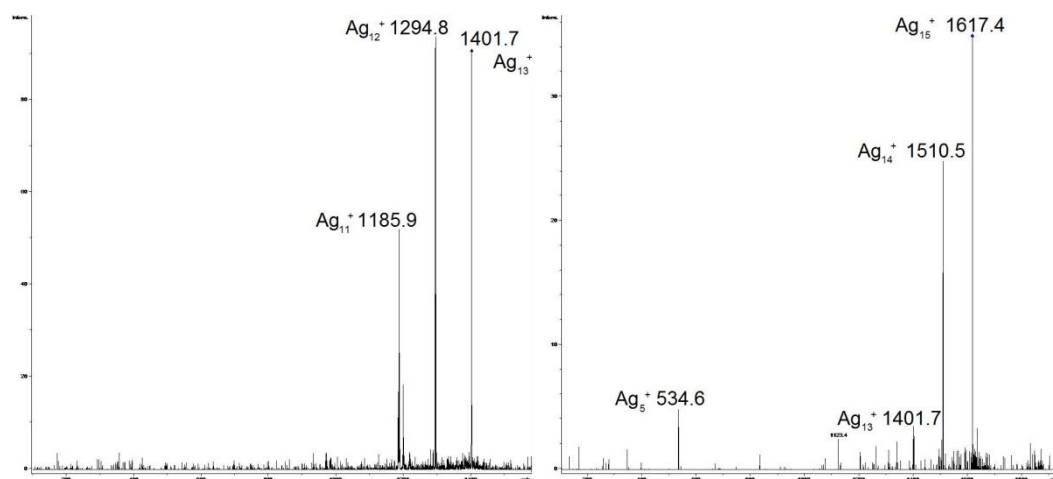


Figure 7.24: Positive-ion mode MS/MS of Ag_{13}^+ , left, and Ag_{15}^+ , right

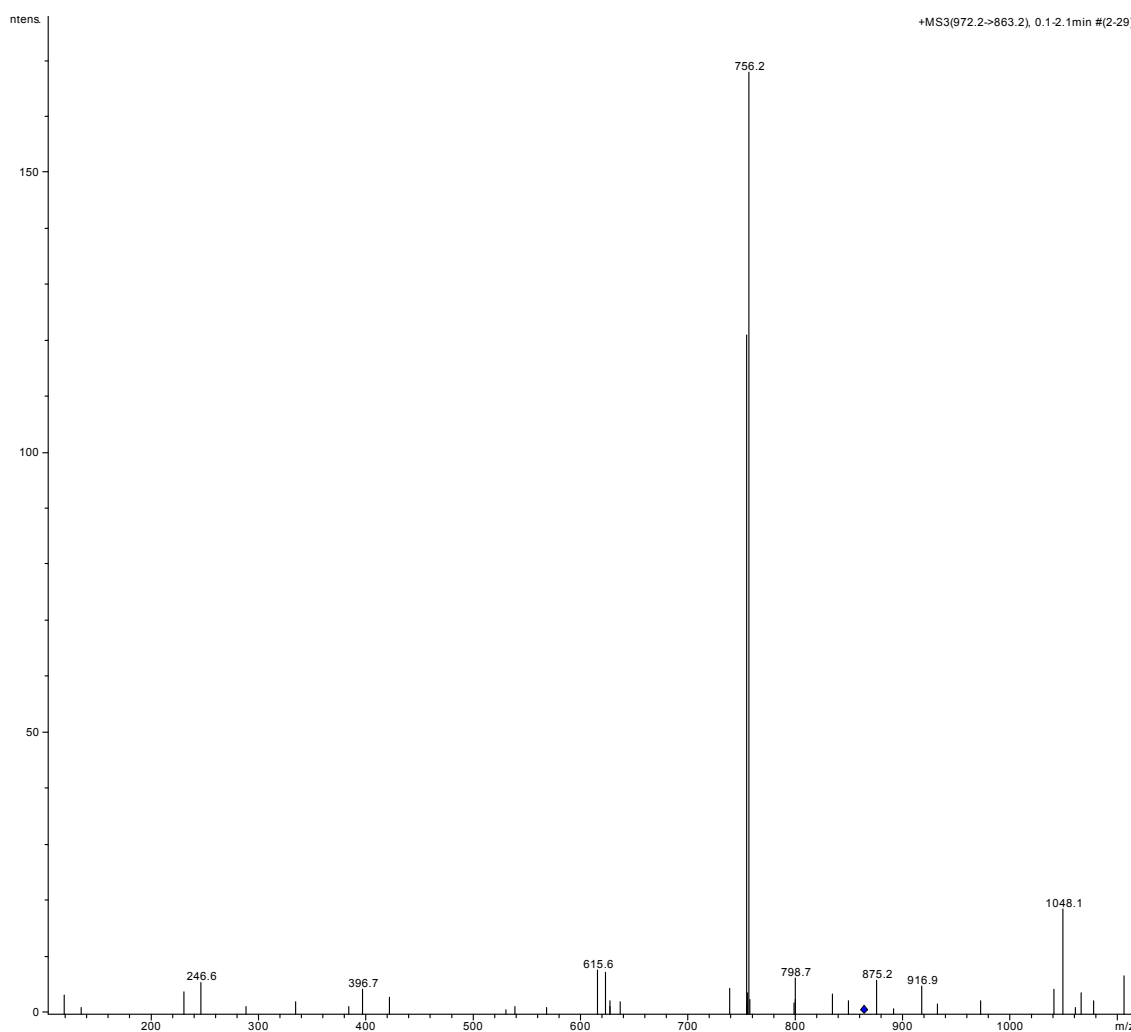
MS^3 experiments were performed on the above clusters when the signal strength would allow to do so:

MS/MS	Cluster	MS ³	Cluster	Main fragment
754.4	Ag ₇ ⁺	538.5	Ag ₅ ⁺	Ag ₃ ⁺
972.2	Ag ₉ ⁺	863.2	Ag ₈ ⁺	Ag ₇ ⁺
972.2	Ag ₉ ⁺	756.3	Ag ₇ ⁺	Ag ₅ ⁺
1401.8	Ag ₁₃ ⁺	1294.8	Ag ₁₂ ⁺	Ag ₁₁ ⁺

Table 7.6: MS³ experiments with the pure Ag clusters

The MS/MS/MS experiments confirm that the odd numbered silver clusters are the stable end product of the dissociations, whereby even numbered fragment clusters are intermediates in dissociations of large clusters, while small clusters show the direct loss of Ag₂ without even numbered intermediate.

An example MS³ spectrum is shown below:

Figure 7.25: Positive-ion mode MS/MS of Ag₉⁺, followed by MS³ of Ag₈⁺

MS/MS of m/z 972.2, Ag_9^+ , followed by MS^3 of m/z 863.2, Ag_8^+ , results in a doublet peak at m/z 754/756.2, representing Ag_7^+ . The peak at m/z 972.2 is composed of 4 $^{106.9}\text{Ag}$, and 5 $^{108.9}\text{Ag}$. The peak at m/z 863.2 has lost one $^{108.9}\text{Ag}$. Therefore, the selected Ag_8^+ now contains an equal mixture of the two silver isotopes. When it decays it loses either a $^{106.9}\text{Ag}$, resulting in the m/z 756.2 peak, or a $^{108.9}\text{Ag}$, resulting in the m/z 754.2 peak. The resulting MS^3 spectrum confirms these considerations by displaying the expected 1:1 doublet of Ag_7^+ .

Conclusion

Clusters of silver and tryptophan molecules have been produced using specific conditions within the ESI source. Pure silver clusters have been produced in the same way and it has been confirmed through MS/MS and MS³ experiments that odd numbered pure silver clusters are more stable than their even numbered counterparts.

For silver / tryptophan hybrid clusters it was found that the tryptophan molecule loses up to two hydrogen atoms to stabilise the silver cluster electronically through the formation of closed shell ions. An even number of silver atoms is relatively unstable as a pure cluster, but is clearly stabilised through the interaction with tryptophan in such clusters. The fragmentation behaviour of the mixed clusters indicates that their structure is in fact composed of a silver cluster which contains the tryptophan molecules attached to it.

In the present study, larger clusters than previously reported have been created. Even larger sizes are also feasible – the largest cluster produced here - Ag₁₁Trp₅, is shown at m/z 2196. This cluster had a fairly strong signal; however, the detection was at the upper mass limit of the esquire2000:

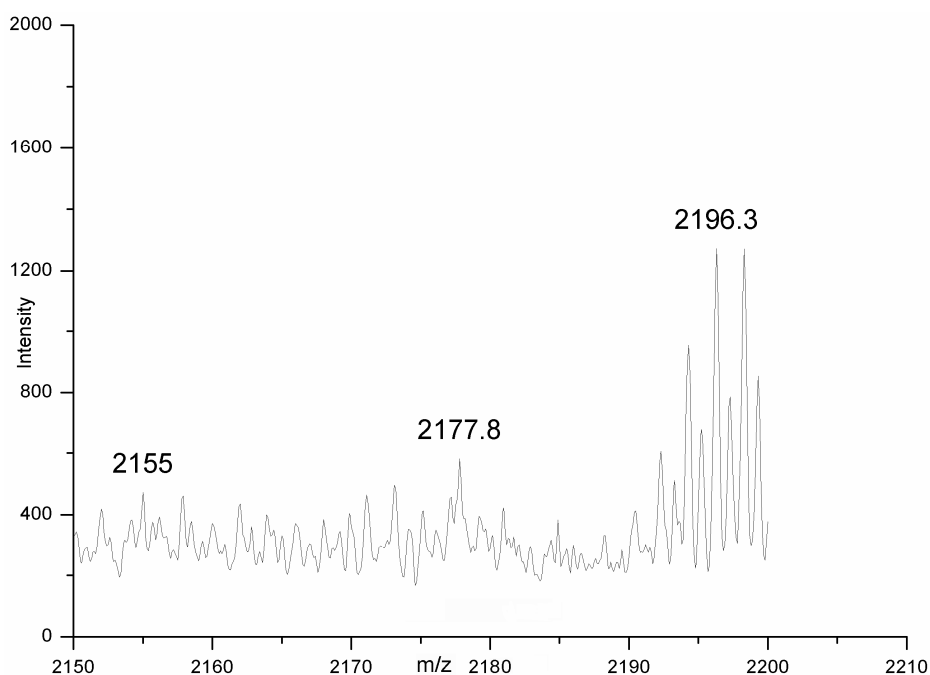


Figure 7.26: Positive-ion mode ESI of AgTFA and Tryptophan, m/z region 2150 - 2200

This suggests that with an instrument with a larger mass range, larger clusters may be detected.

Future work involves cluster formation with different amino acids, with the aim to evaluate further the role of the amino acid in the production of such hybrid clusters.

The study of the interactions of amino acids with other metals, such as gold, is another goal. This could prove difficult, as although previous research has demonstrated that gold binds in a similar fashion as silver to amino acids, further optimisation of the source conditions would be necessary and time consuming¹⁶.

Structure elucidation of these clusters would also be desirable. From the results it is expected that the tryptophan molecules reside on the outside of the clusters. Tryptophan is preferentially lost unless required for stabilisation of the smaller clusters. Additionally, the more tryptophan molecules present in a cluster, the larger the size of the attached silver cluster. This would suggest that a certain number of silver is required per tryptophan molecule wishing to attach. A previous study of silver clusters suggests that for clusters of less than 5 silvers, the silvers are arranged in a planar fashion, but for silver clusters ≥ 5 , the structure is three dimensional¹⁷. It would be logical to assume that a three dimensional cluster formation would allow for the binding of more tryptophan molecules.

References

1. Tabarin, T.; Antoine, R.; Broyer, M.; Dugourd, P., *European Physical Journal D* **2006**, 37 (2), 237-239.
2. Sakairi, M.; Yergey, A. L.; Siu, K. W. M.; Le Blanc, J. C. Y.; Guevremont, R.; Berman, S. S., *Analytical Chemistry* **1991**, 63 (14), 3.
3. Slawson, R. M.; Lee, H.; Trevors, J. T., *BioMetals* **1990**, 3 (3), 151-154.
4. Shin, S.-H.; Ye, M.-K.; Kim, H.-S.; Kang, H.-S., *International Immunopharmacology* **2007**, 7 (13), 1813-1818.
5. Damm, C.; Munstedt, H.; Rosch, A., *Materials Chemistry and Physics* **2008**, 108 (1), 61-66.
6. Murthy, P.; Mohan, Y.; Varaprasad, K.; Sreedhar, B.; Raju, K., *Journal of Colloid and Interface Science* **2008**, 318 (2), 217-224.
7. Jia, H.; Hou, W.; Wei, L.; Xu, B.; Liu, X., *Dental Materials* **2008**, 24 (2), 244-249.
8. Lee, V.; Li, H.; Lau, T.; Guevremont, R.; Siu, K., *Journal of the American Society for Mass Spectrometry* **1998**, 9 (8), 760-766.
9. Perera, B.; Ince, M.; Talaty, E.; Van Stipdonk, M., *Rapid Communications in Mass Spectrometry* **2001**, 15 (8), 615-622.
10. Pereira, B.; Gallardo, A.; Barr, J.; Tekarli, S.; Anbalagan, V.; Talaty, E.; Van Stipdonk, M., *Journal of Mass Spectrometry* **2002**, 37 (4), 401-413.
11. Tabarin, T.; Antoine, R.; Compagnon, I.; Broyer, M.; Dugourd, P.; Mitric, R.; Petersen, J.; Bonacic-Koutecky, V., *European Physical Journal D* **2007**, 43 (1-3), 275-278.
12. Antoine, R.; Tabarin, T.; Broyer, M.; Dugourd, P.; Mitric, R.; Bonacic-Koutecky, V., *ChemPhysChem* **2006**, 7 (2), 524-528.
13. Mitric, R.; Petersen, J.; Kulesza, A.; Bonacic-Koutecky, V.; Tabarin, T.; Compagnon, I.; Antoine, R.; Broyer, M.; Dugourd, P., *Journal of Chemical Physics* **2007**, 127 (13), 134301.
14. Mitric, R.; Petersen, J.; Kulesza, A.; Bonacic-Koutecky, V.; Tabarin, T.; Compagnon, I.; Antoine, R.; Broyer, M.; Dugourd, P., *Chemical Physics* **2008**, 343 (2-3), 372-380.
15. Xiong, Y.; Washio, I.; Chen, J.; Sadilek, M.; Xia, Y., *Angewandte Chemie-International Edition* **2007**, 46 (26), 4917-4921.

16. Pakiari, A.; Jamshidi, Z., *Journal of Physical Chemistry A* **2007**, *111* (20), 4391-4396.
17. Weis, P.; Bierweiler, T.; Gilb, S.; Kappes, M., *Chemical Physics Letters* **2002**, *355* (3-4), 355-364.

Chapter 8: Use of Silver as a cationising agent, and ESI as an analytical tool for the analysis of pure fullerenes and unpolar fullerene derivatives

Introduction

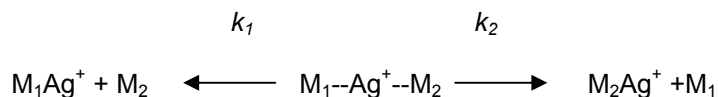
The silver cation is well-known to form a bond with the π electrons in unsaturated hydrocarbons. As discussed in chapter 7, amino acid-silver complexes were created using ESI-MS. It was hoped to use the same technique to create silver bound fullerene dimers, and dissociate these using CID. If successful, it was thought that silver-bound hetero-dimers could be created, using different fullerenes and related compounds. Using the relative intensities of the fragment peaks, the relative silver binding affinities of the fullerenes and related compounds could be evaluated according to the kinetic method.

It was also hoped that conditions within the ESI source could be optimised for the analysis of “bare” fullerenes, without the addition of salts, derivatisation of the sample, or pre-ionisation.

The Kinetic Method

The kinetic method involves the dissociation of a hetero-dimer bound by a charge carrying species in the gas phase whereby the intensities of the resulting fragments are used to calculate each monomer’s affinity for the binding charged species. This can be used to calculate, for example, proton affinities, metal ion binding affinities and ionisation energies¹.

In this instance, it is the relative silver binding affinity that is being sought:



k_1 and k_2 are the rate constants for the competing dissociation reactions.

If you assume that there are no isomers of the activated cluster ion, that there are negligible differences in entropy requirements and negligible reverse activation energies, then the following is true:

$$\ln \frac{k_1}{k_2} = \ln \frac{[M_1Ag]^+}{[M_2Ag]^+} \approx \frac{\Delta(\Delta Ag)}{RT_{eff}}$$

T_{eff} is the effective temperature of the activated hetero-dimer. The ratio of the intensities of the fragment ions is related to the difference in silver ion binding affinity. T_{eff} has been set arbitrarily to 555K. This value is within the T_{eff} range that has been determined by other experiments in the group using the kinetic method with the ion trap. The actual T_{eff} may in fact be different. However, since the measurements need to be compared with each other, the T_{eff} has to be set to a certain value to allow the comparison of the systems under investigation. This approach is valid as only a relative silver ion affinity order is to be established and not absolute values.

The hetero-dimers are formed, isolated from other ions and dissociated to find the relative abundances of the fragment ions. Because of this, it is not necessary to have totally pure samples, as the bound hetero-dimers are isolated prior to fragmentation, meaning any impurities are discarded. This method also has the advantage of being a measurement of relative ion abundances, which means that sources of error that would apply to both fragments would cancel.

There are drawbacks; to begin with, at least two reference samples are required of known affinity to the charge carrier to be able to establish the absolute ion affinities of an unknown. Also, if the reference data is inaccurate, then the resulting determination will also be inaccurate.

There are other issues to take into consideration – if there are multiple binding sites, if there is an entropic barrier not accounted for, or if dynamic factors alter the fragmentation; then these will all affect the ion abundance appearance and not give an accurate measurement of the relative binding affinities.

To calculate the relative silver binding affinities requires a rearrangement of the above equation:

$$\Delta(\Delta Ag^+) = \ln \frac{[M_1 Ag]^+}{[M_2 Ag]^+} \cdot RT_{eff}$$

M_1 is usually the unknown, with M_2 being the series of reference samples.

Silver bound dimers of Fullerenes and Fullerene Derivatives

Fullerenes have a tendency to form dimers; in particular the oxygen bound C_{60} dimer, $C_{120}O$, is formed easily by C_{60} even when in the solid state at an ambient temperature, in as little as

40 hours². This dimer is not easily seen using mass spectrometry; EI-MS produced only a peak for C₆₀.

ESI-MS of C₆₀ dimers is difficult to perform, as is the case for standard fullerene derivatives as discussed in previous chapters. For example, the molecular ion peak of a tetrathiafulvalene bound C₆₀ dimer could only be found through careful alteration of the skimmer voltage³.

Silver-bound dimers of fullerenes and their derivatives have been produced and studied previously, however, not as a means to establish the relative silver binding energies.

Silver complexes with C₆₀ were initially produced in the gas phase using a laser vapourisation cluster source⁴. A silver rod was coated with C₆₀ through sublimation, and a XeCl excimer laser operating at a wavelength of 308nm was used to create the gas phase complexes. The power of the laser played an important role – if too low, only C₆₀ was observed, if too high, only pure silver clusters were formed. Complexes produced were mainly C₆₀ with a silver cluster of between 1 and 5 silver atoms; however, a silver-bound C₆₀ dimer was also produced.

From photodissociation experiments of the [(C₆₀)₂Ag]⁺ complex, it was deduced that it has a sandwich structure, of: [C₆₀--Ag--C₆₀]⁺, as fragments of both C₆₀⁺, and [C₆₀Ag]⁺ were produced. As both C₆₀ and silver have very similar ionisation energies, it was expected that the charge was delocalised.

C₆₀ has been derivatised using a phenathroline in order to create a silver-bound dimer⁵:

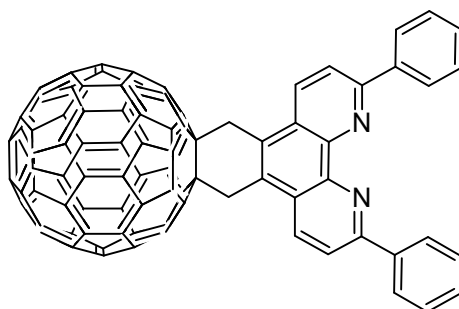


Figure 8.1: Structure of C₆₀ derivatised with a phenathroline

The above compound was mixed with an excess solution of silver ions, and stirred at room temperature under argon overnight. The silver ion was complexed by the four nitrogen atoms to form the dimer. The two planar ligands were at 90° angles with respect to each other.

Synthesis of the derivative was confirmed by IR spectroscopy, $^1\text{H-NMR}$, FD-MS and UV-Vis spectroscopy. Production of the silver bound dimer was confirmed using $^1\text{H-NMR}$, UV-Vis spectroscopy, and positive-ion mode ESI-MS.

The ESI spectrum produced peaks corresponding to the silver-bound dimer, silver attached to one molecule of the C_{60} derivative, and hydrogen addition to the C_{60} derivative.

For polycyclic aromatic hydrocarbons, similar to those attached to C_{60} in chapter 6, silver has been found to interact with the delocalised π electrons⁶.

Using the kinetic method and positive-ion mode ESI-MS, the relative gas phase silver (I) ion affinities of the following PAHs were studied⁷:

Benzene	Pyrene
Napthalene	Triphenylene
Phenanthranene	Chrysene
Anthracene	Benz(a)anthracene
Fluoranthracene	

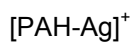
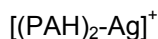
The affinities were calculated relative to benzene. Silver-bound heterodimers of the PAHs were produced with positive-ion mode ESI-MS, and dissociated with CID to produce the relative fragments.

Silver ion cationisation and positive-ion mode ESI-MS were also used in differentiating between isomers of various PAHs, by forming silver (I) bound heterodimers of the individual PAHs, and dissociating them⁸. CID was not performed in the usual way, where ions are subjected to a collision with gas in a collision cell inside the mass analyser. In-source CID, where collisions occur prior to the mass analyser and where the collision gas is the drying gas, was utilised in its place.

It was discovered, as with the fullerene dimers, that the voltages inside the ESI source play an important role. With higher cone voltages, only the PAH ion is seen. At lower voltages, the silver bound PAH dimer is the most abundant, with the $[\text{PAH-Ag}]^+$ complex tending to be the most intense at medium voltages. Depending on which isomers were tested, the ratio of the $[\text{PAH}]^+ : [\text{PAH-Ag}]^+ : [(\text{PAH})_2\text{-Ag}]^+$ peaks altered, and as long as the ESI conditions were kept identical, differentiation between the isomers was possible.

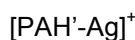
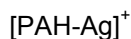
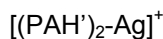
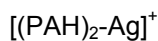
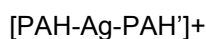
Another example of electrospraying silver and PAHs together comes from the study of the effect of substituents on four different PAHs: anthracene, phenanthrene, pyrene and cyclo[a]phenanthrene⁹.

Solutions of individual PAHs were sprayed with silver ions in positive-ion mode, producing the following complexes:



Increasing the skimmer voltage decreased the abundance of the dimers.

When two PAHs were sprayed with silver, the complexes produced included:



Again, the appearance of the dimers was dependent on the skimmer voltage settings.

It has been demonstrated that it is possible to create silver (I) bound dimers of PAHs using ESI-MS. Using ESI for this project, it was hoped that silver-bound dimers could be produced of fullerenes, and the C₆₀PAH complexes synthesised previously (chapter 6), and to study these using the kinetic method.

ESI as an analytical tool for fullerenes

As discussed in chapter 6, ESI is traditionally difficult for the analysis of fullerenes and their derivatives if they were equally unpolar, as conditions need to be found where the electrospray acts as an electrochemical cell. It was hoped that by utilising the optimised ESI settings found for the C₆₀PAH derivatives in chapter 6, that standard fullerenes could be analysed without the need for addition of salts or for derivatisation prior to analysis.

Experimental

Positive Ion Silver ESI-MS

Compounds analysed for this section include:

- C_{60} , C_{70} , C_{84} , $(C_{59}N)_2$
- An isomer pair from Professor Helena Grennberg, Uppsala University, Sweden, $C_{24}H_{16}$, colloquially called “cis” (below left) and “trans” (below right):

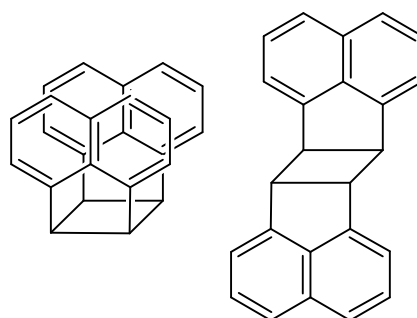


Figure 8.2: Structures of “cis”, left and “trans”, right

- Coronene ($C_{24}H_{12}$), Corannulene ($C_{20}H_{10}$), Pentaïdeno Corannulene ($C_{50}H_{20}$), Cyclopenta[bc]coronene ($C_{26}H_{12}$) and Benzo[a]coronene ($C_{28}H_{14}$) provided by Professor Lawrence Scott at Boston College, MA.

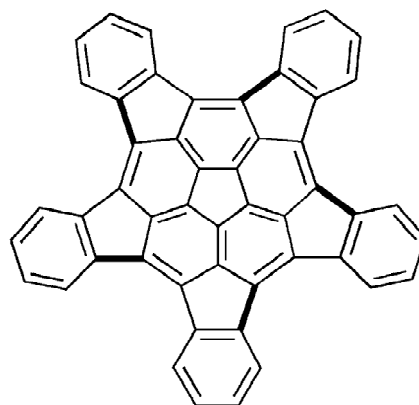


Figure 8.3: Structure of $C_{50}H_{20}$

- $C_{60}A$, $C_{60}T$, $C_{60}P$, synthesized by us (chapter 6)
- $C_{60}C_8H_8$, from Prof. Mike Orfanopoulos and Manolis Trikakakis of the University of Crete
- $(C_{60})_2C_{22}H_{14}(C_6H_5)_2$ (cis-bis[60]fullerene adduct of 6,13-diphenylpentacene) supplied by Professor Glen P. Miller at the University of New Hampshire, NH.

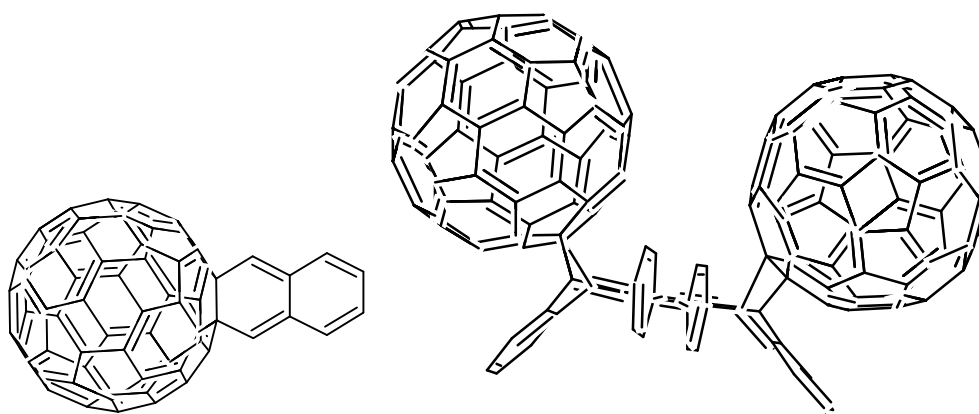


Figure 8.4: Structures of $C_{60}C_8H_8$, left and cis-bis[60]fullerene adduct of 6,13-diphenylpentacene, right

For C_{60} , C_{70} , C_{60} Anthracene, C_{60} Tetracene and C_{60} Pentacene, solution preparation involved dissolving in dichloromethane (DCM) to produce solutions at the concentrations listed below:

C_{60}	69.4 μ M
C_{70}	69.4 μ M
$C_{24}H_{16}$, cis and trans	69.4 μ M
C_{60} Anthracene	55.7 μ M
C_{60} Tetracene	52.7 μ M
C_{60} Pentacene	50.1 μ M
$C_{60}C_8H_8$	69.4 μ M
$(C_{60})_2C_{22}H_{14}(C_6H_5)_2$	69.4 μ M

Table 8.1: Final concentrations of samples initially dissolved in dichloromethane

For the remaining compounds, the samples were dissolved initially in a 1:1 v/v toluene:DCM mixture, and then further diluted with DCM to produce the following concentrations:

C_{84}	138.8 μ M
Coronene ($C_{24}H_{12}$)	69.4 μ M
Corannulene ($C_{20}H_{10}$)	69.4 μ M
Pentaindeno Corannulene ($C_{50}H_{20}$)	69.4 μ M
$C_{26}H_{12}$	69.4 μ M
$C_{28}H_{14}$	69.4 μ M
$(C_{59}N)_2$	69.4 μ M

Table 8.2: Final concentrations of samples initially dissolved in 1:1 toluene:dichloromethane

Silver trifluoroacetate (AgTFA, Aldrich (Sigma-Aldrich), 98%) was dissolved in methanol to make a concentration of 1mM.

The sample solutions were mixed with the silver solution in a 1:1 v/v ratio, to give final concentrations of 500 μ M silver and half the concentration of the sample solutions – for most of the solutions this was 34.7 μ M. For C₈₄ the concentration was doubled, for reasons explained in the results section.

When two samples were mixed to form the hetero-dimers, the concentrations of the final sample dilutions were doubled. 0.5ml of the double concentrated sample solutions were mixed with 1ml of the silver solution, to give the same concentrations of each part as in the “one sample” solutions, usually 34.7 μ M for each sample, and 500 μ M for the silver. This also allowed the solvent ratio to stay constant at 1:1 DCM:Methanol.

For the reaction of C₆₀, anthracene and silver where C₆₀ and anthracene had not been reacted to form the complex, the C₆₀ was in the same concentration as in all other reactions, 34.7 μ M, the silver was also in the same concentration of 500 μ M, and anthracene was in excess of C₆₀, at a concentration of 70.2 μ M. Again, this mixture had the same solvent ratio as all the other reactions, of 1:1 DCM:Methanol.

Positive-ion and Negative-ion mode ESI-MS without Silver

As C₆₀A, C₆₀T and C₆₀P could be observed in ESI-MS without the addition of salts (chapter 6) the same ESI source conditions were tested on the other compounds. This method was compared to the method where sodium acetate is added to the solution to form the sodiated ion. For the sodium acetate method, isopropyl mono was used:

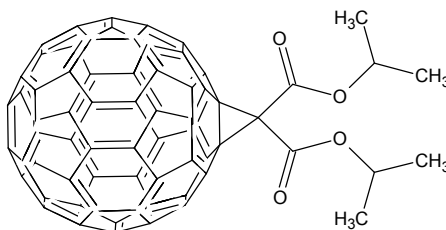


Figure 8.5: Structure of Isopropyl Mono

The positive and negative-ion mode method developed for the C₆₀PAH complexes was also tested on C₈₄ and (C₆₀)₂C₂₂H₁₄(C₆H₅)₂ (cis-bis[60]fullerene adduct of 6,13-diphenylpentacene).

Results

Positive-ion Mode Silver ESI with Fullerenes and Related Compounds

Initial experiments were performed on C₆₀. It was electrosprayed with a silver solution in order to optimise the conditions for silver attachment. The spectra show formation of a silver bound C₆₀ dimer, with various other permutations of C₆₀ bound with silver. An example spectrum is shown below:

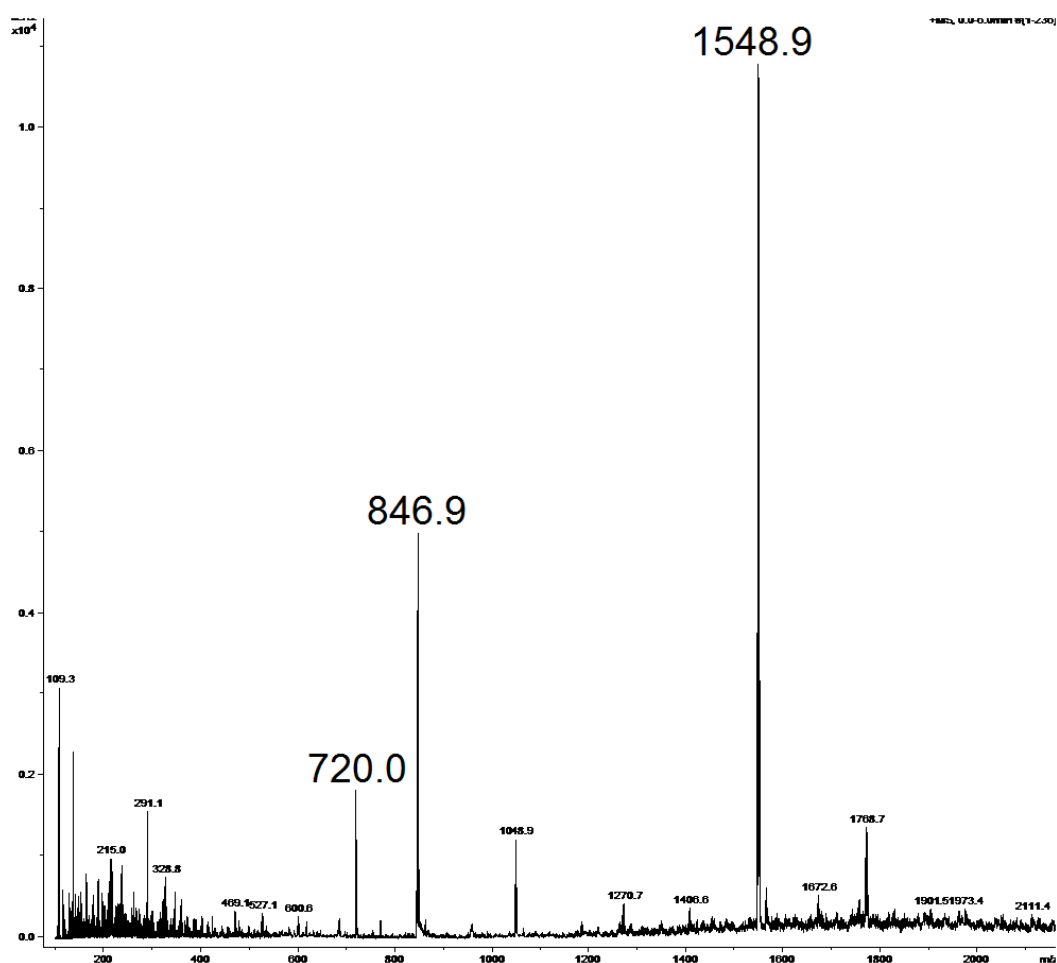


Figure: 8.6: Positive-ion mode ESI spectrum of C₆₀ with AgTFA

The peaks in the above spectrum have been identified and tabulated below.

m/z	Identification
109.3	Ag ⁺
720.0	C ₆₀ ⁺
846.9	[C ₆₀ AgH ₂ O] ⁺

1048.9	$[\text{C}_{60}\text{AgAgTFA}]^+$
1548.9	$[\text{C}_{60}\text{AgC}_{60}]^+$
1768.8	$[\text{C}_{60}\text{AgC}_{60}\text{AgTFA}]^+$

Table 8.3: Identification of the peaks in the C_{60} and AgTFA positive-ion mode ESI spectrum

Confirmation of the production of a silver bound C_{60} dimer came from study of the isotopic pattern and by obtaining an MS/MS spectrum of the peak:

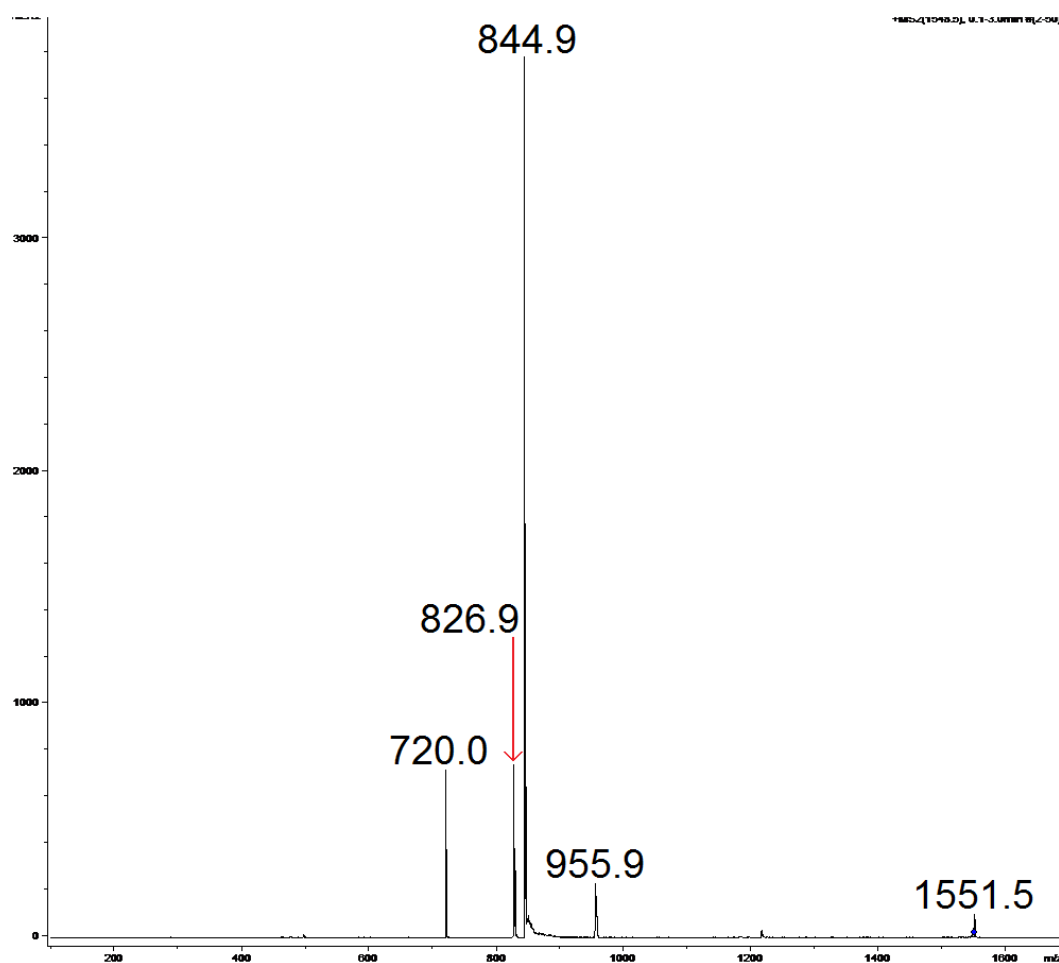


Figure 8.7: Positive-ion mode MS/MS spectrum of 1548.8

The peaks present in this spectrum are identified below:

m/z	Identification
844.9	$[\text{C}_{60}\text{AgH}_2\text{O}]^+$
826.9	$[\text{C}_{60}\text{Ag}]^+$
720.0	C_{60}^+

Table 8.4: Identification of peaks in the MS/MS spectrum of 1548.8

The peak at m/z 955.9 is of unknown origin, it could possibly be addition of trifluoroacetate to the $C_{60}AgH_2O$ complex. Addition of trifluoroacetate had been observed with other compounds; however, it was usually addition of an entire $AgTFA$ unit.

After successful production of a silver-bound C_{60} dimer had been achieved, the other compounds of interest were also electrosprayed individually with $AgTFA$. The resulting spectra were similar to the one obtained for C_{60} , in that dimers and other complexes with silver were observed.

A few example spectra are shown below:

$(C_{59}N)_2$ with $AgTFA$:

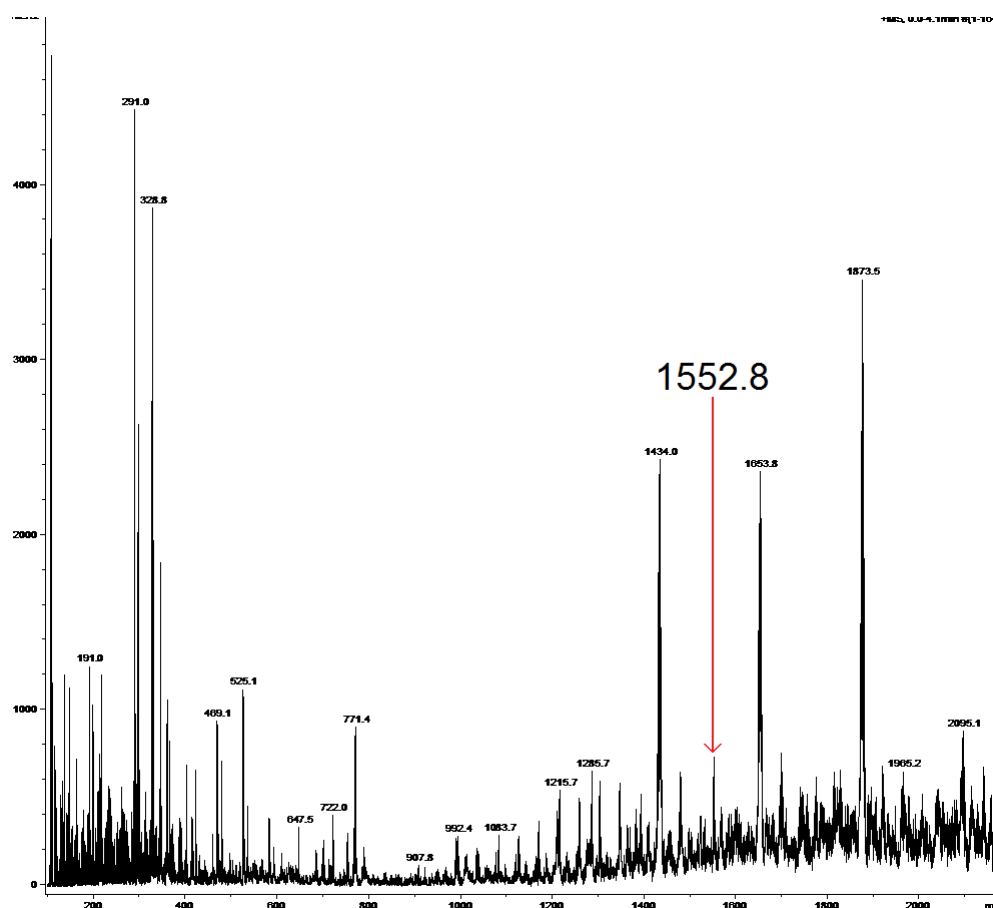


Figure 8.8: Positive-ion mode ESI spectrum of $(C_{59}N)_2$ with $AgTFA$

For $(C_{59}N)_2$ with $AgTFA$, the signal for the silver bound dimer of $C_{59}N$, at m/z 1552.8, is at a very low abundance and obscured by larger peaks. Enhancing the m/z region and simulating the isotopic pattern allows the confirmation of its production. The measured and simulated isotopic pattern is displayed below in the following figure:

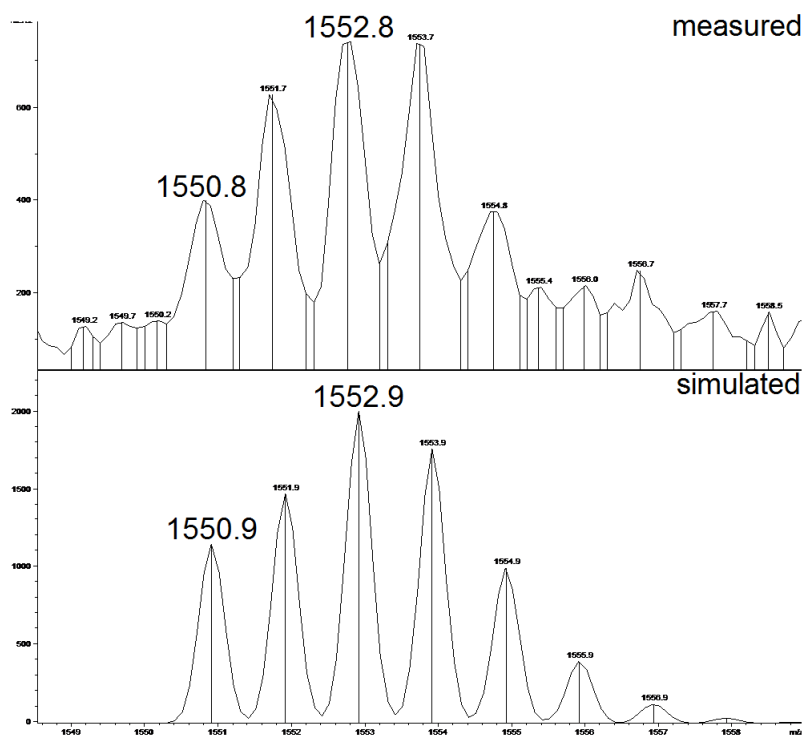


Figure 8.9: Measured, top, and simulated, bottom, isotopic pattern of $[(C_{59}N)_2Ag]^+$

Coronene ($C_{24}H_{12}$) with AgTFA:

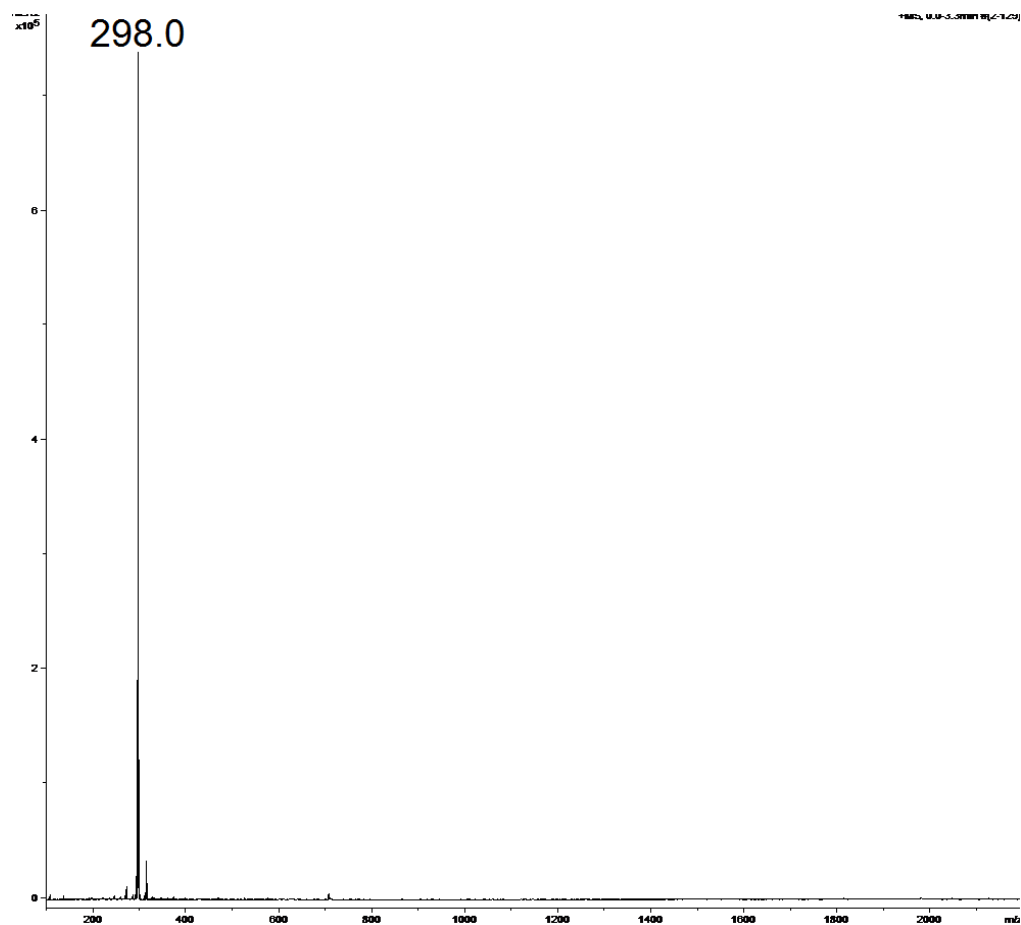


Figure 8.10: Positive-ion mode ESI mass spectrum of $C_{24}H_{12}$ with AgTFA

As can be seen above, the peak for $C_{24}H_{12}^+$ dominates the spectrum. Other peaks are present, including the silver bound homo-dimer, shown with the simulated isotopic pattern:

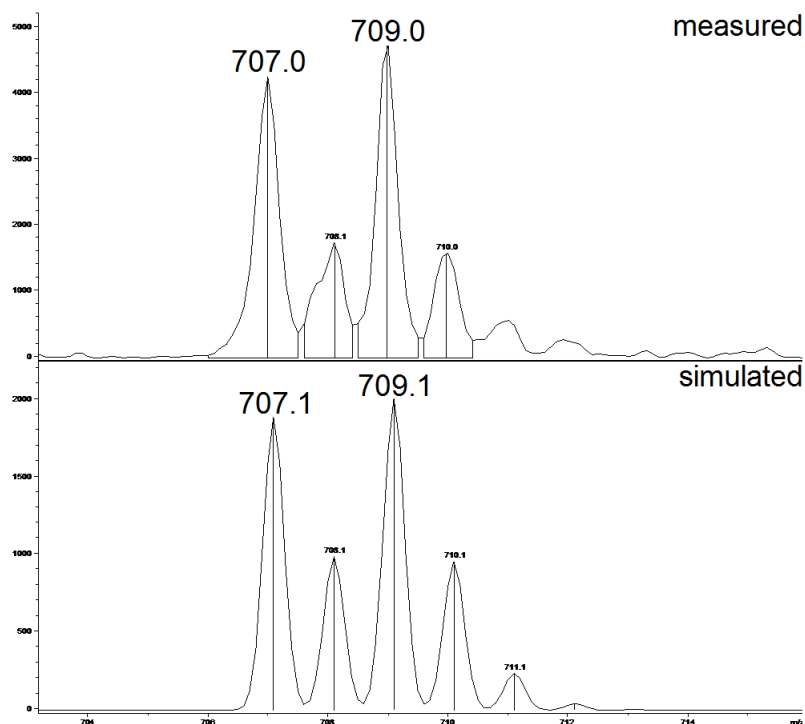


Figure 8.11: Measured, top, and simulated, bottom, isotopic pattern of $[(C_{24}H_{12})_2Ag]^+$

There is a clear match of the simulated isotopic pattern and the actual mass spectrum, the peak at m/z 707 therefore represents the formation of a silver bound $C_{24}H_{12}$ dimer.

For the majority of samples, the silver bound homo-dimer was produced using ESI-MS. In the case of C_{84} , however, it was very difficult to obtain any peaks for either C_{84} or the silver bound C_{84} dimer. In order to overcome this problem different concentrations of C_{84} were tested. When a peak was successfully created, the concentration of C_{84} was twice the standard concentration for the other experiments. When a signal was produced, it was at a much lower intensity when compared to the other compounds analysed. The positive-ion mode spectrum of C_{84} and AgTFA is shown below.

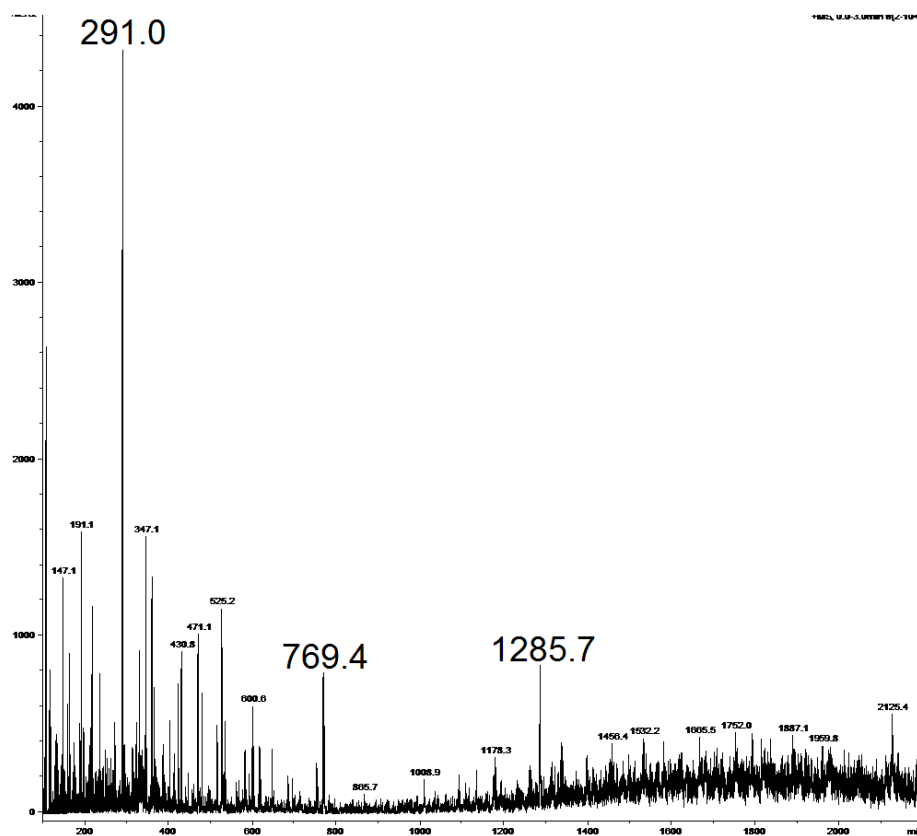


Figure 8.12: Positive-ion mode ESI spectrum of $(C_{84})_2Ag$

Enhancing the molecular ion region for C_{84} demonstrates the low signal-to-noise ratio of the molecular ion peak at m/z 1008:

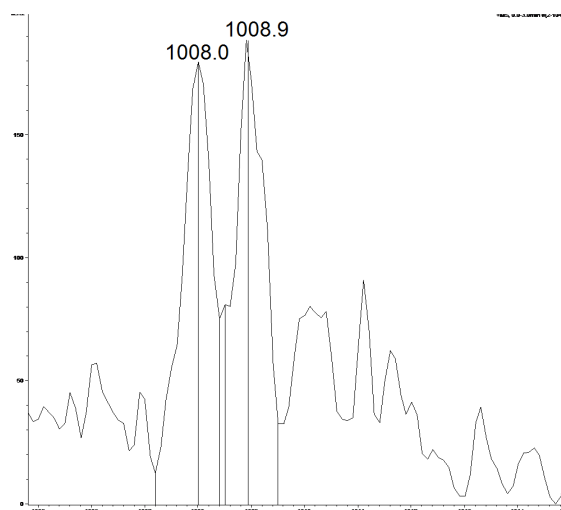


Figure 8.13: The molecular ion peak of C_{84} in the positive-ion mode ESI spectrum

Enhancing the m/z region of the silver bound dimer, at m/z 2125, also demonstrates the low signal-to-noise ratio. When compared to the simulated isotopic pattern for $[(C_{84})_2Ag]^+$, shown below the measured spectrum in figure 8.14, the difficulty in creating silver bound dimers of C_{84} becomes apparent:

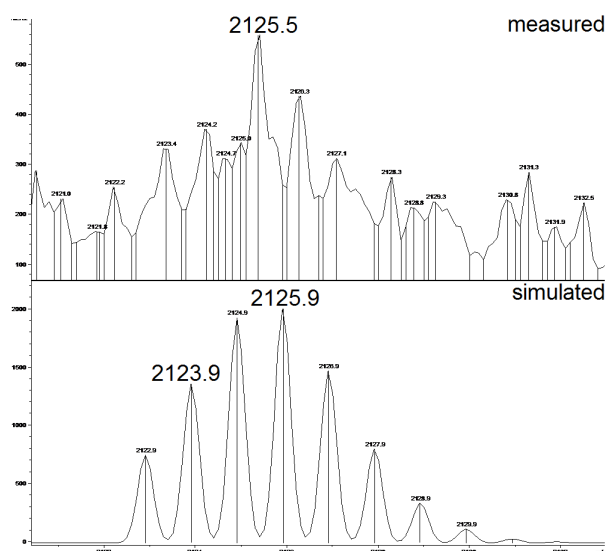


Figure 8.14: Measured, top, and simulated, bottom, isotopic pattern of $[(C_{84})_2Ag]^+$

Performing MS/MS experiments on the silver bound homo-dimers produced similar compounds to the MS/MS of the experiment with C_{60} shown previously. The MS/MS of $[(C_{84})_2Ag]^+$ is shown below:

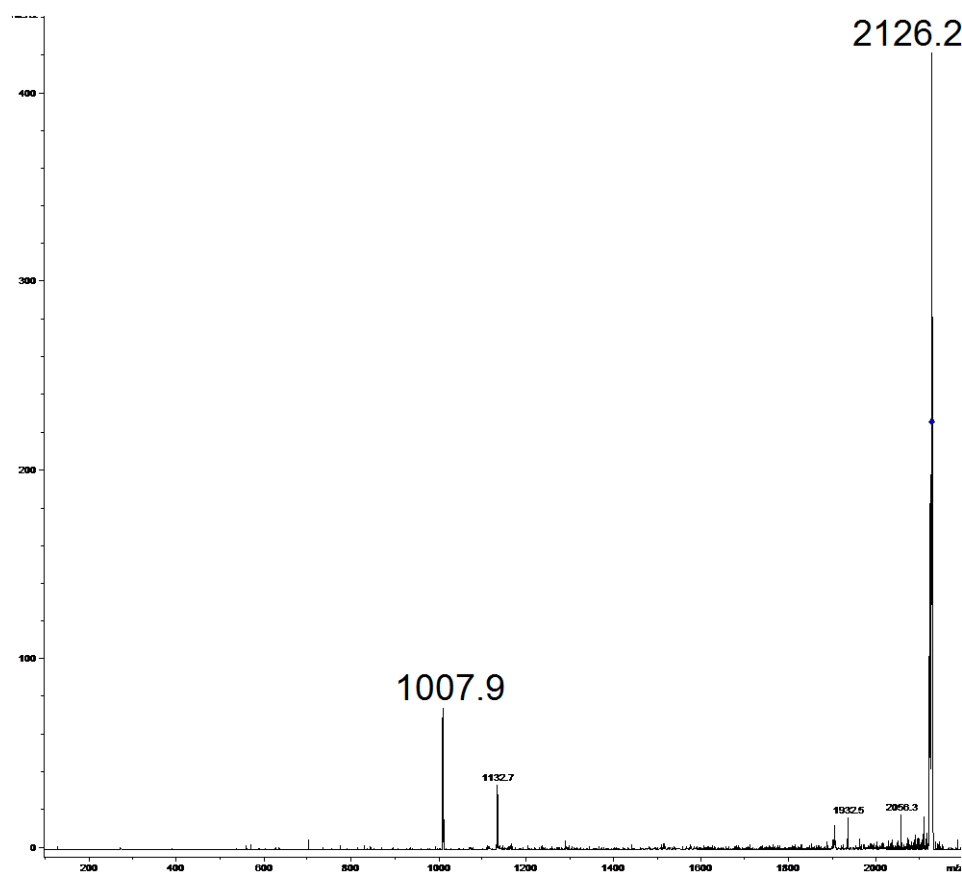


Figure 8.15: Positive-ion mode MS/MS spectrum of m/z 2125.1

Peaks present in the above spectrum:

m/z	Identification
1007.9	C_{84}^+
1132.7	$[C_{84}AgH_2O]^+$
2126.2	$[(C_{84})_2Ag]^+$

Table 8.5: Peaks from the MS/MS spectrum of m/z 2125.1

There is a very small peak at approximately the correct m/z for $[C_{84}Ag]^+$, but due to the very low intensity, it cannot be positively identified as this.

The fragmentation pattern observed here was seen throughout the MS/MS experiments of the silver bound homo-dimers. It is further confirmation that the gas-phase silver cation prefers to bind two ligands. Again water addition is apparent when one of the two initial ligands is lost through fragmentation.

Hetero-dimer formation

Once homo-dimers had been successfully formed and characterised, hetero-dimers were formed by spraying solutions of mixed compounds, with AgTFA. Two series of compounds were electrosprayed with the intention of evaluating relative silver binding affinities. Every possible combination of two compounds within the series was electrosprayed with AgTFA:

Series 1: C_{60} , C_{70} , C_{84} , $(C_{59}N)_2$

Successful formation and MS/MS of a hetero-dimer:

	C_{60}	C_{70}	C_{84}	$(C_{59}N)_2$
C_{60}		✓	✓	✓
C_{70}	✓		✓	✓
C_{84}	✓	✓		✗
$(C_{59}N)_2$	✓	✓	✗	

Table 8.6: Formation and MS/MS spectra of the hetero-dimers of series 1

For C_{84} and $(C_{59}N)_2$ formation of a hetero-dimer proved elusive. Additionally, the homo-dimers were not present. The experiment was repeated on several occasions without success. The lack of formation of a hetero-dimer could be due to the fact that neither C_{84} , nor $(C_{59}N)_2$ attach the silver cation in substantial quantities within the ESI source. The low

solubility of both compounds is also problematic, but was accounted for through the use of sufficiently high concentrations.

Some example spectra of the hetero-dimer formation are shown below:

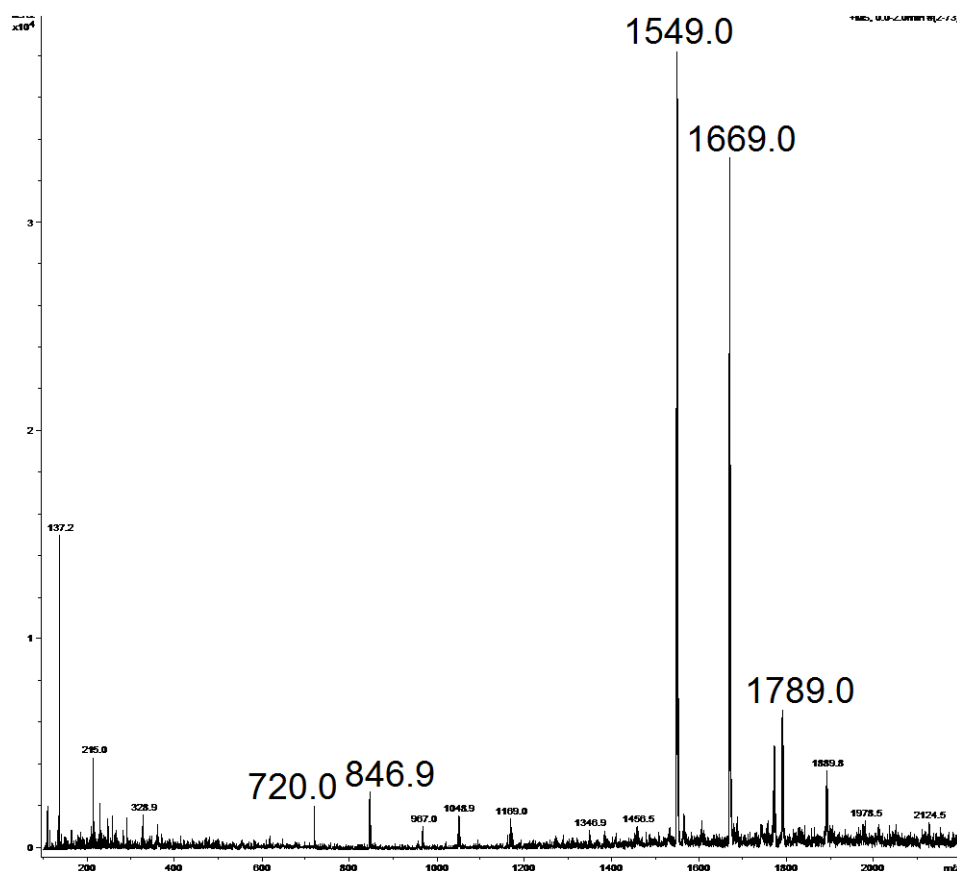


Figure 8.16: Positive-ion mode ESI spectrum of C_{60} , C_{70} and AgTFA

Peaks present and identified in the above spectrum are tabulated below:

m/z	Identification
720.1	C_{60}^+
846.9	$[C_{60}AgH_2O]^+$
967.0	$[C_{70}AgH_2O]^+$
1048.9	$[C_{60}AgAgTFA]^+$
1169.9	$[C_{70}AgAgTFA]^+$
1549.0	$[(C_{60})_2Ag]^+$
1669.0	$[C_{60}AgC_{70}]^+$
1789.0	$[(C_{70})_2Ag]^+$
1889.8	$[C_{60}AgC_{70}AgTFA]^+$

Table 8.7: Peaks from the positive-ion mode ESI spectrum of C_{60} , C_{70} and AgTFA

As can be observed in the “normal” ESI mass spectrum, it appears that C_{60} has the greater silver affinity, due to the greater intensity of the silver bound C_{60} dimer when compared to the C_{70} containing complex peaks. However, as different compounds appear in different intensities dependant on conditions inside the source, MS/MS of the hetero-dimer is necessary to determine which fullerene truly has the larger silver binding affinity.

DCTB-MALDI-MS was also performed on mixed solutions of the fullerenes with silver, to provide a comparison to ESI. The fullerenes were mixed as follows: C_{60} and C_{70} , C_{60} and C_{84} , C_{70} and C_{84} , and C_{60} , C_{70} and C_{84} . The resulting spectra are below:

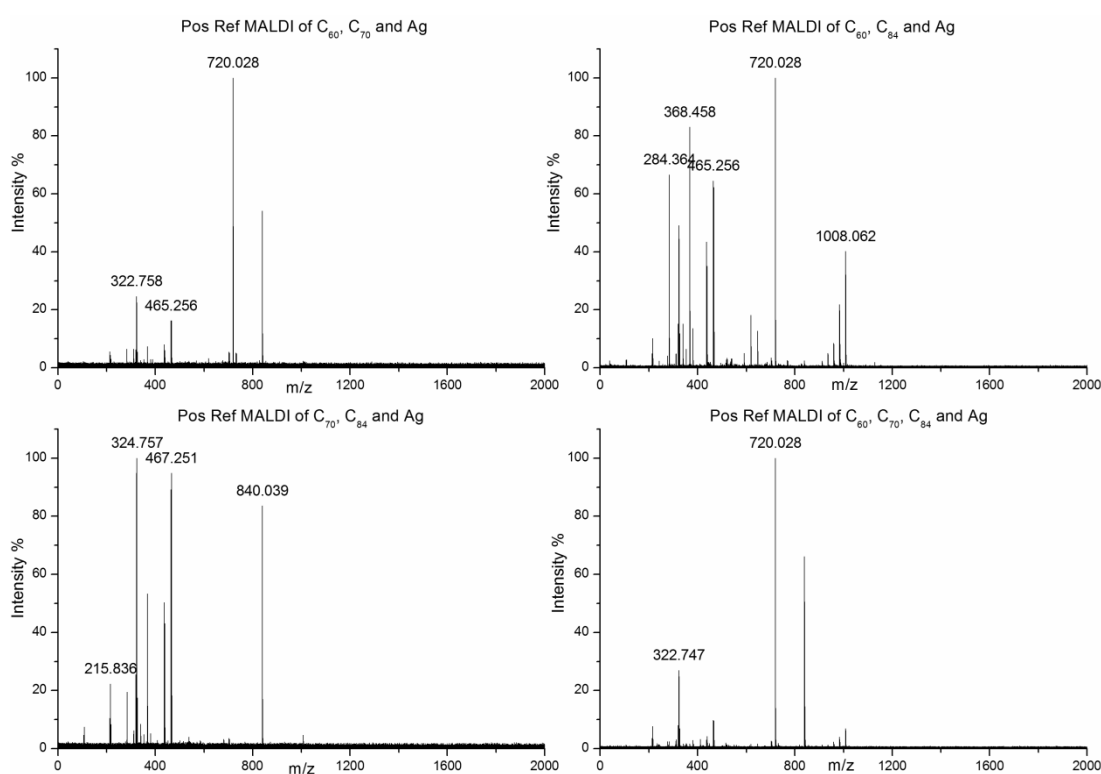


Figure 8.17: Positive-ion mode DCTB-MALDI spectra of fullerene combinations with AgTFA. The dominant peaks in all spectra are those of the bare fullerene ions. Enhancing the m/z region of the respective dimers shows the lack of formation of the silver bound dimers within the MALDI source:

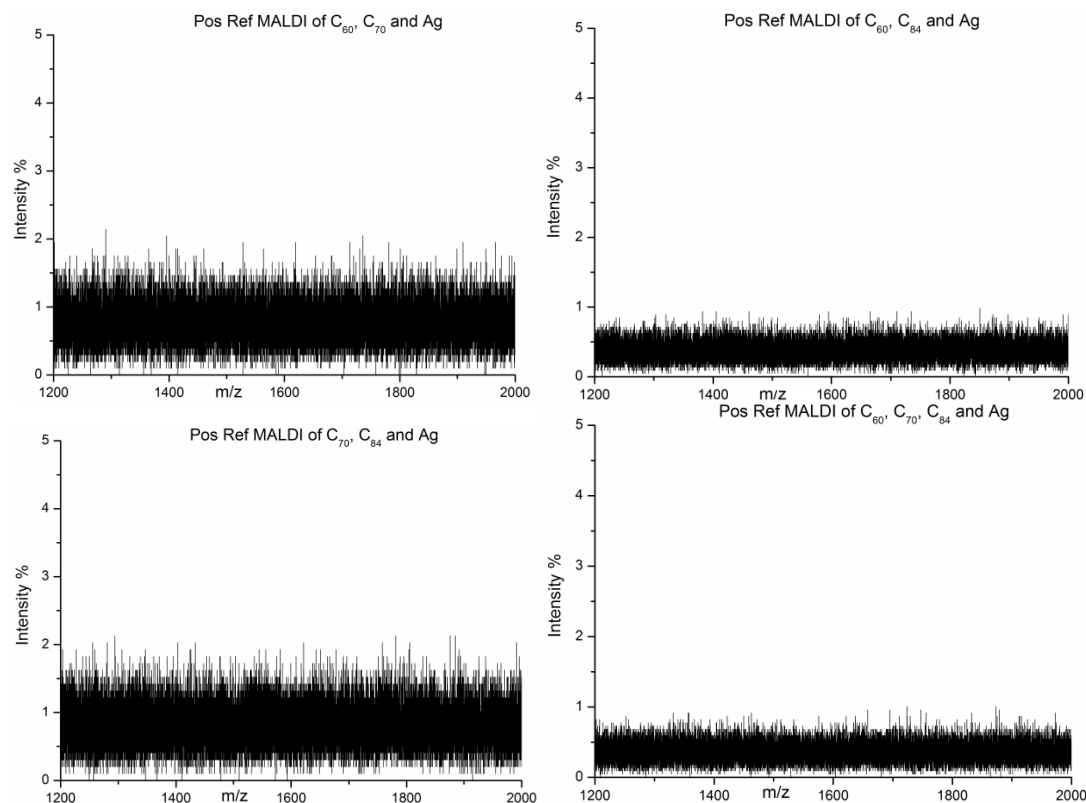


Figure 8.18: Enhancement of the $[\text{Fullerene}_A\text{-Ag-Fullerene}_B]^+$ m/z region of the DCTB-MALDI spectra of fullerenes and AgTFA

Contrasting the DCTB-MALDI-MS and ESI-MS spectra of the fullerene mixtures with silver, it becomes apparent how important the conditions in the ion source are for the formation of the silver bound dimers. Adjusting the right conditions in the electrospray creates the ideal environment in which these complexes are stabilised.

The second series of compounds being analysed for formation of silver bound hetero-dimers are small, non-caged potential fullerene precursors. C_{60} was also analysed in this series, to provide a link to the first series.

Series 2: C_{60} , Coronene ($C_{24}H_{12}$), $C_{20}H_{10}$, $C_{26}H_{12}$, $C_{28}H_{14}$

Successful formation and MS/MS of a hetero-dimer:

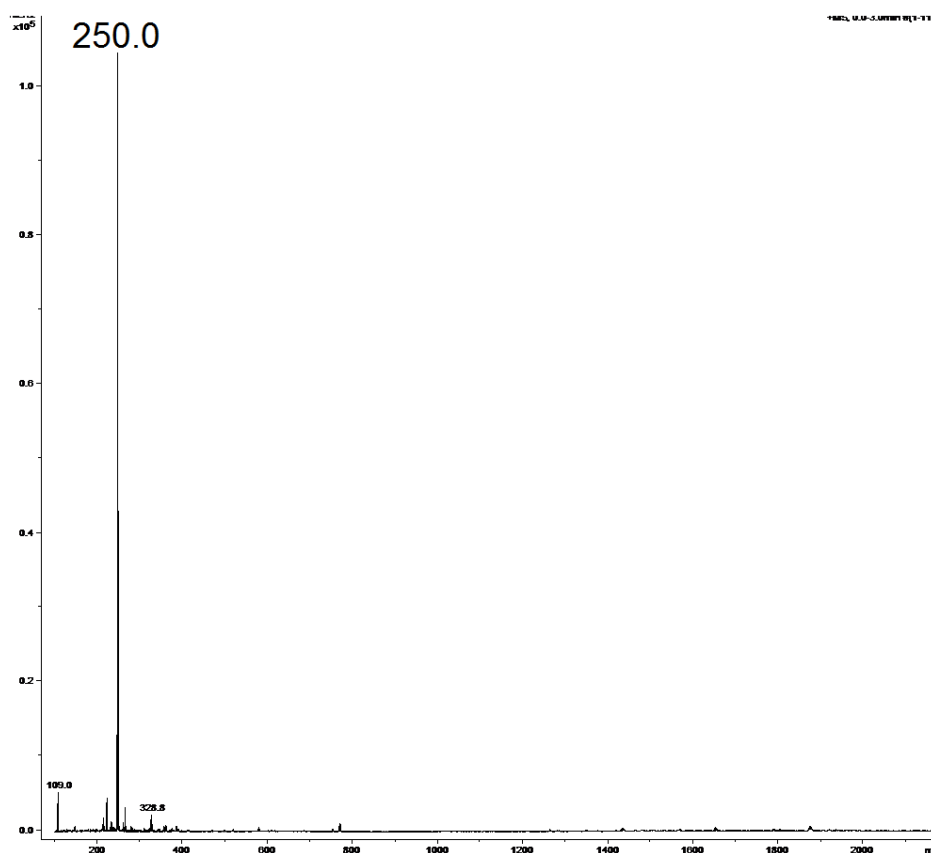
	C_{60}	$C_{24}H_{12}$	$C_{20}H_{10}$	$C_{26}H_{12}$	$C_{28}H_{14}$
C_{60}		✘	✘	✓	✓
$C_{24}H_{12}$	✘		✘	✓	✓

$C_{20}H_{10}$	x	x		x	x
$C_{26}H_{12}$	✓	✓	x		✓
$C_{28}H_{14}$	✓	✓	x	✓	

Table 8.8: Formation and MS/MS spectra of the hetero-dimers of series 2

As can be seen from the above table, $C_{20}H_{10}$ did not form any hetero-dimers with any other sample. A possible explanation is that the silver affinity of the larger compounds was much higher, as there was always formation of the silver bound homo-dimer of the other species in solution when $C_{20}H_{10}$ was present. When electrosprayed with just silver, silver bound dimers of $C_{20}H_{10}$ did form, however, at a very low intensity. If, as with C_{84} , a stronger concentration of sample was required, this could not be tested as there was not enough material supplied for additional experiments.

The full spectrum is displayed below. The $C_{20}H_{10}$ peak dominates the spectrum; this was the case for all of the spectra of these smaller compounds when electrosprayed with silver.

Figure 8.19: Full positive-ion mode ESI spectrum of $C_{20}H_{10}$ with AgTFA

Enhancing the m/z region in which $[(C_{20}H_{10})_2Ag]^+$ was assumed, and simulating the isotopic pattern, it can be seen that the dimer signal is very weak and probably also contains contributions from unwanted ions.

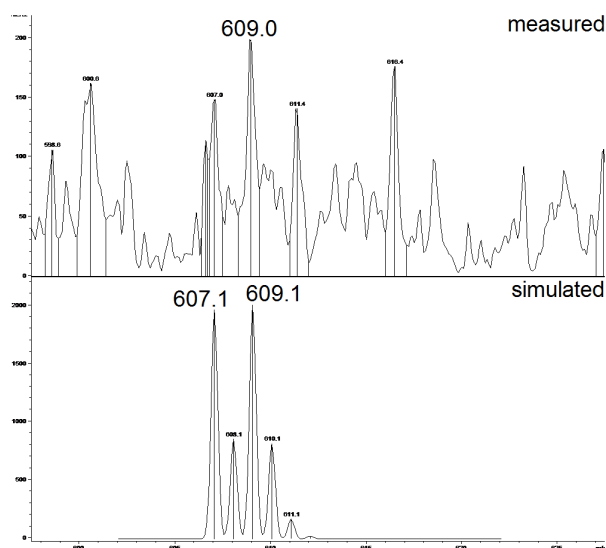


Figure 8.20: Measured, top, and simulated isotopic pattern, bottom, of $[(C_{20}H_{10})_2Ag]^+$

MS/MS of this peak produced the following spectrum:

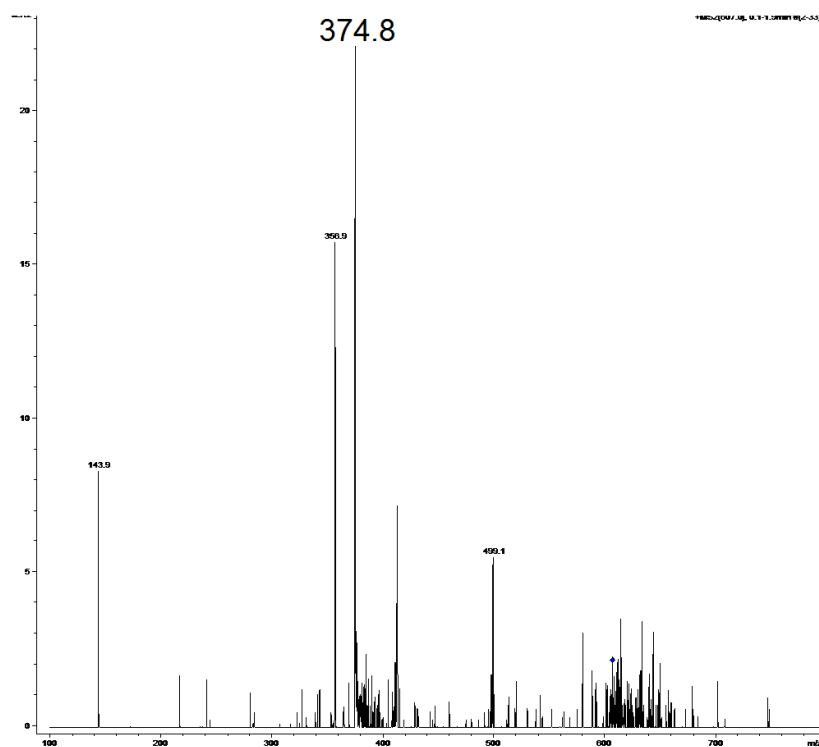


Figure 8.21: MS/MS positive-ion mode ESI spectrum of $[(C_{20}H_{10})_2Ag]^+$

The important peaks present in this spectrum are: m/z 356.9 identified as $[C_{20}H_{10}^{107}Ag]^+$, and m/z 374.8, identified as $[C_{20}H_{10}^{107}AgH_2O]^+$. The intensity of the fragment peaks are small and give an indication of how little of the silver-bound dimer is produced initially.

An example spectrum of a successful hetero-dimer formation for series 2 is below.

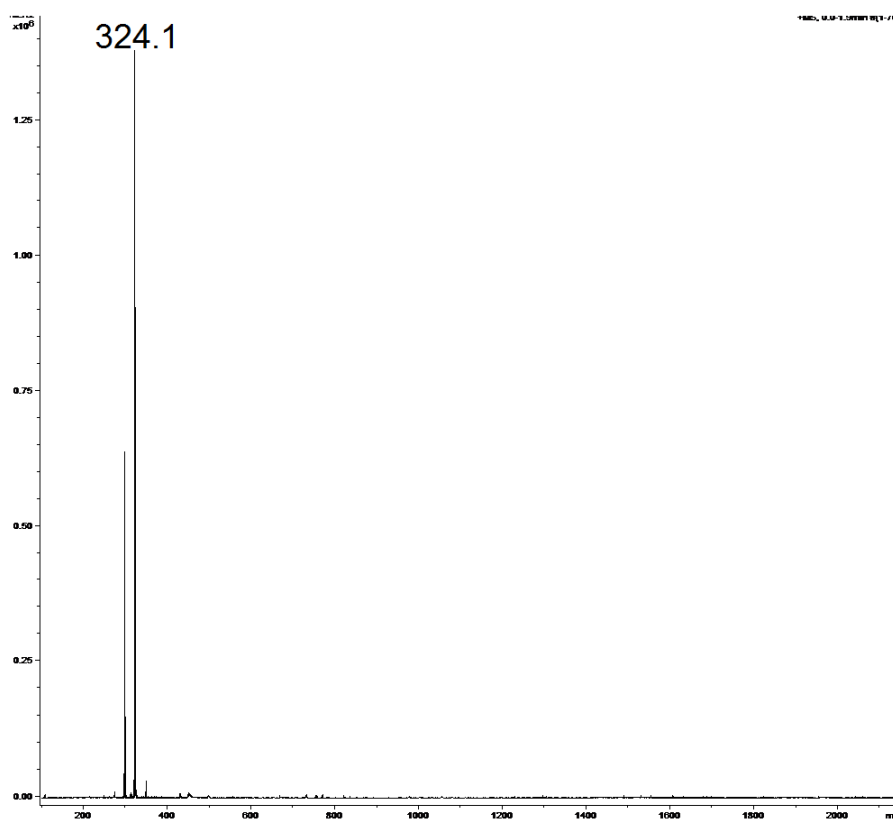


Figure 8.22: Positive-ion mode ESI spectrum of $C_{24}H_{12}$ (coronene), $C_{26}H_{12}$ and AgTFA. $C_{24}H_{12}$ and $C_{26}H_{12}$ dominate the spectrum. However, there was dimer formation and both homo-dimers and the hetero-dimer were clearly seen. The measured and simulated isotopic patterns of the hetero-dimer are shown below:

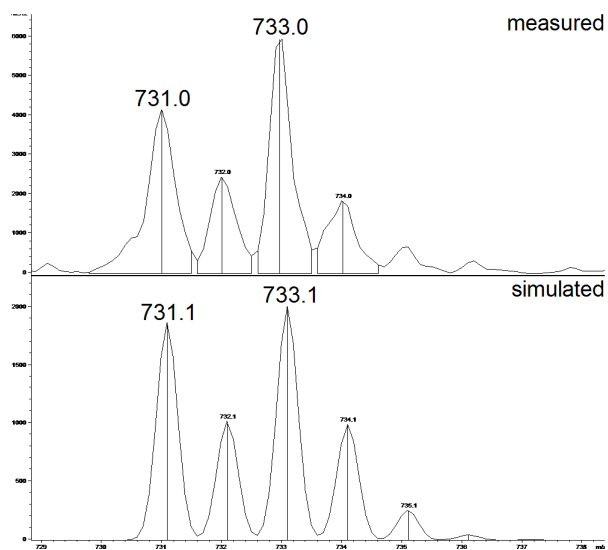


Figure 8.23: Measured, top, and simulated, bottom, isotopic pattern of $[C_{24}H_{12}AgC_{26}H_{12}]^+$

Collision Induced Dissociation

MS/MS experiments were performed on the silver bound dimers to dissociate them into silver bound monomers. From the relative peak intensities of the monomeric fragment ions, it was intended to evaluate the relative binding affinities, using the kinetic method.

Because of the water addition to the fragment ions, it is important to include the intensities of the water adducts in the calculations, as their abundance is part of the initial intensity of the monomeric fragment ion. The water addition occurs after formation through dissociation of the dimeric precursor.

Series 1: C_{60} , C_{70} , C_{84} , $(C_{59}N)_2$, m/z values of the dimers:

	C_{60}	C_{70}	C_{84}	$(C_{59}N)_2$
C_{60}		1669	1836	1550
C_{70}	1669		1957	1668
C_{84}	1836	1957		*
$(C_{59}N)_2$	1550	1668	*	

Table 8.9: m/z values of the hetero-dimers of series 1

Series 2: C_{60} , Coronene ($C_{24}H_{12}$), $C_{26}H_{12}$, $C_{28}H_{14}$, m/z values of the dimers:

	C_{60}	$C_{24}H_{12}$	$C_{26}H_{12}$	$C_{28}H_{14}$
C_{60}		*	1153	1178.9
$C_{24}H_{12}$	*		733	759
$C_{26}H_{12}$	1153	733		783
$C_{28}H_{14}$	1178.9	759	783	

Table 8.10: m/z values of the hetero-dimers of series 2

$C_{20}H_{10}$ is intentionally excluded from series 2, as a dimer could not be formed with any of the other samples, as discussed above.

Relative Silver Binding Affinity

By using one sample from each set of samples as a reference for which the silver ion affinity was set to zero, the silver binding affinities relative to this reference can be calculated.

For series 1, the reference sample was C_{60} . For series 2, the reference sample was $C_{28}H_{14}$.

Also for series 2, C_{60} would have been the preferred reference sample; however, as it did

not form a hetero-dimer with $C_{24}H_{12}$, the calculation would not have been possible. $C_{28}H_{14}$ has formed hetero-dimers with all of the other compounds in the series, and was selected as the reference compound.

Series 1:

$[C_{60}\text{-Ag-X}]^+$ dissociation gave the following intensities:

X	Fragment Intensities					
	$[C_{60}]^+$	$[C_{60}\text{Ag}]^+$	$[C_{60}\text{AgH}_2\text{O}]^+$	$[X]^+$	$[X\text{Ag}]^+$	$[X\text{AgH}_2\text{O}]^+$
C_{70}	10.27	4.86, 2.73	18.89, 10.50	30.30	12.05, 9.18	100, 56.21
C_{84}	2.29	0.49, 0.43	4.81, 3.38	100	0.68, 1.18	60.61, 54.06
$C_{59}\text{N}$	11.50	0.24, 0	1.64, 0	16.99	6.21, 5.50	57.11, 53.53

Table 8.11: Fragment intensities of series 1

The intensities were recorded of the lowest carbon isotope peak, and as percentages of the dominant peak set at 100%. For peaks containing silver, the intensities recorded are for the ^{107}Ag containing peak and the ^{109}Ag peak, with the lowest carbon isotope.

For $C_{59}\text{N}$ and C_{60} , the peaks often overlapped. For the peaks containing C_{60} and a ^{109}Ag or $C_{59}\text{N}$ and a ^{107}Ag , which would be at approximately the same m/z value, the isotope pattern in separate peaks were observed. For the overlapping peaks, it was assumed that the peaks belonged to the $C_{59}\text{N}^{107}\text{Ag}$ containing fragments, as the $C_{60}^{107}\text{Ag}$ peaks were very small, and the $C_{59}\text{N}^{109}\text{Ag}$ containing peaks had similar intensities to the peaks under study.

Series 2:

$[C_{28}H_{14}\text{-Ag-X}]^+$ dissociation gave the following intensities:

X'	Fragment Intensities					
	$[C_{28}H_{14}]^+$	$[C_{28}H_{14}\text{Ag}]^+$	$[C_{28}H_{14}\text{AgH}_2\text{O}]^+$	$[X']^+$	$[X'\text{Ag}]^+$	$[X'\text{AgH}_2\text{O}]^+$
C_{60}	100	4.26, 4.28	27.55, 47.32	9.01	0.31, 0.63	1.76, 6.11
$C_{24}H_{12}$	70.61	4.98, 14.64	21.94, 100	74.66	1.71, 2.33	8.25, 25.27
$C_{26}H_{12}$	67.66	19.20, 23.54	24.97, 89.70	100	6.49, 11.77	23.14, 83.94

Table 8.12: Fragment intensities of series 2

In order to use these intensities to establish the relative silver binding affinities, the kinetic method must be employed.

$$\Delta(\Delta Ag^+) = \ln \frac{[M_1 Ag]^+}{[M_2 Ag]^+} \cdot RT_{eff}$$

T_{eff} is assumed to be 555K as explained previously. M_1 is the reference sample, and M_2 the unknown. R is the gas constant, $8.314\ 472\ J\ K^{-1}\ mol^{-1}$

$[M_1 Ag]^+$ and $[M_2 Ag]^+$ refers to all the related fragmentation peaks, including the signals for the water addition. The total intensities are listed below:

Series 1:

X	C ₆₀ fragments	X fragments	$\Delta Ag^+ / J\ mol^{-1} *$	$\Delta Ag^+ / Kcal\ mol^{-1} *$
C ₇₀	47.25	207.74	-6833.36	-1.633
C ₈₄	11.4	216.53	-13585.72	-3.246
C ₅₉ N	13.38	139.34	-10812.57	-2.583

Table 8.13: Total fragment intensities of series 1 (*relative to C₆₀ set at 0)

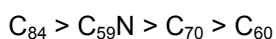
Series 2:

X'	C ₂₈ H ₁₄ fragments	X' fragments	$\Delta Ag^+ / J\ mol^{-1} *$	$\Delta Ag^+ / Kcal\ mol^{-1} *$
C ₆₀	183.41	17.82	10758.33	2.570
C ₂₄ H ₁₂	212.17	112.22	2939.12	0.702
C ₂₆ H ₁₂	225.07	225.34	-5.53	-1.32 x 10 ⁻³

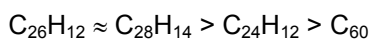
Table 8.14: Total fragment intensities of series 2 (*relative to C₂₈H₁₄ set at 0)

The values for the relative silver affinities may not be correct (T_{eff} etc); however, a qualitative silver-ion affinity can be obtained from the study of the total fragment intensities.

For series 1:



For series 2:



The affinity order in these series can be checked by the study of the MS/MS experiments with the remaining series members.

For example, series 1: MS/MS spectra of C₇₀ with C₈₄ and C₅₉N are shown below:

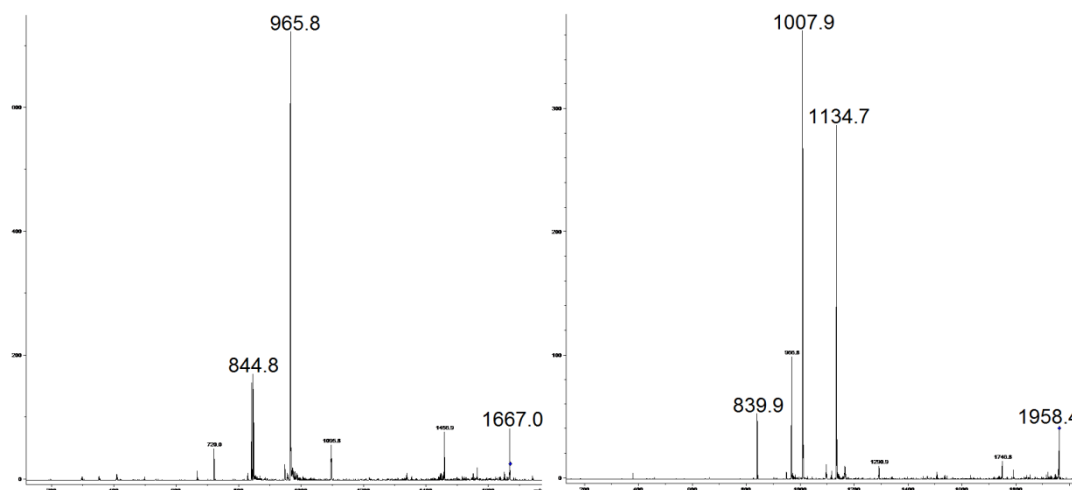
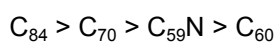


Figure 8.24: MS/MS of $[C_{70}AgC_{59}N]^+$, left, MS/MS of $[C_{70}AgC_{84}]^+$, right

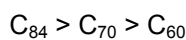
For $[C_{70}AgC_{59}N]^+$, the C_{70} containing peaks can be observed as being far more intense than the peaks for $C_{59}N$. This is at odds with the obtained affinity order from the above measurements. From the present experiment, the relative silver-ion binding affinities for series 1 would follow the following order:



Unfortunately, as C_{60} and $C_{59}N$ differ by two mass units and as the silver isotopes also differ by two mass units, it follows that combinations of all four species can lead to overlap of different species of the same nominal mass, which cannot be resolved with the present ion trap. In fact, for the combination of C_{60} and $C_{59}N$ with the two silver isotopes both mixed silver-bound hetero-dimers overlap with ions of other composition but of same nominal mass: for instance: at m/z 1549 $[C_{60}^{107}AgC_{59}N]^+$ overlaps with $[C_{60}^{109}AgC_{60}]^+$ and at m/z 1551 $[C_{60}^{109}AgC_{59}N]^+$ overlaps with $[C_{59}N^{107}AgC_{59}N]^+$. However, the ion of $[C_{60}^{107}AgC_{60}]^+$ at m/z 1549 cannot be contributed to by any $C_{59}N$ containing ions and since it was very low in abundance, it was thought that $C_{59}N$ would be the main contributor to the overlapping ions. In the hetero-dimer with C_{70} , $[C_{59}N^{107}AgC_{70}]^+$ and $[C_{60}^{109}AgC_{70}]^+$ overlap at m/z 1669. Unfortunately, $[C_{59}N^{109}AgC_{70}]^+$ cannot be contributed to by any C_{60} containing ions, but is too low in abundance to be studied.

In summary, it must be concluded that the experiments with $C_{59}N$ were not successful. A possible reason for this is that there may not have been enough $C_{59}N$ in solution. The $(C_{59}N)_2$ dimer is most likely less soluble than C_{60} due to its size and it would have to dissociate initially to provide the monomer before silver bound dimers could be formed. The

possible ion $[(C_{59}N)_2AgC_{60}]^+$ is beyond the mass range of the instrument. However, the positive outcome of the above experiments is the establishment and confirmation of the Ag^+ ion affinity order of the pure fullerenes:



Series 2: MS/MS spectra of $C_{26}H_{12}$ with C_{60} and $C_{24}H_{12}$:

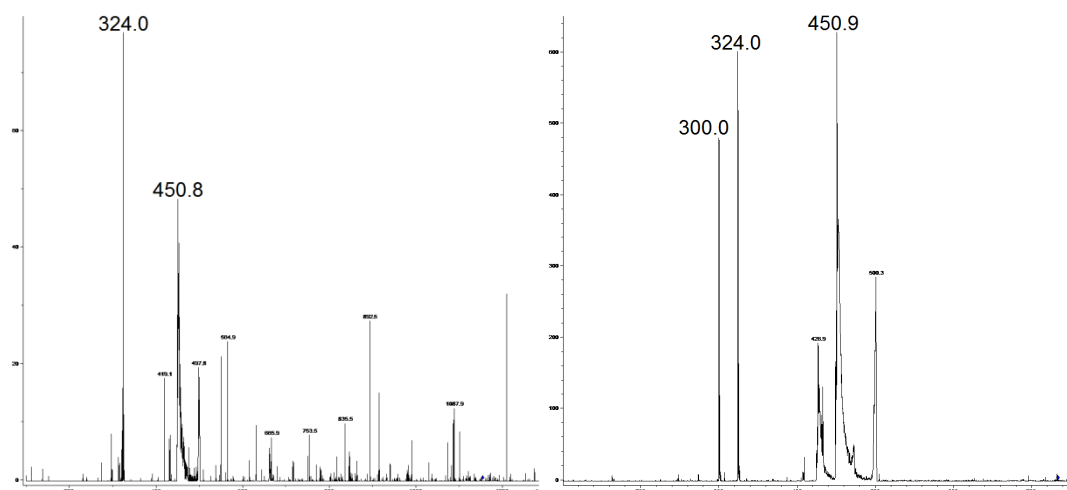


Figure 8.25: MS/MS of $[C_{26}H_{12}AgC_{60}]^+$, left and $[C_{26}H_{12}AgC_{24}H_{12}]^+$, right

In the case of $C_{26}H_{12}$ electrosprayed with C_{60} and silver, the only fragments produced relate to $C_{26}H_{12}$ when MS/MS is being performed on the silver bound hetero-dimer. For $C_{26}H_{12}$ and $C_{24}H_{12}$, it can be observed that the peak intensities are similar, with the $C_{26}H_{12}$ peaks being slightly higher in intensity, confirming its higher silver-ion affinity.

It could be argued that the calculations relative to C_{60} would give inaccurate results, due to the dissimilarity of C_{60} to the remaining compounds within the series. However, it is clear that qualitatively C_{60} has a smaller silver-ion affinity compared to $C_{24}H_{12}$, $C_{26}H_{12}$ and $C_{28}H_{14}$.

C_{60} PAHs and Silver

Working along the same principles as for the fullerenes and smaller organic compounds studied, it was thought to electrospray the synthesized C_{60} PAHs with silver and calculate the relative silver binding affinity of the polyaromatic hydrocarbons using C_{60} as the reference sample. As has been previously described in the introduction to this chapter, ESI-MS has been employed to study the relative silver binding affinity of polyaromatic hydrocarbons. It was hoped that silver would insert between the C_{60} and the polyaromatic hydrocarbon and

that MS/MS experiments of the $[\text{C}_{60}\text{-Ag-PAH}]^+$ complex would result in $[\text{C}_{60}\text{-Ag}]^+$ and $[\text{PAH-Ag}]^+$ fragments.

The samples analysed were the synthesised C_{60}A , C_{60}T and C_{60}P from chapter 5, $\text{C}_{60}\text{C}_8\text{H}_8$ from the University of Crete, and $(\text{C}_{60})_2\text{C}_{22}\text{H}_{12}(\text{C}_6\text{H}_5)_2$ from the University of New Hampshire. Example spectra of the compounds electrosprayed with AgTFA are below, starting with C_{60}A and AgTFA:

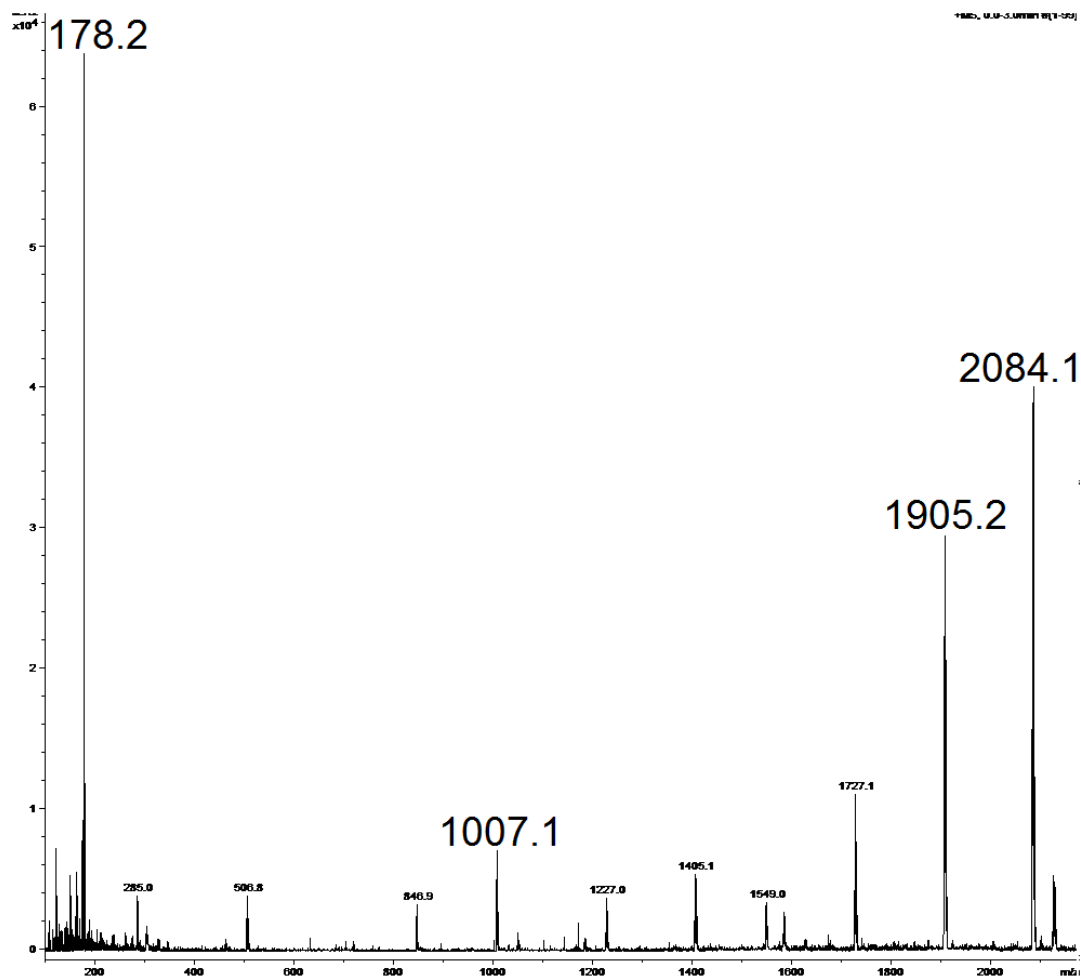


Figure 8.26: Positive-ion mode ESI spectrum of C_{60}A with AgTFA

The spectrum of C_{60}A plus AgTFA has many peaks present which can be attributed to the following:

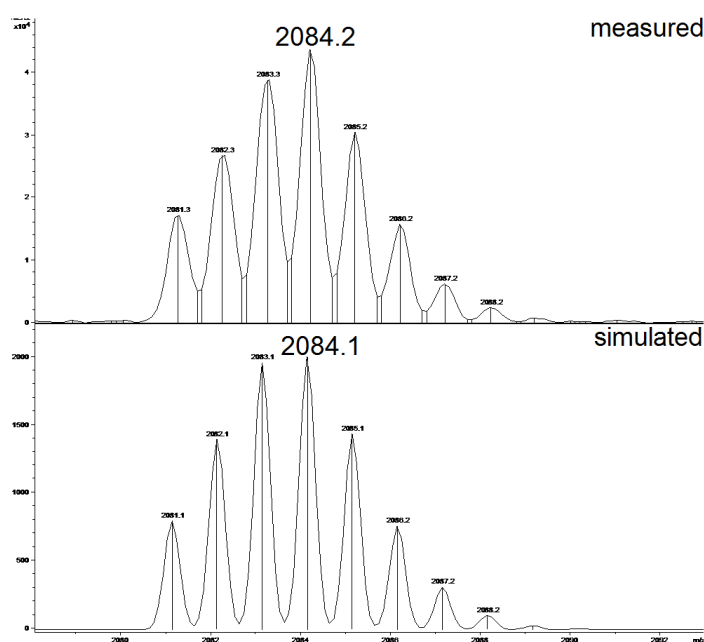
m/z	Identification
846.9	$[\text{C}_{60}\text{AgH}_2\text{O}]^+$
1007.1	$[\text{C}_{60}\text{-Ag-A}]^+$
1227.0	$[(\text{C}_{60}\text{A})\text{AgTFA}]^+$

1405.1	$[(C_{60}A_2)AgTFA]^+$
1549.0	$[(C_{60})_2Ag]^+$
1727.1	$[(C_{60}A_2)Ag]^+$
1905.2	$[(C_{60}A)_2Ag]^+$
2084.1	$[(C_{60}A)Ag(C_{60}A_2)]^+$

Table 8.15: Table of peaks for the ESI spectrum of $C_{60}A$ with AgTFA

All peaks present are related to $C_{60}A$ complexing with AgTFA. There is also the presence of $C_{60}A_2$, which was not seen in the MALDI spectra. Note that for all ions silver has acquired two ligands. Proof that the silver has inserted as: $[C_{60}-Ag-A]^+$ comes from the observation that this ion cannot attach an additional water molecule, as observed with $[C_{60}AgH_2O]^+$.

Confirmation of the peak identity comes from MS/MS experiments, and study of the isotopic pattern. The simulated isotopic pattern of $[(C_{60}A)Ag(C_{60}A_2)]^+$ is shown below the measured mass spectrum, and demonstrates an almost exact match:

Figure 8.27: Measured, top, and simulated, bottom, isotopic pattern of $[(C_{60}A)Ag(C_{60}A_2)]^+$

DCTB-MALDI-MS was also performed on the synthesized $C_{60}PAH$ compounds with silver, to see if a comparable result could be found:

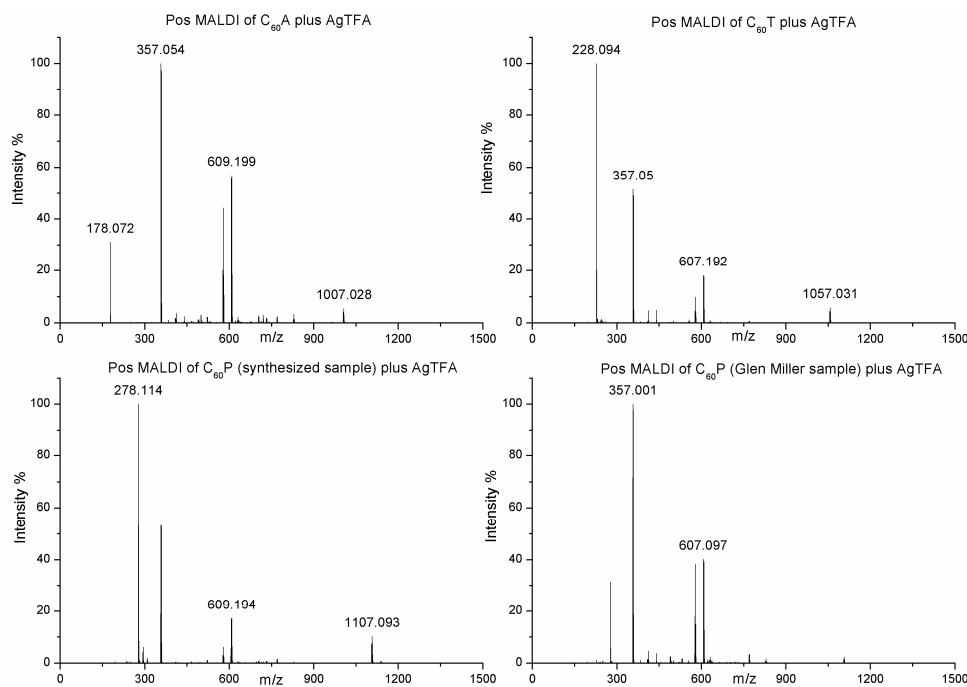


Figure 8.28: DCTB-MALDI of the $C_{60}PAH$'s with AgTFA

Enhancement of the m/z region of the respective $[C_{60}PAH-Ag]^+$ complexes demonstrates their formation:

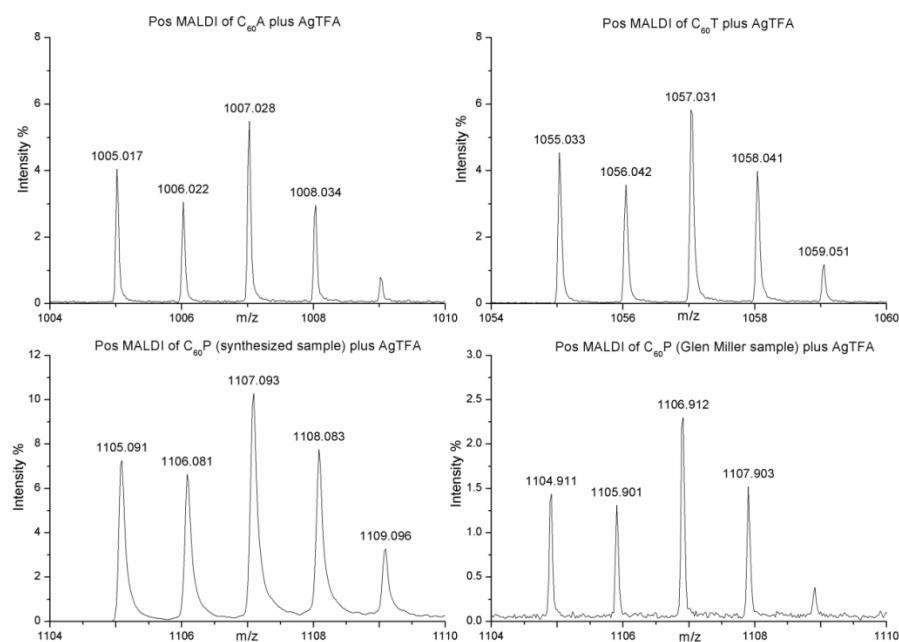


Figure 8.29: The m/z regions of $[C_{60}PAH-Ag]^+$ complexes

As can be seen from the MALDI spectra, there is addition of one silver per $C_{60}PAH$ molecule. There is no dimer formation as can be seen in the ESI spectra. Conditions within the ESI source are clearly more favourable for promoting addition of silver to the compounds.

The ESI spectrum of $C_{60}C_8H_8$ and AgTFA is below:

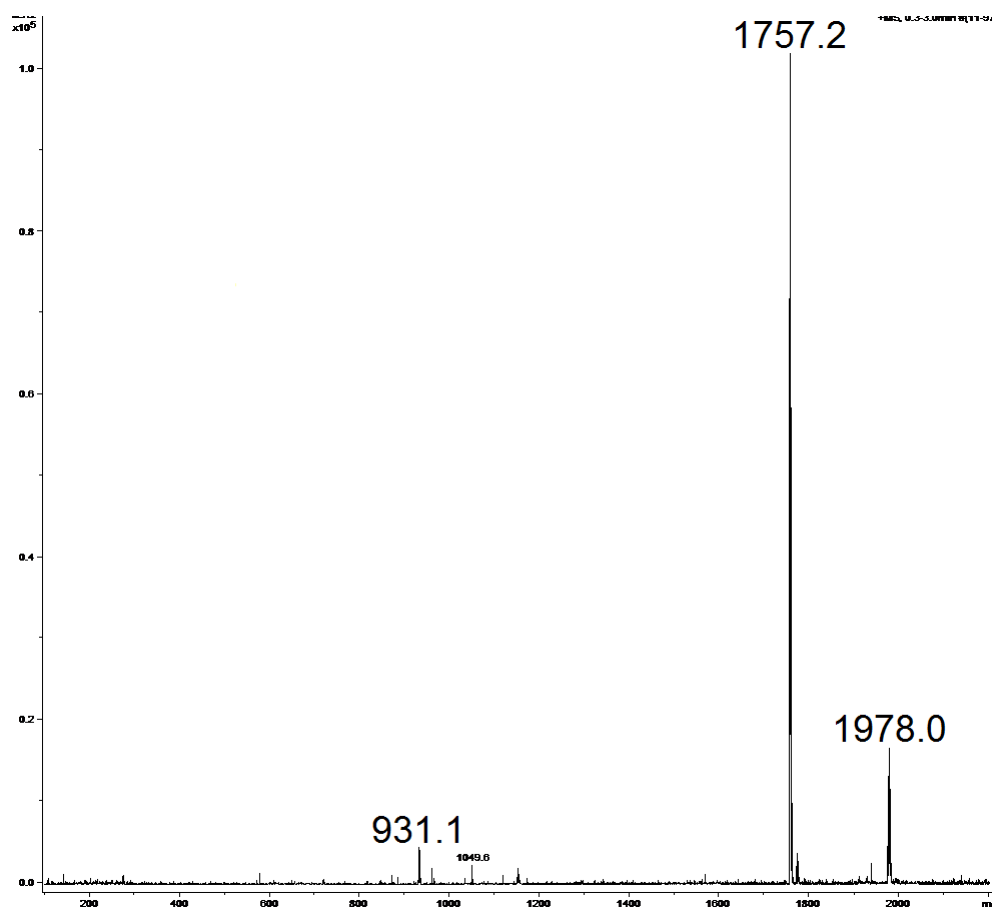


Figure 8.30: Positive-ion mode ESI spectrum of $C_{60}C_8H_8$ and AgTFA

Due to this sample being purified after synthesis, there are fewer peaks present than for the samples synthesized here. They can be identified as:

m/z	Identification
931.1	$[C_{60}C_8H_8Ag]^+$
1757.2	$[(C_{60}C_8H_8)_2Ag]^+$
1978.0	$[(C_{60}C_8H_8)_2Ag_2TFA]^+$

Table 8.16: Peaks from the ESI spectrum of $C_{60}C_8H_8$ and AgTFA

Confirmation of identity comes from MS/MS experiments and comparison of the isotopic pattern with the simulated isotopic pattern. The simulated isotopic pattern of $(C_{60}C_8H_8)_2Ag$ is shown below the measured mass spectrum:

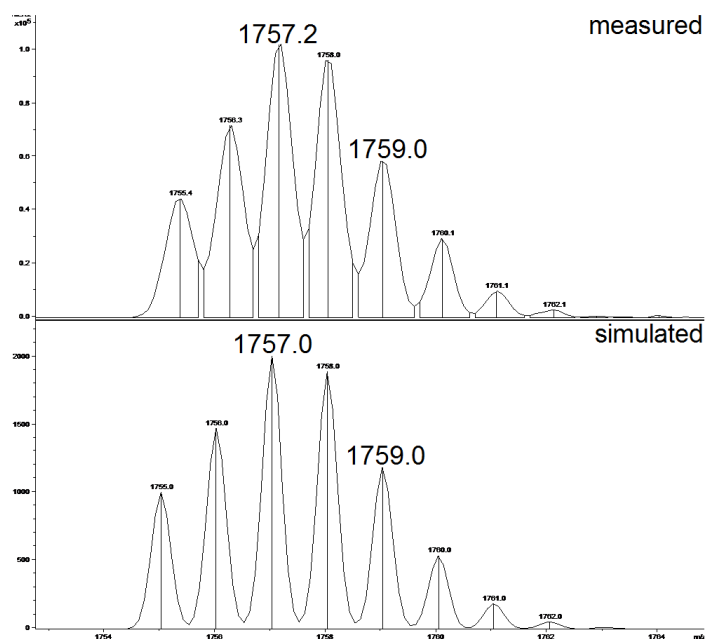


Figure 8.31: The measured, top, and simulated, bottom, isotope pattern of $[(C_{60}C_8H_8)_2Ag]^+$. Again, DCTB-MALDI-MS of $C_{60}C_8H_8$ with silver was performed, resulting in the following spectrum:

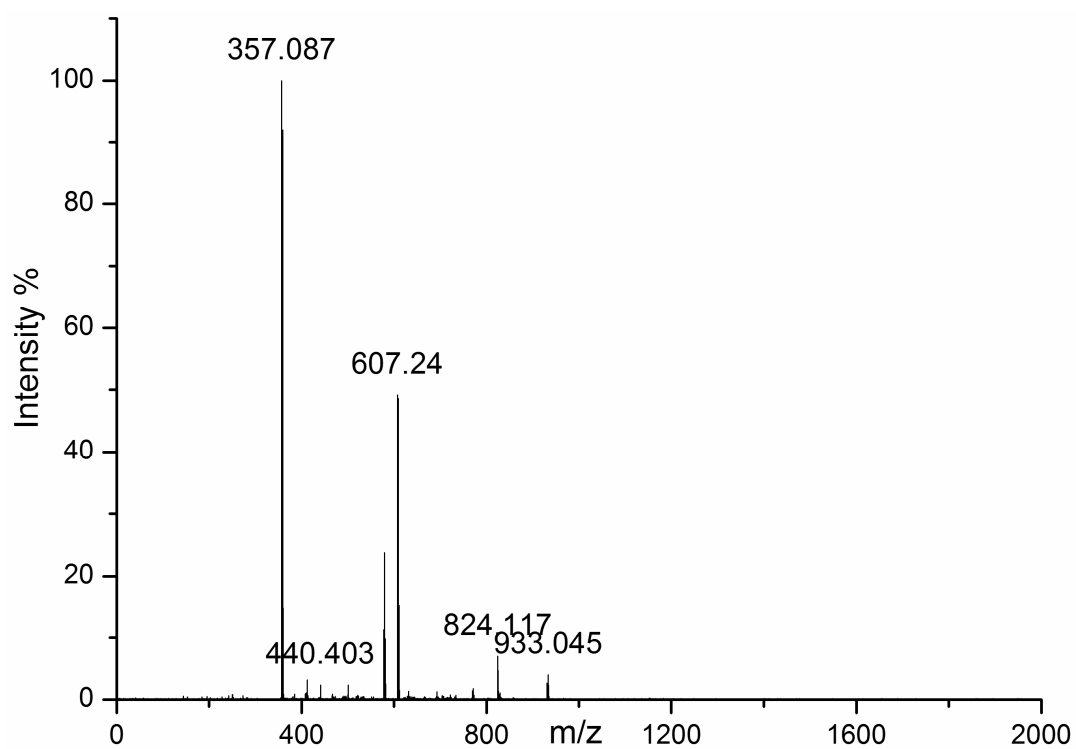


Figure 8.32: Positive-ion mode MALDI of $C_{60}C_8H_8$ and AgTFA

Enhancing the molecular ion region displays the isotopic pattern:

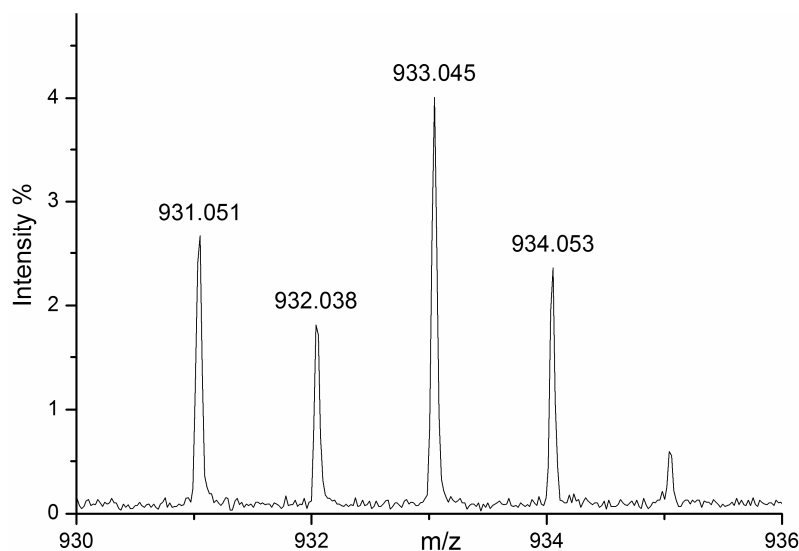


Figure 8.33: Molecular ion region of $[\text{C}_{60}\text{C}_8\text{H}_8\text{Ag}]^+$

Again, there is only addition of one silver per molecule of $\text{C}_{60}\text{C}_8\text{H}_8$, unlike in the ESI spectrum, which demonstrates dimer formation as well. Dimer formation was expected to be the prominent complex formation of this compound, as the ligand is attached through a stronger bond than anthracene, tetracene and pentacene are attached to C_{60} .

The ESI spectrum of $(\text{C}_{60})_2\text{C}_{22}\text{H}_{12}(\text{C}_6\text{H}_5)_2$ and AgTFA is below:

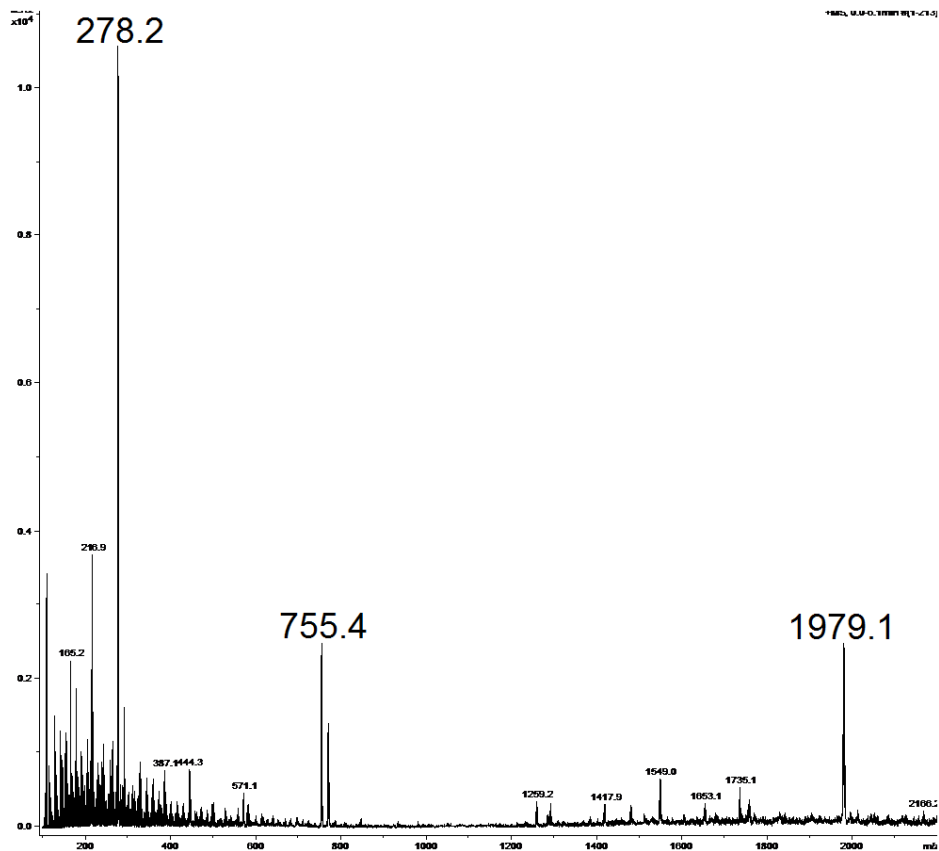


Figure 8.34: Positive-ion mode ESI spectrum of $(\text{C}_{60})_2\text{C}_{22}\text{H}_{12}(\text{C}_6\text{H}_5)_2$ and AgTFA

The peaks present in this spectrum can be identified as the following:

m/z	Identification
278.0	Pentacene
1259.2	$C_{60}C_{22}H_{14}(C_6H_5)_2Ag$
1549.0	$(C_{60})_2Ag$
1979.1	$(C_{60})_2C_{22}H_{12}(C_6H_5)_2Ag$

Table 8.17: Peaks of the ESI spectrum of $(C_{60})_2C_{22}H_{12}(C_6H_5)_2$ and AgTFA

Positive-ion mode DCTB-MALDI-MS with silver was performed on this compound, producing the following spectrum:

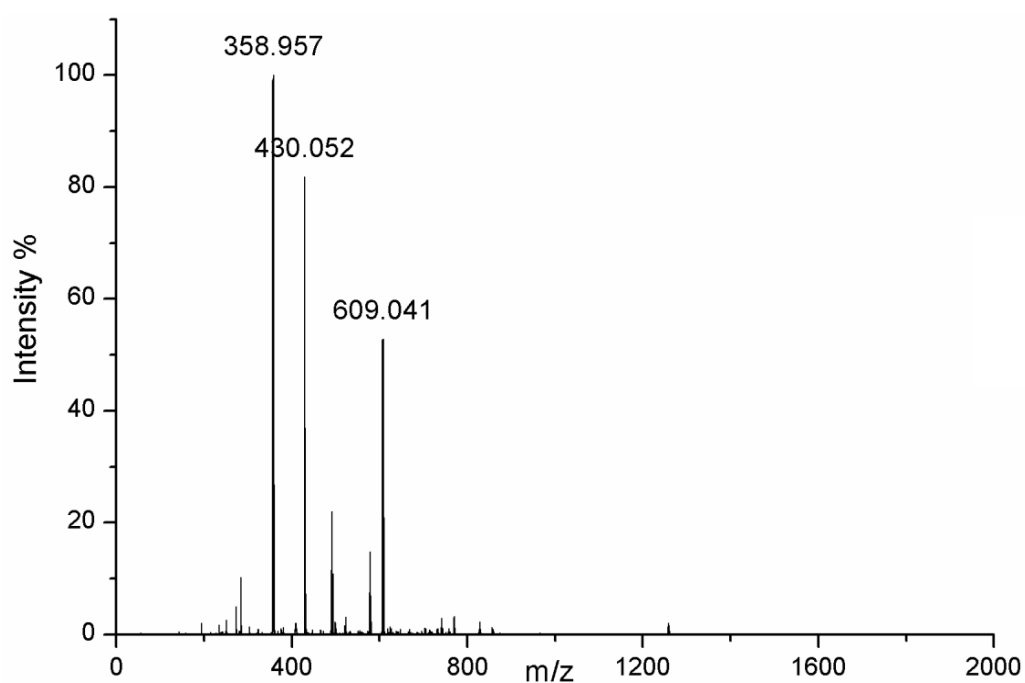


Figure 8.35: Positive-ion mode DCTB-MALDI of $(C_{60})_2C_{22}H_{12}(C_6H_5)_2$ with AgTFA

Enhancing the m/z region 1256 to 1262 demonstrates the isotopic pattern of a peak with a very low intensity. The silver addition has occurred to the compound but is always accompanied by a loss of one C_{60} . There is no evidence of the intact, undissociated compound with silver.

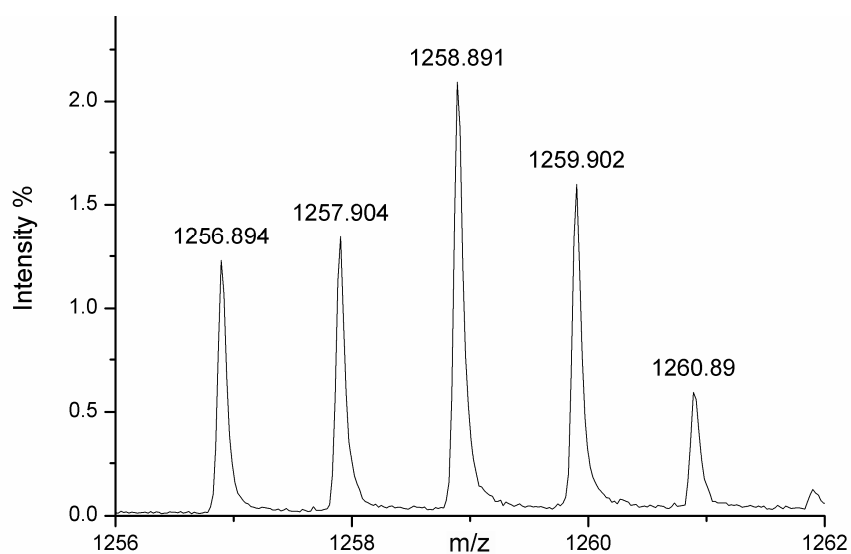


Figure 8.36: The isotopic pattern of $C_{60}C_{22}H_{12}(C_6H_5)_2Ag^+$

With the silver bound C_{60} PAH complexes formed, the next step was to fragment them, to see which ligand the silver preferentially binds to, and to calculate a silver binding affinity relative to C_{60} for the PAH's.

An example MS/MS spectrum, of $[C_{60}TAg]^+$ is below:

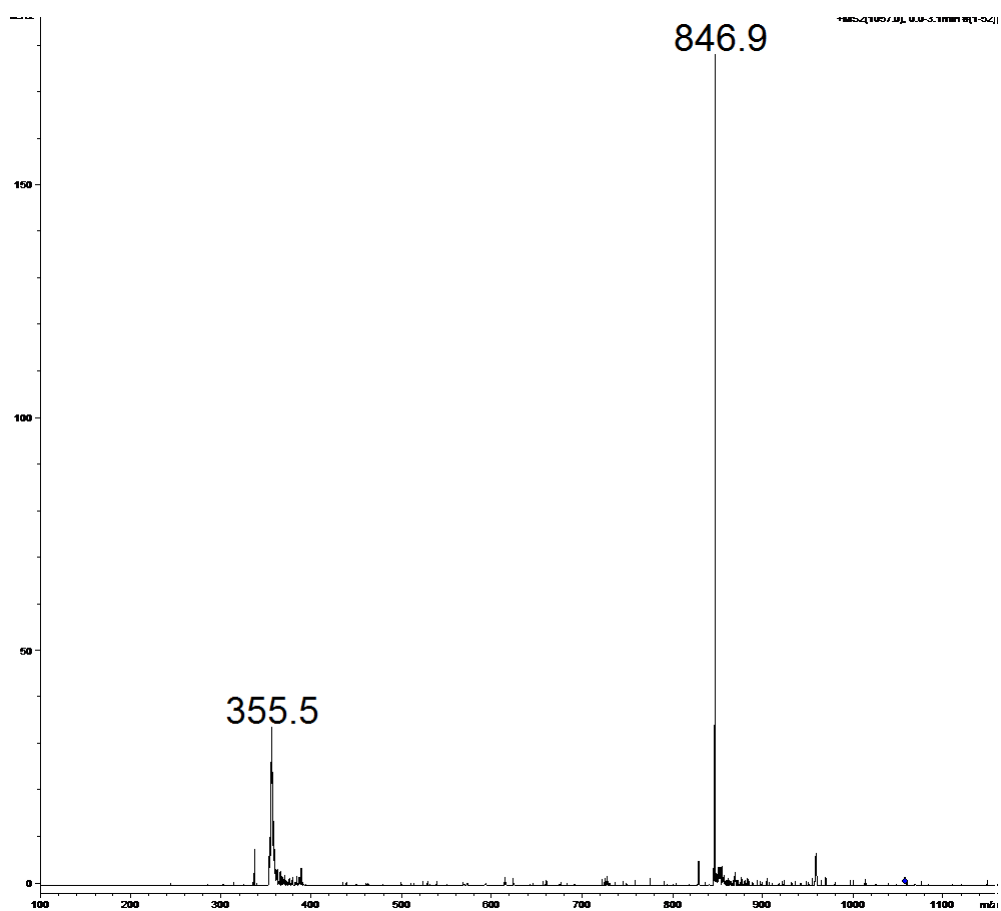


Figure 8.37: Positive-ion mode MS/MS spectrum of m/z 1057.0

This table has the intensities of each fragment peak relating to either C₆₀ or the PAH, measured from the ESI MS/MS spectra, which can be found in the appendix.

MS/MS	C ₆₀ Ag	C ₆₀ AgH ₂ O	PAHAg	PAHAgH ₂ O
C ₆₀ A	0.18, 1.30	14.39, 100	2.68, 2.56	2.37, 2.53
C ₆₀ T	2.82	100	4.28	19.07
C ₆₀ P	0.90	100	0.65	26

Table 8.18: Intensities of the fragments resulting from MS/MS of [C₆₀PAHAg]⁺ complexes

Where both isomers of silver were present, the intensity of both was recorded. The intensity of the ¹⁰⁷Ag peak is listed first in the table.

Total intensities and preliminary calculations are presented below:

	C ₆₀ Fragments	PAH fragments	Ln(PAH/C ₆₀)
C ₆₀ A	115.87	10.14	-2.436
C ₆₀ T	102.82	23.35	-1.477
C ₆₀ P	100.90	26.65	-1.331

Table 8.19: Intensities of C₆₀ fragments and PAH fragments

It can be observed that a qualitative order of silver-ion binding affinity can be noted as:



In the case of ESI, C₆₀ appears to have a greater silver binding affinity than all three polyaromatic hydrocarbons tested. Using C₆₀ as the reference compound for silver binding affinity, and setting the silver binding affinity of C₆₀ at 0, the relative silver binding affinities of anthracene, tetracene and pentacene can be calculated as follows:

$$\Delta(\Delta Ag^+) = \ln \frac{[M_1 Ag]^+}{[M_2 Ag]^+} \cdot RT_{eff}$$

Positive-ion mode LIFT on the Bruker Ultraflex II of the C₆₀AgPAH complexes was also obtained. Although MALDI is considered too unreliable for quantification, it was decided to compare the resulting relative silver-ion affinities from MALDI with ESI. The resulting spectra for C₆₀A, C₆₀T and C₆₀P are as follows:

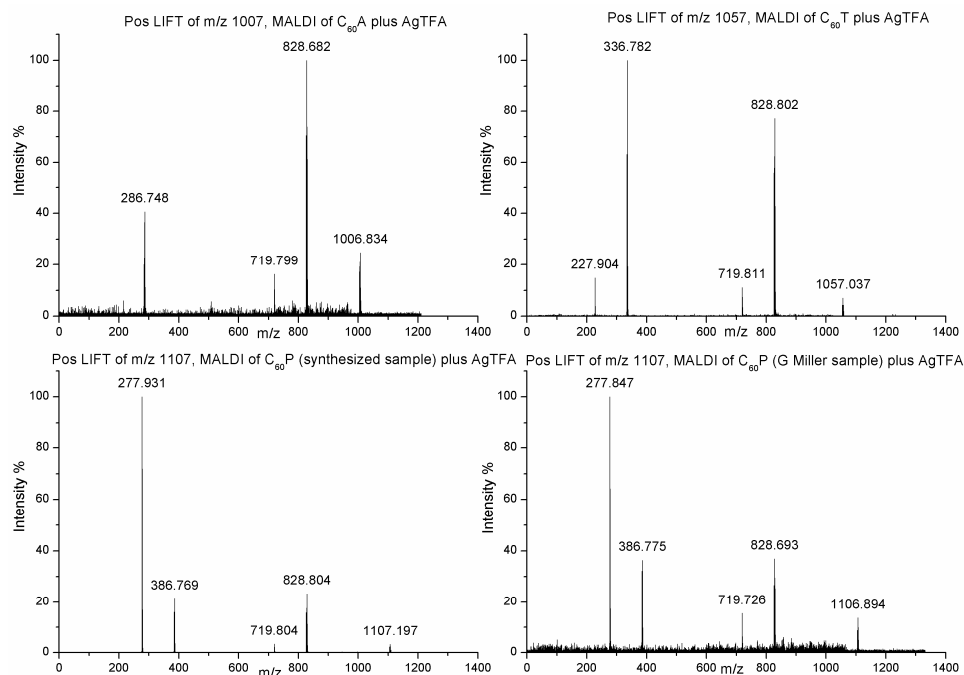


Figure 8.38: DCTB-MALDI spectra of the C_{60} PAH complexes with AgTFA

The spectra are different from those produced using ESI-MS. There is no water addition, as would be expected from the different detection techniques. The fragmentation using LIFT is also comparatively stronger, as both C_{60} and the PAH can be seen without Ag.

In summary, the peaks produced in all four MALDI spectra are of either C_{60} or the polyaromatic hydrocarbons, with and without Ag.

In spite of the supposed unreliability of MALDI for quantification purposes, the same pattern of relative silver binding affinity can be seen as from the ESI spectra:



However, there are differences, in that from the MALDI spectra it appears that C_{60} has a stronger affinity than anthracene, but a smaller affinity than tetracene and pentacene. From the ESI spectra, it appears that C_{60} has a stronger silver affinity than all three PAHs. The actual intensity measurements from the spectra are below.

LIFT	C_{60}	$C_{60}Ag$	PAH	PAHAg
$C_{60}A$	97	419, 594	21	133, 241
$C_{60}T$	506	2632, 3510	672	2873, 4548
$C_{60}P$	1649	5218, 7009	31204	4600, 7077

Table 8.20: Fragment intensities of LIFT experiments of $[C_{60}\text{-Ag-PAH}]^+$

The total fragment intensities and preliminary calculations are presented below:

	C ₆₀ Fragments	PAH fragments	Ln(PAH/C ₆₀)
C ₆₀ A	1110	395	-1.033
C ₆₀ T	6648	8093	0.197
C ₆₀ P	13876	42881	1.128

Table 8.21: Total intensities of C₆₀ fragments and PAH fragments

The MS/MS of the related C₆₀PAH compounds were interesting. C₆₀C₈H₈Ag fragmented as follows:

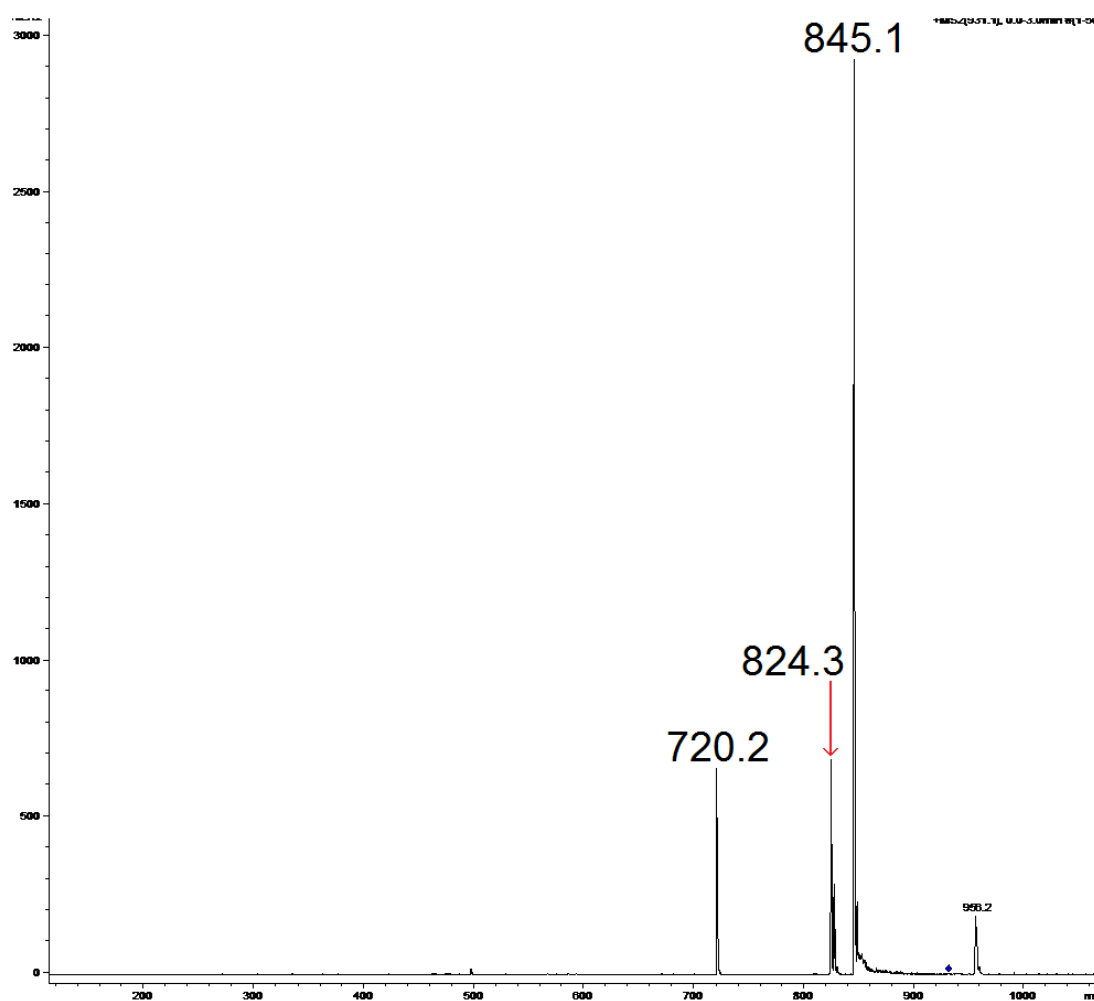


Figure 8.39: Positive-ion mode MS/MS spectrum of m/z 931.1

There is considerable fragmentation into C₆₀, which is not seen in ESI with the C₆₀A, C₆₀T and C₆₀P samples analysed. There is also no sign of bare silver or of C₈H₈ with or without silver.

Enhancement of the main cluster of peaks shows that at around m/z 825, there are two sets of peaks – $C_{60}C_8H_8$ at m/z 824, and $C_{60}Ag$ at m/z 827.

The $C_{60}C_8H_8$ fragmentation is less intense than that of $C_{60}Ag$ and $C_{60}AgH_2O$ combined, and suggests that loss of C_8H_8 is the preferential fragmentation route. However, the fact that $C_{60}C_8H_8$ does remain intact, even if in small quantities, is further evidence that C_8H_8 has stronger bonding to C_{60} than the polyaromatic hydrocarbons.

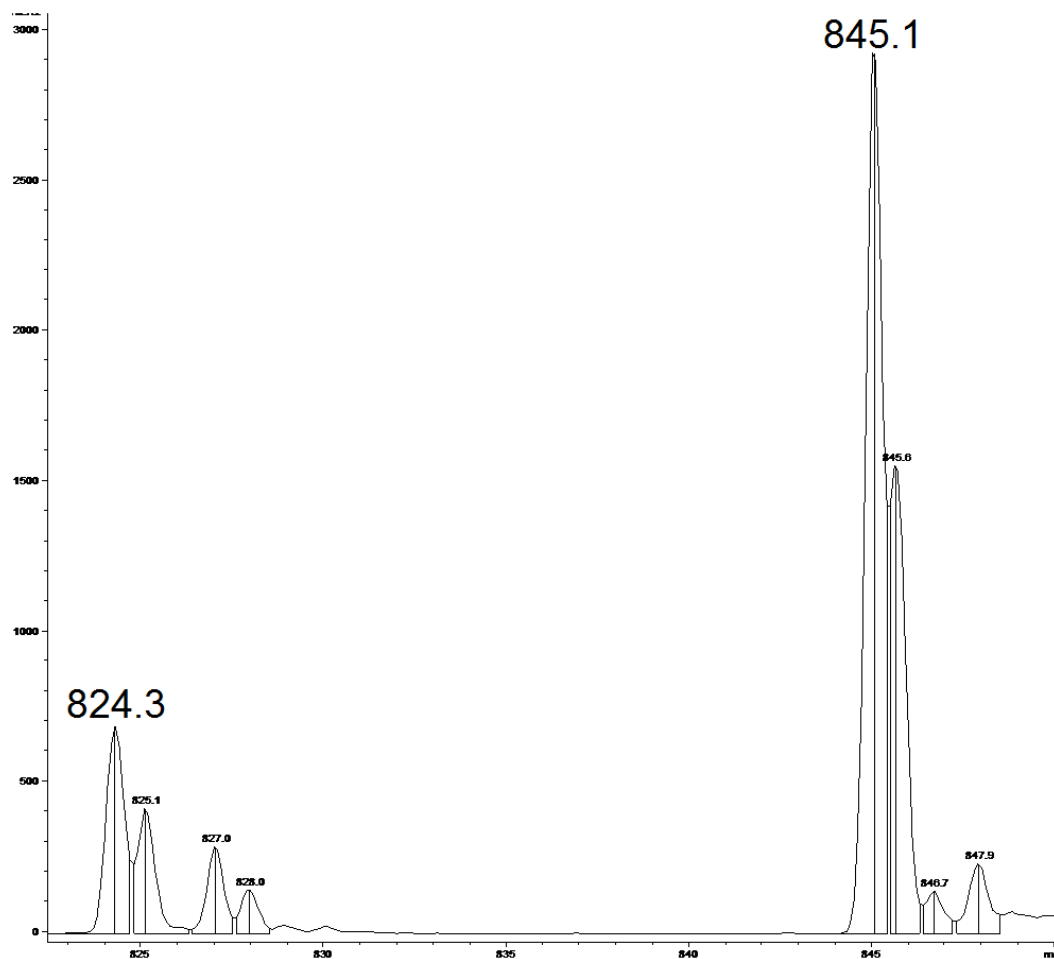


Figure 8.40: The m/z region 822 to 850 of the ESI spectrum of $C_{60}C_8H_8$ and AgTFA

Positive-ion mode LIFT with MALDI conditions of $C_{60}C_8H_8Ag$ gave the spectrum below:

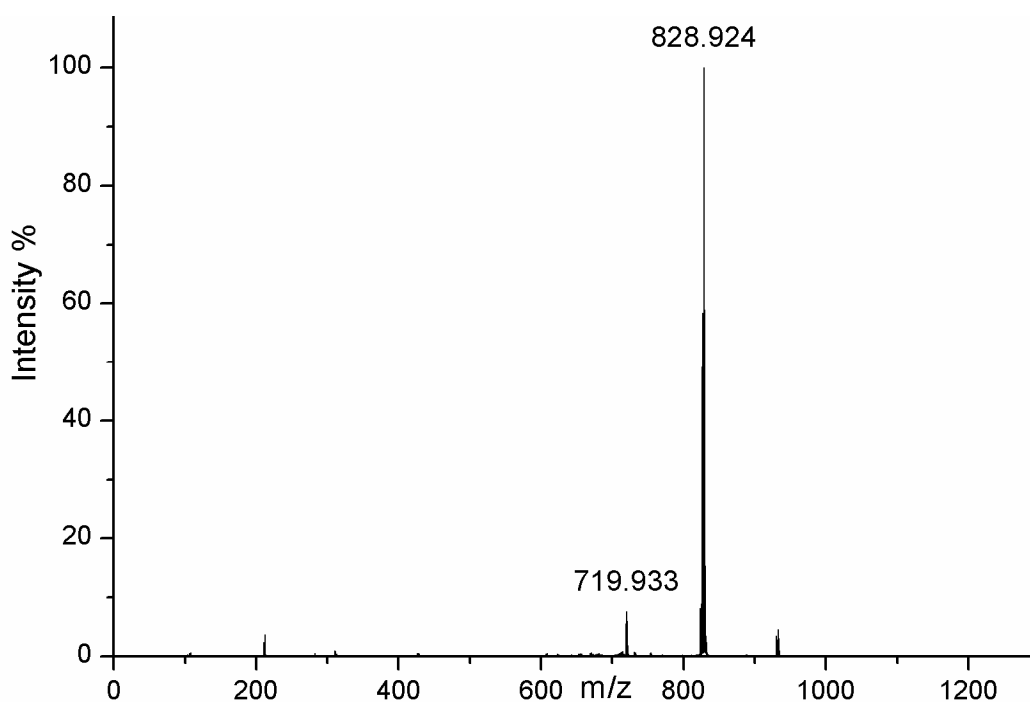


Figure 8.41: Positive-ion mode LIFT spectrum of m/z 933

The peaks present are C_{60} at m/z 719.9 and $C_{60}Ag$ at m/z 828.9. This is similar to the ESI spectrum in that there is no evidence of C_8H_8 retaining the silver. Enhancing the m/z region 822 to 834:

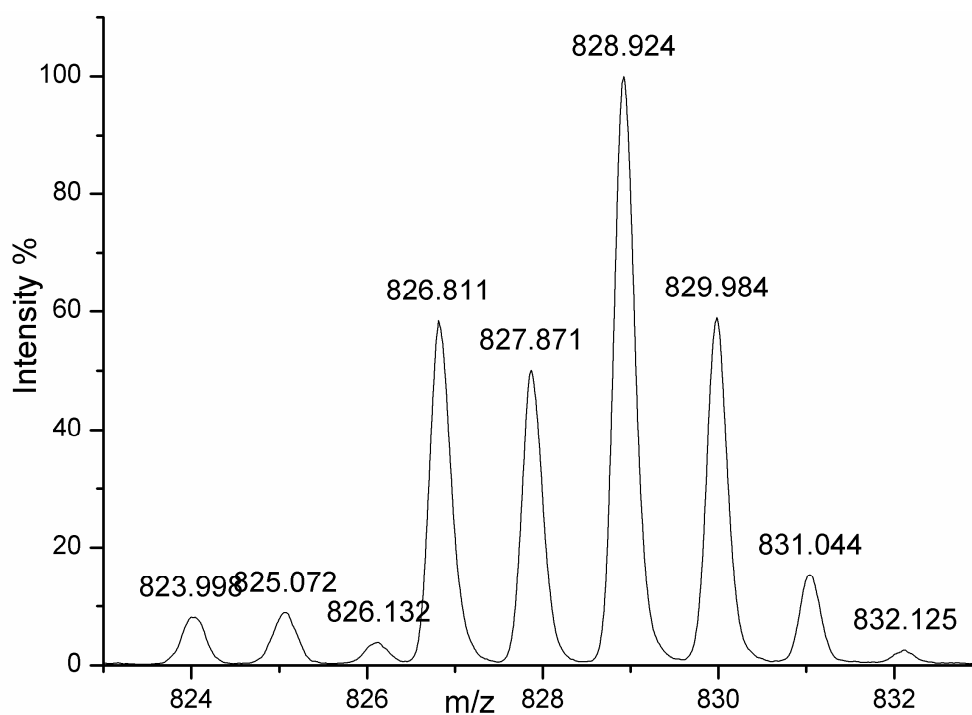


Figure 8.42: m/z region 823 to 833 of the positive-ion mode LIFT spectrum of m/z 933

There are peaks present which indicate formation of $C_{60}C_8H_8$, however, the preferential fragmentation route is to lose C_8H_8 , as is the case for ESI.

The MS/MS spectrum of $(C_{60})_2C_{22}H_{12}(C_6H_5)_2Ag$ is below:

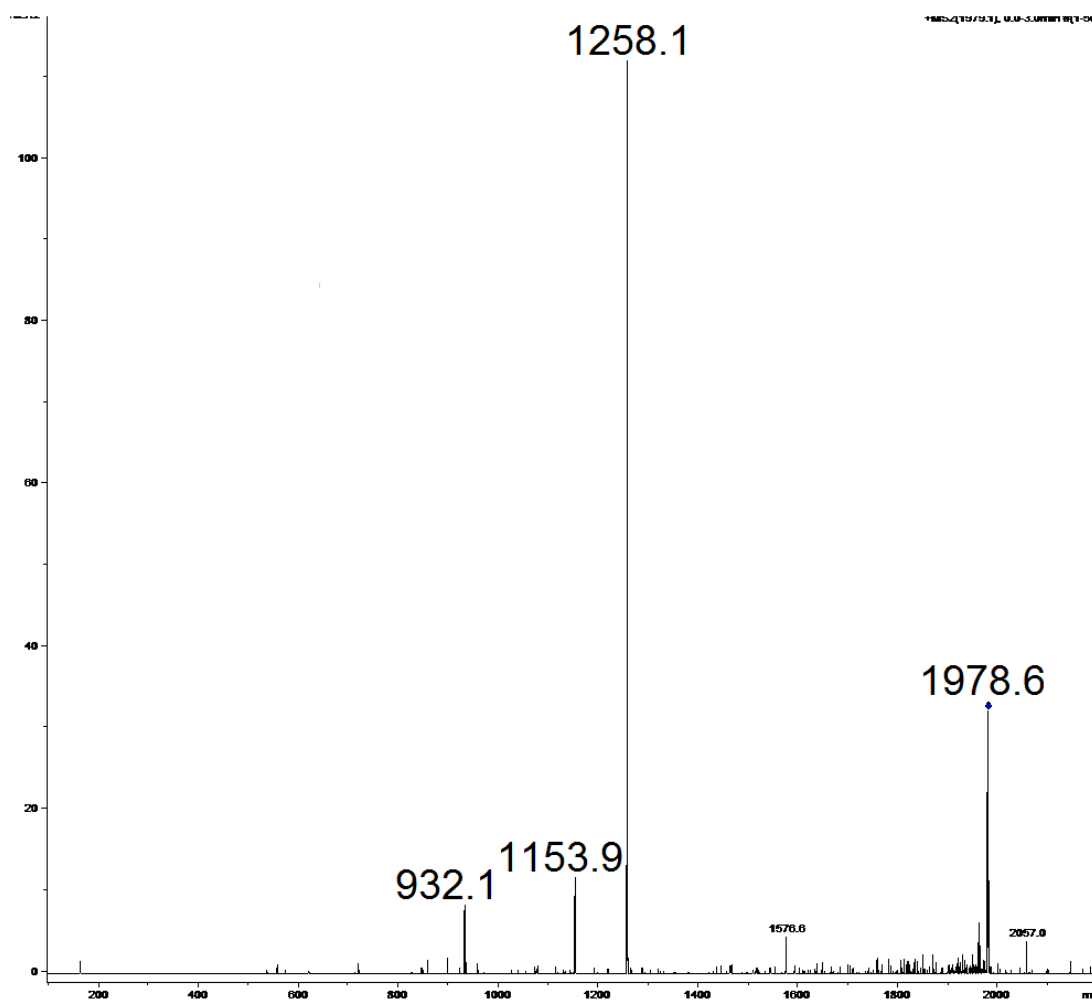


Figure 8.43: Positive-ion mode MS/MS spectrum of m/z 1979.1

The dominant fragment at m/z 1258.1 is loss of one of the C_{60} molecules.

LIFT was performed under MALDI conditions. Even though DCTB was present, the conditions appeared too harsh for the retention of both C_{60} molecules, and as such the LIFT had to be performed on the silver adduct of the compound missing one C_{60} , at m/z 1259: $(C_{60})C_{22}H_{12}(C_6H_5)_2Ag$. The resulting spectrum:

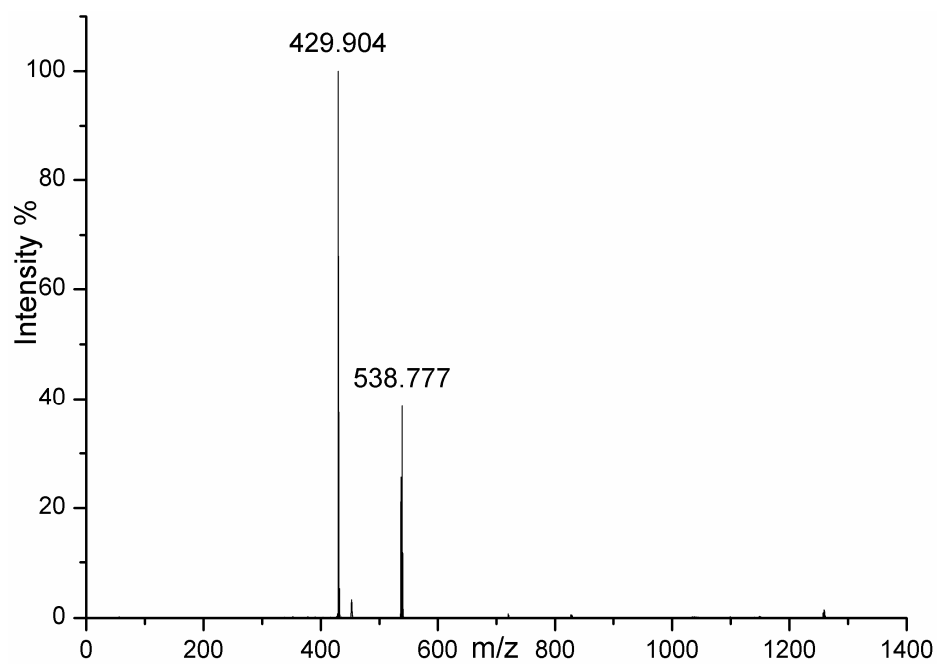


Figure 8.44: Positive-ion mode LIFT spectrum of m/z 1259

These peaks can be identified as:

m/z 429.9 - $[\text{C}_{22}\text{H}_{12}(\text{C}_6\text{H}_5)_2]$

m/z 538.7 - $[\text{C}_{22}\text{H}_{12}(\text{C}_6\text{H}_5)_2\text{Ag}]$

The corresponding MS/MS ESI spectrum of m/z 1259 is below:

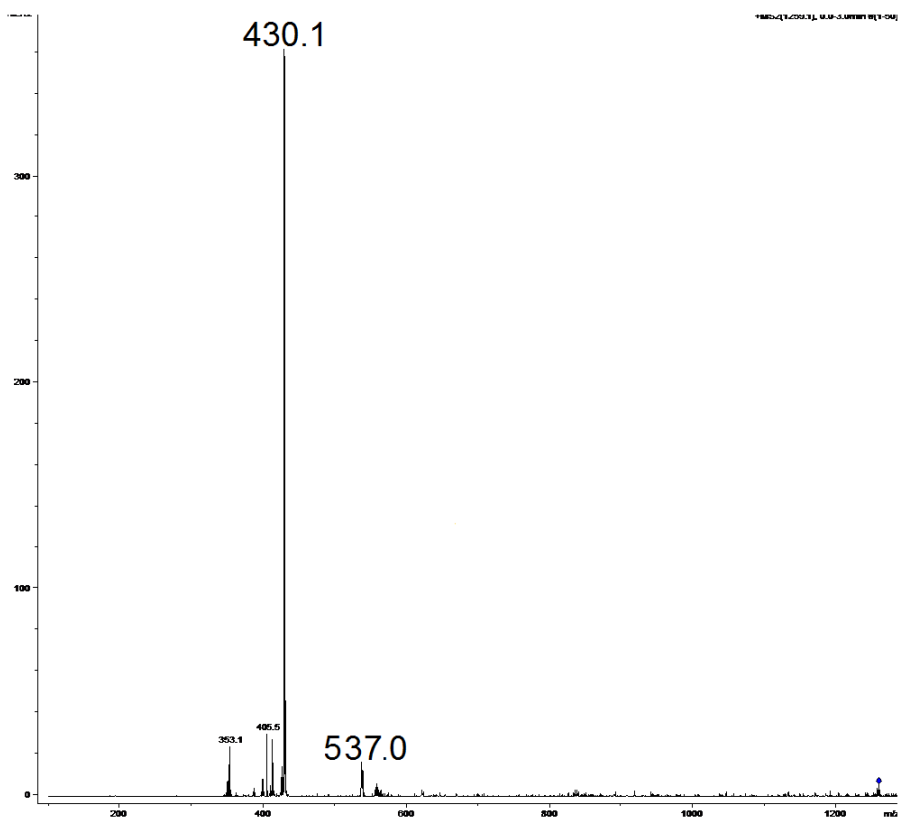


Figure 8.45: Positive-ion mode MS/MS spectrum of m/z 1259.1

The ESI spectrum has the same fragments and some additional peaks at m/z 353 and 405.

C₆₀, Silver and Anthracene

It was thought to attempt the creation of the silver bound complex of [C₆₀AgA] using C₆₀ and anthracene that had not been reacted together. This experiment was performed employing both MALDI and ESI-MS.

As can be seen from the positive-ion mode ESI spectrum below, the affinity of C₆₀ is so much greater than that of anthracene that there is only formation of the silver bound C₆₀ dimer.

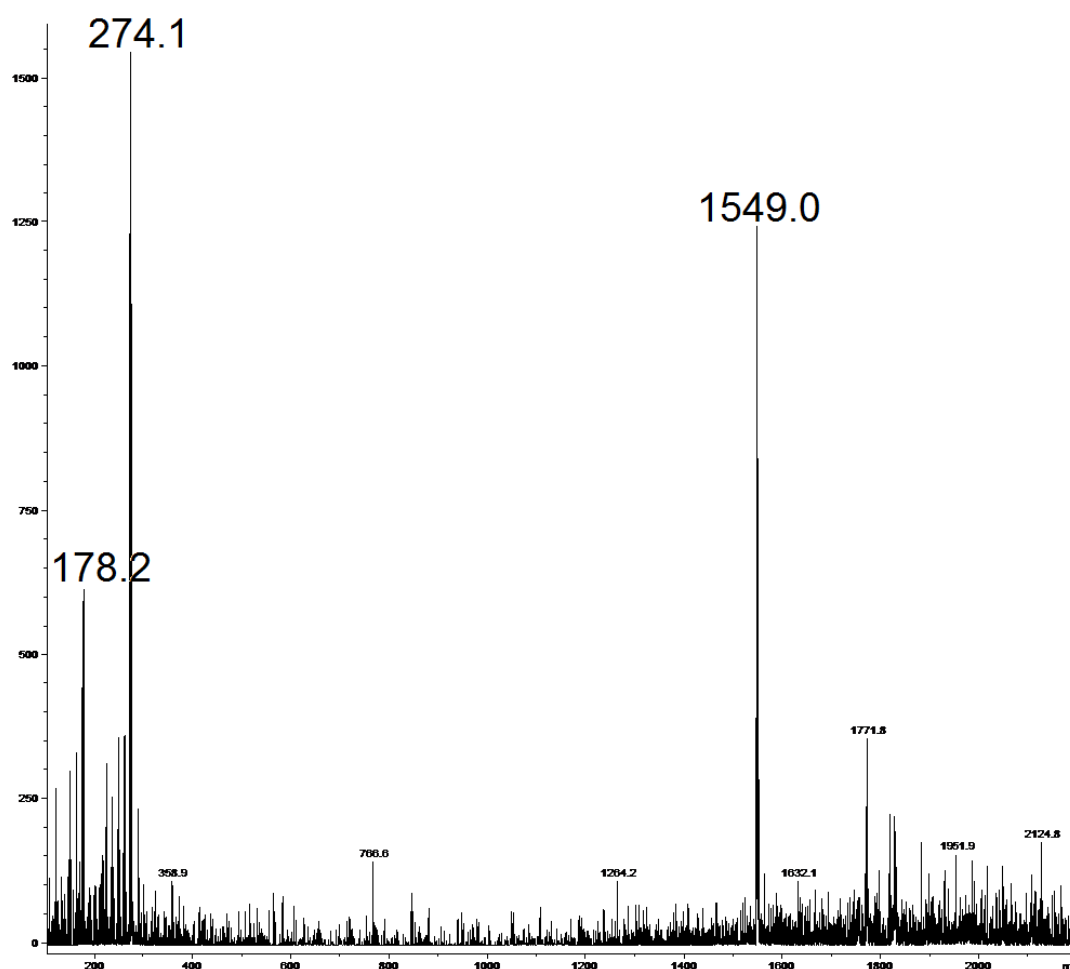


Figure 8.46: Positive-ion mode ESI spectrum of C₆₀, Anthracene and AgTFA

The MALDI spectrum is below:

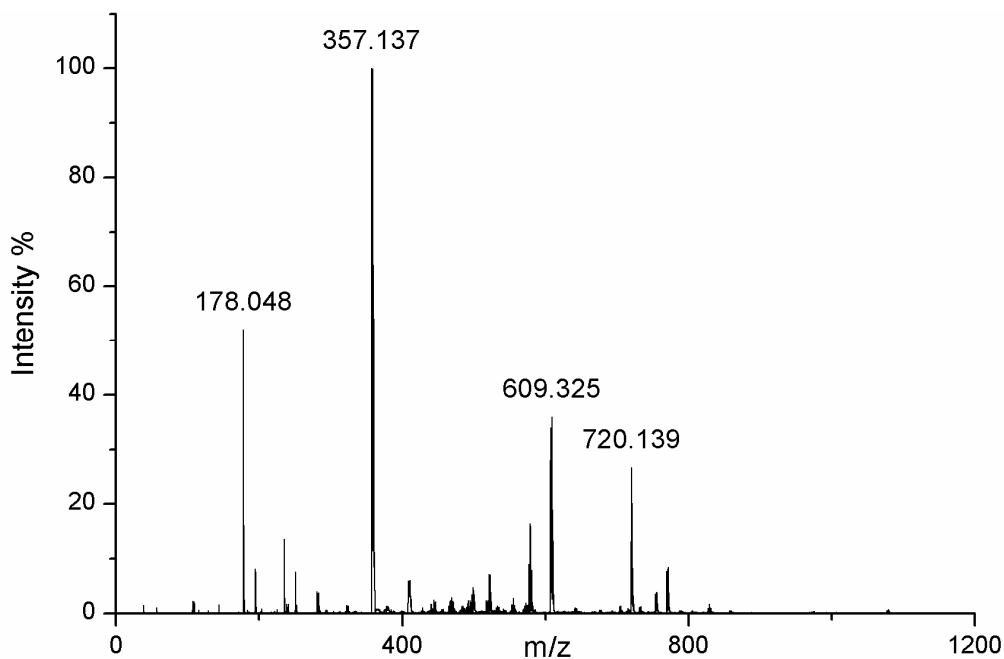


Figure 8.47: Positive-ion mode MALDI spectrum of C_{60} , Anthracene and AgTFA

When MALDI conditions are employed there is no silver addition to anthracene or C_{60} . The peak at m/z 357 is of silver addition to DCTB. m/z 609 is silver addition to two DCTB molecules. However, enhancing the m/z region 1004 to 1010 demonstrates the possible formation of $[C_{60}AgA]$, at an extremely low intensity:

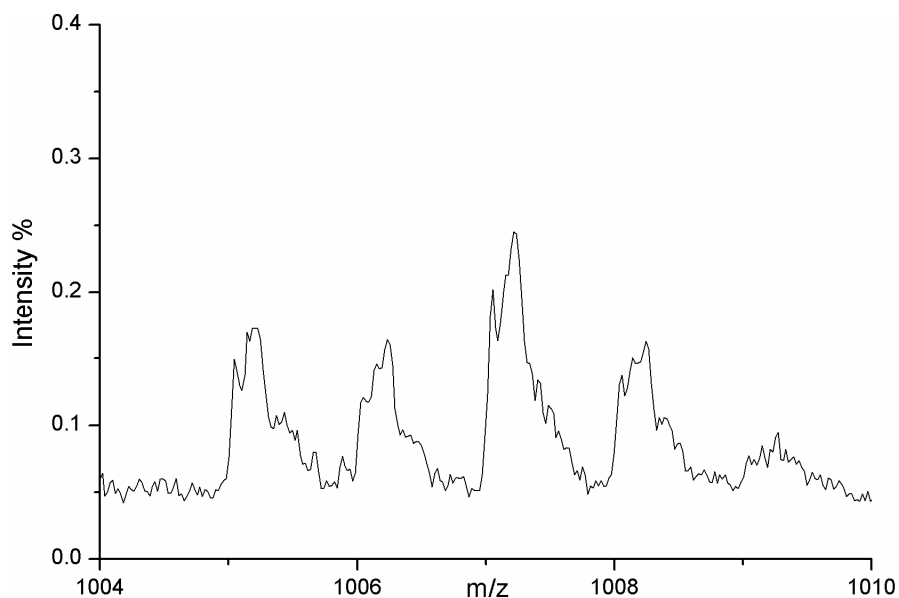


Figure 8.48: Positive-ion mode MALDI of C_{60} , Anthracene and AgTFA

To check if formation of the complex had occurred, LIFT was performed on the peak:

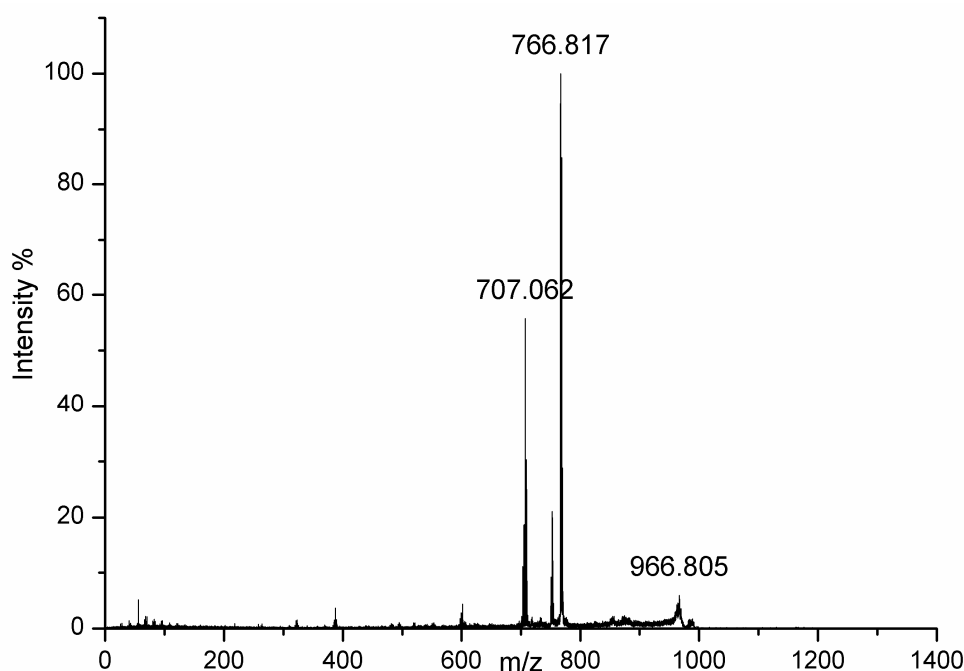


Figure 8.49: Positive-ion mode LIFT spectrum of m/z 1005

There is no indication of C_{60} , or anthracene. Therefore the peak at m/z 1005 cannot be assigned as the $[C_{60}AgA]$ complex, despite the isotopic pattern being an almost exact match. It is apparent that the peak appears at a very low intensity, and perhaps this is why no fragments can be found. The fragments in the LIFT spectrum are most likely due to something at a similar m/z value, which has managed to pass through the initial parent ion selection.

“Cis”, “trans” and Silver

It was thought to bind silver to “cis” and “trans”, the two stereoisomers supplied by Professor Helena Grennberg at Uppsala University, Sweden. It was hoped that the stereoisomers could be differentiated by exploiting the tendency of silver to attach two ligands in the gas phase. The structure of “cis” would allow silver to form two bonds within one “cis” molecule, if interaction occurs with the aromatic rings, as would be expected.

Initially, the compounds were electrosprayed without silver, in order to check that ionisation and detection was possible. The resulting negative-ion mode spectra did not appear to give any indication of “cis” and “trans” and were very noisy, much like the MALDI spectra. The

spectra shown below were obtained at 100% compound stability, which appeared to give a better signal than at 500% compound stability.

“Cis”:

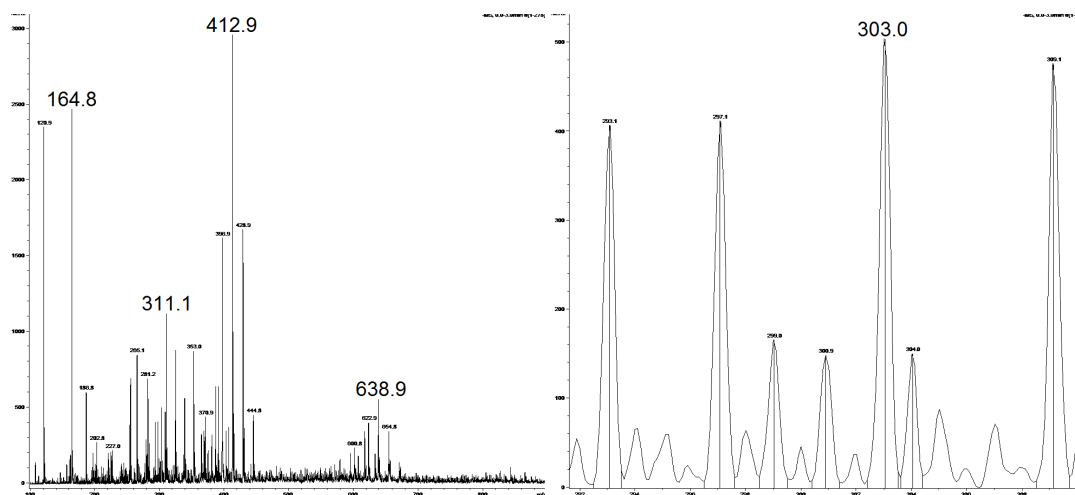


Figure 8.50: Positive-ion mode ESI spectrum of “cis”, enhanced molecular ion region on right

“Trans”:

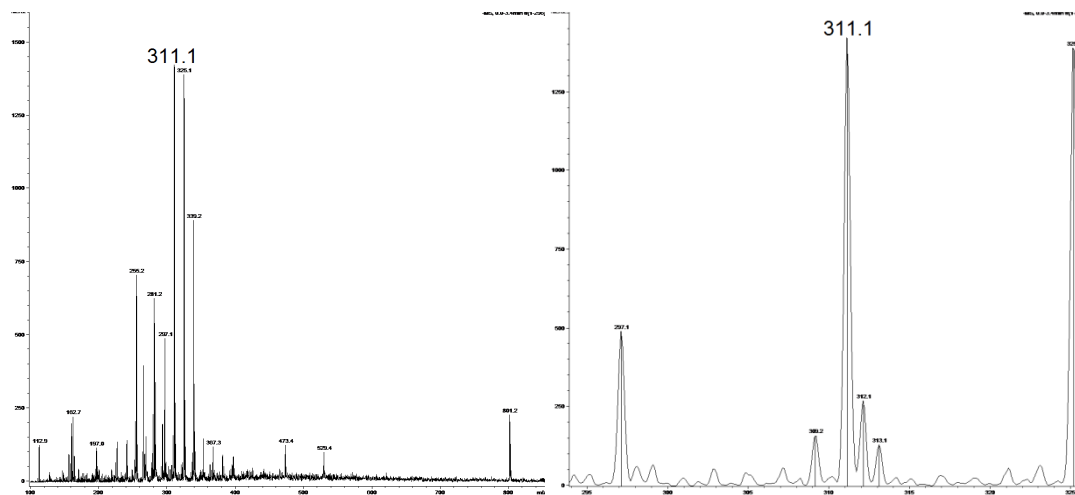


Figure 8.51: Positive-ion mode ESI spectrum of “trans”, enhanced molecular ion region on right

Regardless, “cis” and “trans” were electrospayed with AgTFA, resulting in the following spectra:

“Cis” and AgTFA:

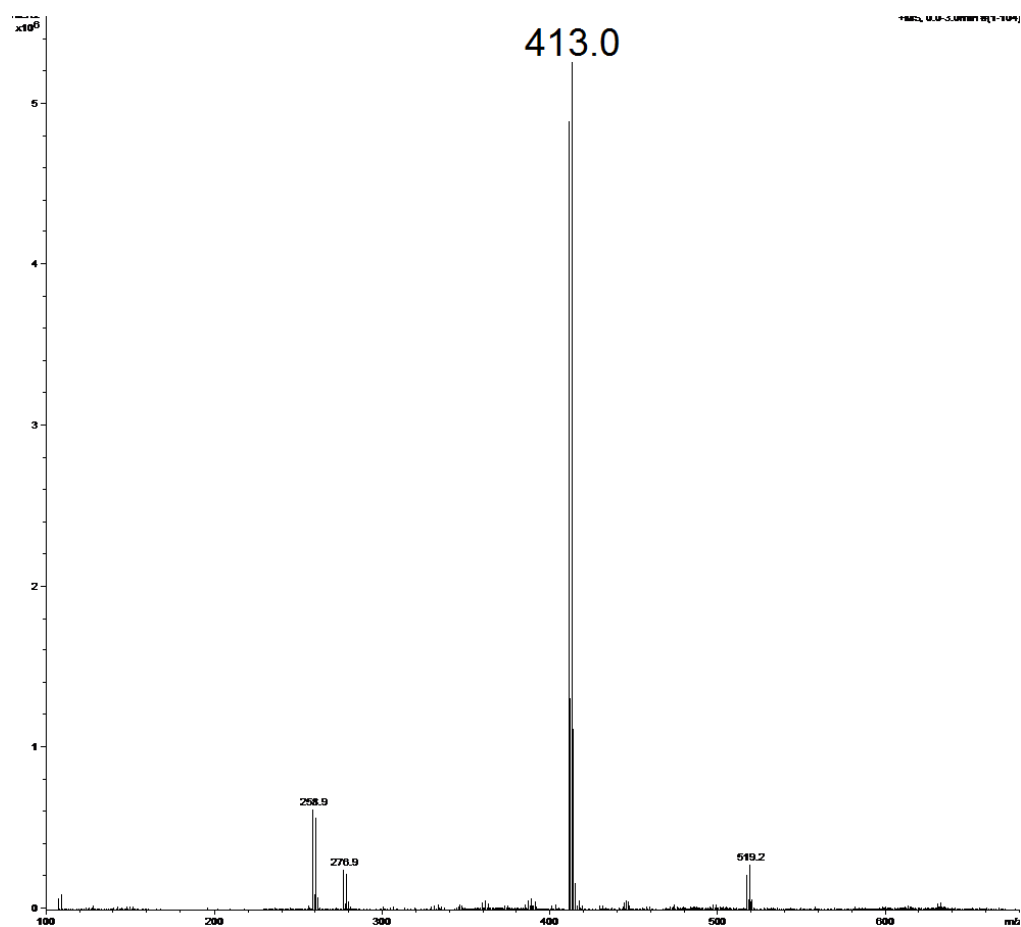


Figure 8.52: Positive-ion mode ESI spectrum of “cis” and AgTFA

In contrast to the spectrum of just “cis”, the spectrum of “cis” with silver is cleaner with a definite dominant peak at m/z 413.0, with a slightly less intense peak at m/z 411.0. These peaks corresponds to the expected m/z value of $[\text{“cis”Ag}]^+$.

MS/MS confirms this and demonstrates an initially unexpected fragmentation pathway:

MS/MS of "cis" and AgTFA:

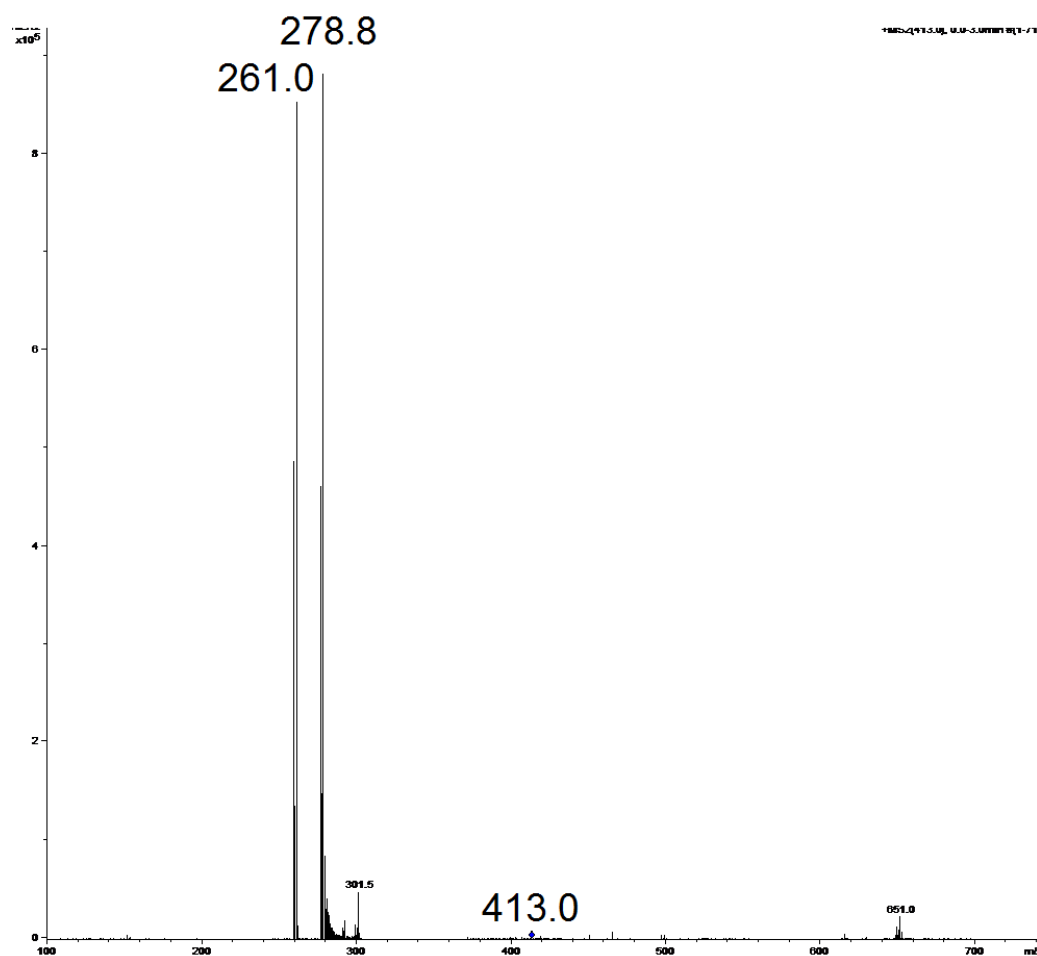


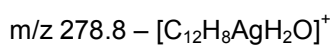
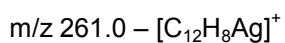
Figure 8.53: Positive-ion mode of "cis" and AgTFA, MS/MS of m/z 413.0

The MS/MS spectrum shows the same two peaks that are also present in the initial MS spectrum, at m/z 261.0 and 278.8. Both of these peaks contain one silver, demonstrated by the isotopic pattern. The ^{109}Ag containing peaks are much larger than the ^{107}Ag containing peaks. The peak that was selected for MS/MS was 413 – the ^{109}Ag "cis" compound. Due to its proximity to the selected mass, some of the ^{107}Ag "cis" compound would also have fragmented, however not in as great quantities as the ^{109}Ag "cis" complex.

The two peaks at m/z 261.0 and 278.8, when the silver is removed, have mass values of 152 Da, and 170 Da respectively. They are separated by 18 mass units.

152 Da is half the mass of "cis" and "trans". It appears that for "cis", the silver inserts itself in between the aromatic rings. When it fragments, "cis" appears to break exactly in half, with the silver retaining one half of the molecule. As silver preferentially binds two ligands, it then

binds a water molecule in the ion trap, leading to the identification of the two fragment peaks as:



For “trans”, the story is similar to “cis”. The standard MS spectrum of “trans” and AgTFA is shown below:

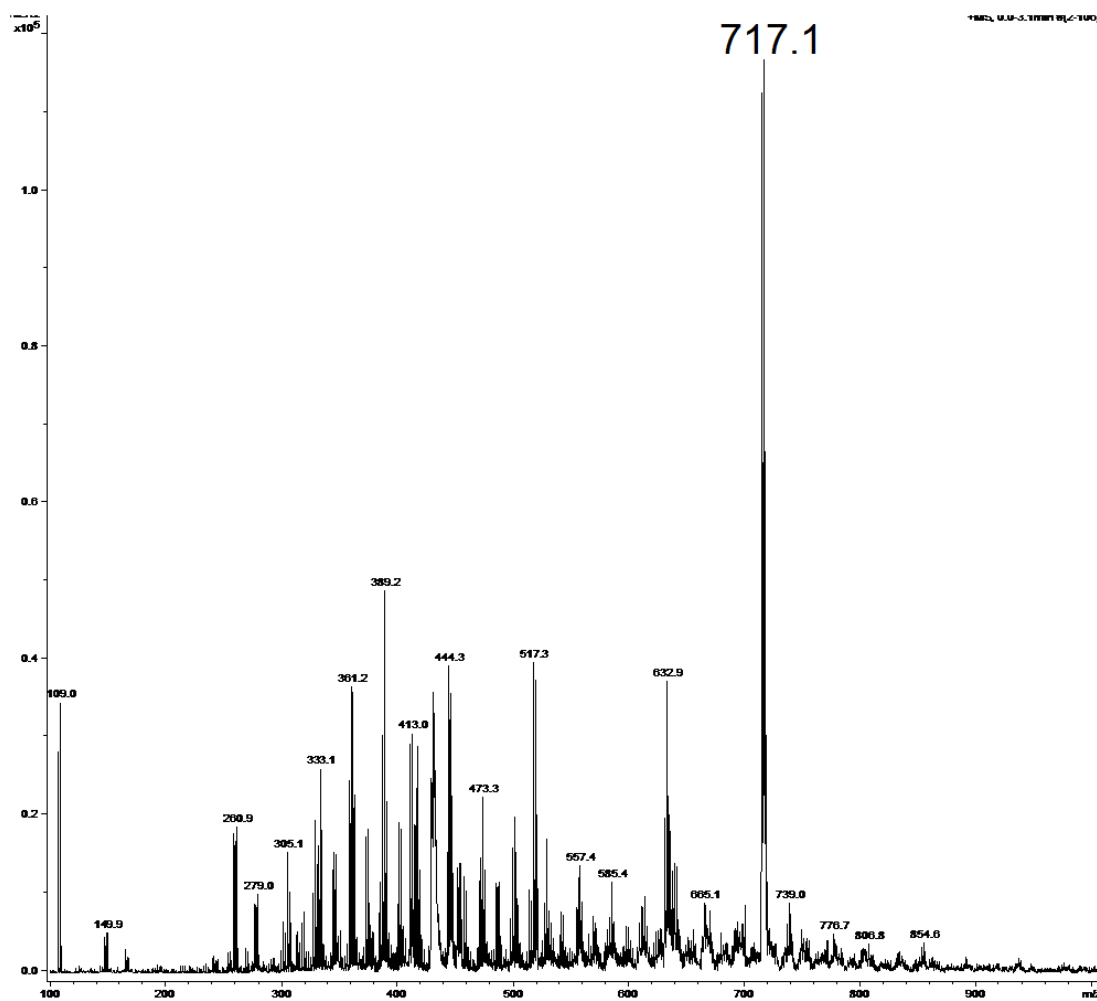


Figure 8.54: Positive-ion mode ESI spectrum of “trans” and AgTFA

The isotopic pattern of the peak at m/z 717.1 is enhanced overleaf:

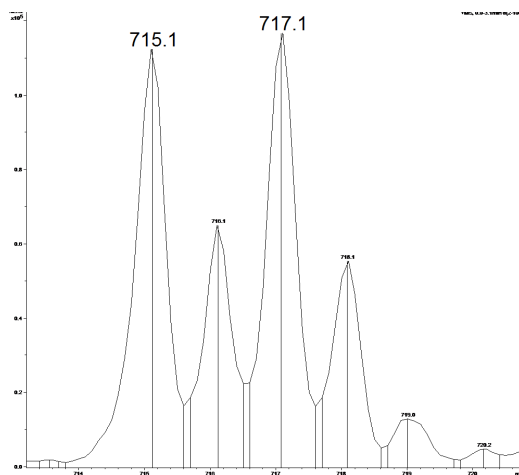


Figure 8.55: The isotopic pattern of the peak at m/z 717.1 from the ESI spectrum of “trans” and AgTFA

From the isotopic pattern it is clear that this compound contains one silver. The m/z values are the expected m/z values of [“(trans”)₂Ag]⁺. MS/MS was performed on this peak, resulting in the following spectrum:

MS/MS of [“(trans”)₂Ag]⁺:

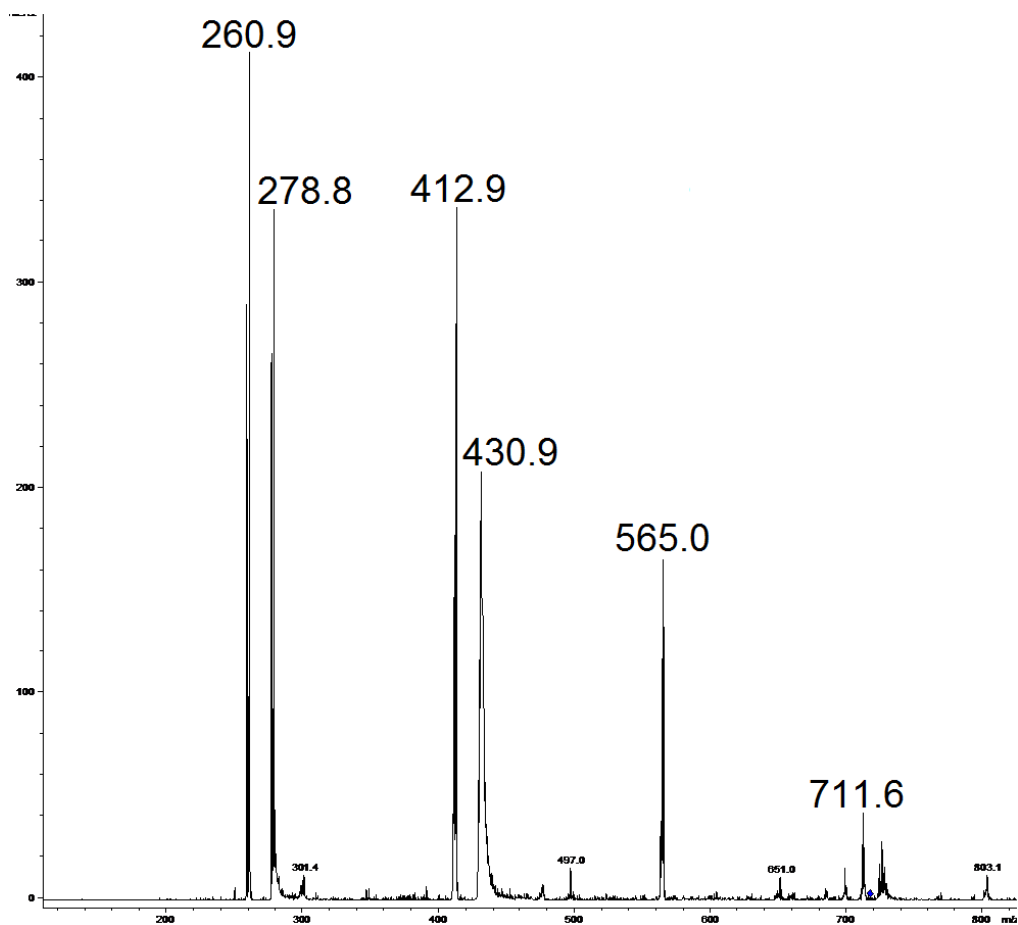


Figure 8.56: Positive-ion mode spectrum of “trans” and AgTFA, MS/MS of m/z 717.1

In this spectrum, the same peaks are present as in the MS/MS of “cis” and AgTFA, at m/z 261 and 279. The peaks have been identified as below:

m/z	Identification
260.9	$[\text{C}_{12}\text{H}_8\text{Ag}]^+$
278.9	$[\text{C}_{12}\text{H}_8\text{AgH}_2\text{O}]^+$
412.9	$[\text{“trans”Ag}]^+$
430.9	$[\text{“trans”AgH}_2\text{O}]^+$
565.0	$[\text{“trans”Ag C}_{12}\text{H}_8]^+$

Table 8.22: Peaks in the positive-ion mode spectrum of “trans” and AGTFA, MS/MS of m/z 717.1

It appears that, similar to “cis”, the “trans” molecule breaks in half in preference to losing the silver ion. The two spectra also demonstrate the different ways that silver has interacted with the two compounds inside the ESI source, and is further proof that silver preferentially binds two ligands. In the case of “trans”, as it cannot bind twice with the same molecule, it has to bind two molecules. When it loses one of those, it binds water, which can be found inside the ion trap.

For “cis”, silver can bind twice within one molecule, and as such does not bind water, until the molecule has fragmented in half, and silver only has one ligand. From these it can be conjectured that the silver inserts in between the aromatic rings for “cis”, and it is to the aromatic rings that silver binds to the respective molecules:

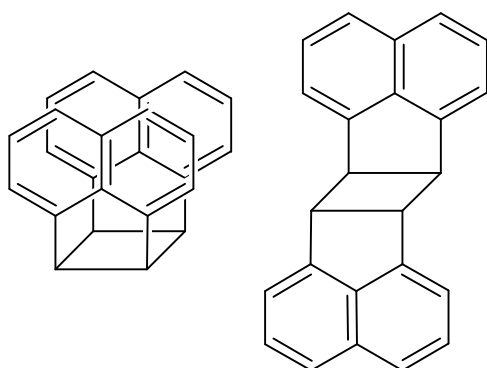


Figure 8.57: Structure of “cis”, left, and “trans”, right

Positive-ion mode MALDI-MS and LDI-MS was performed on these compounds with silver, to see if the same result could be achieved. LDI-MS was also performed due to the small size of the samples, as matrix peaks could obscure the sample peaks.

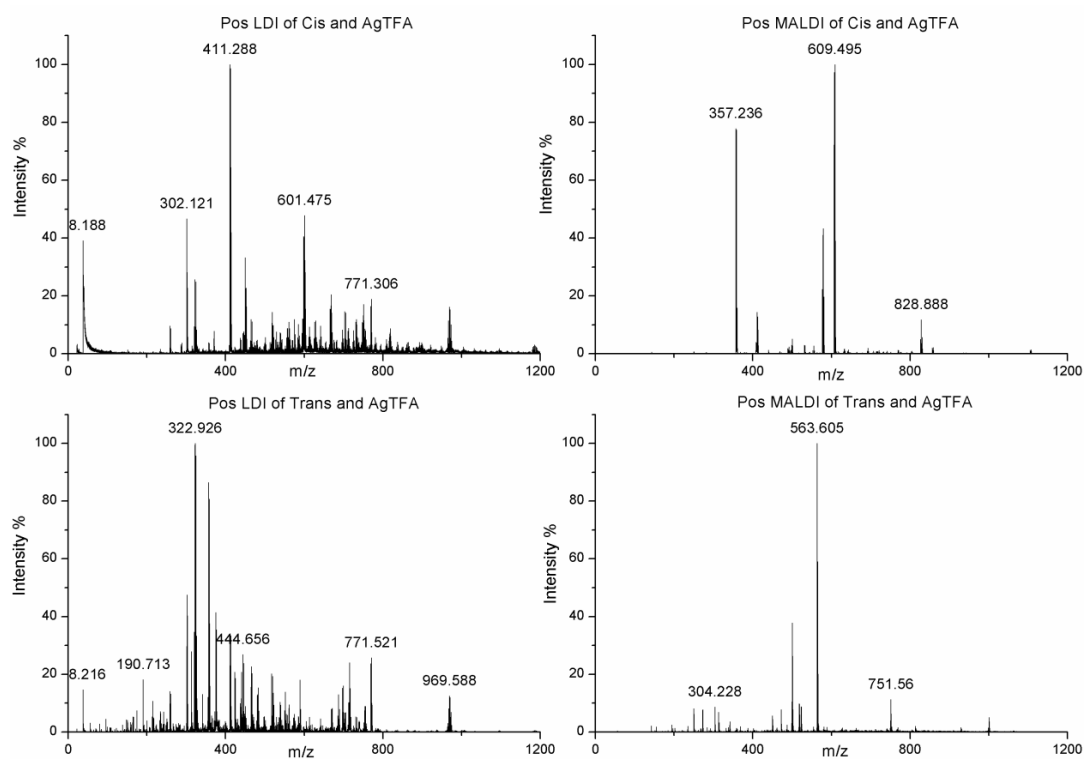


Figure 8.58: LDI and MALDI spectra of “cis” and “trans” with AgTFA

Enhancing the m/z region of 406 to 420 demonstrates addition of one silver to either “cis” or “trans”, displayed below:

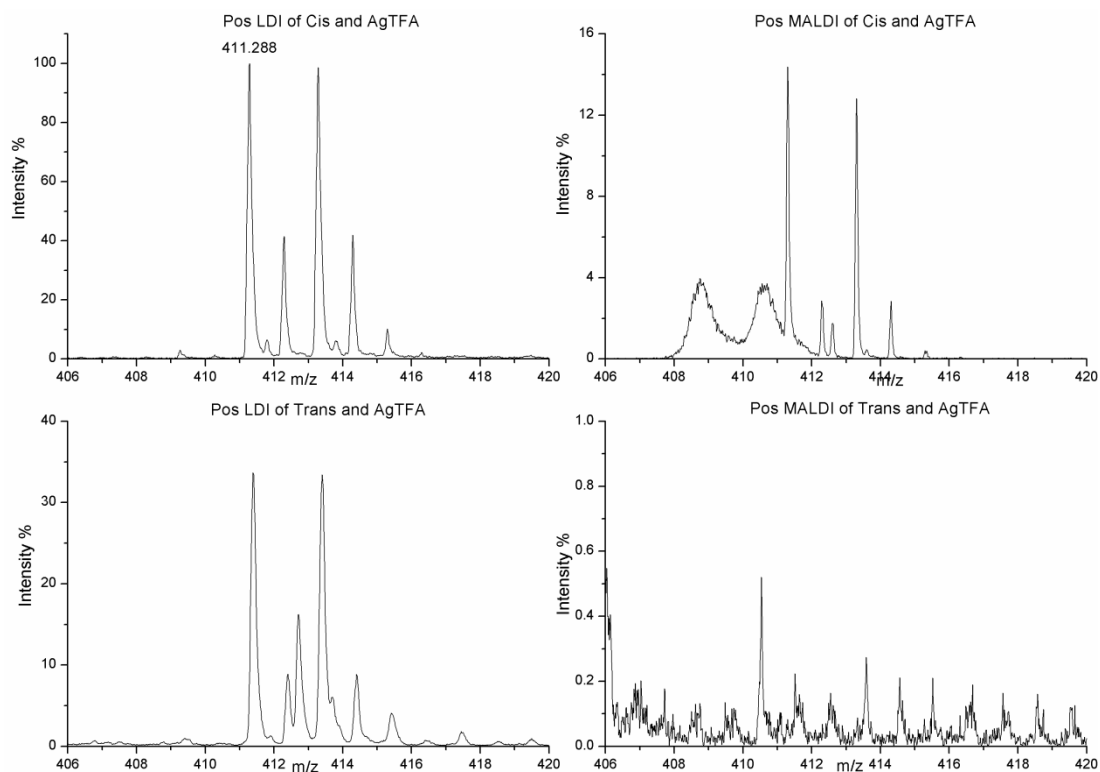


Figure 8.59: Positive-ion mode LDI and MALDI of “cis” and “trans” with AgTFA

As can be seen from the intensity values there is greater addition in LDI-MS compared to MALDI-MS. There is less addition to “trans” than to “cis”, it is almost non-existent in the MALDI spectrum of “trans”. This could be due to silver preferring to bind two ligands, in which case for “trans”, one silver would attach two “trans” molecules:

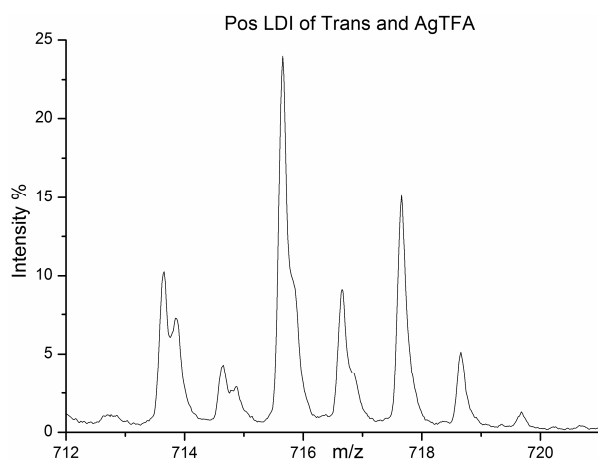


Figure 8.60: Positive-ion mode LDI of “trans” with AgTFA, m/z region 712 to 721

It appears that two sets of peaks are overlapping in the enhancement of the m/z region of [“trans”₂Ag]. It cannot be said with any certainty that [“trans”₂Ag] is present, as the isotopic pattern does not match the simulated pattern, unless it is the smaller of the two sets of peaks, and is therefore obscured by the larger peaks.

LIFT experiments were performed on the silver complexes, with and without DCTB present:

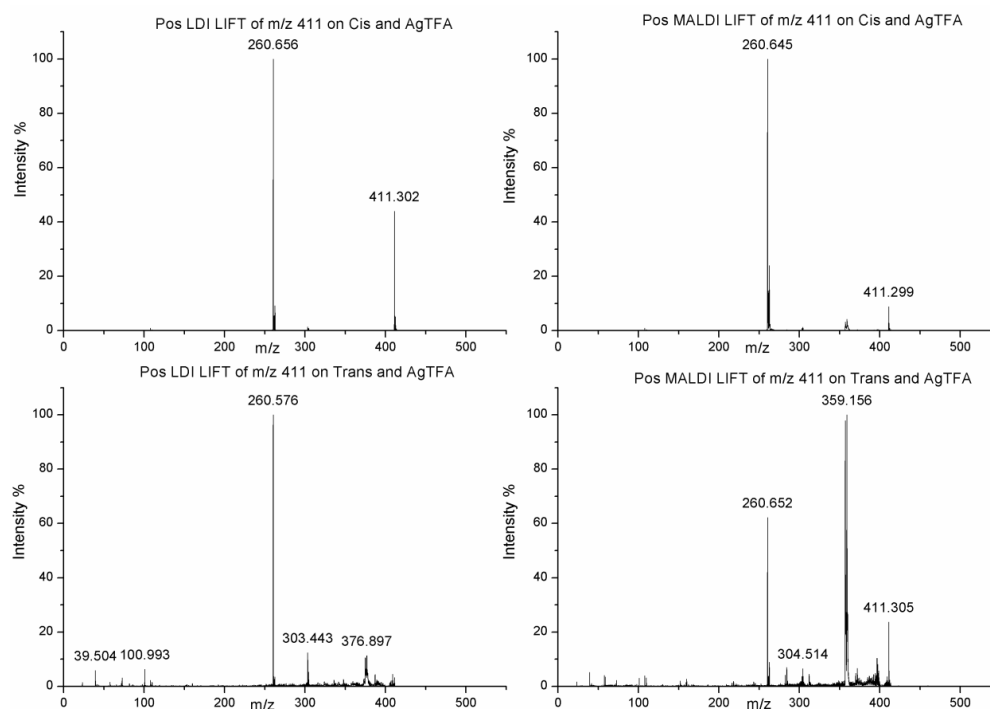


Figure 8.61: Positive-ion mode LIFT of 411 for “cis” and “trans” with AgTFA, LDI and MALDI. The same fragmentation pattern can be seen in the MALDI and LDI LIFT spectra of m/z 411, for both “cis” and “trans”. It is also identical to the ESI spectra, in that “cis” and “trans” appear to break in half with one half retaining the silver. In the “trans” spectra there is, however, also some evidence of the silver being lost and the “trans” remaining whole and retaining the charge, with small peaks at approximately m/z 304.

C₆₀, C₆₀PAH and Gold

An extension of the research was to test if other metals could be encouraged to form complexes with the fullerenes and related compounds. Initial tests were performed using gold. A gold solution was mixed with C₆₀A, under the same conditions as for silver. Positive-ion mode ESI and positive and negative-ion mode MALDI-MS were performed.

The positive-ion mode ESI spectrum of C₆₀A with Au is below:

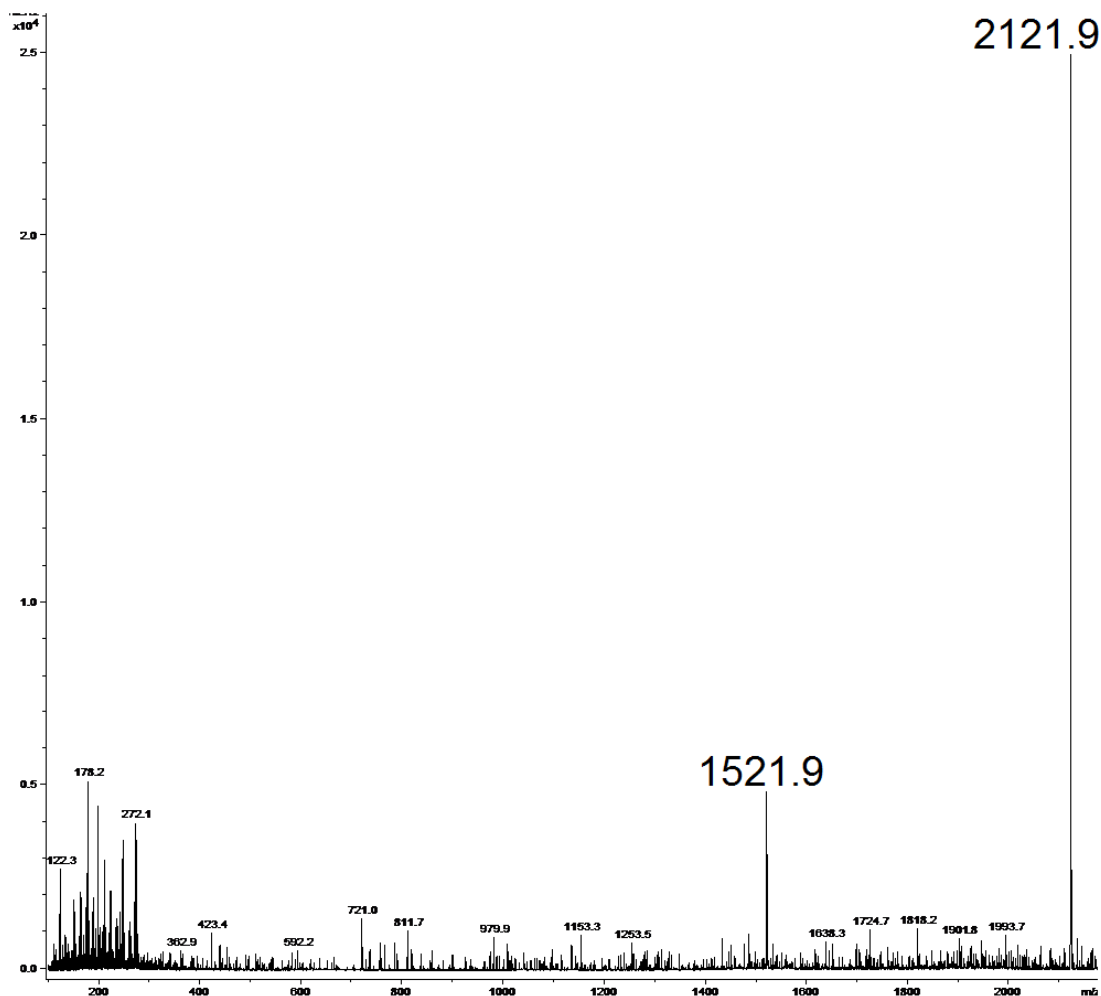


Figure 8.62: Positive-ion mode ESI spectrum of $C_{60}A$ with $AuCl_3$

The expected m/z value of $[C_{60}AAu]$ is 1095. The expected m/z of a gold bound $C_{60}A$ dimer would be at 1993. There is a peak at m/z 1993.7; however, it is of such a low intensity as to be indistinguishable from the noise. There is no sign of a peak at m/z 1095.

MS/MS was performed on m/z 2121.9:

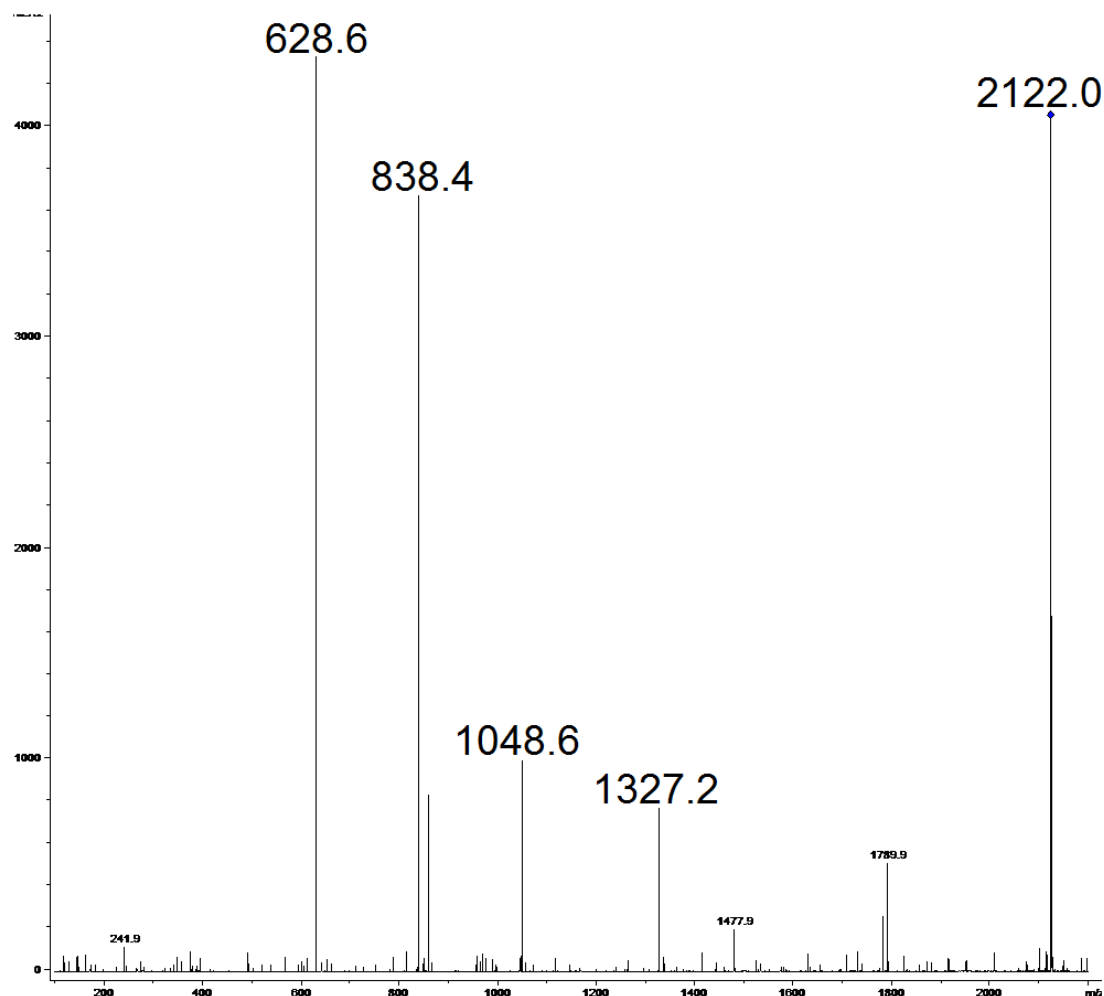


Figure 8.63: Positive-ion mode MS/MS spectrum of m/z 2121.9

There are no indications of $C_{60}A$, or gold in any of the fragment peaks in the MS/MS spectrum. m/z 2121.9 was presumably just a contaminant inside the ESI. The machine is open access, and although a large volume of solvent was flushed through the system prior to starting the experiments, some particularly strong contaminants were always present.

The positive and negative-ion MALDI-MS spectra for $C_{60}A$ are below:

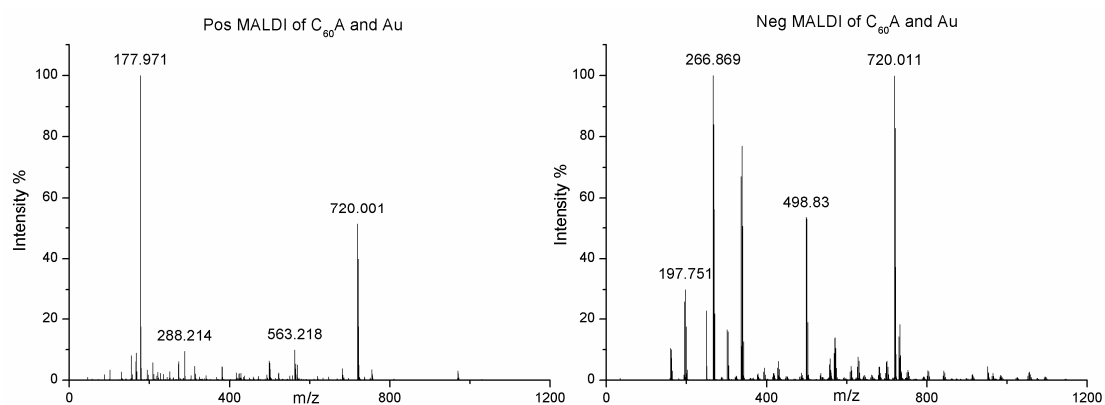


Figure 8.64: Positive and negative-ion mode MALDI of $C_{60}A$ with Au

In positive-ion mode, there are peaks indicating anthracene and C_{60} . In negative-ion mode there are peaks for Au and C_{60} .

Enhancing the m/z region 1088 to 1104 shows a series of peaks at the expected value for $[C_{60}AAu]$ in negative-ion mode. In positive-ion mode there is also a very small peak at the correct m/z value:

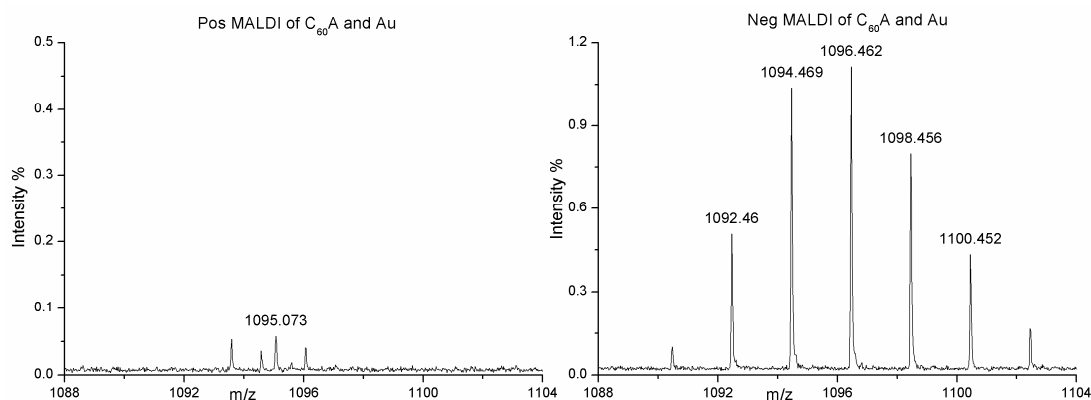


Figure 8.65: Positive and negative-ion mode MALDI of $C_{60}A$ and Au, m/z region 1088 to 1104

The intensities of the possible $C_{60}AAu$ peak for both positive and negative-ion mode are very low, below 1% intensity of the dominant peak in their respective spectra.

Initial attempts at producing gold bound dimers or even a gold- $C_{60}A$ complex have failed. The intensity of the possible $C_{60}AAu$ peaks are too low in MALDI. As negative-ion mode appeared to produce a cleaner peak, and a peak for gold, which was absent in positive-ion mode, perhaps negative-ion mode ESI would be more successful. It seems further optimisation would be required, which could not be performed during the course of this PhD due to time constraints.

Standard ESI of Fullerenes

Both positive and negative-ion mode methods have been reported that produce ions of fullerenes and fullerene derivatives in ESI.

Initially attempts were made to replicate the positive-ion mode work performed by Wilson et al.¹⁰. Instead of potassium acetate, sodium acetate was used. Additionally, instead of tagging the fullerene with a crown ether, the assumption was made that isopropyl mono, as a

fullerene derivatised with a ligand, should ionise within the ESI source. Sodium acetate was added to the solution, in order to produce a peak of the sodium adduct of the molecular ion. It was immediately obvious that altering the target mass of the machine drastically altered the appearance of the spectra. With the target mass set at m/z 2200, the following spectrum was produced:

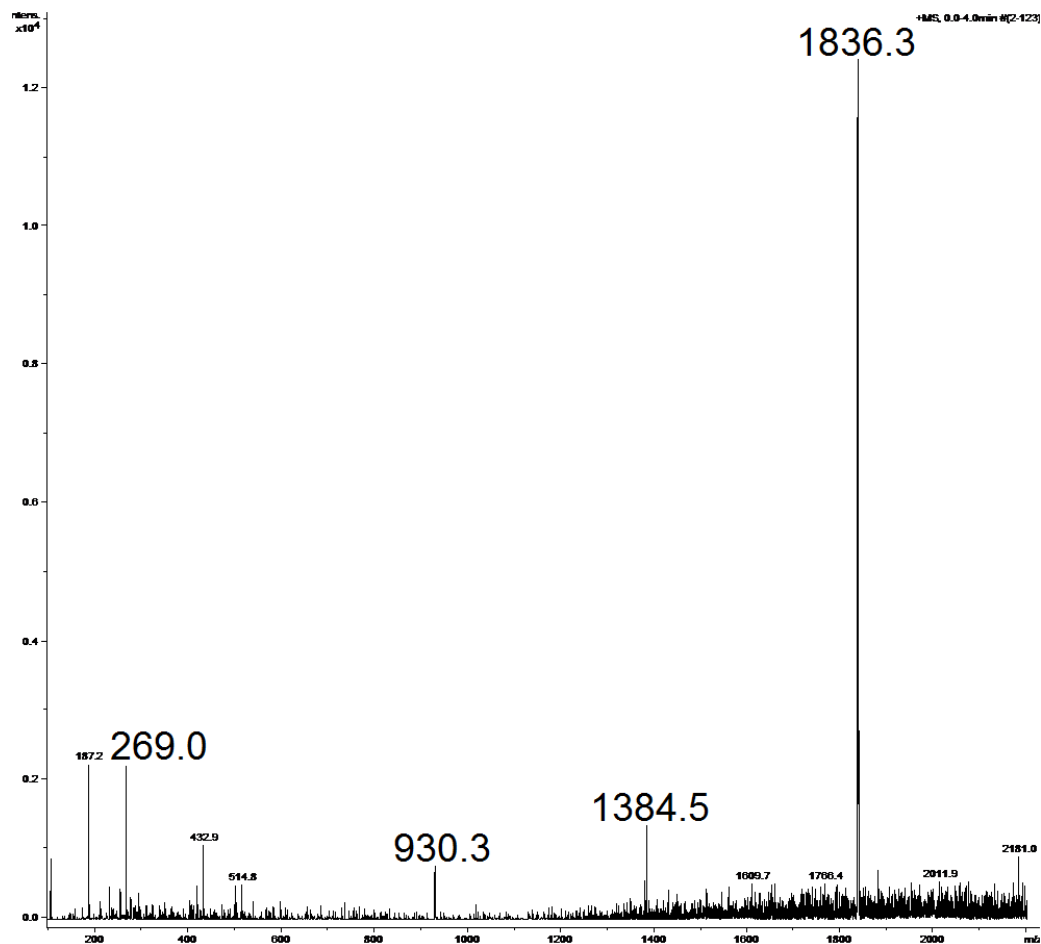


Figure 8.66: Positive-ion mode ESI spectrum of isopropyl mono with sodium acetate

With the target mass set at m/z 1400, the following spectrum was produced:

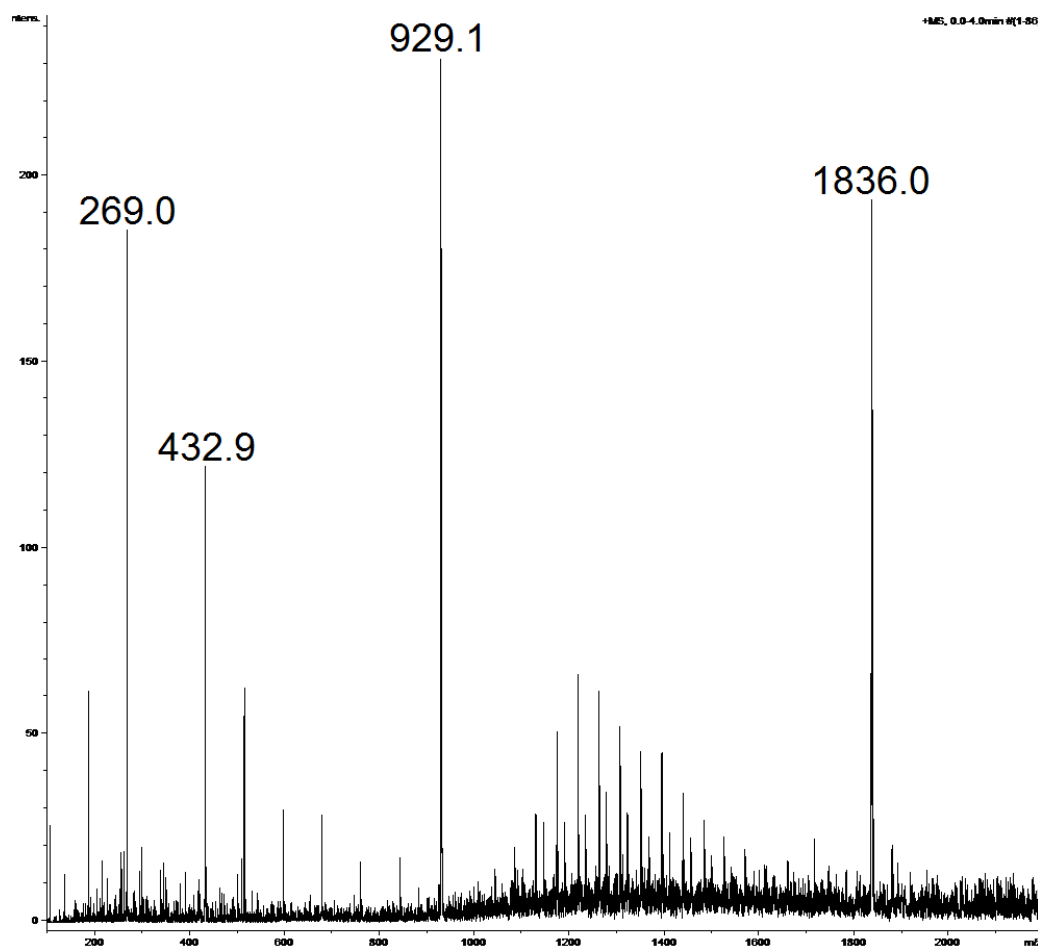


Figure 8.67: Positive-ion mode ESI spectrum of isopropyl mono with sodium acetate

In the first spectrum, the peak at m/z 929 is extremely low in intensity, especially when compared to the peak at m/z 1836. In the second spectrum, the peak at m/z 929 is larger in intensity.

The peak at m/z 929 corresponds to the sodium adduct of isopropyl mono. The peak at m/z 1836 is more interesting in that it appears to be a sodium bound dimer of isopropyl mono.

The isotopic patterns of the two peaks are displayed below, with m/z 929 shown left, and 1836, right.

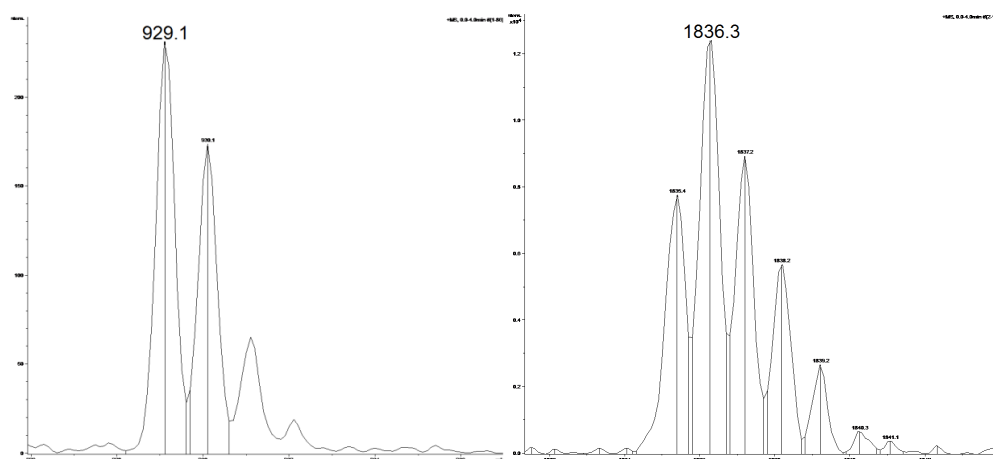


Figure 8.68: Isotopic pattern from the measured mass spectrum of m/z 929, left, and m/z 1836, right

For the sodium-bound dimer, the peak at m/z 1836 is higher in intensity than the peak at m/z 1835. This is due entirely to the presence of carbon-13. The isotopic pattern is identical to the simulated pattern for $[(C_{69}O_4H_{14})_2Na]$.

MS/MS of the peaks at m/z 1836 confirmed the identity of the peaks. MS/MS of m/z 1836 is shown below:

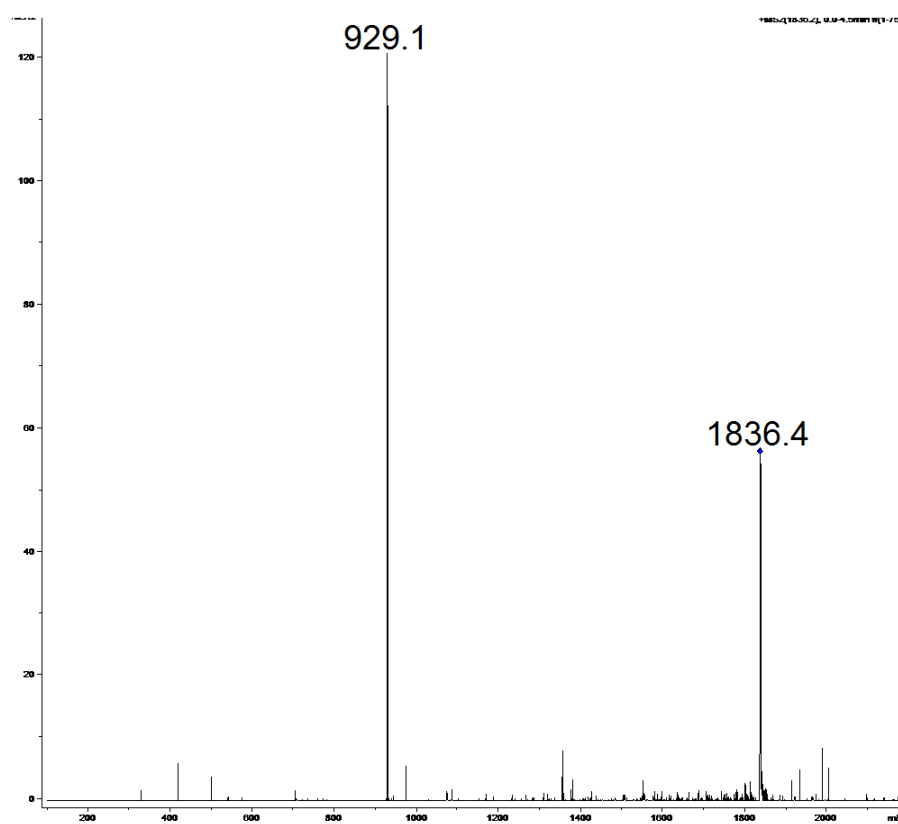


Figure 8.69: Positive-ion mode ESI spectrum of isopropyl mono and sodium, MS/MS of m/z 1836.2

The peak at 1836.2 loses one isopropyl mono molecule to produce the peak at 929.1.

The method for producing negative-ion mode spectra of fullerenes has also been repeated. Addition of sodium methoxide is reported to produce signals for C_{60}^- and the addition of odd numbered methoxy groups, such as $C_{60}(OCH_3)^-$, $C_{60}(OCH_3)_3^-$, and so forth. Minor signals for oxidised products, such as $C_{60}O^-$ and $C_{60}O(OCH_3)_3^-$, were also produced. The experiments were repeated here with C_{60} , and produced the following spectrum:

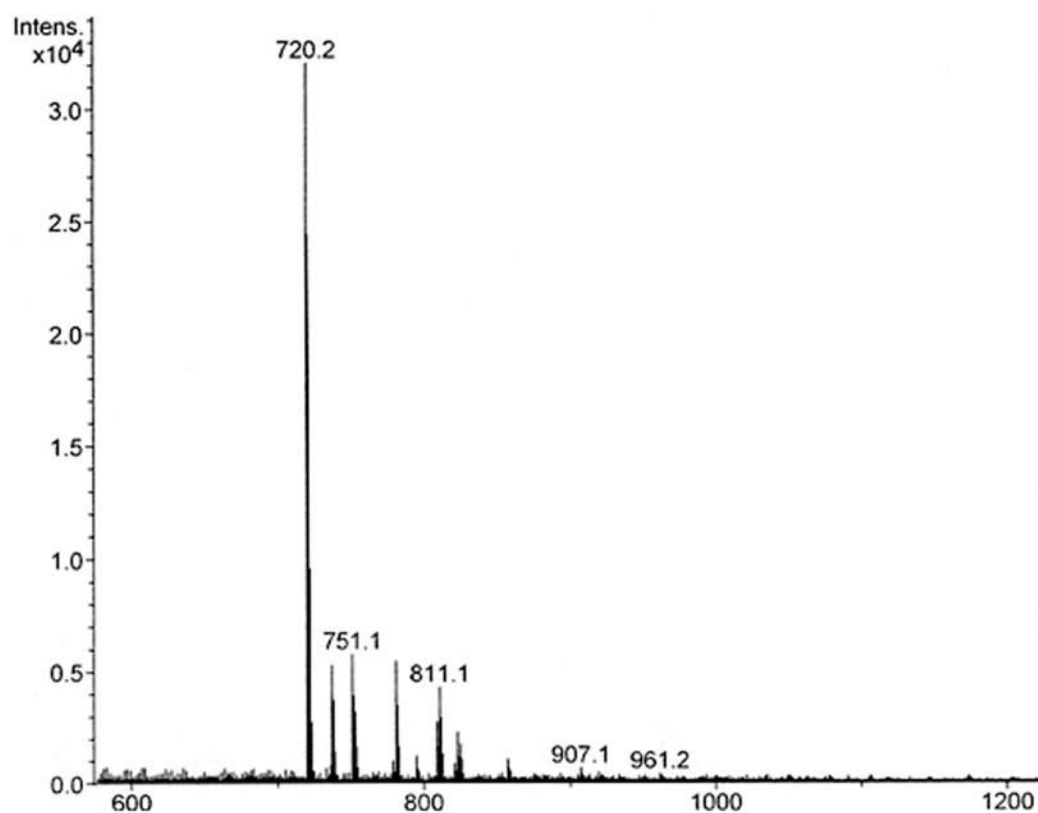


Figure 8.70: Negative-ion mode ESI spectrum of C_{60} with sodium methoxide

The peaks produced here have been identified as below:

m/z	Identification
720	C_{60}^-
721	$C_{60}H^-$?
737	$C_{60}OH^-$
751	$C_{60}OCH_3^-$
781	$C_{60}(OCH_3)_2^- - H$
811	$C_{60}(OCH_3)_3^- - 2H$

Table 8.23: Peaks from the negative-ion mode ESI spectrum of C_{60} and Sodium Methoxide

The peak at m/z 721 has a larger intensity than would be expected of $^{12}\text{C}_{59}^{13}\text{C}$, and has been tentatively identified as C_{60}H . As was been discussed in chapter 6, the negative ESI spectra of the C_{60} PAHs also demonstrated a massively enhanced m/z 721 peak. Addition of a negative hydrogen appears to be the most likely scenario, however, further experiments are required in order to ascertain the ionisation processes involved.

In summary, previously reported methods for ionising fullerene samples have been repeated here. Both successfully produced ions, however many additional ions were also created. This may prove confusing with determining which peak is the molecular ion peak in the case of samples with unknown masses.

It has been found that simply optimising conditions within the ESI source allowed for the production of underivatised fullerenes in both ion modes without the addition of salts.

The following negative-ion mode spectra of C_{84} are examples:

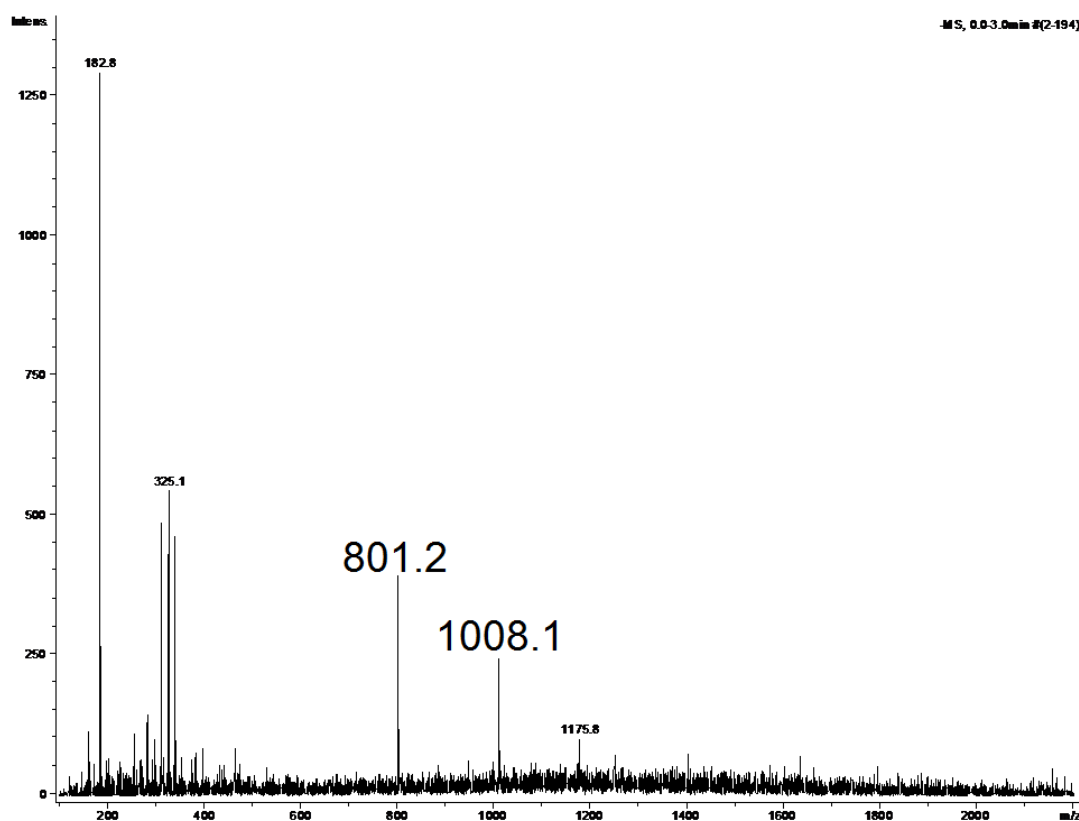


Figure 8.71: Negative-ion mode ESI spectrum of C_{84} at 100% Compound Stability

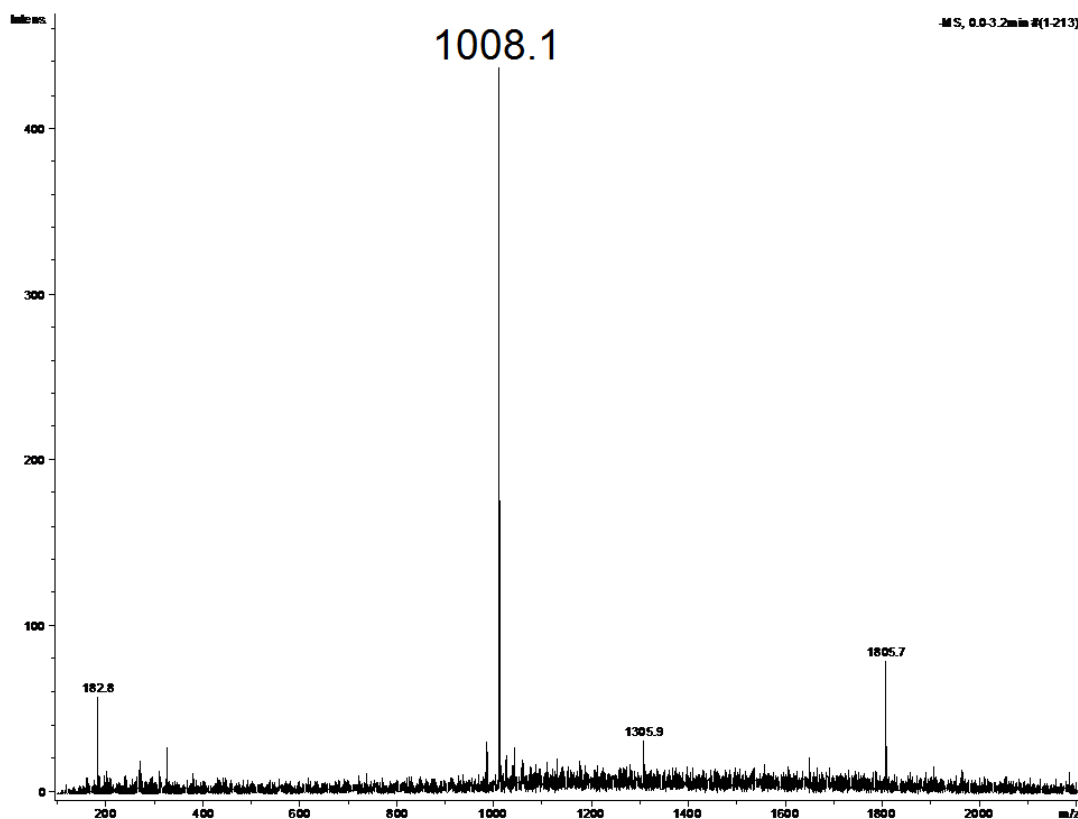


Figure 8.72: Negative-ion mode ESI spectrum of C_{84} at 500% Compound Stability

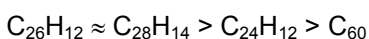
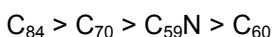
As seen in previous spectra, the compound stability has a drastic effect on the quality of the spectra. The two spectra of C_{84} were obtained at 100% and 500% compound stability. All other source settings were constant – the drying gas temperature at 100°C and the target mass was set at 1250 Da. The compound stability, as explained previously, is the voltage gradient that affects the ions after they exit the capillary. The lower the compound stability, the smaller the voltage gradient and the softer the field the ions face. In the case of fullerenes, it appears harder conditions are required for ionisation. However, in both spectra the intensity of the C_{84} peaks are relatively similar, it is the absence of other peaks in the 500% CS spectrum that makes it appear cleaner. This could be explained as the fullerenes being fairly resilient to the voltage gradient, but the molecules creating the background noise in the first spectrum not surviving the harsh conditions in the second spectrum. Either way, further optimisation of the conditions is required in order to produce cleaner spectra of a greater intensity.

Conclusion

In this chapter it has been demonstrated that the use of silver in electrospray experiments can assist in the formation of positive-ions from traditionally difficult to ionise samples, such as fullerenes and non-polar organic molecules.

Attempts have been made to determine the relative silver binding affinity of these various fullerenes and related compounds, however as has been demonstrated with C₅₉N and C₆₀, where there are differences in the ability of a sample to form ions in ESI, there will be an inaccurate calculation. At present, only a relative order of binding affinity can be presented for the samples, rather than actual figures.

It appears the larger the molecule in a series, the higher silver affinity it has:



Pentacene > Tetracene > Anthracene

Additionally, it has been found that optimisation of the conditions within the ESI source is sufficient to ionise traditionally difficult to ionise samples, without the need for addition of salts, or silver. This helps to produce clearer spectra in the sense that there are fewer peaks produced, however, the signal-to-noise ratio is fairly low, resulting in spectra of low quality. There is also the occasional addition of one mass unit in negative ion mode, which could suggest addition of a negative hydrogen ion.

Further optimisation of the conditions should help produce cleaner spectra; however, further experiments are required in order to ascertain the ionisation process that results in the plus one addition to the molecular ion peaks.

The experiments with “cis”, “trans” and silver produced some spectacular spectra which demonstrated beyond doubt that silver (I) in the gas phase preferentially binds two ligands. Fragmentation of [“trans”₂Ag]⁺ showed how the molecules will split in half, with silver retaining one half, and subsequently attaching a water molecule. The exception being the

original complex, in which silver already has two ligands. The two molecules also confirmed the location of the interaction with silver being through the aromatic rings, as in the case of “cis”, silver could interact twice with the same molecule, and subsequently did not attach two “cis” molecules or a water molecule. Due to the separation of the aromatic rings in the case of “trans”, silver could not interact twice with the same molecule, demonstrated by the abundant dimer formation.

References

1. Cooks, R. G.; Wong, P. S. H., *Accounts of Chemical Research* **1998**, 31 (7), 379.
2. Taylor, R.; Barrow, M.; Drewello, T., *Chemical Communications* **1998**, (22), 2497-2498.
3. Rondeau, D.; Kreher, D.; Cariou, M.; Hudhomme, P.; Gorgues, A.; Richomme, P., *Rapid communications in mass spectrometry: RCM* **2001**, 15 (18), 1708-1712.
4. Reddic, J. E.; Robinson, J. C.; Duncan, M. A., *Chemical Physical Letters* **1997**, 279, 203.
5. Shu, L.; Pyo, S.; Rivera, J.; Echegoyen, L., *Inorganica Chimica Acta* **1999**, 292, 34.
6. Munakata, M.; Wu, L. P.; Ning, G. L.; Kuroda-Sowa, T.; Maekawa, M.; Suenaga, Y.; Maeno, N., *Journal of the American Chemical Society* **1999**, 121 (21), 4968-4976.
7. Ng, K.; Ma, N.; Tsang, C., *Rapid communications in mass spectrometry* **1998**, 12 (22), 1679-1684.
8. Ng, K.; Ma, N.; Tsang, C., *Rapid communications in mass spectrometry* **2003**, 17 (18), 2082-2088.
9. Laali, K. K.; Hupertz, S.; Temu, A. G.; Galembeck, S. E., *Organic & biomolecular chemistry* **2005**, 3 (12), 2319-2326.
10. Wilson, S.; Wu, Y., *Journal of the Chemical Society-Chemical Communications* **1993**, (9), 784-786.

Chapter 9: Conclusion

The gas-phase behaviour of a variety of different fullerene derivatives and related compounds has been studied using the ionisation techniques of MALDI and ESI.

Performing MALDI-MS on the various fullerene derivatives including the open-cage fullerenes provided more than just confirmation of synthesis. The open-cage fullerenes were found to reheat the cage differently under elevated laser fluences. The size of the orifice and the elements present within the orifice appear to have a direct relation to the caged structure that the open-cage fullerene reheated to.

An in depth study of $C_{60}H_2$ demonstrated how easily this molecule oxidises over time, yet is relatively stable as a powder under ambient conditions, with no degradation or cage shrinkage over the course of the four weeks for which it was studied. Key to this investigation was the establishment of MALDI conditions that would not lead to decomposition of $C_{60}H_2$. This was achieved and for the first time a meaningful mass spectrum of this compound was obtained.

Using pencil as an efficient matrix compound for fullerene derivatives proved unsuccessful. DCTB, the standard fullerene matrix was, however, proved to be far superior for fullerene derivatives in producing fragmentation-free, clean spectra. With the pencil lead, however, the very easy addition of sodium and potassium to the compound was observed, which appeared to increase stability of the target compound when compared to the behaviour of the same compound under LDI conditions. Attempts to utilise the extraordinarily easy sodium and potassium addition to distinguish isomeric compounds was successful for the open-cage fullerenes. Sodiated isomers showed the same fragment ions, but in distinctly different abundances, which allowed to distinguish them. Attempts to create sodium and potassium adducts in the past have relied upon the addition of a salt layer to the target slide, using pencil, however, is just as successful, but easier and cheaper.

C_{60} and polyaromatic hydrocarbon complexes were successfully synthesised and characterised using MALDI and ESI. A purified sample of $C_{60}P$ (P = pentacene), obtained from Glen Miller at the University of New Hampshire, allowed demonstration of the softness of the ionisation techniques for producing a molecular ion peak. Notoriously labile, the peak

intensities of C_{60} and $C_{60}P$ were almost equal using DCTB-MALDI-MS, with the molecular ion peak larger than previously reported.

The presence of silver ions when studying various compounds with the ESI-MS led to many interesting results.

Cluster formation, with and without the amino acid tryptophan, presented cluster sizes larger than those previously seen with ESI-MS. Indeed, the formation of pure silver clusters in ESI-MS without tryptophan had not been published before. Dissociation of the mixed tryptophan-silver clusters revealed many interesting facts – tryptophan is preferentially lost for all cluster sizes, unless the silver clusters had 8 or less silver atoms present, as these appeared to be stabilised by the presence of one tryptophan molecule. If only one tryptophan molecule was present, then two silver atoms were lost in preference. The exception to this rule was Ag_7^+ , and to some extent Ag_3^+ , which were stable without tryptophan. The larger cluster sizes lost the tryptophan molecules initially, and preferentially, until the bare silver cluster was produced.

Study of the hydrogen loss of the tryptophan molecules within the cluster through MS/MS experiments produced some generic tendencies, however, some exceptions were observed. The main tendency appeared to be that each tryptophan molecule would lose at most two hydrogen atoms. This is in line with the general observation that for each cluster, the maximum number of hydrogen atoms lost was two per tryptophan present. Some clusters appeared to show loss of the occasional tryptophan molecule with 4 hydrogen atoms missing. This could, however, be a consequence of the inability of the ion trap used to select precisely one exact m/z , and that clusters of the same composition but with different silver isotopes are present. Additionally, there could be hydrogen transfer within the clusters. Initial observations have shown that smaller silver clusters can be stabilised by one tryptophan molecule that has lost only one hydrogen atom. In the case of these smaller clusters, the number of hydrogen atoms that is lost from the entire cluster has not reached the maximum hydrogen loss. In this case tryptophan molecules missing two hydrogen atoms are lost first, leaving tryptophan molecules lacking only one hydrogen atom in the cluster. Although there are other competitive dissociations, the main mechanisms involve loss of either a tryptophan molecule or two silver atoms. A less preferred pathway, seen with a few of the clusters is the

loss of one silver atom and one tryptophan; it is assumed they are lost as one unit. This dissociation tends to be observed for larger clusters with an even number of silver atoms present, presumably as the result of this dissociation is an odd-numbered silver cluster. Odd-numbered silver clusters are, due to the even number of electrons, more stable than their even-numbered counterparts. These complexes have produced many interesting results, but have also raised many questions that are beyond the scope of this thesis. These will be subject of further study in the group.

With the success of utilising silver ions in ESI-MS with tryptophan, the kinetic method was attempted on several fullerenes and smaller compounds to calculate the relative silver binding affinities. The differences between MALDI and ESI were obvious in the case of the synthesised C_{60} and polyaromatic hydrocarbon complexes. The use of silver ions was effective in helping to produce ions of compounds that typically cannot be analysed with ESI-MS, such as the family of pure fullerenes. The fact that these silver-bound dimers have been produced, and then subsequently dissociated is already exciting. Even if absolute values for the silver ion affinities are still elusive and experiments with $C_{59}N$ were not successful, a relative order of silver-ion affinities of the compounds studied was obtained.

Silver was also used successfully where sodium and potassium had failed, in the differentiation of the small organic compounds, "cis" and "trans".

Many of the experiments confirmed the observation that silver tends to bind two ligands in the gas-phase. Dissociation of the silver-bound hetero- and homo-dimers under ESI conditions demonstrated that when silver lost one of the ligands, it acquired a water molecule from the ion trap in order to fulfil its need for two ligands. The differentiation experiments with "cis" and "trans" were successful due to the location at which the silver ion interacted with the compounds – the polyaromatic rings. With "cis", silver could insert in between the polyaromatic parts of the molecule, forming two bonds with one molecule. With "trans", silver had to bind two "trans" molecules, as the polyaromatic parts of the "trans" molecule were too far apart for silver to successfully interact with only one molecule. Further evidence of the bi-dentate character of gas-phase silver complexes comes from MS/MS experiments of the "cis"/"trans" complexes with silver. These fragment through the loss of one half of the "cis" or "trans" molecule. In this case, the silver would again acquire a water

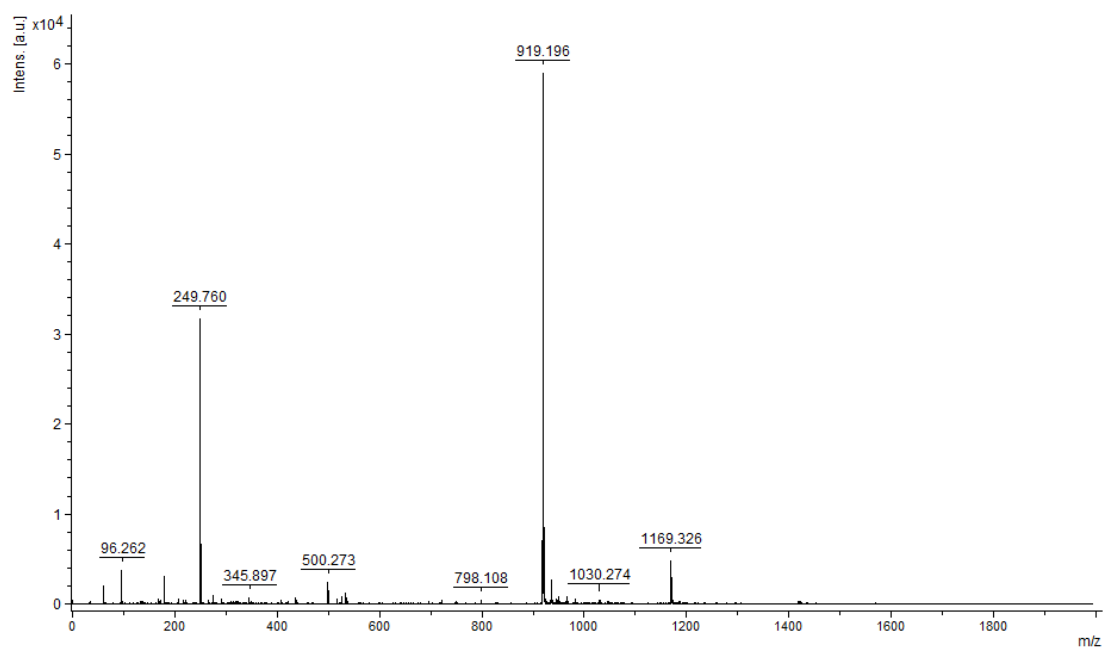
molecule. The “trans” molecule can also show ligand dissociations retaining two ligands on silver, which cannot add water in the trap.

“Bare” fullerenes have also been studied using ESI-MS without any addition of an ion forming agent. Anions were successfully formed by the addition of one mass unit, however, the signal-to-noise ratio was low, and further studies are required to ascertain the ion formation mechanism. “Bare” fullerenes appear to produce spectra of a better quality in negative-ion mode; however, both ion modes still need further optimisation for the production of better quality spectra with a greater signal-to-noise ratio of the molecular ion peaks.

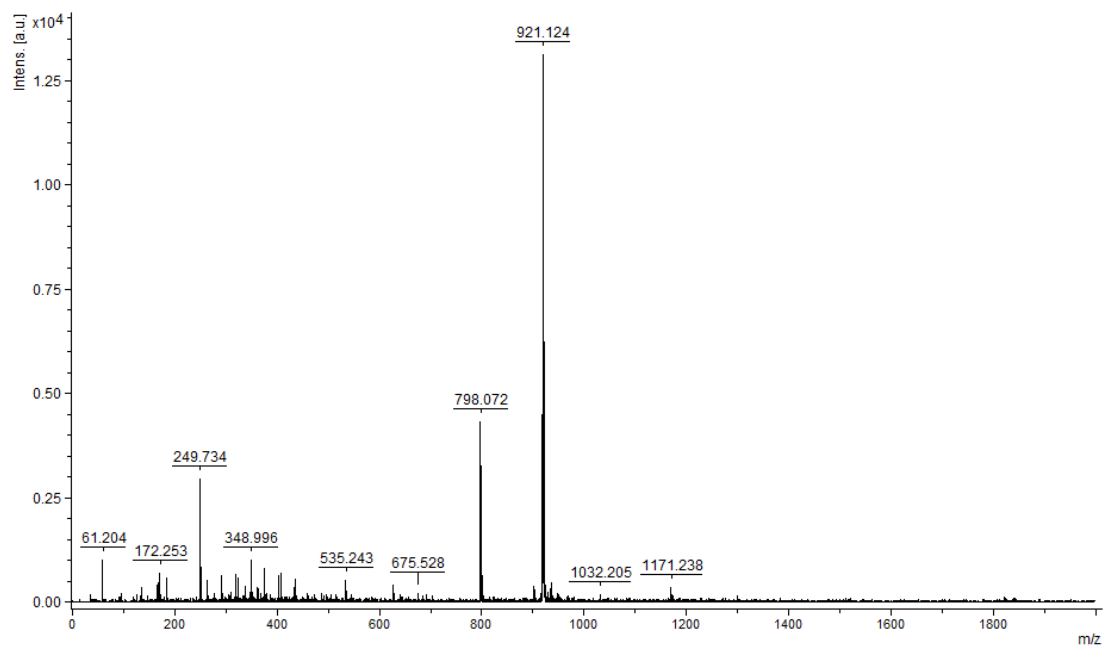
Appendix

Chapter 3 Additional Spectra

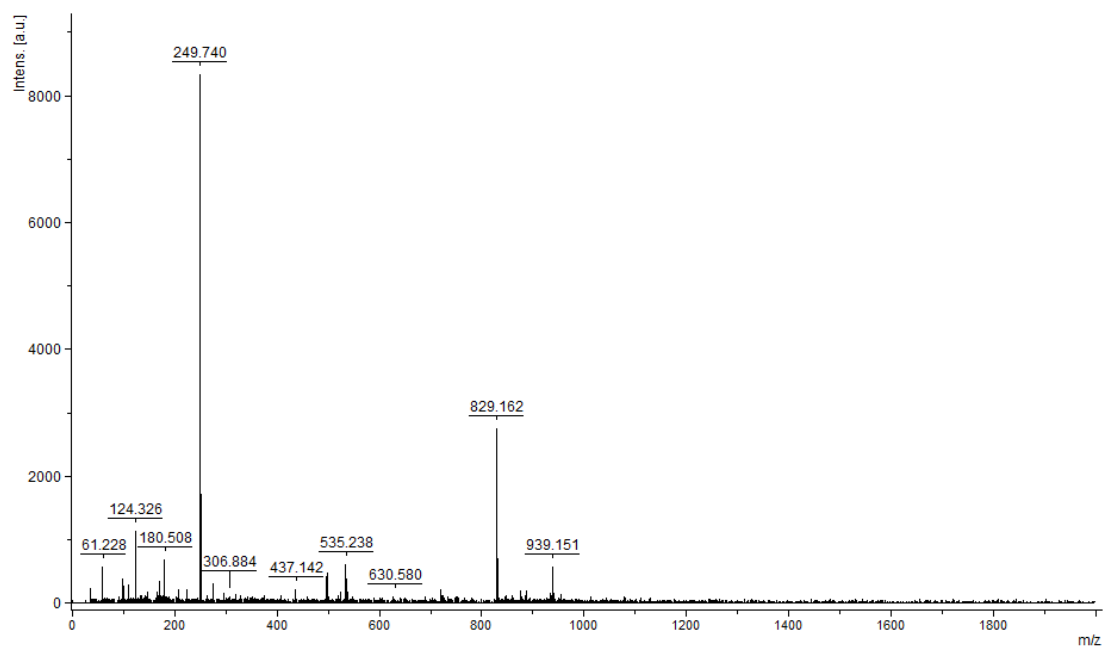
MALDI spectra



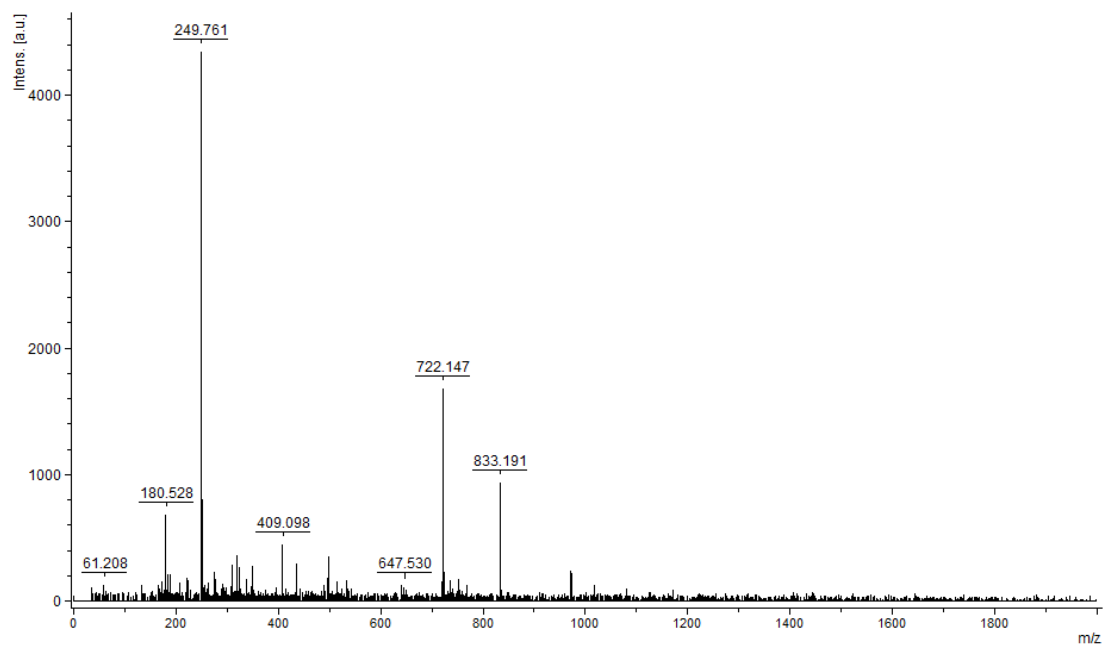
Sample 1.1, negative-ion mode MALDI



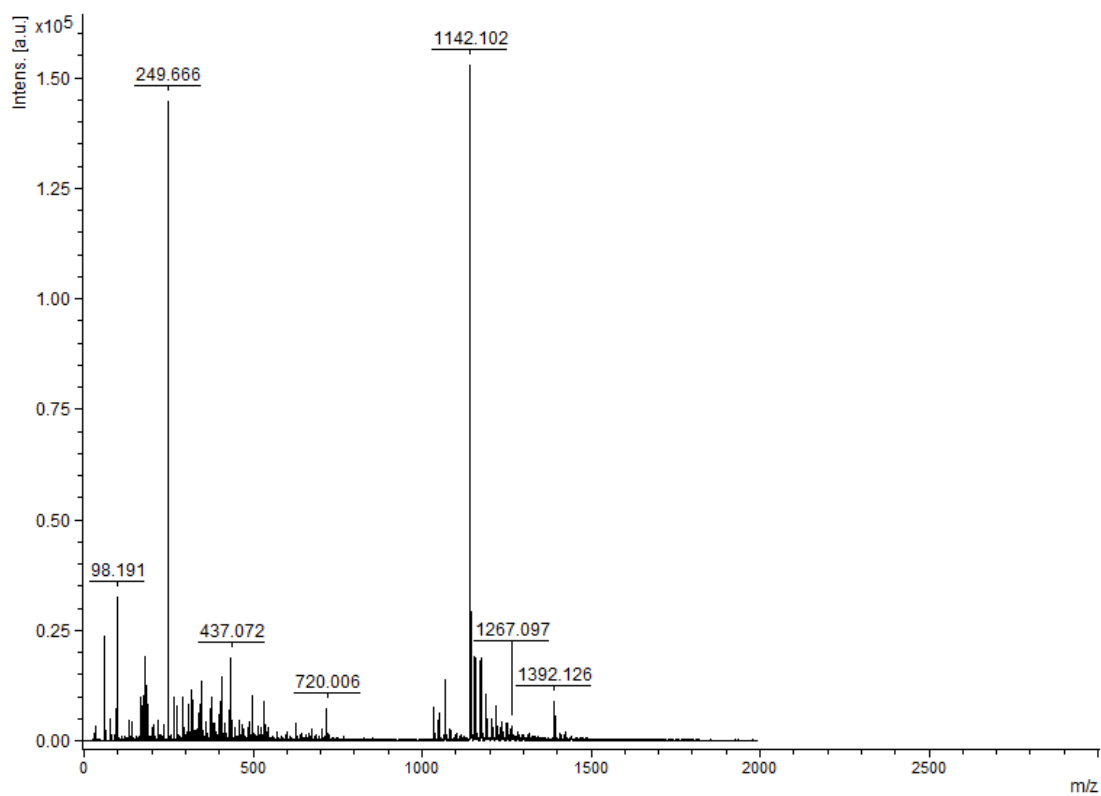
Sample 1.6, negative-ion mode MALDI



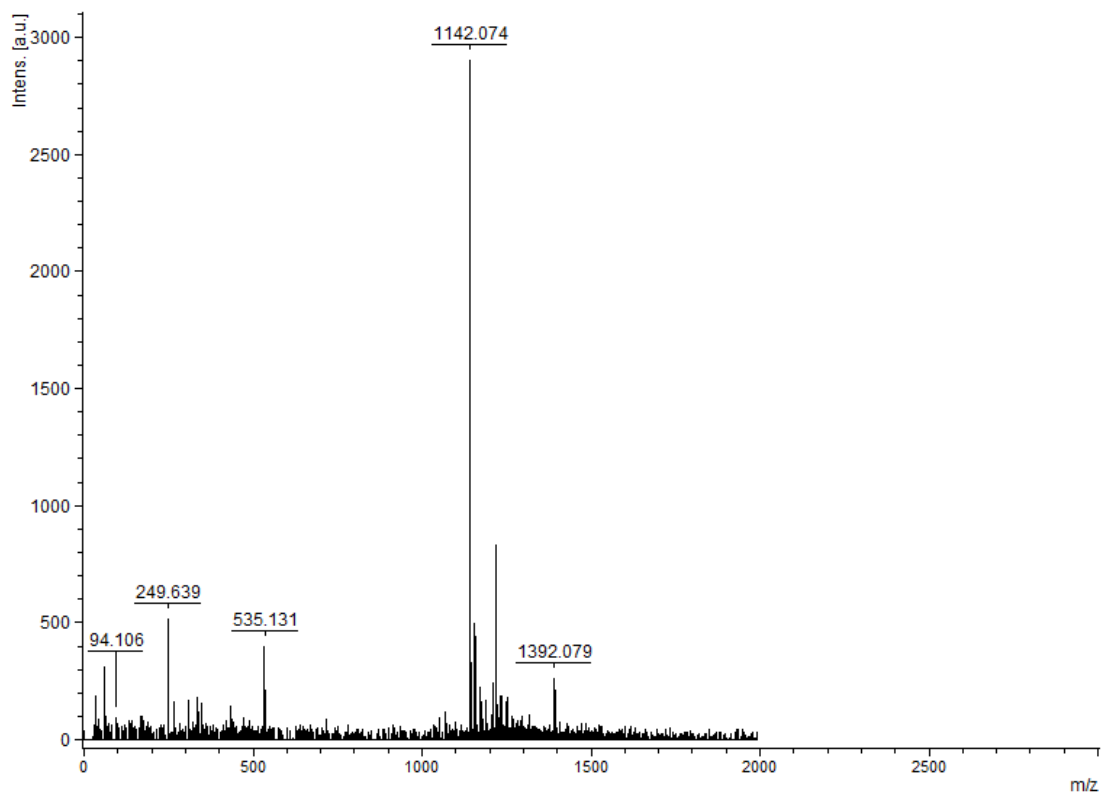
Sample 1.7, negative-ion mode MALDI



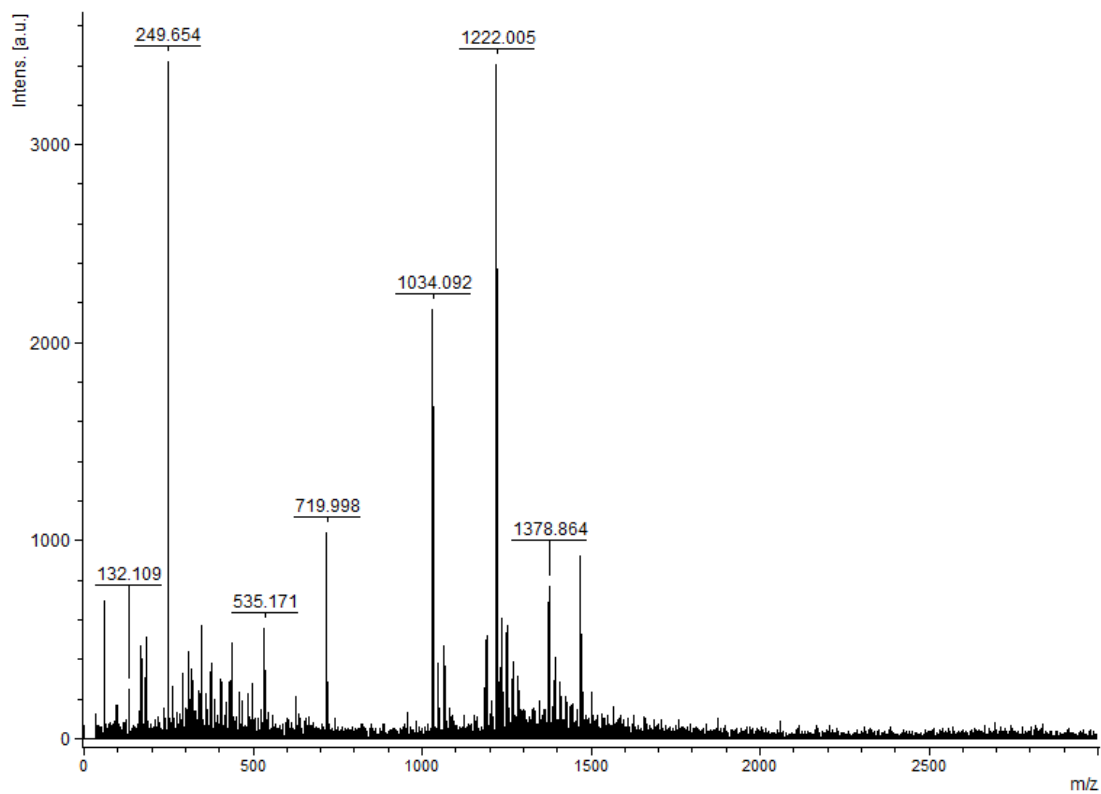
Sample 1.8, negative-ion mode



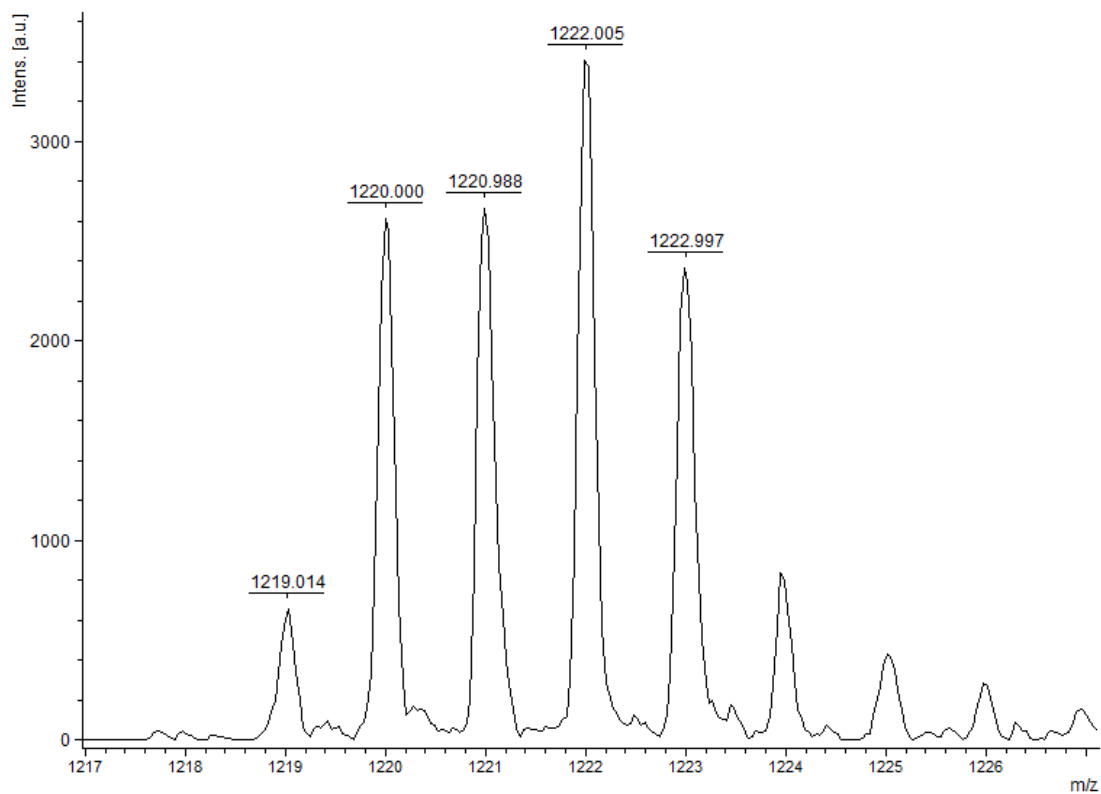
Sample 2.1, negative-ion mode MALDI



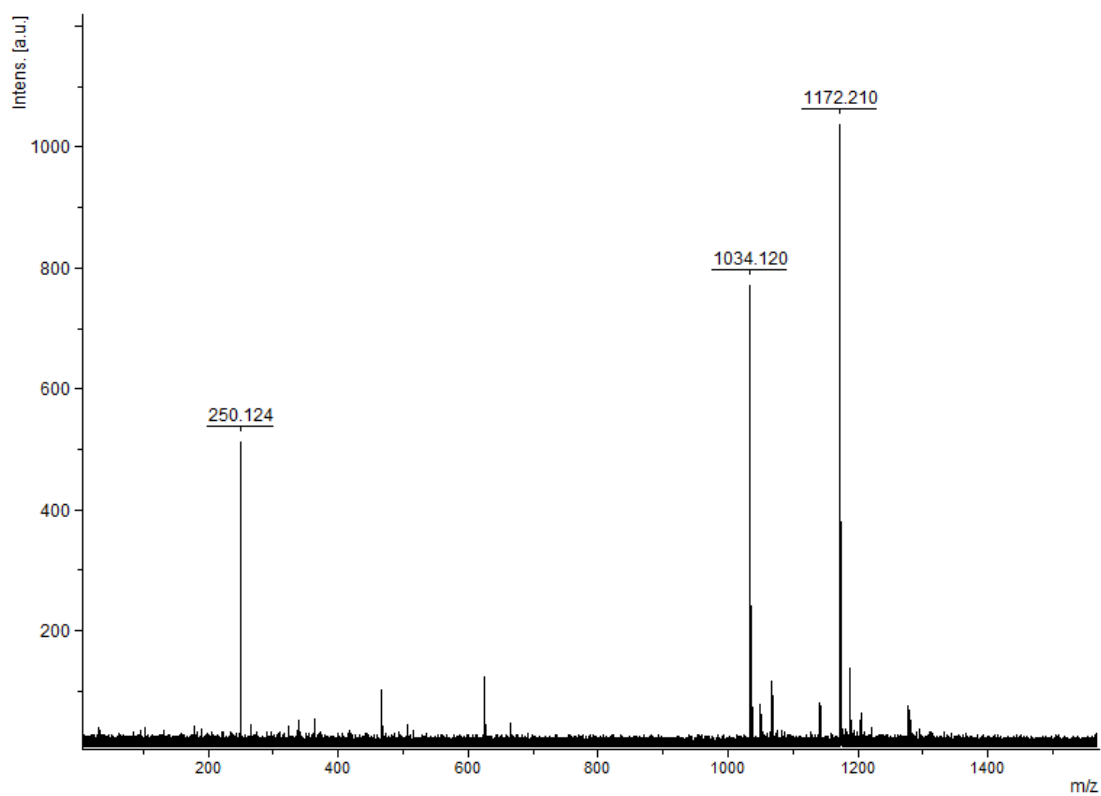
Sample 2.2, negative-ion mode MALDI



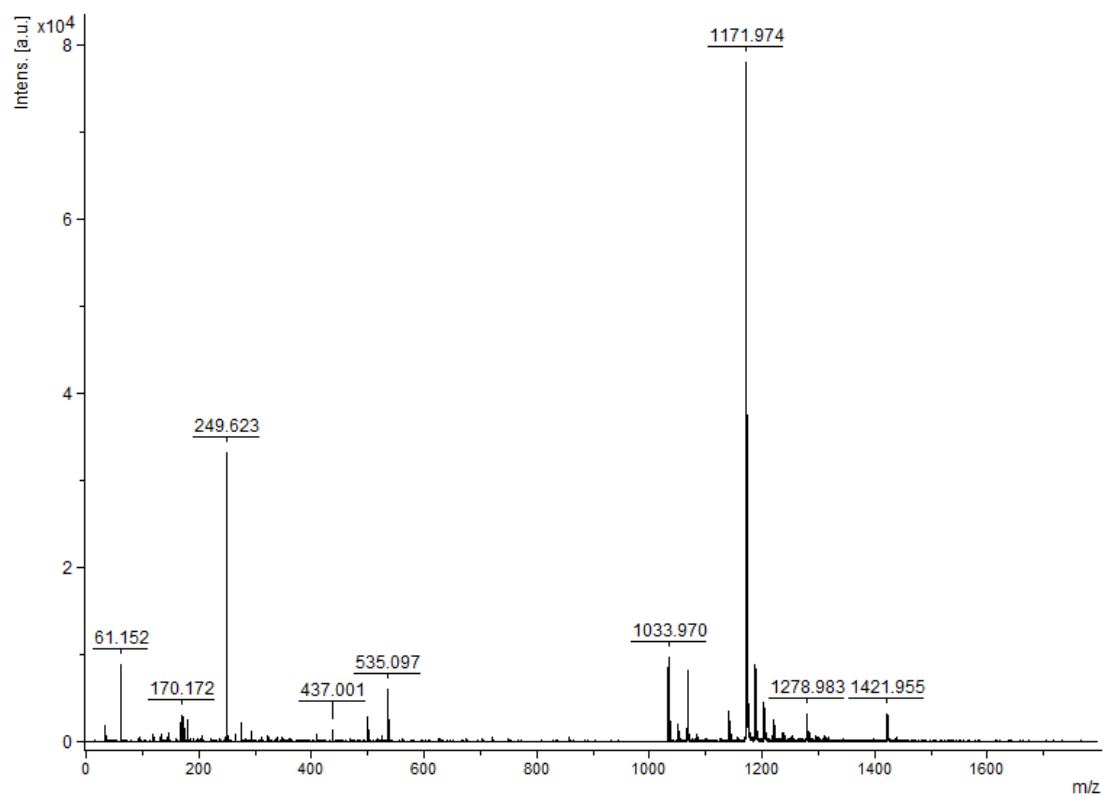
Sample 2.4, negative-ion mode MALDI



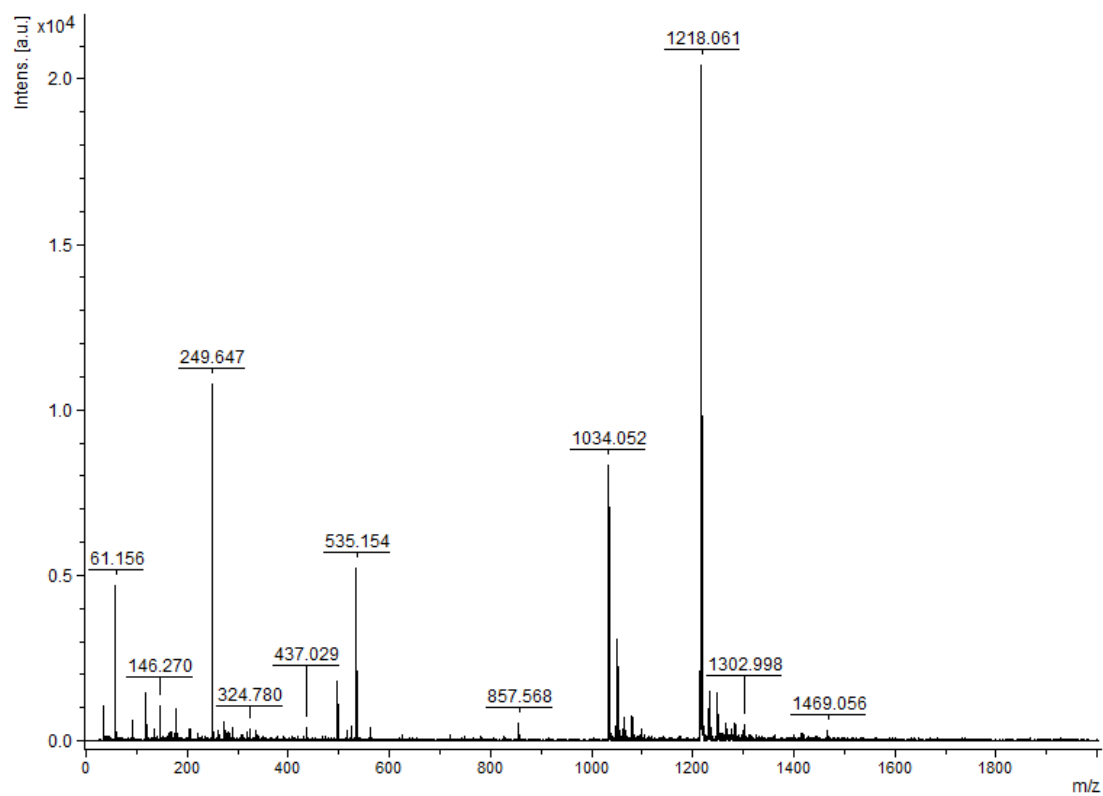
Sample 2.4, negative-ion mode MALDI, isotopic pattern



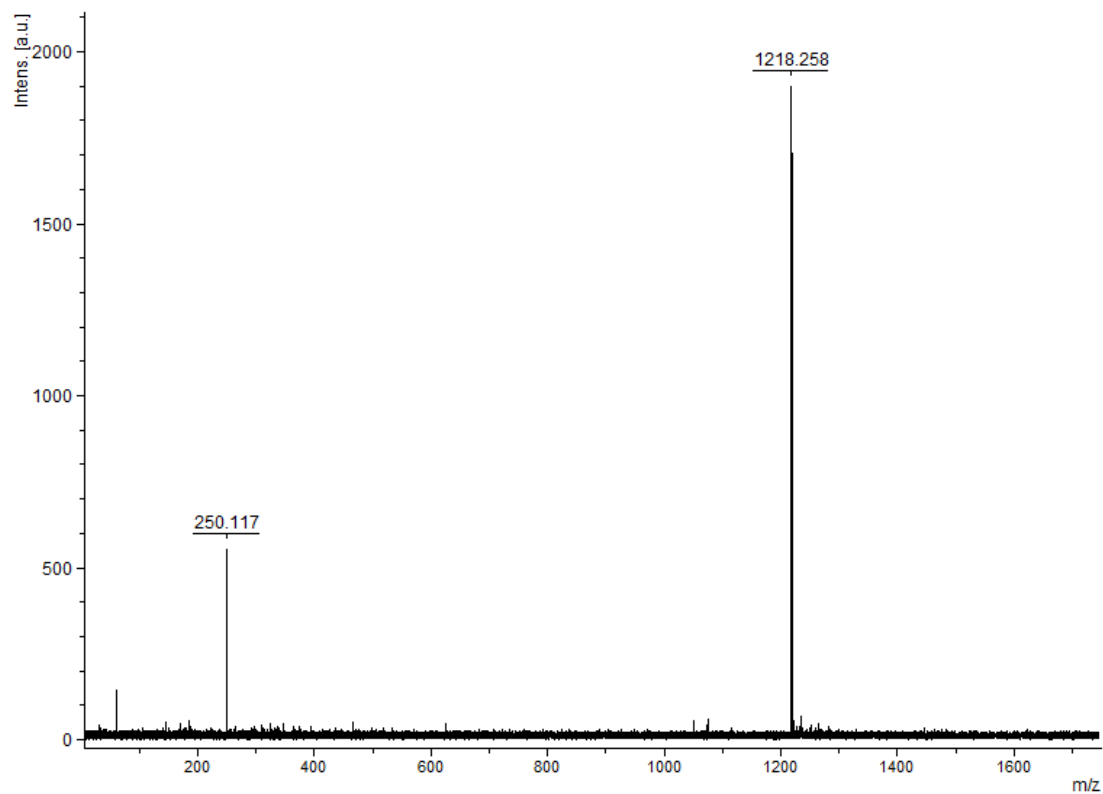
Sample 2.5, negative-ion mode MALDI



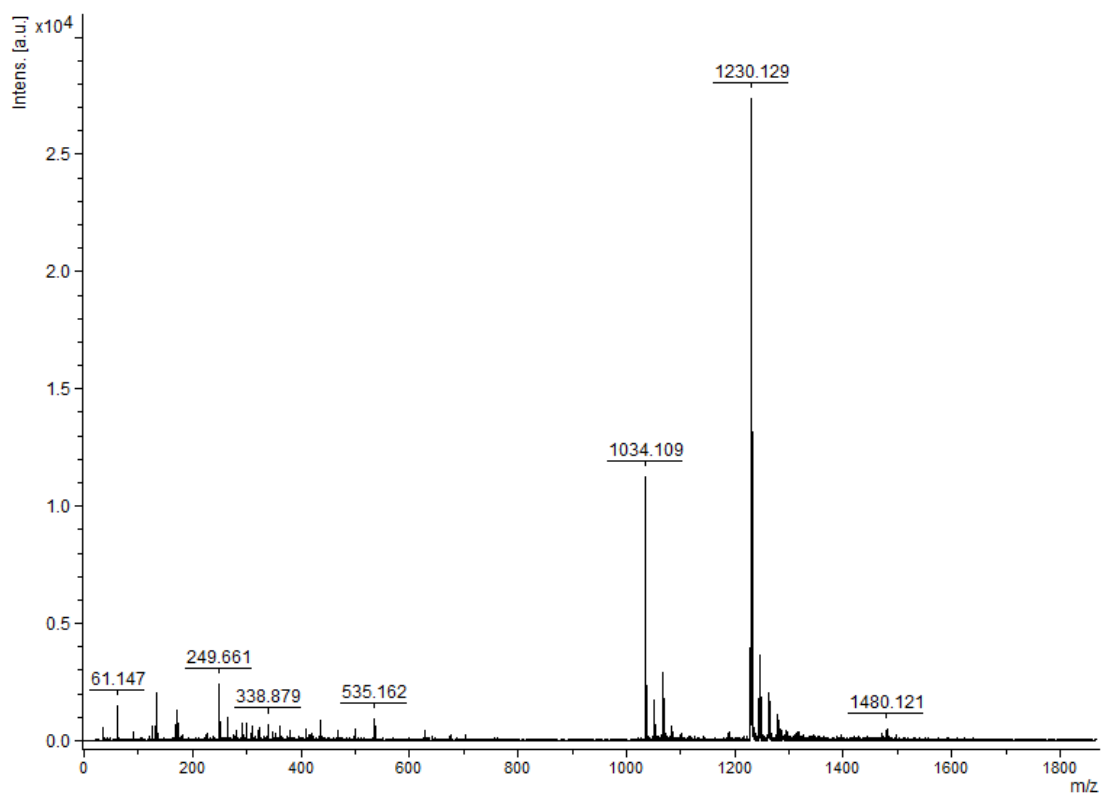
Sample 2.6, negative-ion mode MALDI



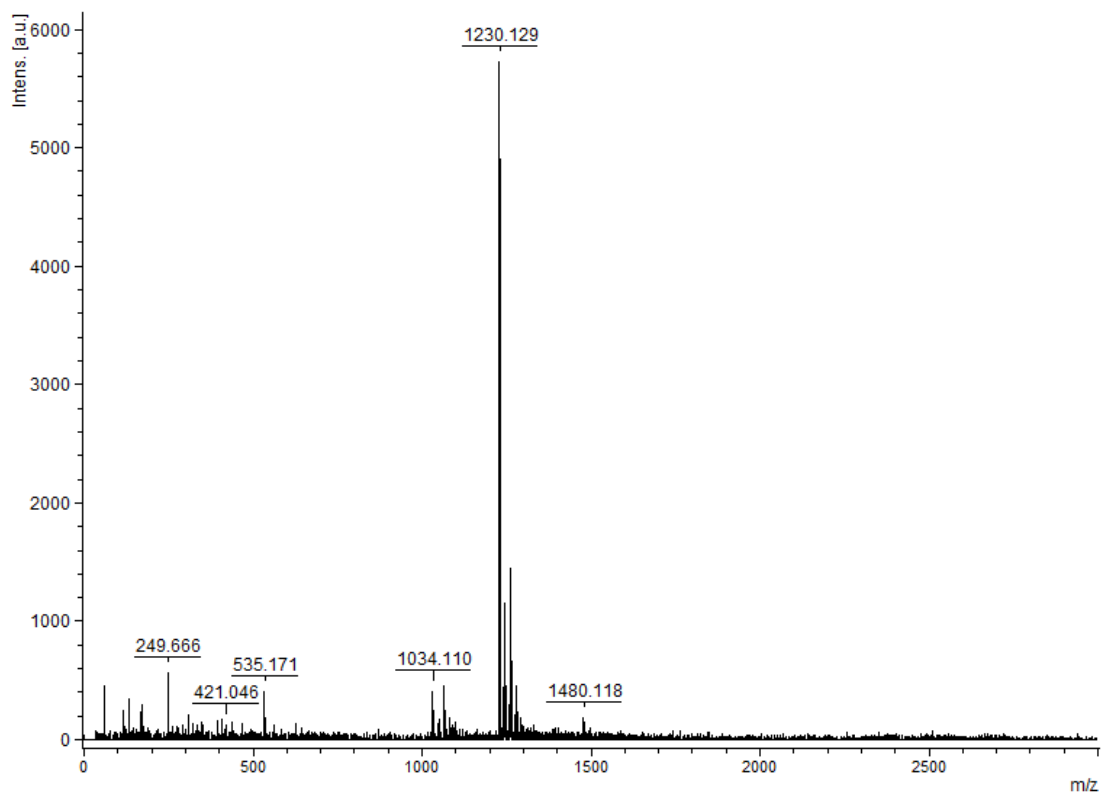
Sample 2.7, negative-ion mode MALDI



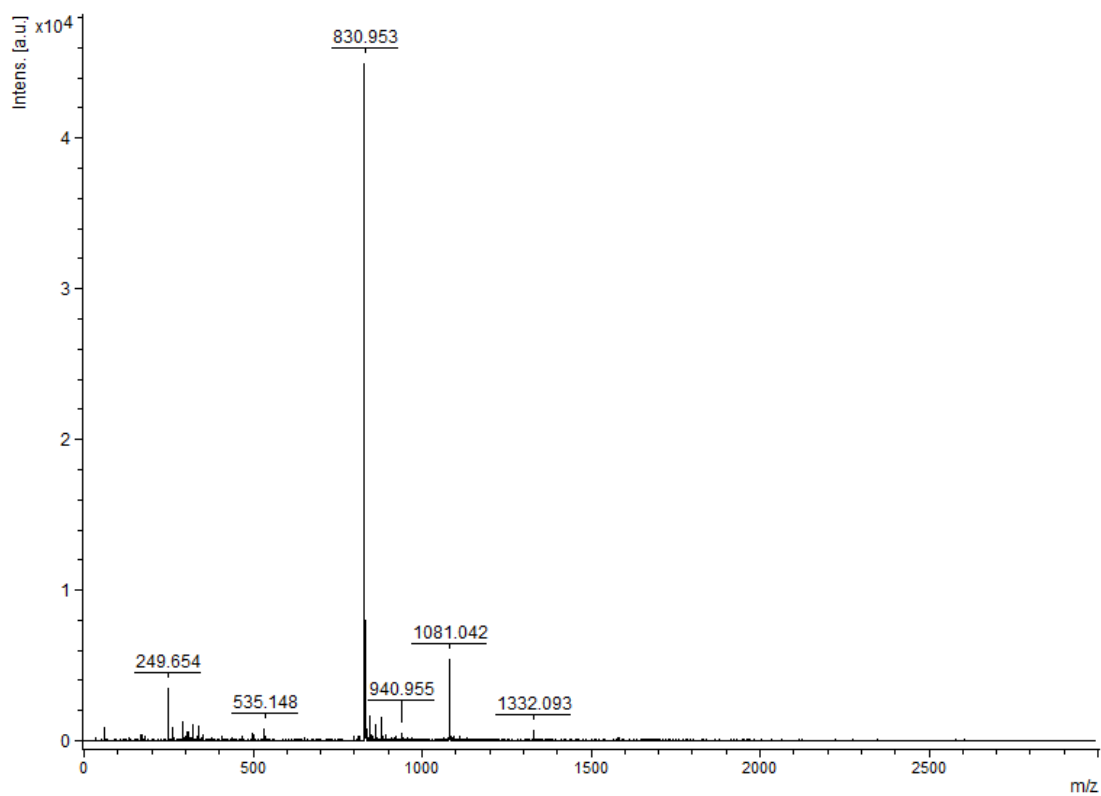
Sample 2.8, negative-ion mode MALDI



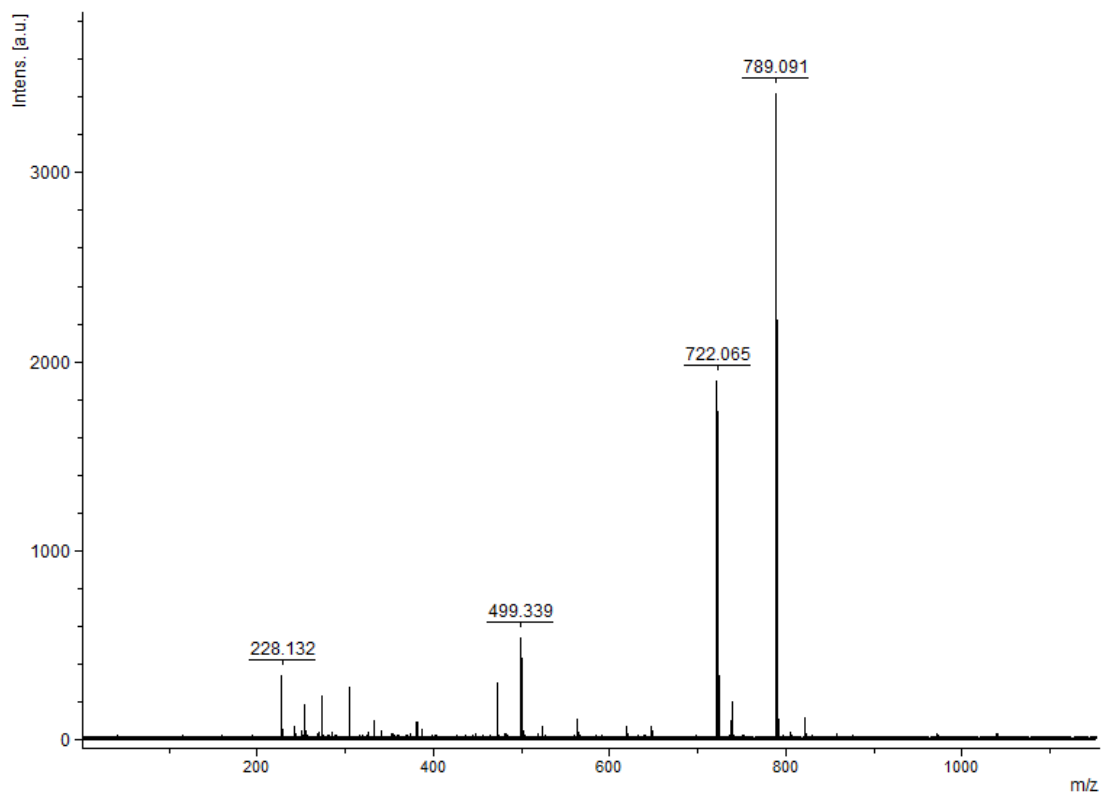
Sample 2.9, negative-ion mode MALDI



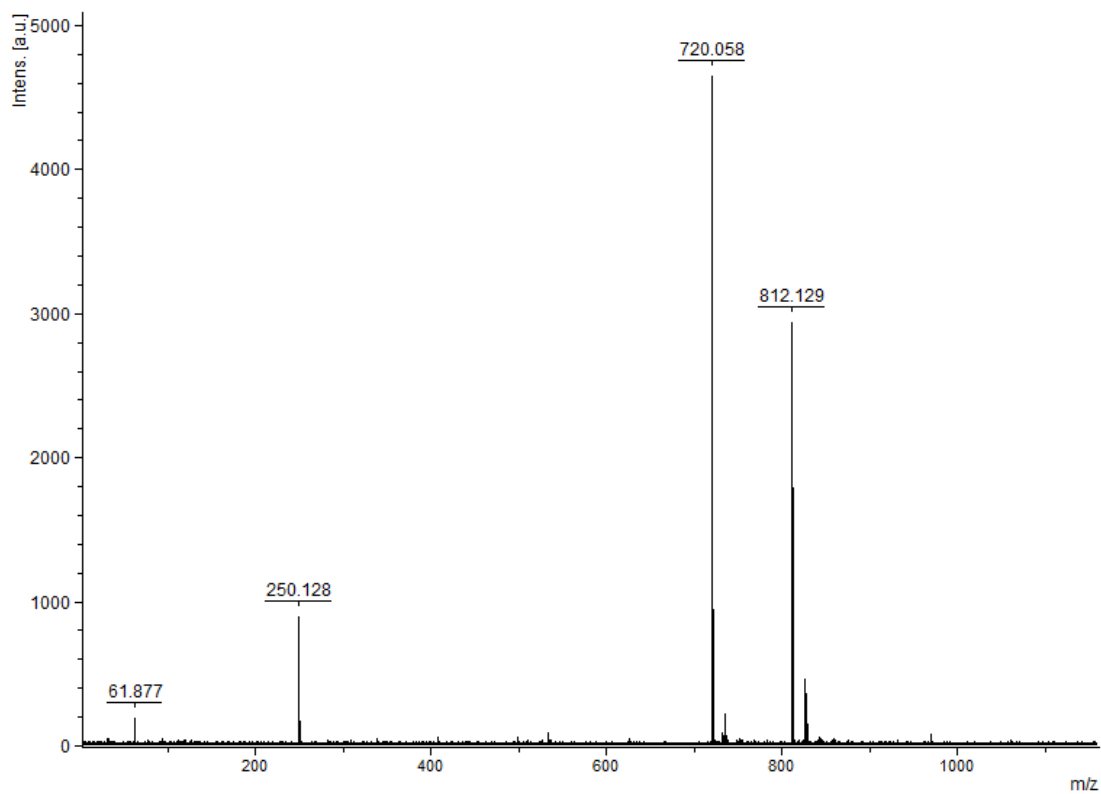
Sample 2.10, negative-ion mode MALDI



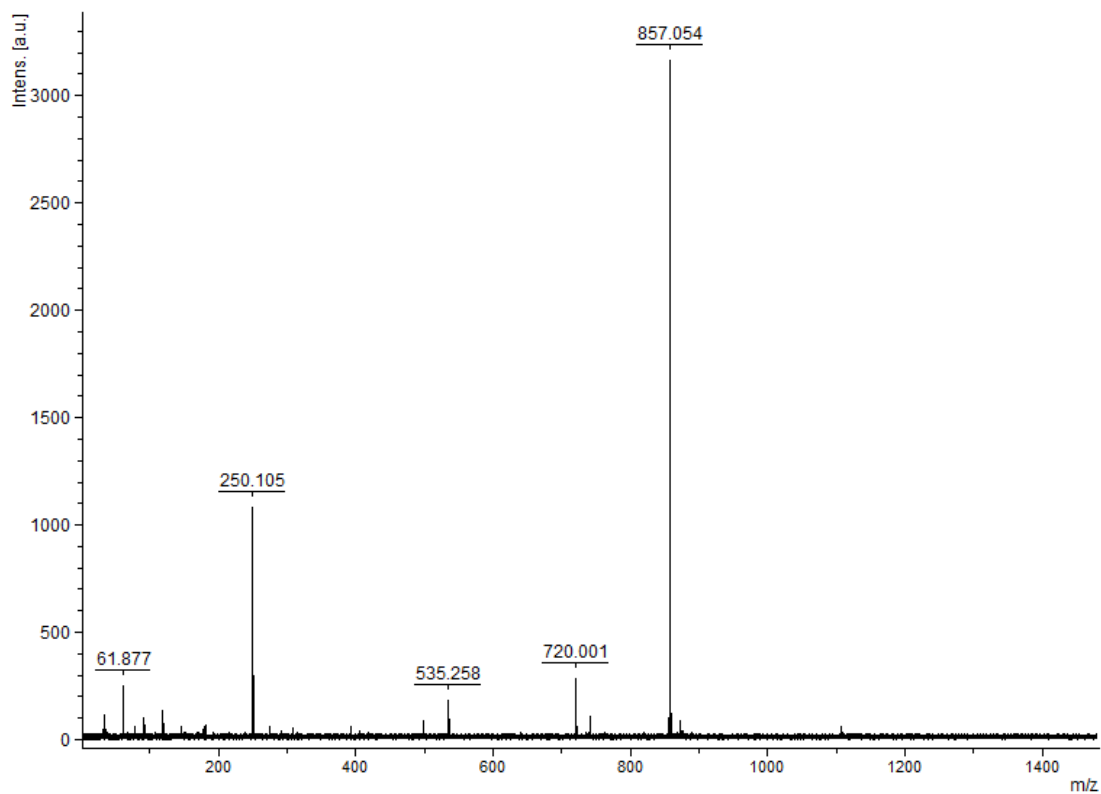
Sample 2.11, negative-ion mode MALDI



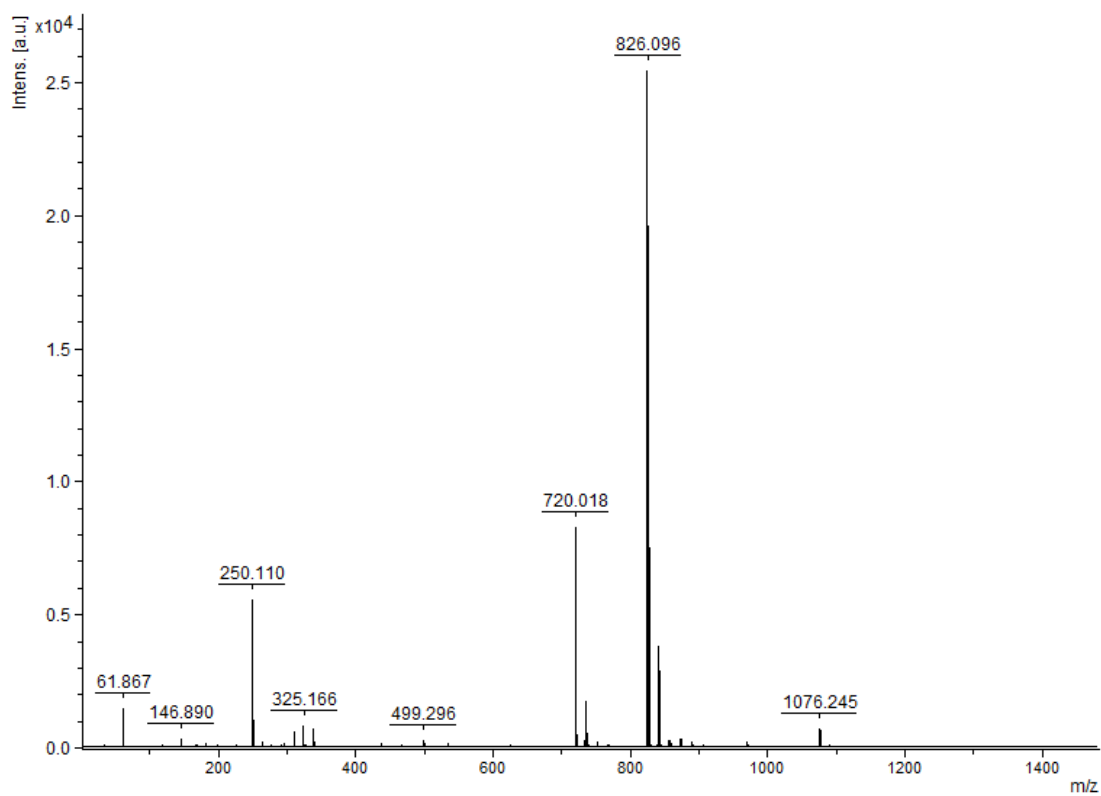
Sample 3.7, positive-ion mode MALDI



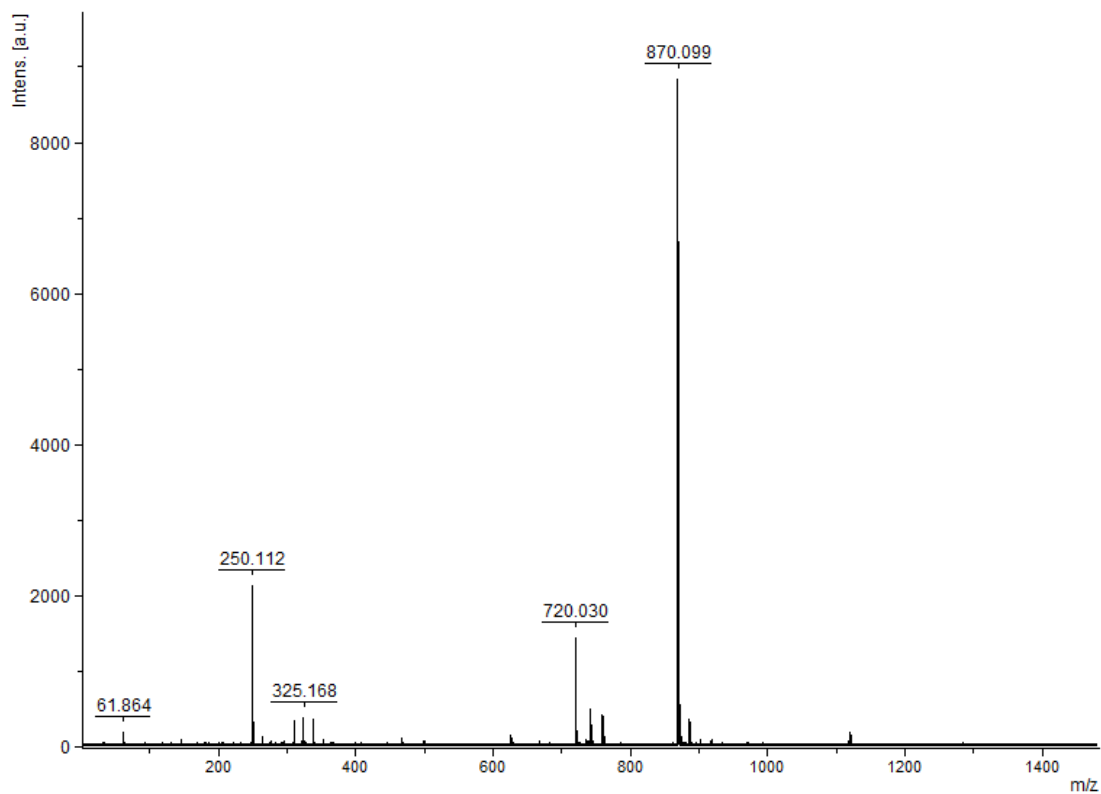
Sample 3.8, negative-ion mode MALDI



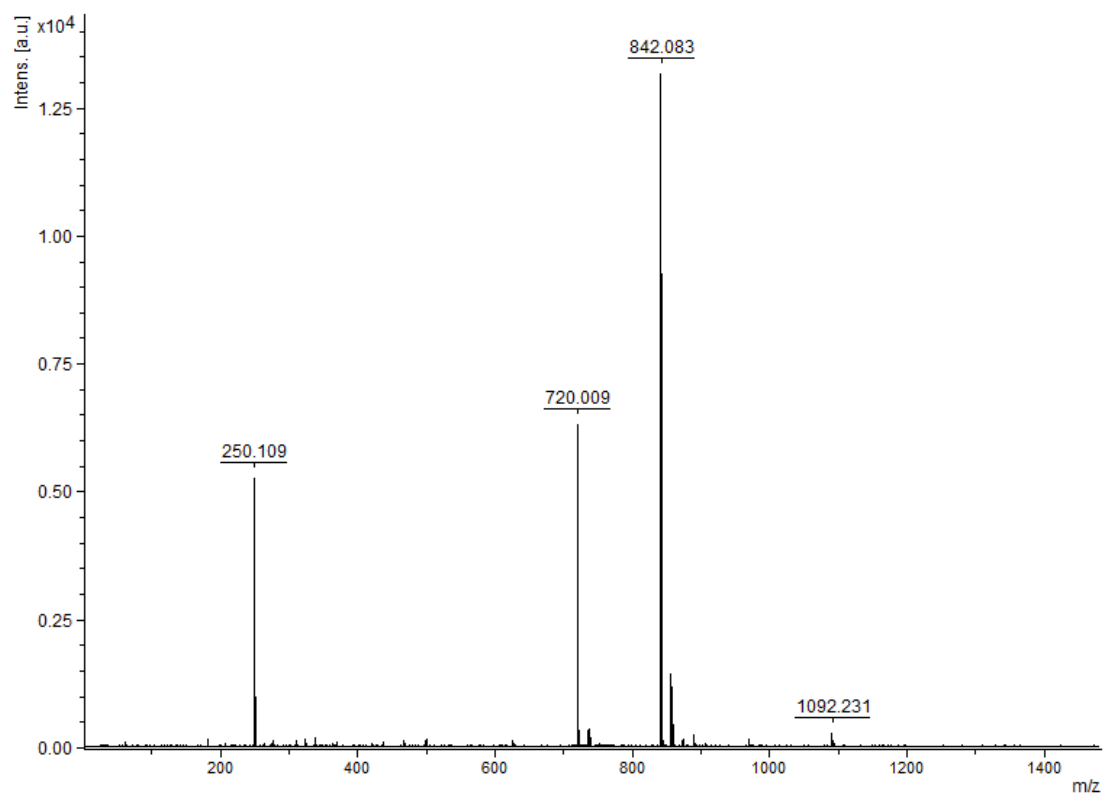
Sample 3.9, negative-ion mode MALDI



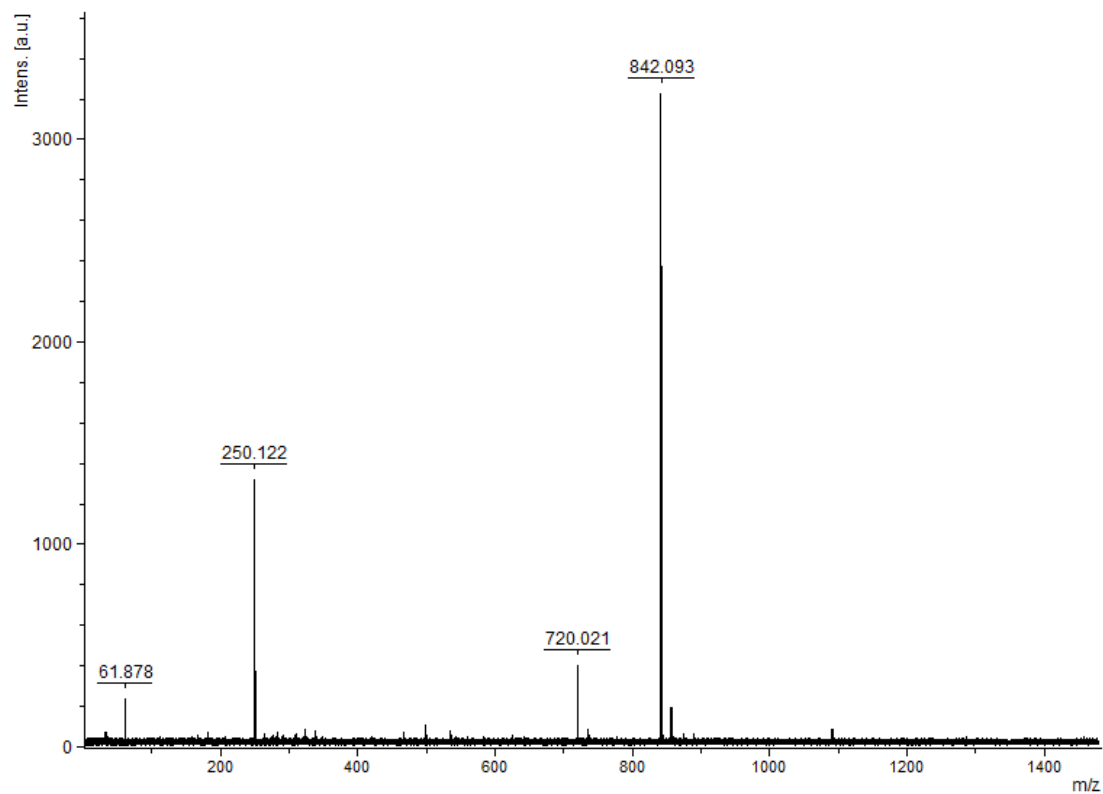
Sample 3.11, negative-ion mode MALDI



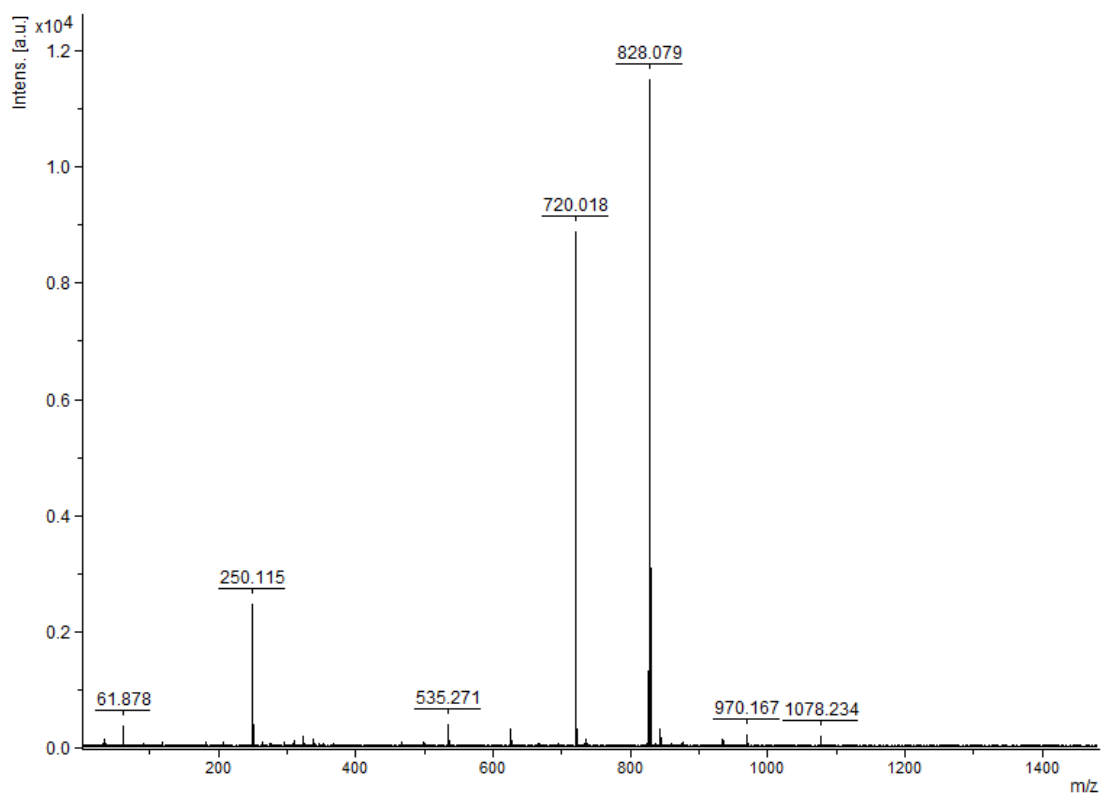
Sample 3.12, negative-ion mode MALDI



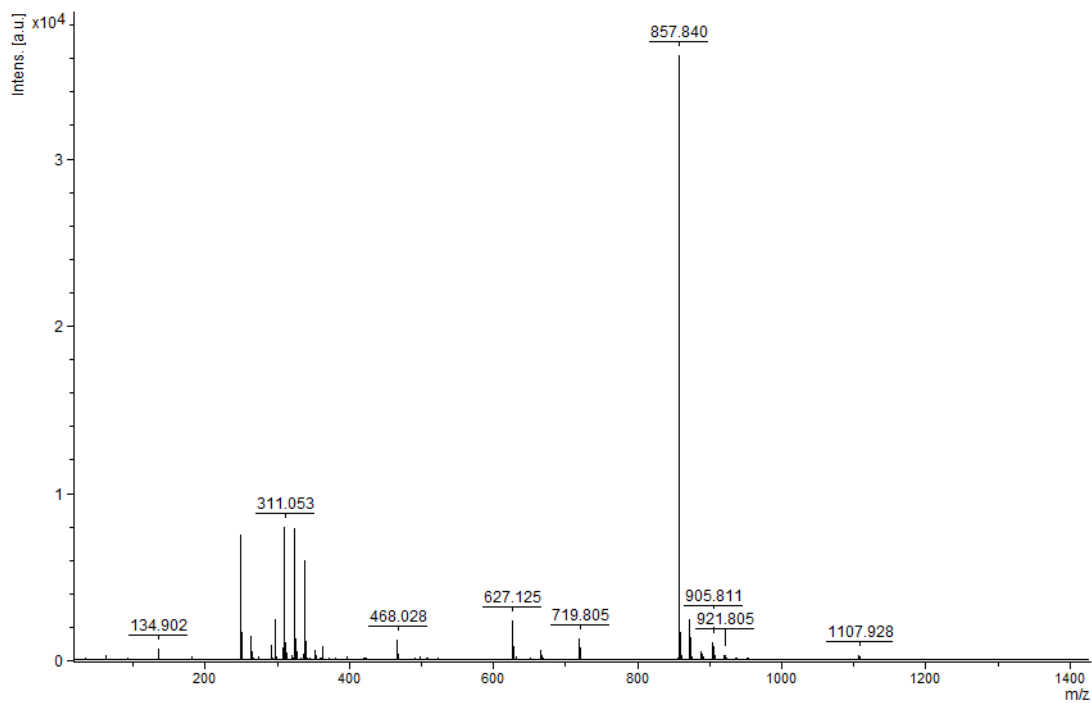
Sample 3.13, negative-ion mode MALDI



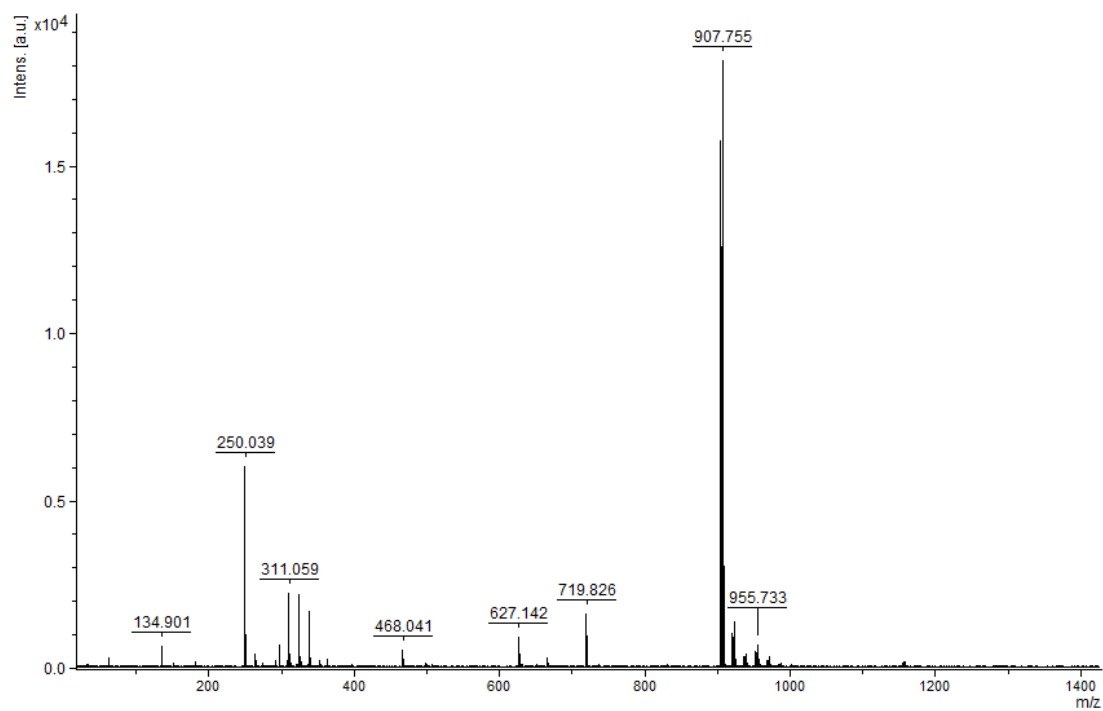
Sample 3.14, negative-ion mode MALDI



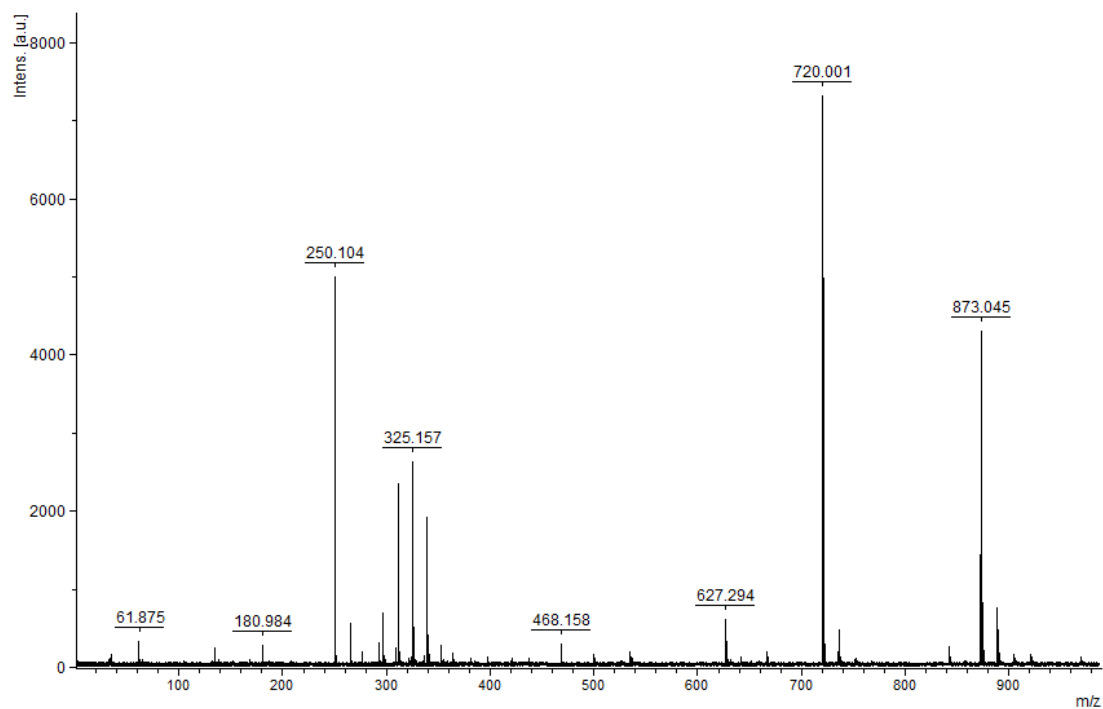
Sample 3.15, negative-ion mode MALDI



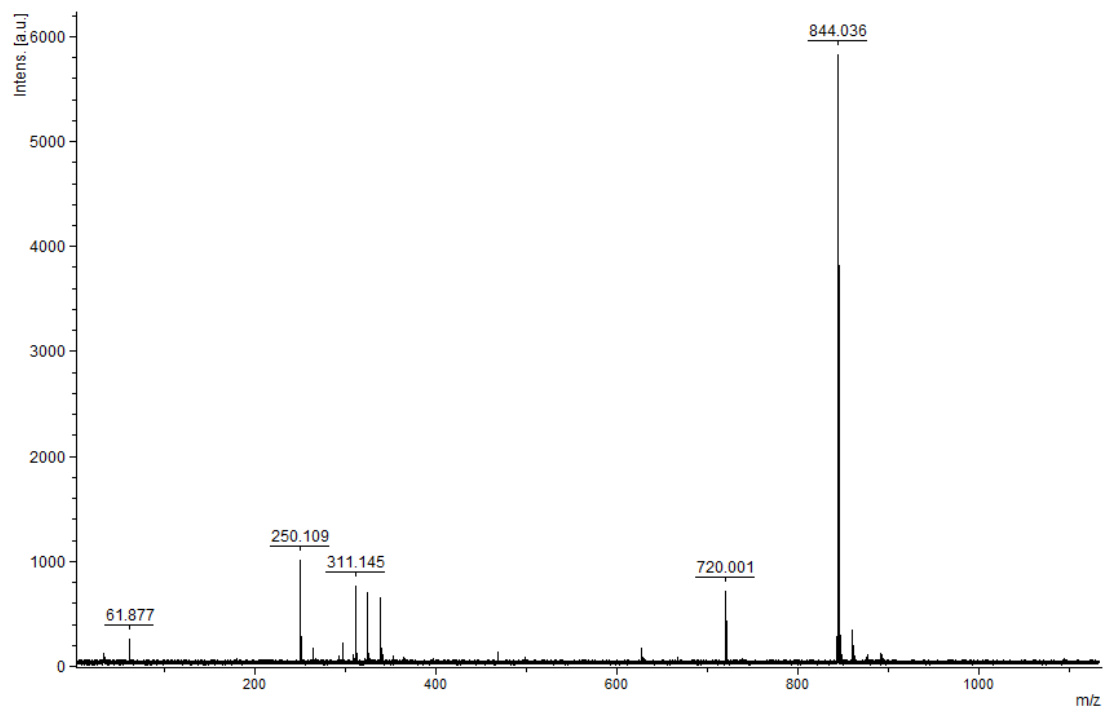
Sample 4.1, negative-ion mode MALDI



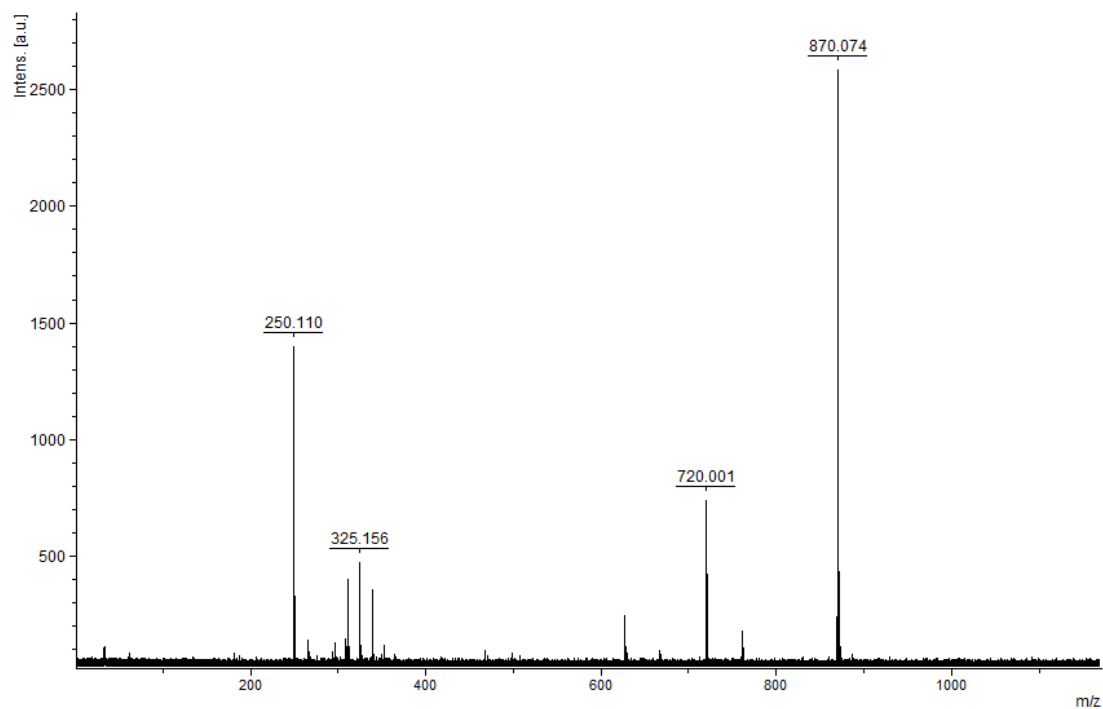
Sample 4.2, negative-ion mode MALDI



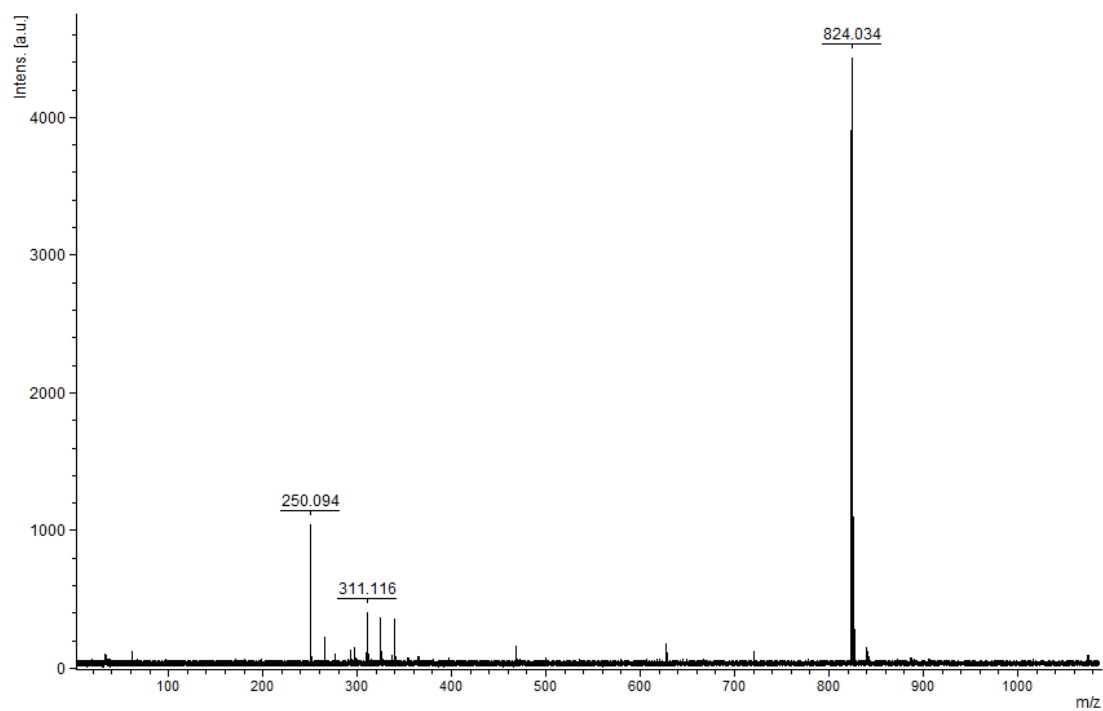
Sample 4.3, negative-ion mode MALDI



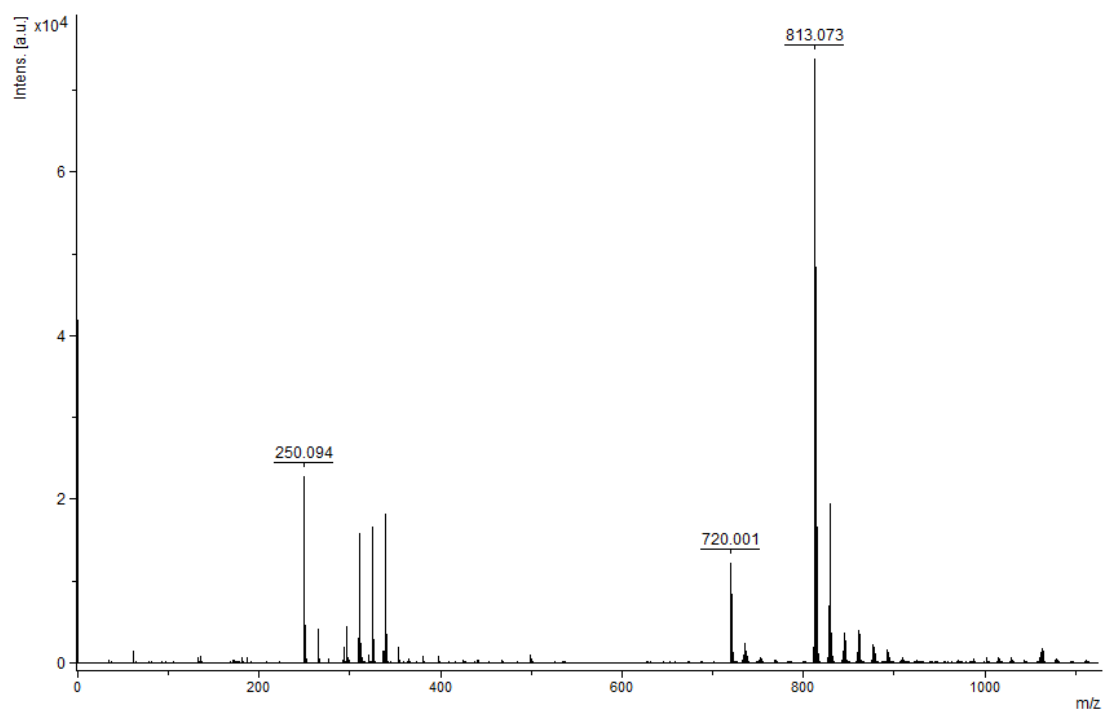
Sample 4.5, negative-ion mode MALDI



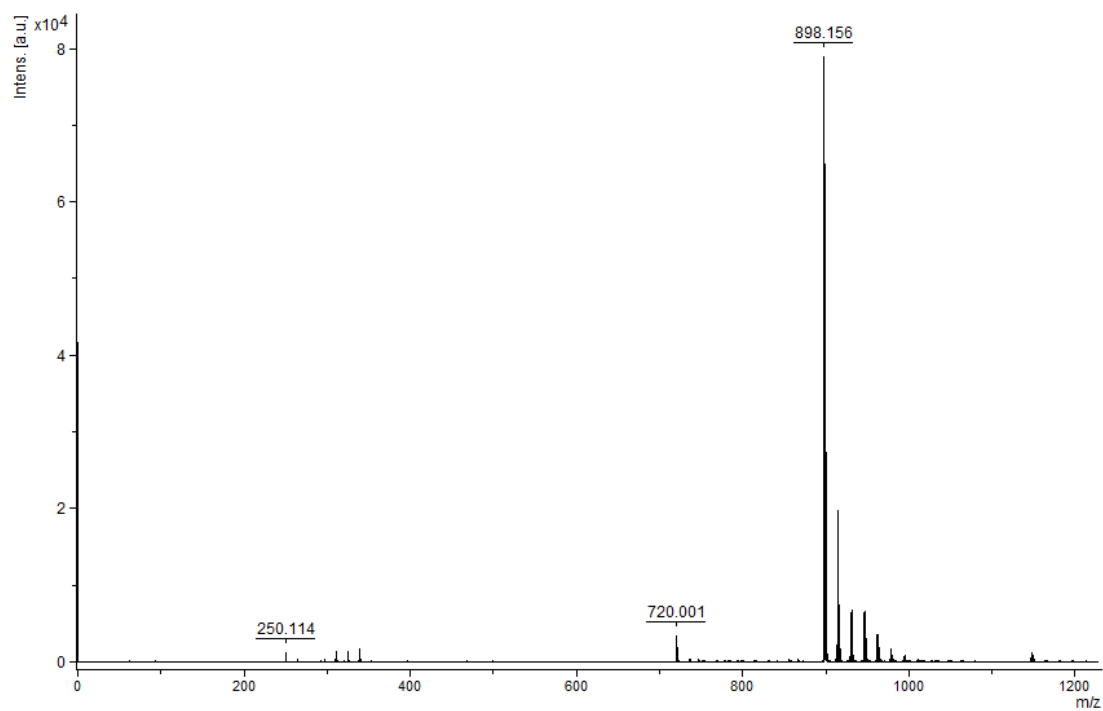
Sample 4.6, negative-ion mode MALDI



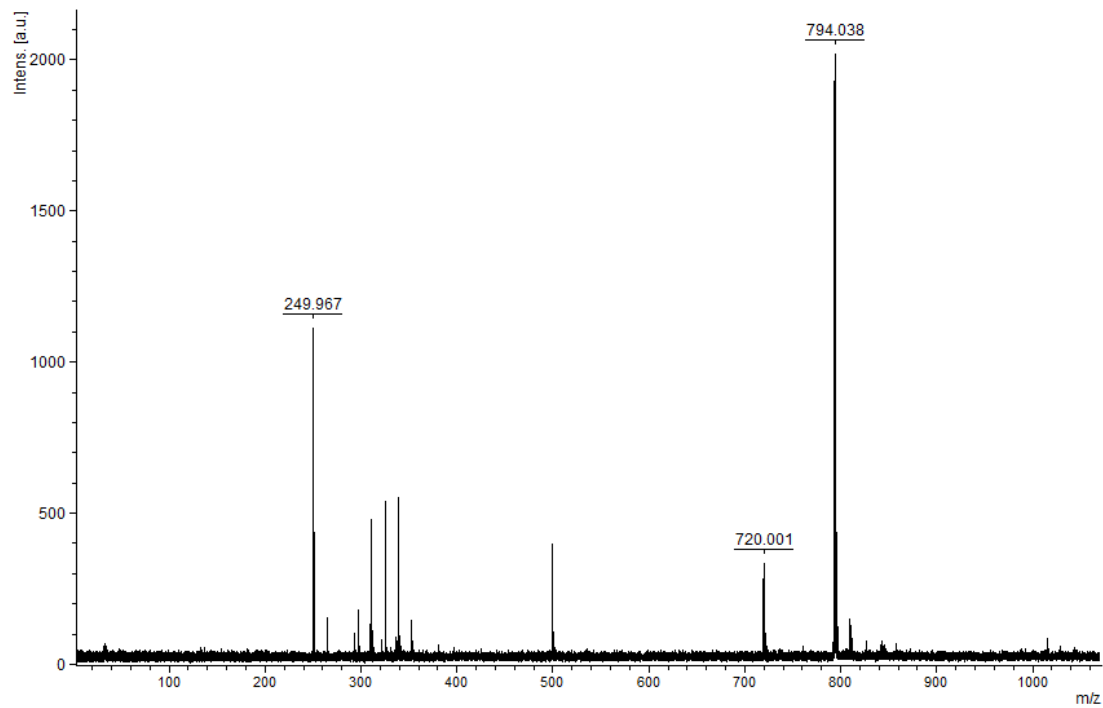
Sample 4.7, negative-ion mode MALDI



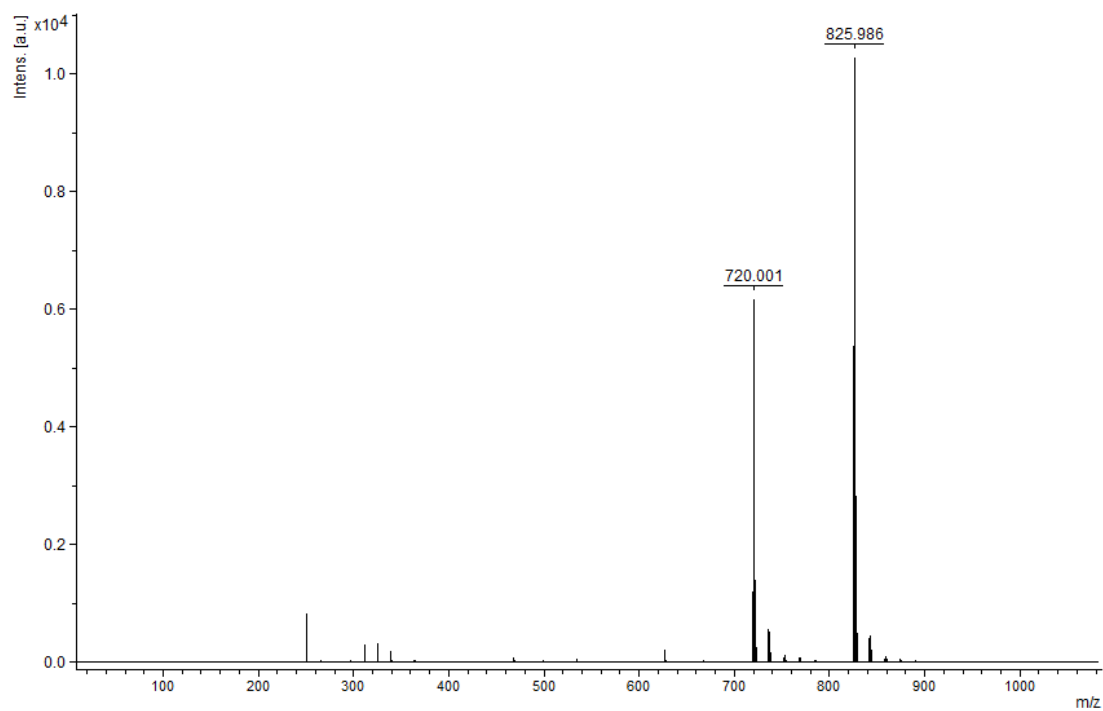
Sample 5.1, negative-ion mode MALDI



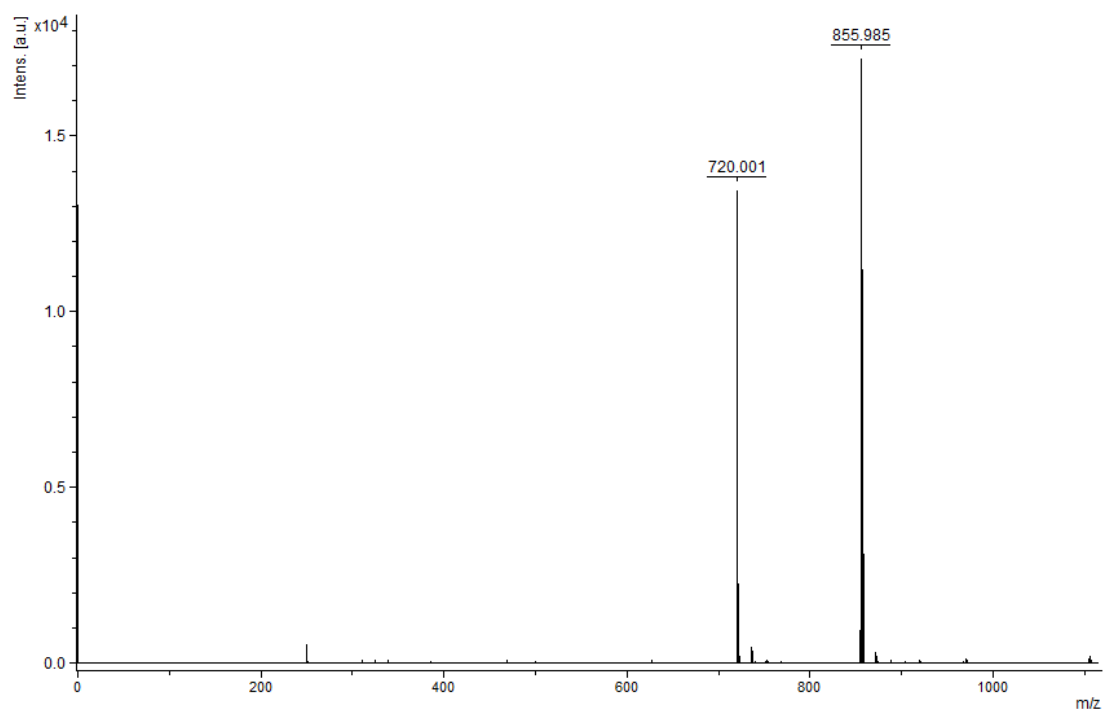
Sample 5.3, negative-ion mode MALDI



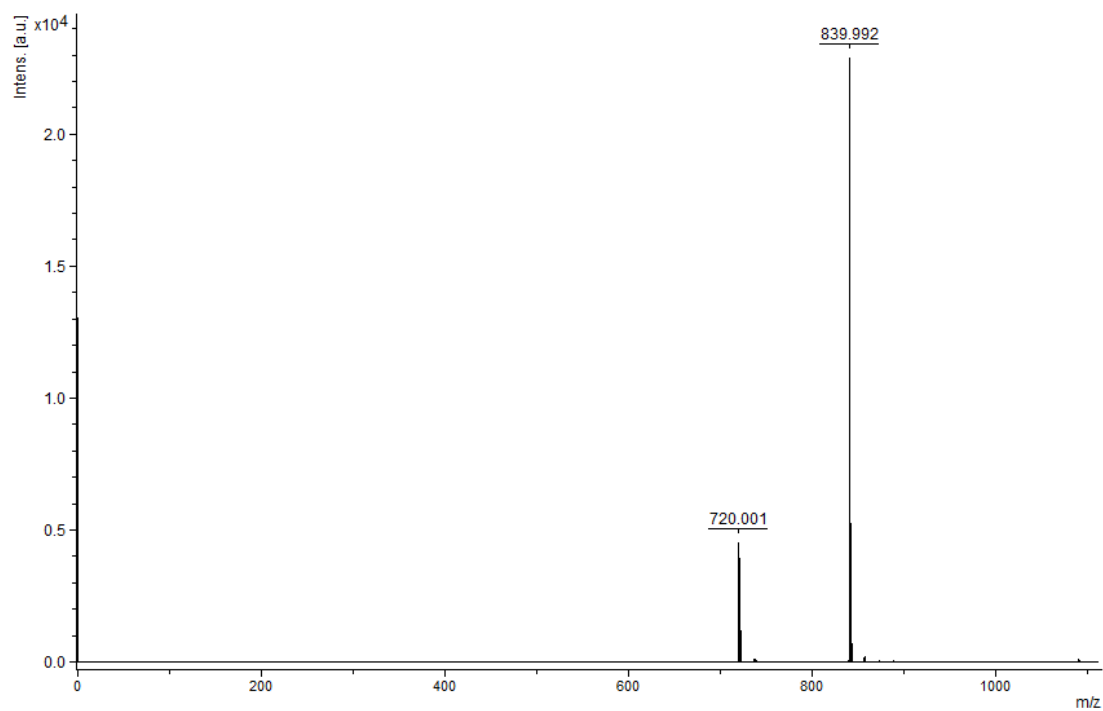
Sample 5.5, negative-ion mode MALDI



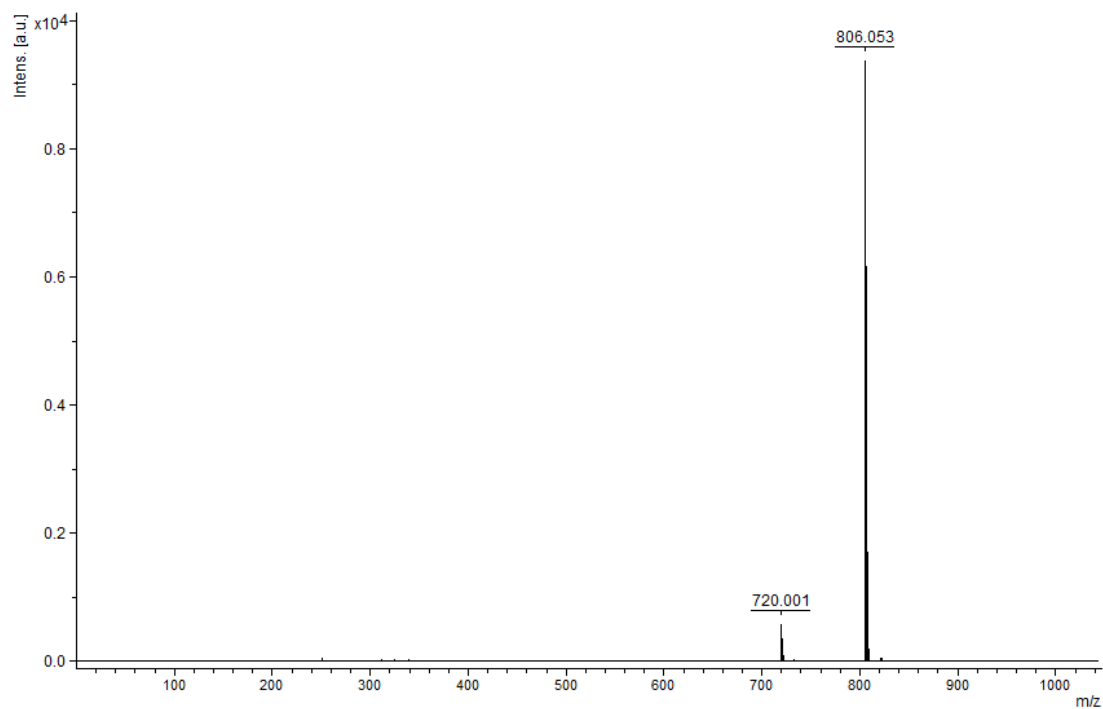
Sample 6.1, negative-ion mode MALDI



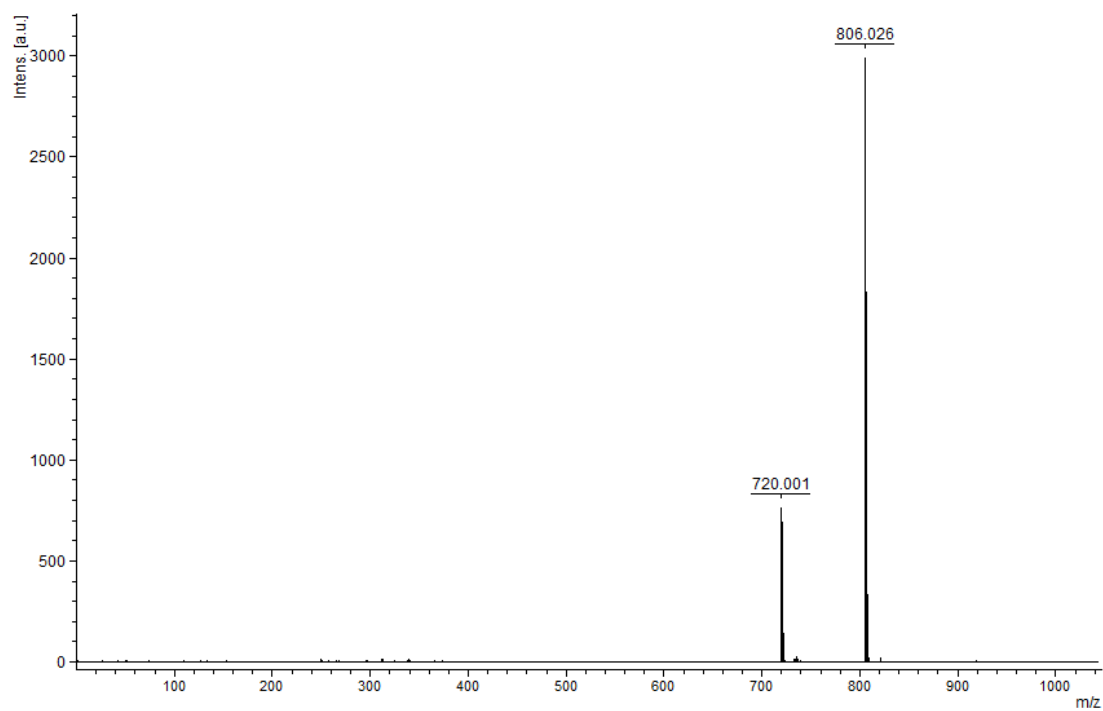
Sample 6.2, negative-ion mode MALDI



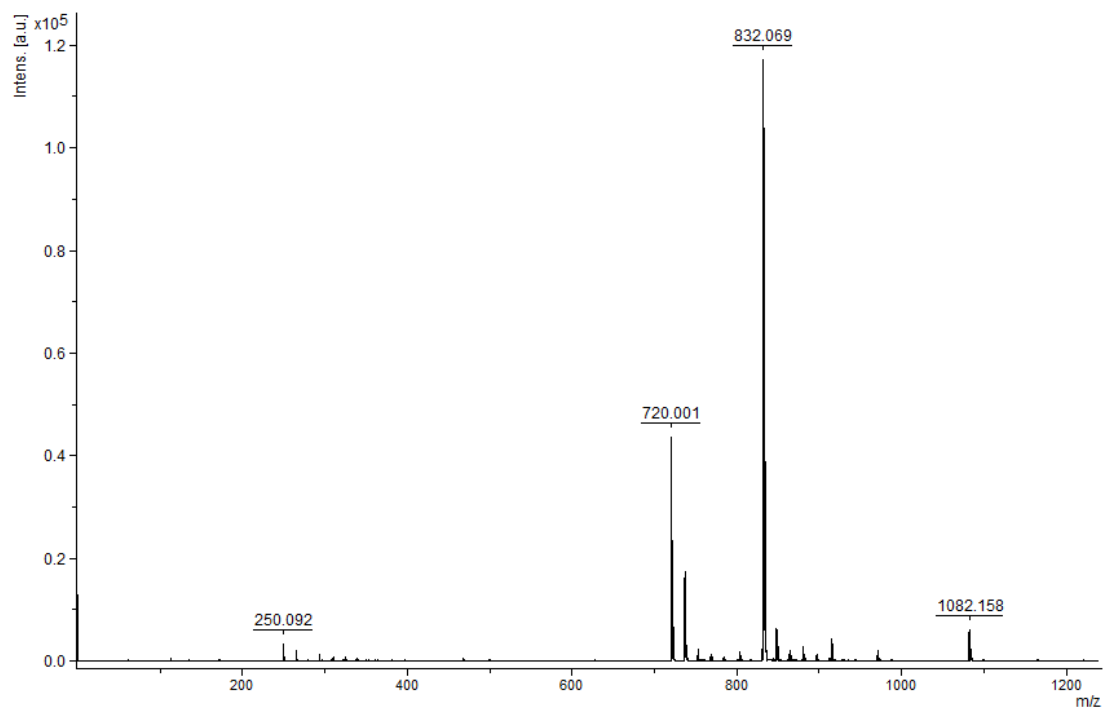
Sample 6.3, negative-ion mode MALDI



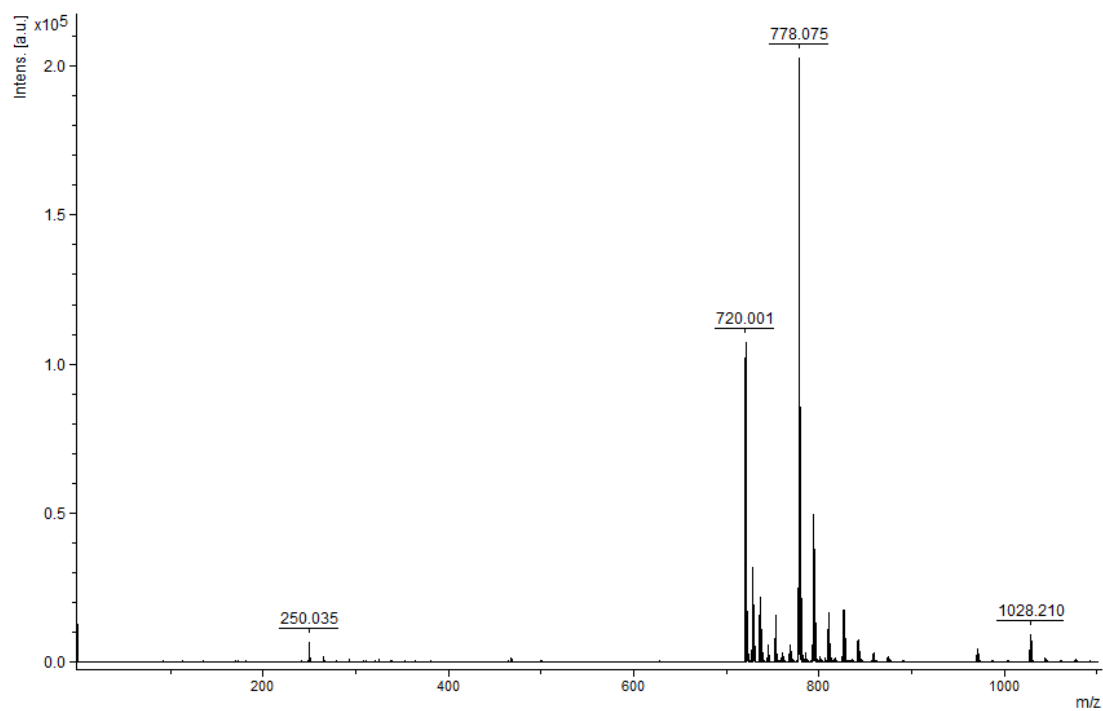
Sample 6.5, negative-ion mode MALDI



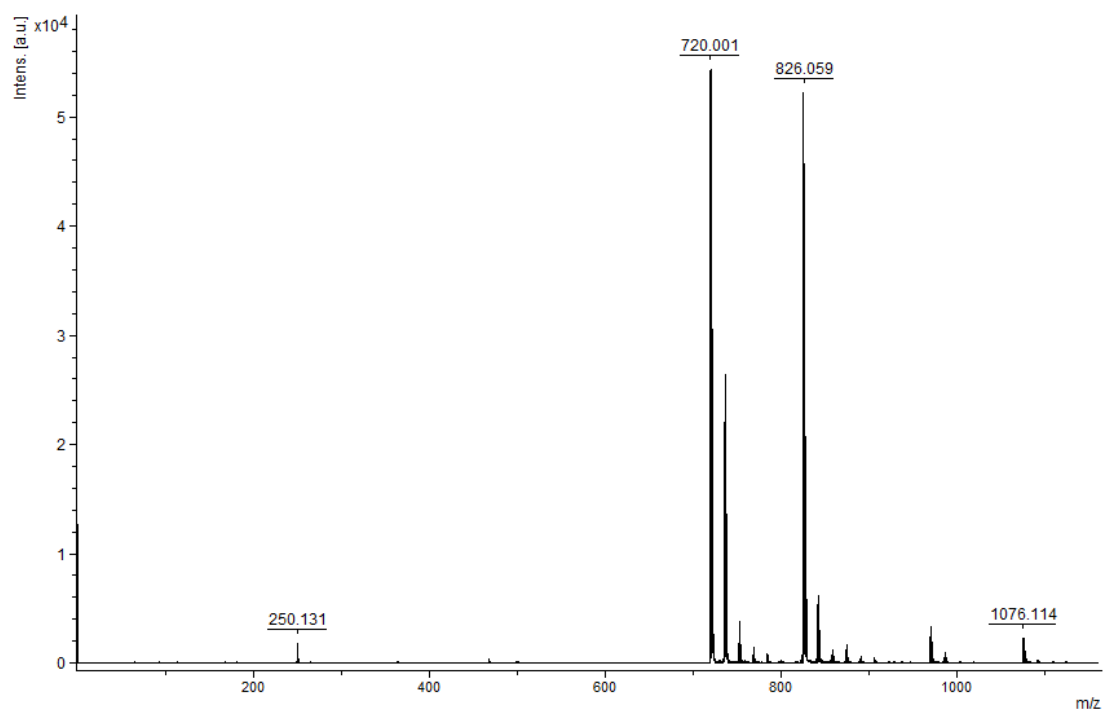
Sample 6.6, negative-ion mode MALDI



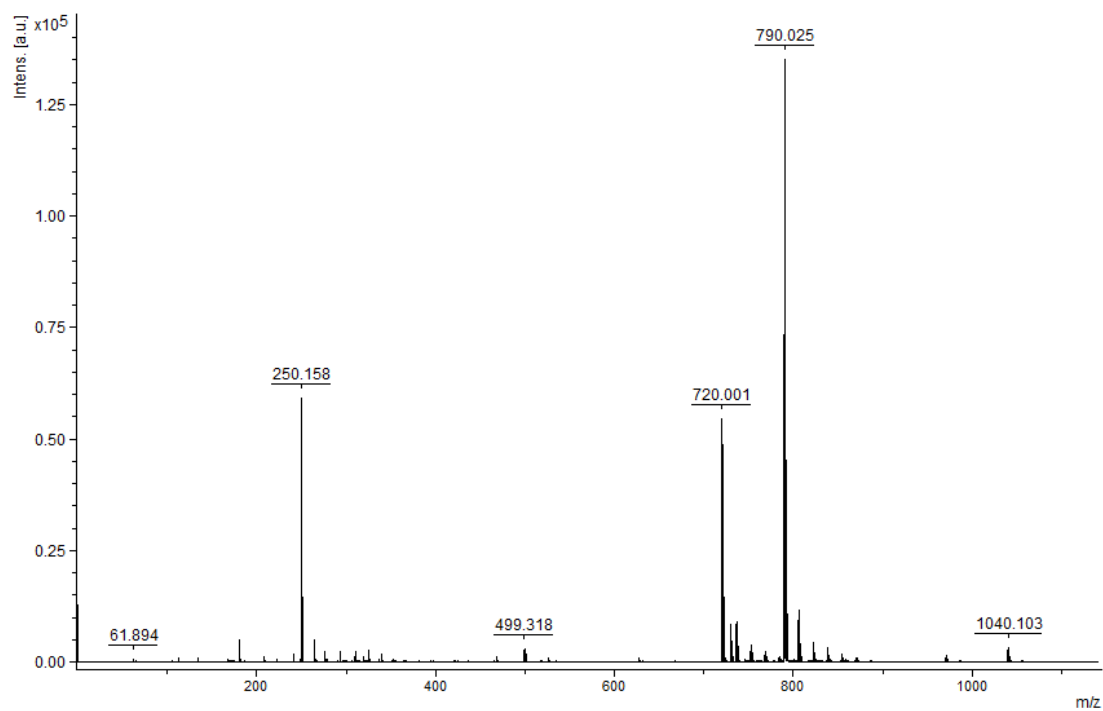
Sample 7.1, negative-ion mode MALDI



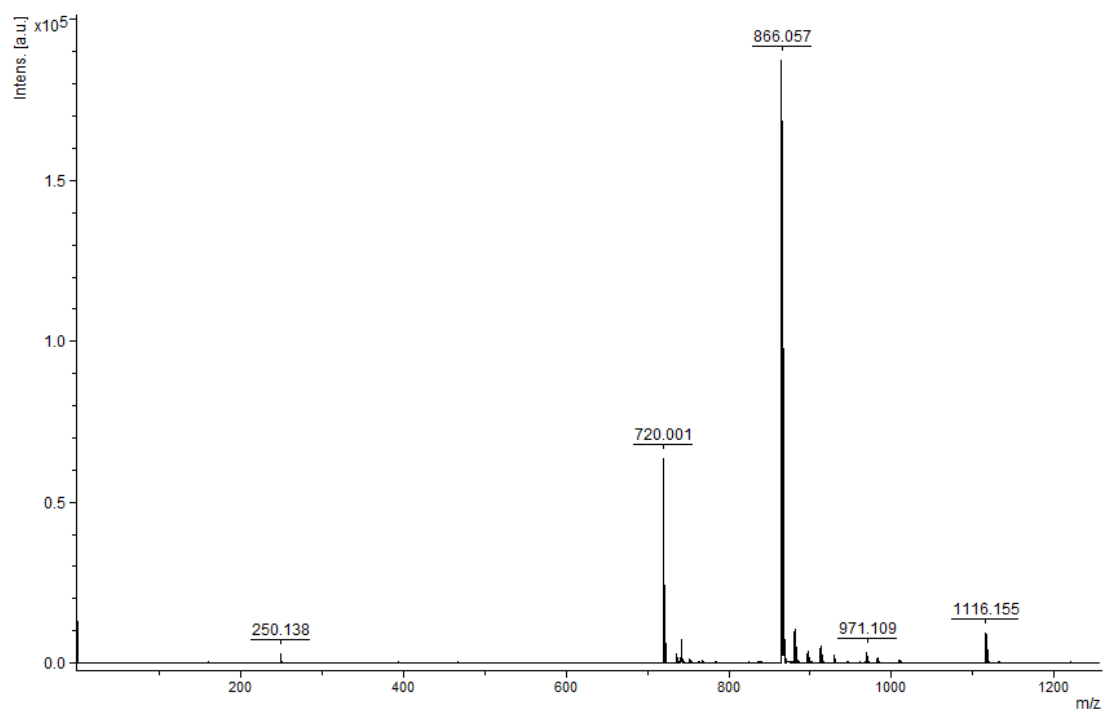
Sample 7.2, negative-ion mode MALDI



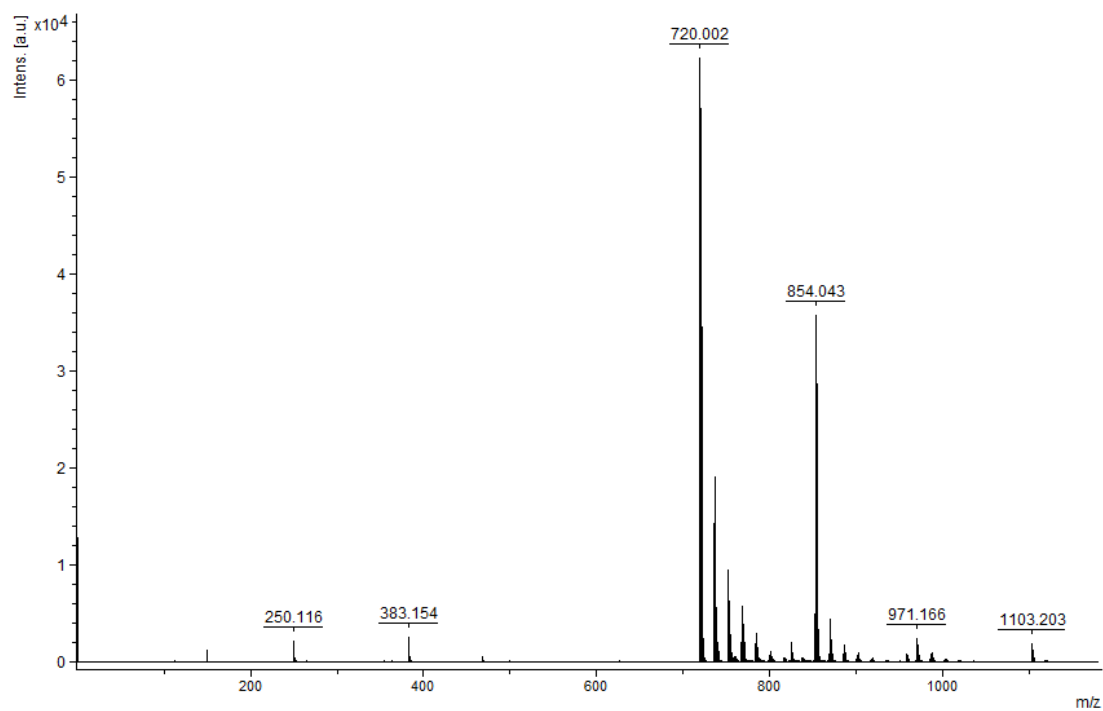
Sample 7.3, negative-ion mode MALDI



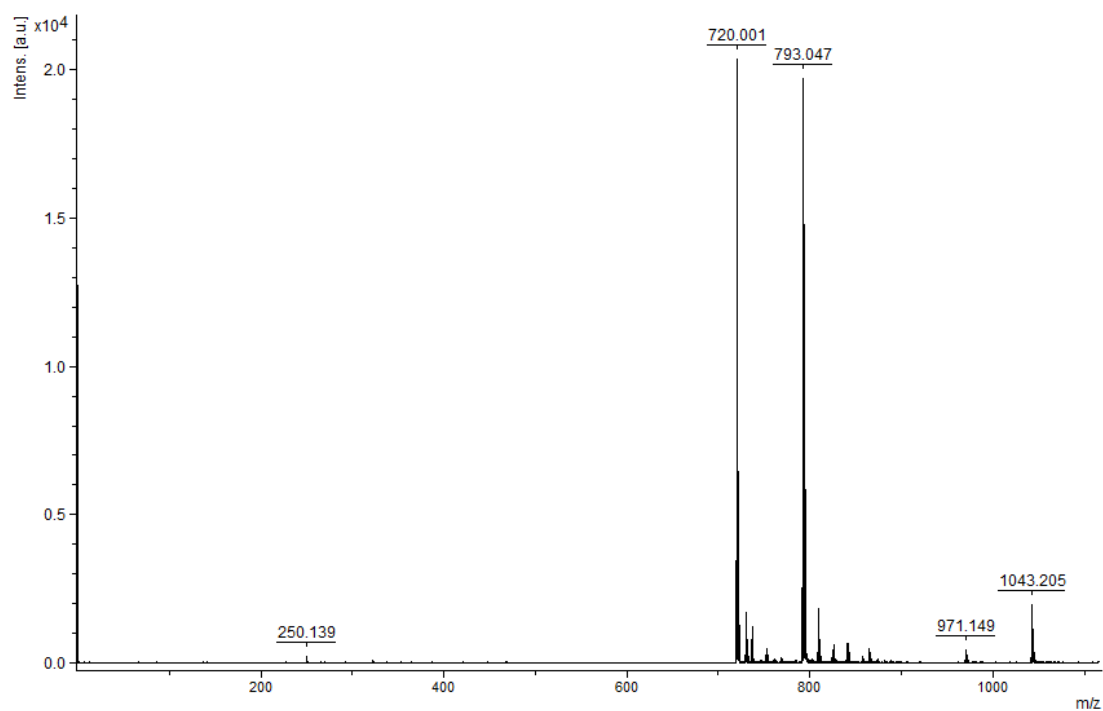
Sample 7.4, negative-ion mode MALDI



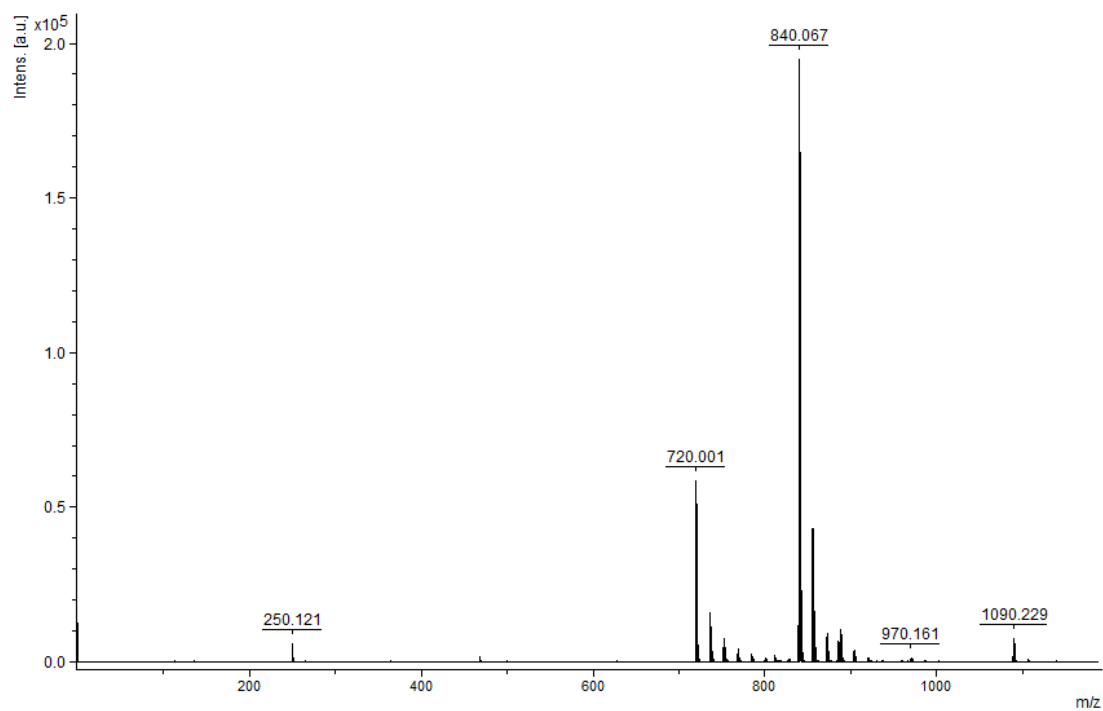
Sample 7.5, negative-ion mode MALDI



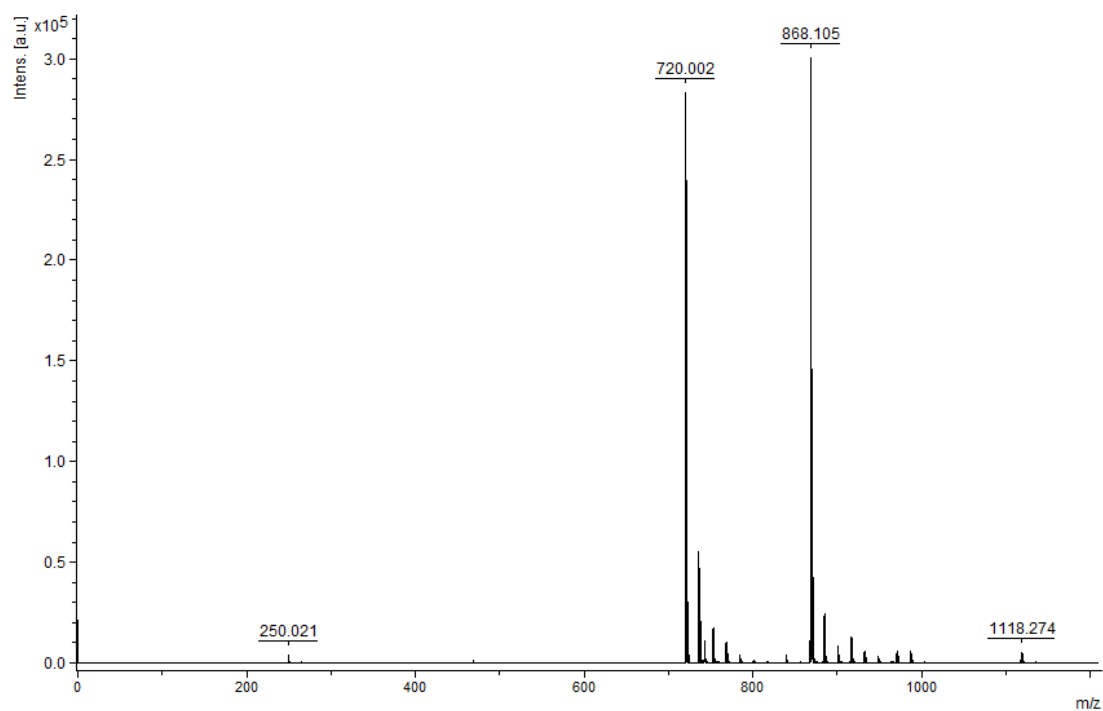
Sample 7.6, negative-ion mode MALDI



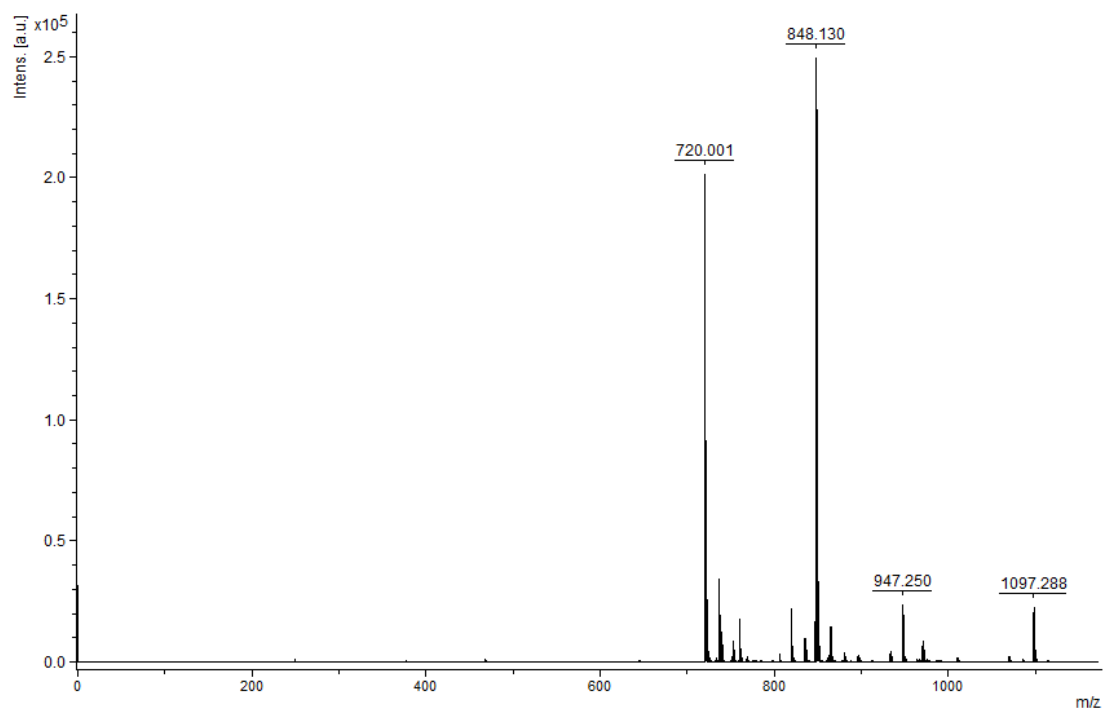
Sample 7.7, negative-ion mode MALDI



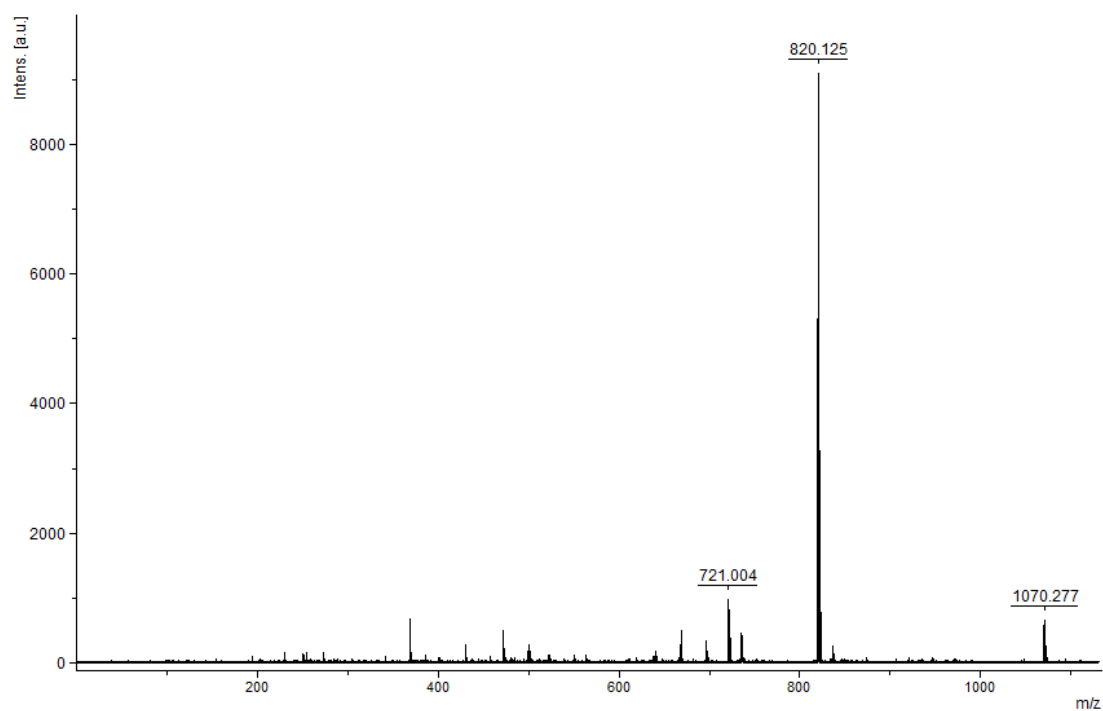
Sample 7.8, negative-ion mode MALDI



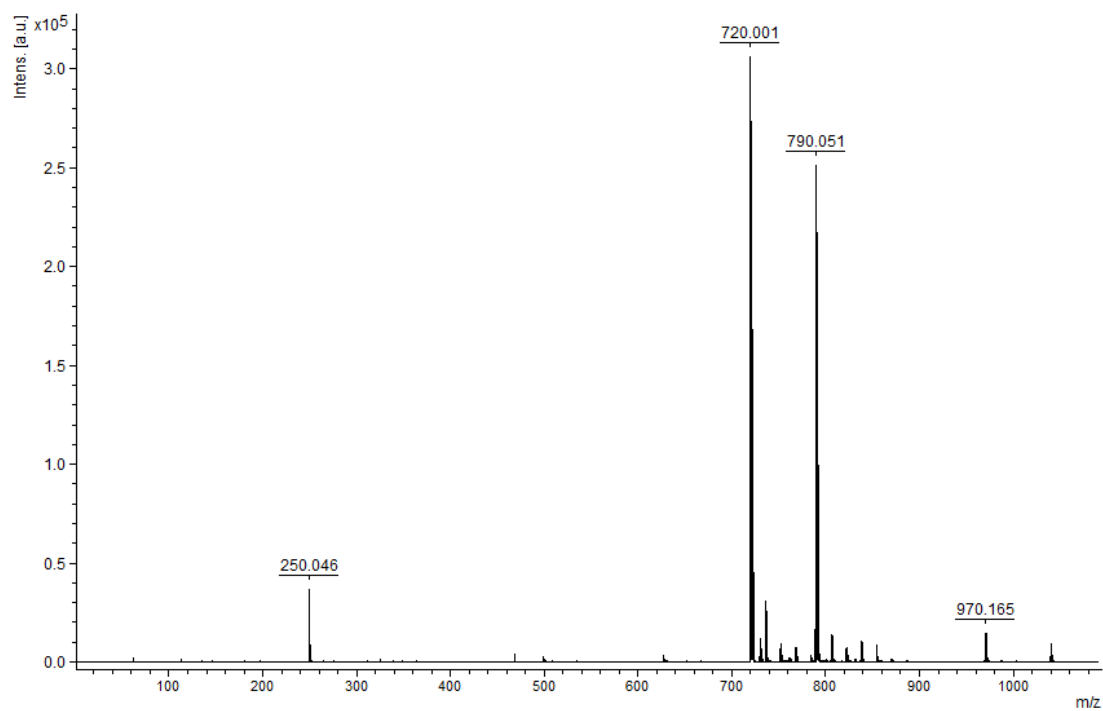
Sample 8.1, negative-ion mode MALDI



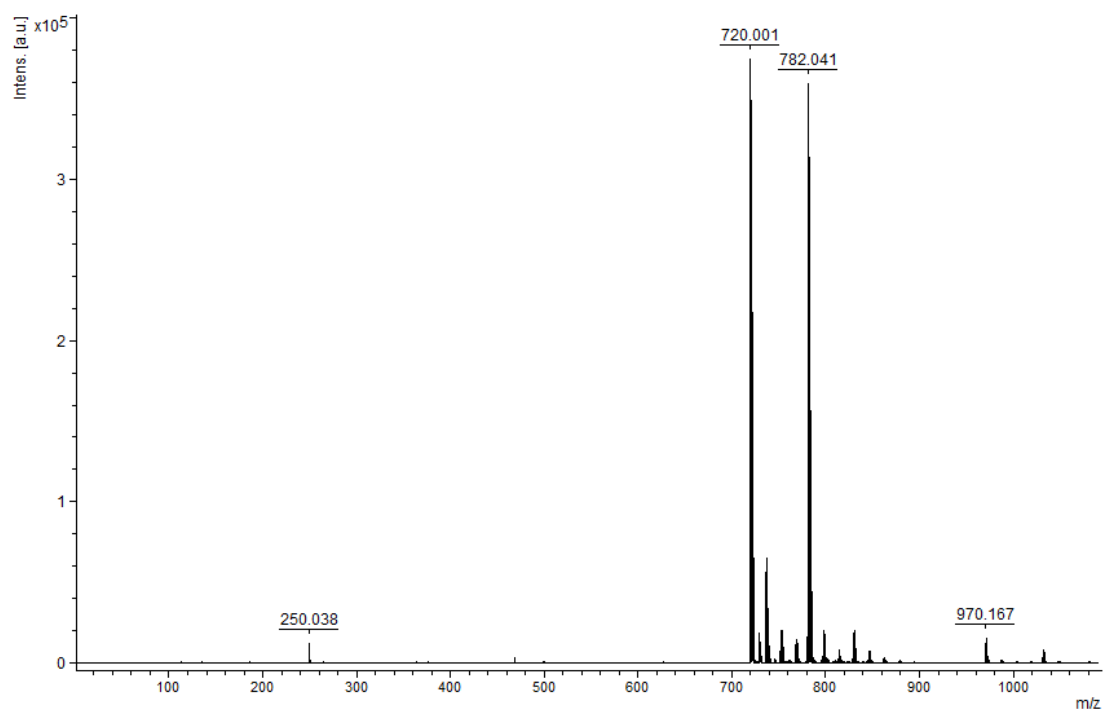
Sample 8.2, negative-ion mode MALDI



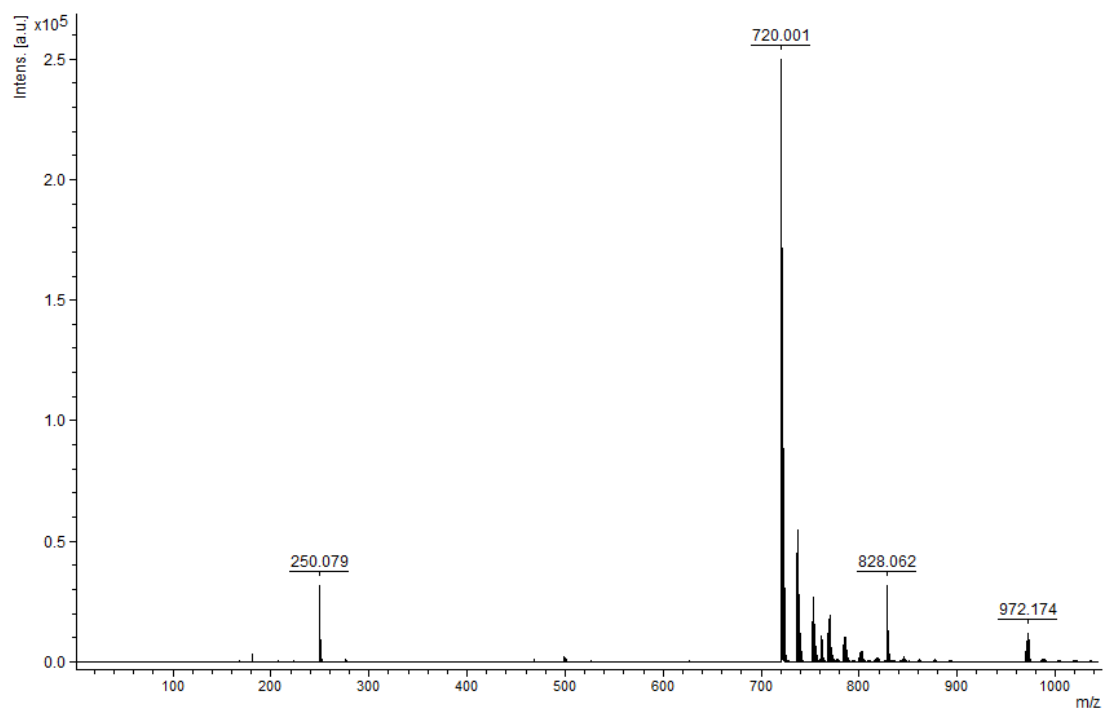
Sample 8.3, positive-ion mode MALDI



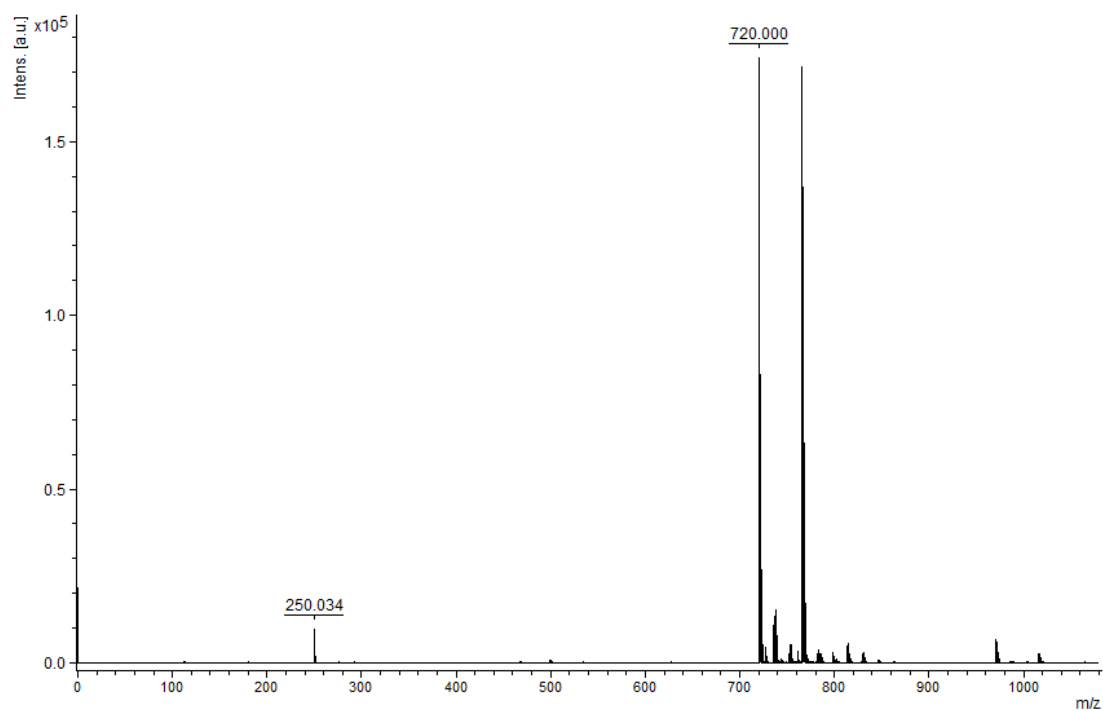
Sample 8.4, negative-ion mode MALDI



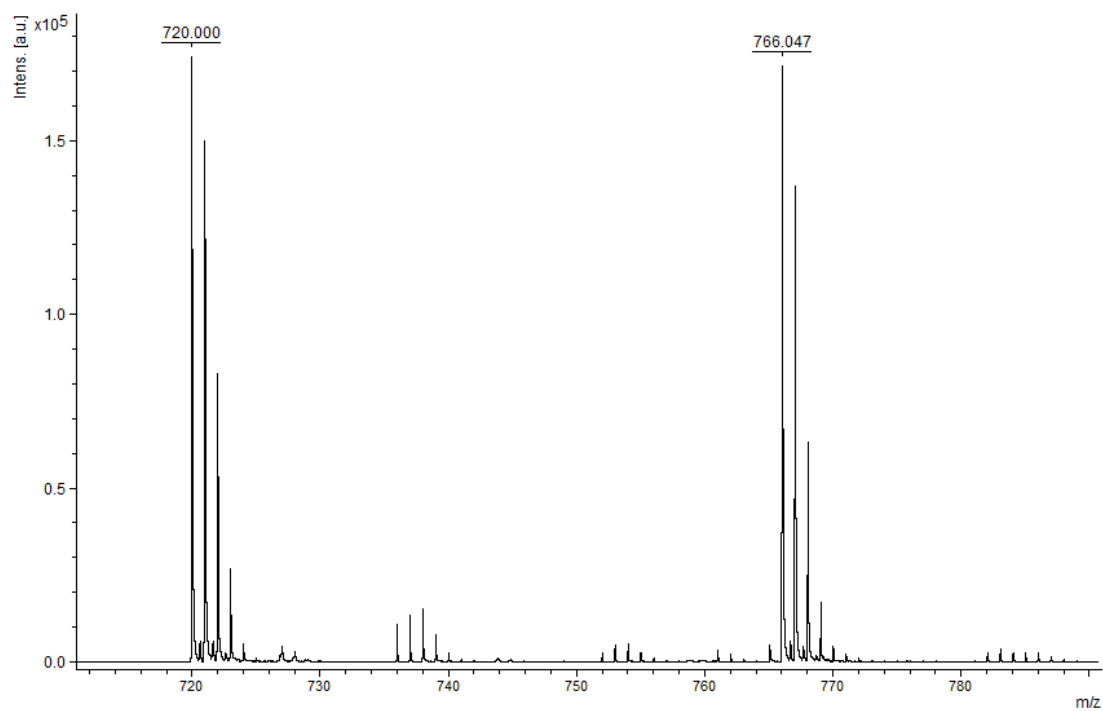
Sample 8.5, negative-ion mode MALDI



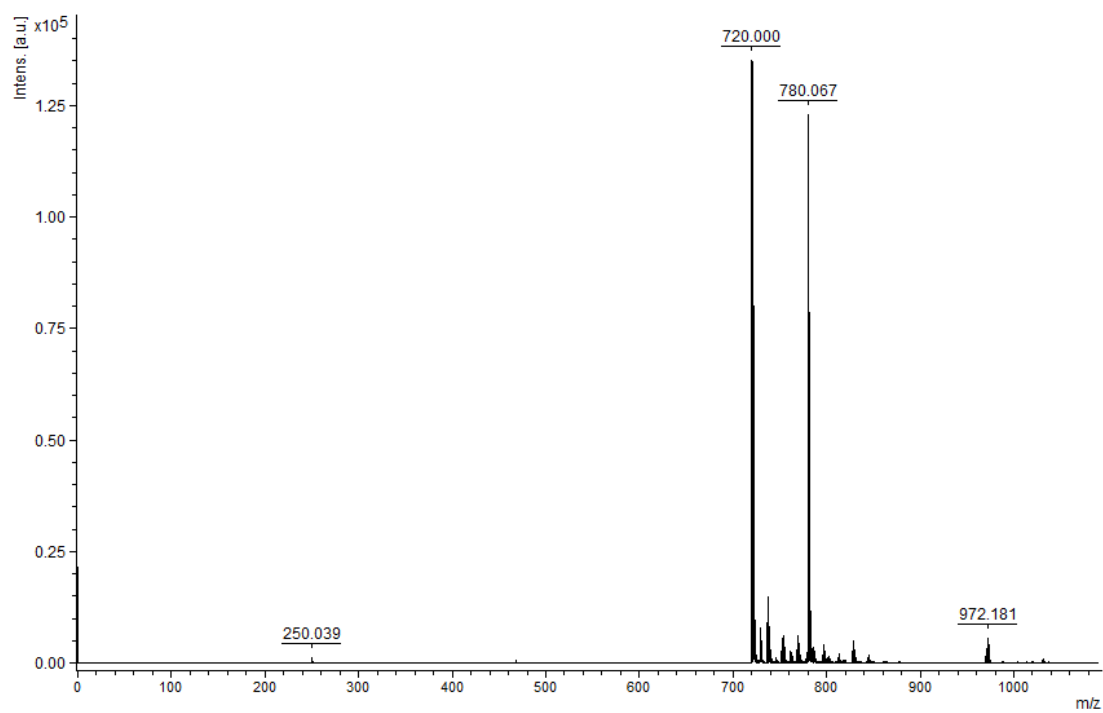
Sample 8.6, negative-ion mode MALDI



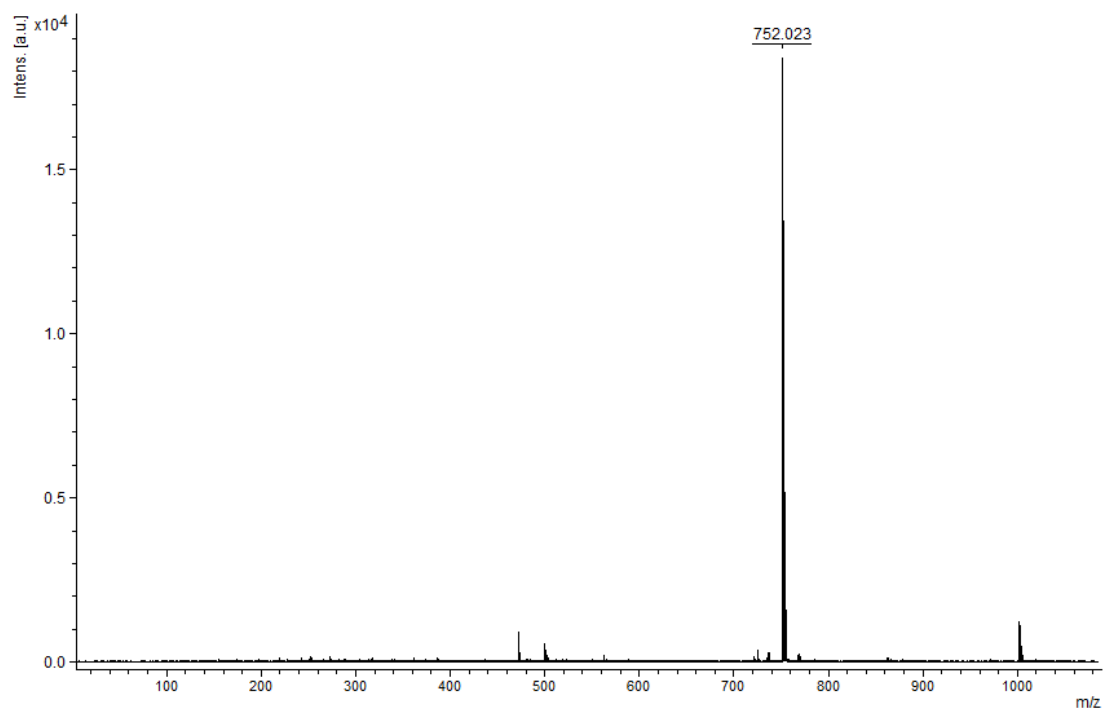
Sample 8.7, negative-ion mode MALDI



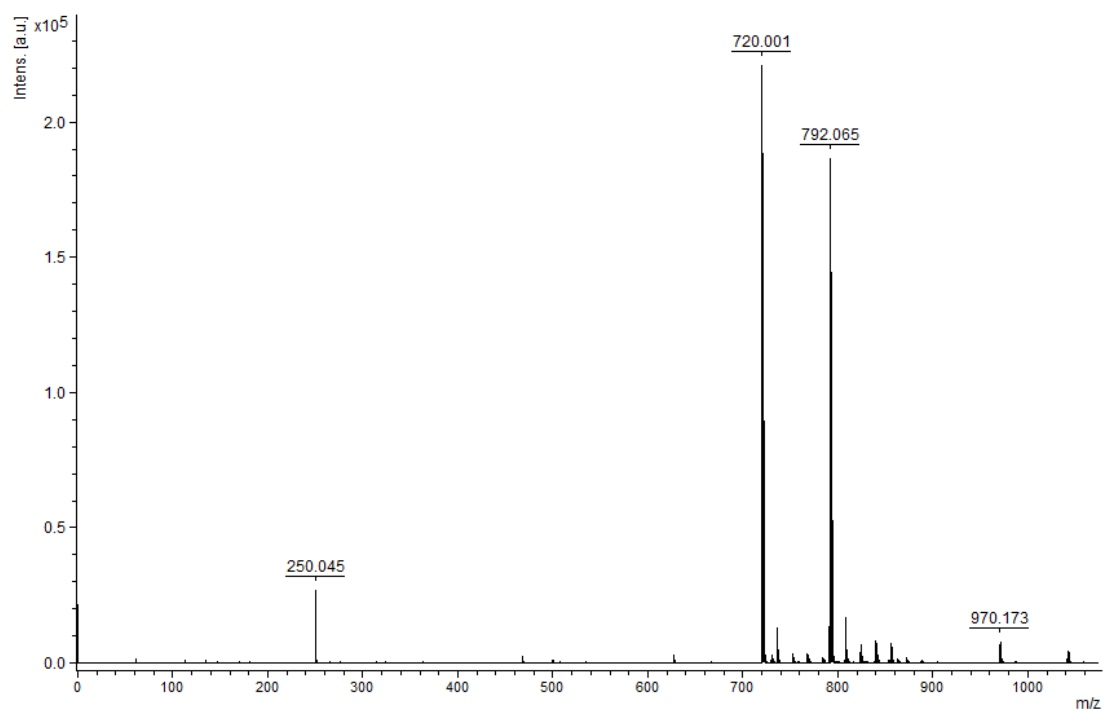
Sample 8.7, negative-ion mode MALDI



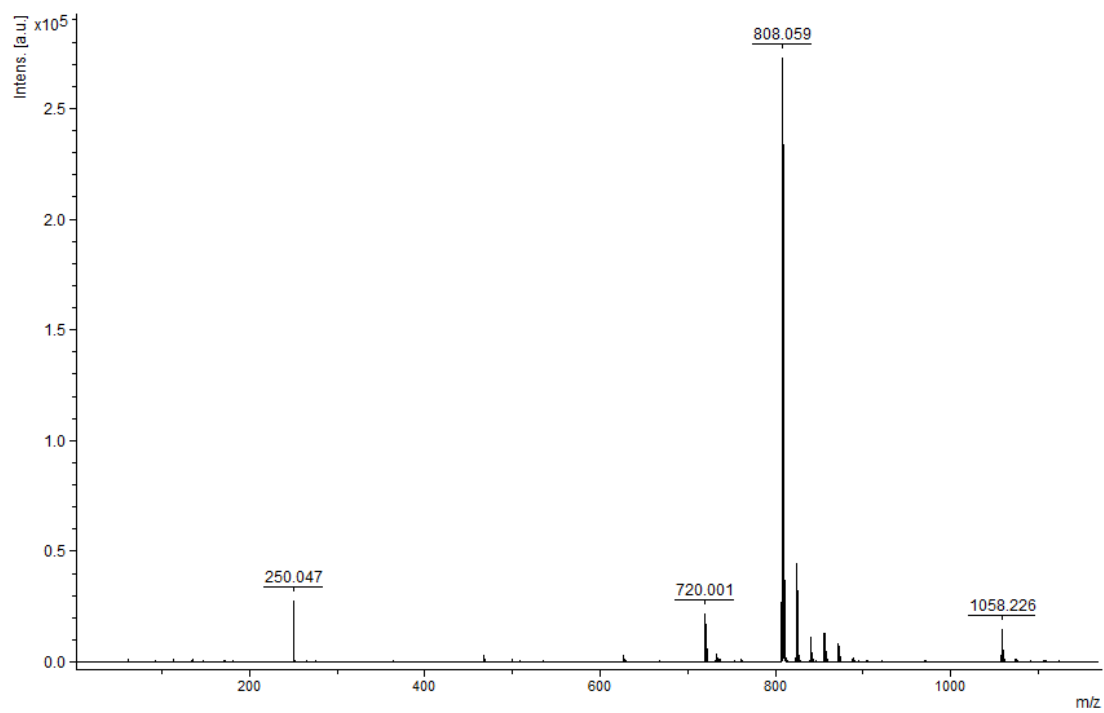
Sample 8.8, negative-ion mode MALDI



Sample 8.9, positive-ion mode MALDI

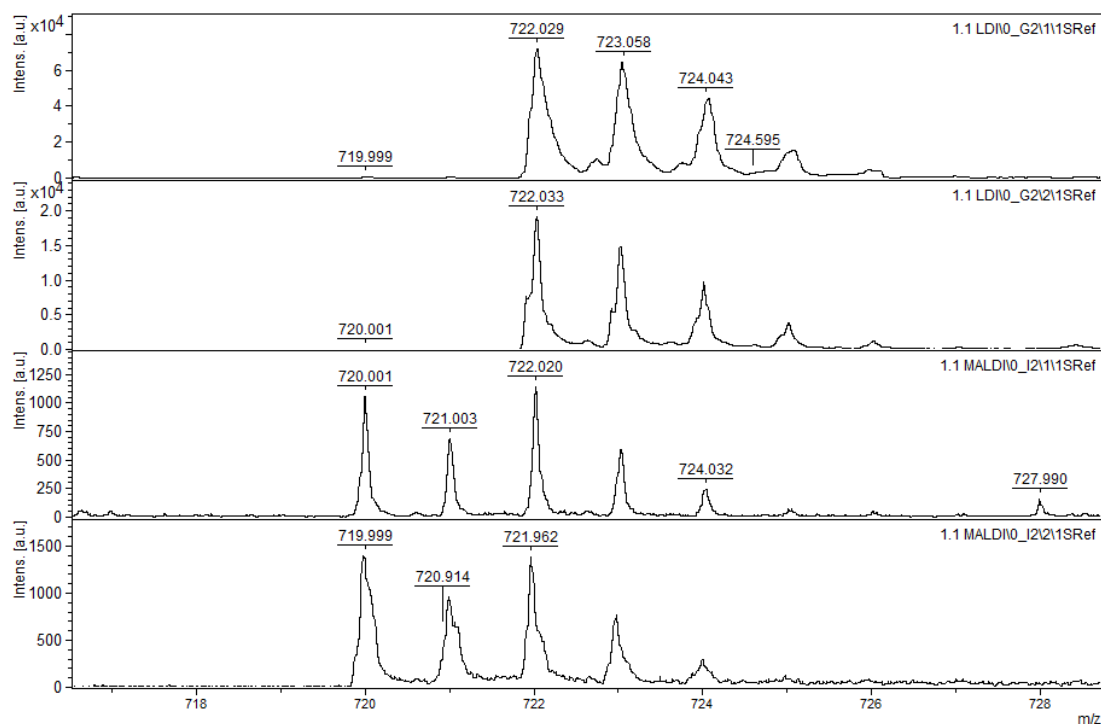


Sample 8.11, negative-ion mode MALDI

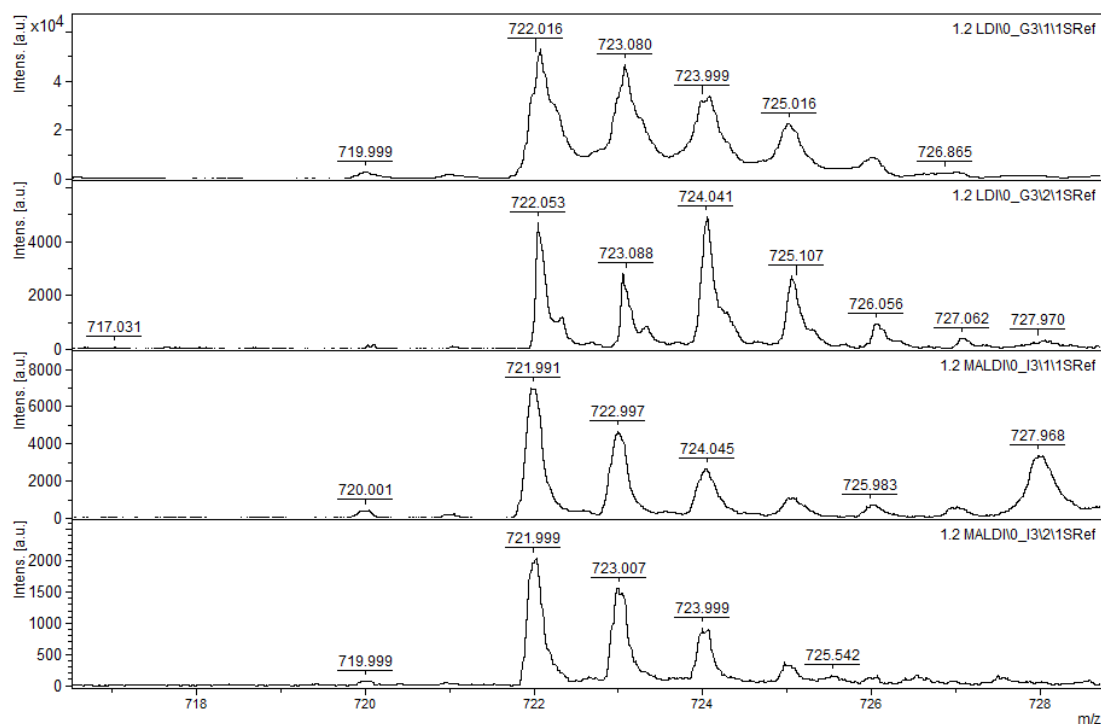


Sample 8.12, negative-ion mode MALDI

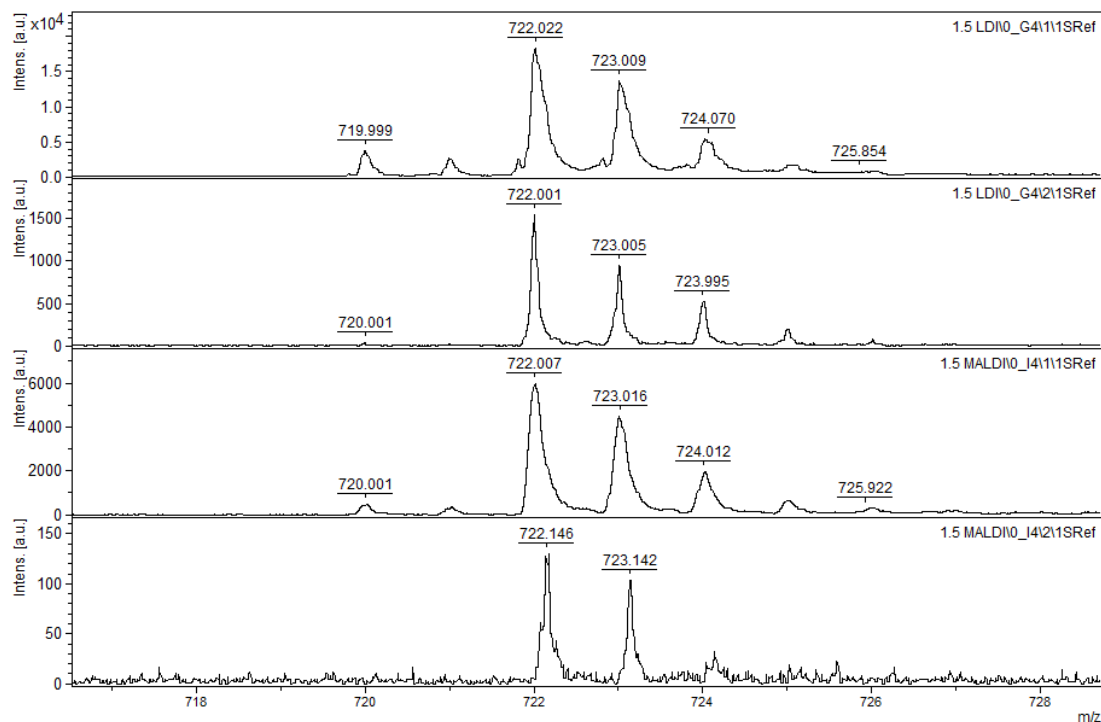
High Laser power MALDI spectra of OCF's



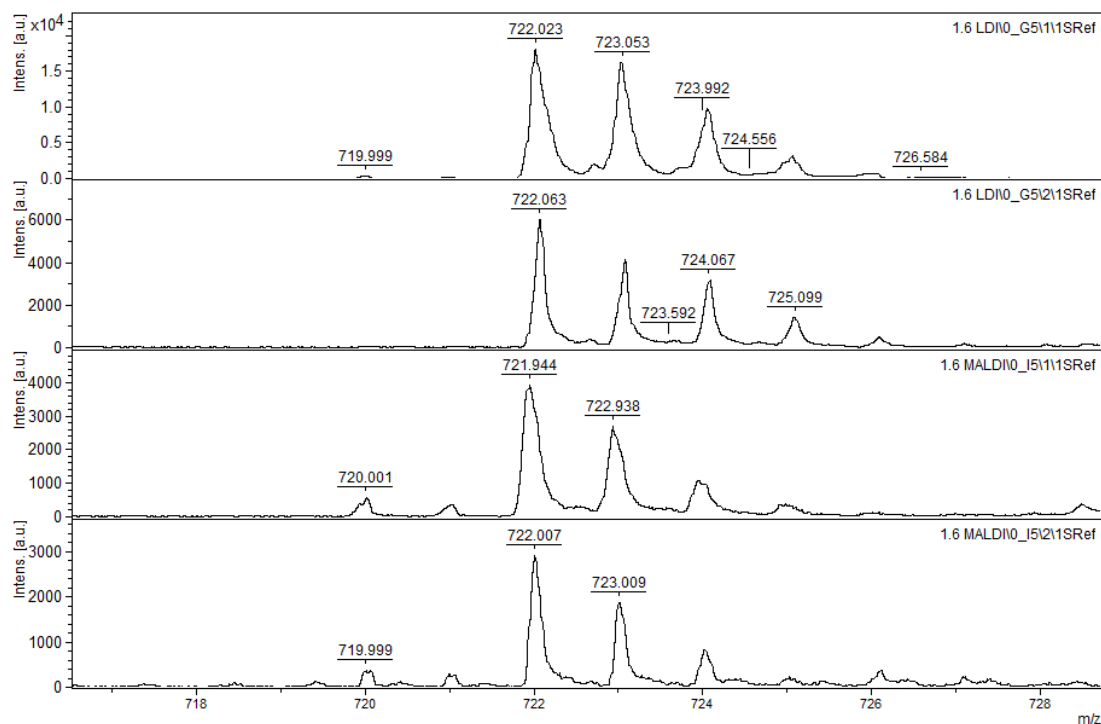
Sample 1.1, top to bottom – positive-ion mode LDI, negative-ion mode LDI, negative-ion mode MALDI, positive-ion mode MALDI



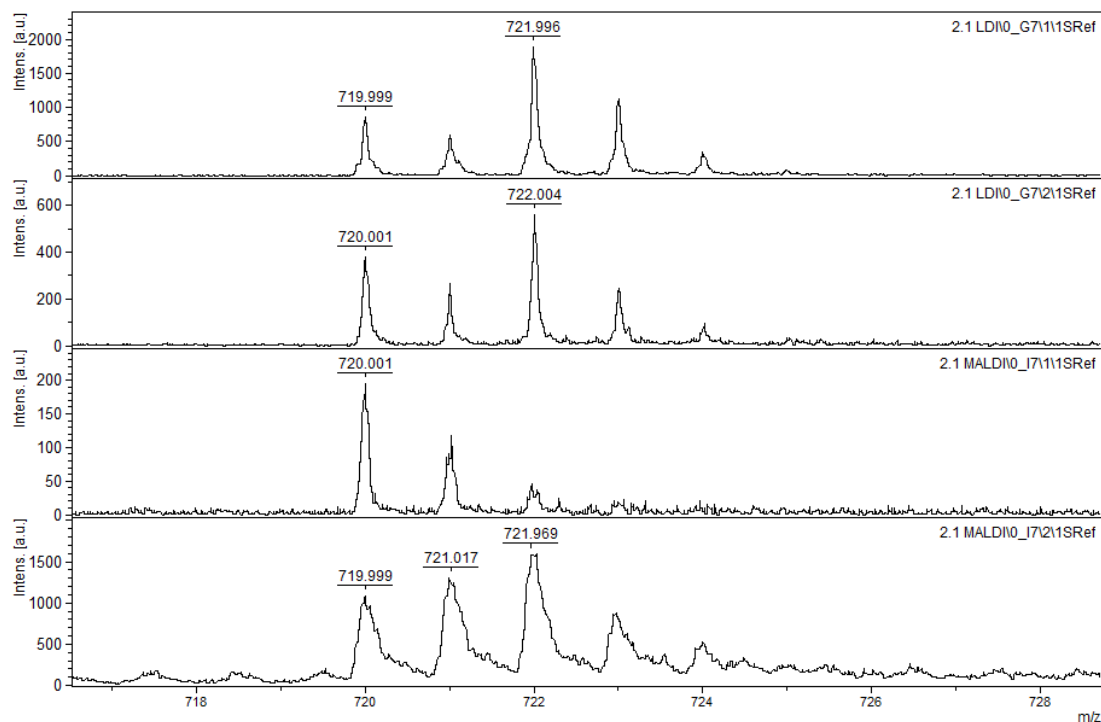
Sample 1.2, top to bottom – positive-ion mode LDI, negative-ion mode LDI, negative-ion mode MALDI, positive-ion mode MALDI



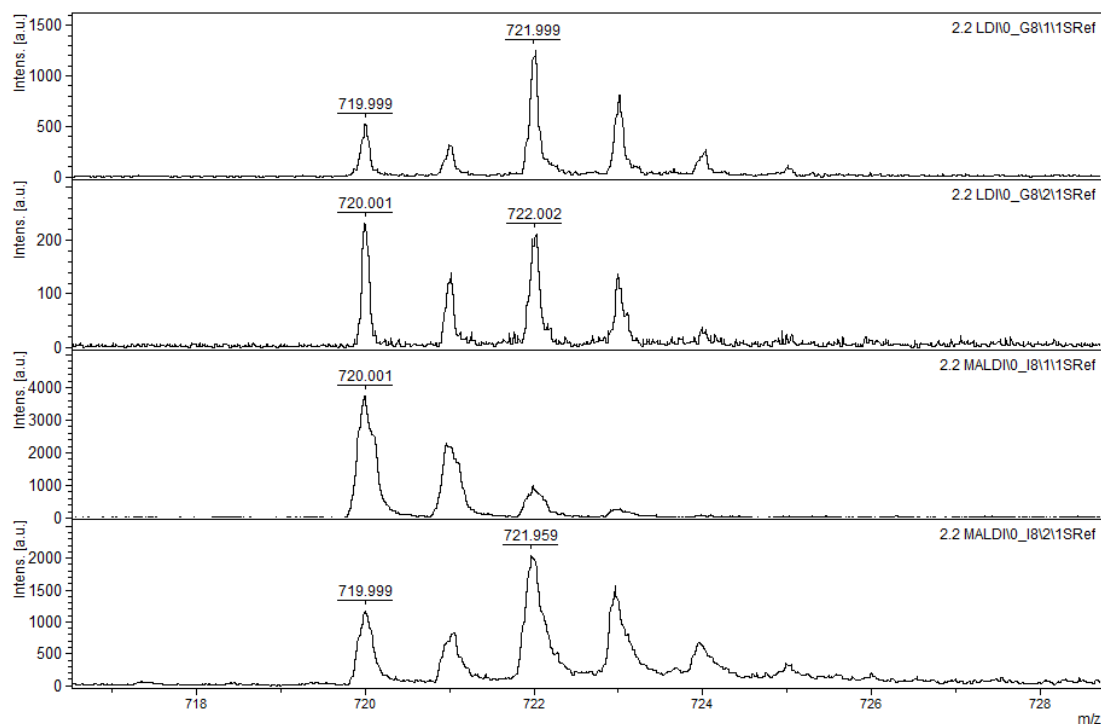
Sample 1.5, top to bottom – positive-ion mode LDI, negative-ion mode LDI, negative-ion mode MALDI, positive-ion mode MALDI



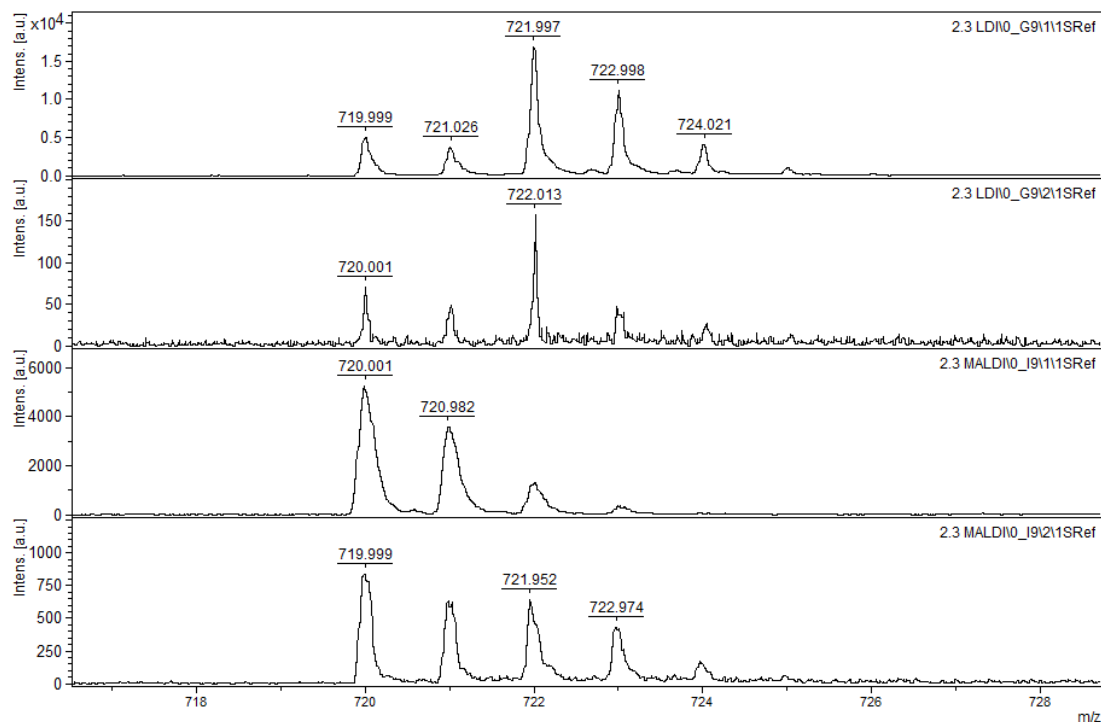
Sample 1.6, top to bottom – positive-ion mode LDI, negative-ion mode LDI, negative-ion mode MALDI, positive-ion mode MALDI



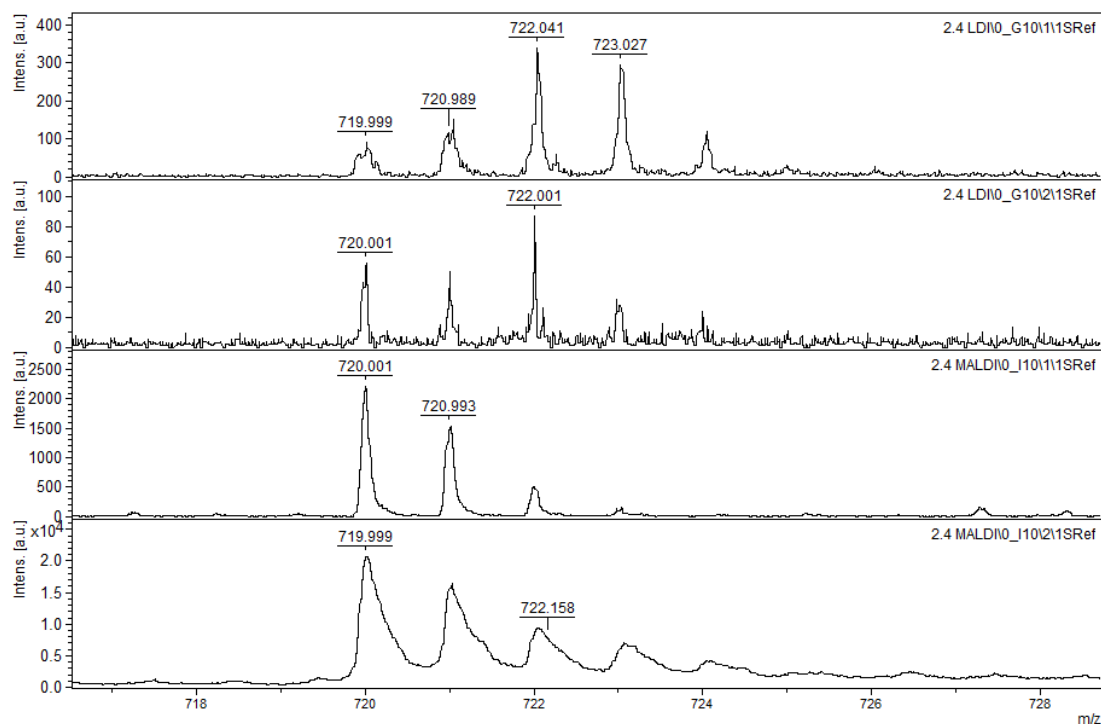
Sample 2.1, top to bottom – positive-ion mode LDI, negative-ion mode LDI, negative-ion mode MALDI, positive-ion mode MALDI



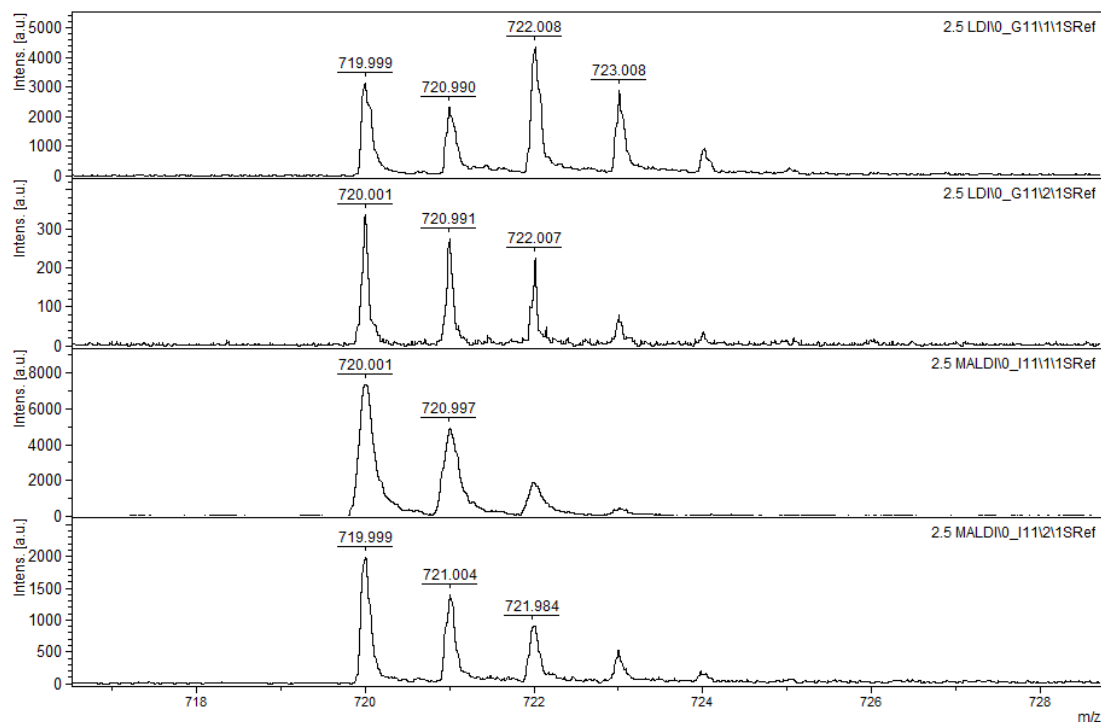
Sample 2.2, top to bottom – positive-ion mode LDI, negative-ion mode LDI, negative-ion mode MALDI, positive-ion mode MALDI



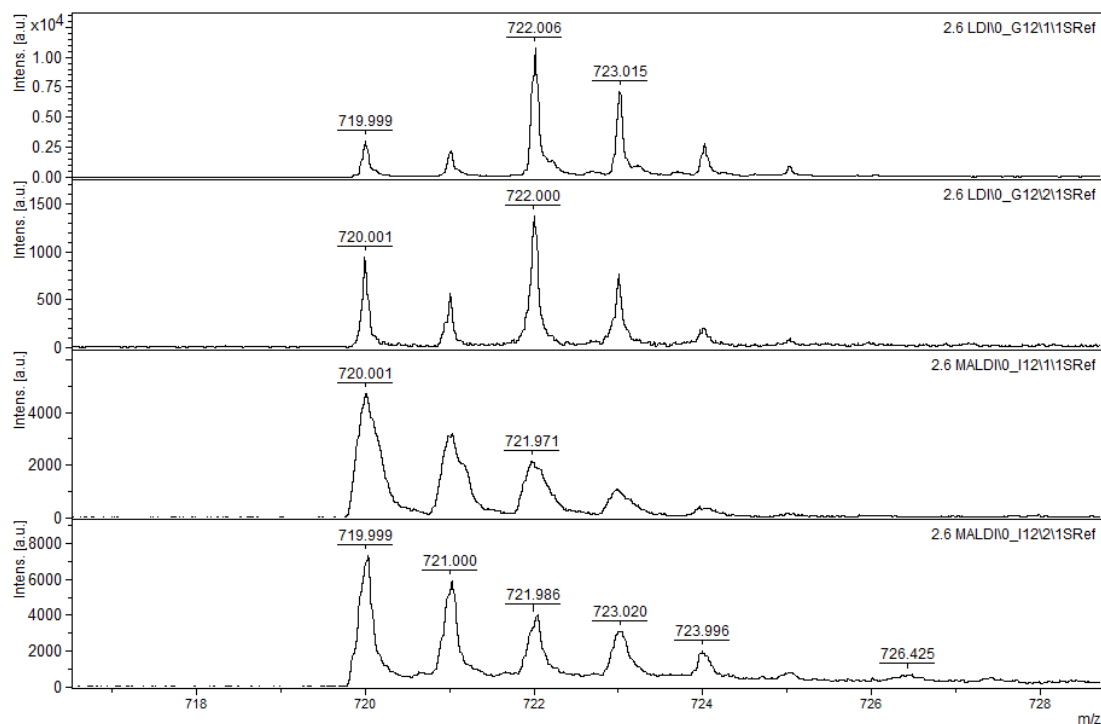
Sample 2.3, top to bottom – positive-ion mode LDI, negative-ion mode LDI, negative-ion mode MALDI, positive-ion mode MALDI



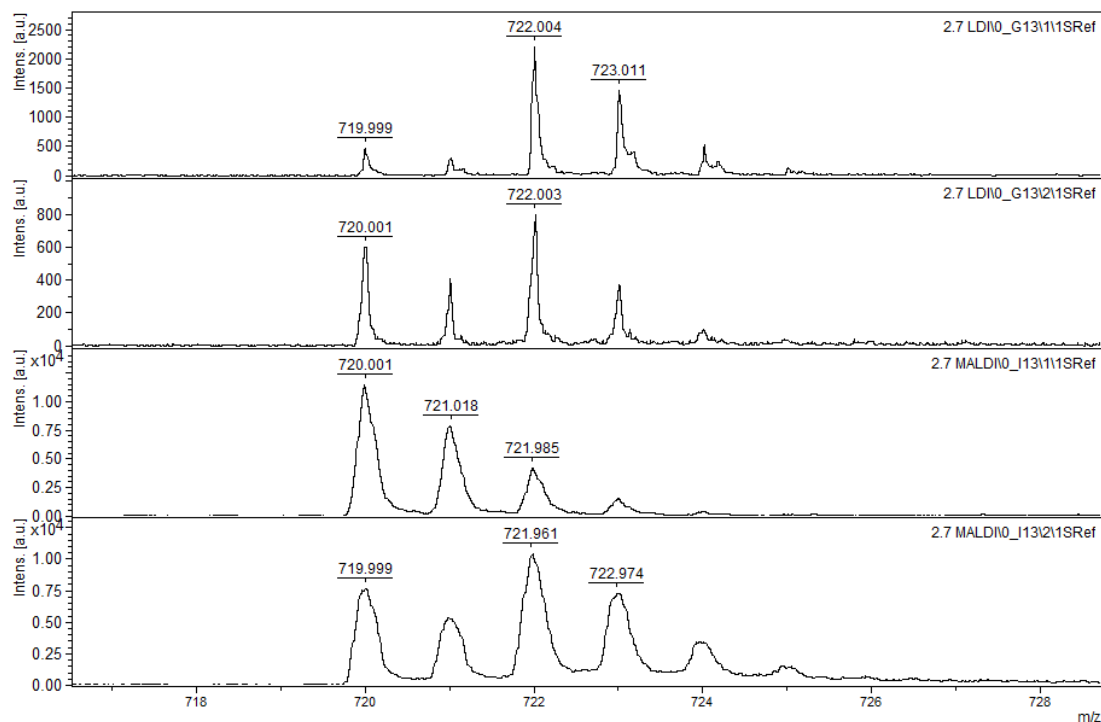
Sample 2.4, top to bottom – positive-ion mode LDI, negative-ion mode LDI, negative-ion mode MALDI, positive-ion mode MALDI



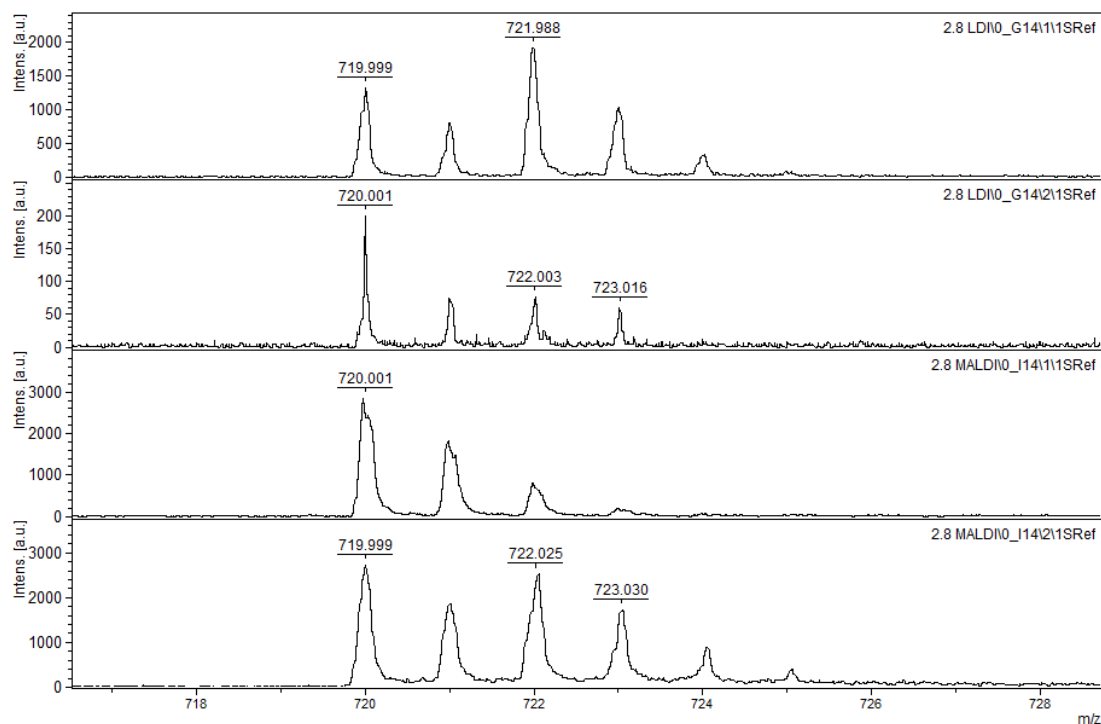
Sample 2.5, top to bottom – positive-ion mode LDI, negative-ion mode LDI, negative-ion mode MALDI, positive-ion mode MALDI



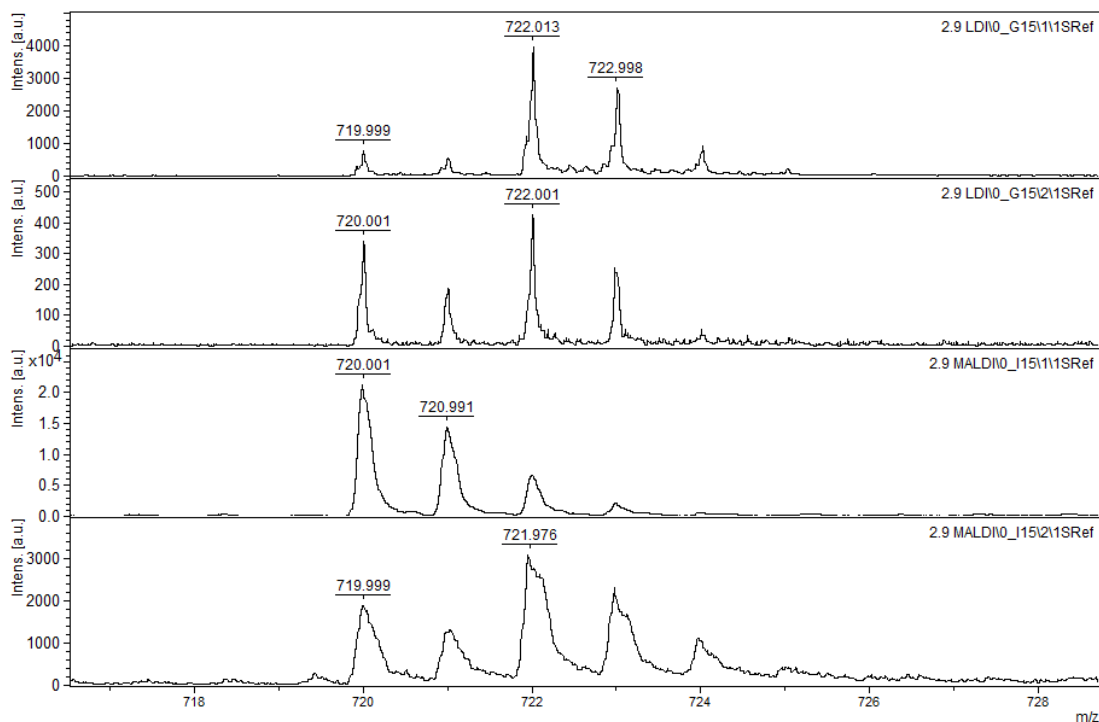
Sample 2.6, top to bottom – positive-ion mode LDI, negative-ion mode LDI, negative-ion mode MALDI, positive-ion mode MALDI



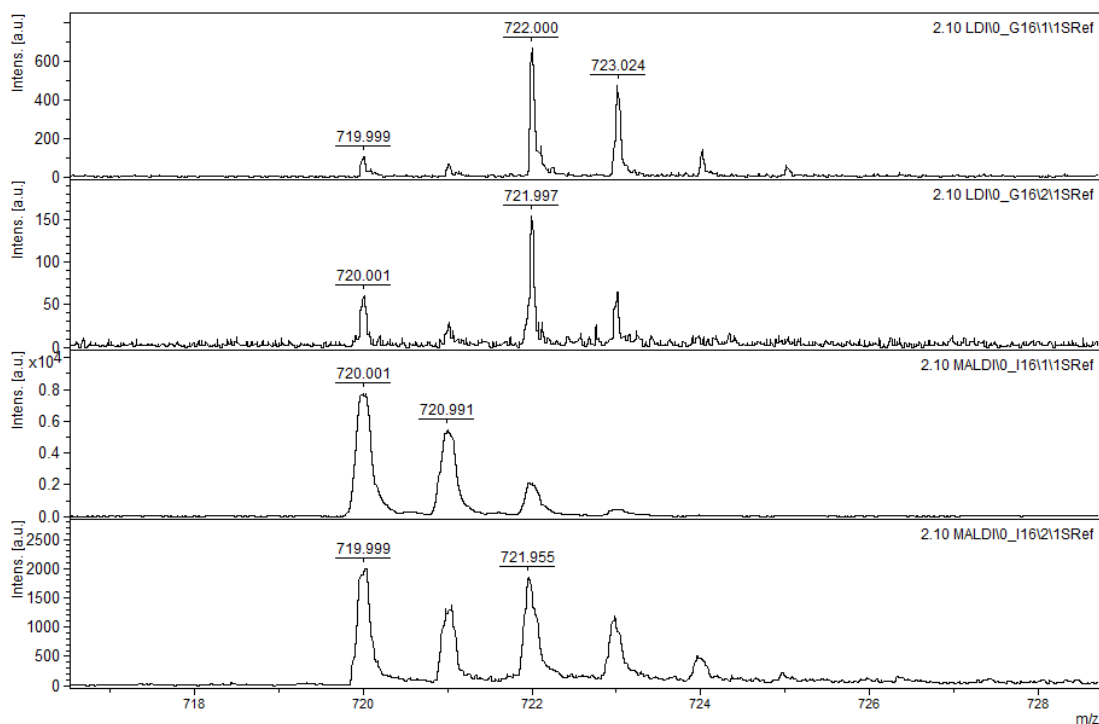
Sample 2.7, top to bottom – positive-ion mode LDI, negative-ion mode LDI, negative-ion mode MALDI, positive-ion mode MALDI



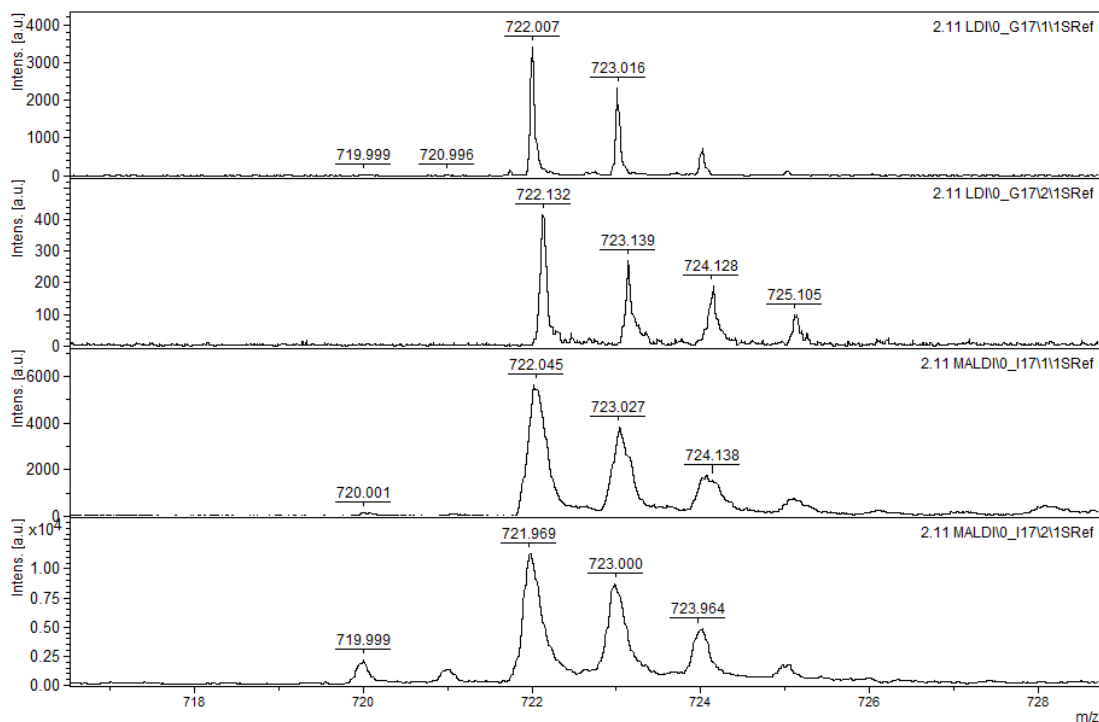
Sample 2.8, top to bottom – positive-ion mode LDI, negative-ion mode LDI, negative-ion mode MALDI, positive-ion mode MALDI



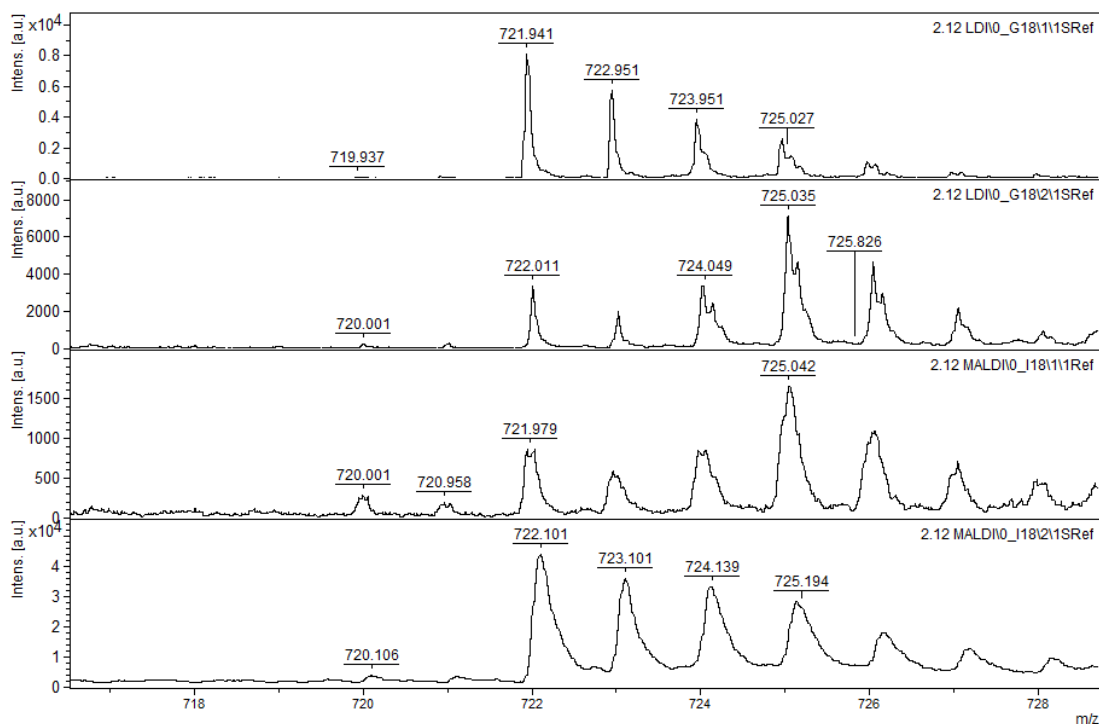
Sample 2.9, top to bottom – positive-ion mode LDI, negative-ion mode LDI, negative-ion mode MALDI, positive-ion mode MALDI



Sample 2.10, top to bottom – positive-ion mode LDI, negative-ion mode LDI, negative-ion mode MALDI, positive-ion mode MALDI



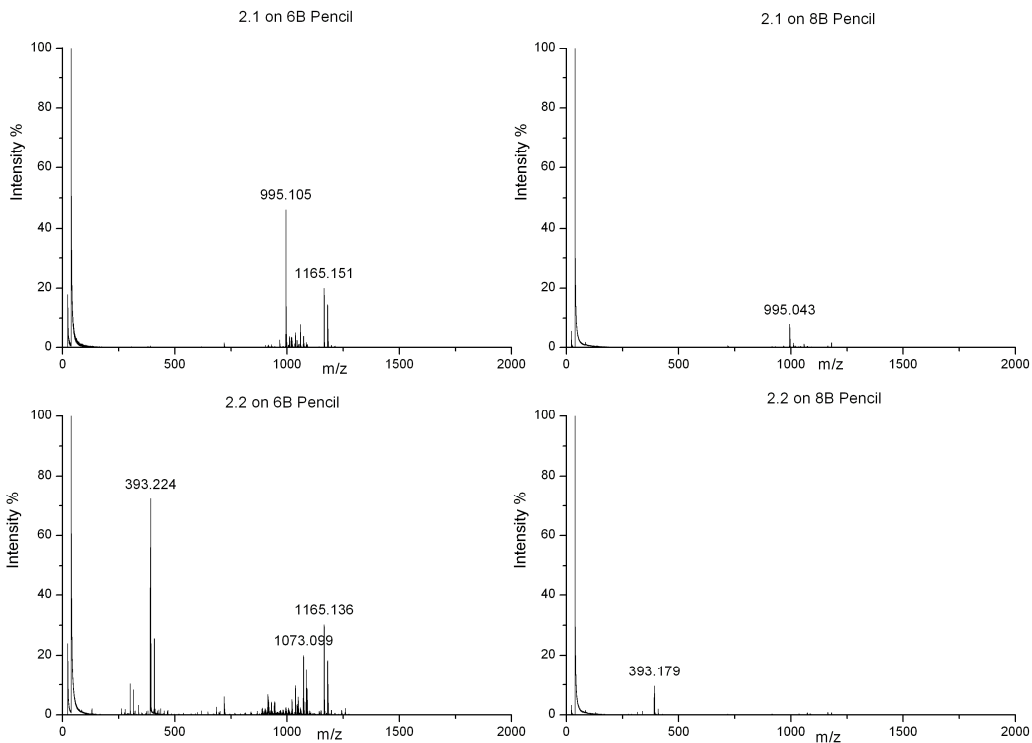
Sample 2.11, top to bottom – positive-ion mode LDI, negative-ion mode LDI, negative-ion mode MALDI, positive-ion mode MALDI



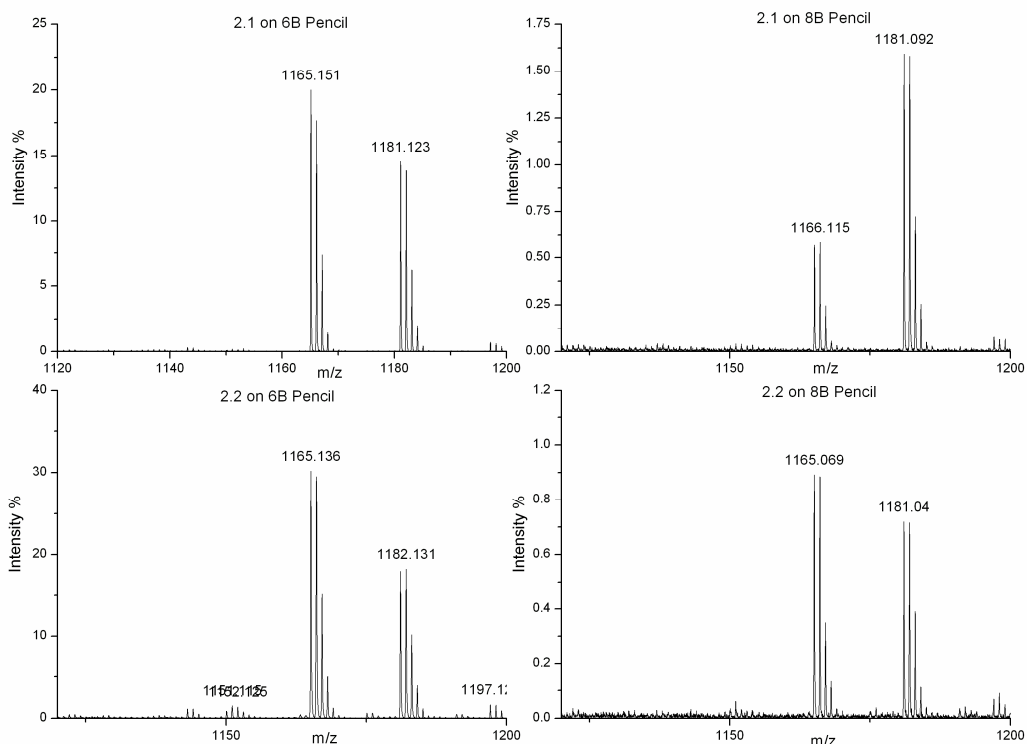
Sample 2.12, top to bottom – positive-ion mode LDI, negative-ion mode LDI, negative-ion mode MALDI, positive-ion mode MALDI

Chapter 5 Additional Spectra

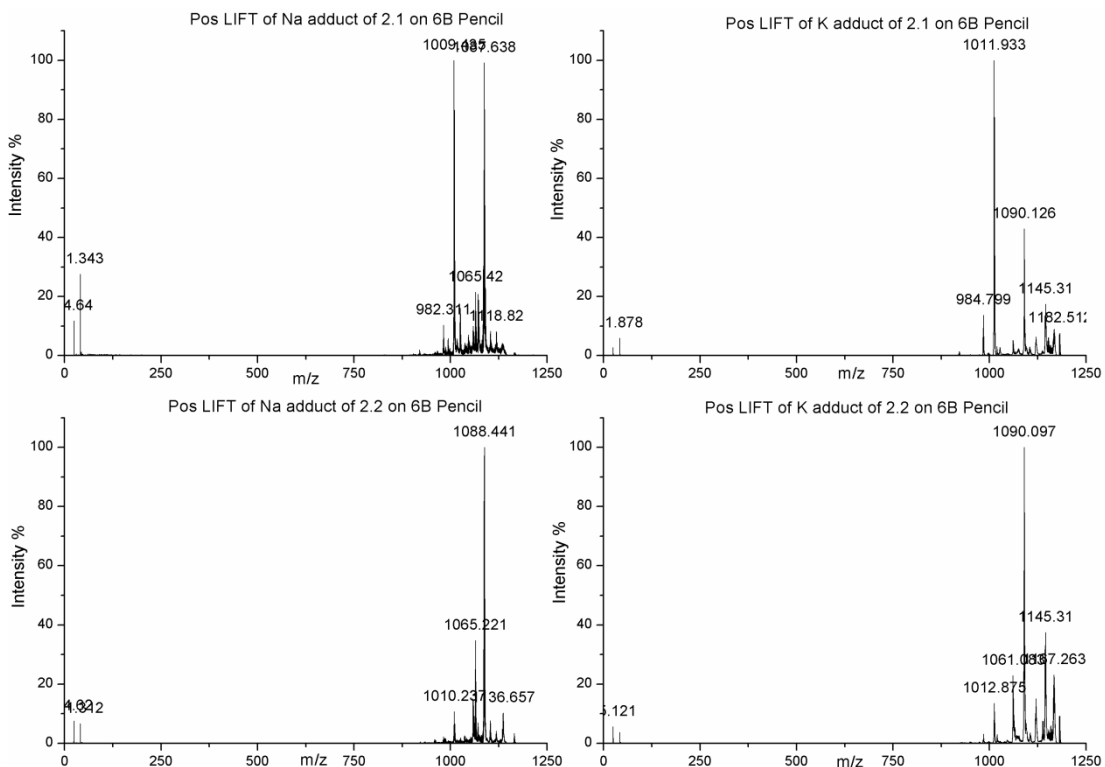
Additional OCF on pencil spectra



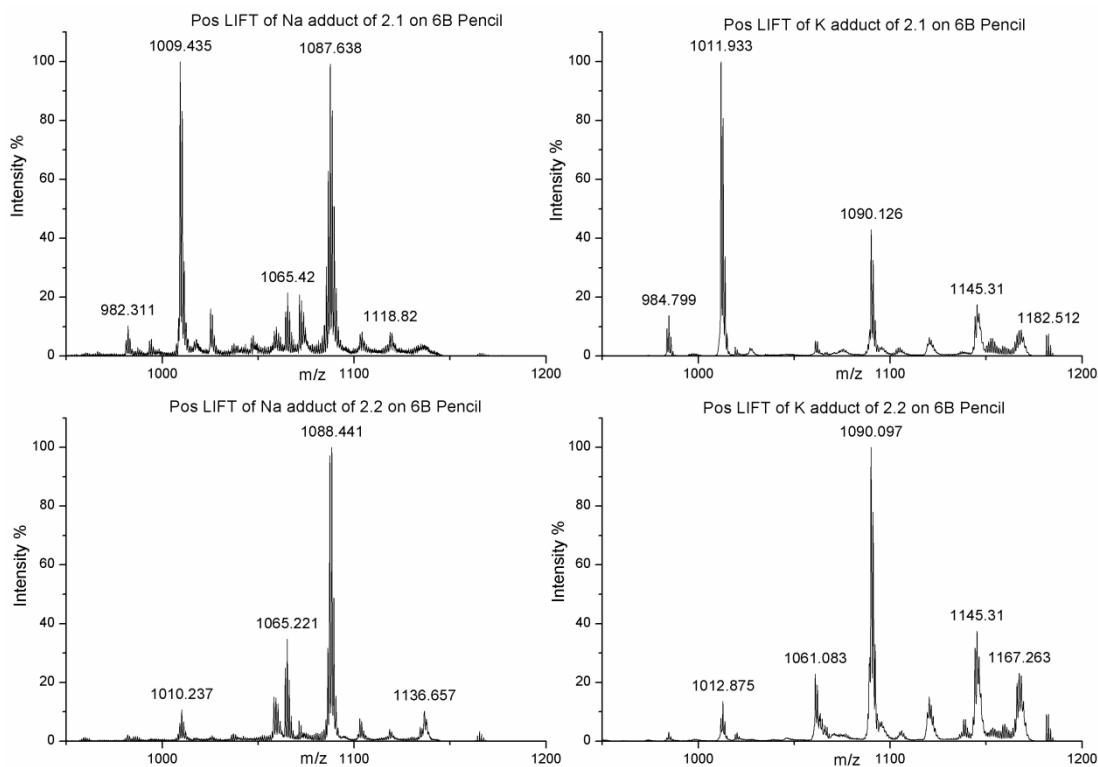
Compounds 2.1 and 2.3 on 6B and 8B Pencil



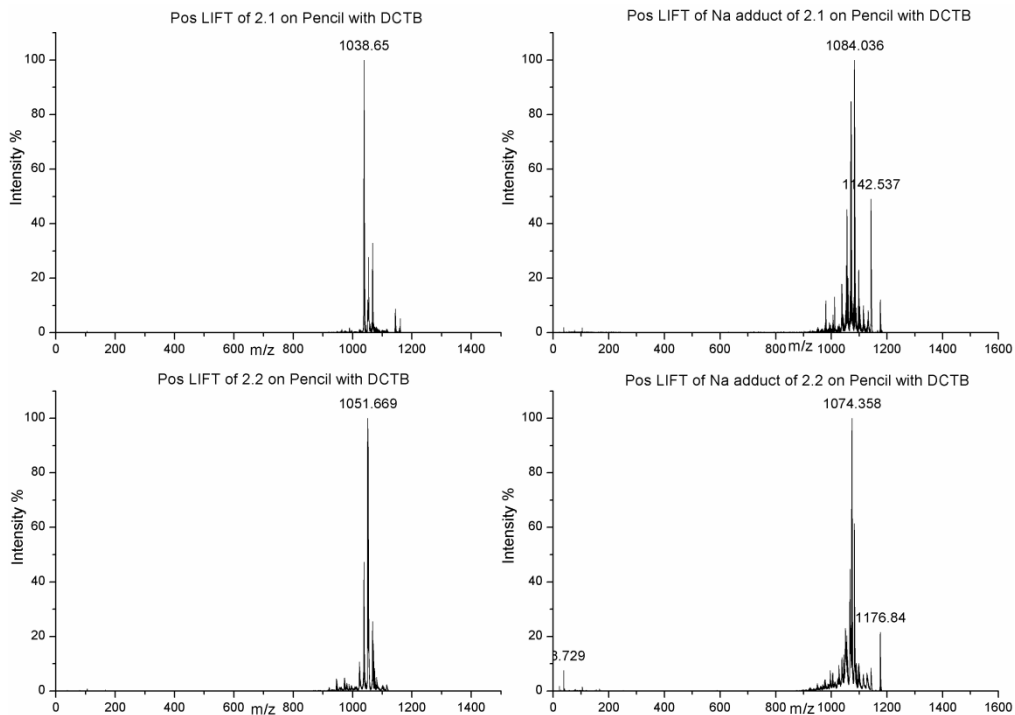
Enhancement of the molecular ion region for compounds 2.1 and 2.2



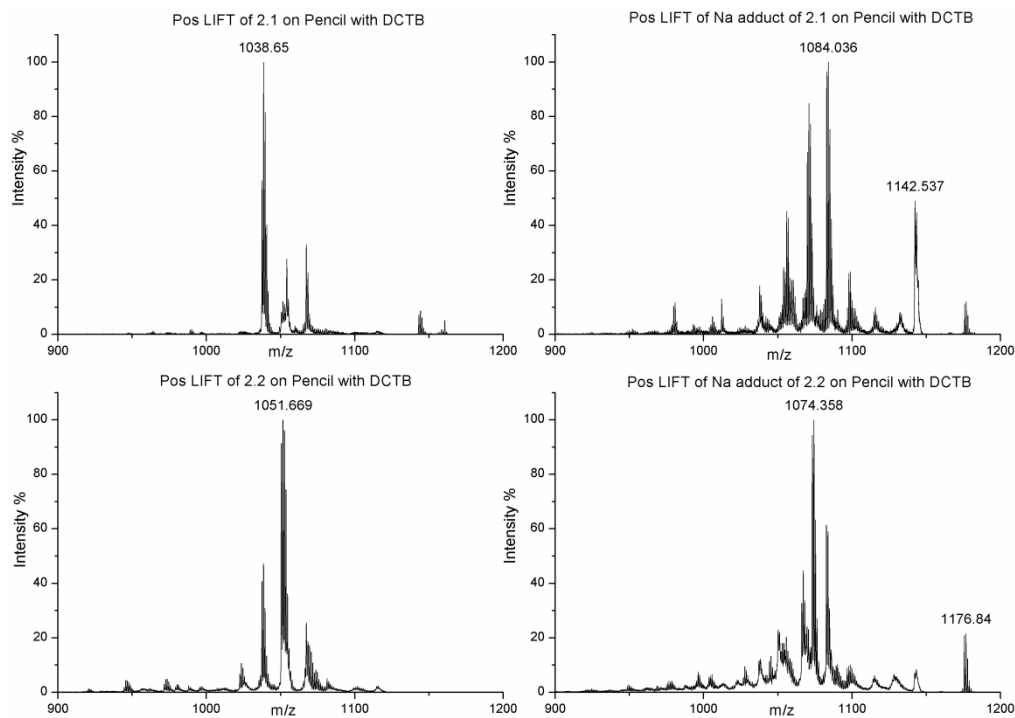
Positive-ion mode LIFT of the Na and K adducts of 2.1 and 2.2 on 6B pencil



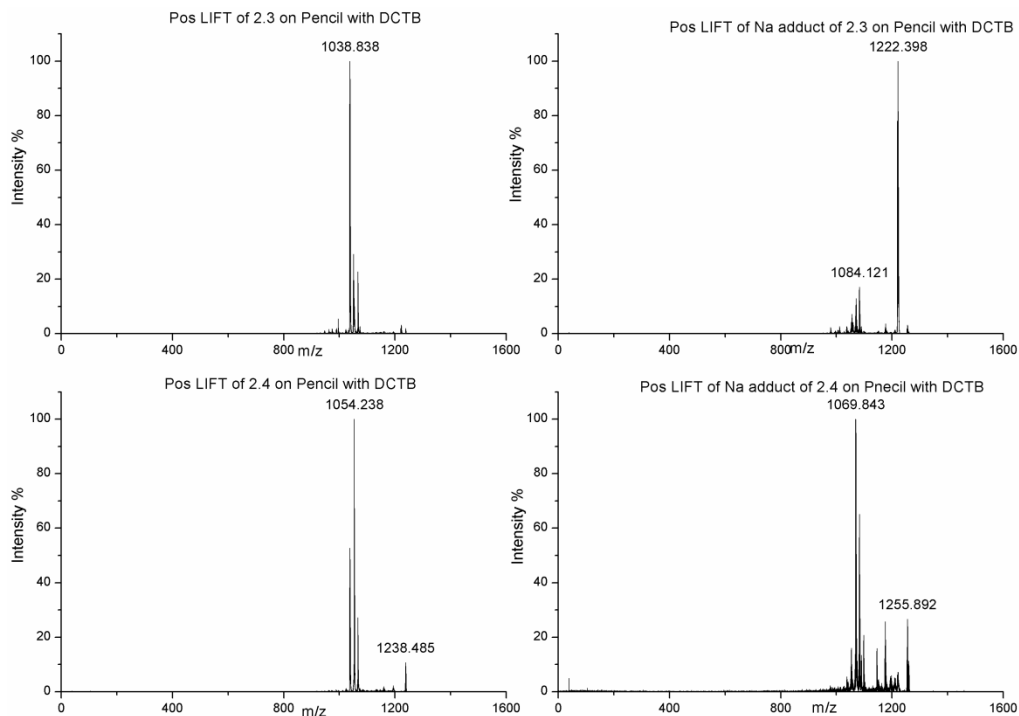
Enhancement of the fragment peaks for the LIFT experiments of the Na and K adducts of 2.1 and 2.2 on 6B pencil



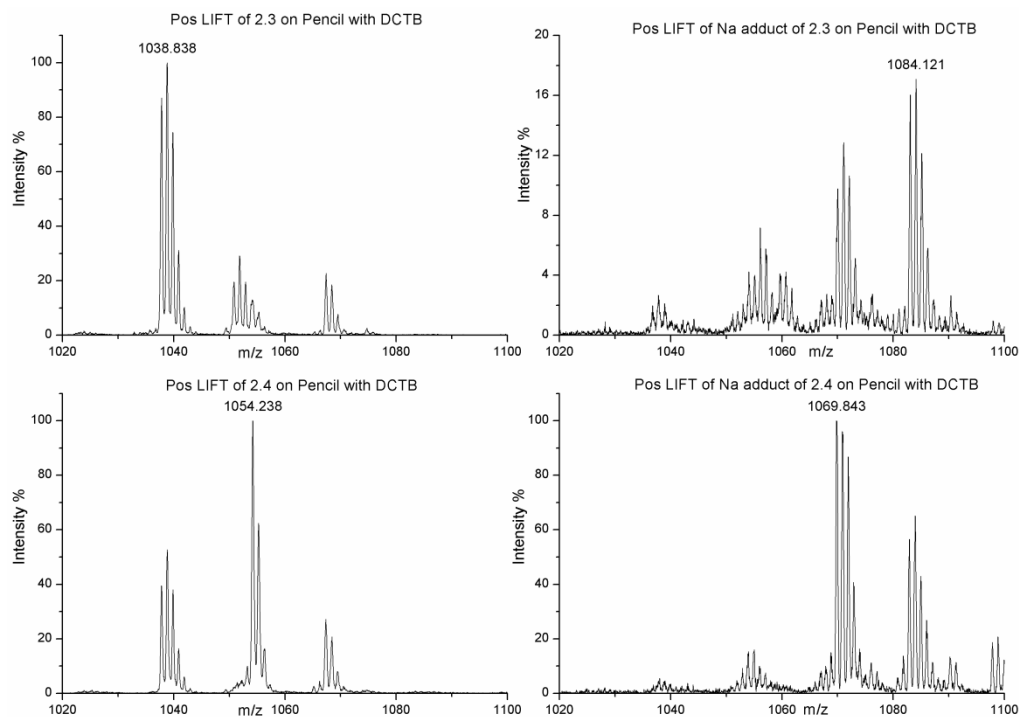
Positive-ion mode LIFT of the “bare” and the Na adducts of 2.1 and 2.2 on HB pencil with DCTB present



Enhancement of the fragment ions of the positive-ion mode LIFT of the “bare” and the Na adducts of 2.1 and 2.2 on HB pencil with DCTB present

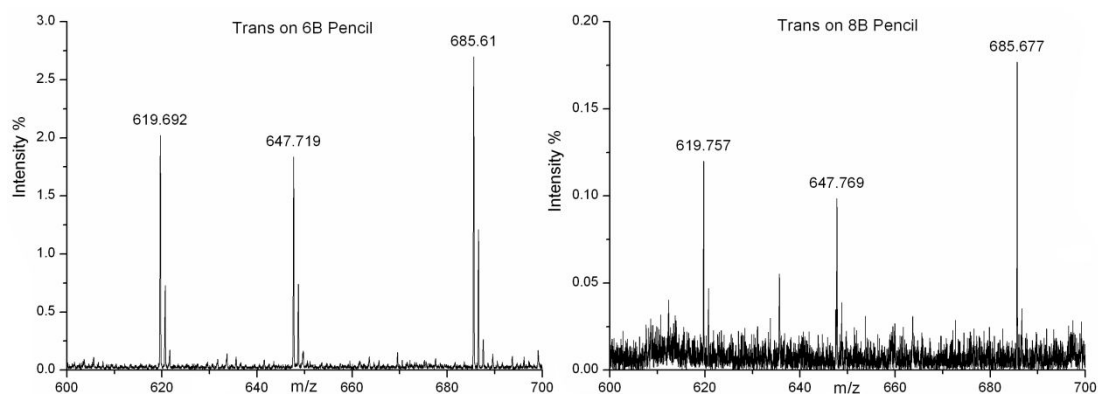


Positive-ion mode LIFT of the “bare” and the Na adducts of 2.3 and 2.4 on HB pencil with DCTB present

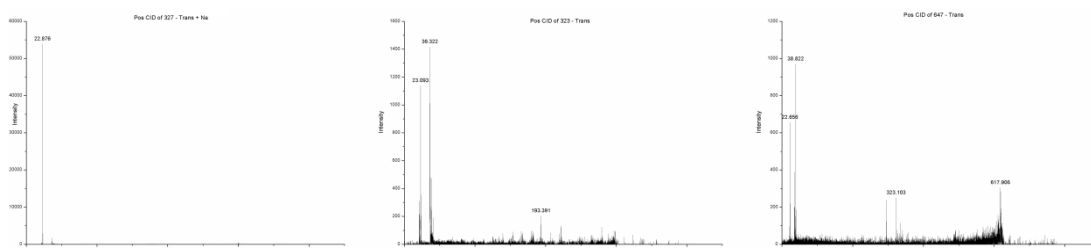


Enhancement of the fragment ion region of the positive-ion mode LIFT of the “bare” and the Na adducts of 2.1 and 2.2 on HB pencil with DCTB present

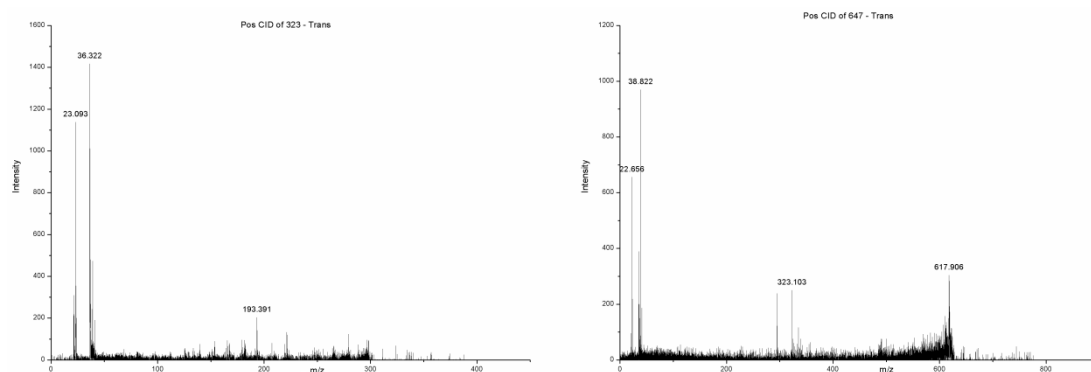
Additional (Z)- and (E)-acenaphthalene ("Cis" and "Trans") Spectra



Enhancement of the higher mass range for "Trans" on 6B and 8B pencil



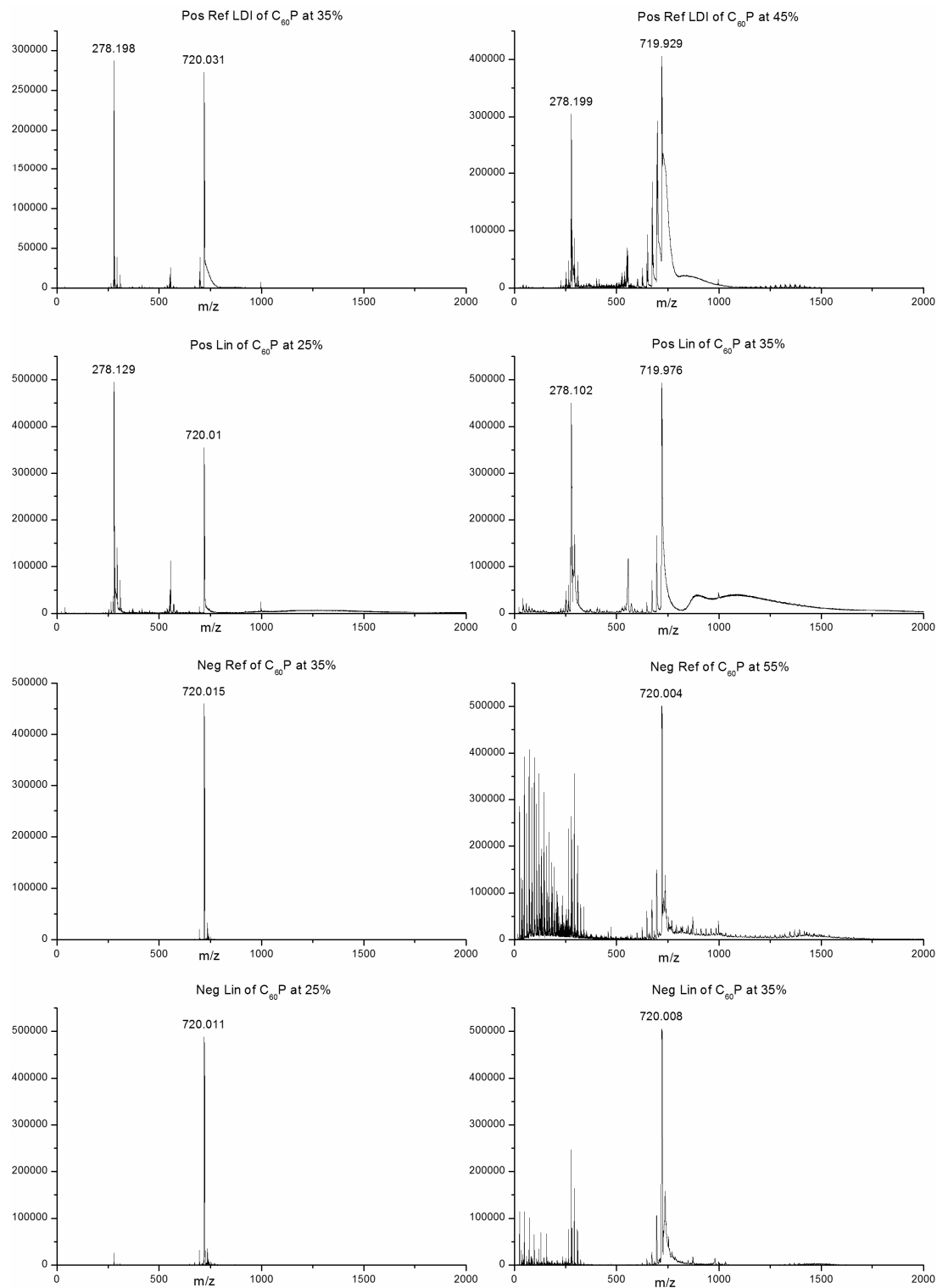
Various CID experiments of "Trans" on pencil



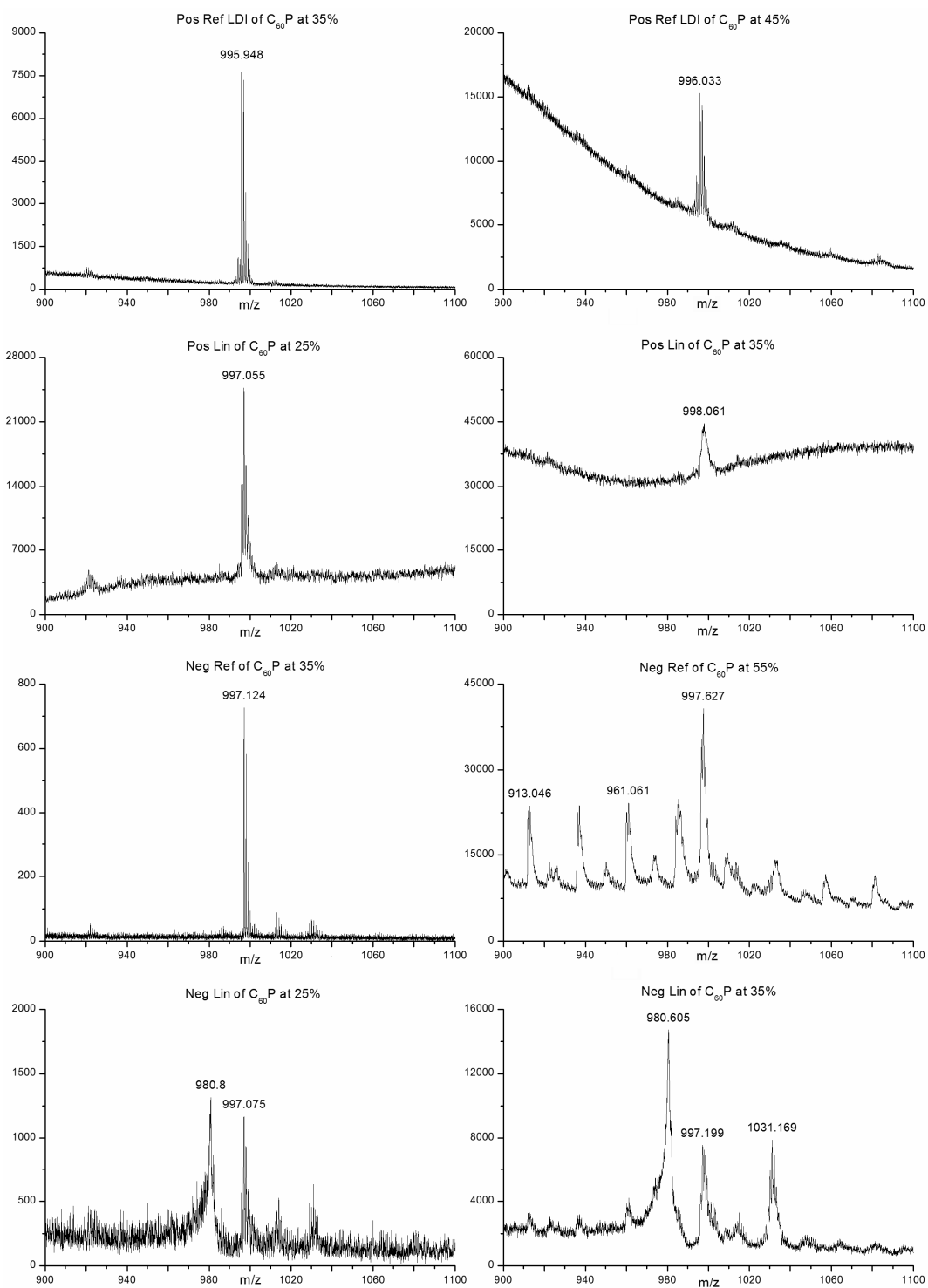
More CID experiments of "Trans" on pencil

Chapter 6 Additional Spectra

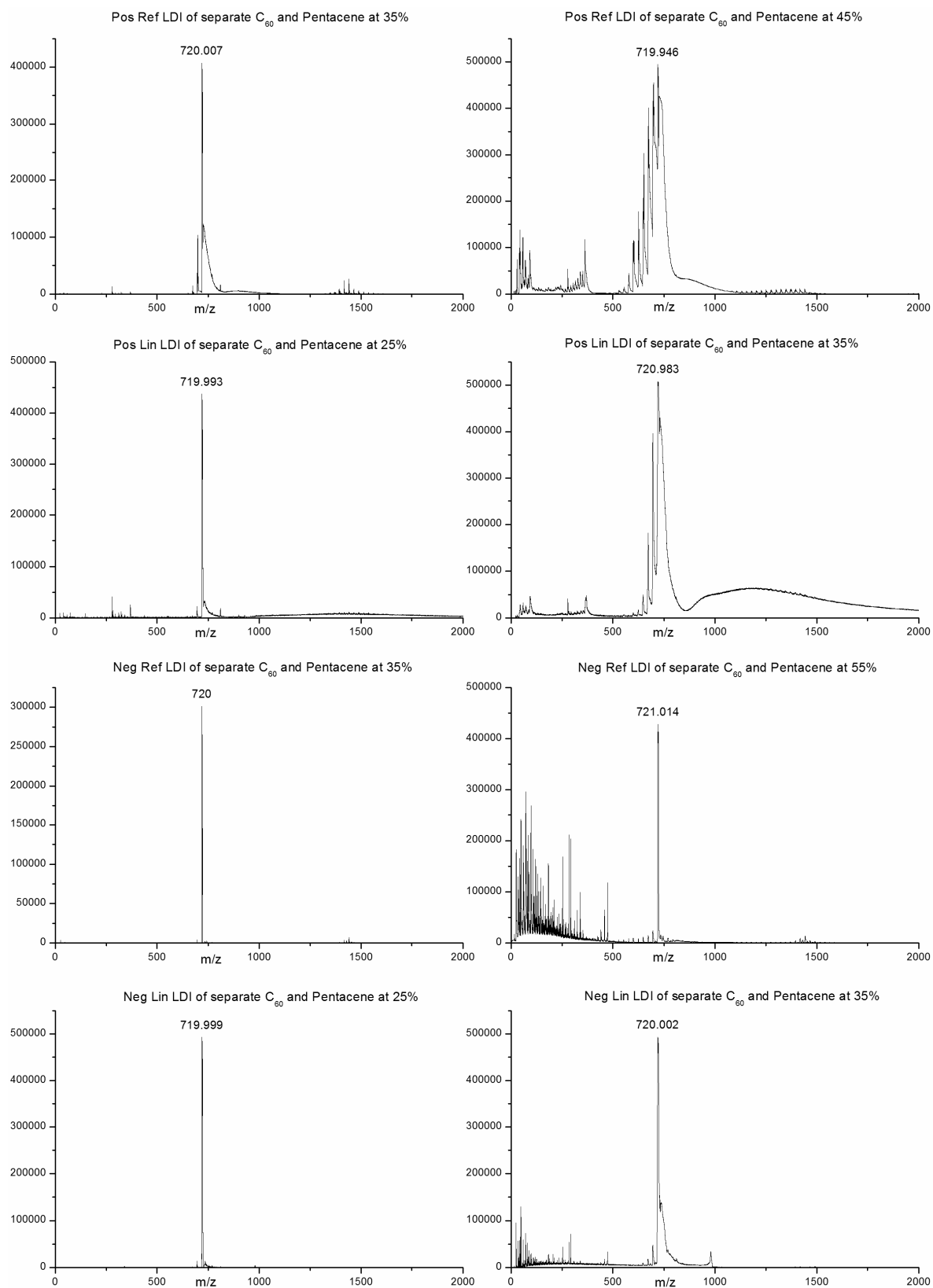
C₆₀P Spectra at elevated Laser Fluences

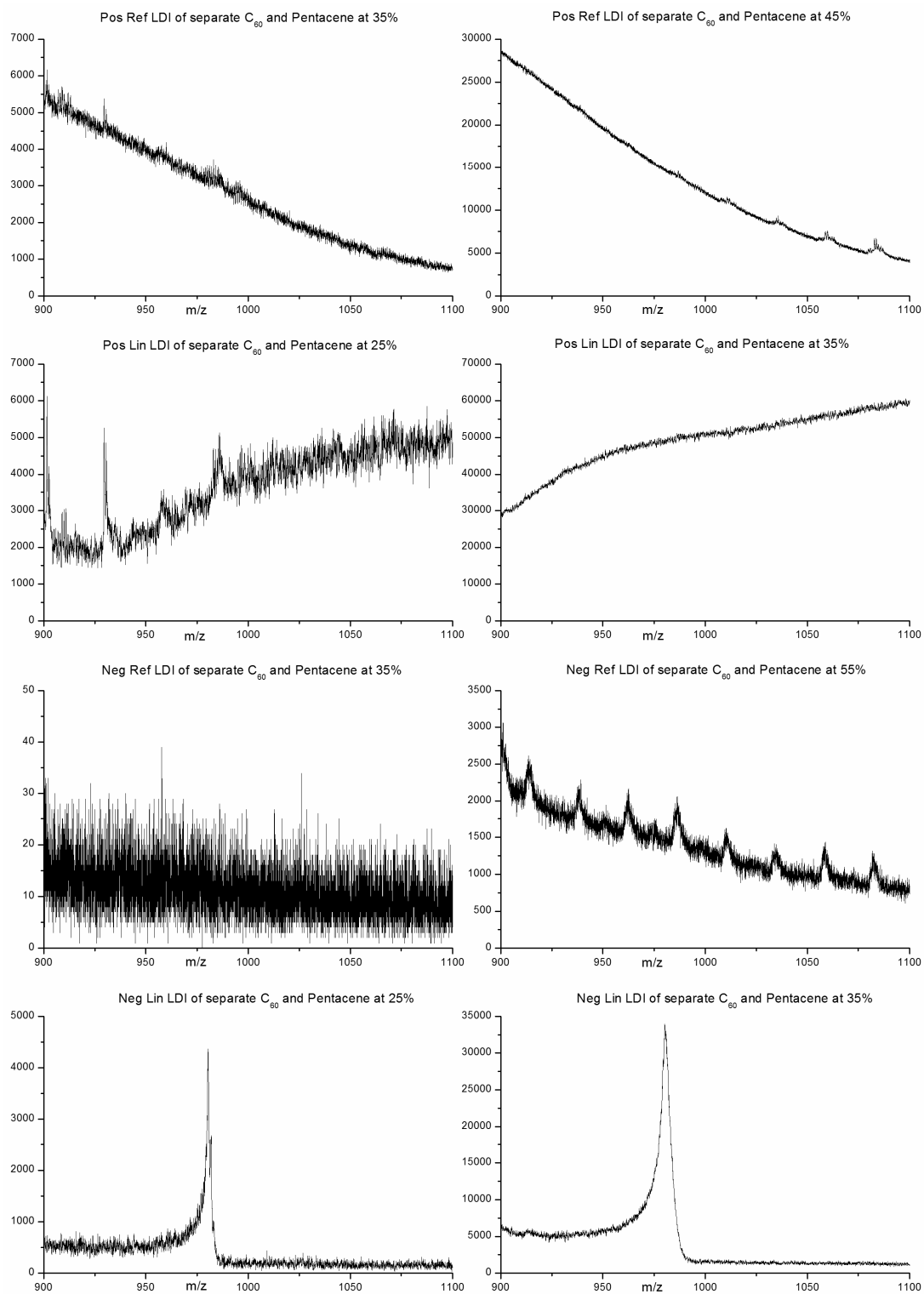


Full range spectra of the LDI experiments on C₆₀P at elevated Laser Fluences



Enhancement of the molecular ion region for the LDI experiments with elevated laser fluences on $C_{60}P$

Spectra of the LDI experiments with separate C_{60} and pentacene at elevated laser fluences

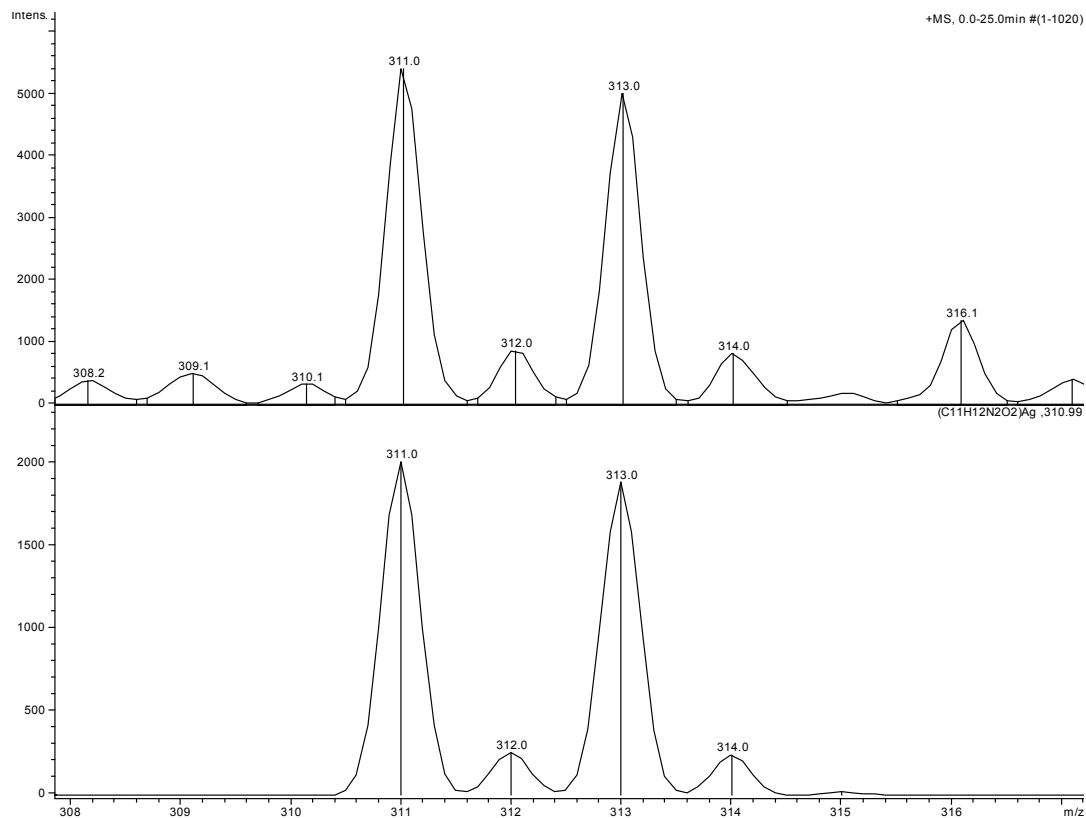


Spectra of the LDI experiments of separate C_{60} and pentacene at elevated laser fluences, enhancement of the quasi-molecular ion region

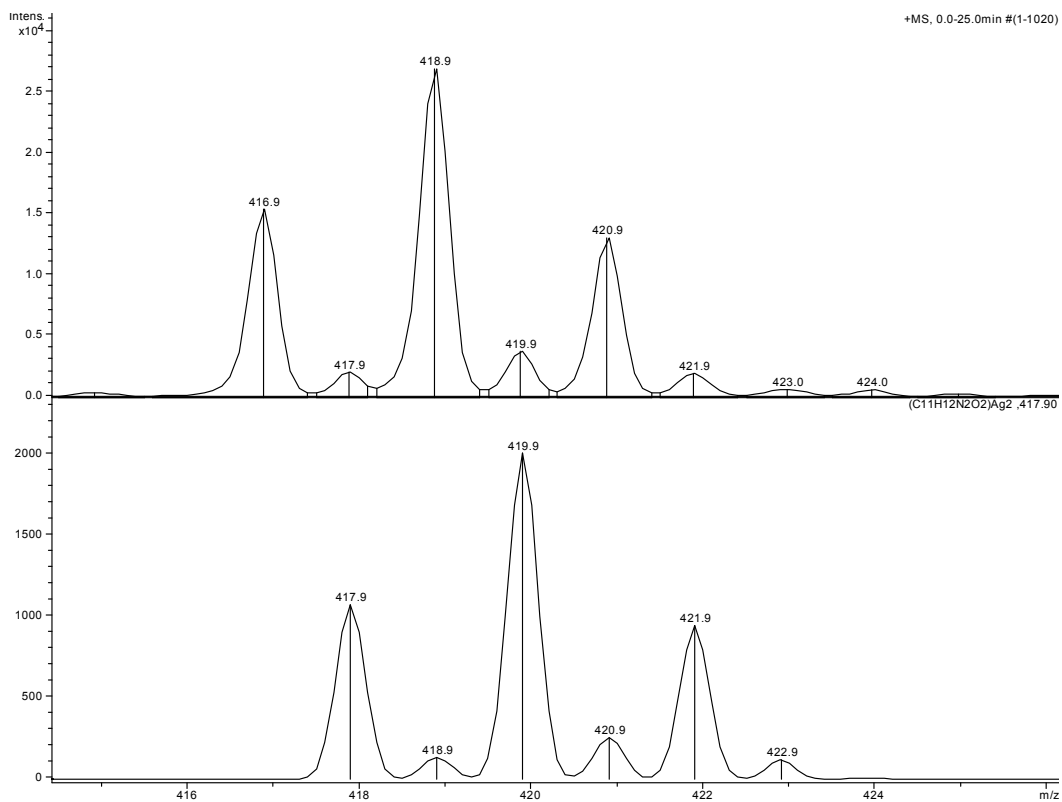
Chapter 7 Additional Spectra

Actual and Simulated Isotopic pattern of the different Clusters

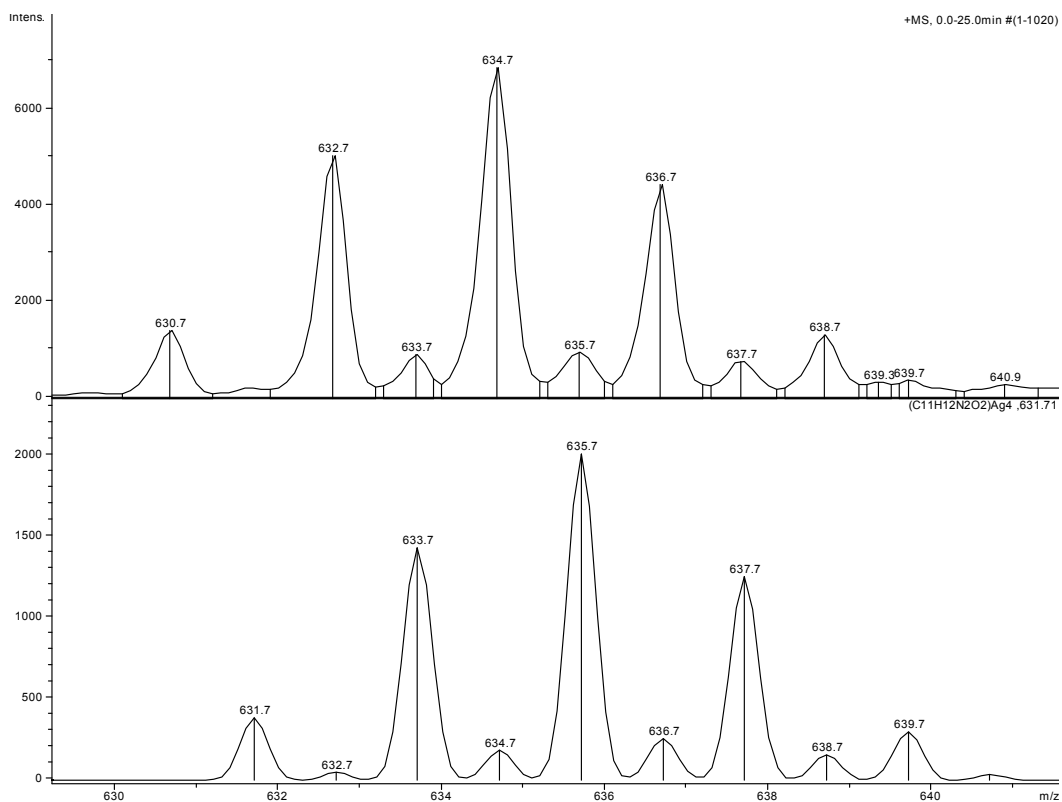
Individual clusters with the simulated isotopic patterns displayed below the actual mass spectrum. The simulated isotopic pattern has the “intact” version of tryptophan i.e. the hydrogen atom loss is not simulated, which is why the simulated and actual do not align.



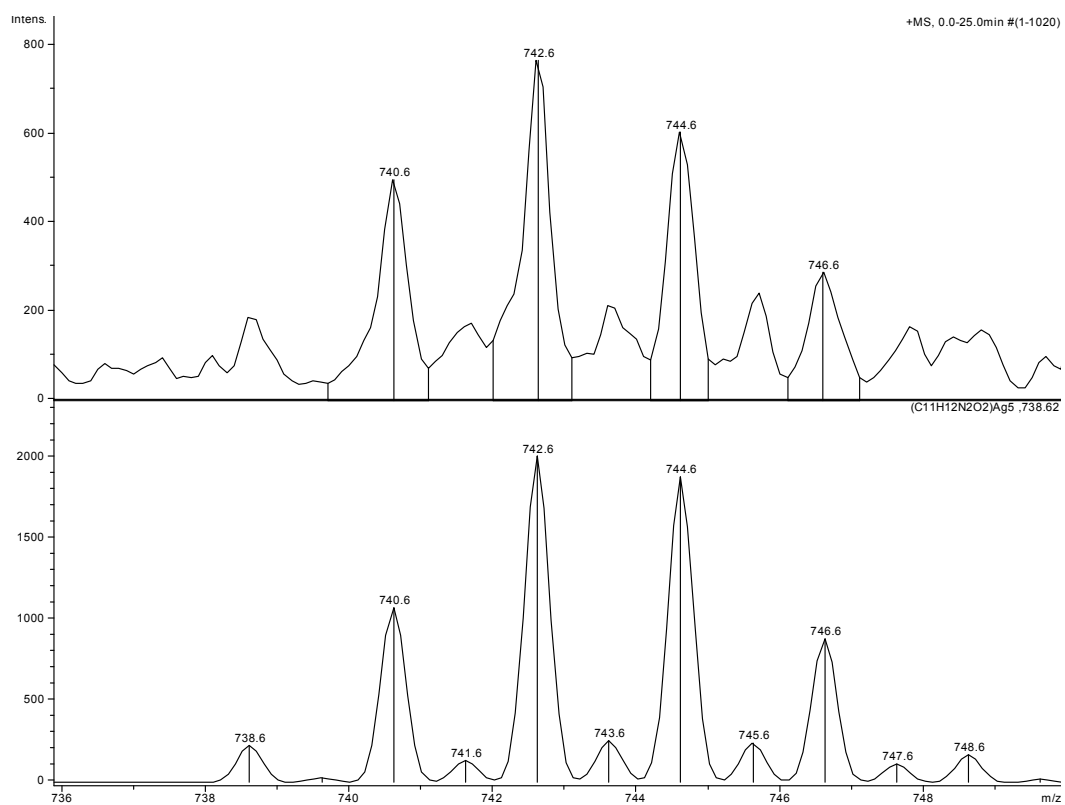
$[AgTrp]^+$ cluster, actual, top and simulated, bottom



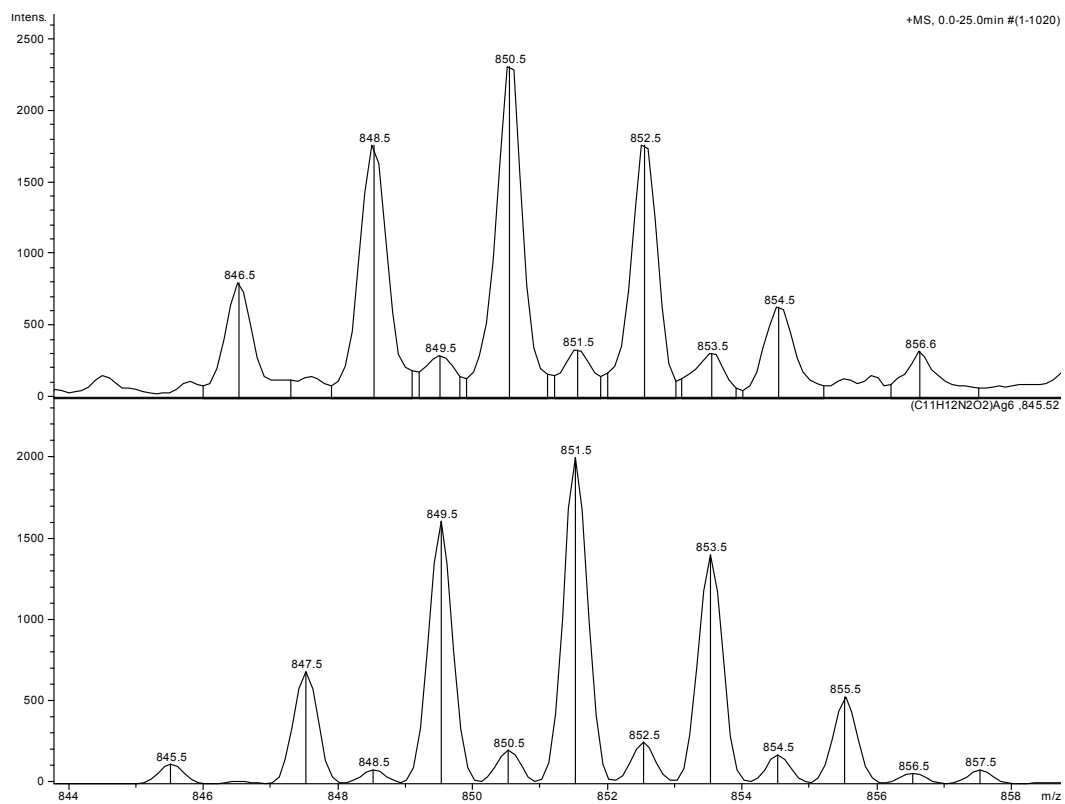
$[Ag_2Trp]^+$ cluster, actual, top and simulated, bottom



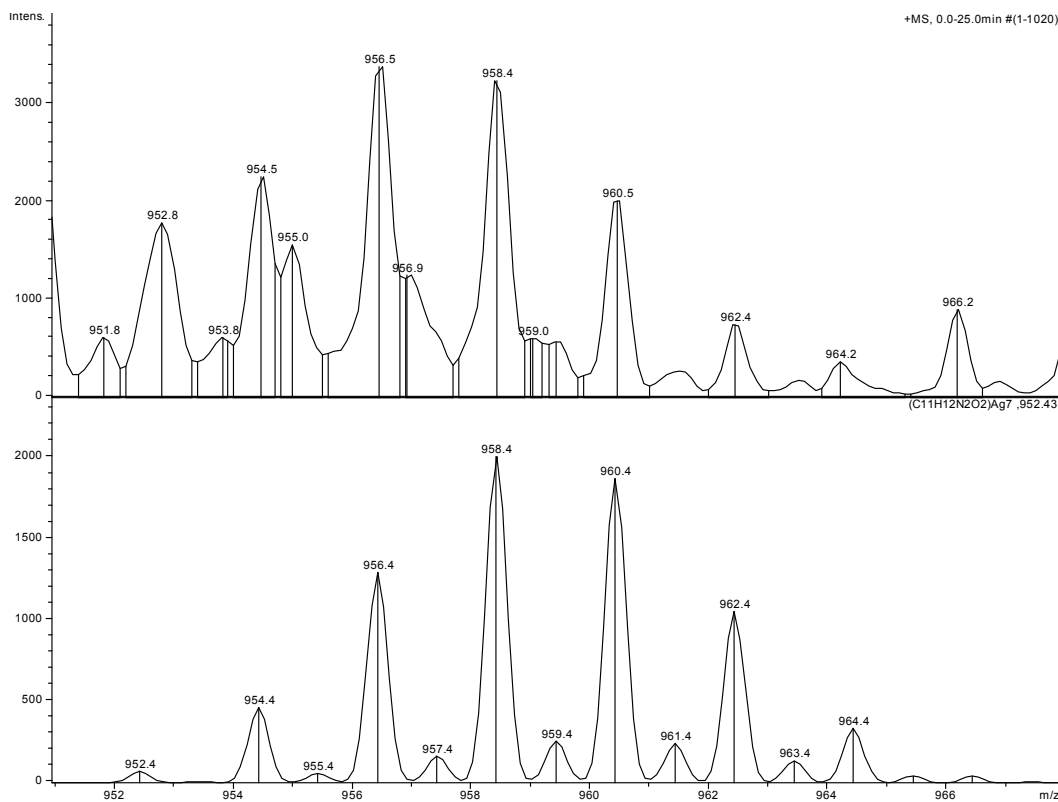
$[Ag_4Trp]^+$ cluster, actual, top and simulated, bottom



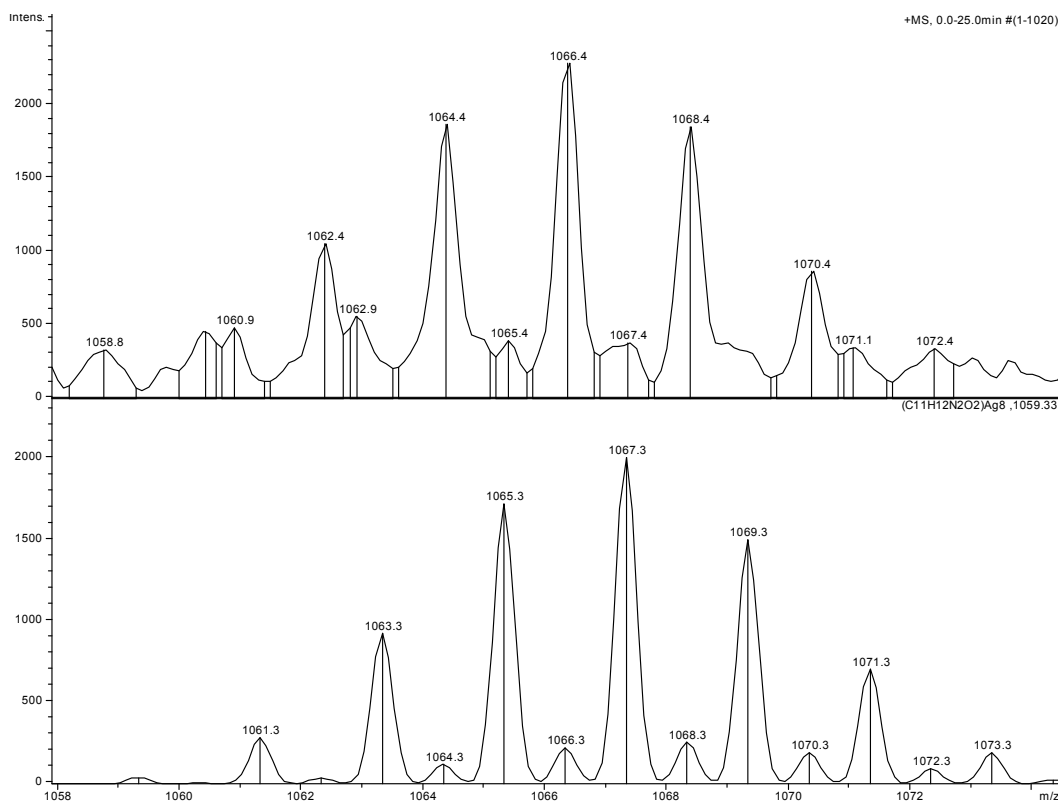
[Ag₅Trp]⁺ cluster, actual, top and simulated, bottom



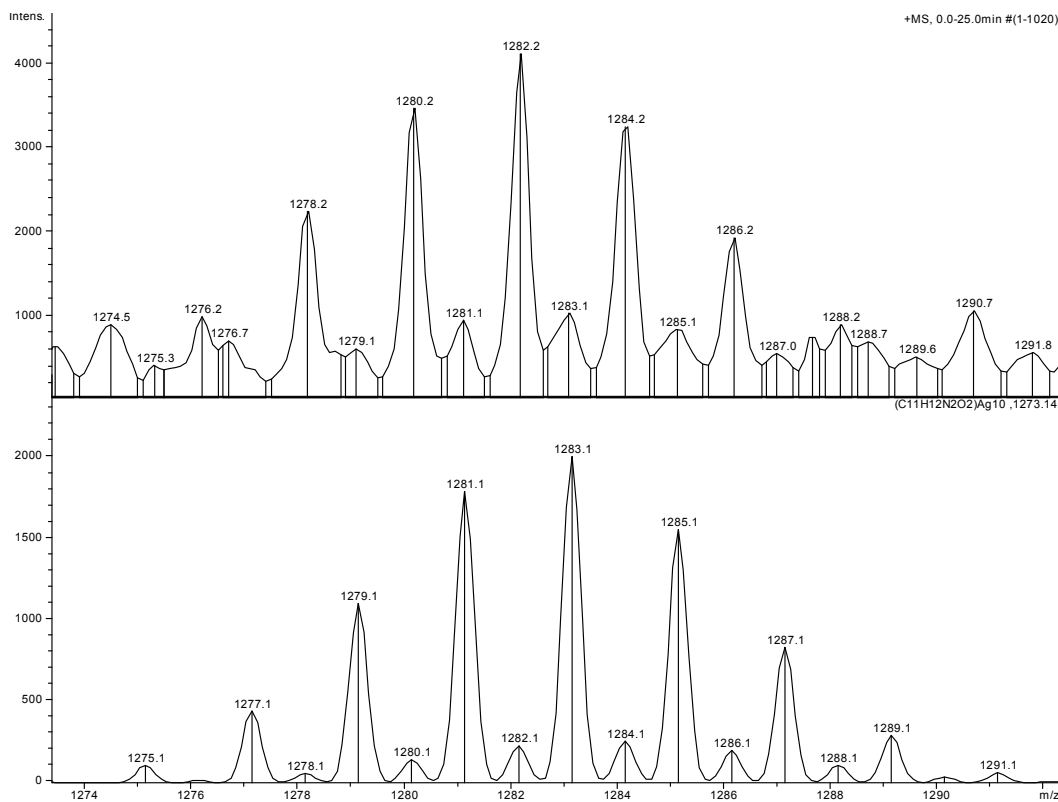
[Ag₆Trp]⁺ cluster, actual, top and simulated, bottom



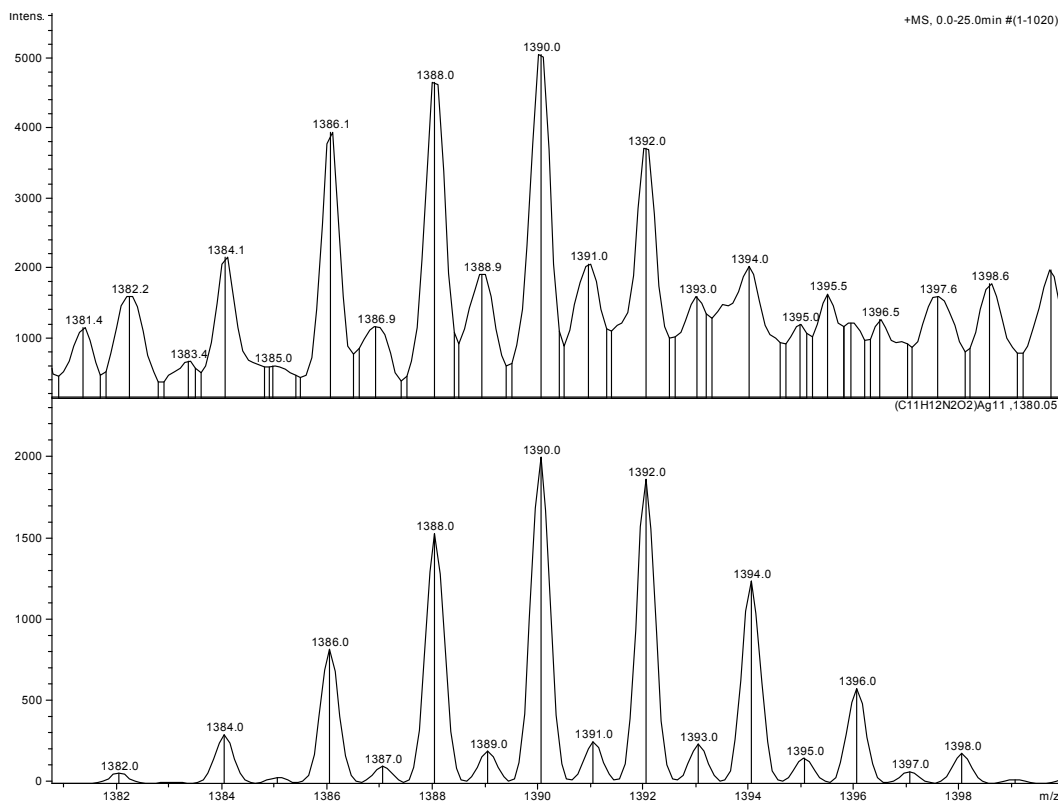
[Ag₇Trp]⁺ cluster, actual, top and simulated, bottom



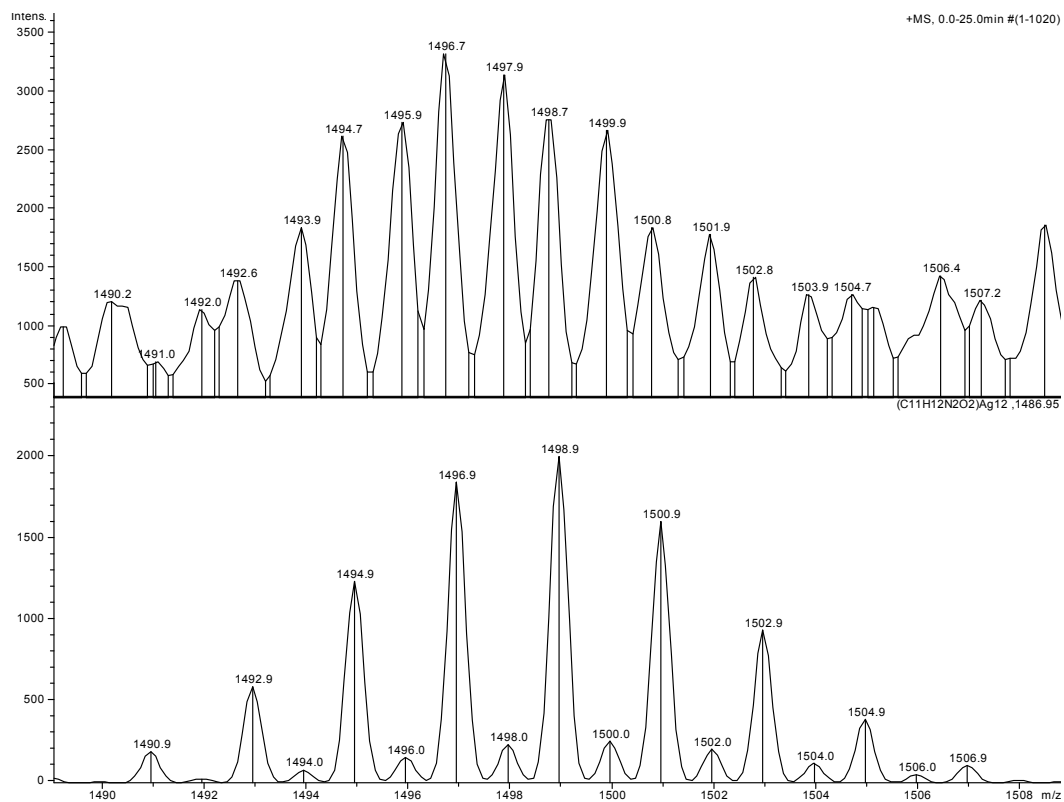
[Ag₈Trp]⁺ cluster, actual, top and simulated, bottom



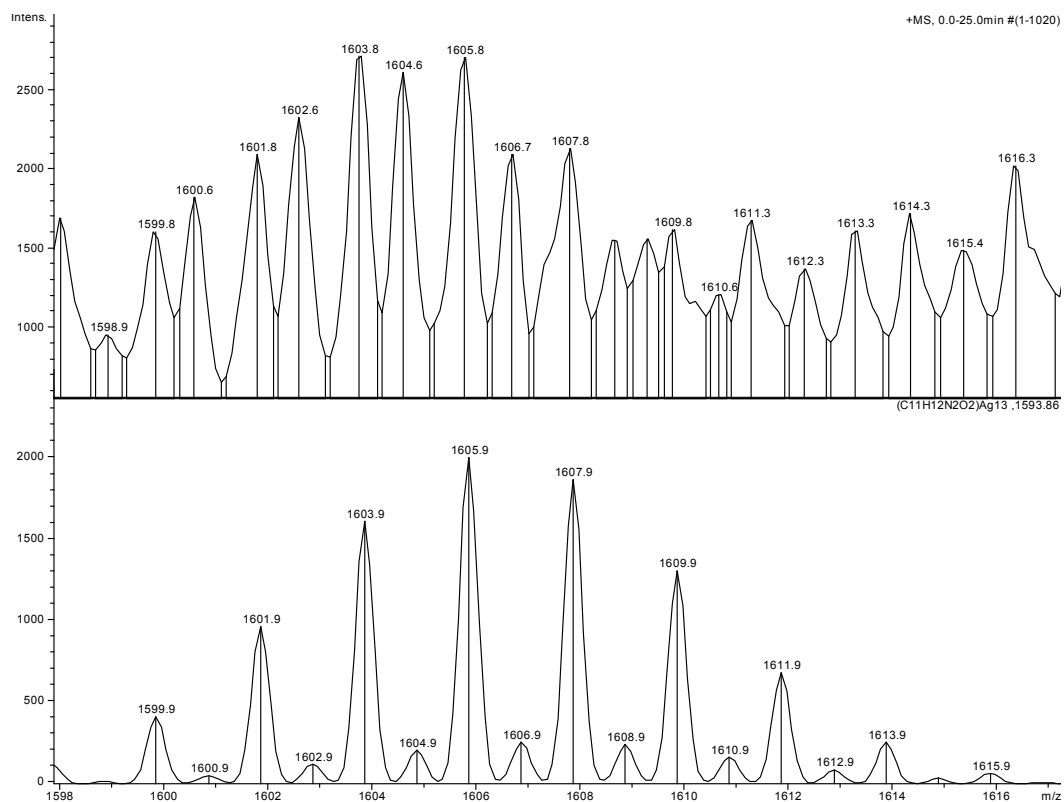
[Ag₁₀Trp]⁺ cluster, actual, top and simulated, bottom



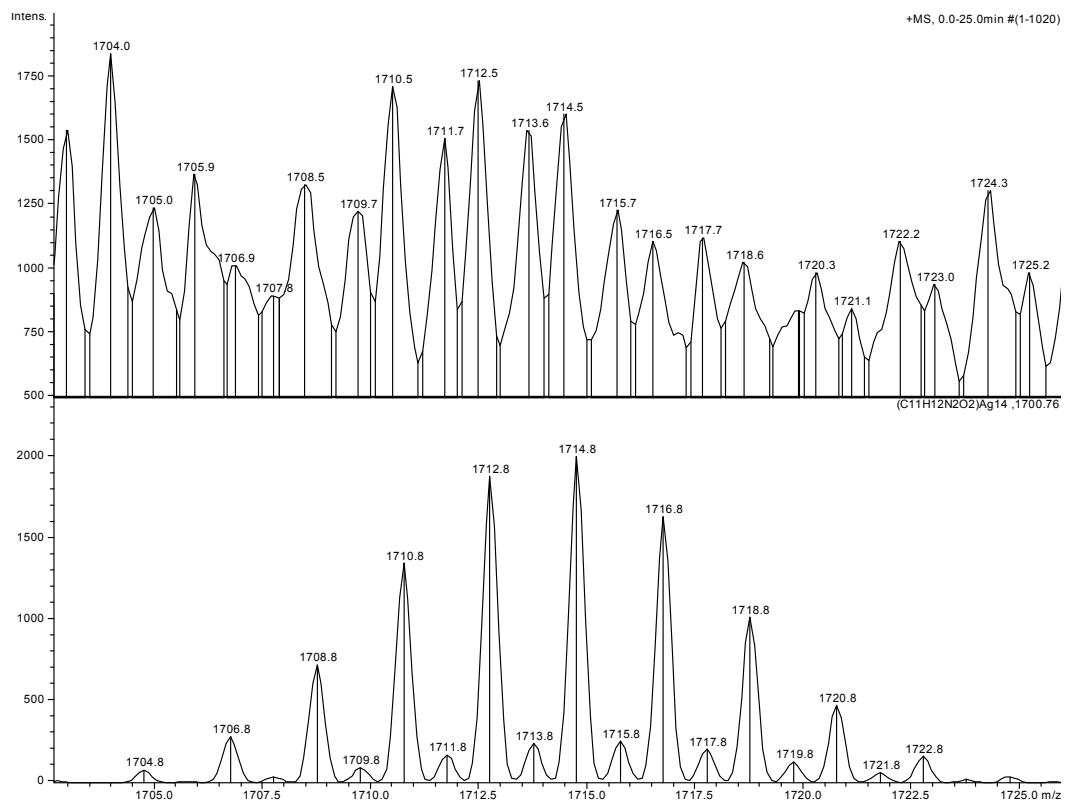
[Ag₁₁Trp]⁺ cluster, actual, top and simulated, bottom



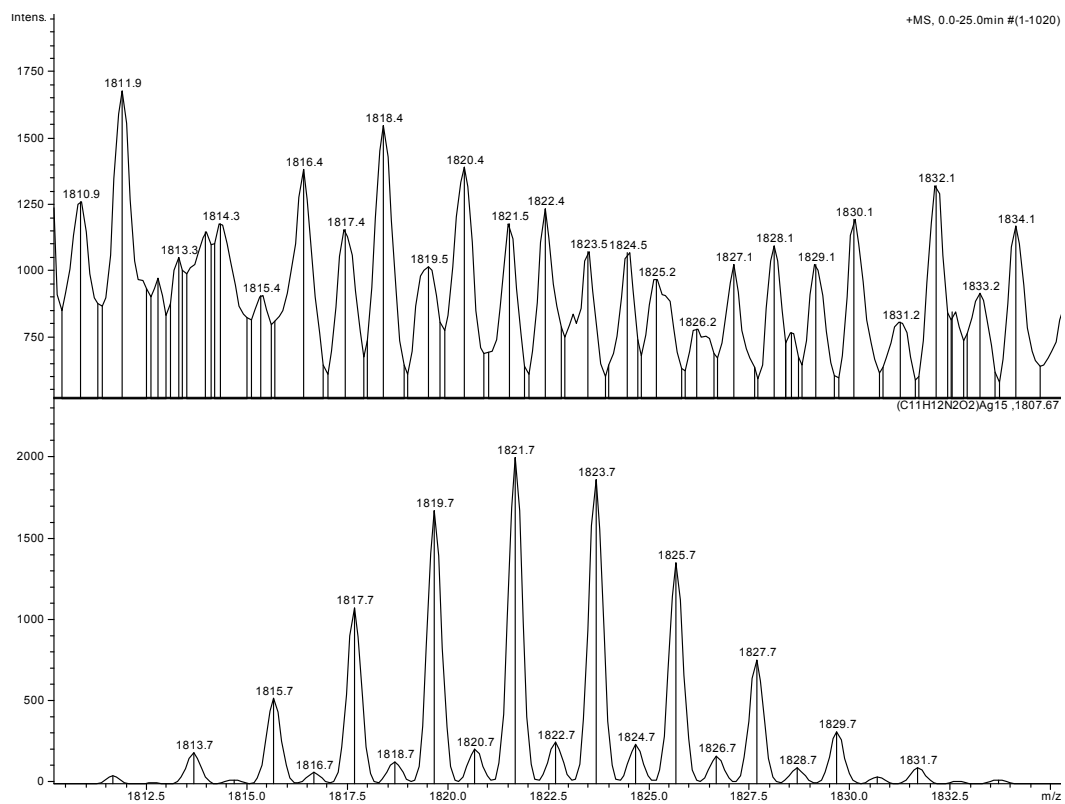
[Ag₁₂Trp]⁺ cluster, actual, top and simulated, bottom



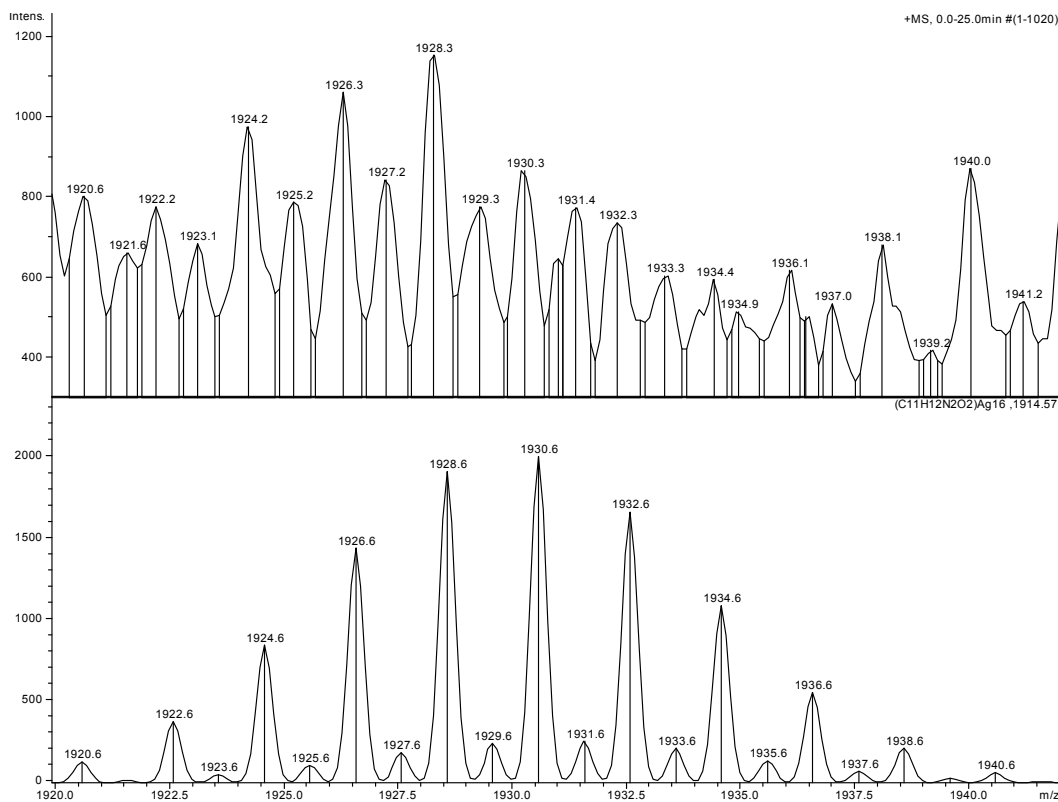
[Ag₁₃Trp]⁺ cluster, actual, top and simulated, bottom



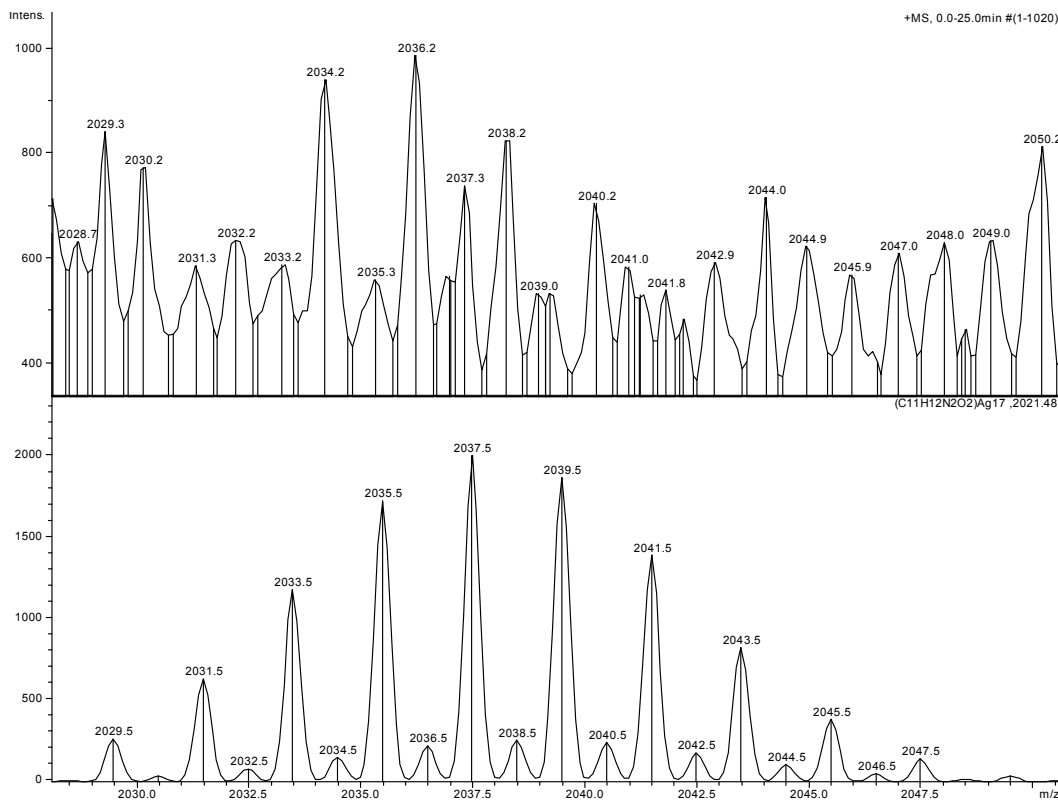
[Ag₁₄Trp]⁺ cluster, actual, top and simulated, bottom



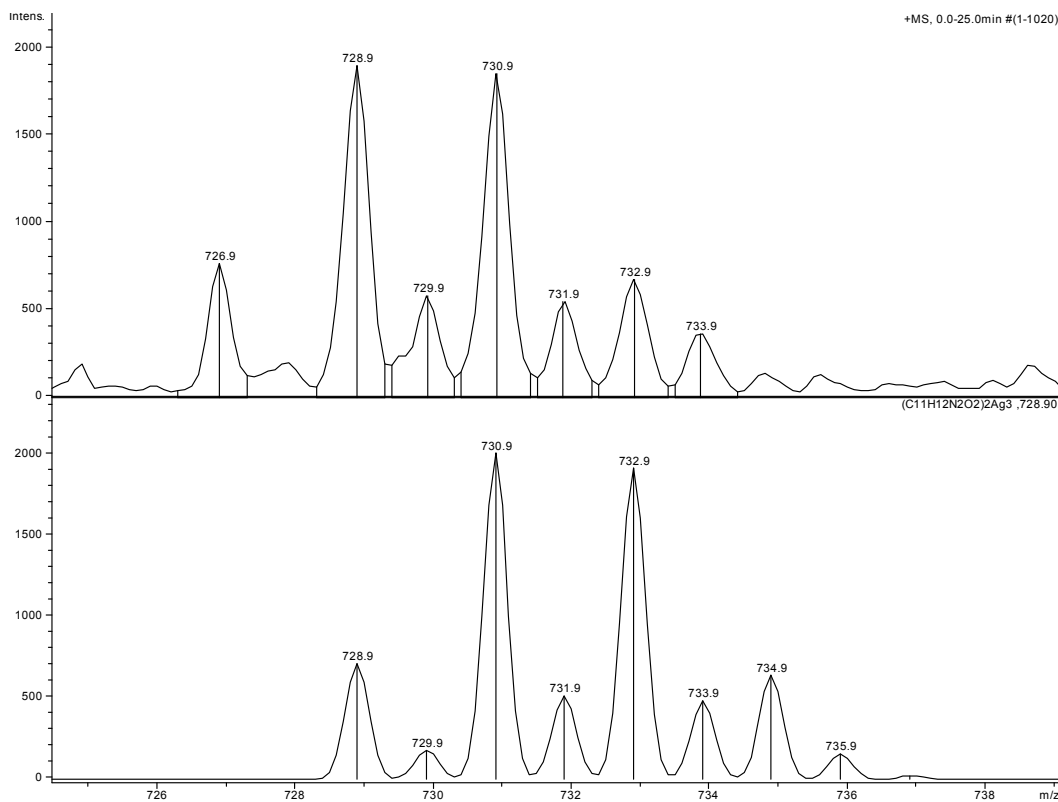
[Ag₁₅Trp]⁺ cluster, actual, top and simulated, bottom



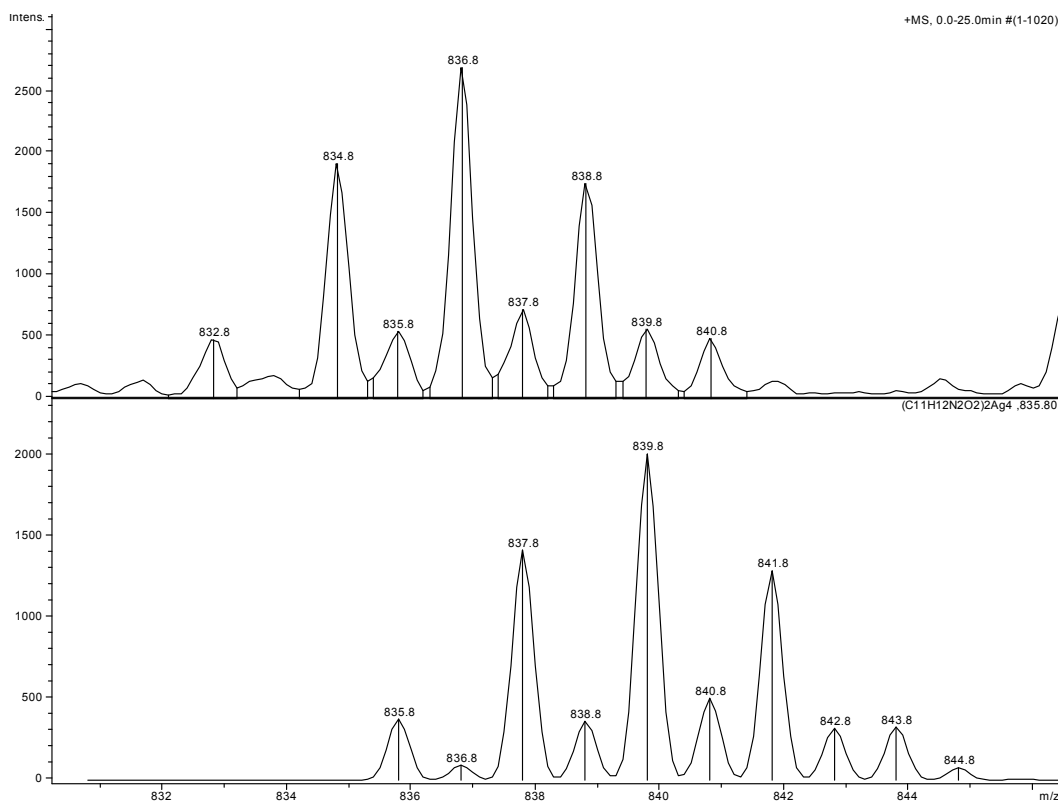
$[Ag_{16}Trp]^+$ cluster, actual, top and simulated, bottom



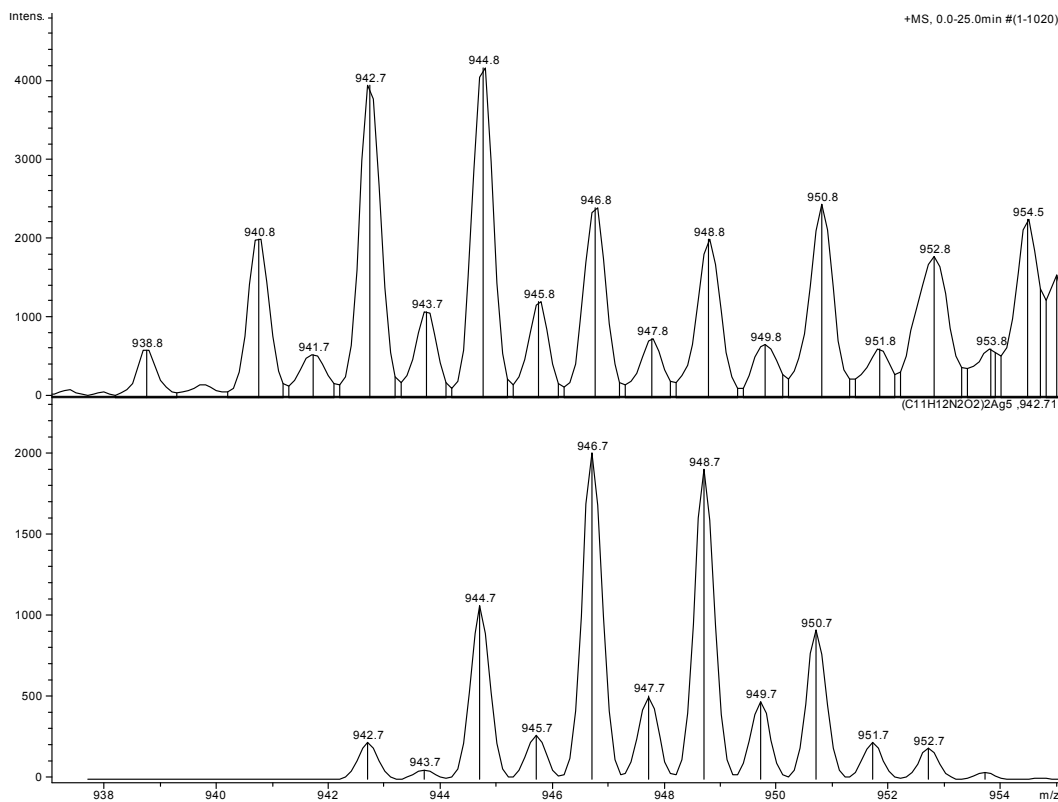
$[Ag_{17}Trp]^+$ cluster, actual, top and simulated, bottom



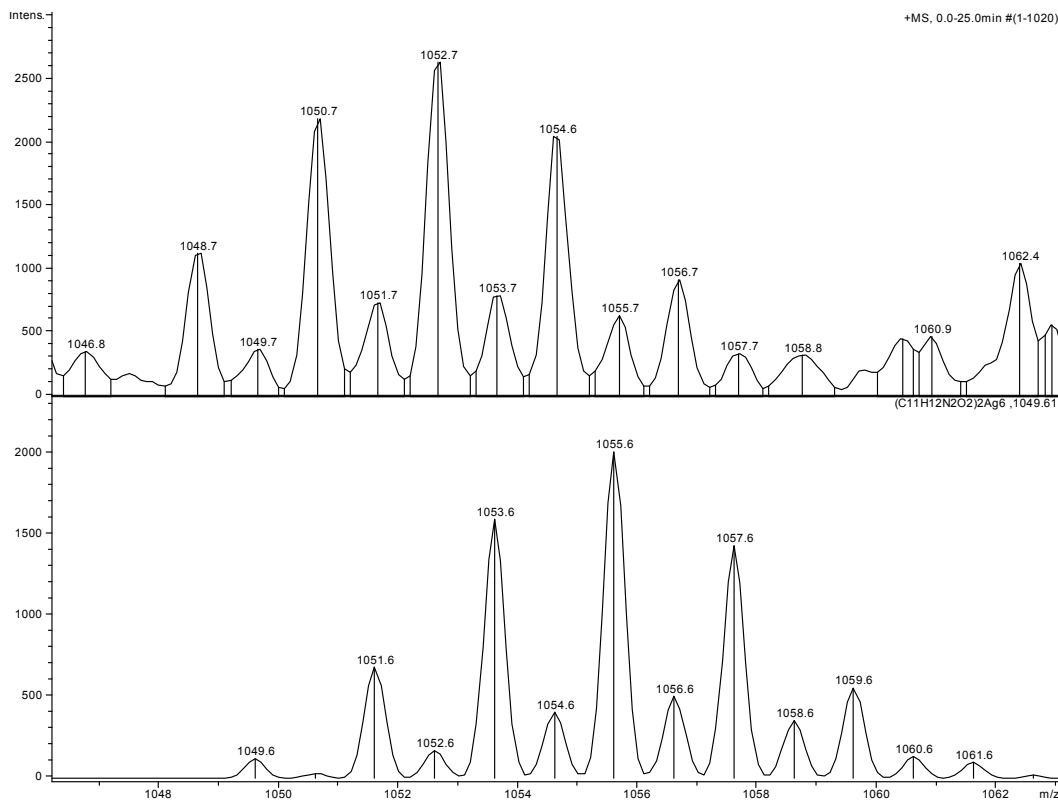
$[Ag_3Trp_2]^+$ cluster, actual, top and simulated, bottom



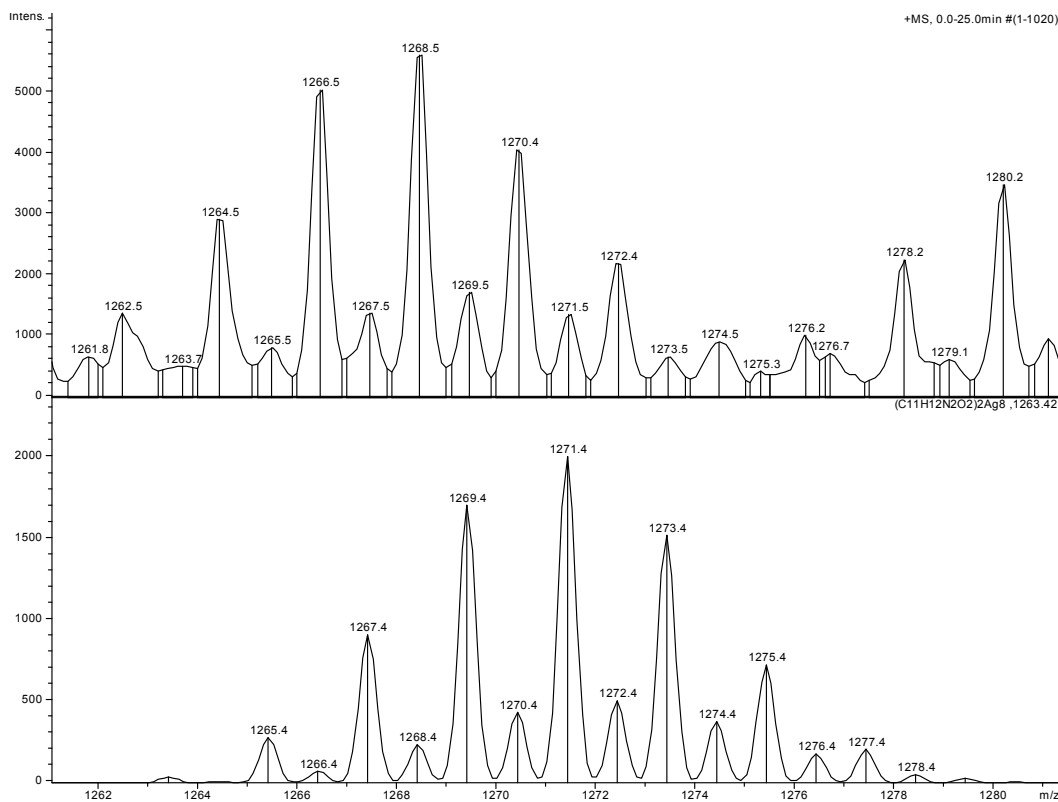
$[Ag_4Trp_2]^+$ cluster, actual, top and simulated, bottom



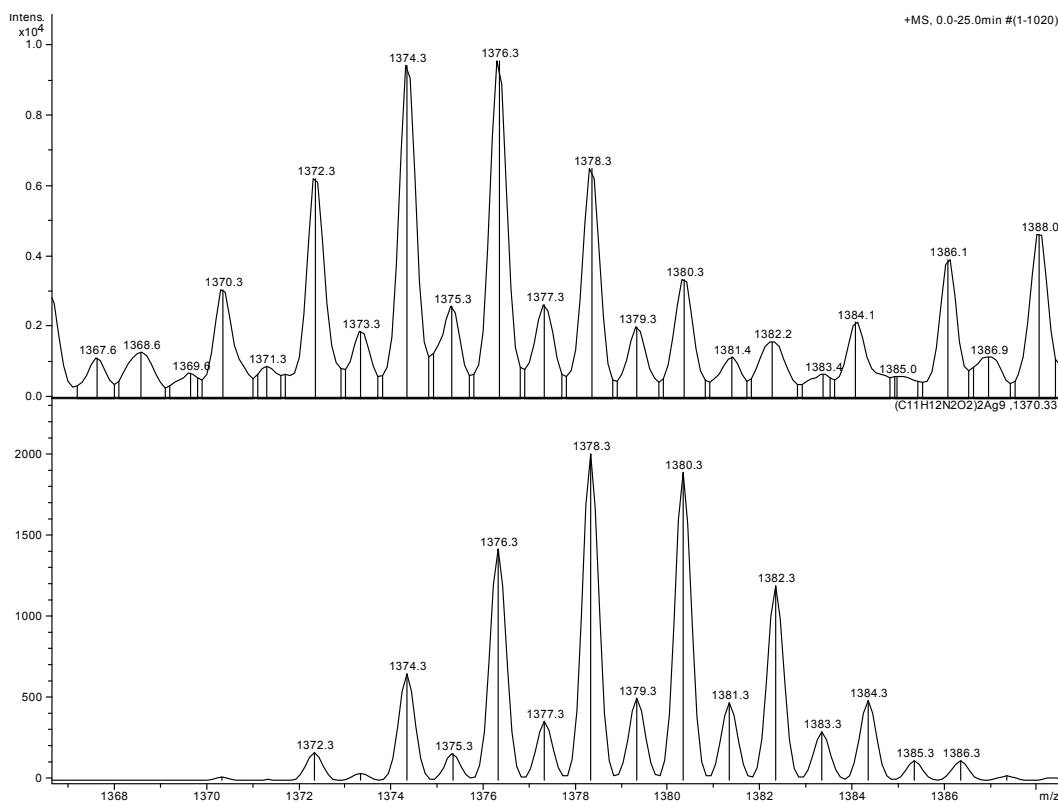
$[Ag_5Trp_2]^+$ cluster, actual, top and simulated, bottom



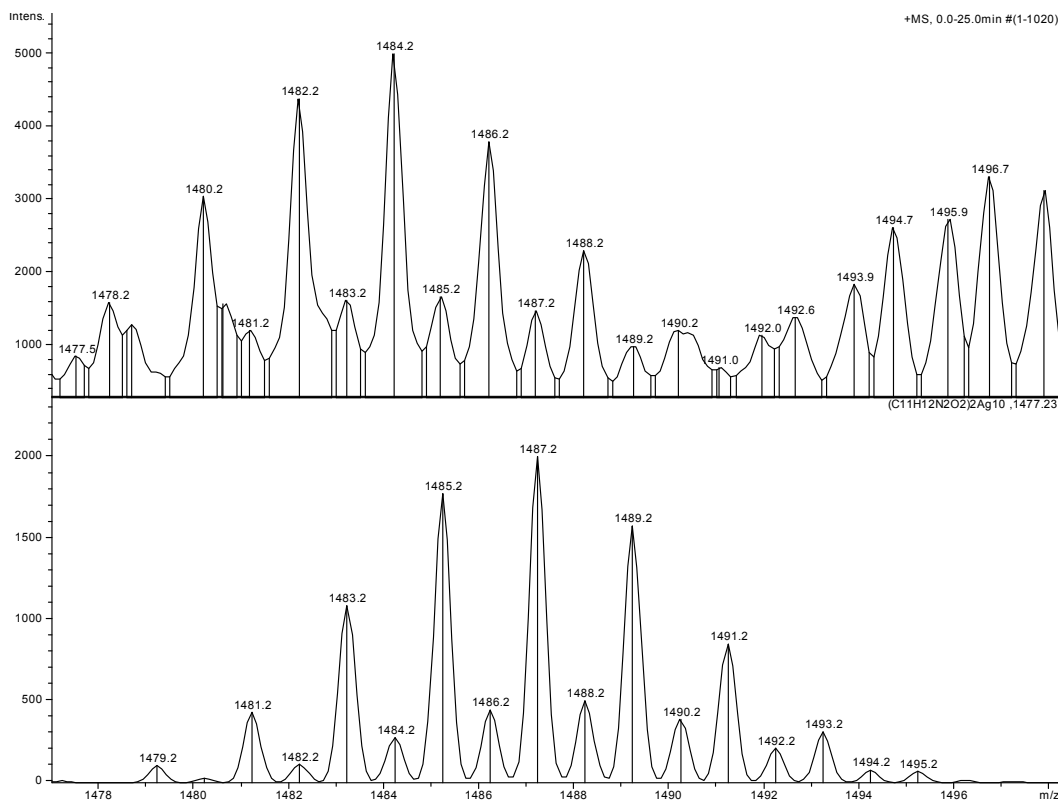
$[Ag_6Trp_2]^+$ cluster, actual, top and simulated, bottom



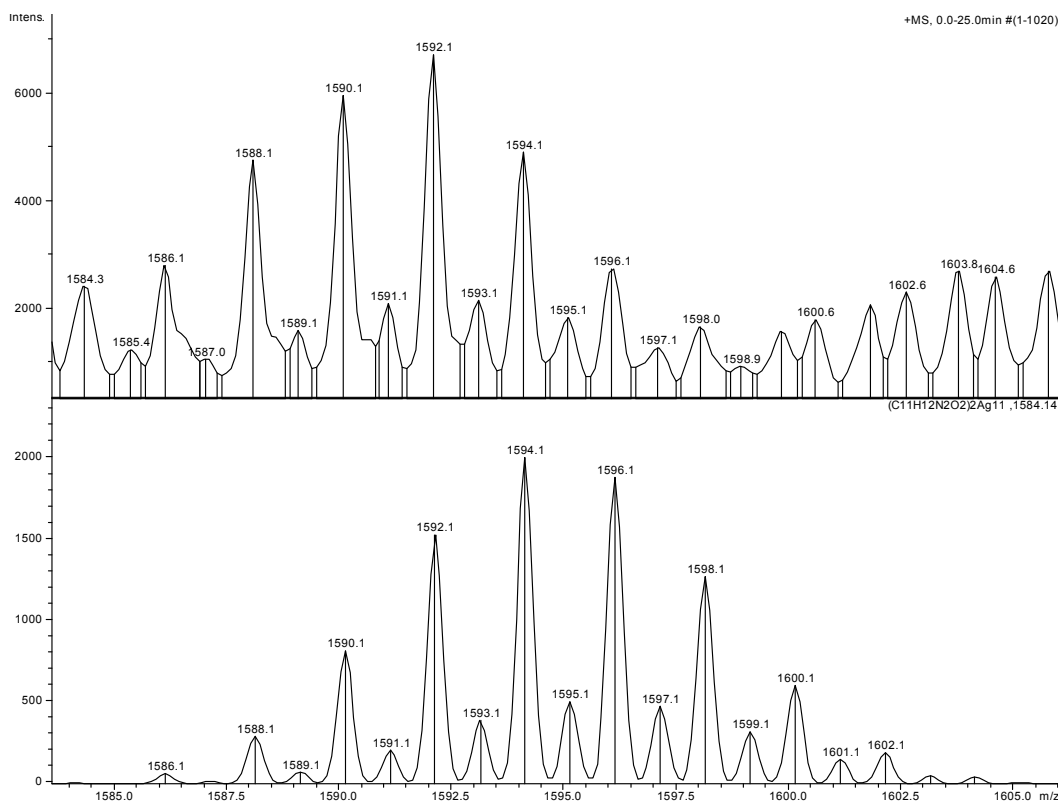
$[Ag_8Trp_2]^+$ cluster, actual, top and simulated, bottom



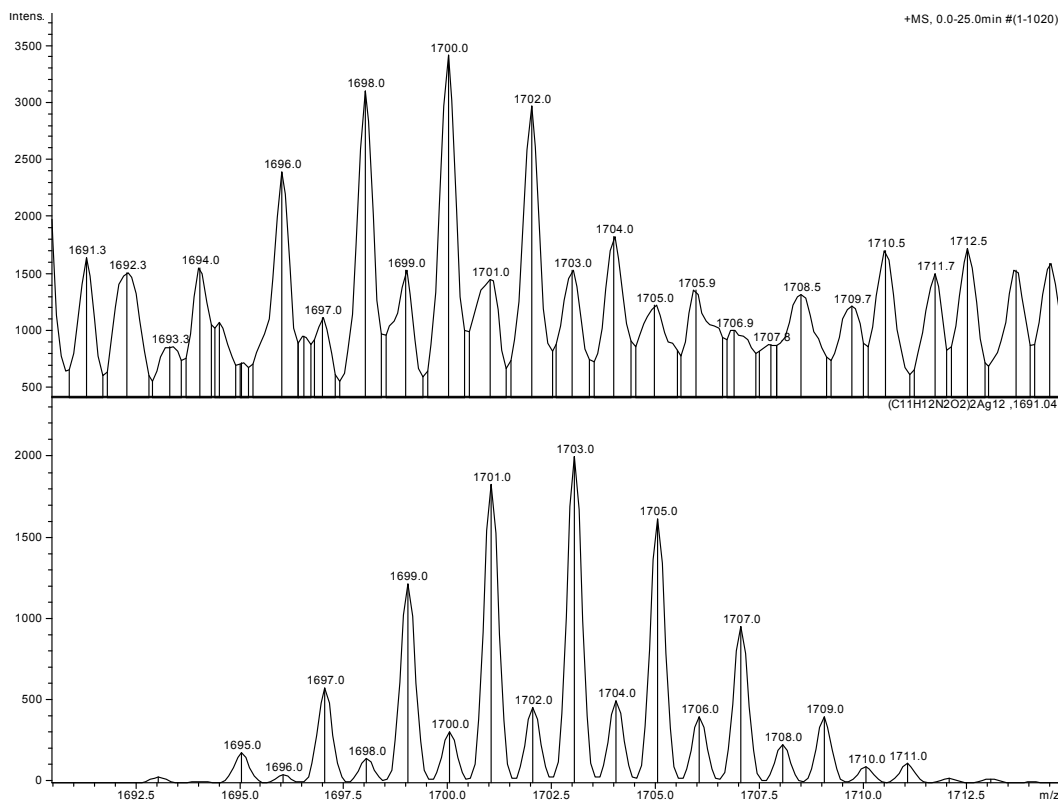
$[Ag_9Trp_2]^+$ cluster, actual, top and simulated, bottom



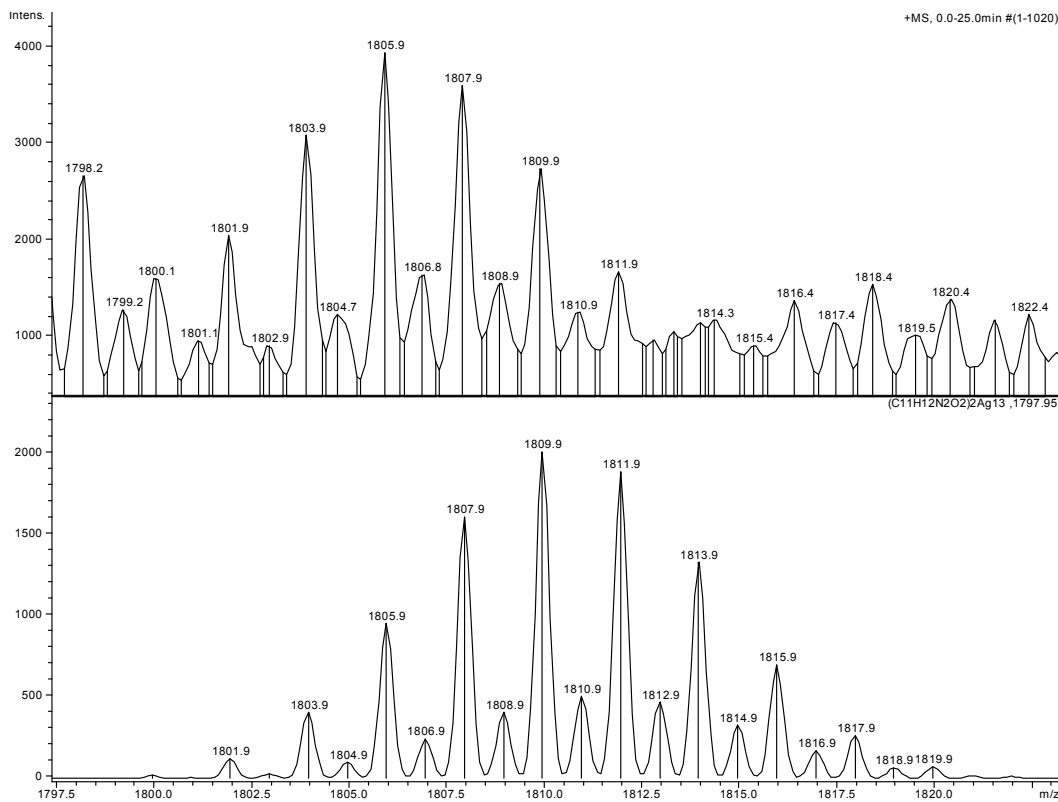
[Ag₁₀Trp₂]⁺ cluster, actual, top and simulated, bottom



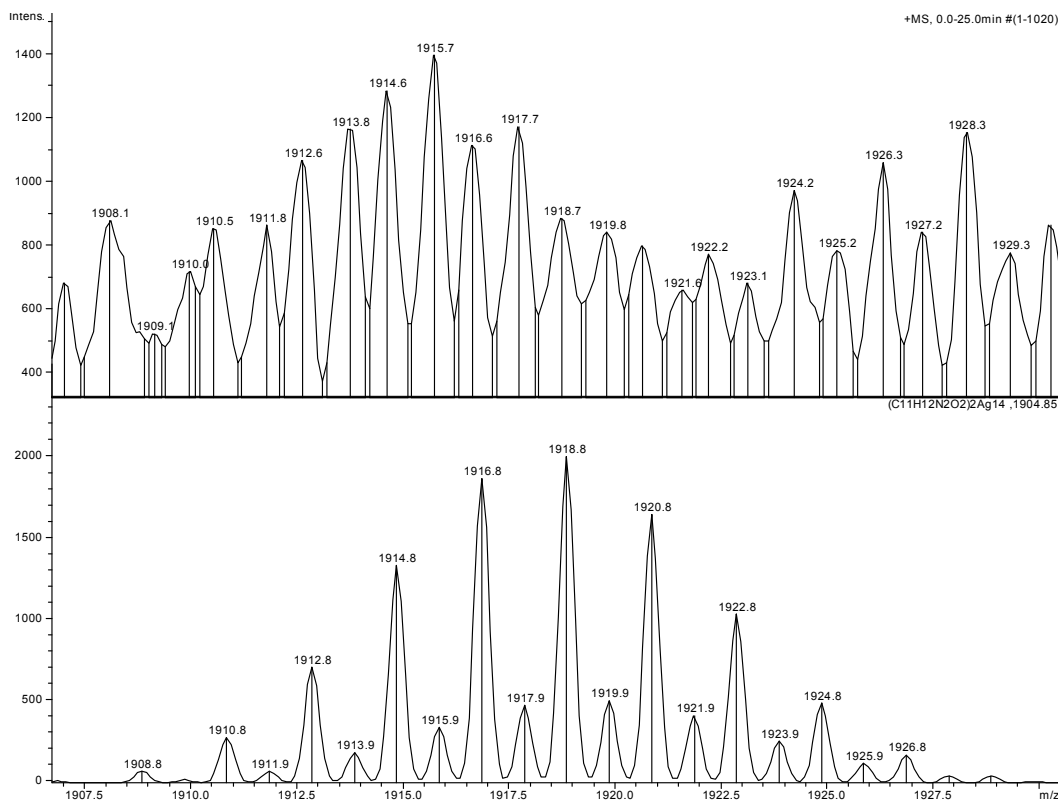
[Ag₁₁Trp₂]⁺ cluster, actual, top and simulated, bottom



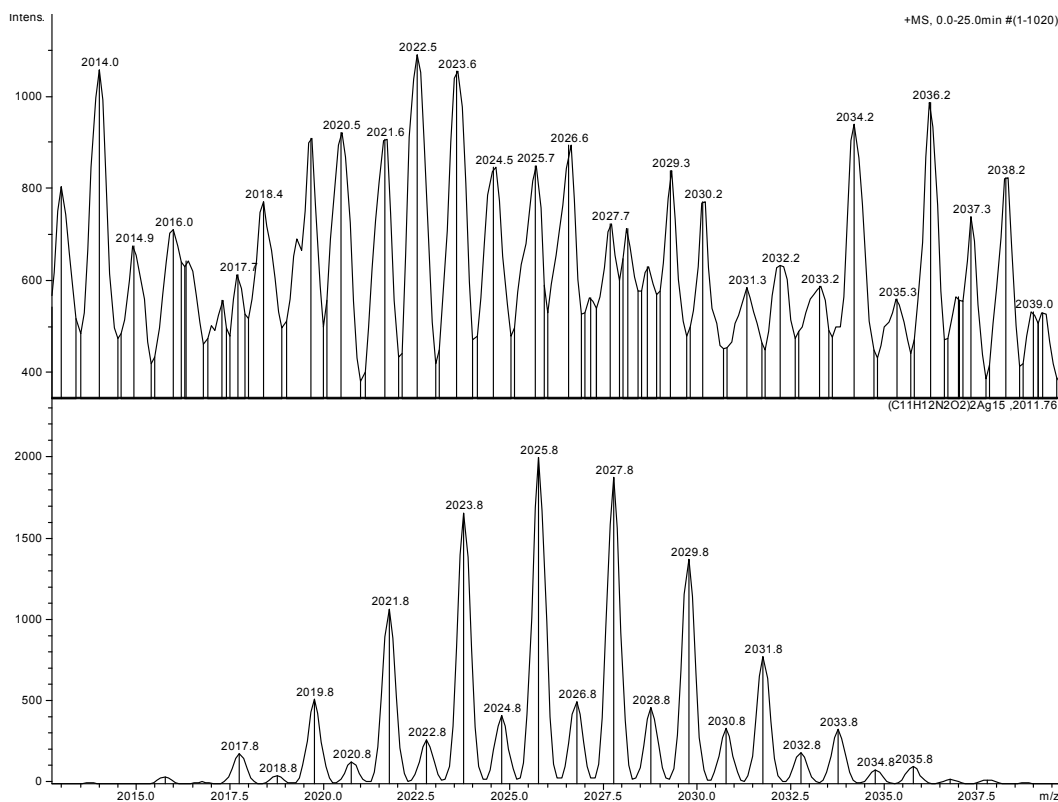
$[Ag_{12}Trp_2]^+$ cluster, actual, top and simulated, bottom



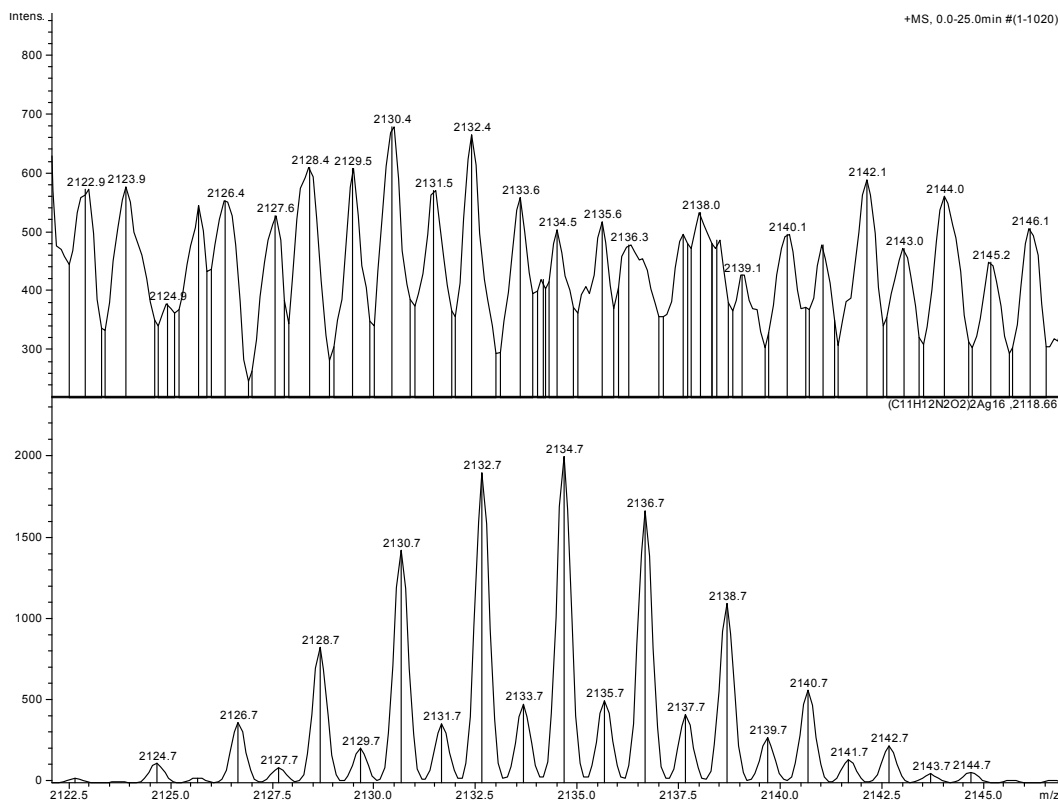
$[Ag_{13}Trp_2]^+$ cluster, actual, top and simulated, bottom



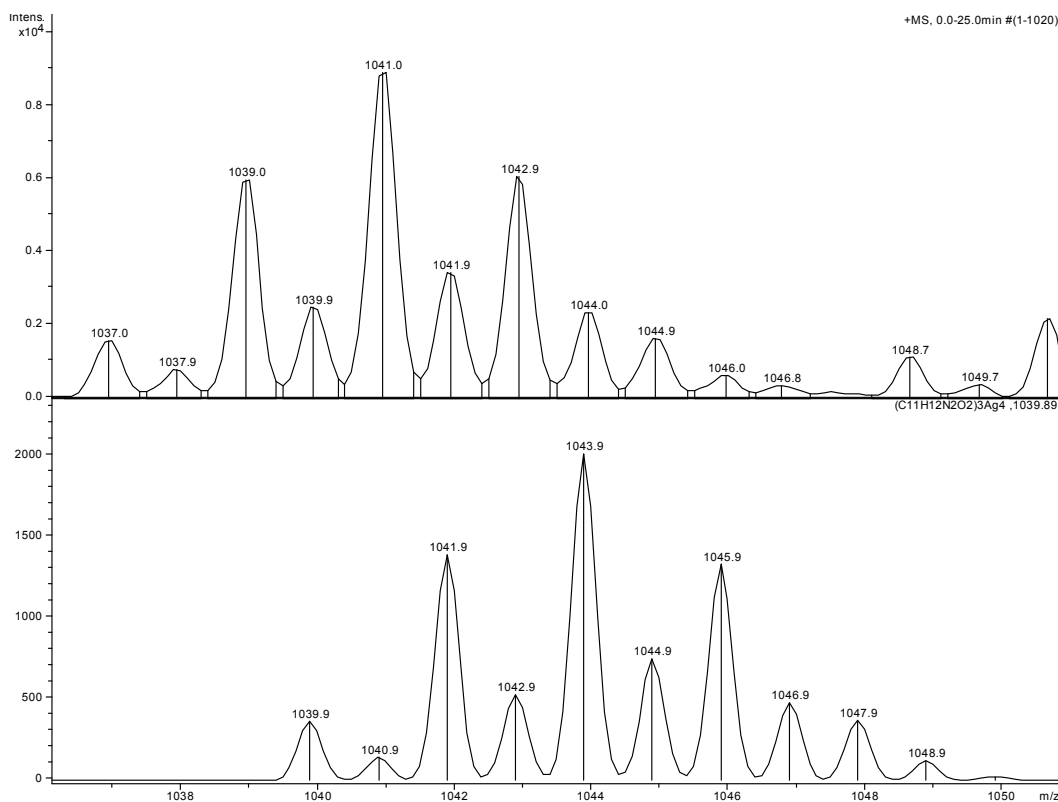
[Ag₁₄Trp₂]⁺ cluster, actual, top and simulated, bottom



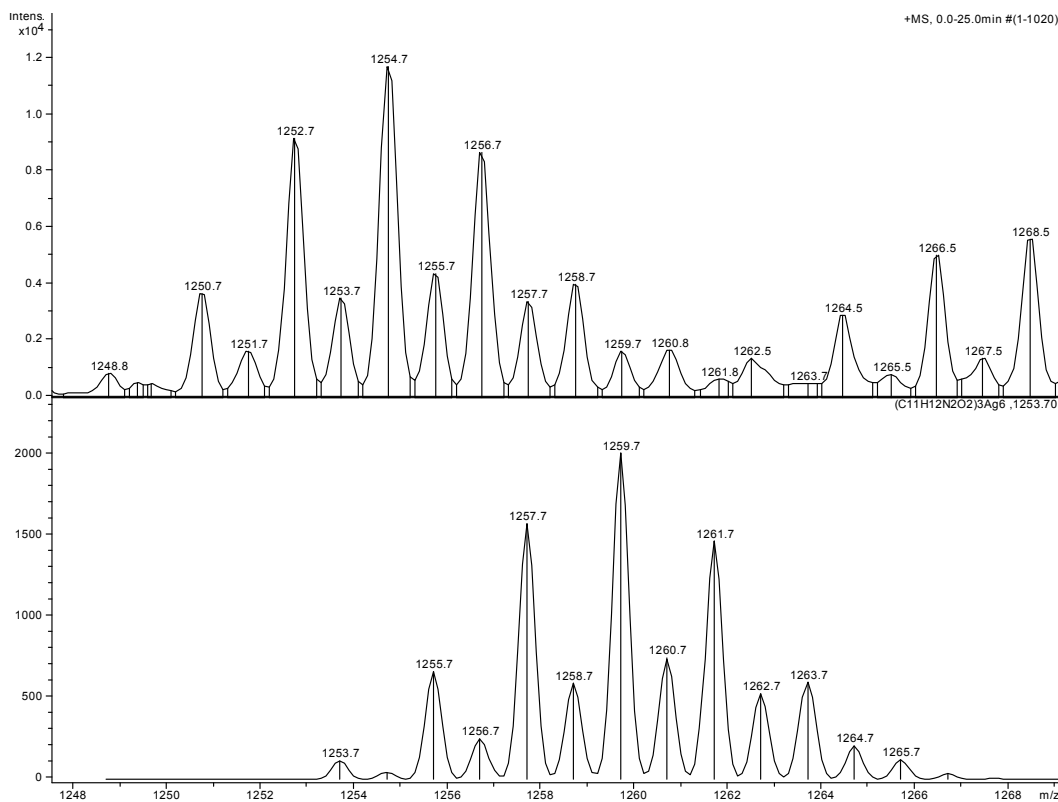
[Ag₁₅Trp₂]⁺ cluster, actual, top and simulated, bottom



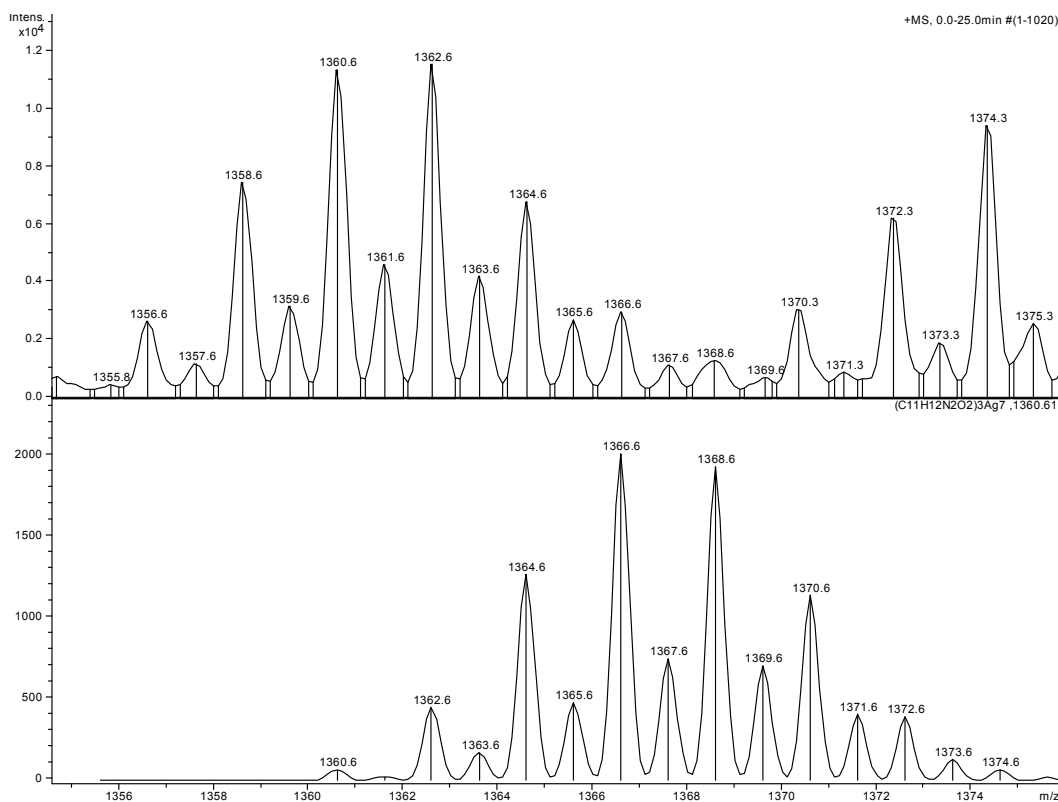
[Ag₁₆Trp₂]⁺ cluster, actual, top and simulated, bottom



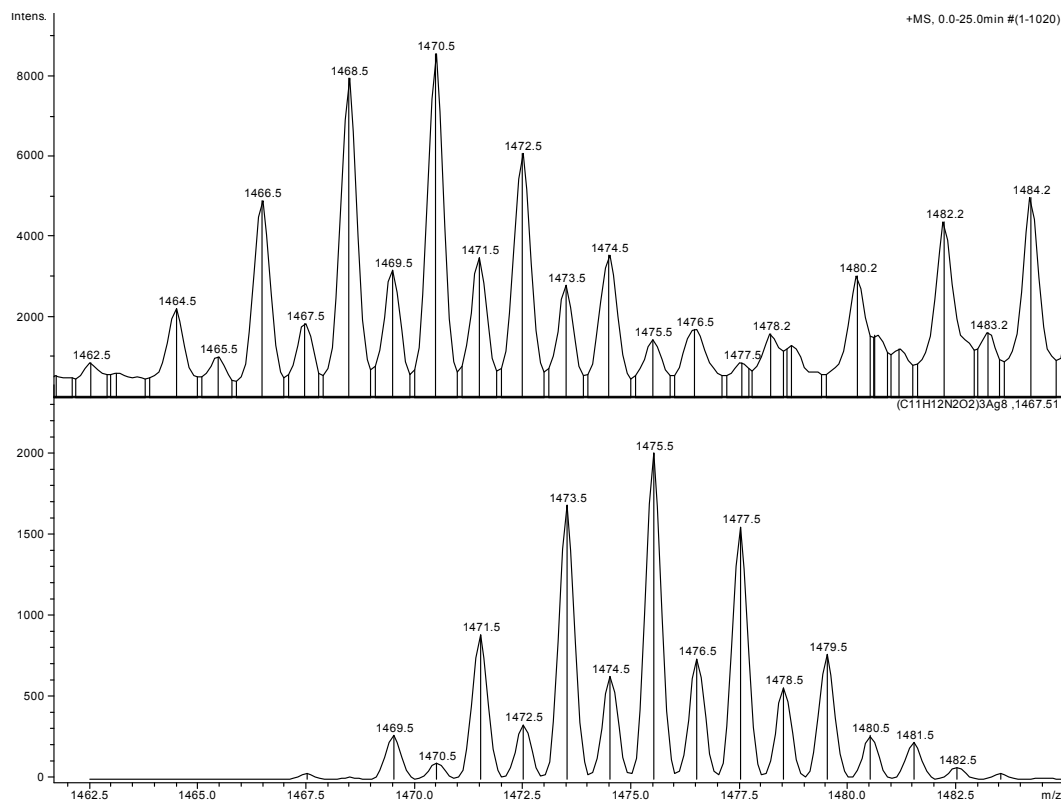
[Ag₄Trp₃]⁺ cluster, actual, top and simulated, bottom



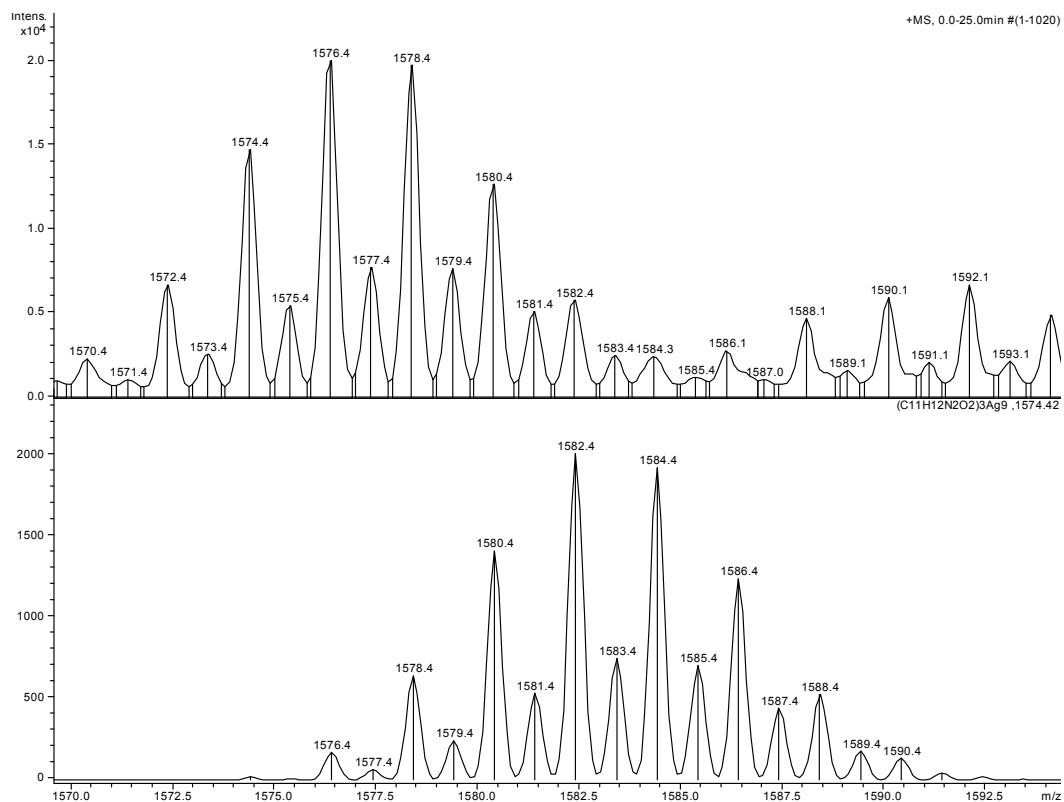
[Ag₆Trp₃]⁺ cluster, actual, top and simulated, bottom



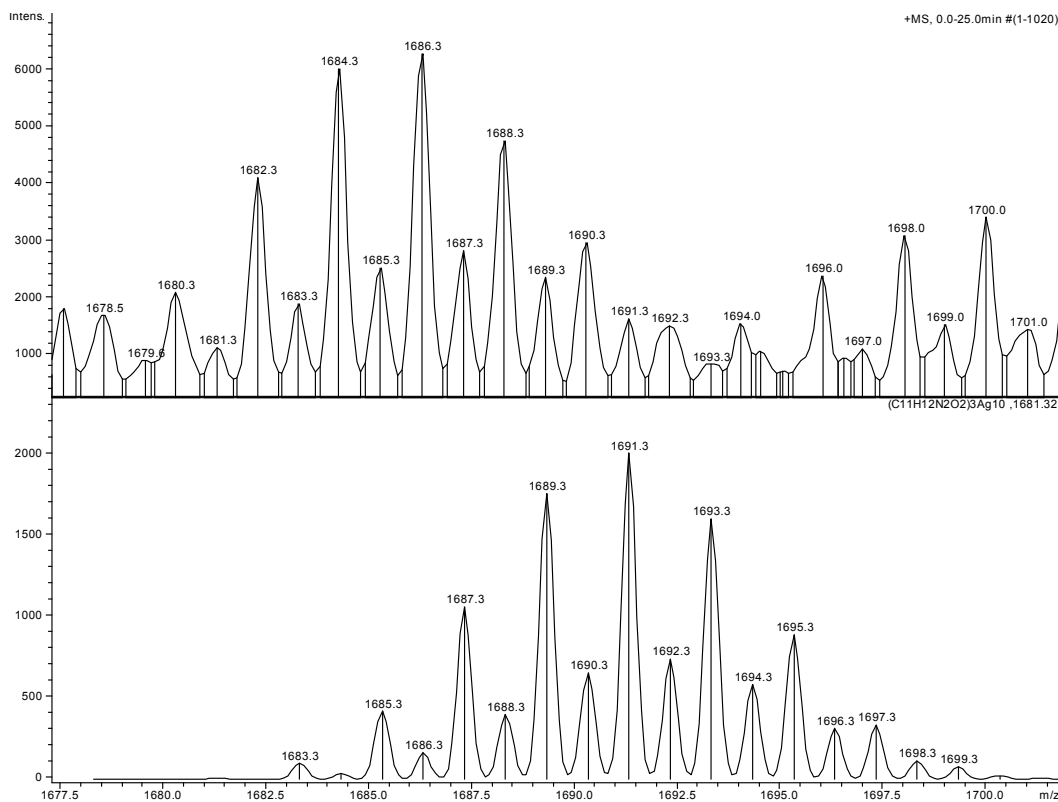
[Ag₇Trp₃]⁺ cluster, actual, top and simulated, bottom



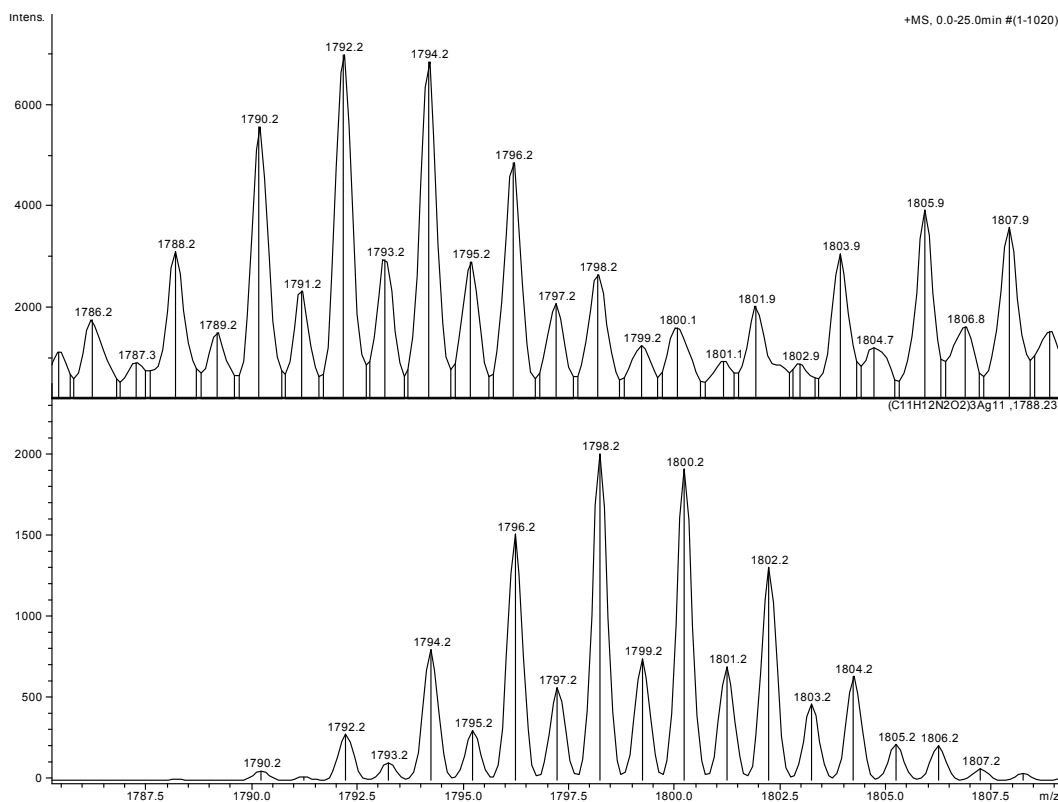
$[Ag_8Trp_3]^+$ cluster, actual, top and simulated, bottom



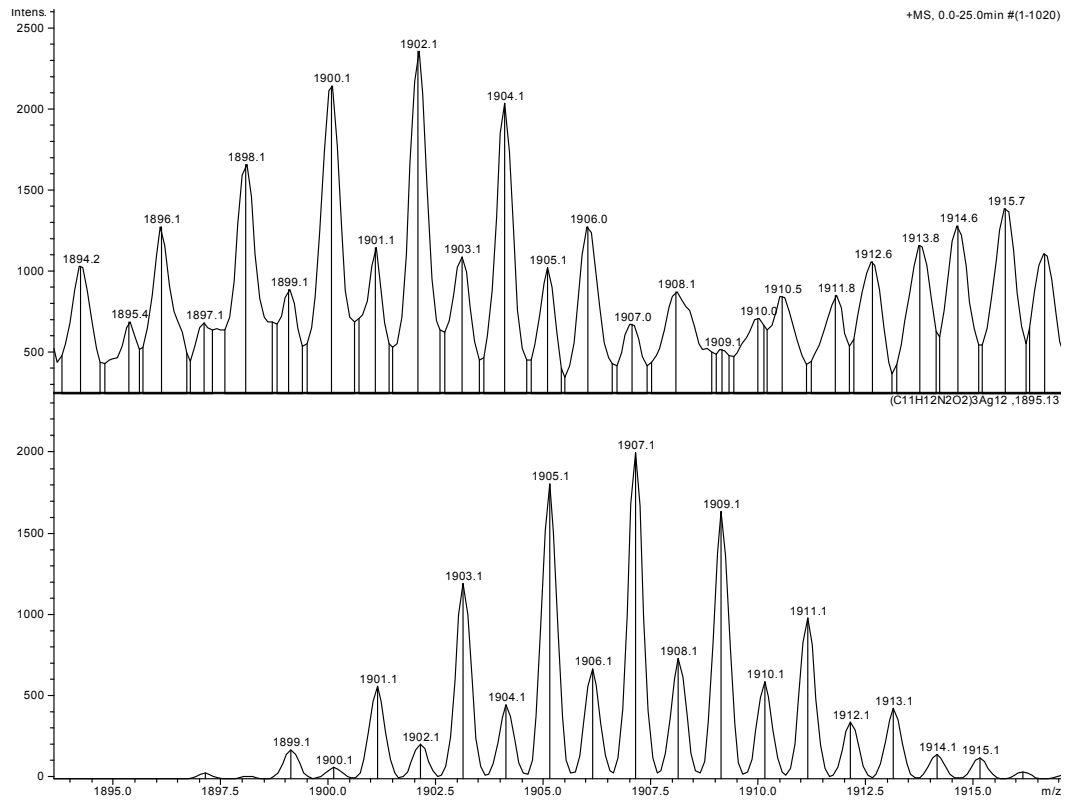
$[Ag_9Trp_3]^+$ cluster, actual, top and simulated, bottom



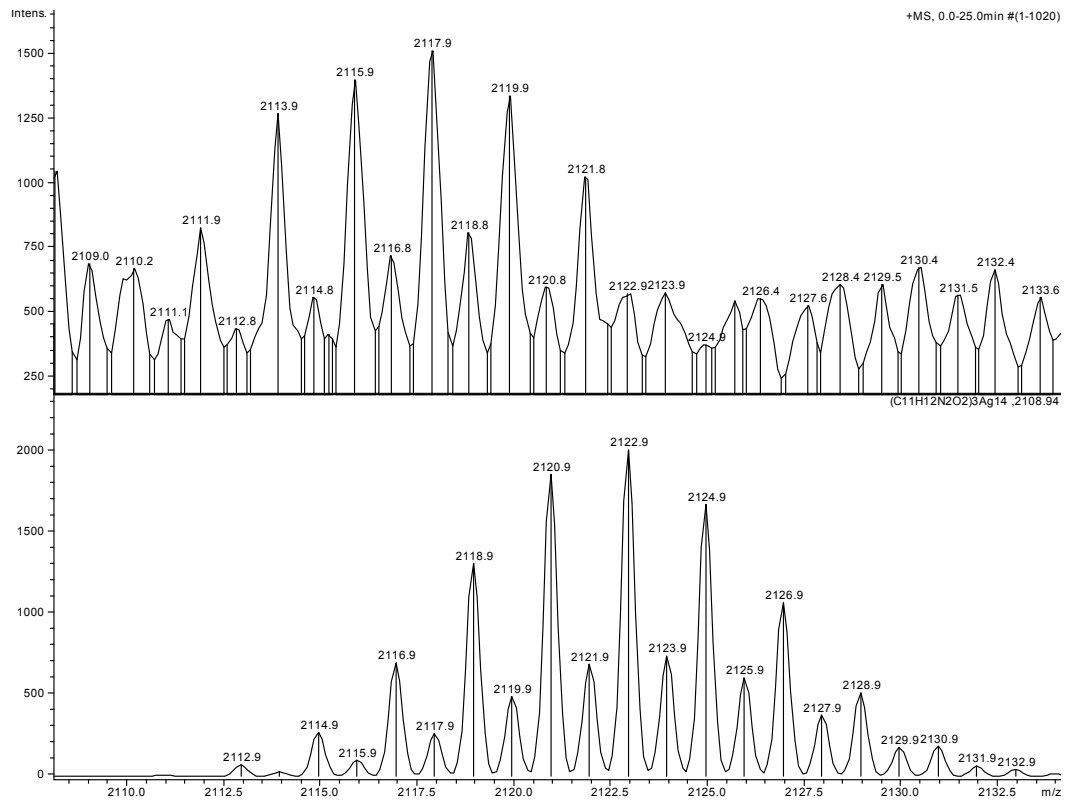
[Ag₁₀Trp₃]⁺ cluster, actual, top and simulated, bottom



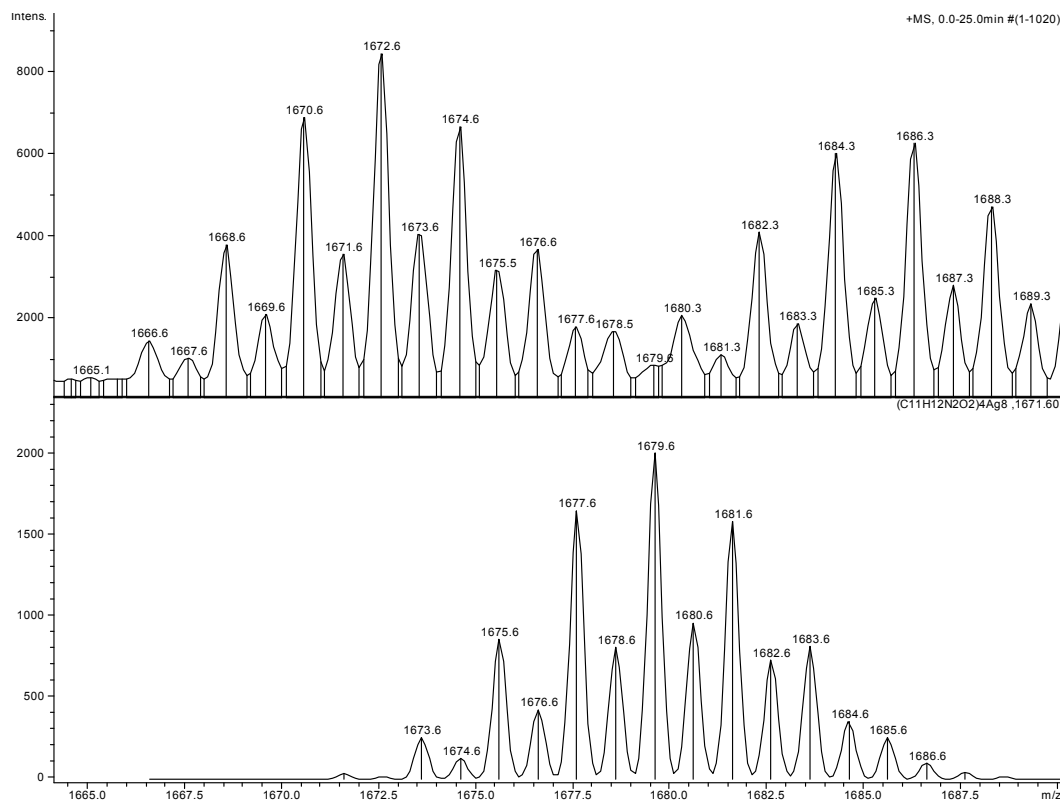
[Ag₁₁Trp₃]⁺ cluster, actual, top and simulated, bottom



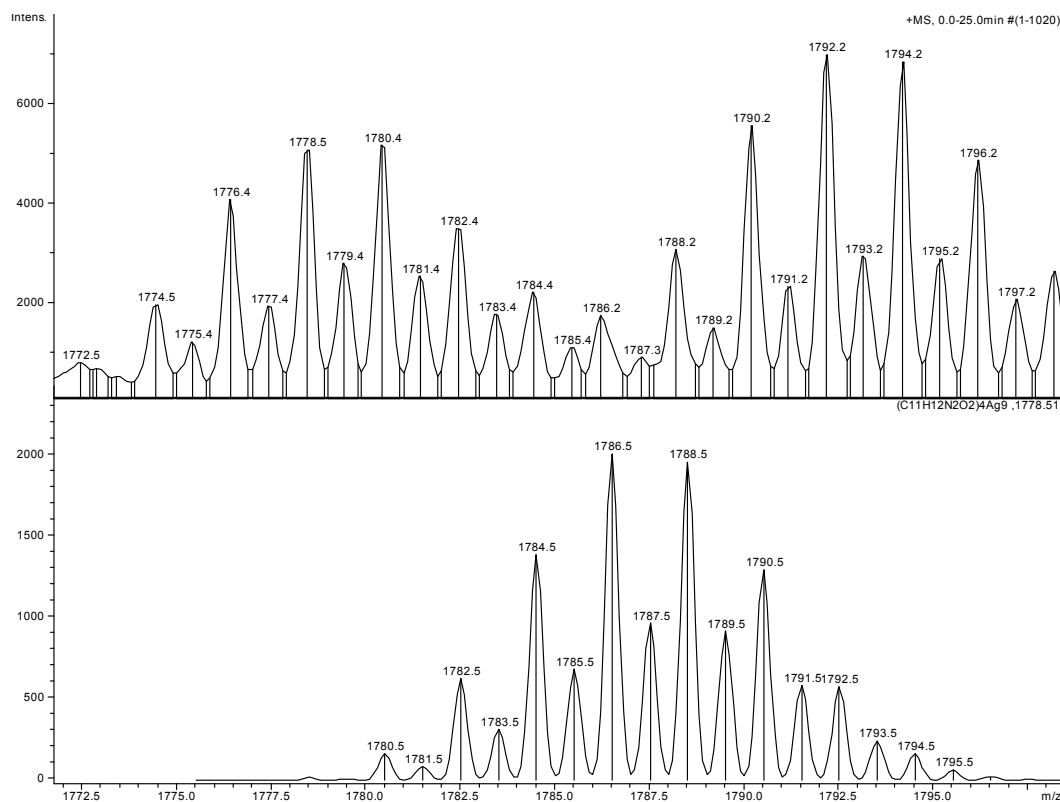
$[Ag_{12}Trp_3]^+$ cluster, actual, top and simulated, bottom



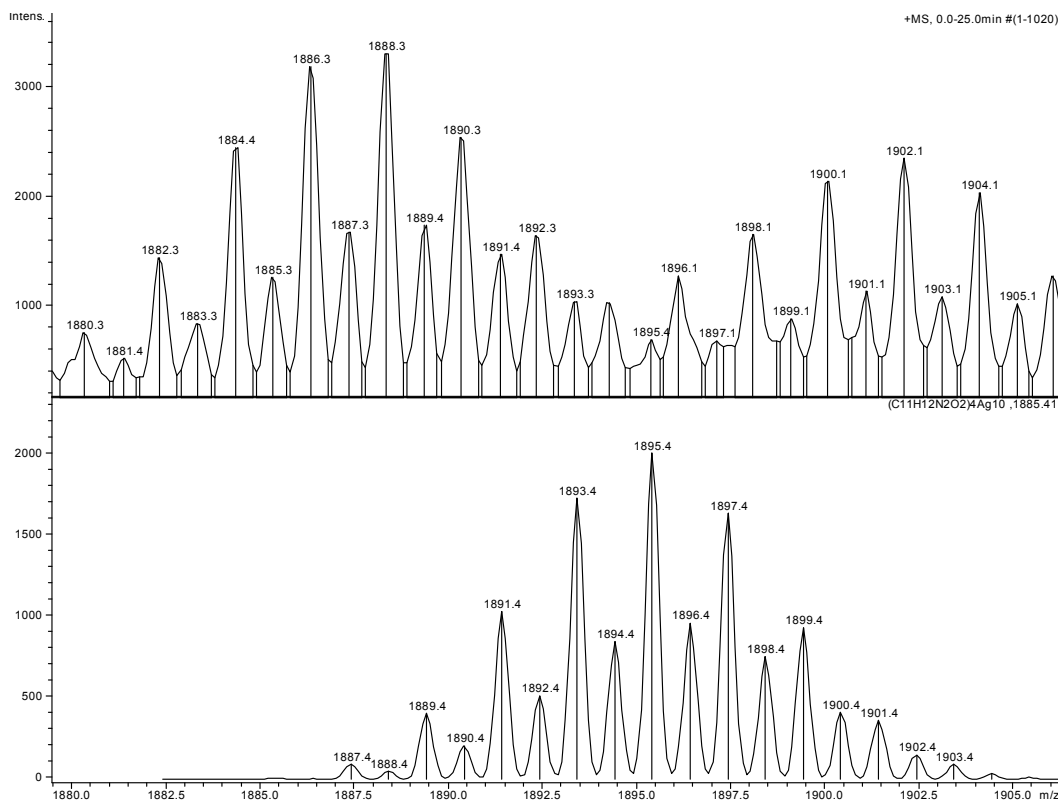
$[Ag_{14}Trp_3]^+$ cluster, actual, top and simulated, bottom



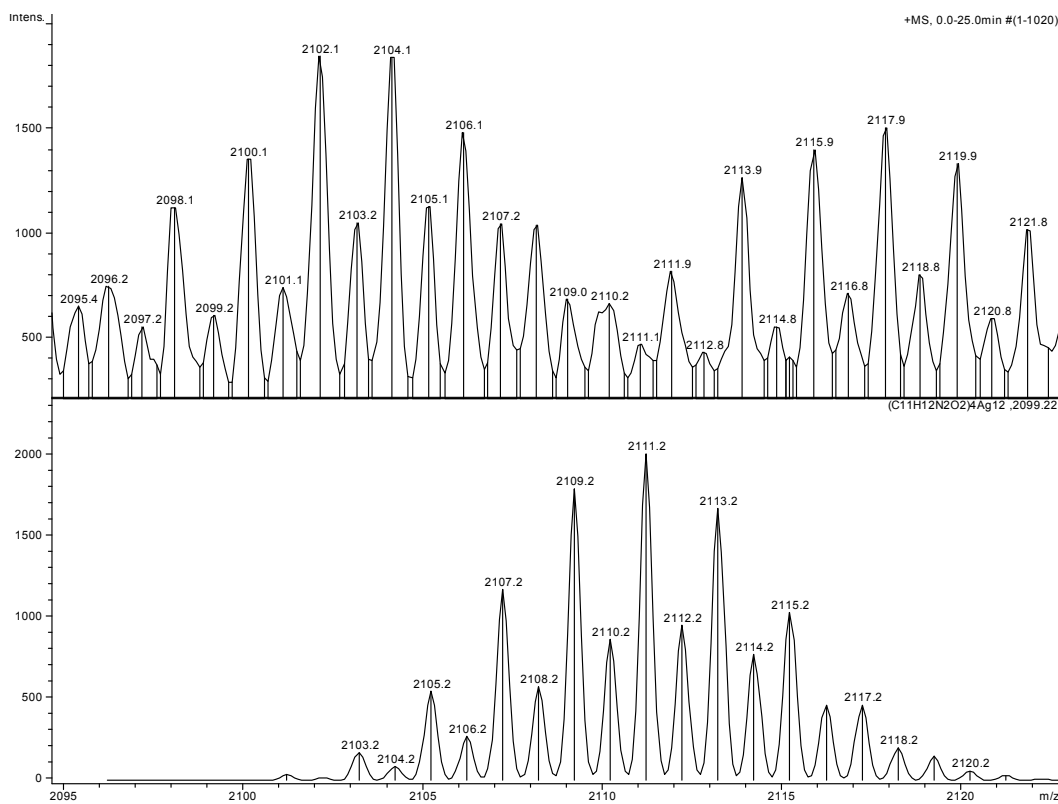
$[Ag_8Trp_4]^+$ cluster, actual, top and simulated, bottom



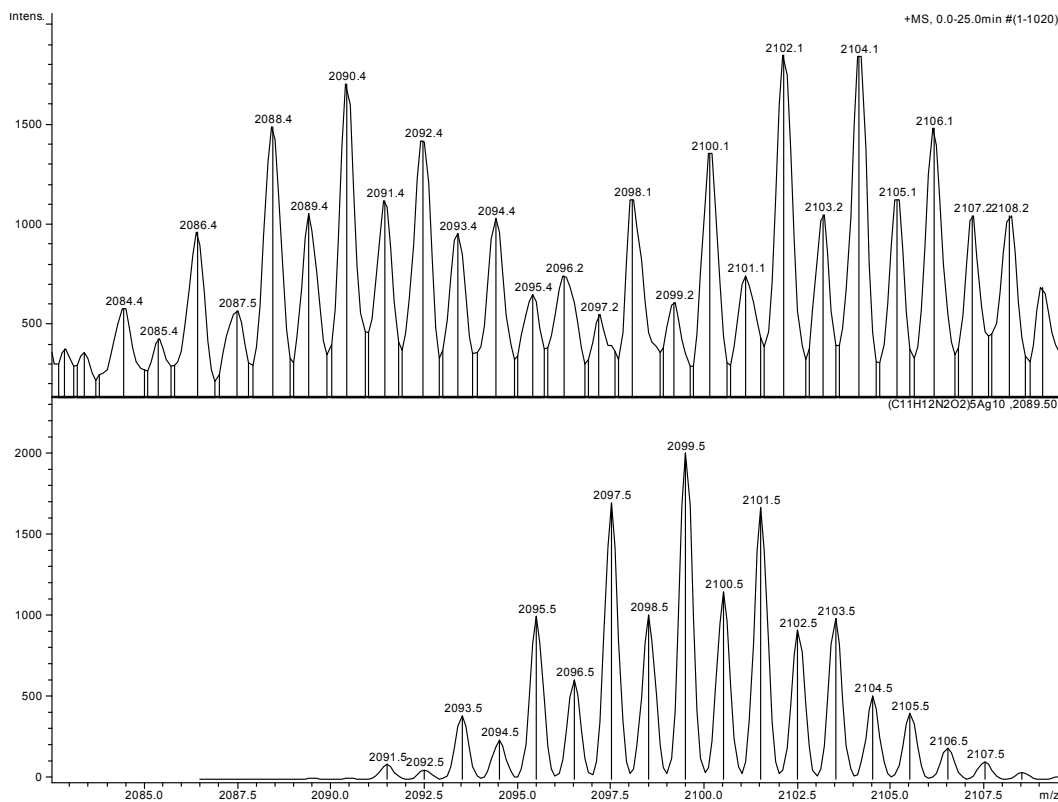
$[Ag_9Trp_4]^+$ cluster, actual, top and simulated, bottom



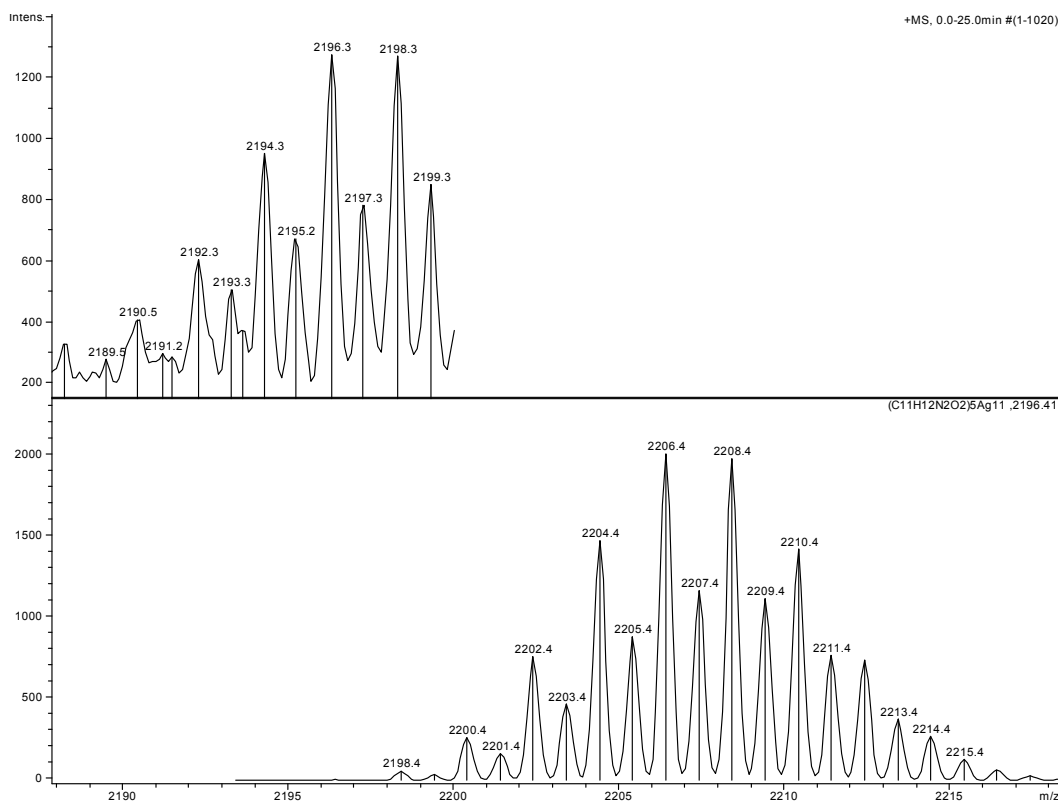
[Ag₁₀Trp₄]⁺ cluster, actual, top and simulated, bottom



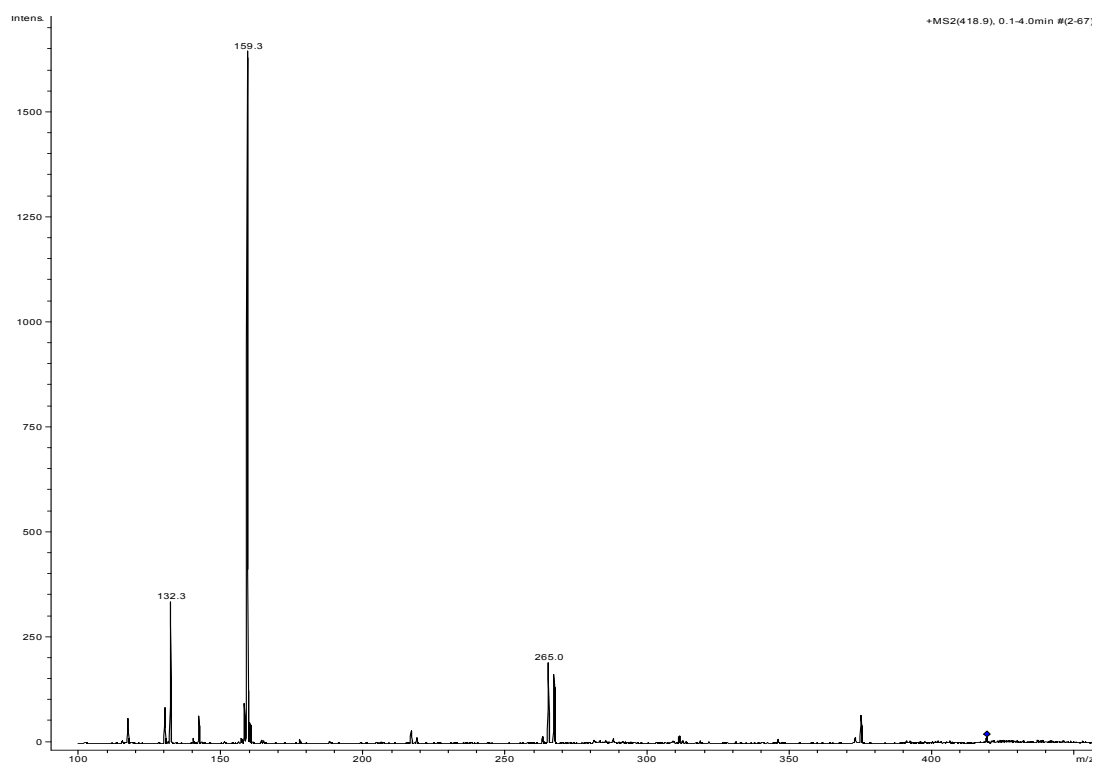
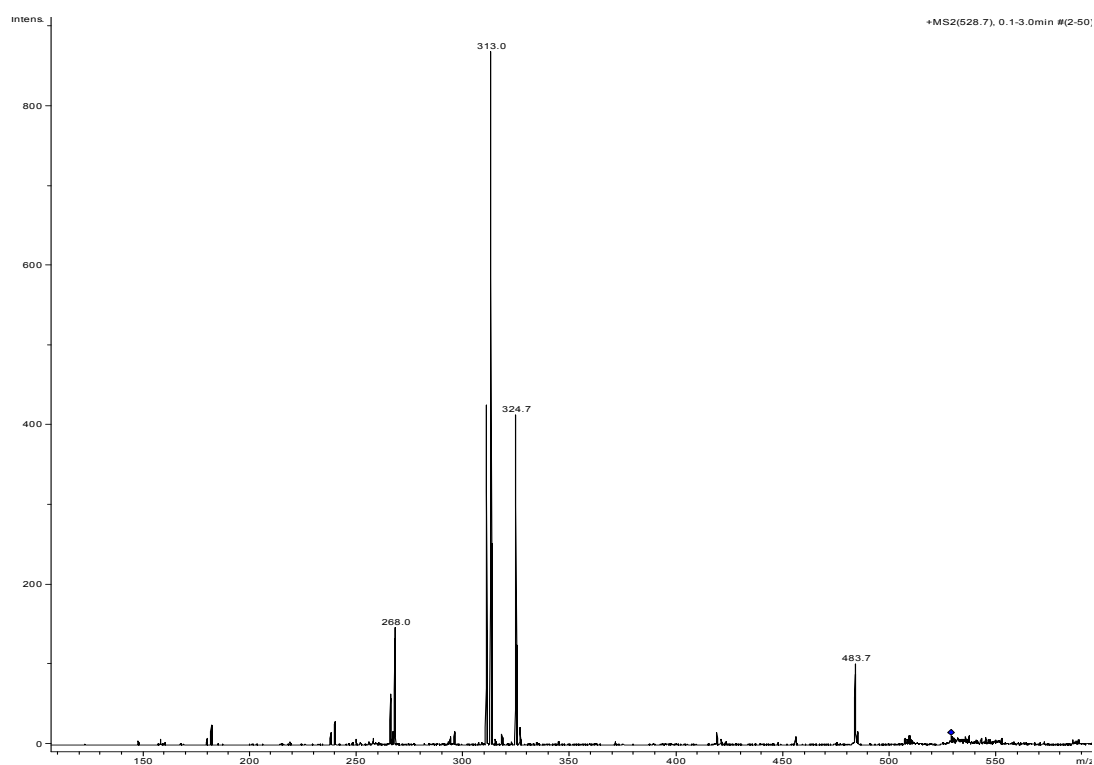
[Ag₁₂Trp₄]⁺ cluster, actual, top and simulated, bottom

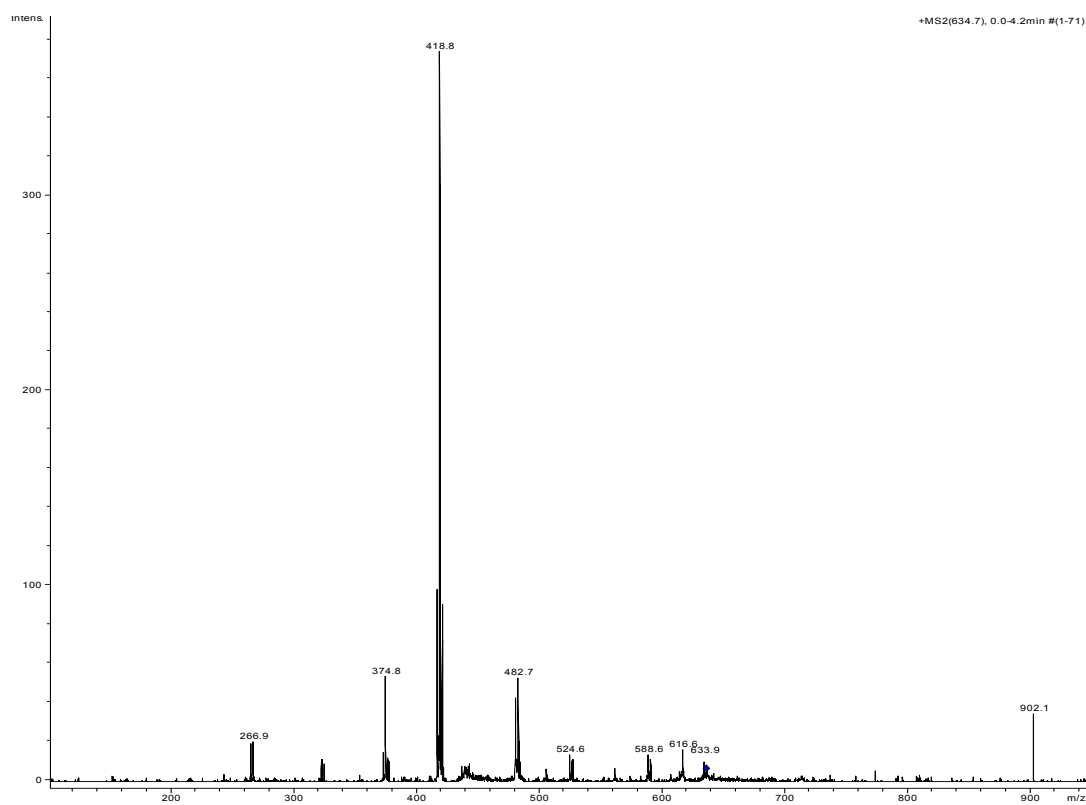
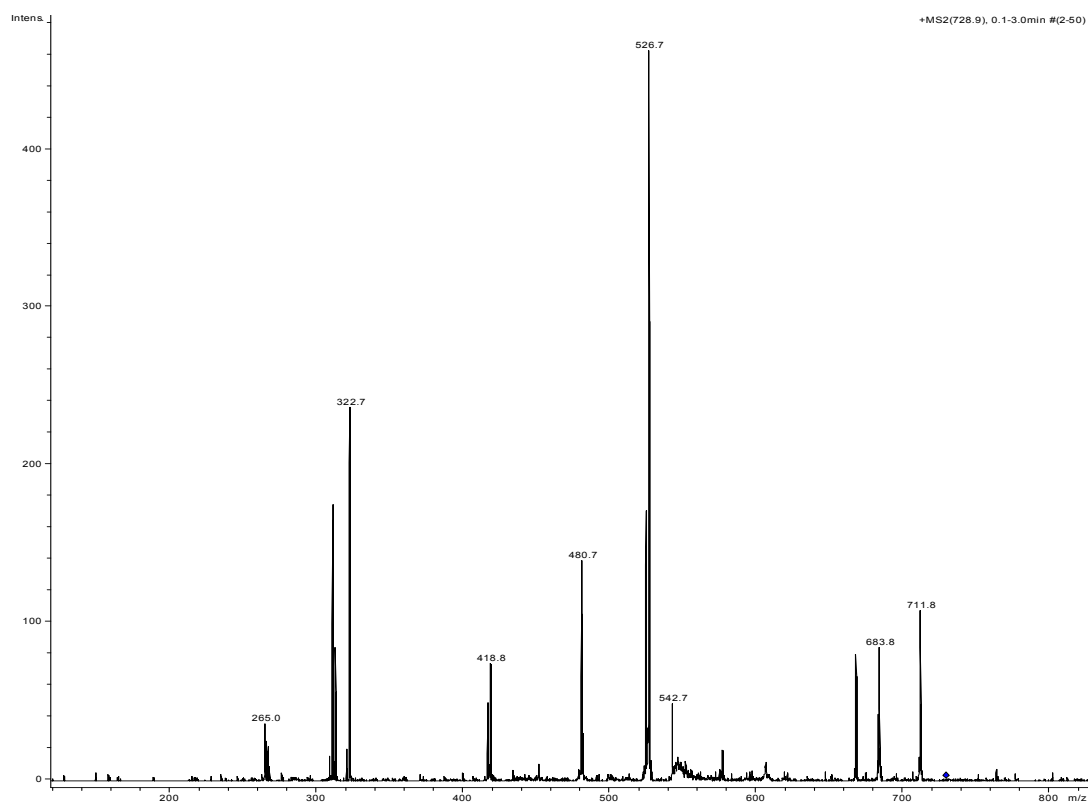


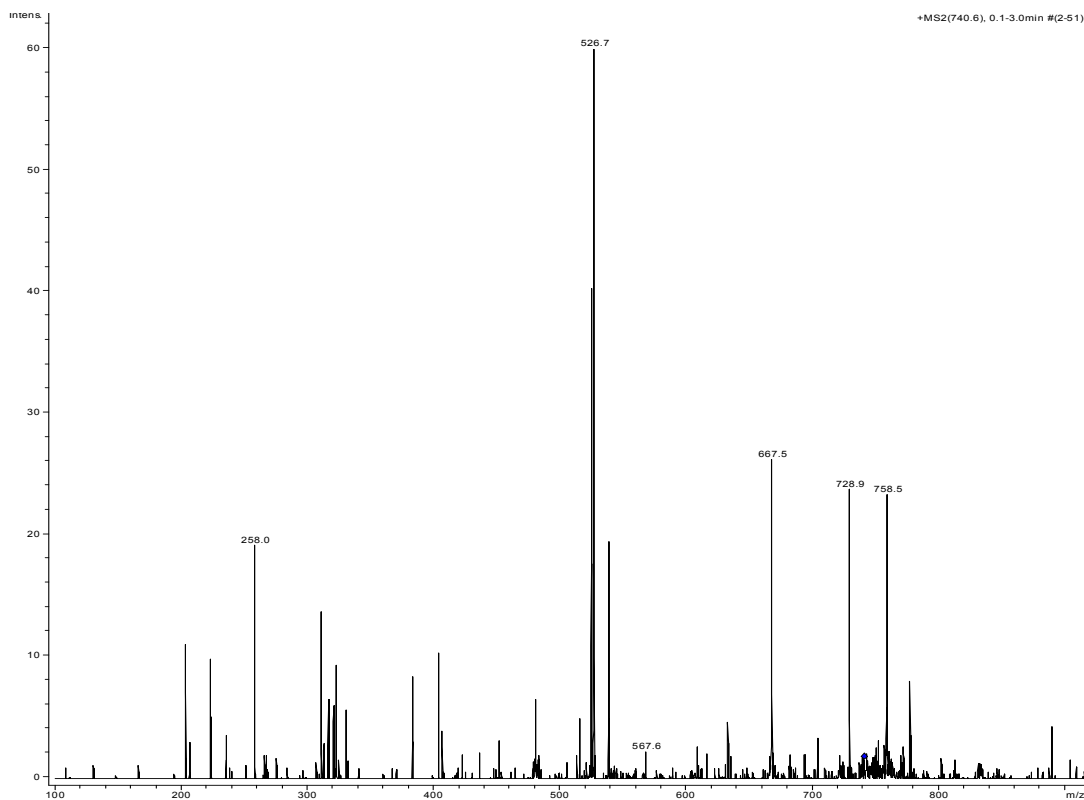
[Ag₁₀Trp₅]⁺ cluster, actual, top and simulated, bottom



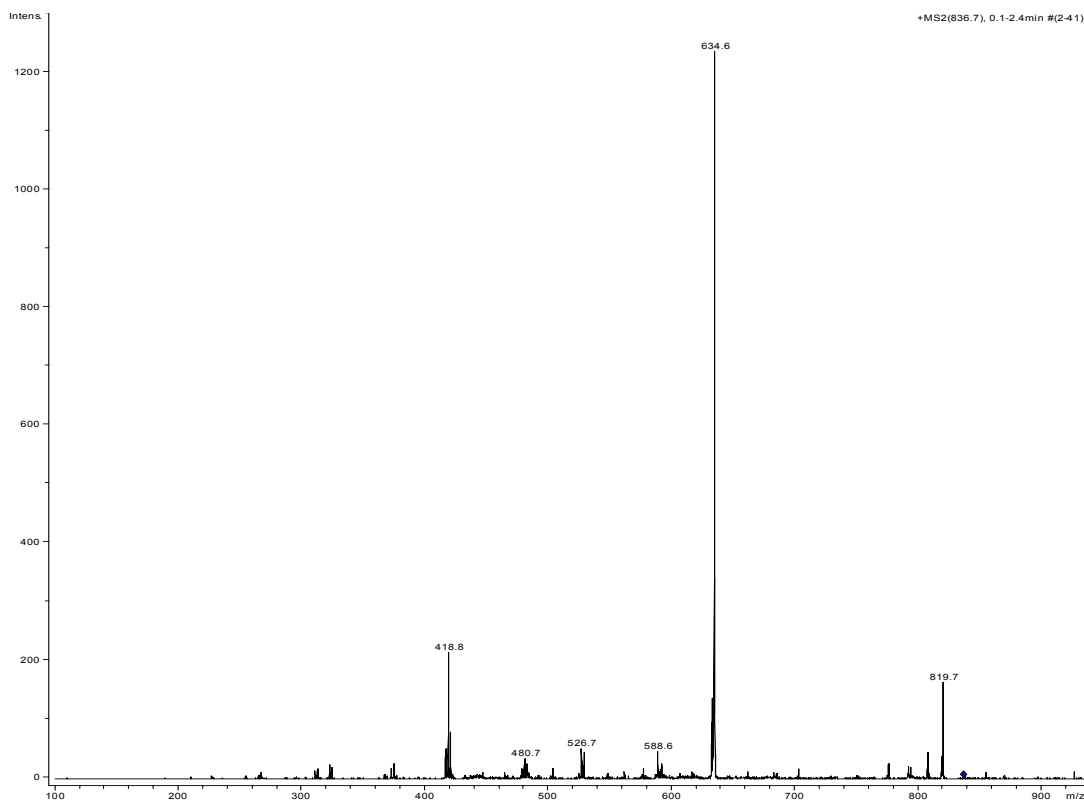
[Ag₁₁Trp₅]⁺ cluster, actual, top and simulated, bottom

MS/MS of Trp-Ag clusters, positive-ion mode ESI spectra**MS/MS of Ag_2 Trp, m/z 418.9****MS/MS of Ag_3 Trp, m/z 528.7**

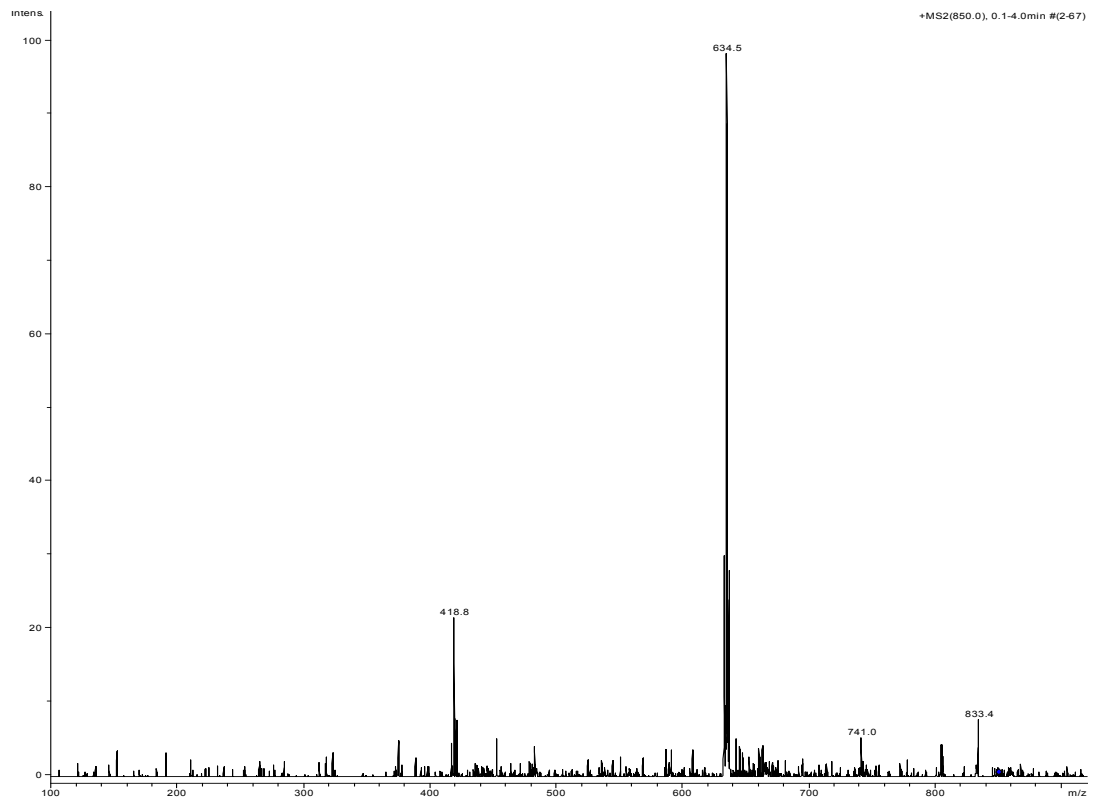
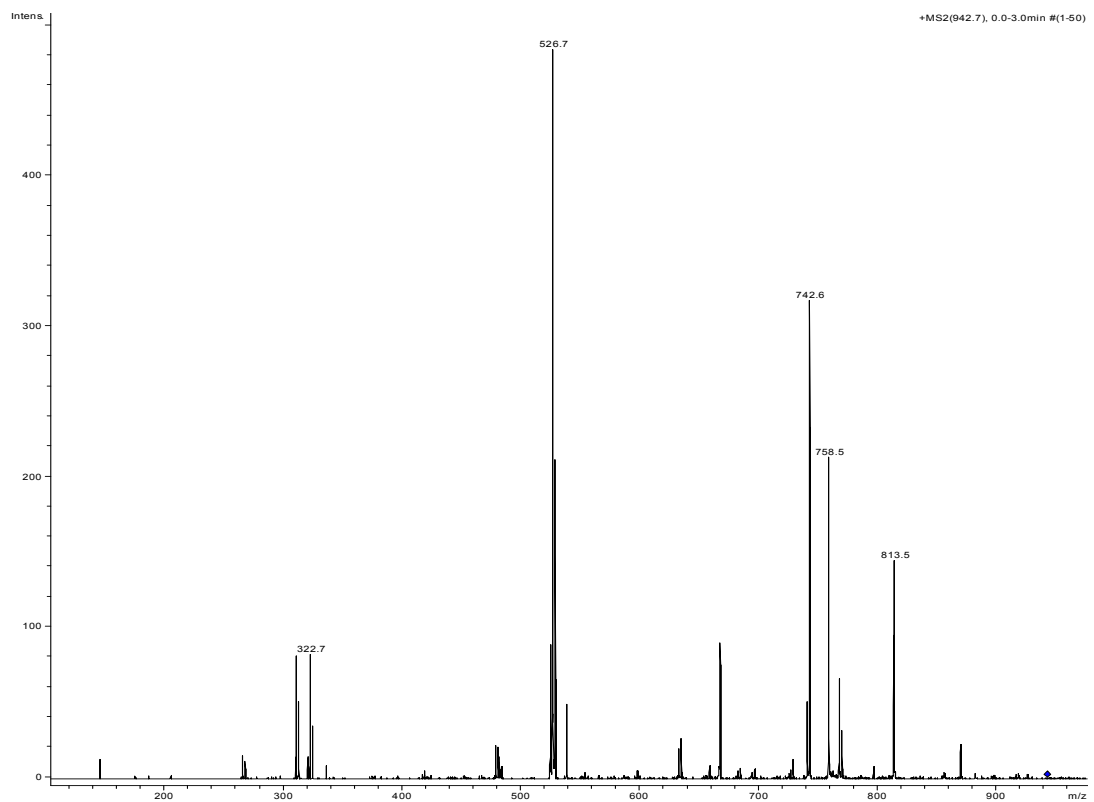
MS/MS of Ag₄Trp, m/z 634.7MS/MS of Ag₃Trp₂, m/z 728.8

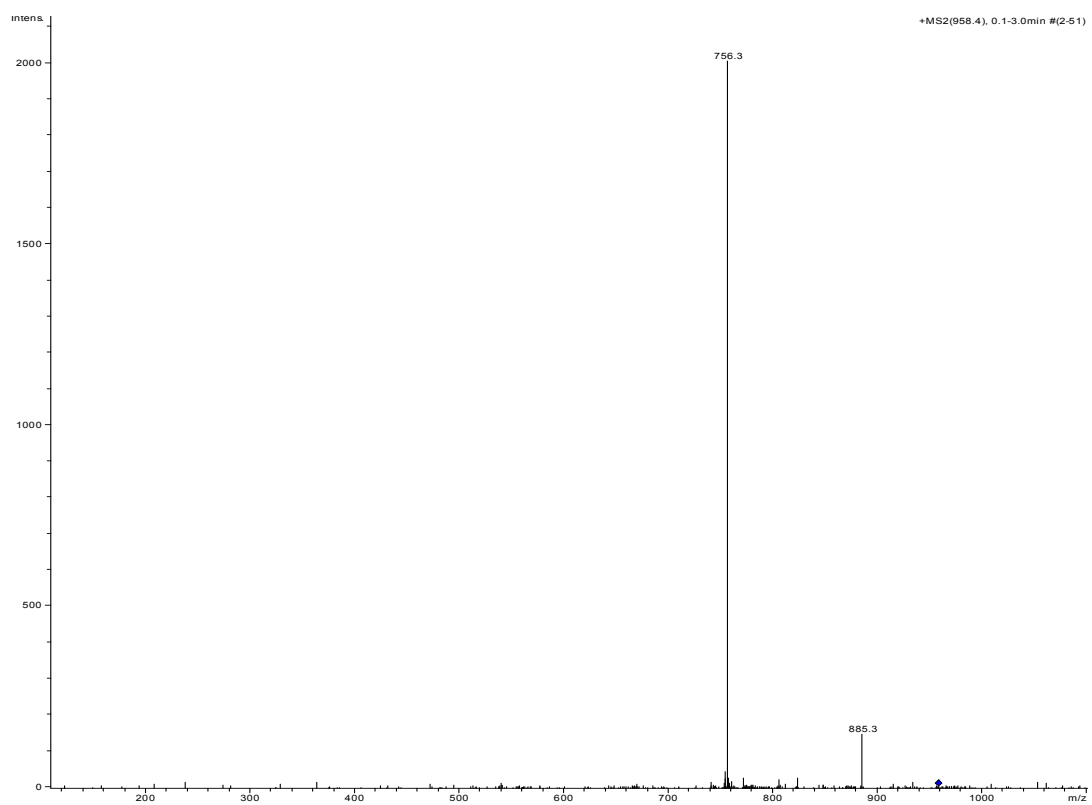
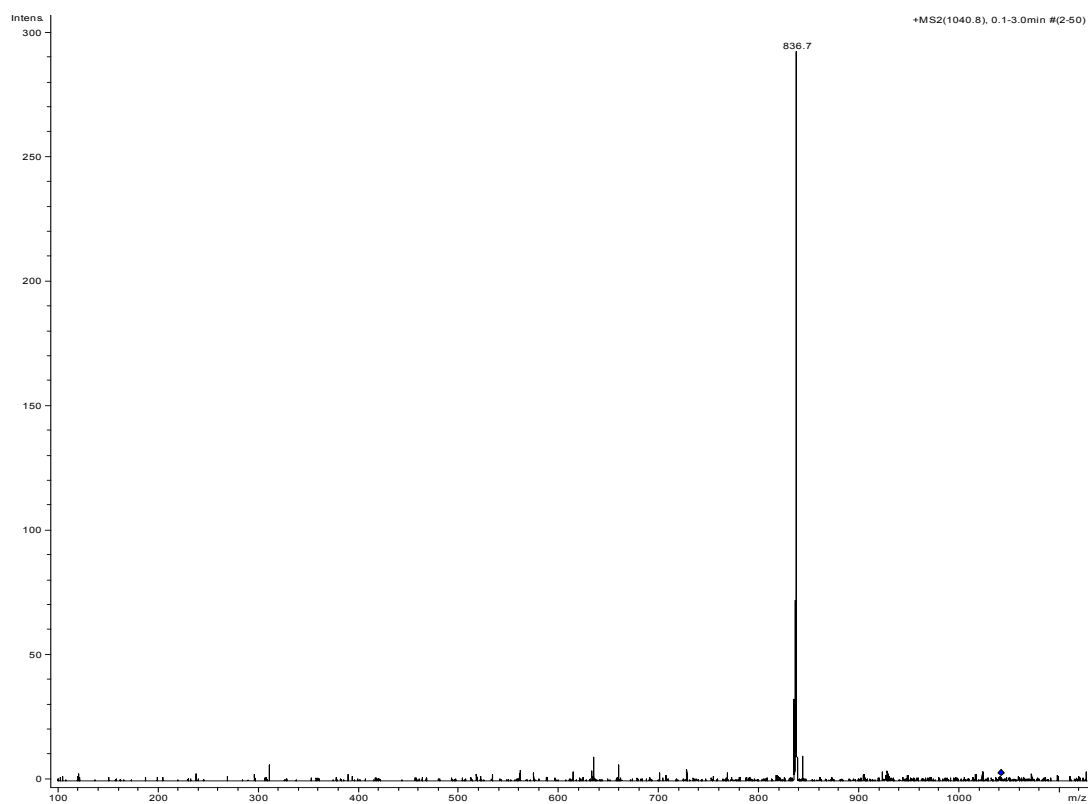


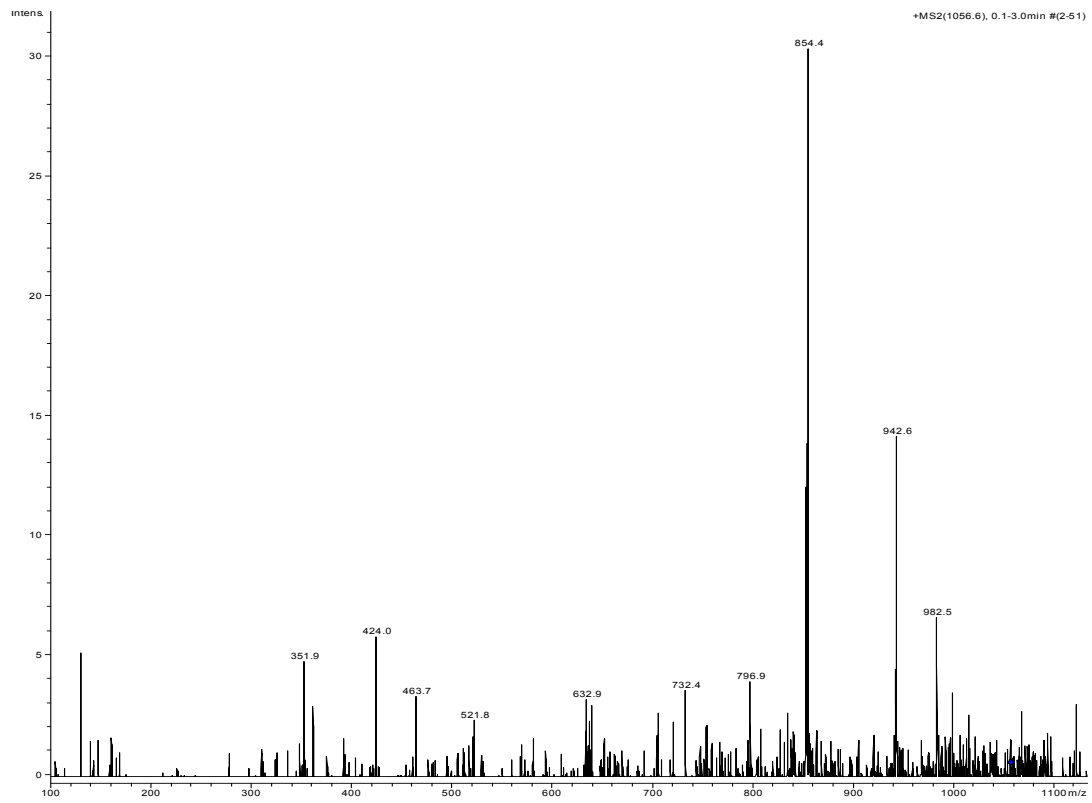
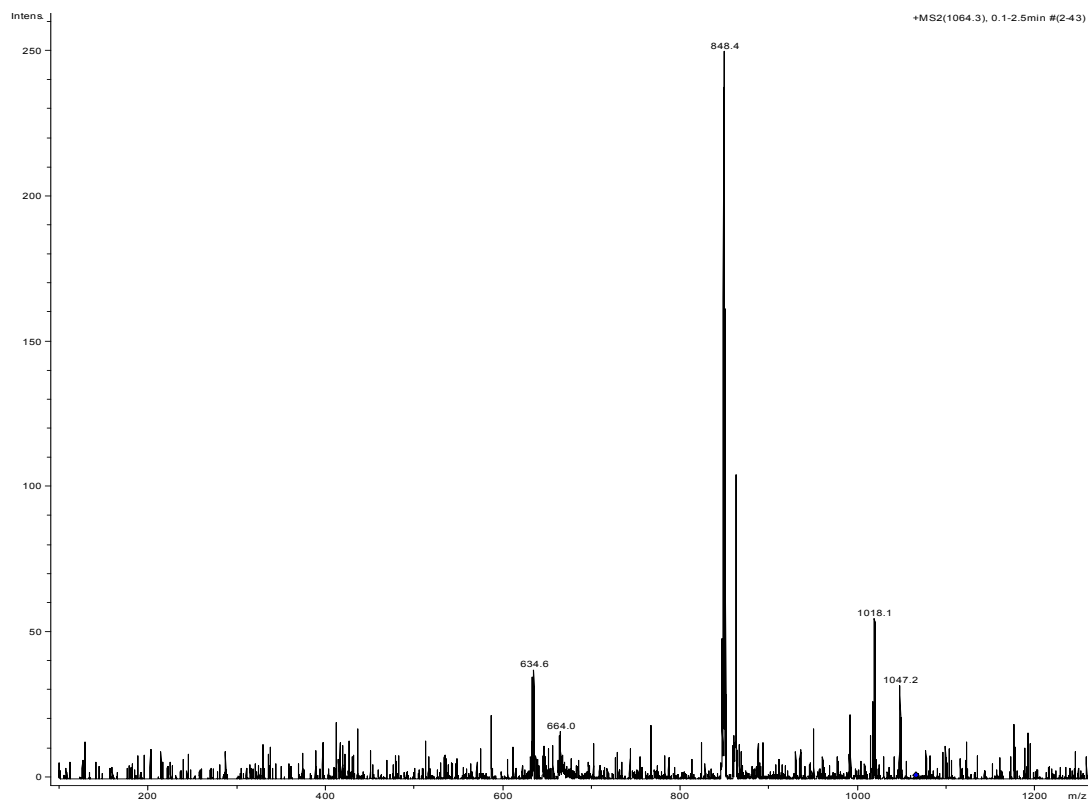
MS/MS Ag₅Trp, m/z 740.6

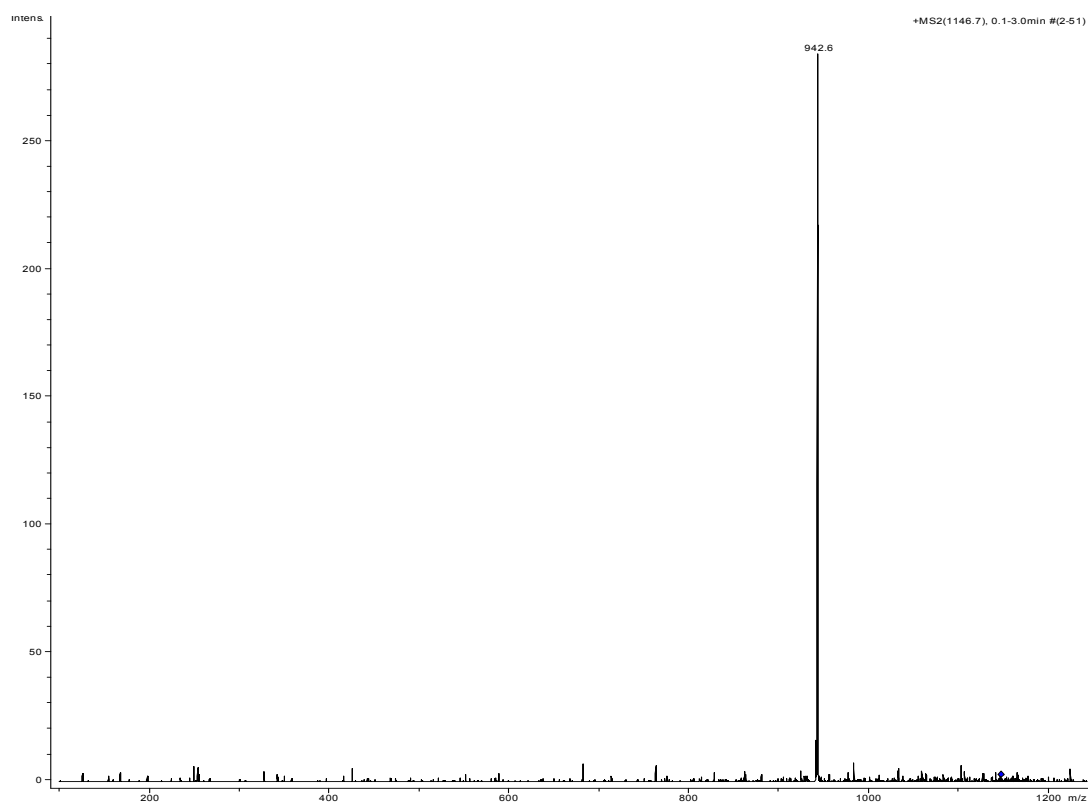
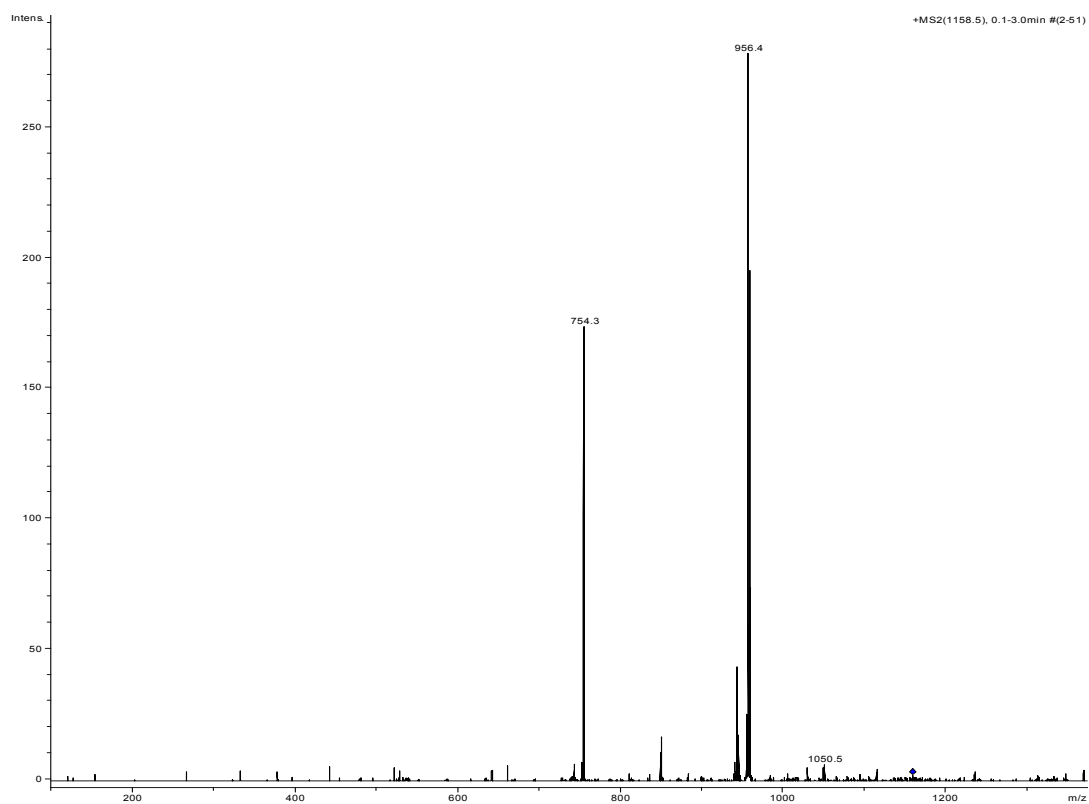


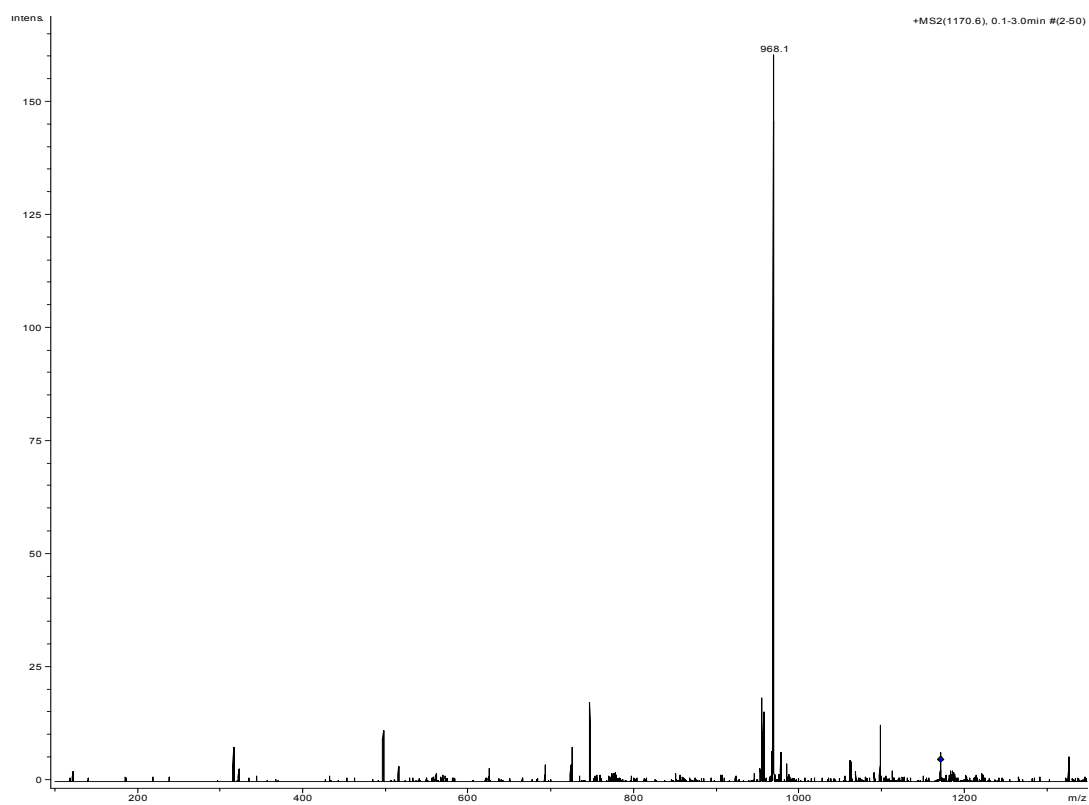
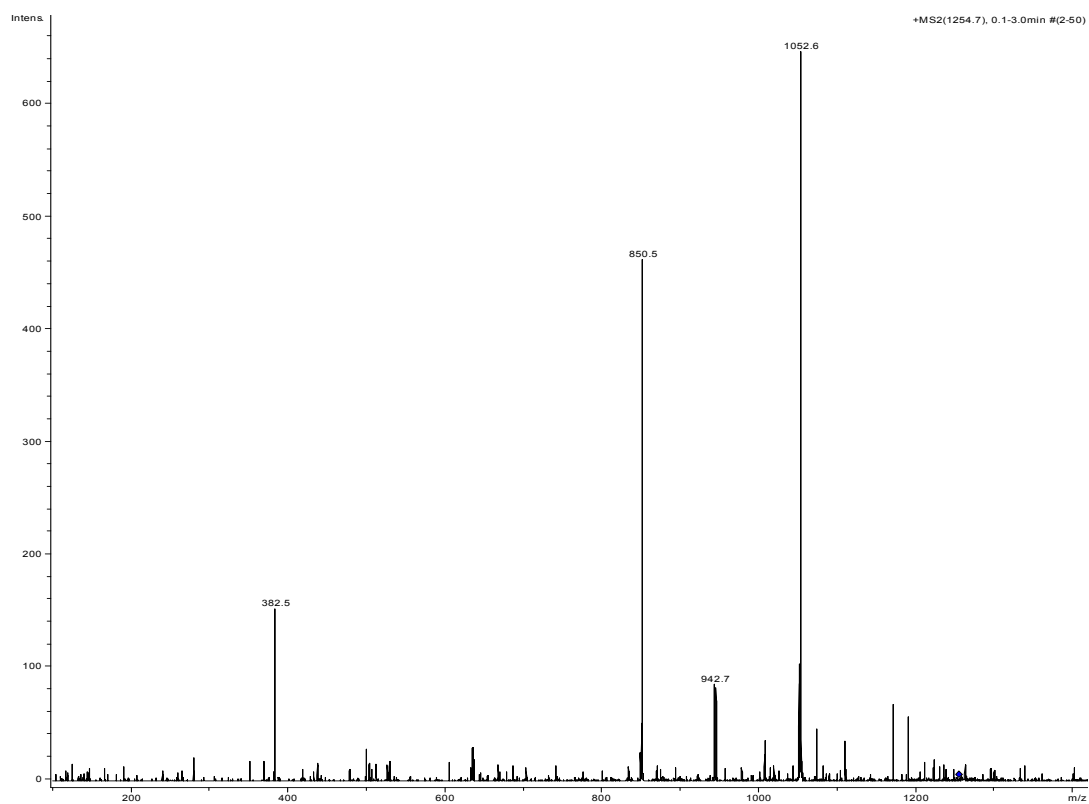
MS/MS of Ag₄Trp₂, m/z 836.7

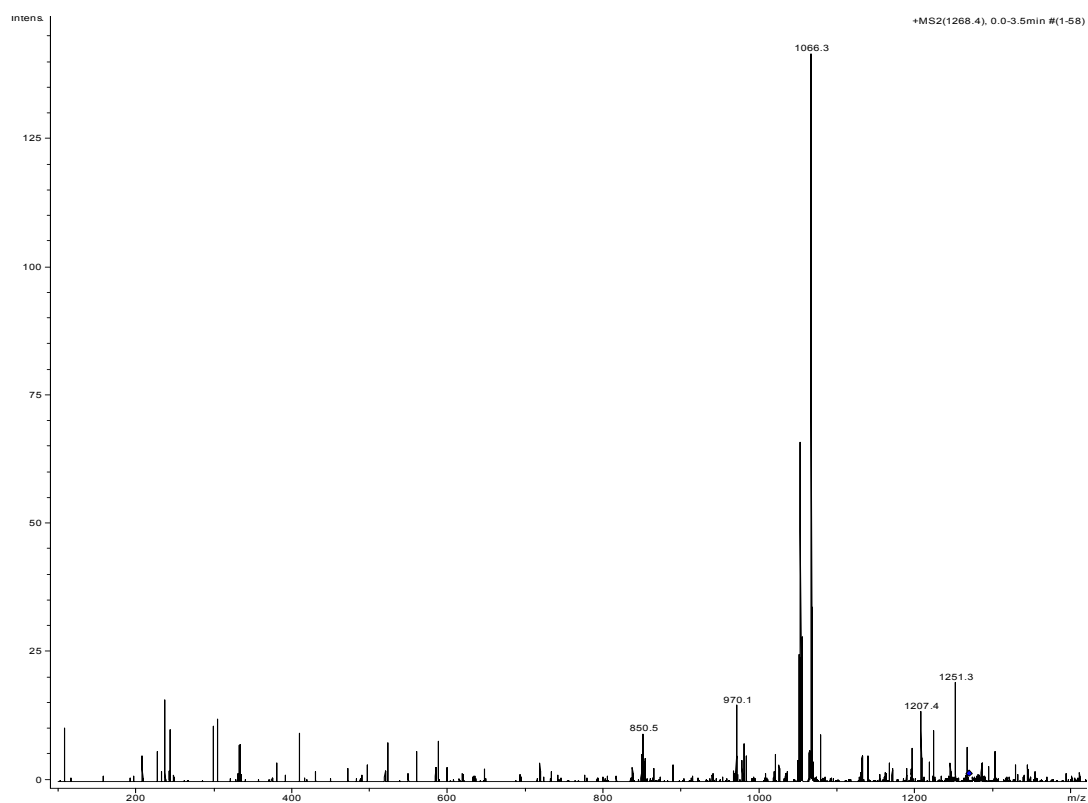
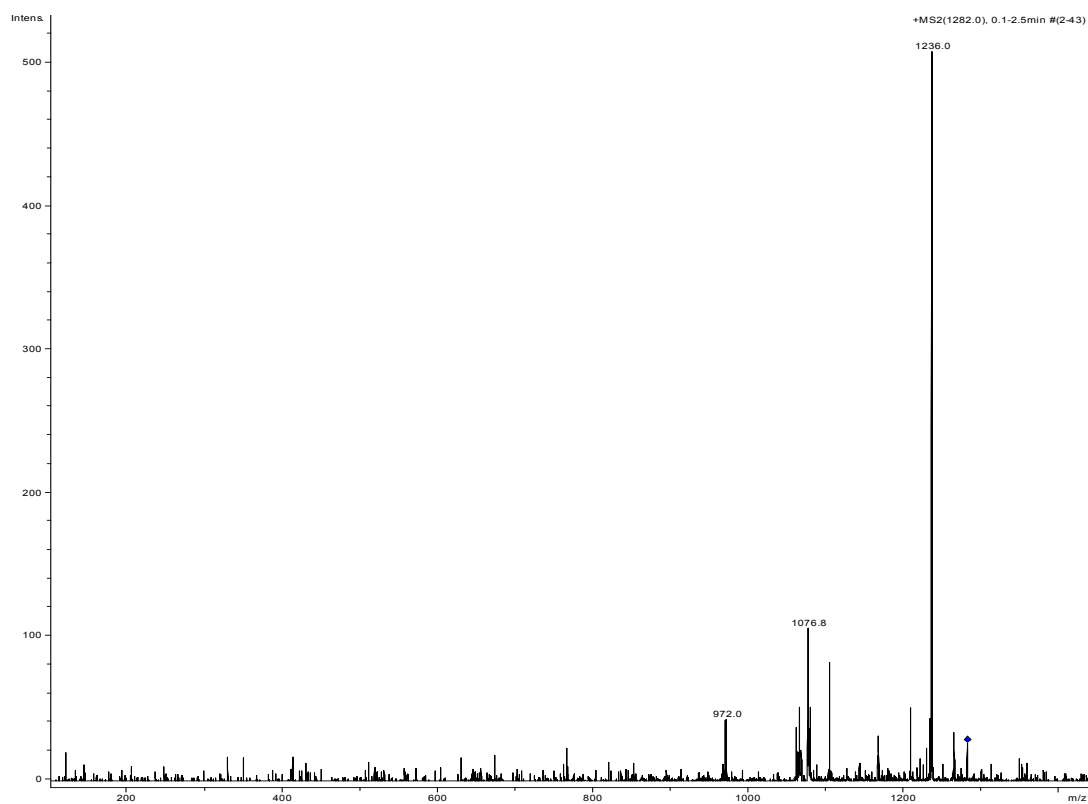
MS/MS of Ag₆Trp, m/z 850.0MS/MS of Ag₅Trp₂, m/z 942.7

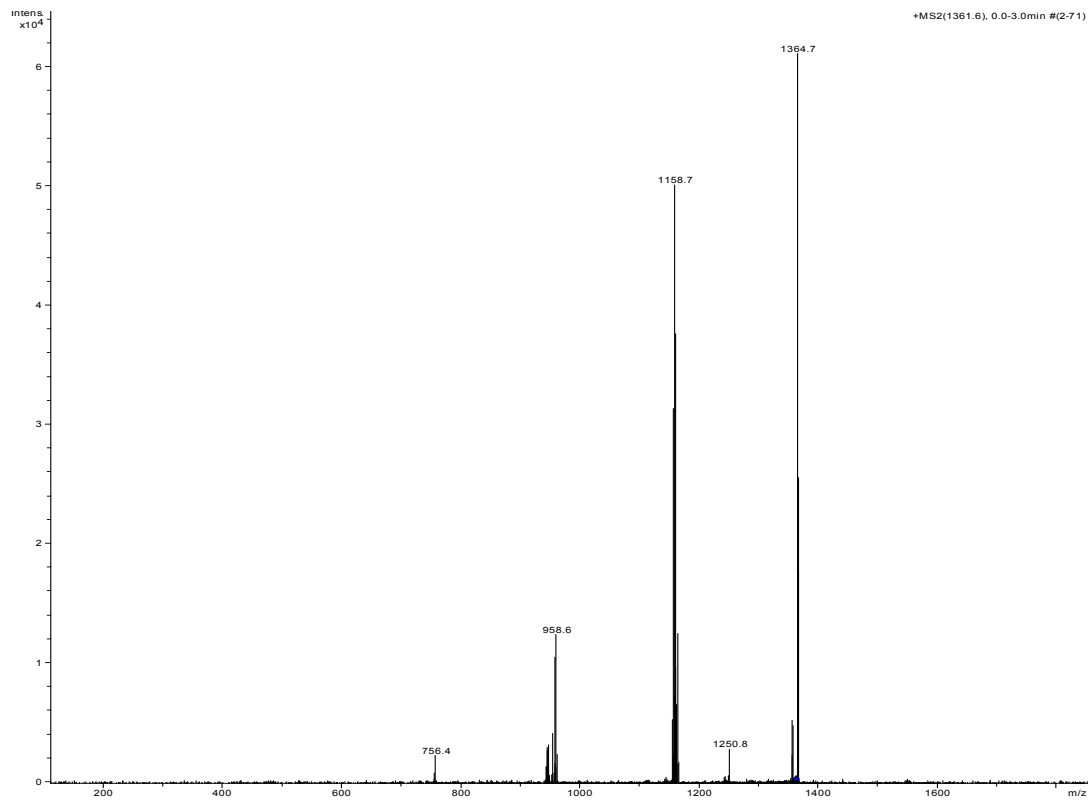
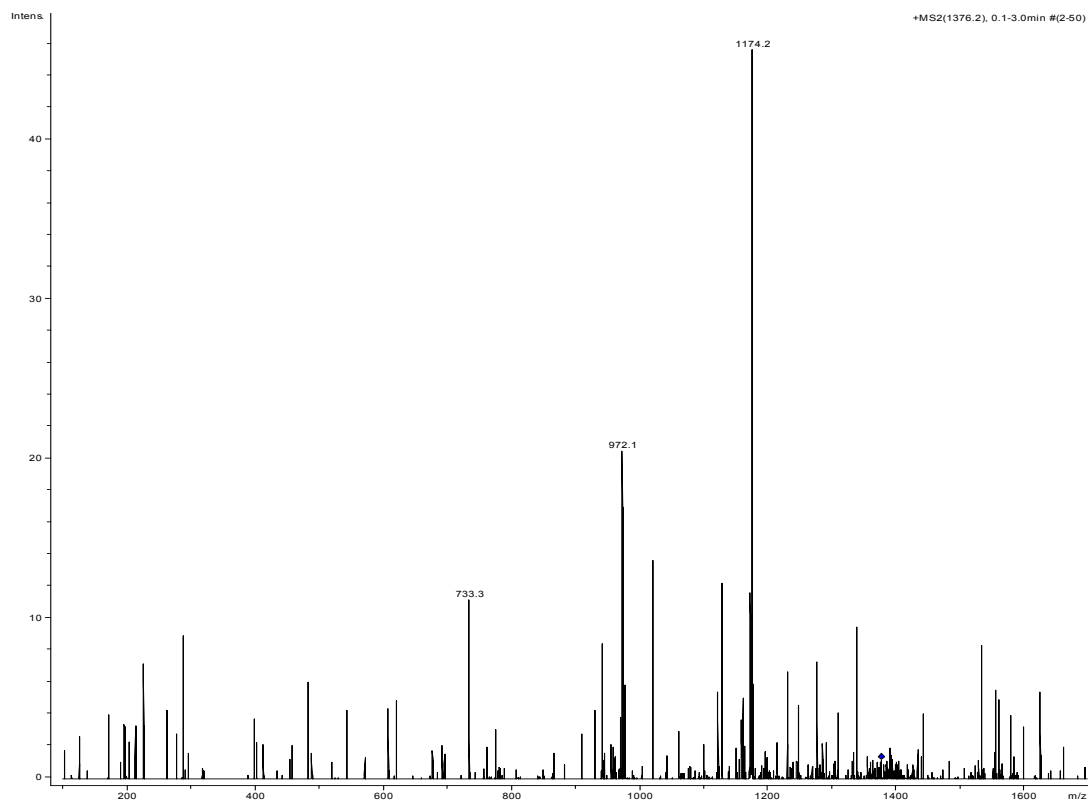
MS/MS of Ag₇Trp, m/z 958.4MS/MS of Ag₄Trp₃, m/z 1040.8

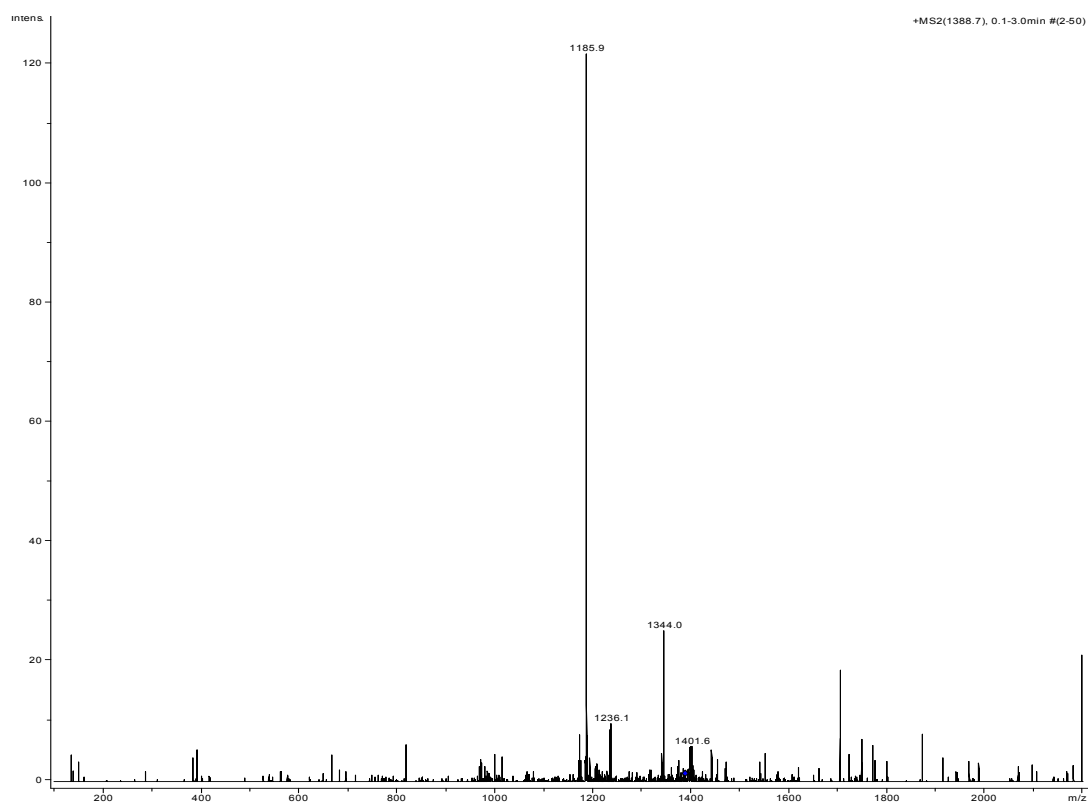
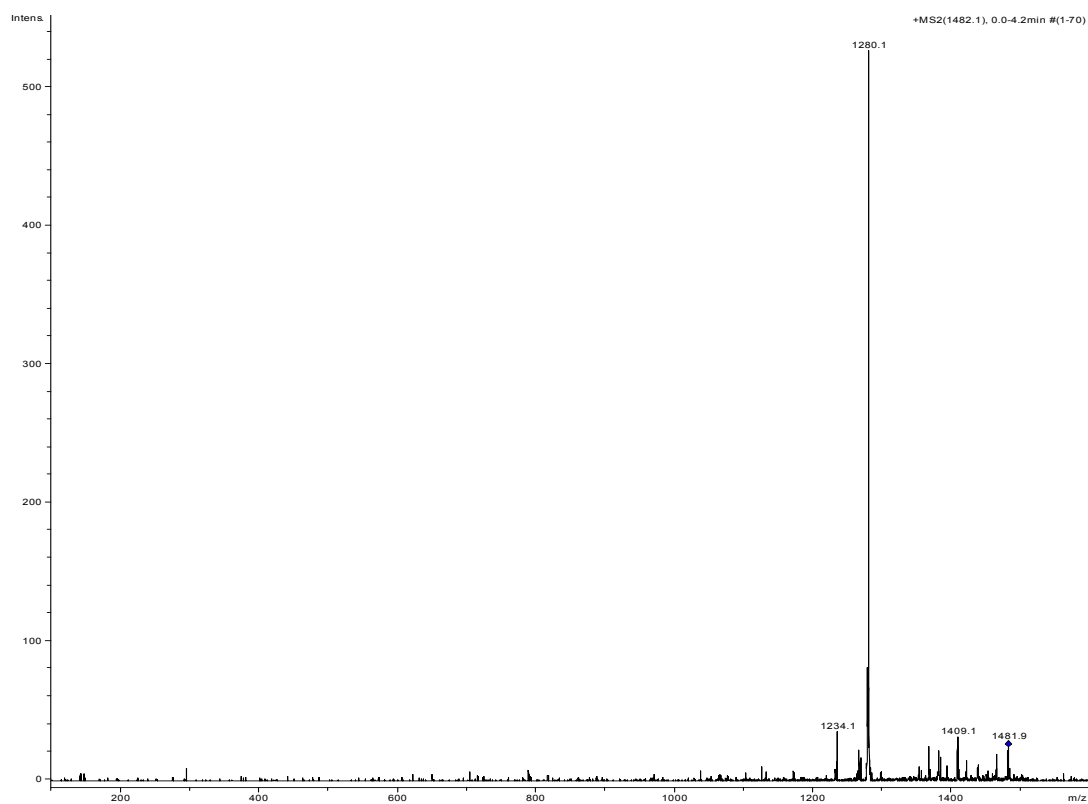
MS/MS of Ag_6Trp_2 , m/z 1056.6MS/MS of Ag_8Trp , m/z 1064.3

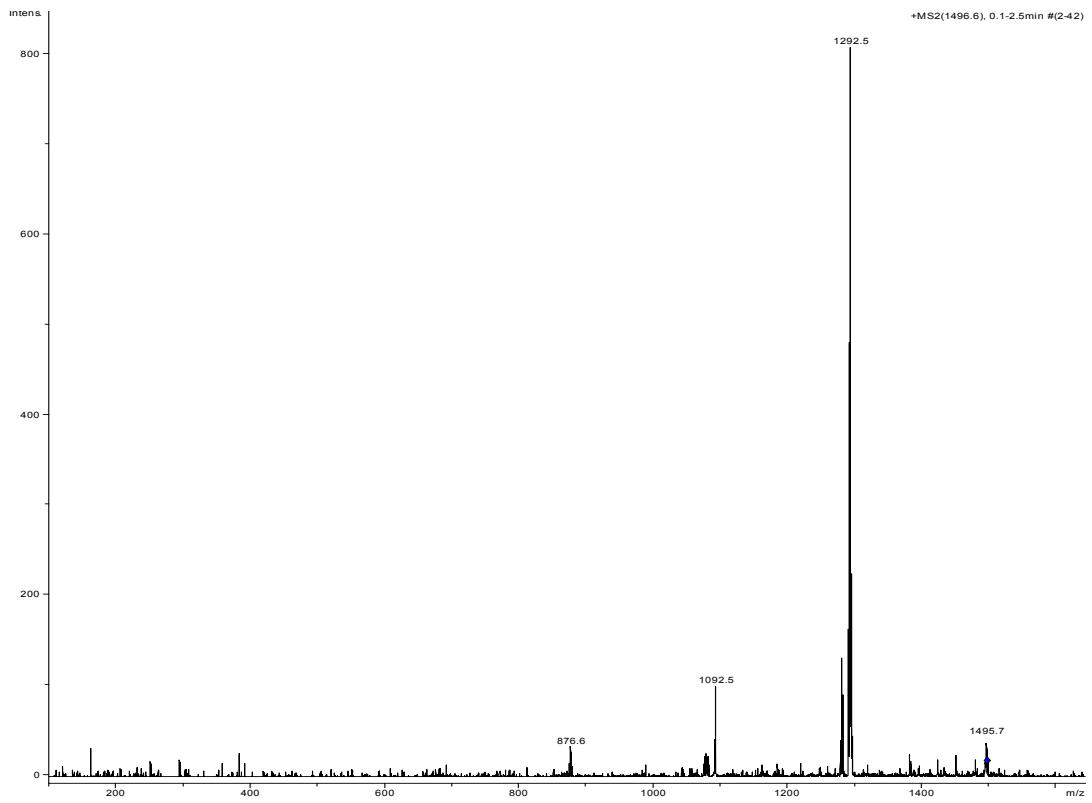
MS/MS of Ag₅Trp₃, m/z 1146.7MS/MS of Ag₇Trp₂, m/z 1158.5

MS/MS of Ag₉Trp, m/z 1170.6MS/MS of Ag₆Trp₃, m/z 1254.7

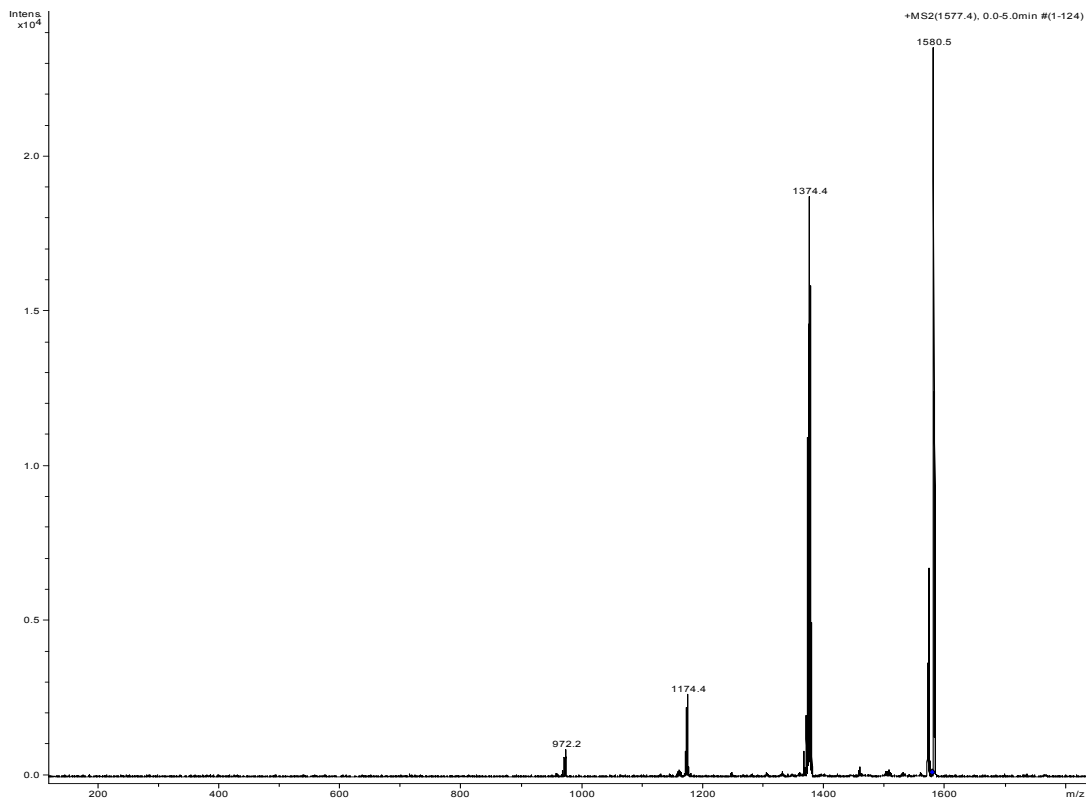
MS/MS of Ag_8Trp_2 , m/z 1268.4MS/MS of $Ag_{10}Trp$, m/z 1282.0

MS/MS of Ag_7Trp_3 , m/z 1361.6MS/MS of Ag_9Trp_2 , m/z 1376.2

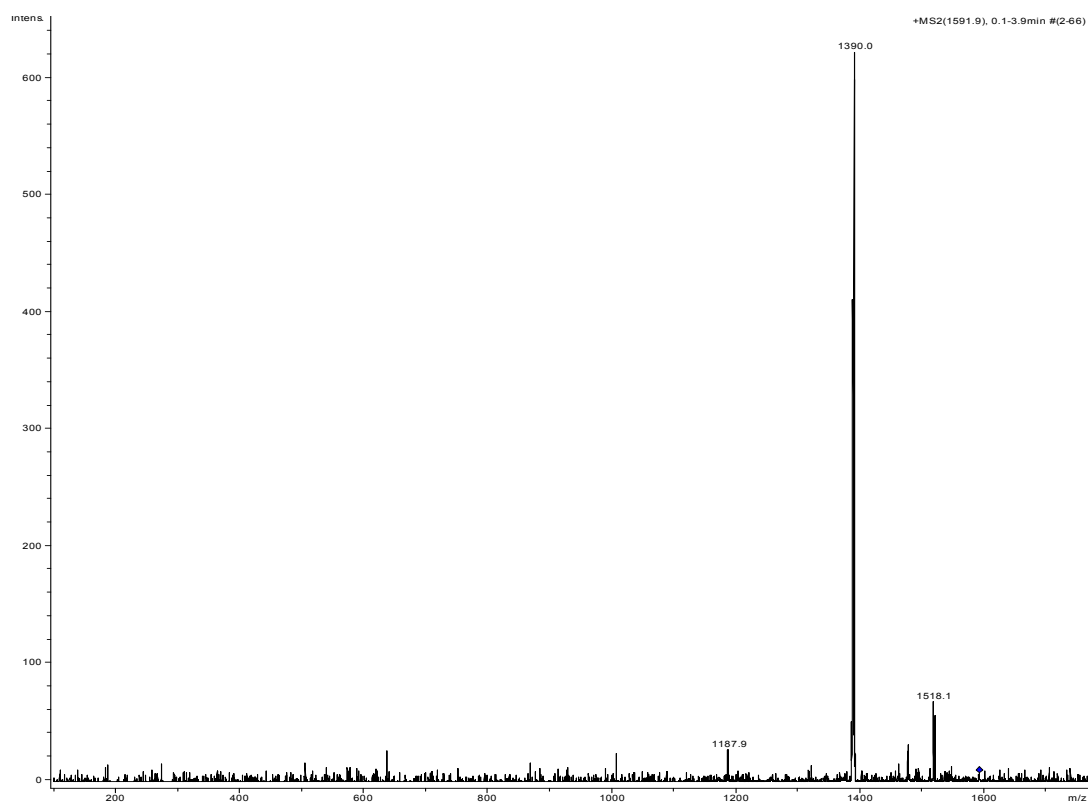
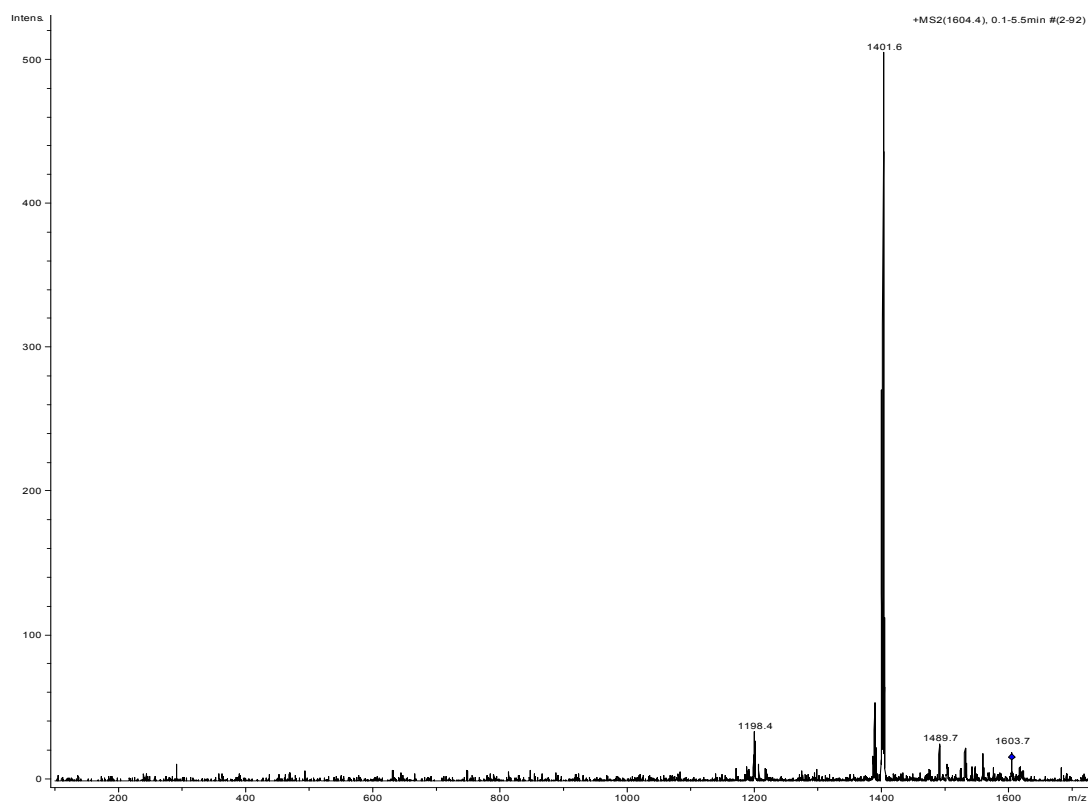
MS/MS of Ag₁₁Trp, m/z 1388.7MS/MS of Ag₁₀Trp₂, m/z 1482.1

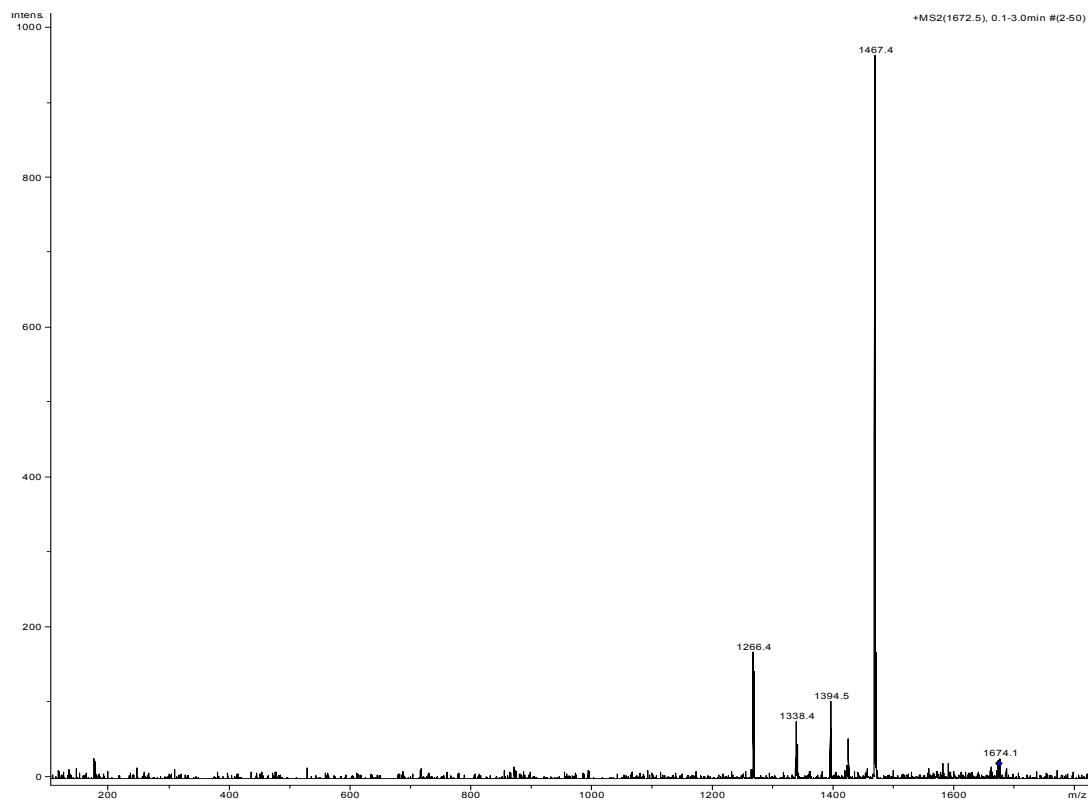
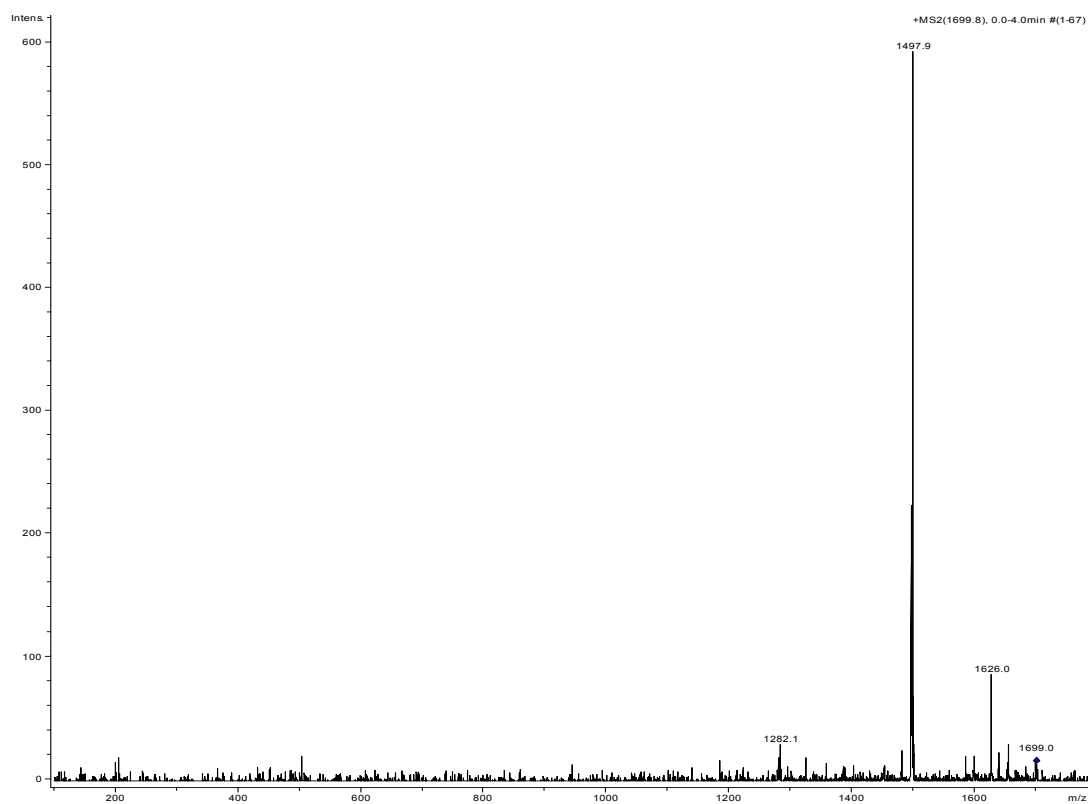


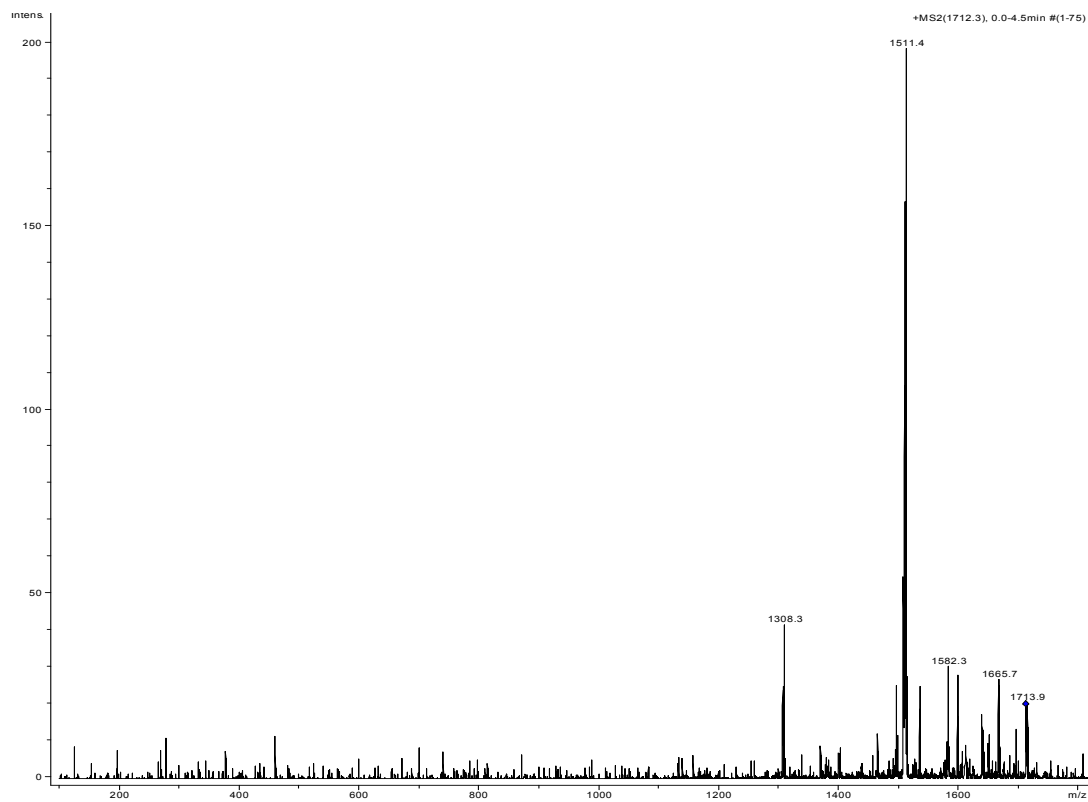
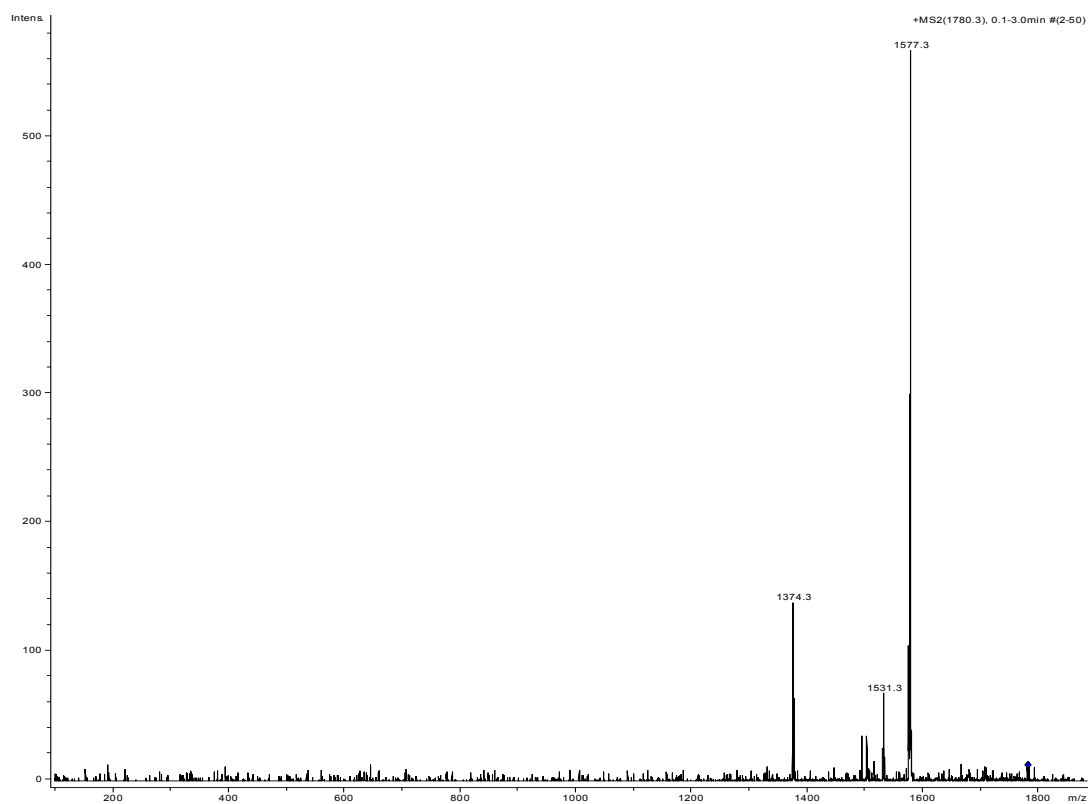
MS/MS of Ag₁₂Trp, m/z 1496.6

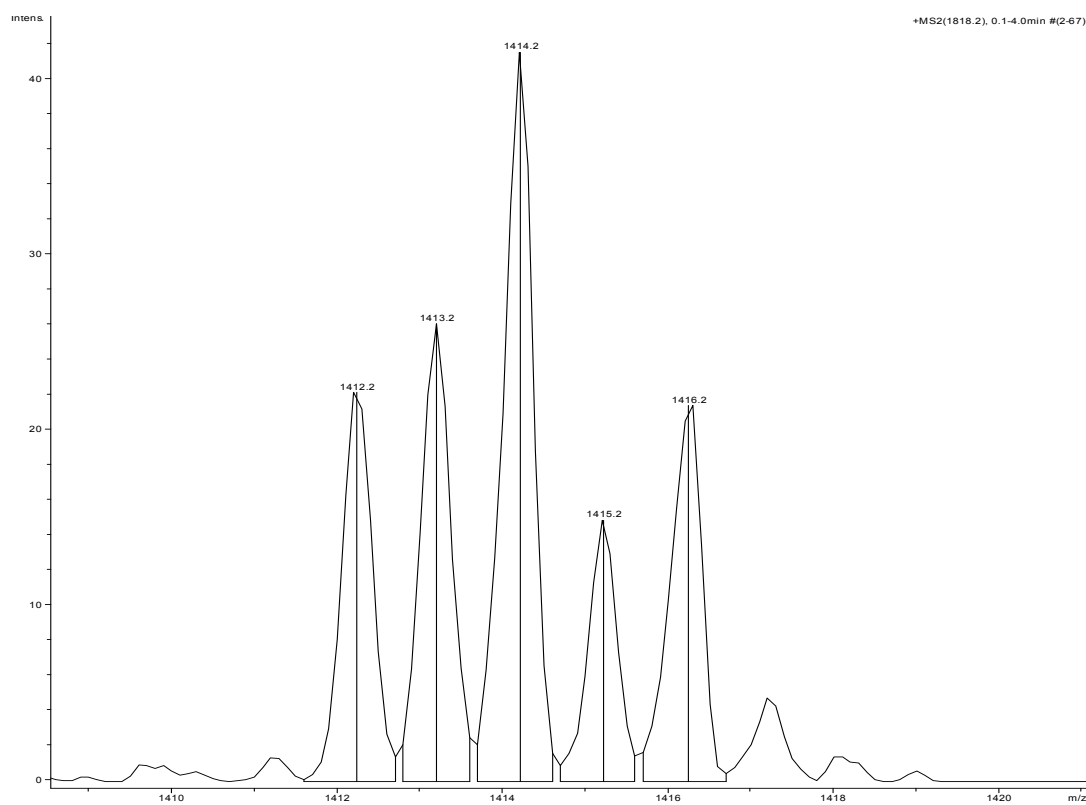
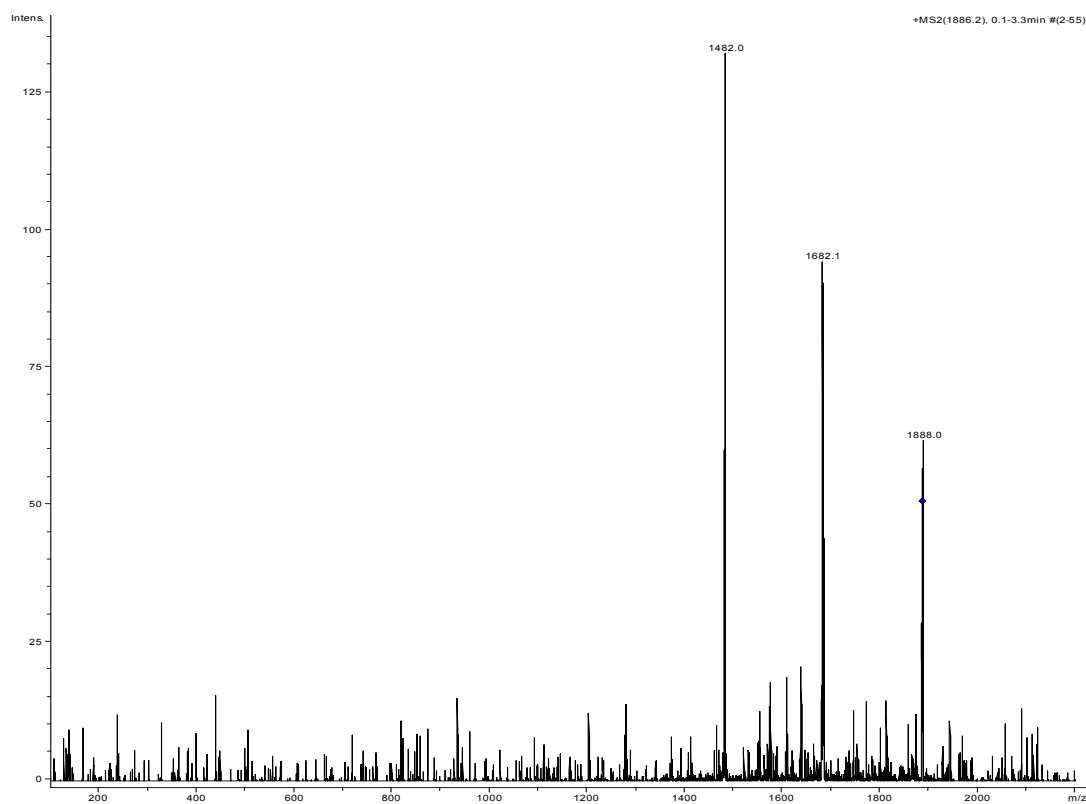


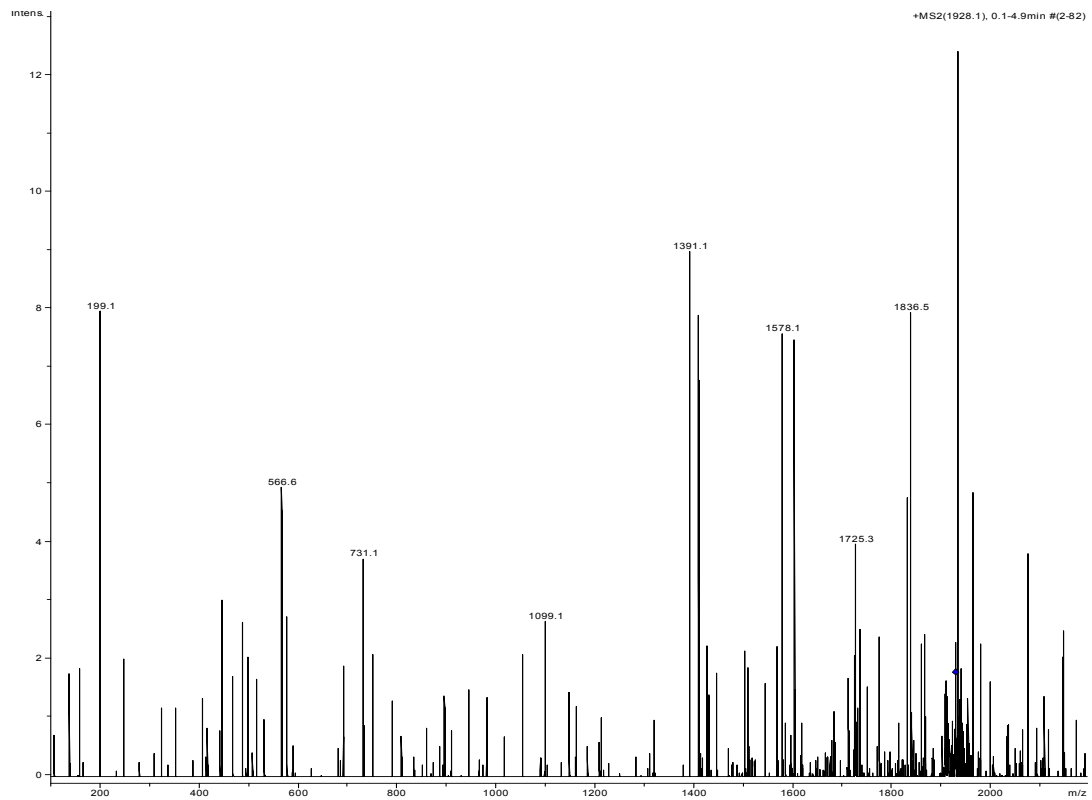
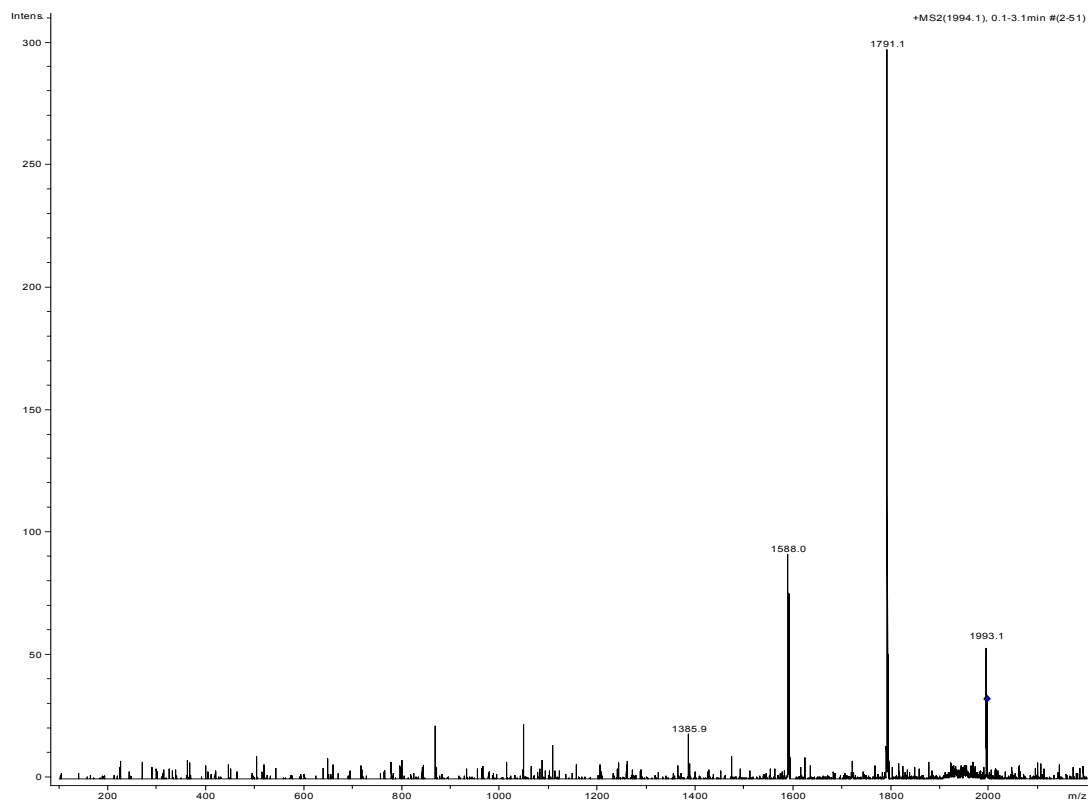
MS/MS of Ag₉Trp₃, m/z 1578.1

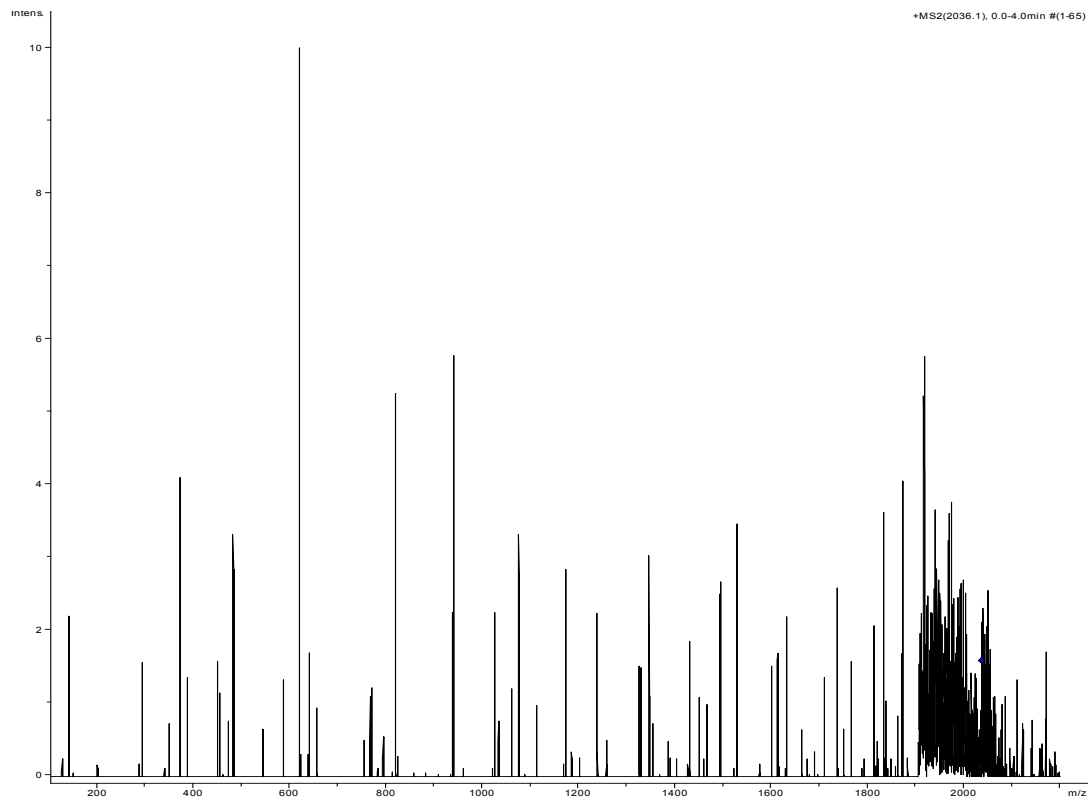
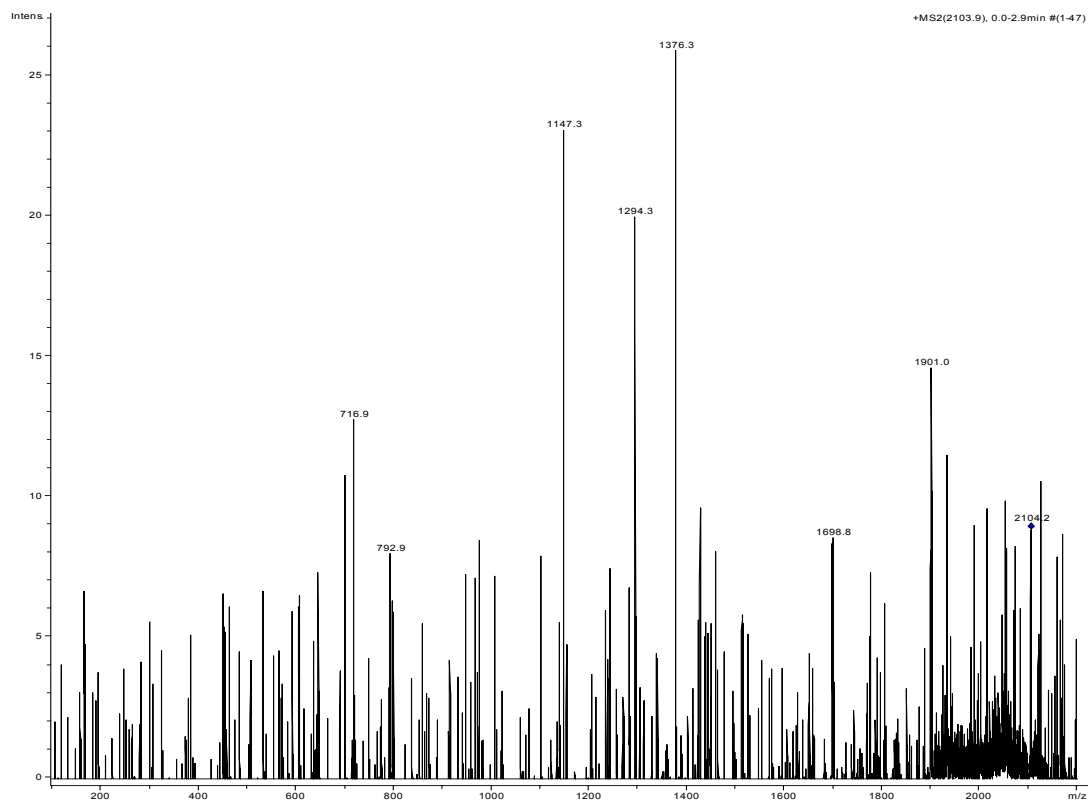
MS/MS of Ag₁₁Trp₂, m/z 1591.9MS/MS of Ag₁₃Trp, m/z 1604.4

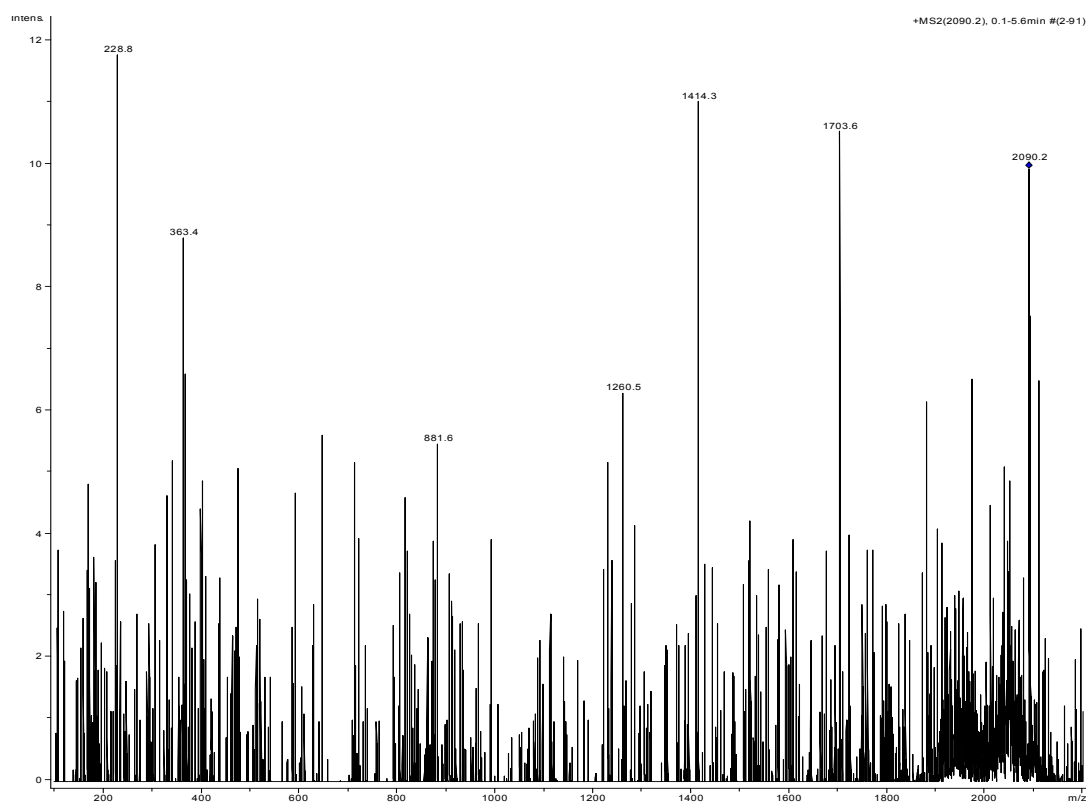
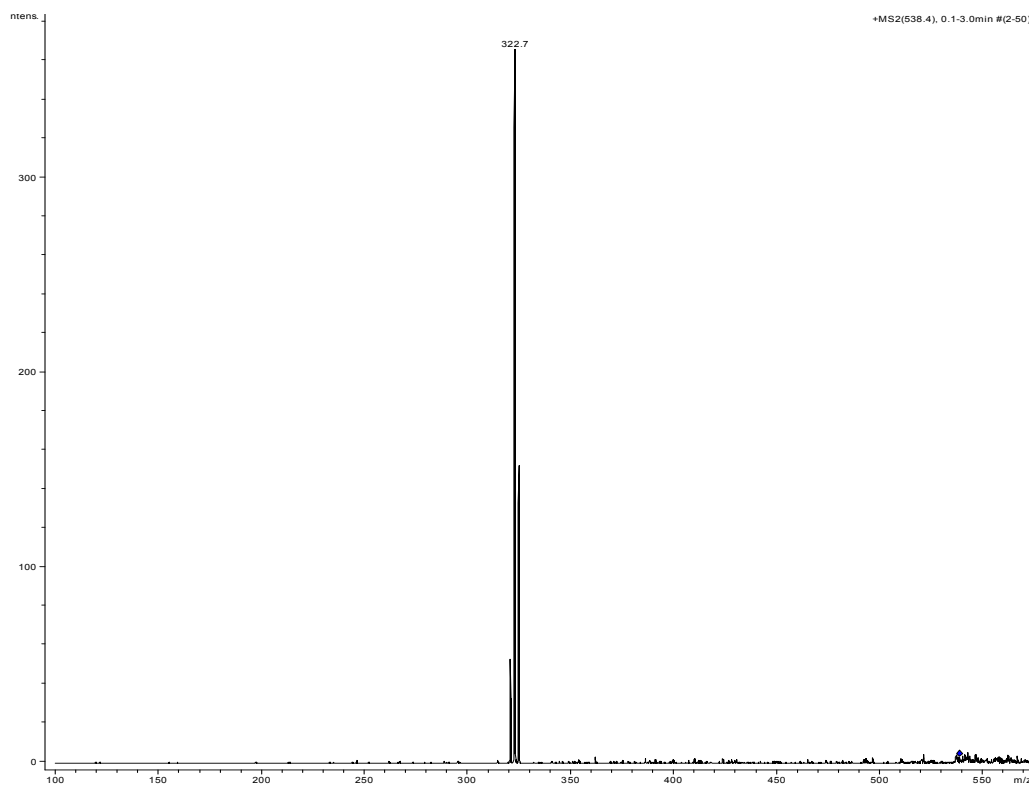
MS/MS of Ag₈Trp₄, m/z 1672.5MS/MS of Ag₁₂Trp₂, m/z 1699.8

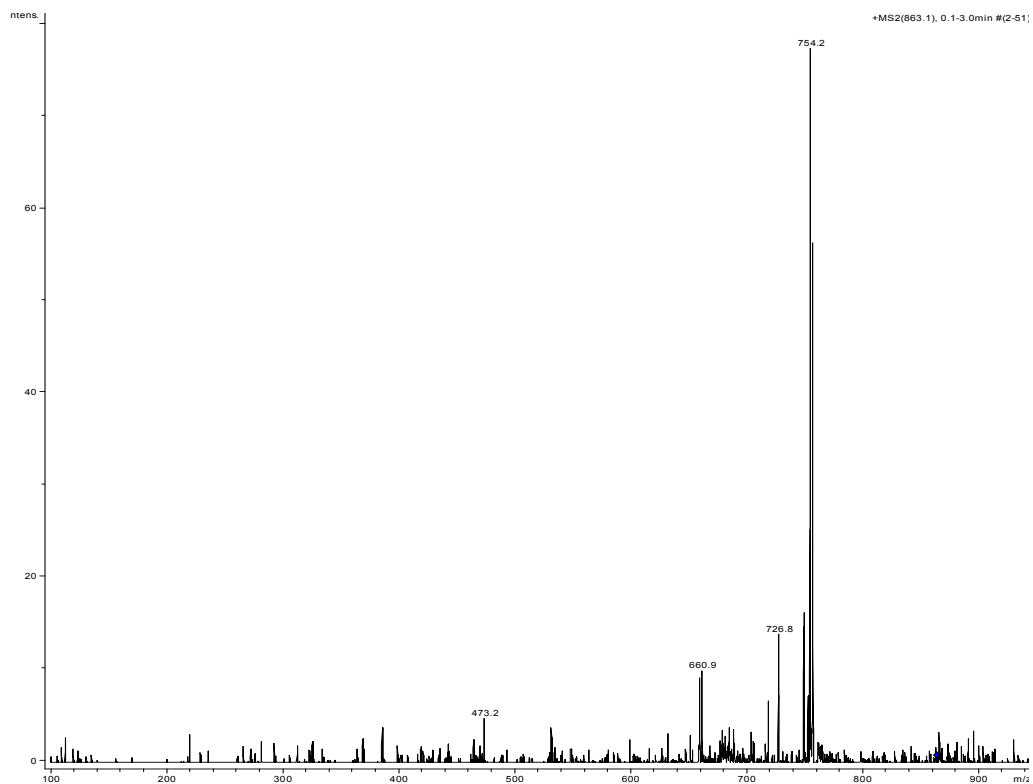
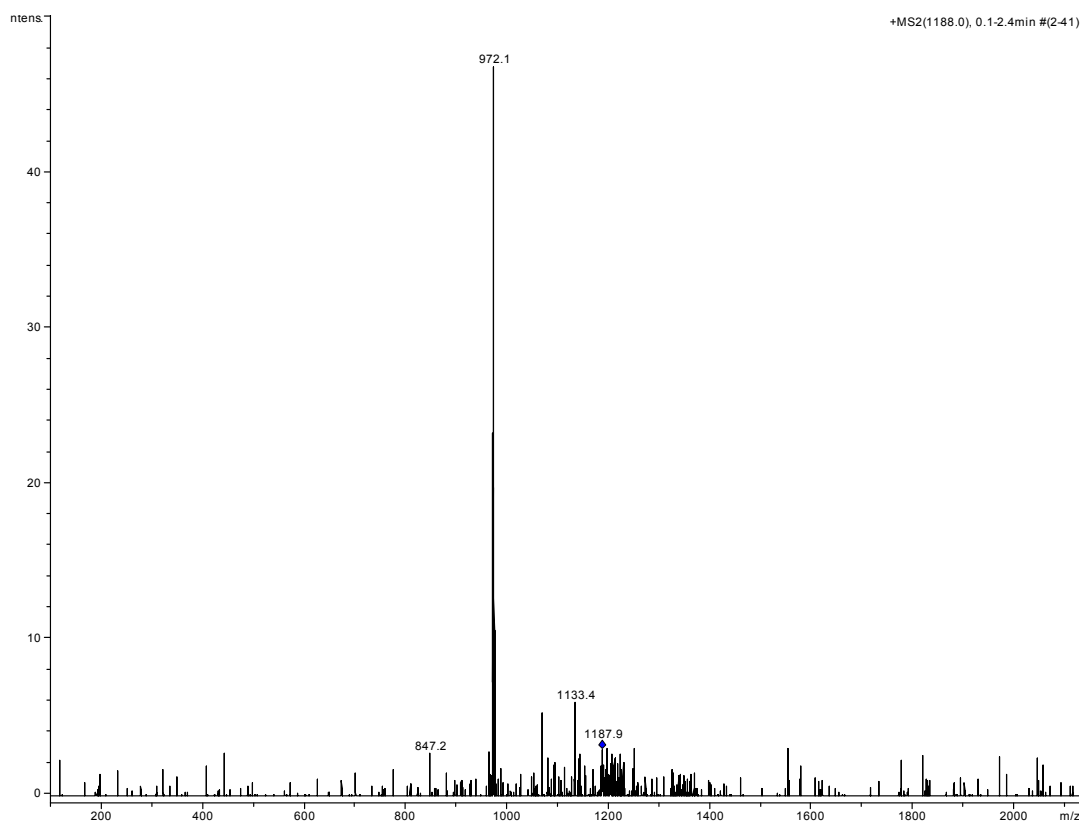
MS/MS of Ag₁₄Trp, m/z 1712.3MS/MS of Ag₉Trp₄, m/z 1780.3

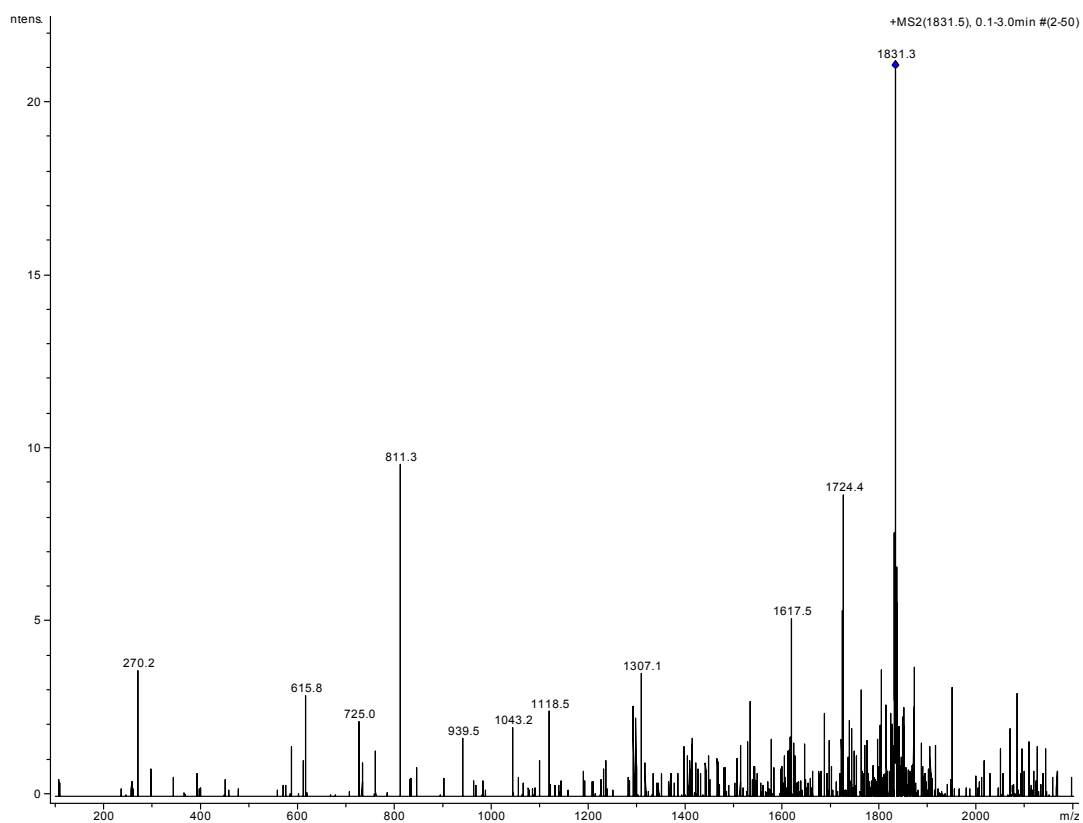
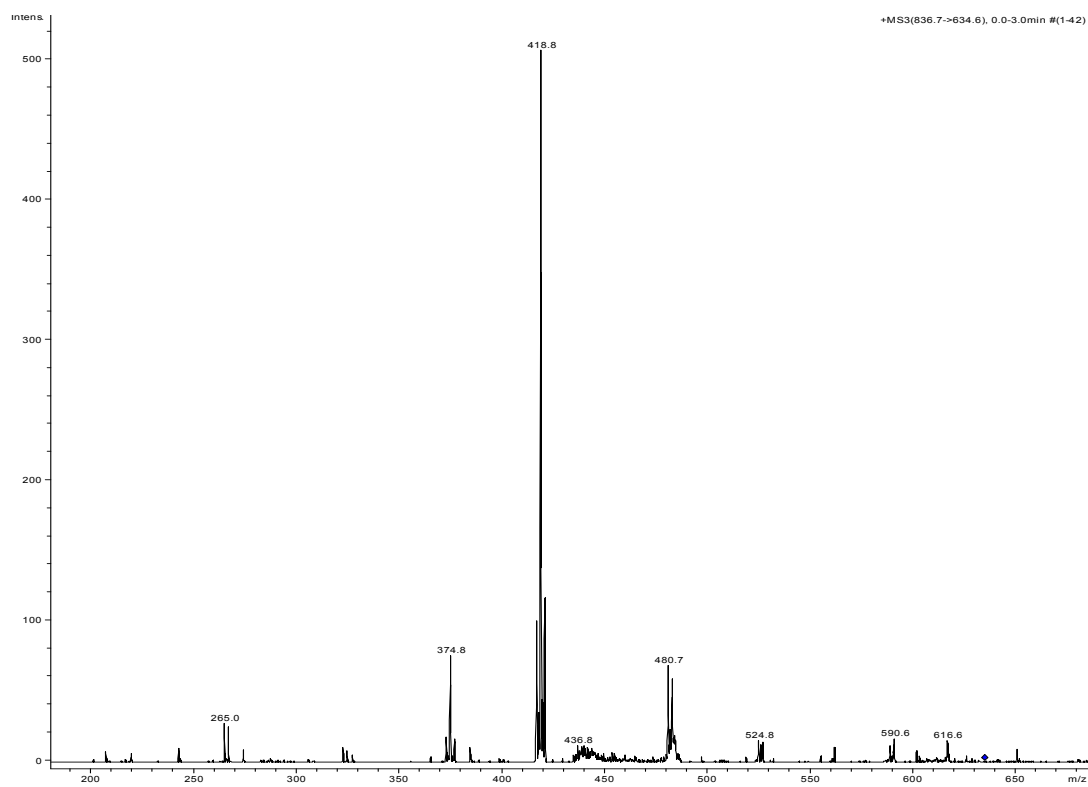
MS/MS of Ag₁₅Trp, m/z 1818.2MS/MS of Ag₁₀Trp₄, m/z 1886.2

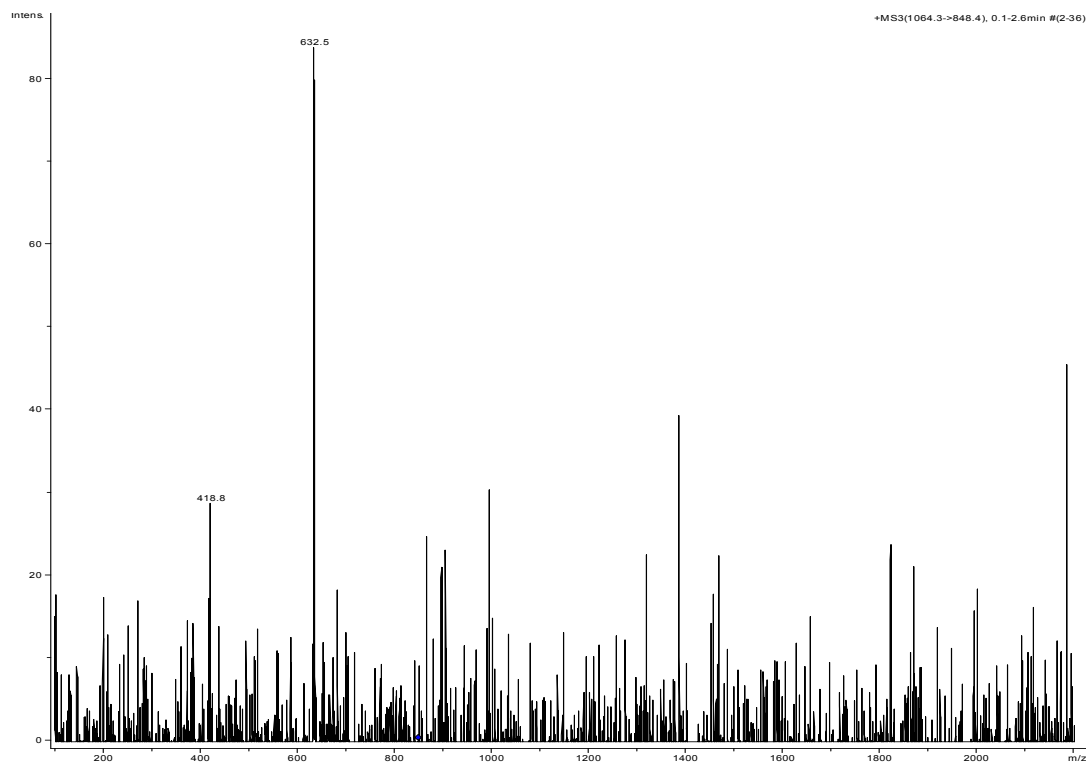
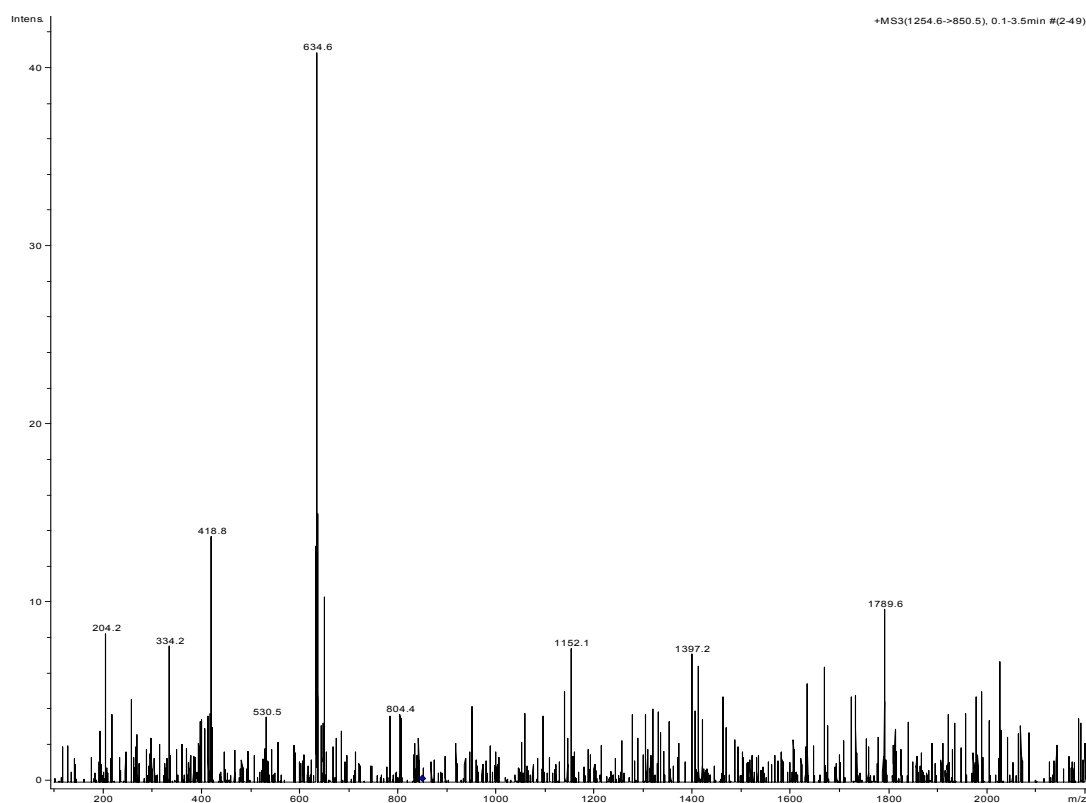
MS/MS of $Ag_{16}Trp$, m/z 1928.1MS/MS of $Ag_{11}Trp_4$, m/z 1994.1

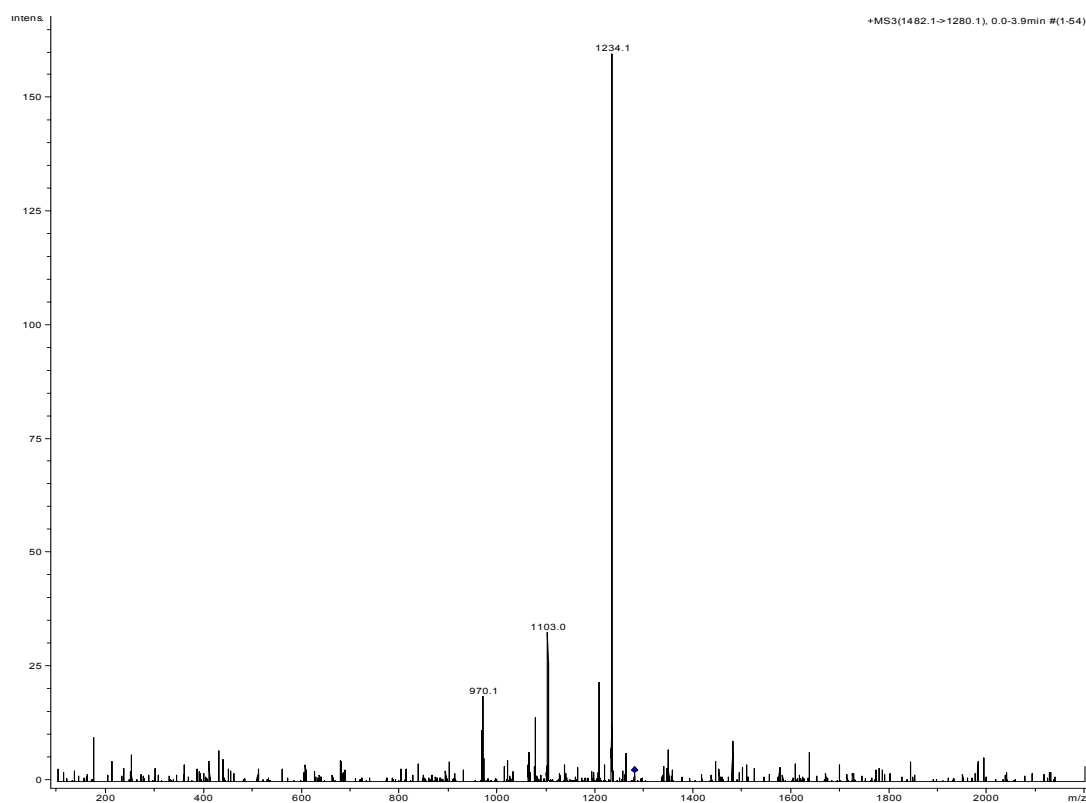
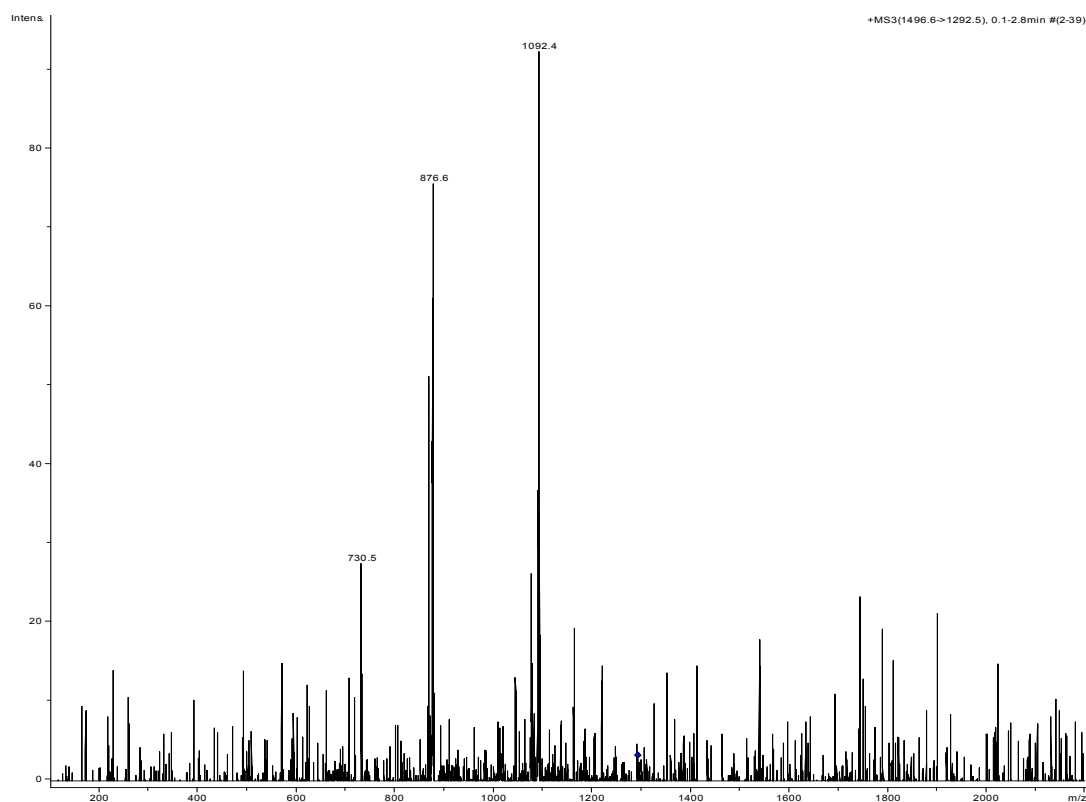
MS/MS of Ag₁₇Trp, m/z 2036.1MS/MS of Ag₁₀Trp₅, m/z 2090.2

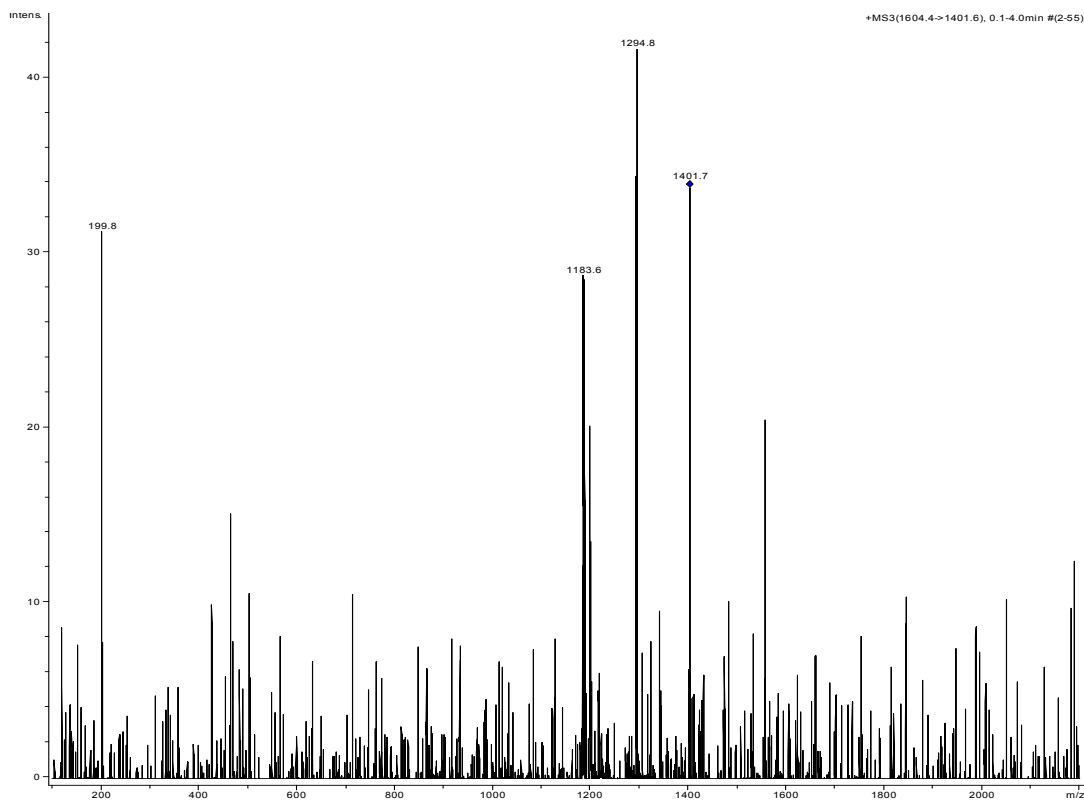
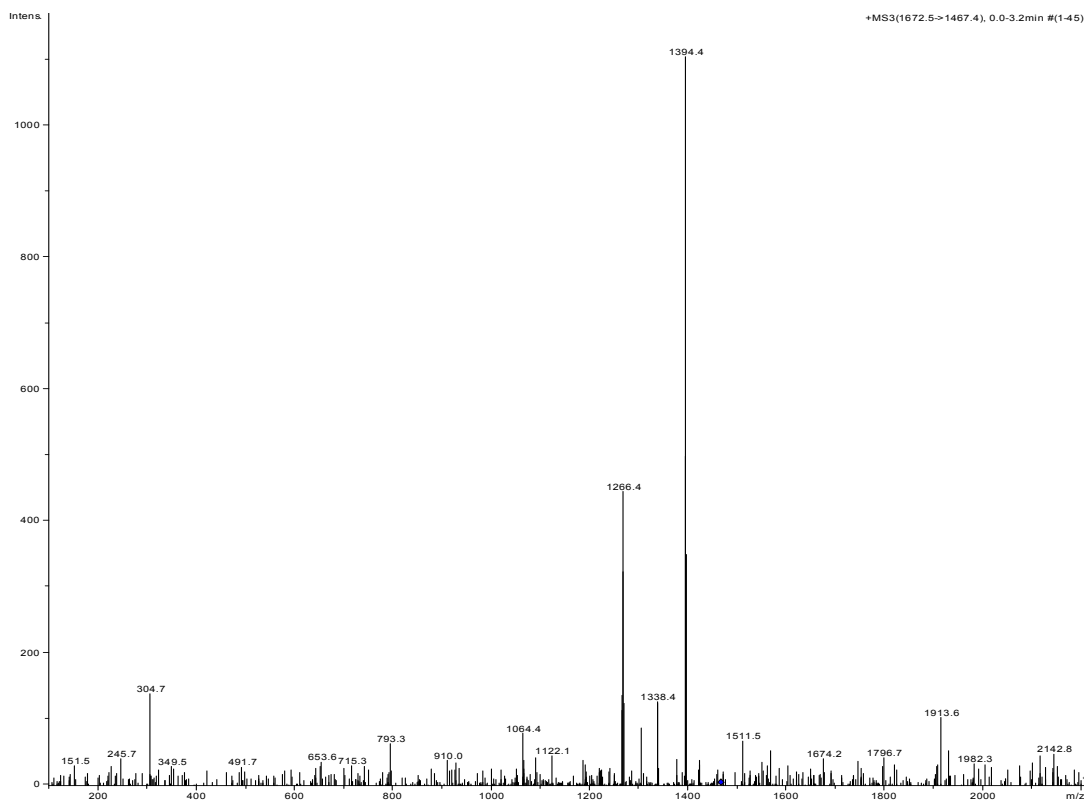
MS/MS of Ag₁₂Trp₄, m/z 2103.9**MS/MS of Silver clusters, positive-ion mode ESI spectra**MS/MS of Ag₅

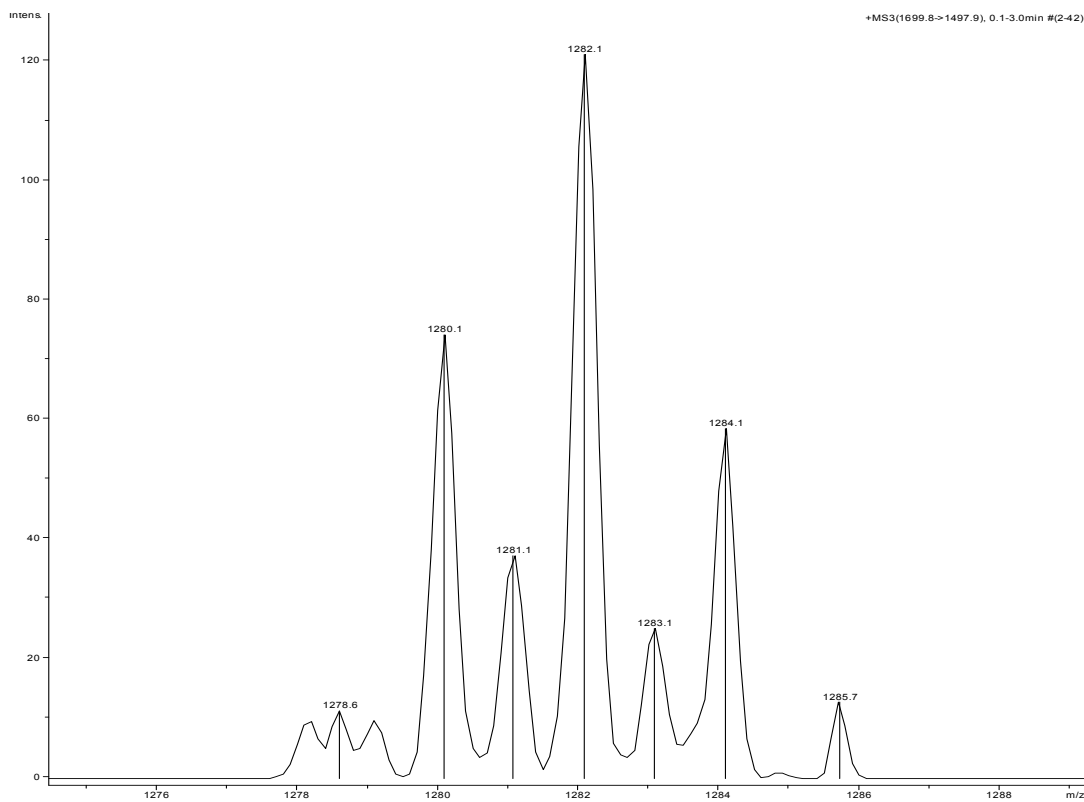
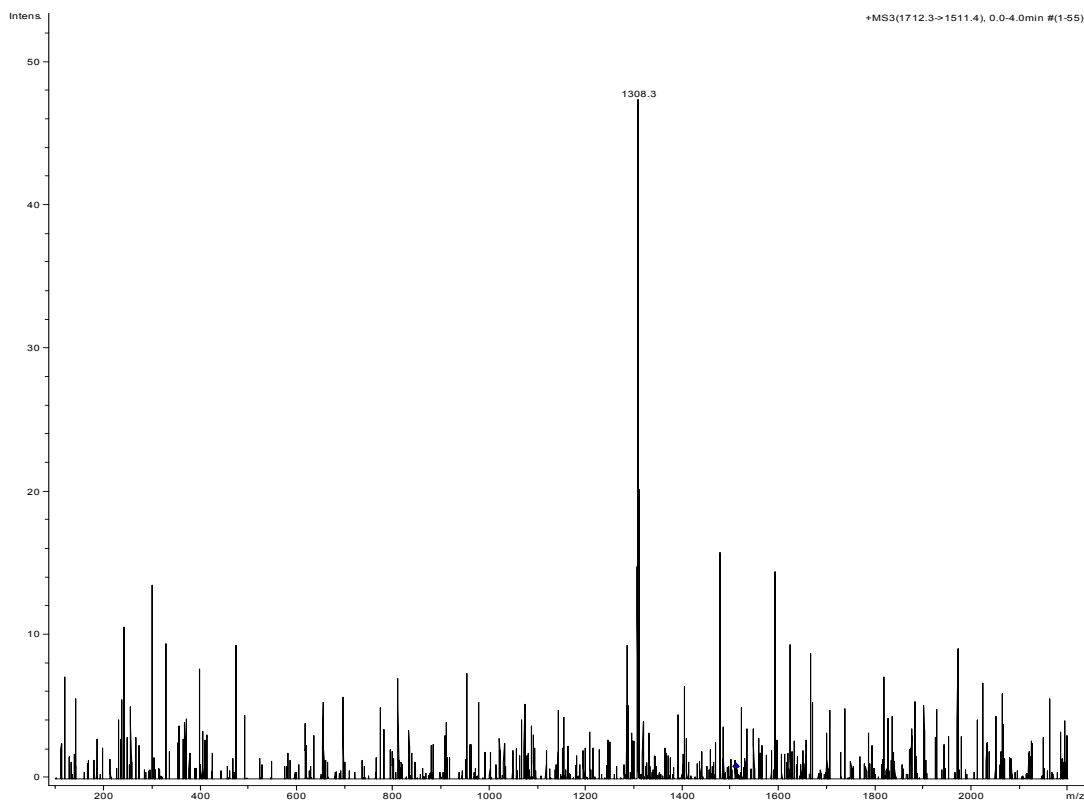
MS/MS of Ag₈MS/MS of Ag₁₁

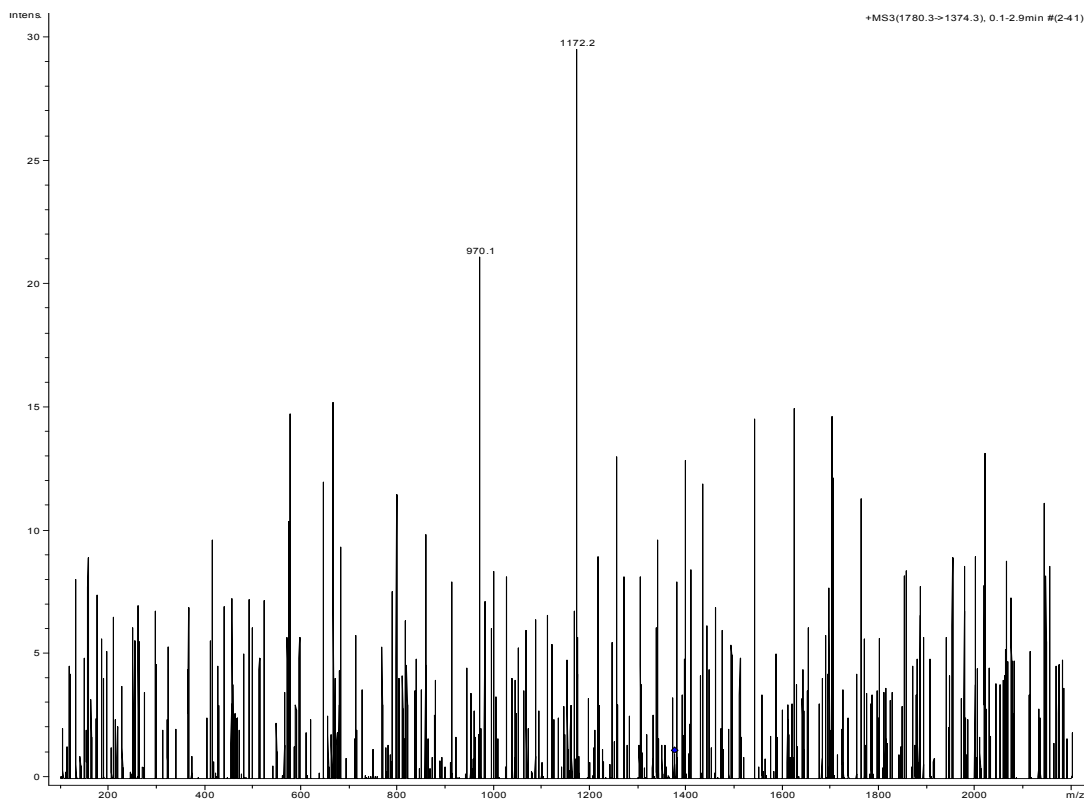
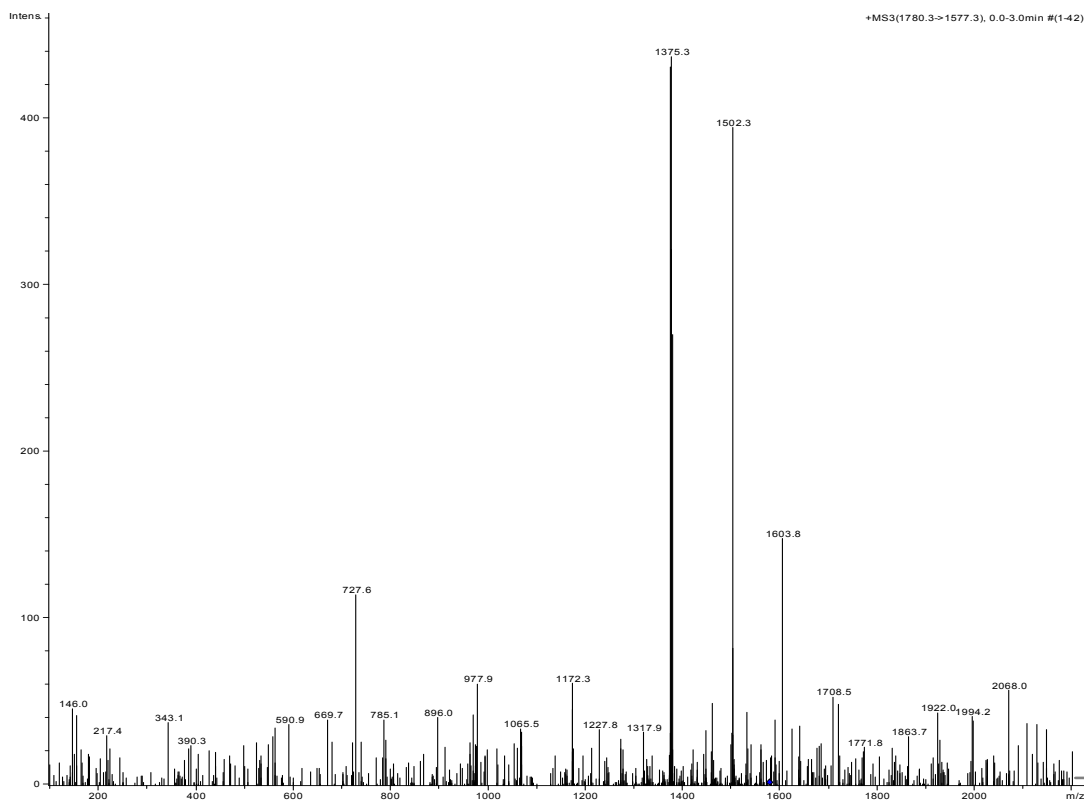
MS/MS of Ag_{17} **MS(3) of the Trp- Ag clusters, positive-ion mode ESI spectra**MS/MS of Ag_4Trp_2 , m/z 836.7; MS(3) of Ag_4Trp , m/z 634.6

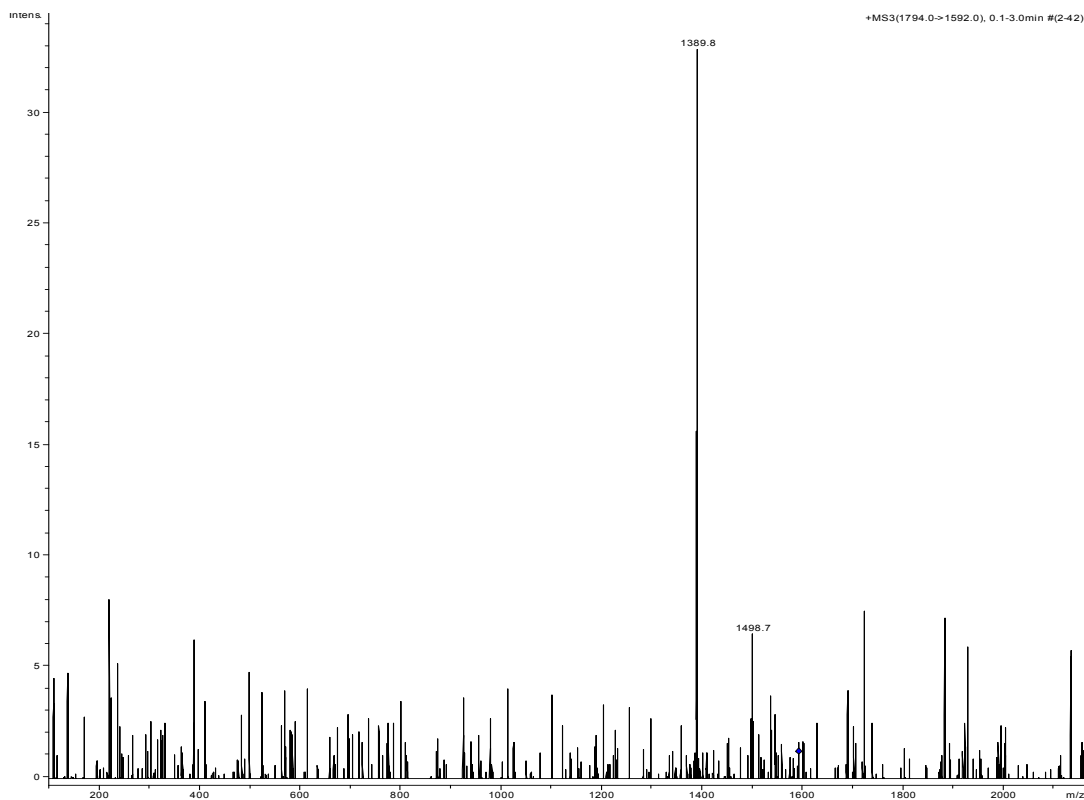
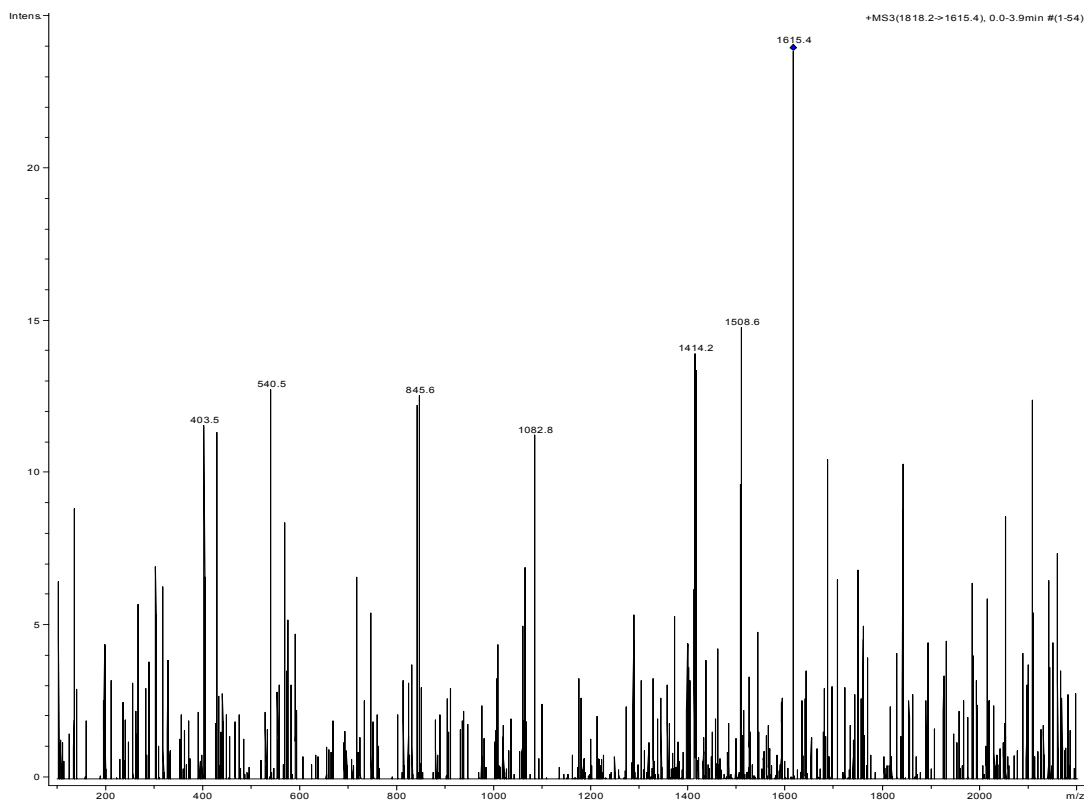
MS/MS of Ag₈Trp, m/z 1064.3; MS(3) of Ag₆Trp, m/z 848.4MS/MS of Ag₆Trp₃, m/z 1254.6; MS(3) of Ag₆Trp, m/z 850.5

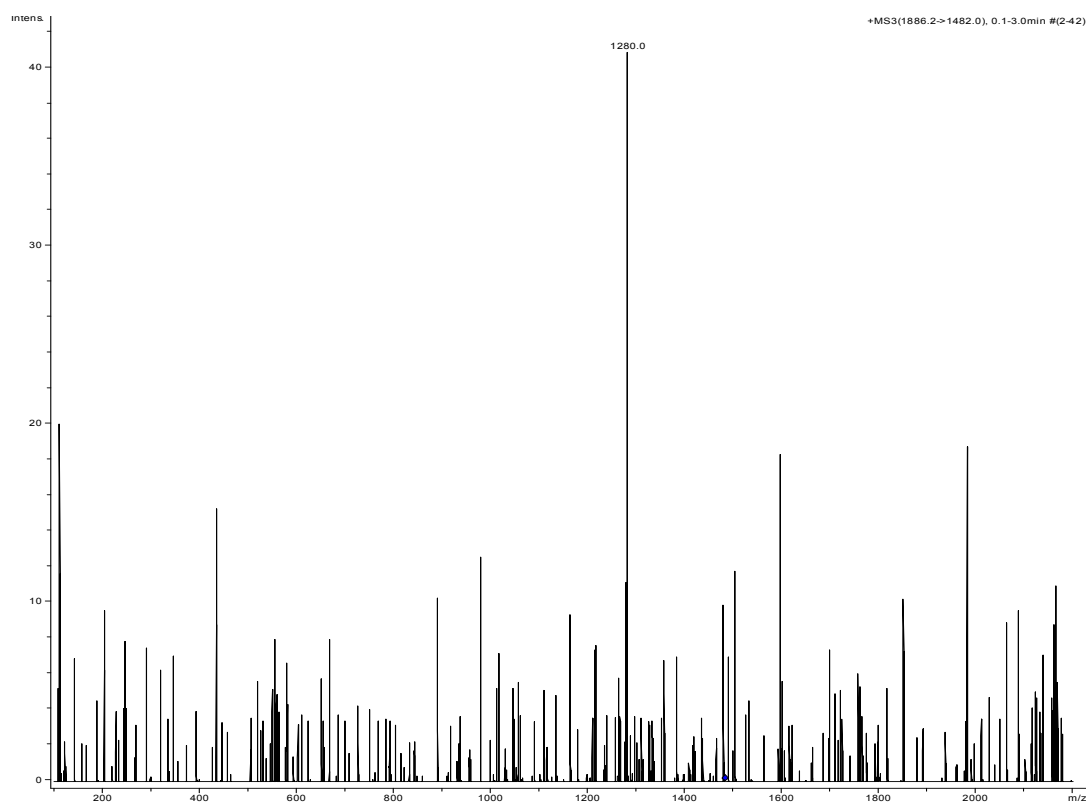
MS/MS of Ag₁₀Trp₂, m/z 1482.1; MS(3) of Ag₁₀Trp, m/z 1280.1MS/MS of Ag₁₂Trp, m/z 1496.6; MS(3) of Ag₁₂, m/z 1292.5

MS/MS of Ag₁₃Trp, m/z 1604.4; MS(3) of Ag₁₃, m/z 1401.6MS/MS of Ag₈Trp₄, m/z 1672.5; MS(3) of Ag₈Trp₃ m/z 1467.4

MS/MS of Ag₁₂Trp₂, m/z 1699.8; MS(3) of Ag₁₂Trp, m/z 1497.9MS/MS of Ag₁₄Trp, m/z 1712.3; MS(3) of Ag₁₄, m/z 1511.4

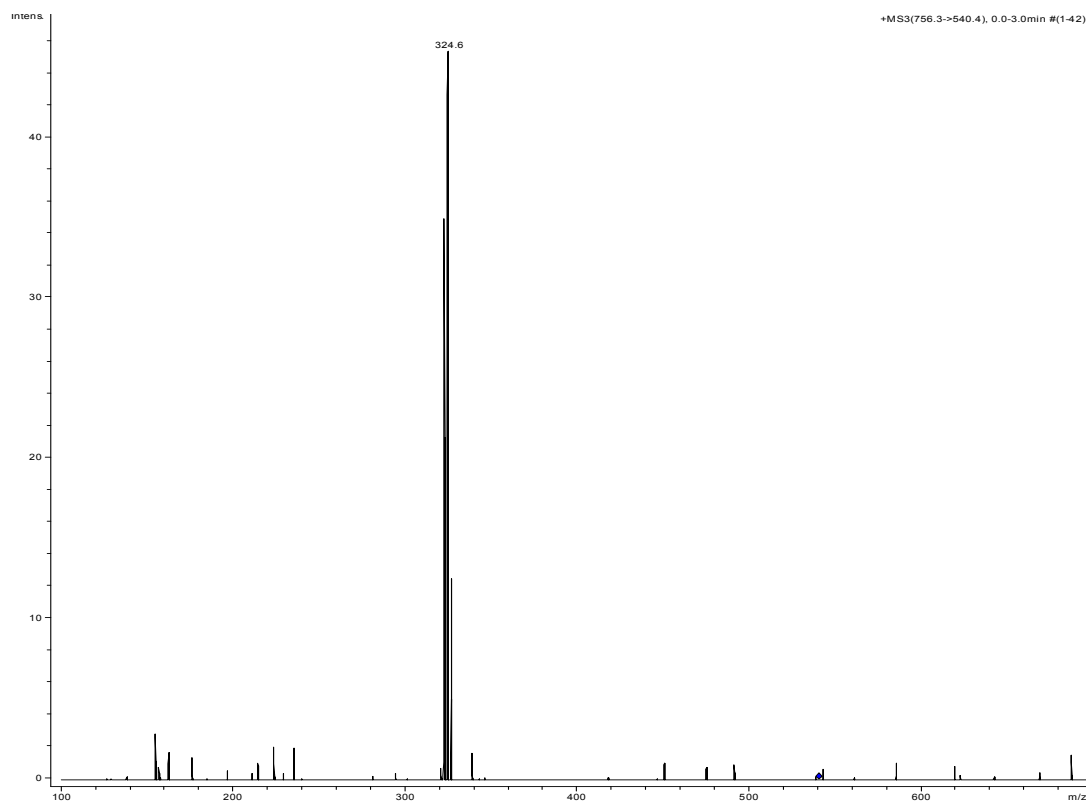
MS/MS of Ag_9Trp_4 , m/z 1780.3; MS(3) of Ag_9Trp_2 , m/z 1374.3MS/MS of Ag_9Trp_4 , m/z 1780.3; MS(3) of Ag_9Trp_3 , m/z 1577.3

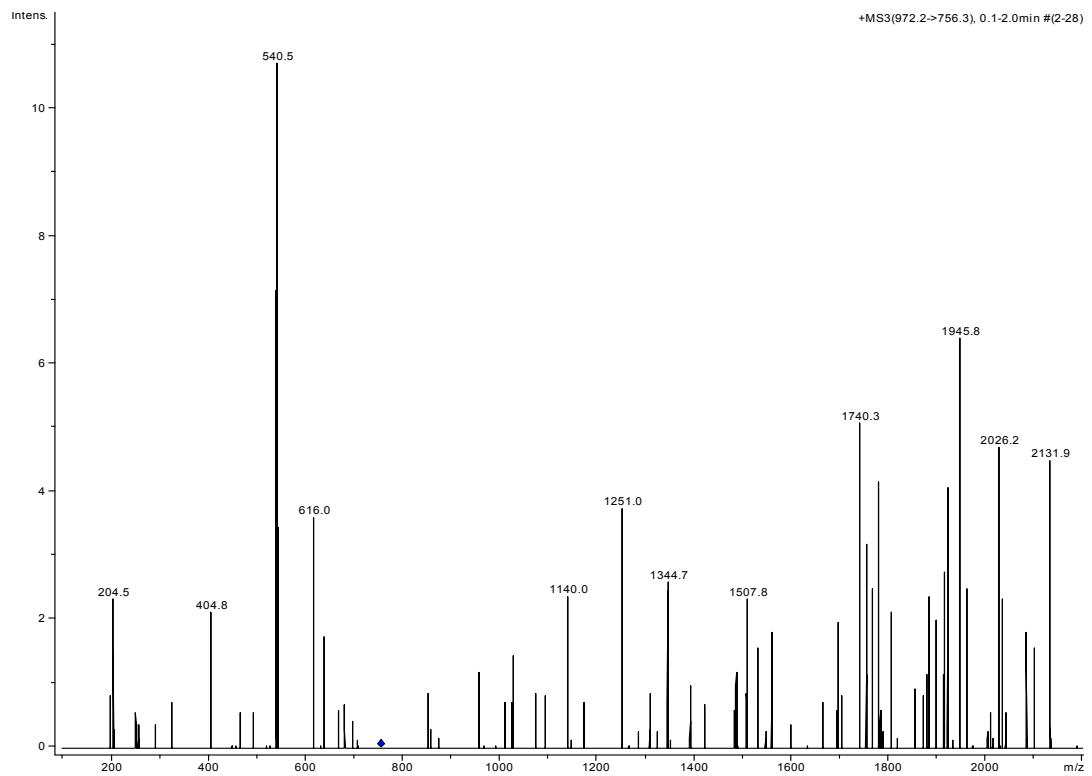
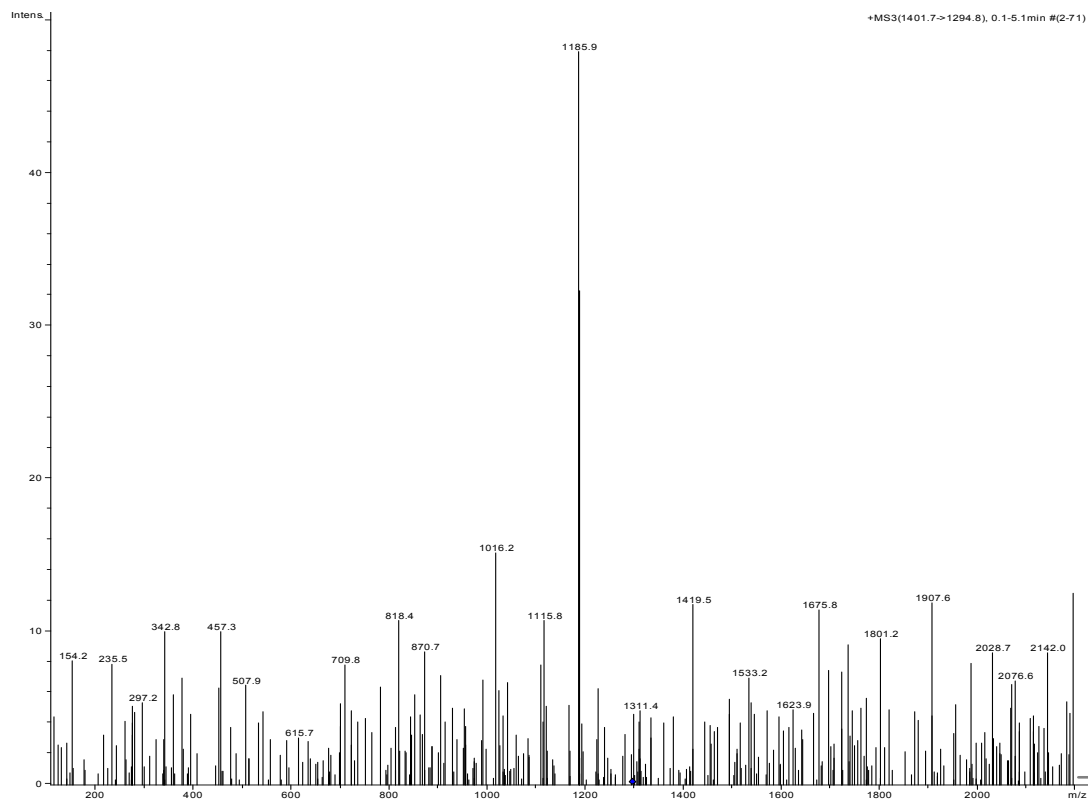
MS/MS of Ag₁₁Trp₃, m/z 1792.0; MS(3) of Ag₁₁Trp₂, m/z 1590.0MS/MS of Ag₁₅Trp, m/z 1818.2; MS(3) of Ag₁₅, m/z 1615.4



MS/MS of $\text{Ag}_{10}\text{Trp}_4$, m/z 1886.2; MS(3) of $\text{Ag}_{10}\text{Trp}_2$, m/z 1482.0

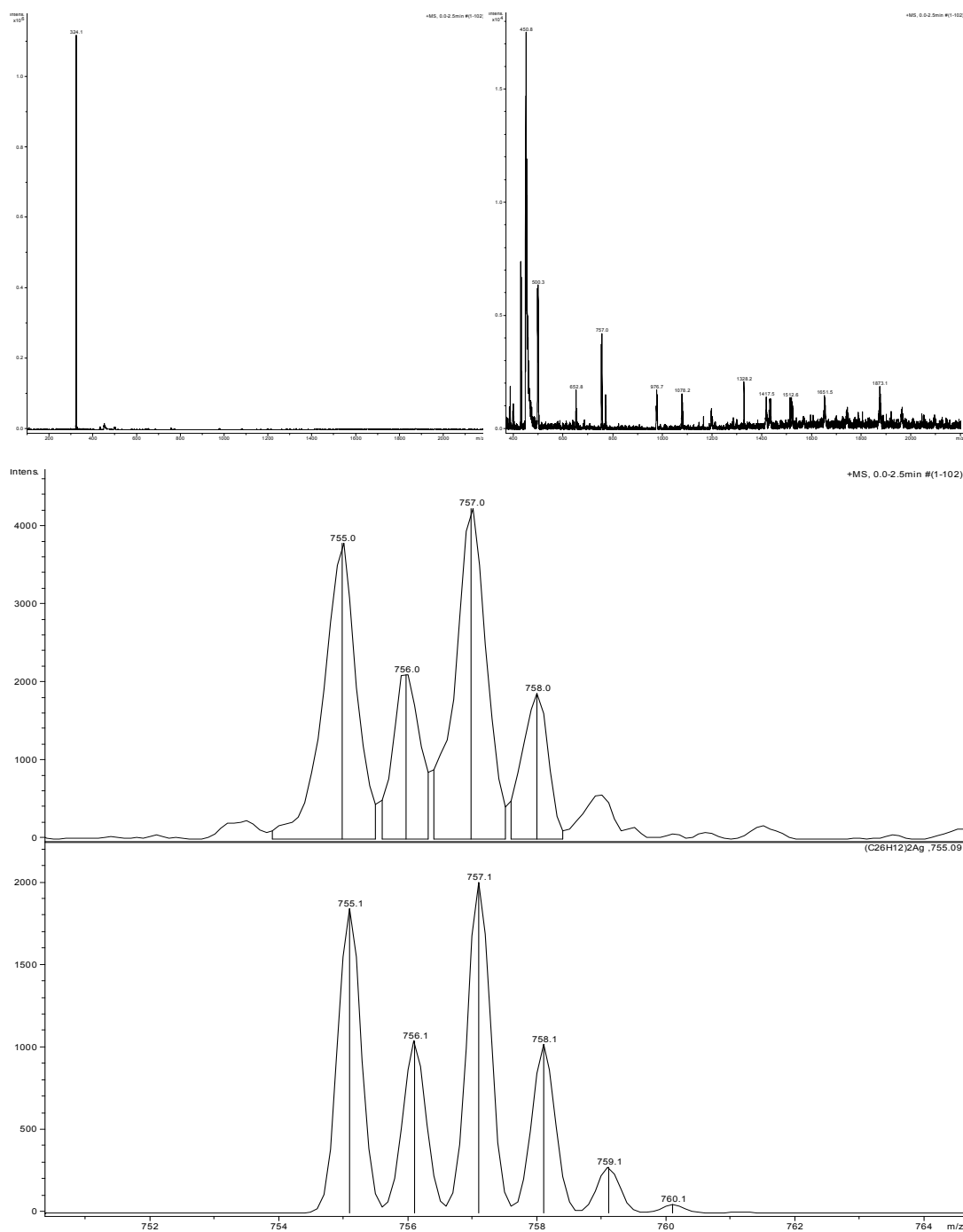
MS(3) of Silver clusters, positive-ion mode ESI spectra

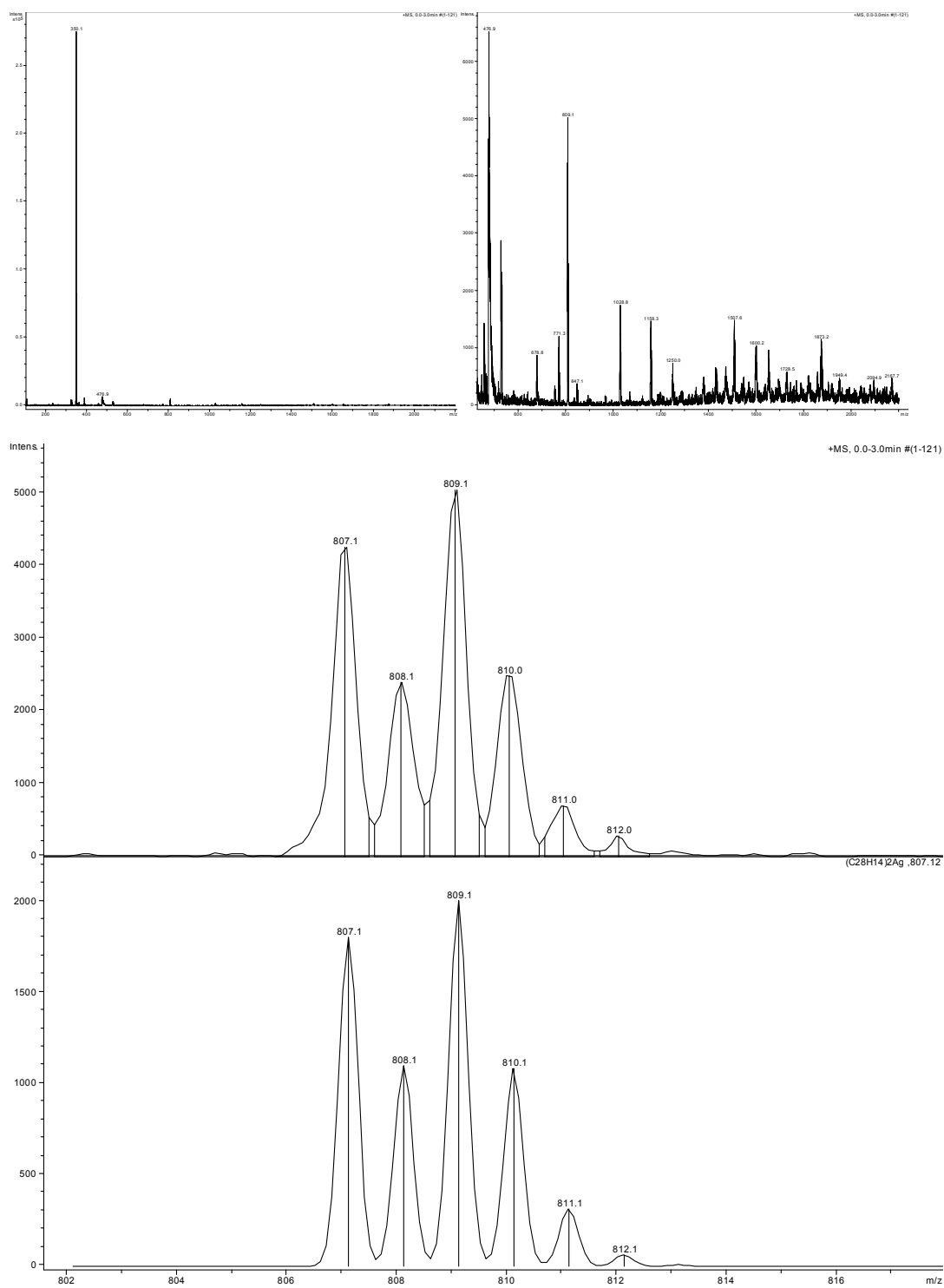


MS/MS of Ag₇, m/z 754.4; MS(3) of Ag₅, m/z 538.5MS/MS of Ag₉, m/z 972.2, MS(3) of Ag₇, m/z 756.3MS/MS of Ag₁₃, m/z 1401.8, MS(3) of Ag₁₂, m/z 1294.8

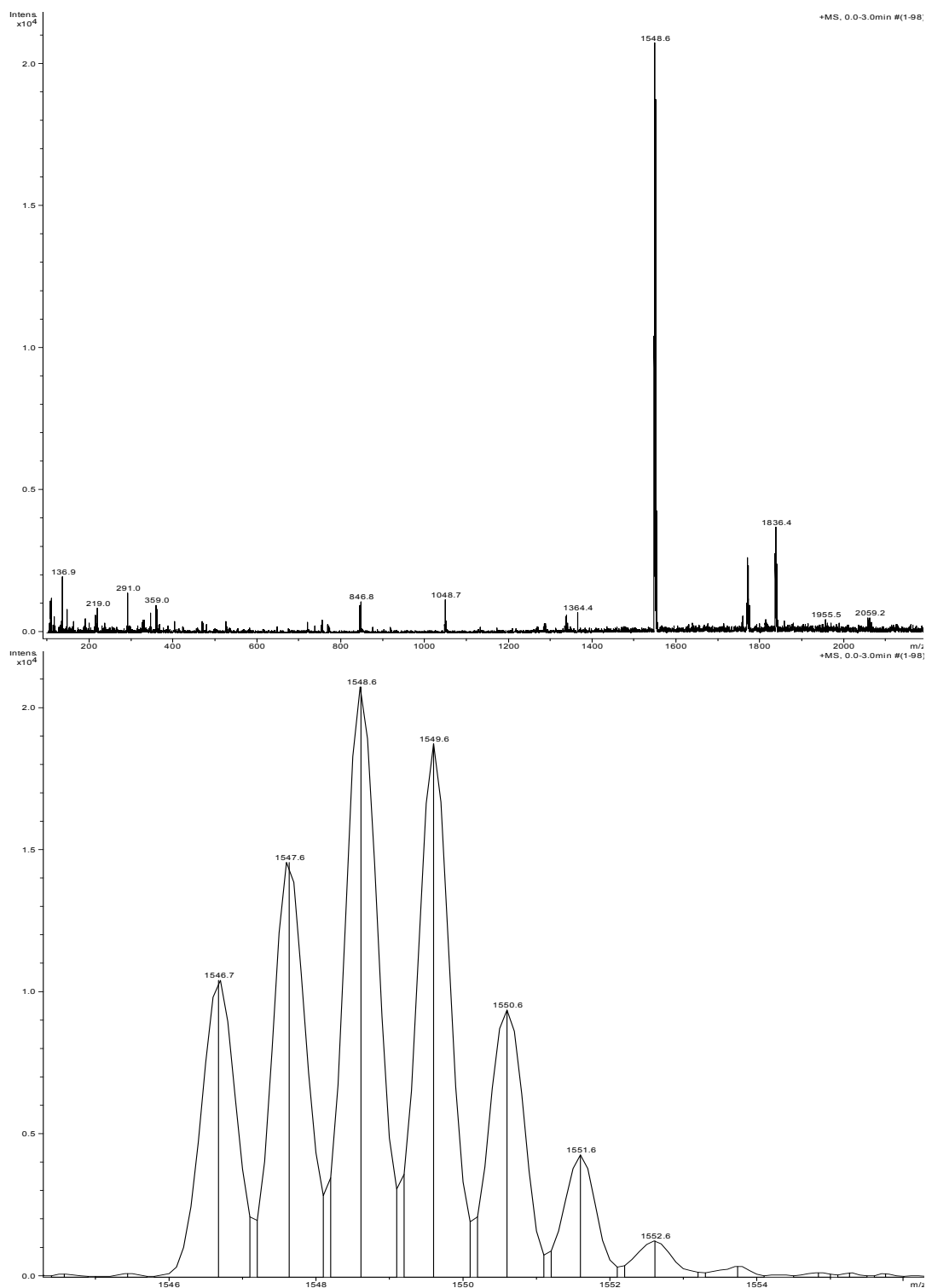
Chapter 8 Additional Spectra

Homo-dimer formation with silver, positive-ion mode ESI spectra

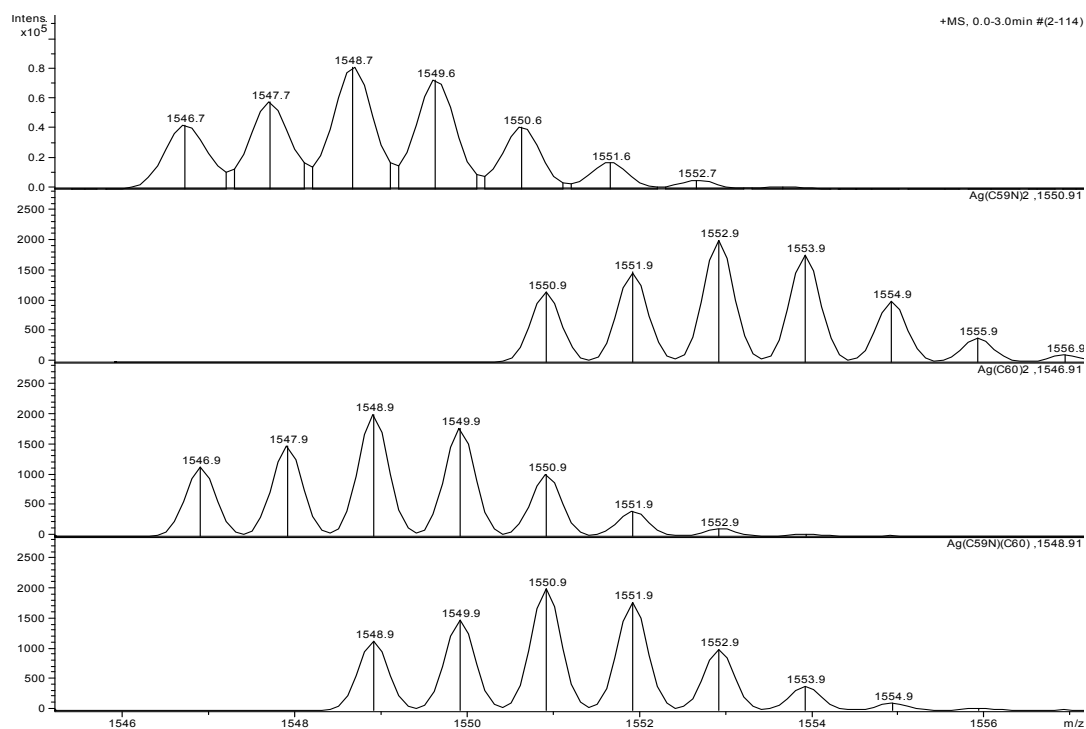
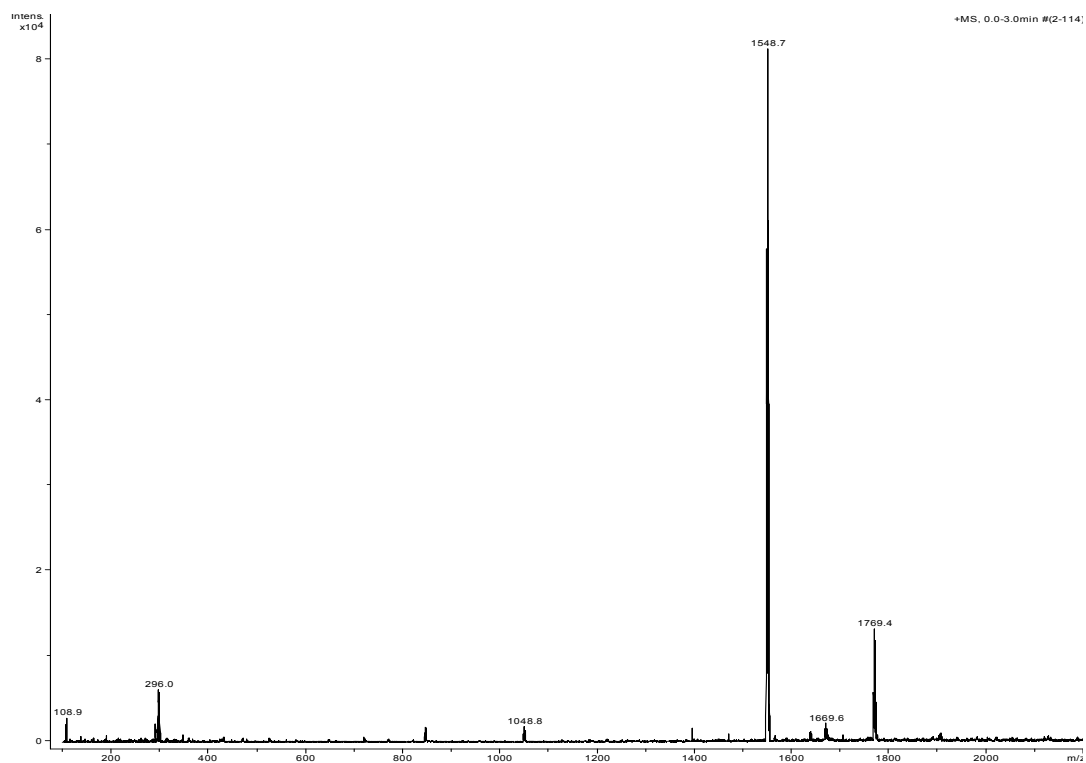
 $C_{26}H_{12}$:

$C_{28}H_{14}$:

Top left: full spectrum; top right: spectrum from m/z 450; bottom: actual and simulated spectrum of $[C_{28}H_{12}AgC_{28}H_{12}]^+$

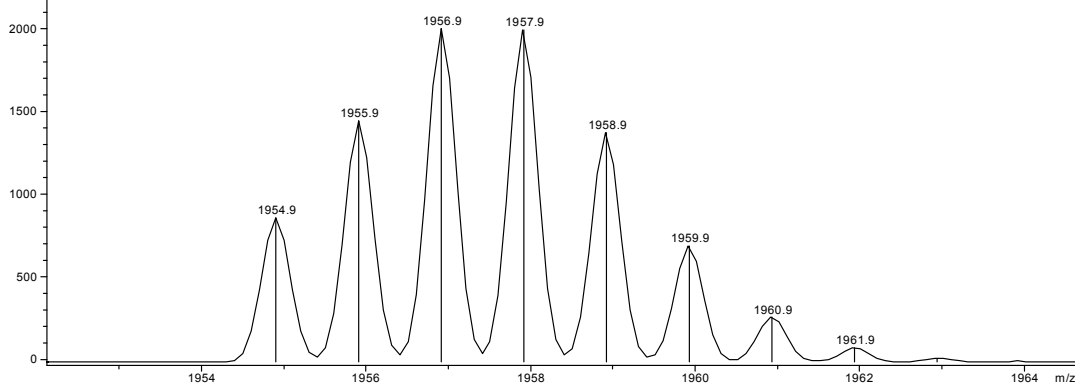
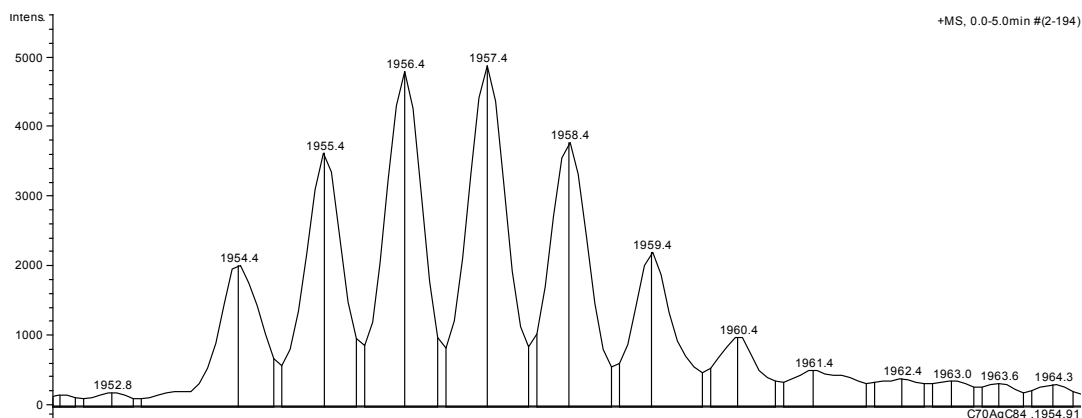
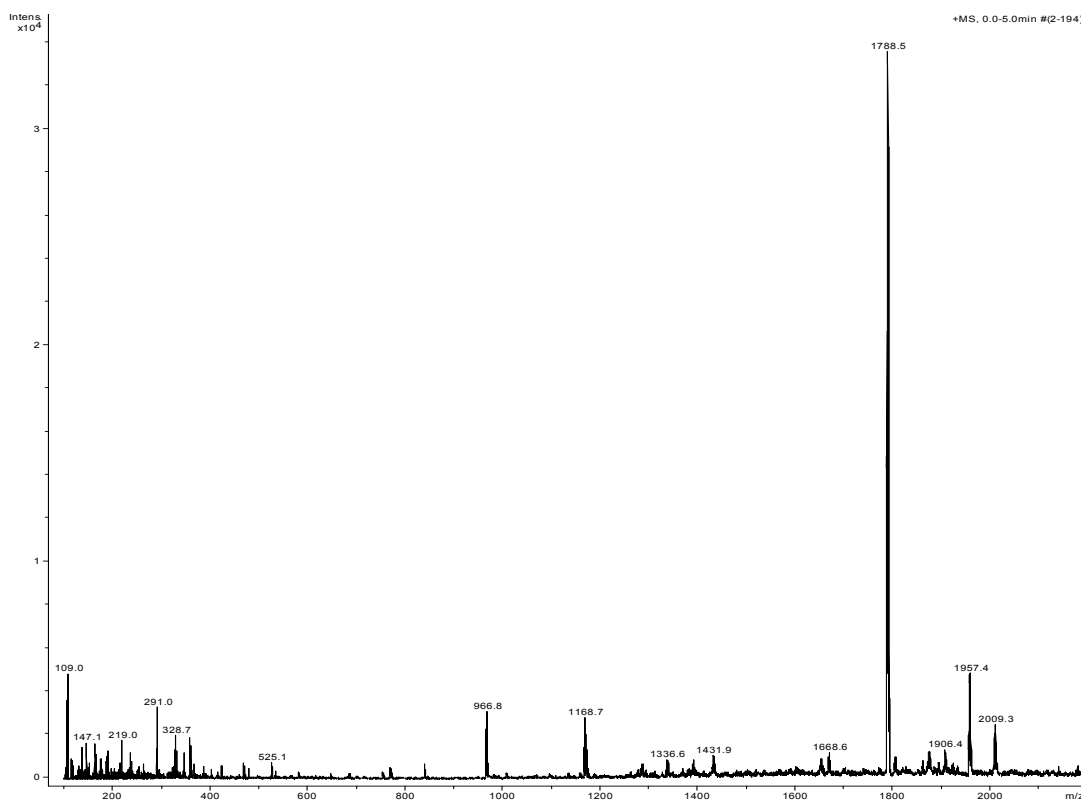
Hetero-dimer formation with silver, positive-ion mode ESI spectra C_{60} , C_{84} and Ag:Top: full spectrum; bottom: Isotopic pattern of $[C_{60}AgC_{84}]^+$

C_{60} , $C_{59}N$ and Ag:



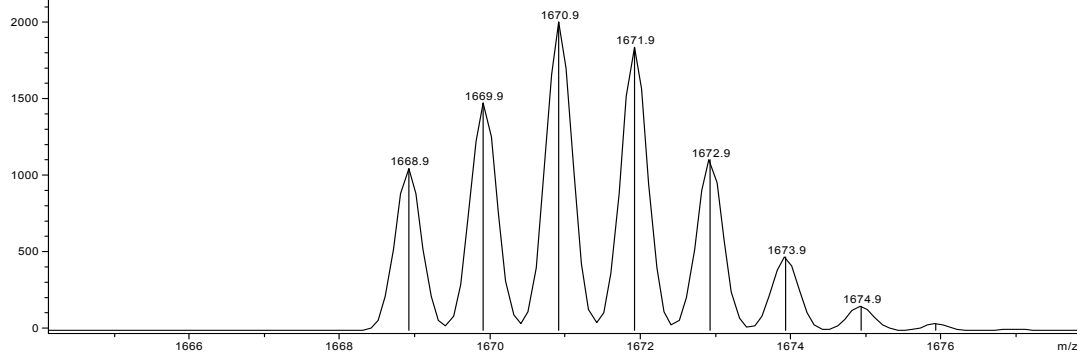
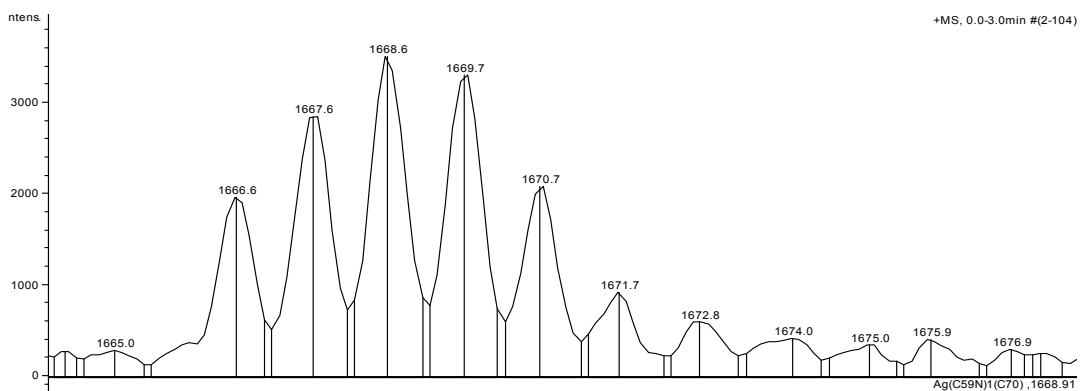
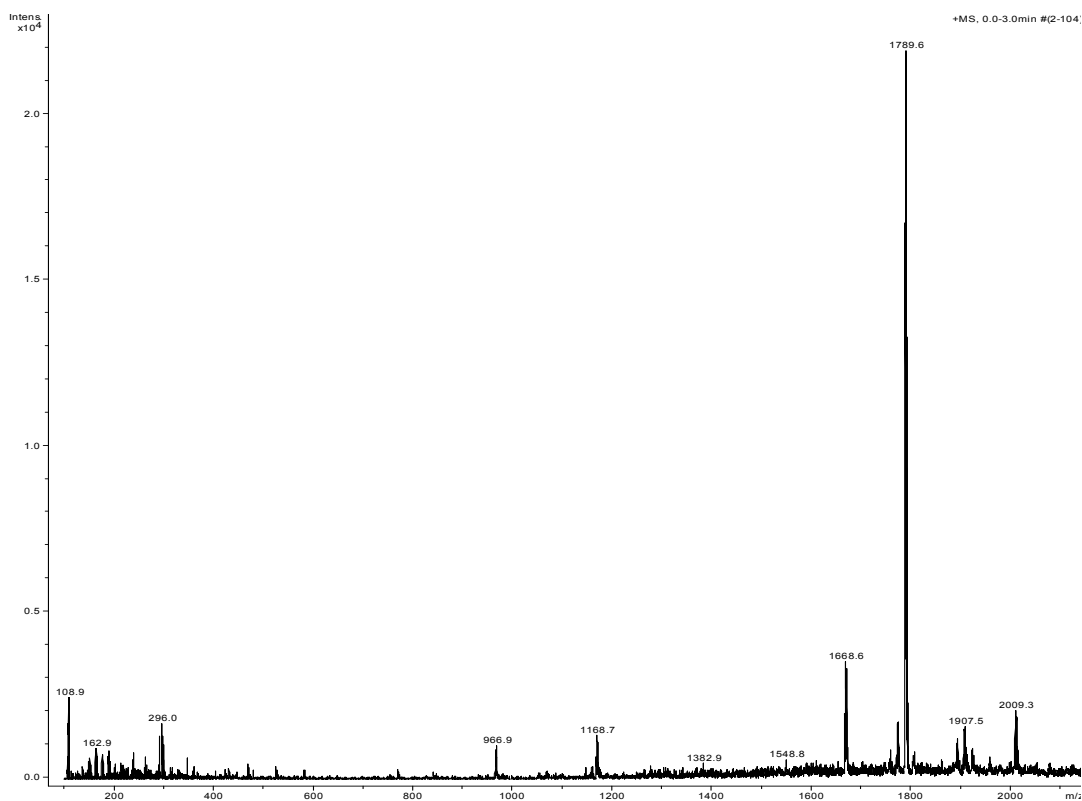
Top: full spectrum; bottom: isotopic pattern of $[C_{60}AgC_{59}N]^+$, with simulated patterns top to bottom: $[(C_{59}N)_2Ag]$, $[(C_{60})_2Ag]^+$, $[C_{60}AgC_{59}N]^+$

C₇₀, C₈₄ and Ag:

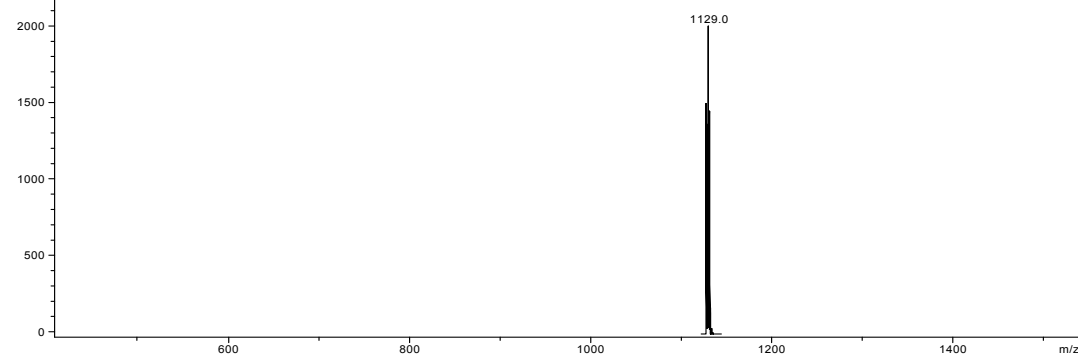
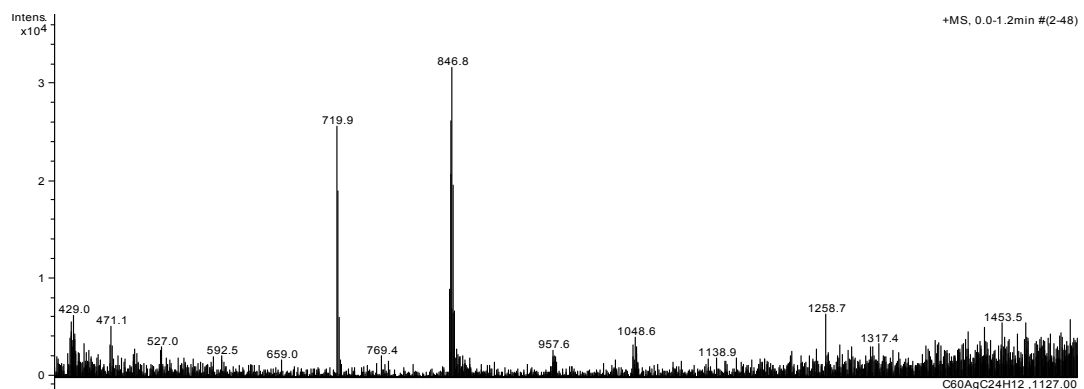
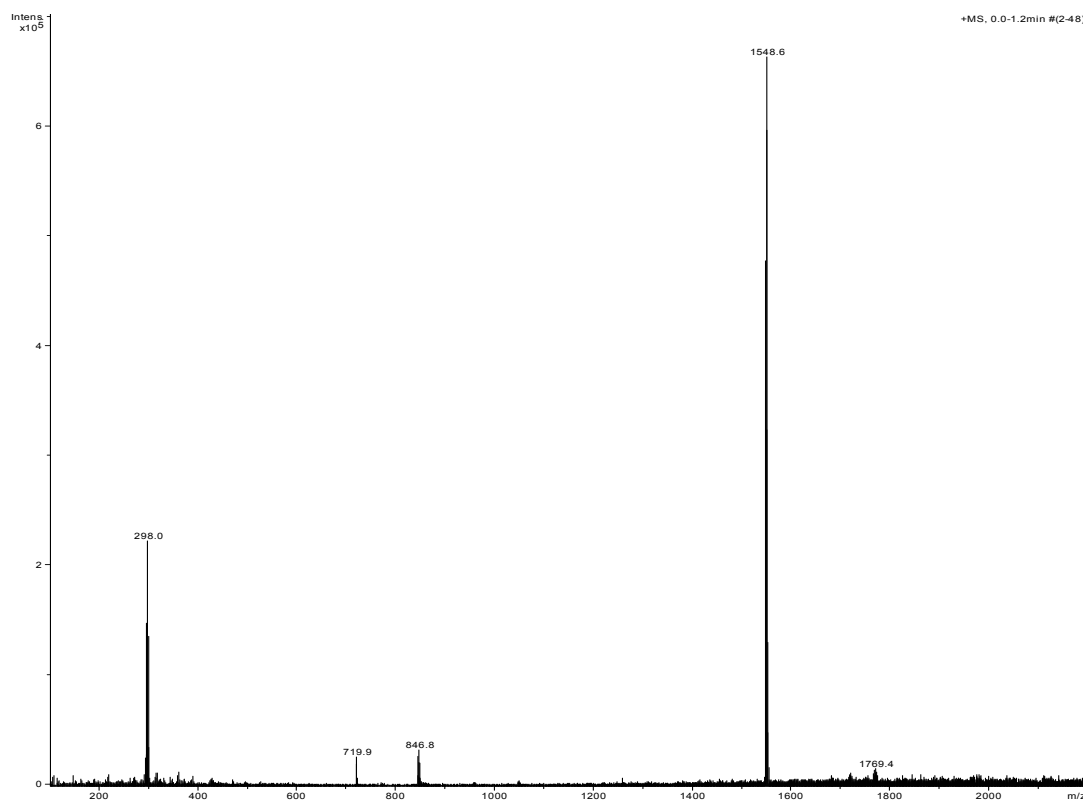


Top: full spectrum, bottom: actual and simulated isotopic pattern of [C₇₀AgC₈₄]⁺

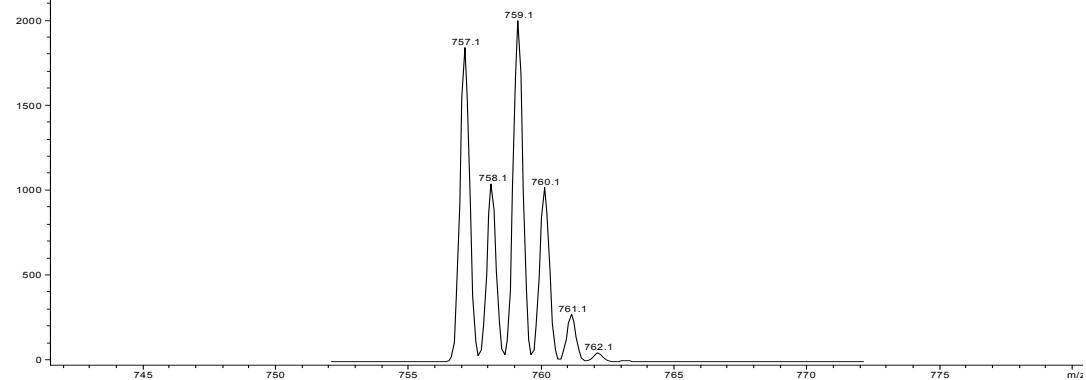
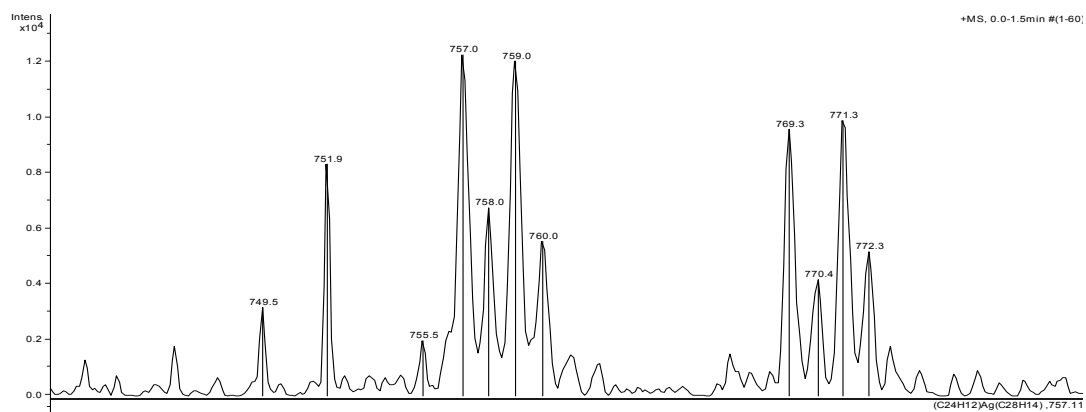
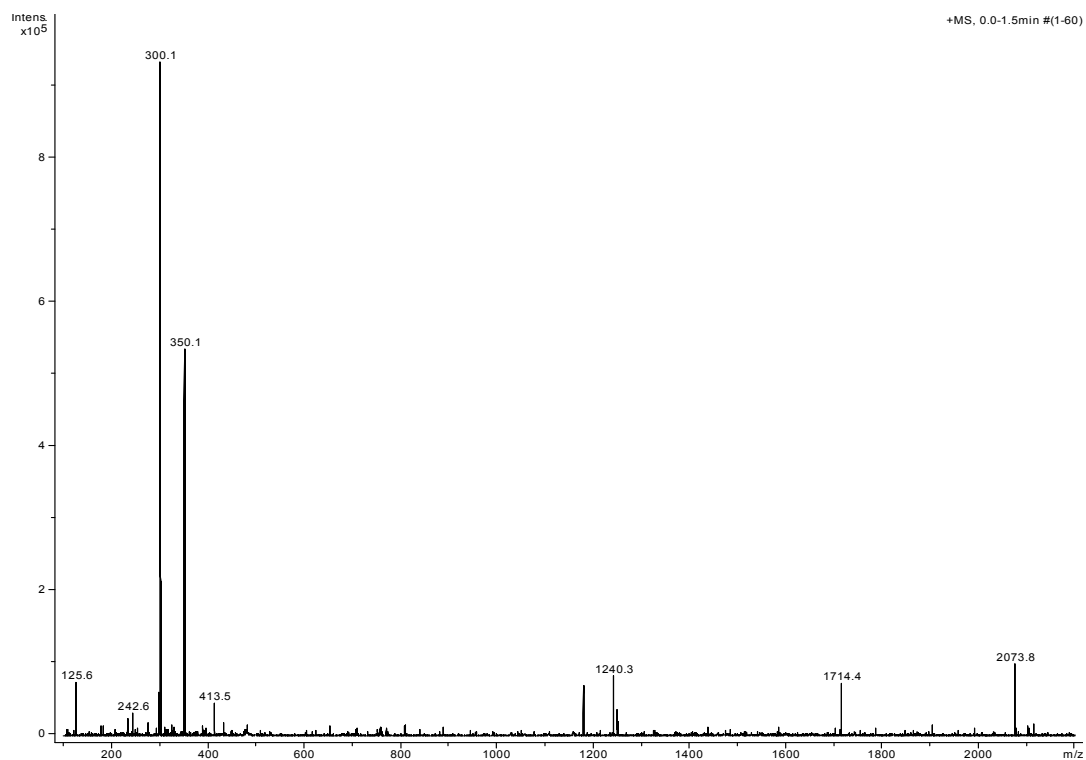
C₇₀, C₅₉N and Ag:



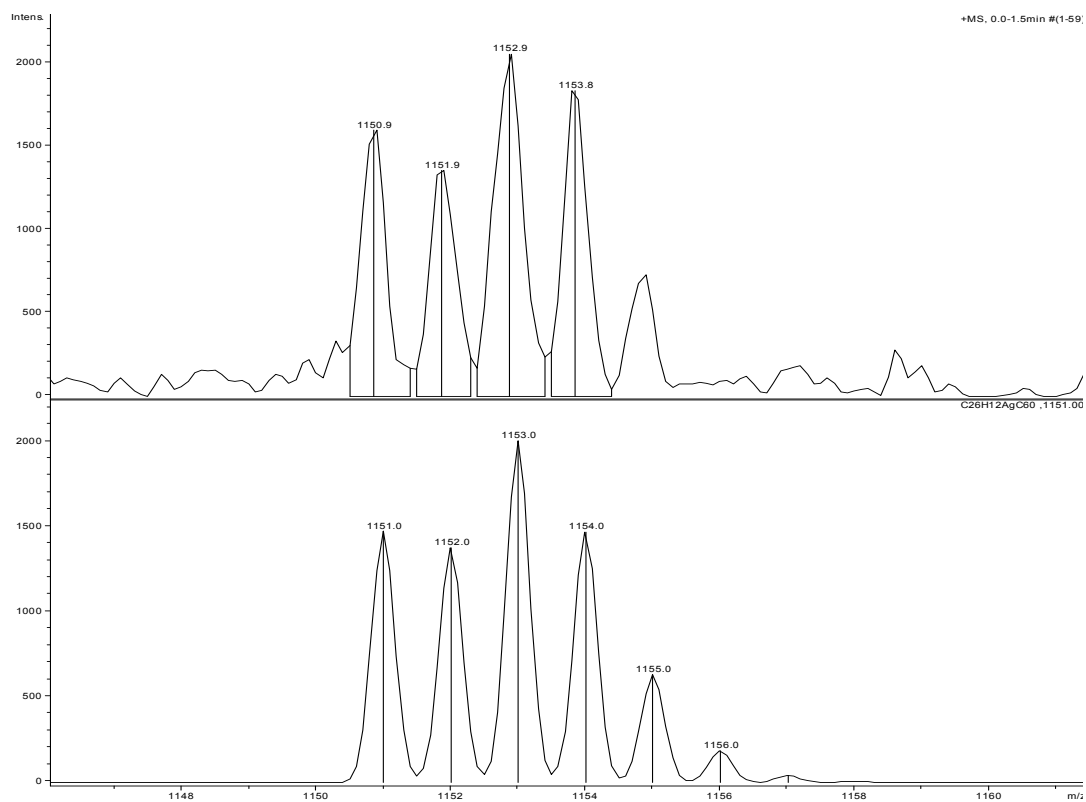
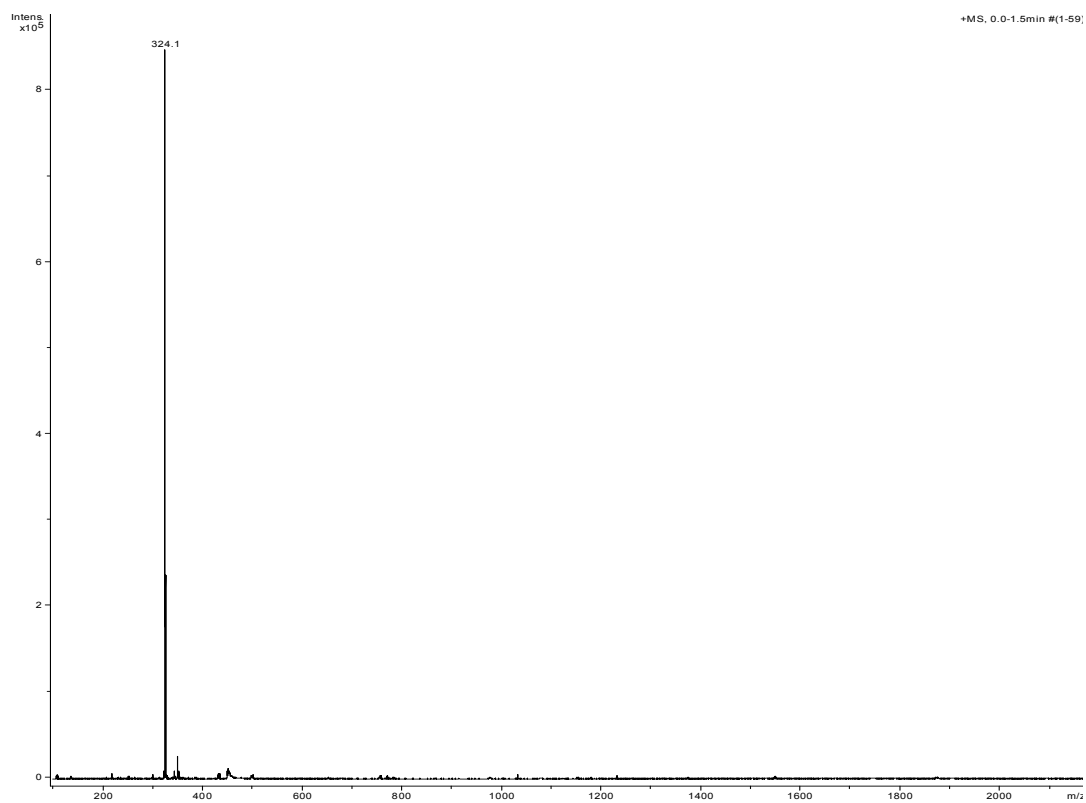
Top: full spectrum, bottom: actual and simulated pattern of [C₅₉NAgC₇₀]⁺

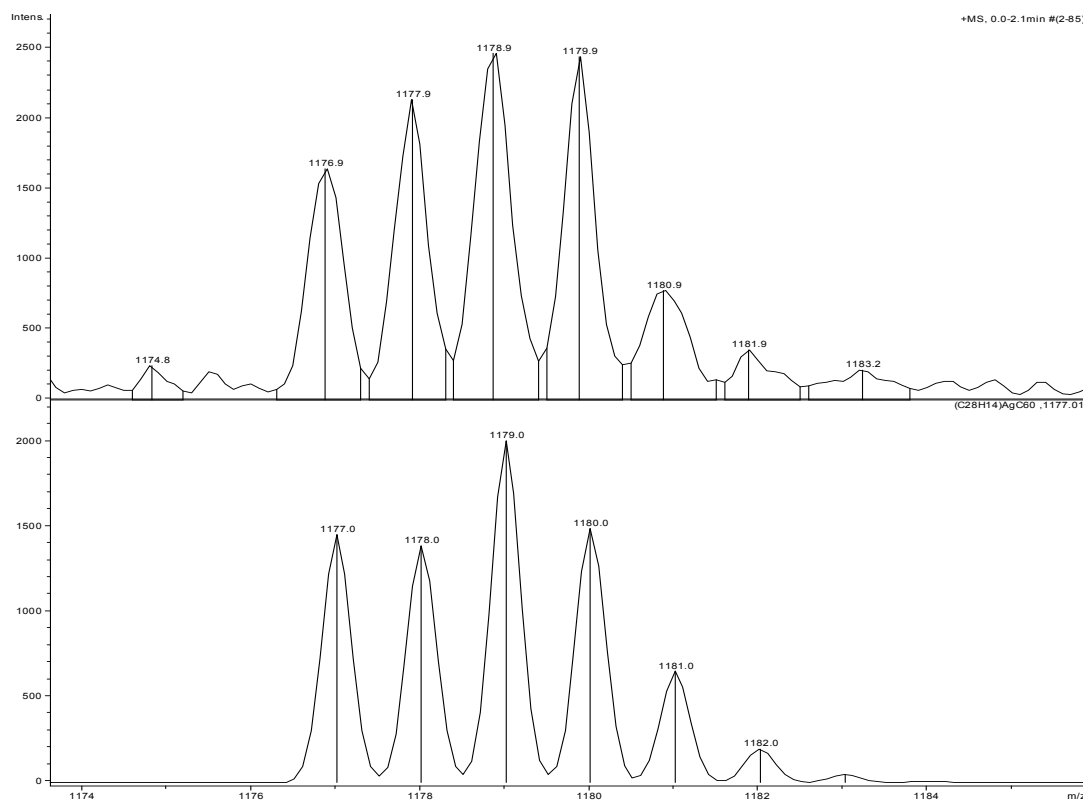
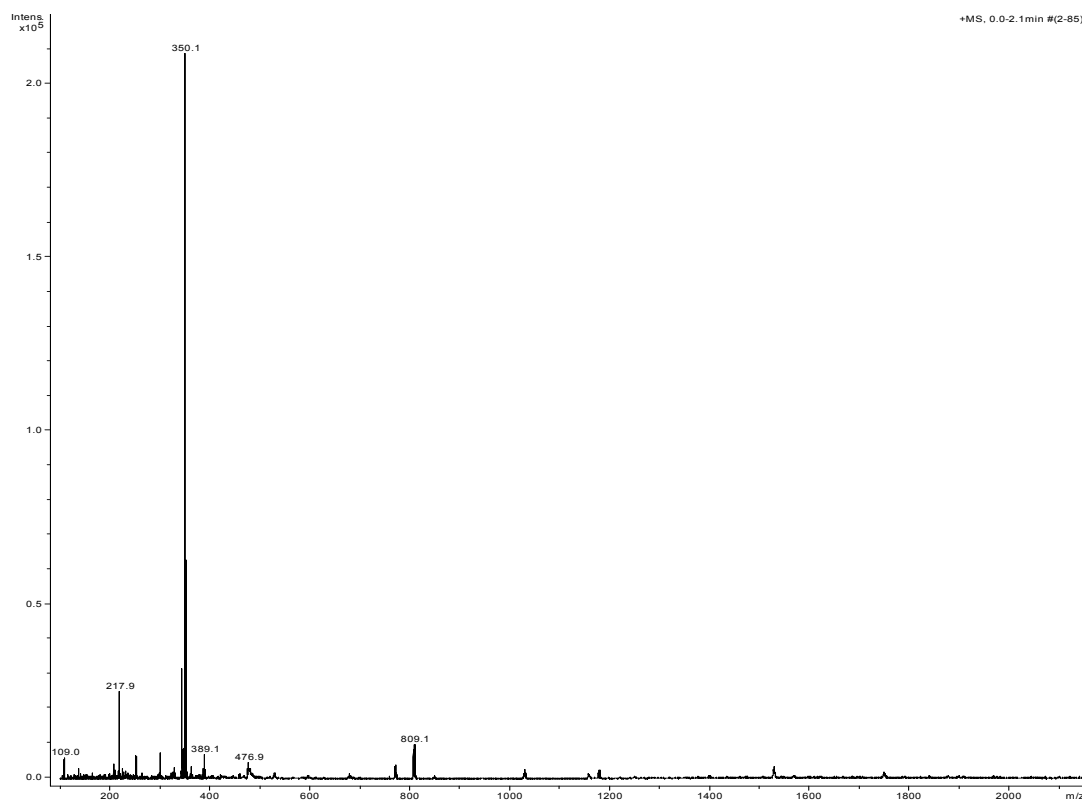
Coronene (C₂₄H₁₂), C₆₀ and Ag:

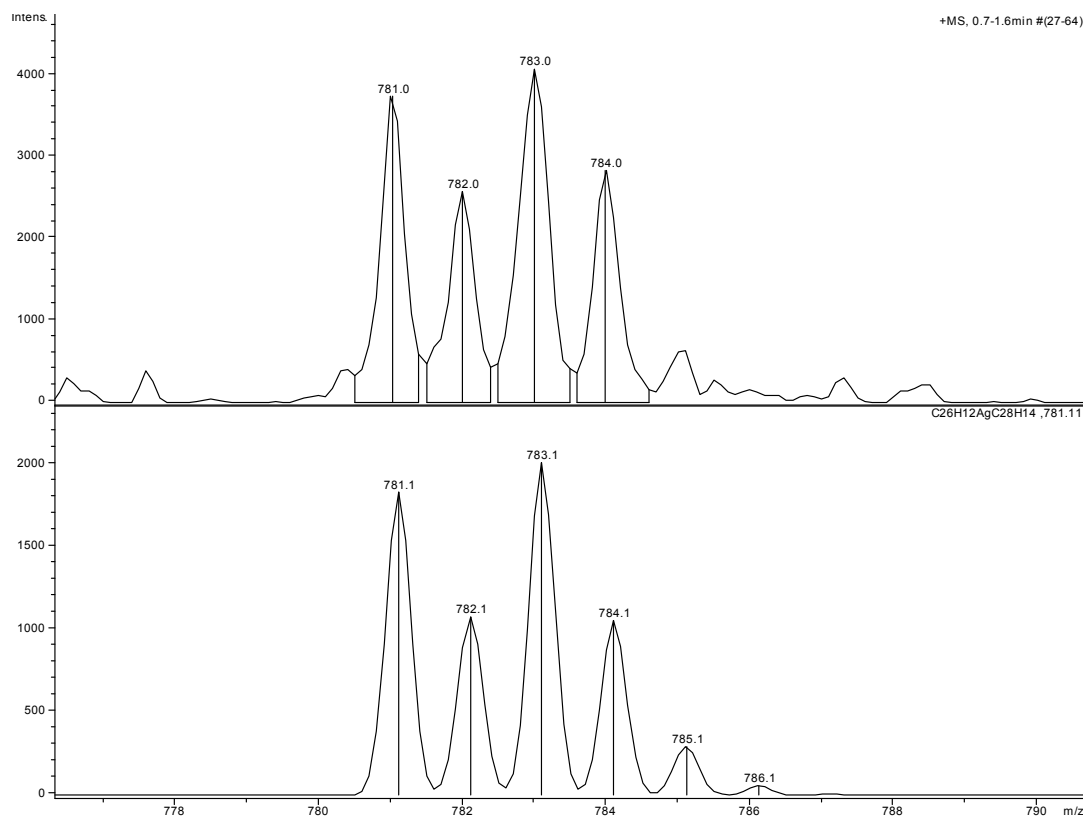
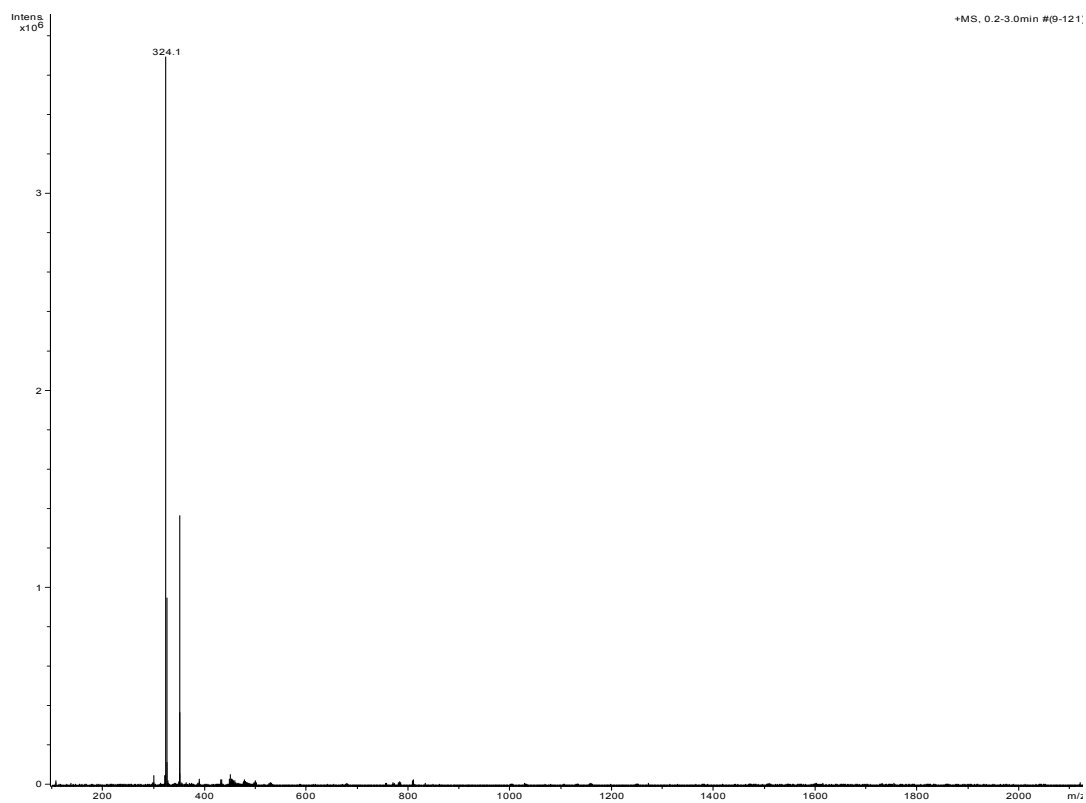
Top: full mass spectrum of C₆₀ and coronene, bottom, actual and simulated mass spectrum of [C₆₀AgC₂₄H₁₂]⁺

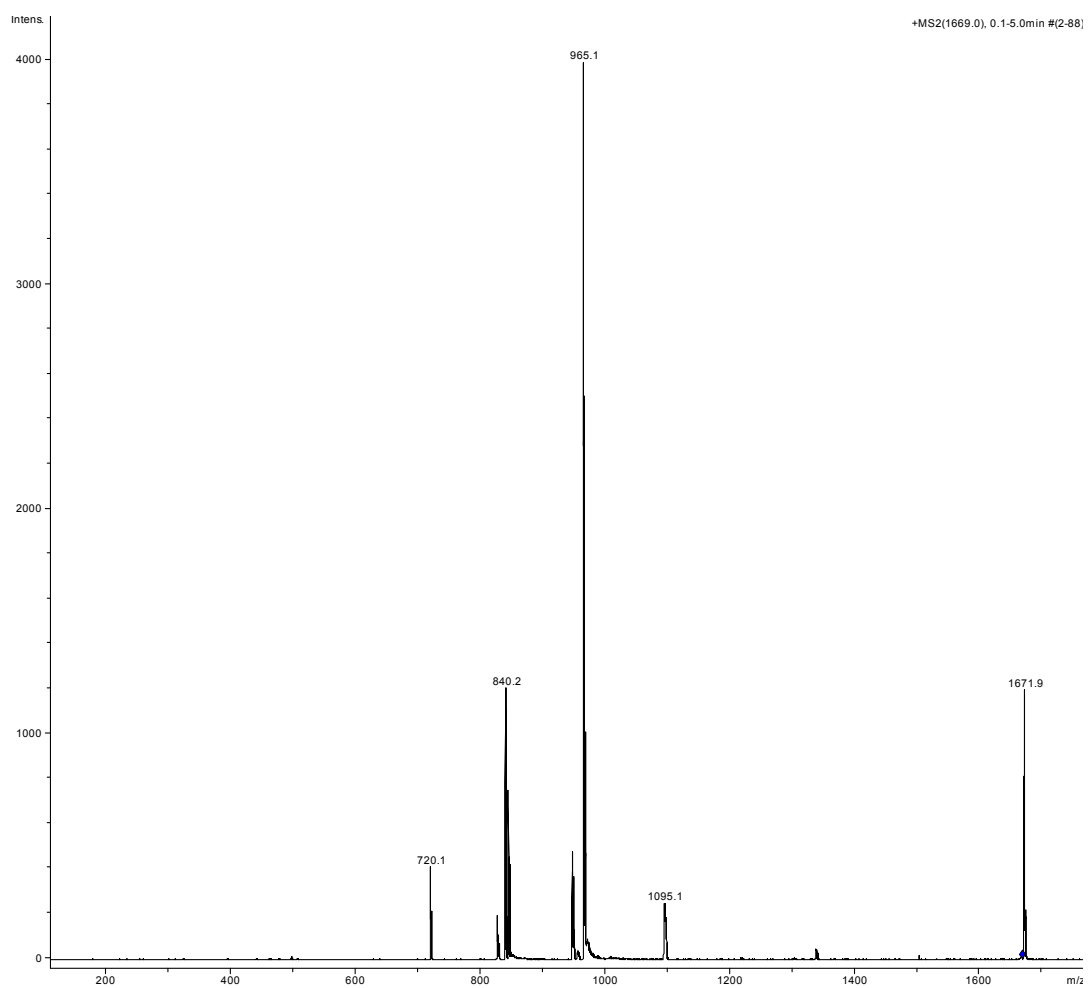
Coronene, C₂₈H₁₄ and Ag:

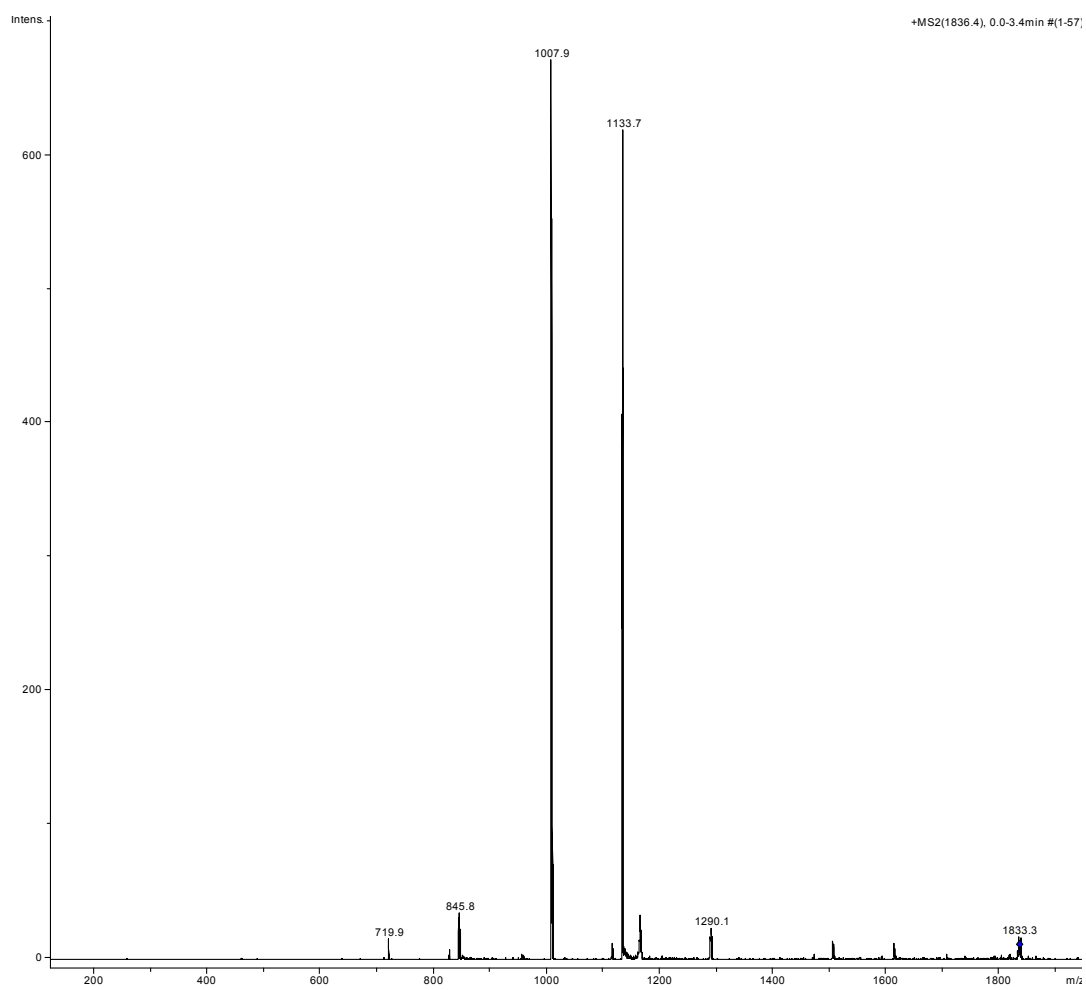
Top: full mass spectrum, bottom: actual and simulated mass spectrum of [C₂₄H₁₂AgC₂₈H₁₄]⁺

C_{60} , $C_{26}H_{12}$ and Ag:Top: full mass spectrum, bottom: actual and simulated mass spectrum of $[C_{60}AgC_{24}H_{12}]^+$

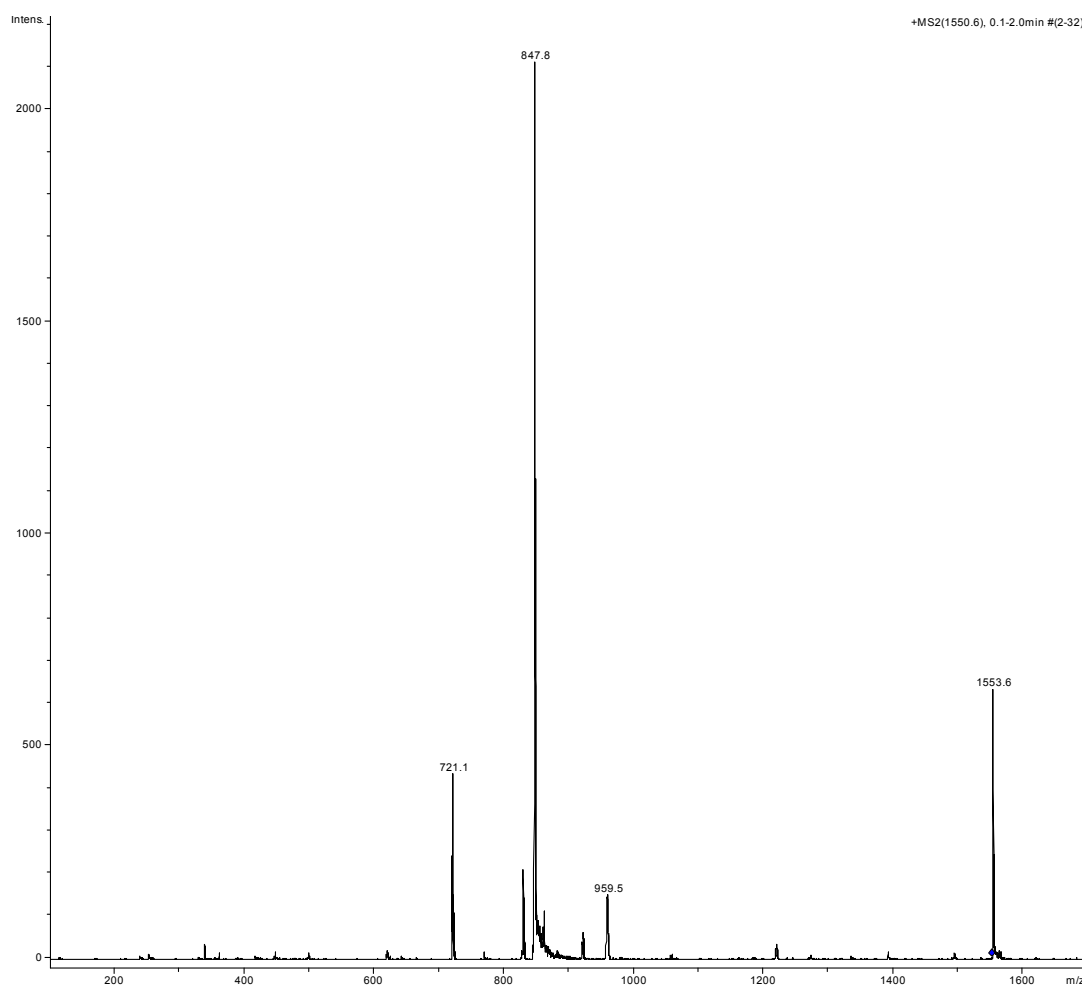
C_{60} , $C_{28}H_{14}$ and Ag:Top: full mass spectrum, bottom: actual and simulated mass spectrum of $[C_{60}AgC_{28}H_{14}]^+$

$C_{26}H_{12}$, $C_{28}H_{14}$ and Ag:Top: full mass spectrum, bottom: actual and simulated mass spectrum of $[C_{26}H_{12}AgC_{28}H_{14}]^+$

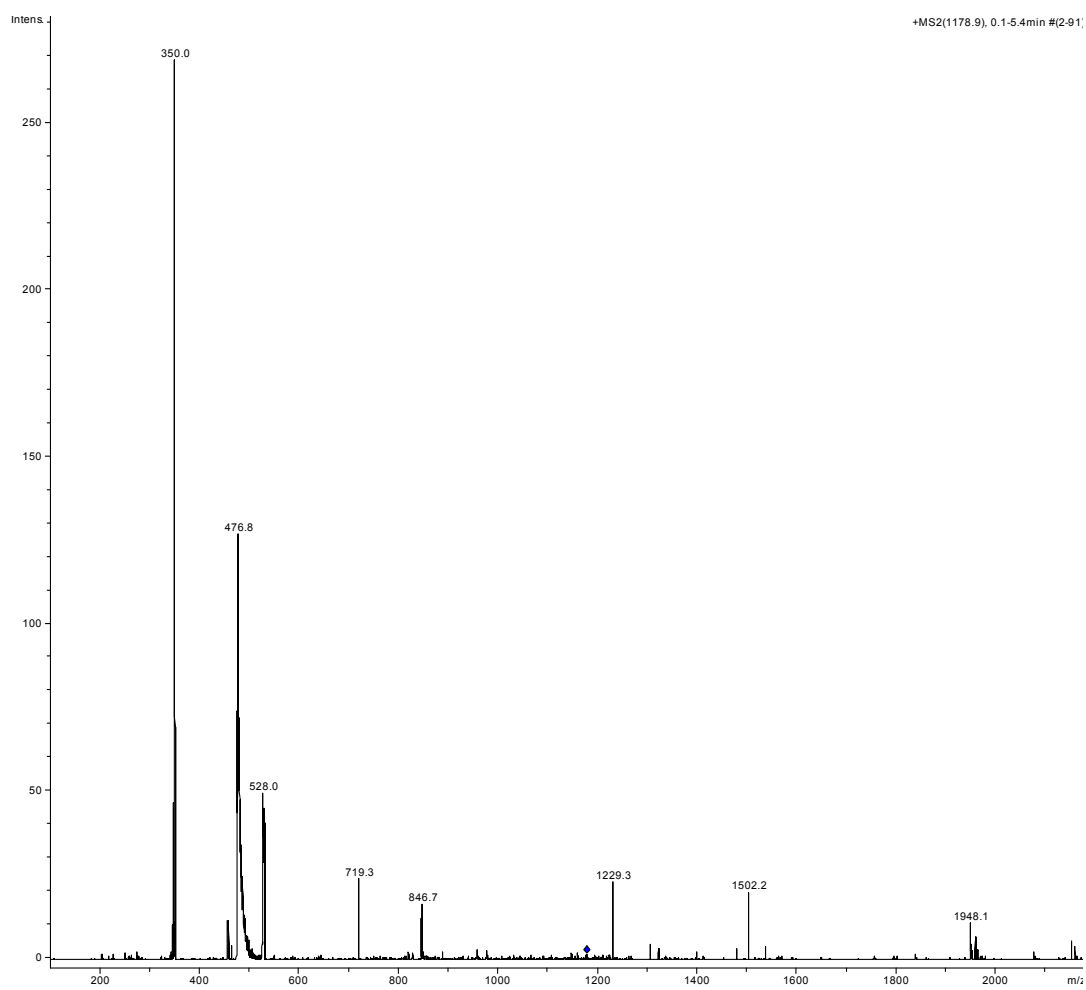
CID of the silver bound hetero-dimers, positive-ion mode ESI spectra C_{60} , C_{70} , and Ag:MS/MS of $[C_{60}AgC_{70}]^+$

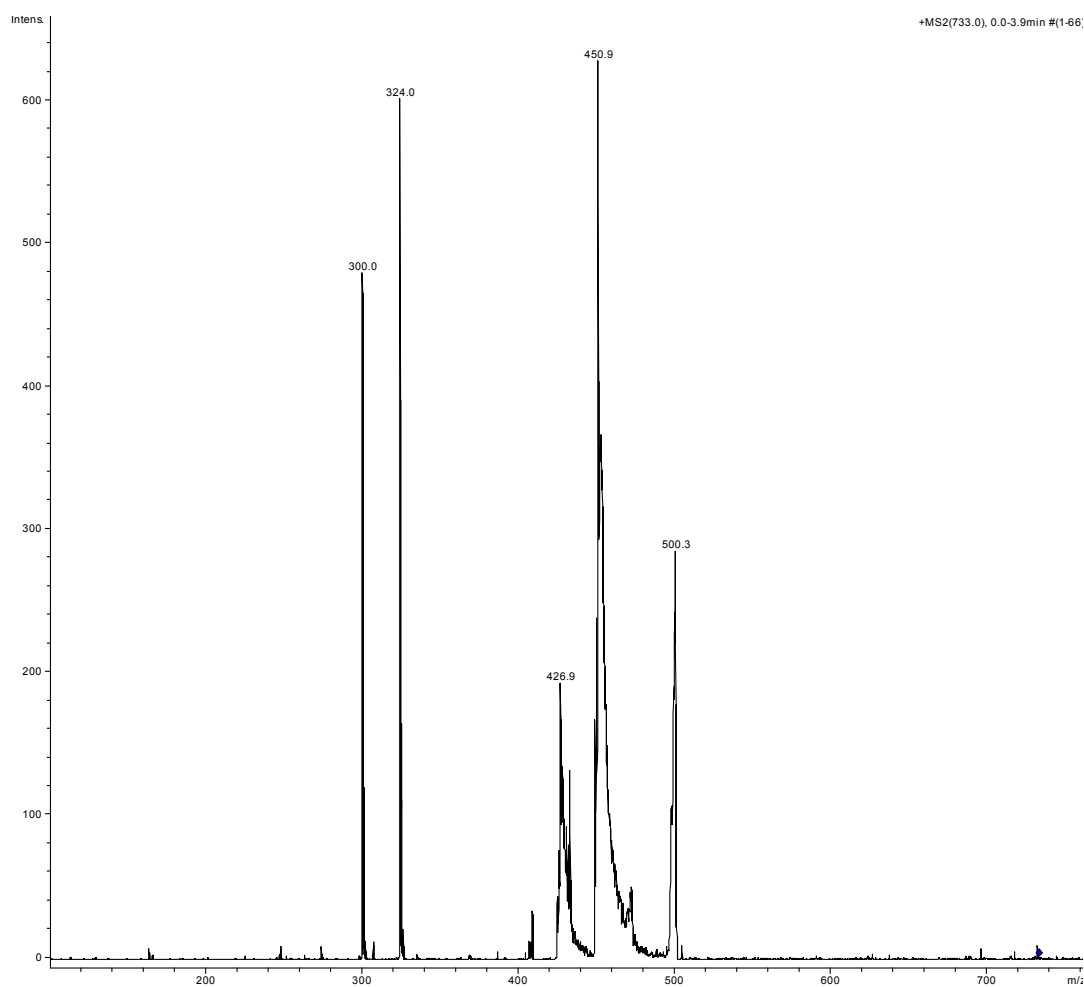
C_{60} , C_{84} and Ag:MS/MS of $[C_{60}AgC_{84}]^+$

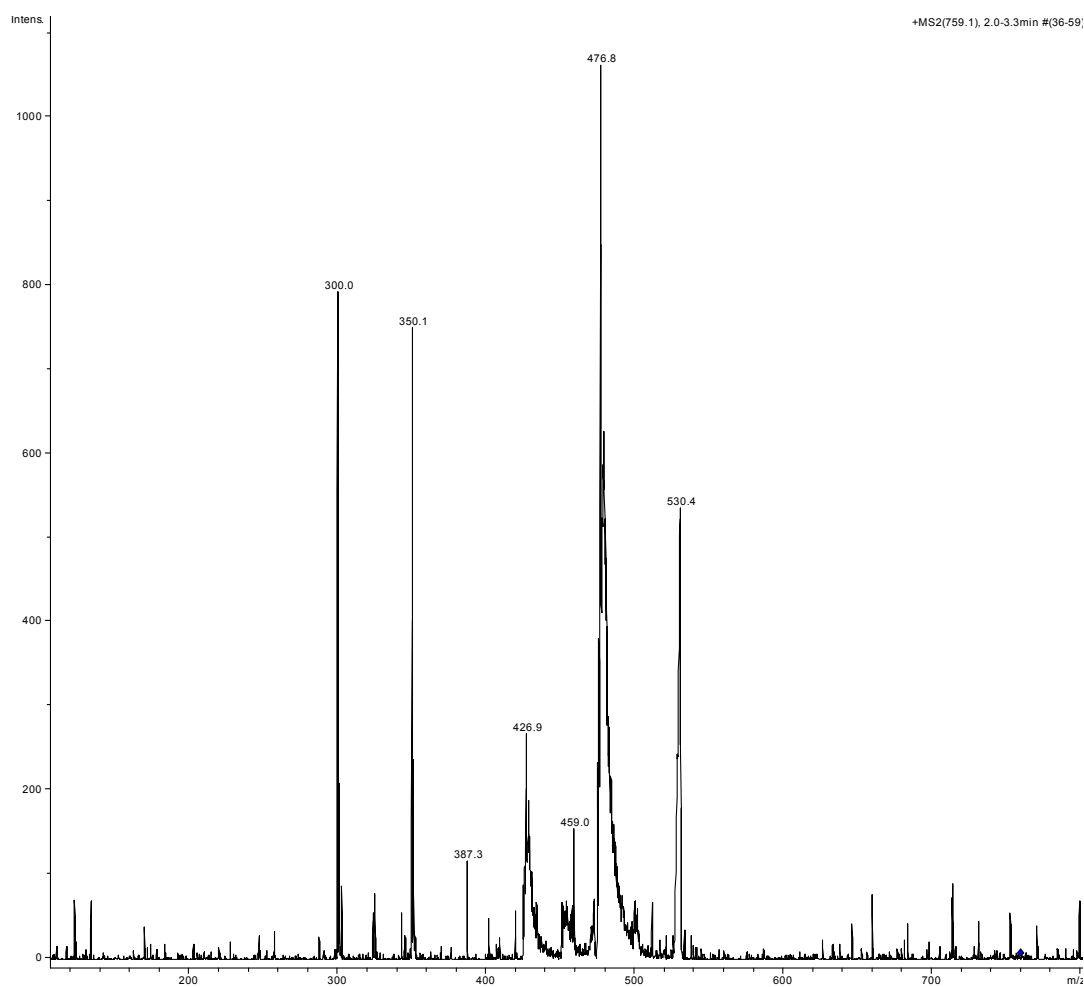
C_{60} , $(C_{59}N)_2$ and Ag:



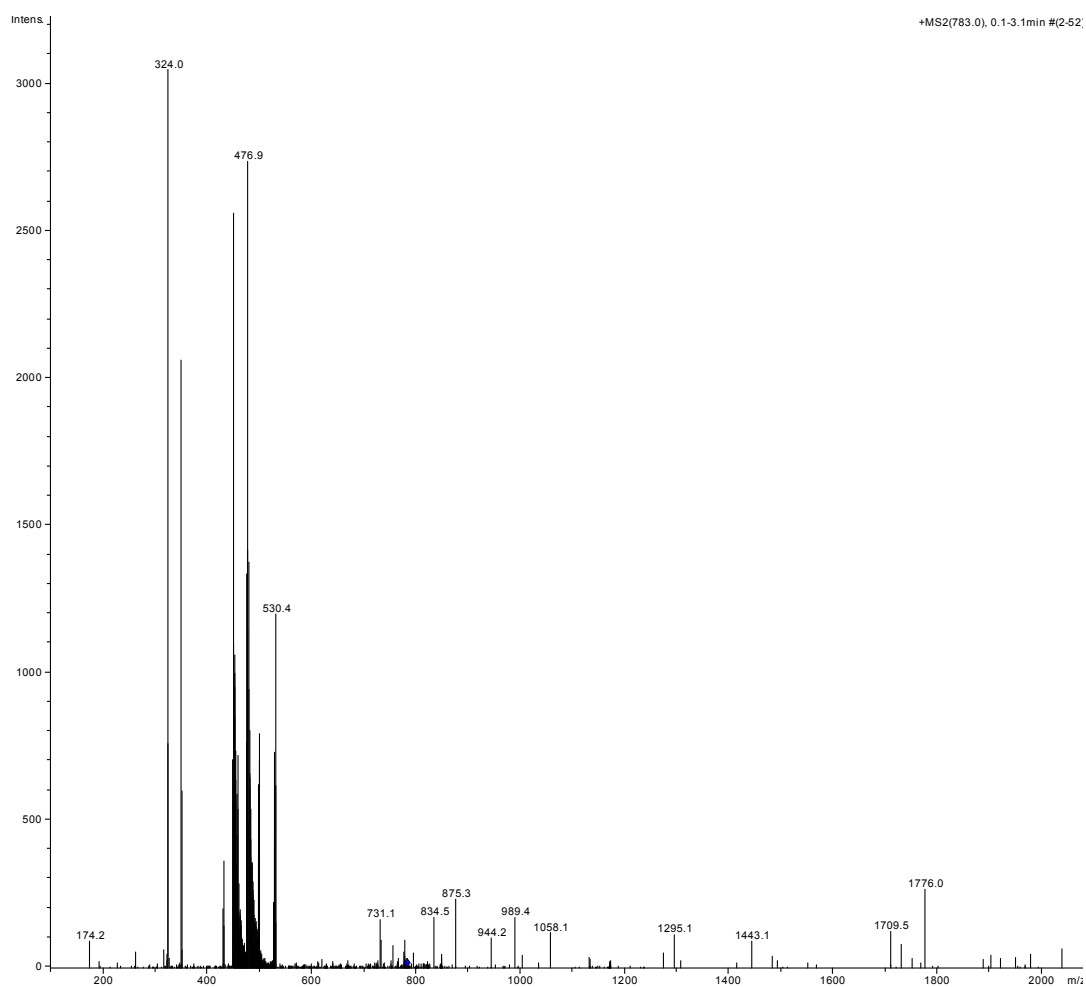
MS/MS of $[C_{60}AgC_{59}N]^+$

C_{60} , $C_{28}H_{14}$ and Ag:MS/MS of $[C_{60}AgC_{28}H_{14}]^+$

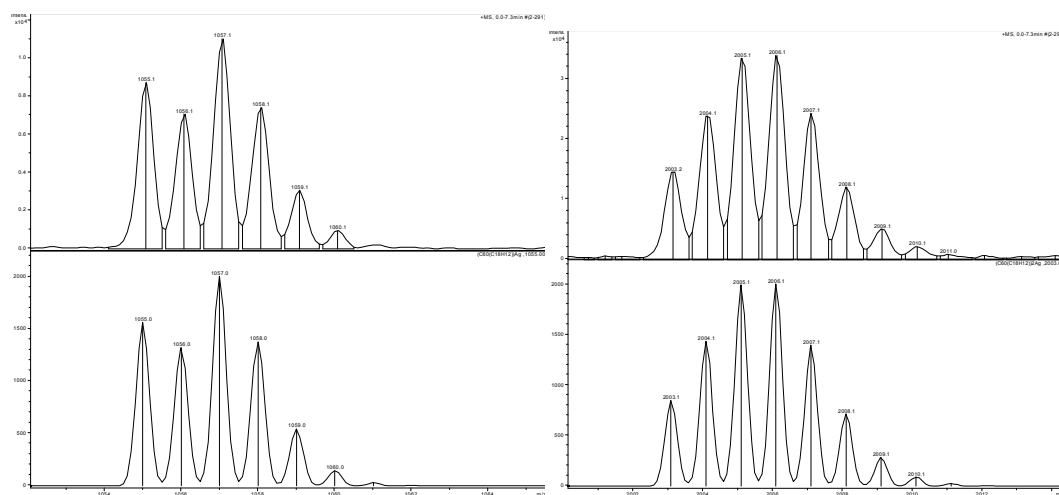
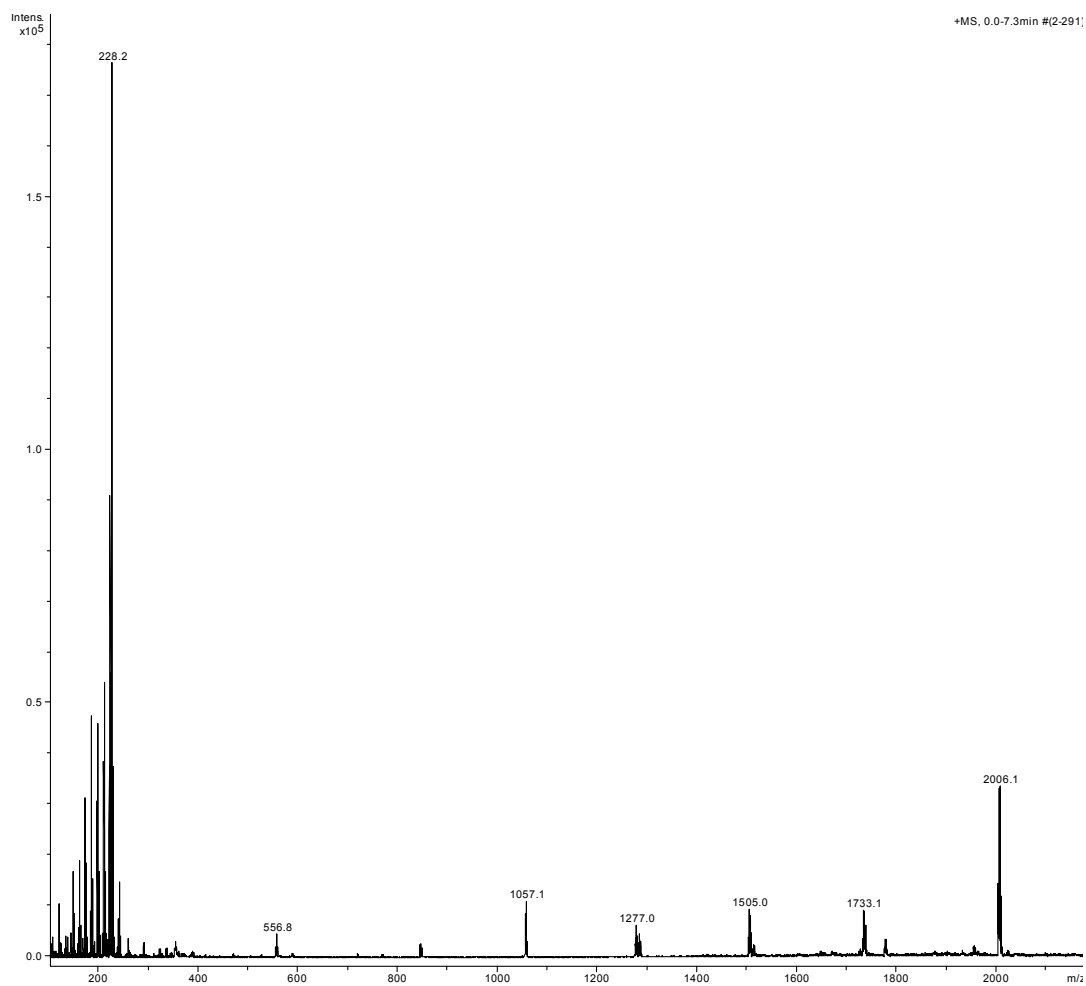
Coronene, C₂₆H₁₂ and Ag:MS/MS of [C₂₄H₁₂AgC₂₆H₁₂]⁺

Coronene, C₂₈H₁₄ and Ag:MS/MS of [C₂₄H₁₂AgC₂₈H₁₄]⁺

$C_{26}H_{12}$, $C_{28}H_{14}$ with Ag:

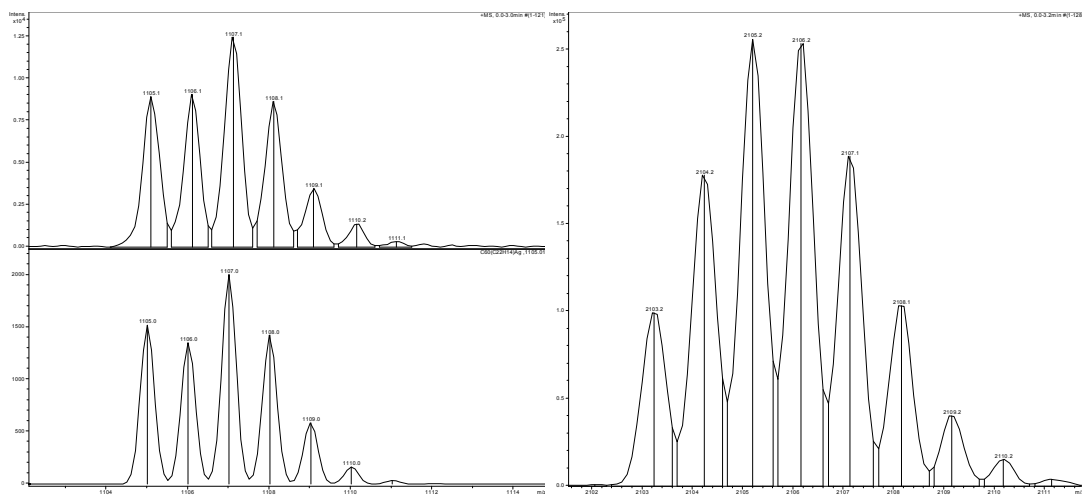
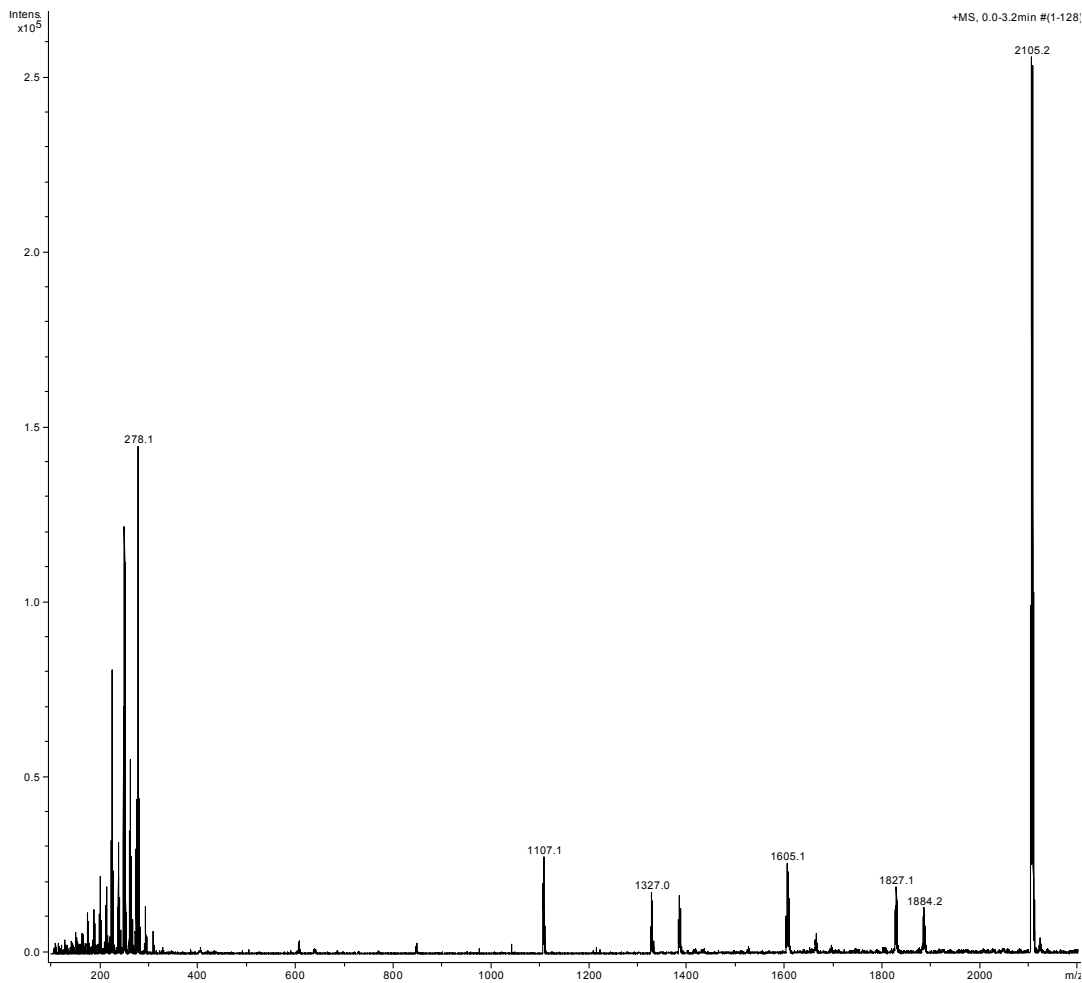


MS/MS of $[C_{26}H_{12}AgC_{28}H_{14}]^+$

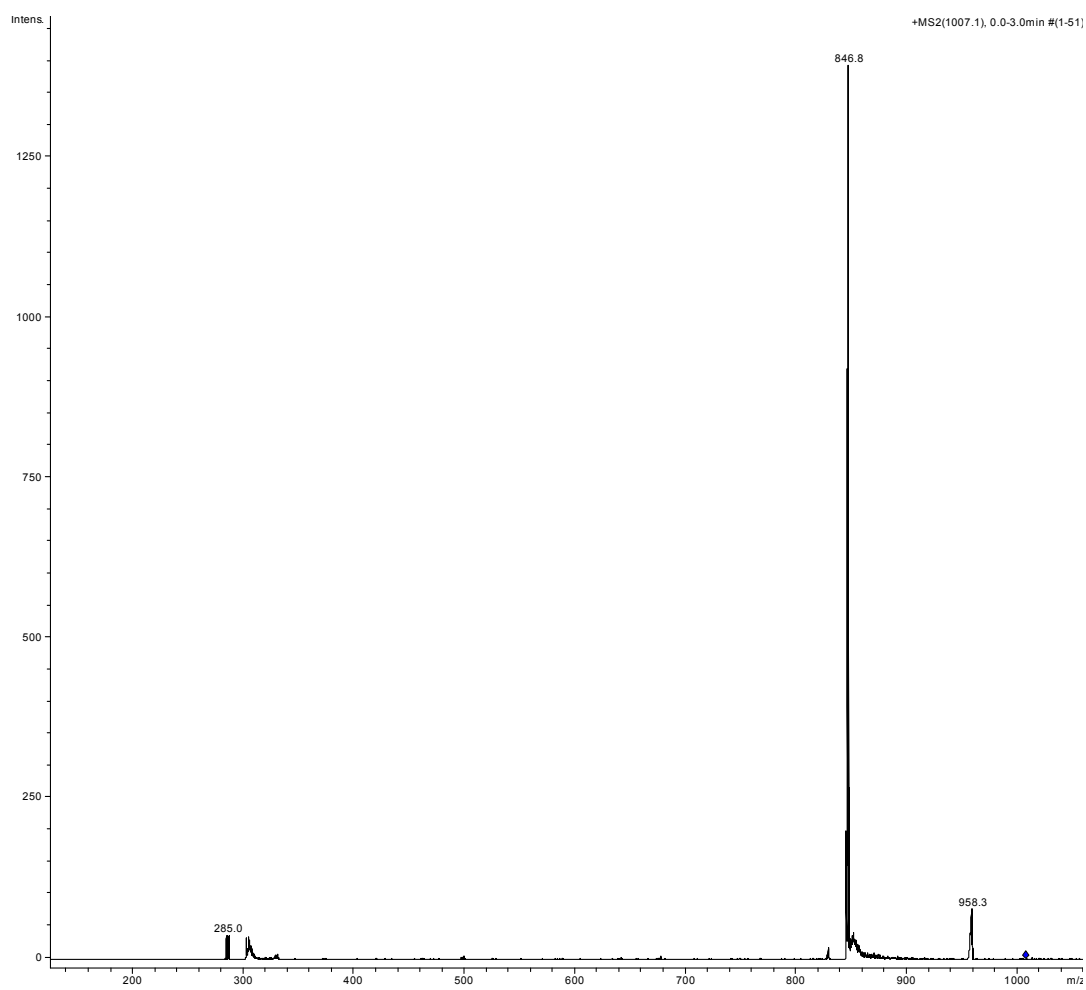
C₆₀PAH's and AgTFA positive-ion mode ESI spectraPositive-ion mode C₆₀Tetracene with AgTFA

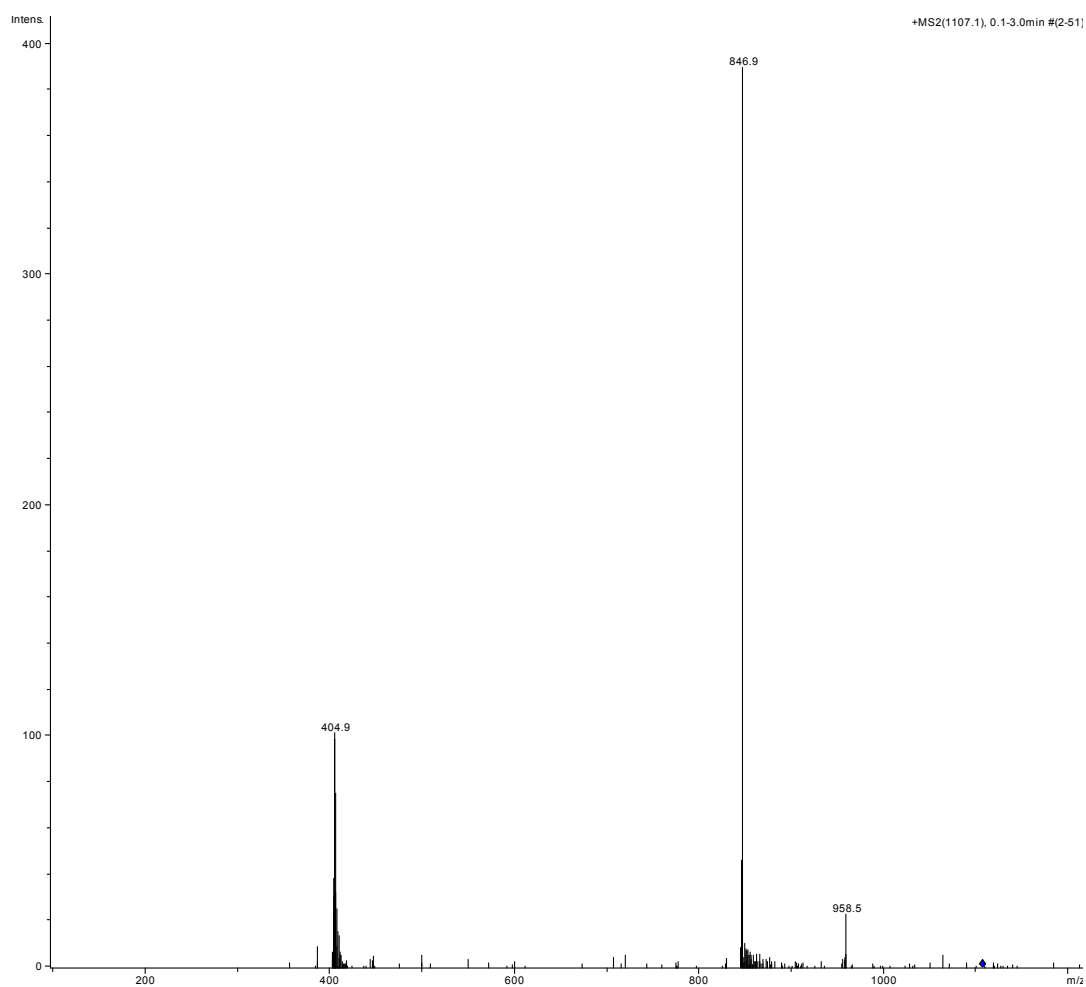
Top: full mass spectrum of C₆₀T with AgTFA, bottom left: actual and simulated mass spectrum of [C₆₀AgT]⁺, bottom right: actual and simulated mass spectrum of [(C₆₀T)₂Ag]⁺

Positive-ion mode C₆₀Pentacene with AgTFA



Top: full positive-ion mode spectrum of $C_{60}P$ with AgTFA, bottom left: actual and simulated mass spectrum of $[C_{60}AgP]^+$, bottom right: isotopic pattern of $[(C_{60}P)_2Ag]^+$

Positive-ion mode MS/MS ESI spectra of C₆₀A with AgTFAMS/MS of [C₆₀AgA]⁺

Positive-ion mode MS/MS ESI spectra of C₆₀P with AgTFAMS/MS of [C₆₀AgP]⁺